COMPUTATIONAL MODELING OF SPINTRONIC MATERIALS

EDITED BY: Xiaotian Wang, Gokhan Surucu and Zhenxiang Cheng
PUBLISHED IN: Frontiers in Materials, Frontiers in Chemistry and Frontiers in Physics

frontiers Research Topics

frontiers

ISSN 1664-8714
ISBN 978-2-88966-486-3
DOI 10.3389/978-2-88966-486-3

About Frontiers

Frontiers is more than just an open-access publisher of scholarly articles: it is a pioneering approach to the world of academia, radically improving the way scholarly research is managed. The grand vision of Frontiers is a world where all people have an equal opportunity to seek, share and generate knowledge. Frontiers provides immediate and permanent online open access to all its publications, but this alone is not enough to realize our grand goals.

Frontiers Journal Series

The Frontiers Journal Series is a multi-tier and interdisciplinary set of open-access, online journals, promising a paradigm shift from the current review, selection and dissemination processes in academic publishing. All Frontiers journals are driven by researchers for researchers; therefore, they constitute a service to the scholarly community. At the same time, the Frontiers Journal Series operates on a revolutionary invention, the tiered publishing system, initially addressing specific communities of scholars, and gradually climbing up to broader public understanding, thus serving the interests of the lay society, too.

Dedication to Quality

Each Frontiers article is a landmark of the highest quality, thanks to genuinely collaborative interactions between authors and review editors, who include some of the world's best academicians. Research must be certified by peers before entering a stream of knowledge that may eventually reach the public - and shape society; therefore, Frontiers only applies the most rigorous and unbiased reviews.
Frontiers revolutionizes research publishing by freely delivering the most outstanding research, evaluated with no bias from both the academic and social point of view. By applying the most advanced information technologies, Frontiers is catapulting scholarly publishing into a new generation.

What are Frontiers Research Topics?

Frontiers Research Topics are very popular trademarks of the Frontiers Journals Series: they are collections of at least ten articles, all centered on a particular subject. With their unique mix of varied contributions from Original Research to Review Articles, Frontiers Research Topics unify the most influential researchers, the latest key findings and historical advances in a hot research area! Find out more on how to host your own Frontiers Research Topic or contribute to one as an author by contacting the Frontiers Editorial Office: frontiersin.org/about/contact

COMPUTATIONAL MODELING OF SPINTRONIC MATERIALS

Topic Editors:
Xiaotian Wang, Southwest University, China
Gokhan Surucu, Middle East Technical University, Turkey
Zhenxiang Cheng, University of Wollongong, Australia

Citation: Wang, X., Surucu, G., Cheng, Z., eds. (2021). Computational Modeling of Spintronic Materials. Lausanne: Frontiers Media SA. doi: 10.3389/978-2-88966-486-3

Table of Contents

frontiers in Materials

EDITORIAL
published: 15 January 2021
doi: 10.3389/fmats.2020.634712

Editorial: Computational Modeling of Spintronic Materials

Xiaotian Wang[1], Zhenxiang Cheng[2] and Gokhan Surucu[3,4]**

[1]School of Physical Science and Technology, Southwest University, Chongqing, China, [2]Institute for Superconducting and Electronic Materials (ISEM), University of Wollongong, Wollongong, NSW, Australia, [3]Department of Physics, Middle East Technical University, Ankara, Turkey, [4]Department of Electric and Energy, Ahi Evran University, Kirsehir, Turkey

Keywords: first-principle calculations, density-functional theory, material simulation calculations, spintronic materials, electronic structrue

Editorial on the Research Topic

Computational Modeling of Spintronic Materials

In research topic "Computational Modeling of Spintronic Materials", we collected 17 articles dealing with themes as below:

i. Recent advances of spintronic materials;
ii. Frontiers in computational modeling of functional materials.

OPEN ACCESS

Edited by:
Roberto Brighenti, University of Parma, Italy

Reviewed by:
Xiaojun Wu, University of Science and Technology of China, China

****Correspondence:***
Xiaotian Wang
xiaotianwang@swu.edu.cn
Gokhan Surucu
g_surucu@yahoo.com

Specialty section:
This article was submitted to Computational Materials Science, a section of the journal Frontiers in Materials

Received: *28 November 2020*
Accepted: *14 December 2020*
Published: *15 January 2021*

Citation:
Wang X, Cheng Z and Surucu G (2021) Editorial: Computational Modeling of Spintronic Materials. Front. Mater. 7:634712. doi: 10.3389/fmats.2020.634712

Heulser alloys are famous spintronic materials due to they usually host high Curie temperature and adjustable structures. Zhang et al. (Zhang et al., 2020) proposed quaternary Heusler compound CoCrScSn is a half-metal with 100% spin-polarization. Moreover, the elastic constants and half-metallic states under different lattice constants are touched by Zhang et al. Classic Heusler ferromagnets consist of transition-group d-metals and main-group p-elements. As a new direction of Heusler alloy, Wu et al. (Wu et al., 2020) studied a series of all-d-metal Heusler alloys X_2MnTi (X = Pd, Pt, Ag, Au, Cu and Ni). X_2MnTi alloys are without main-group p-elements. Wu et al. also investigated the competition of the cubic $L2_1$ and tetragonal $L1_0$ states of these X_2MnTi alloys. It is hoped that the possible martensitic transformation of these all-d-metal X_2MnTi can be confirmed experimentally.

Half-metals have two spin-directions, one spin channel shows metallic property and the other one features insulating/semiconducting behaviors, resulting in 100% spin-polarization. Also, half-metals can be used for efficient spin injection in spintronics. Doumi et al. (Doumi et al., 2020) proposed that $Ca_{1-x}Cr_xO$ (x = 0.25, 0.5, 0.75) are half-metals, where the ferromagnetism is mainly coming from the direct exchange splitting instead of the crystal field. Deng et al. (Deng et al., 2020) studied the magnetic structure and the Curie temperature of LiMgN with Cu doping, they found that these Cu doped LiMgN systems are dilute magnetic semiconductors with high Curie temperature. More interestingly, $Li(Mg_{0.875}Cu_{0.125})N$ is predicted to be half-metal with a net magnetic moment. Chen et al. (Chen et al., 2020) investigated the electronic structures and magnetism of $Li_{1\pm y}(Mg_{1-x}Cr_x)P$ (x, y = 0.125). They found that Li $(Mg_{0.875}Cr_{0.125})P$ magnet is half-metal.

A series of materials co-exhibiting half-metallic state and topological elements are predicted via first-principles calculations. Chang et al. (Chang et al., 2020) proposed a rhombohedral type $GdMnO_3$ is a half-metal with multiple Dirac-like band crossing points. Li (Li, 2020) proposed $CsCrCl_3$ ferromagnet $P6_3/mmc$ structure is a hypothetical half metal and it also belongs to nodal surface materials. Jia et al. (Jia et al., 2020) reported sandwich-like hexagonal VI_3 monolayer is a half-metal with Weyl fermions. Moreover, a series of topological semimetals and topological metals are reported in the research topic collection: 1) Zhang and Wang (Zhang and Wang, 2020) found that

pure Zr is a topological material with type II nodal line and nodal surface states; 2) Li and Xia (Li and Xia, 2020) reported that cubic HfN is a topological semimetal with zero-dimensional (0-D) and one-dimensional (1-D) topological elements (TEs); 3) Li et al. (Li et al., 2020) proposed that tetragonal PtO is a topological material with nodal point and nodal line states; 4) Xu (Xu, 2020) studied the electronic structures and the topological signatures of XPt (X = Sc, Y, and La) via first-principles calculations. XPt (X = Sc, Y and La) materials are proposed to be novel systems with rich nodal line and nodal point states. Remarkably, we can observe opened and closed nodal lines, and triply degenerate and Dirac nodal points in these systems; 5) Xu et al. (Xu et al., 2020) predicted that hexagonal Zr_3X (X = Al, Ga, In) are metallic systems with high stability and perfect 0-D and 1-D TEs.

Some functional materials and their related physics behaviors are also investigated by first-principles calculations: 1) Ke et al. (Ke et al., 2020) performed a band-gap engineering work to study the band structures and band-gap tailoring of C-mono-doped, C-Ge, and C-Sn co-doped GaN nanosheets; 2) Y_2O_3:Ce magnetic semiconductor with R-3 group symmetry was identified by Ju et al. (Ju et al., 2020) via CALYPSO, and the structural behaviors, doping site locations as well as electronic structures of Y_2O_3:Ce are also studied by Ju et al. via first-principles calculations in details; 3) Yan et al. (Yan et al., 2020) investigated the reaction pathways of H_2 release from the hydrolytic NH_3BH_3 and examined the catalytic roles of small NiCu clusters; 4) Chen et al. (Chen et al., 2020) built an ultrathin van der Waals Fe_3GeTe_2/In_2Se_3 heterostructure and they reported that this heterostructure hosts tunable magnetic anisotropy and Dzyaloshinskii-Moriya Interaction (DMI).

We hope this research topic will attract readers. And we would like to thank all the authors, reviewers and editors who contributed to our research topic.

AUTHOR CONTRIBUTIONS

All authors listed have made a substantial, direct, and intellectual contribution to the work and approved it for publication.

FUNDING

This study has been funded by the National Natural Science Foundation of China (Grant No. 51801163), and the Fundamental Research Funds for the Central Universities (Grant No. XDJK 2019C112).

Conflict of Interest: The authors declare that the research was conducted in the absence of any commercial or financial relationships that could be construed as a potential conflict of interest.

frontiers in Chemistry

ORIGINAL RESEARCH
published: 28 April 2020
doi: 10.3389/fchem.2020.00338

The Microstructure and Electronic Properties of Yttrium Oxide Doped With Cerium: A Theoretical Insight

Meng Ju[1,2], Jingjing Wang[2], Jing Huang[1], Chuanzhao Zhang[3]*, Yuanyuan Jin[3], Weiguo Sun[4], Shichang Li[5] and Yunhong Chen[2]*

[1] School of Physical Science and Technology, Southwest University, Chongqing, China, [2] College of Computer and Information Engineering, Hubei Normal University, Huangshi, China, [3] Department of Physics and Optoelectronic Engineering, Yangtze University, Jingzhou, China, [4] Centre for Science at Extreme Conditions and School of Physics and Astronomy, Scottish Universities Physics Alliance (SUPA), University of Edinburgh, Edinburgh, United Kingdom, [5] School of Science, Chongqing University of Posts and Telecommunications, Chongqing, China

OPEN ACCESS

Edited by:
Zhenxiang Cheng,
University of Wollongong, Australia

Reviewed by:
Li Zhu,
Carnegie Institution for Science (CIS), United States
Hui Li,
Temple University, United States

***Correspondence:**
Jingjing Wang
scu_wjj@163.com
Chuanzhao Zhang
zcz19870517@163.com

Specialty section:
This article was submitted to Theoretical and Computational Chemistry, a section of the journal Frontiers in Chemistry

Received: *05 March 2020*
Accepted: *01 April 2020*
Published: *28 April 2020*

Citation:
Ju M, Wang J, Huang J, Zhang C, Jin Y, Sun W, Li S and Chen Y (2020) The Microstructure and Electronic Properties of Yttrium Oxide Doped With Cerium: A Theoretical Insight. Front. Chem. 8:338. doi: 10.3389/fchem.2020.00338

Trivalent Cerium (Ce^{3+}) doped Yttrium Oxide (Y_2O_3) host crystal has drawn considerable interest due to its popular optical 5d-4f transition. The outstanding optical properties of Y_2O_3:Ce system have been demonstrated by previous studies but the microstructures still remain unclear. The lacks of Y_2O_3:Ce microstructures could constitute a problem to further exploit its potential applications. In this sense, we have comprehensively investigated the structural evolutions of Y_2O_3:Ce crystals based on the CALYPSO structure search method in conjunction with density functional theory calculations. Our result uncovers a new rhombohedral phase of Y_2O_3:Ce with R-3 group symmetry. In the host crystal, the Y^{3+} ion at central site can be naturally replaced by the doped Ce^{3+}, resulting in a perfect cage-like configuration. We find an interesting phase transition that the crystallographic symmetry of Y_2O_3 changes from cubic to rhombohedral when the impurity Ce^{3+} is doped into the host crystal. With the nominal concentration of Ce^{3+} at 3.125%, many metastable structures are also identified due to the different occupying points in the host crystal. The X-ray diffraction patterns of Y_2O_3:Ce are simulated and the theoretical result is comparable to experimental data, thus demonstrating the validity of the lowest energy structure. The result of phonon dispersions shows that the ground state structure is dynamically stable. The analysis of electronic properties indicate that the Y_2O_3:Ce possesses a band gap of 4.20 eV which suggests that the incorporation of impurity Ce^{3+} ion into Y_2O_3 host crystal leads to an insulator to semiconductor transition. Meanwhile, the strong covalent bonds of O atoms in the crystal, which may greatly contribute to the stability of ground state structure, are evidenced by electron localization function. These obtained results elucidate the structural and bonding characters of Y_2O_3:Ce and could also provide useful insights for understanding the experimental phenomena.

Keywords: crystal structure prediction (CSP), electronic propercies, structural evolution, rare earth element, theoretical calculation DFT

INTRODUCTION

The rare-earth Cerium ions doped crystals constitute an attractive class of materials that have been extensively used in many kinds of fields including scintillation phosphors, laser medium, and white light emitting diode phosphors (Han et al., 2019; Lin et al., 2019; Masanori et al., 2020). The outstanding optical behaviors of trivalent Cerium ion (Ce^{3+}) has drawn considerable interest due to its popular optical 5d-4f transition. Among various host materials, Yttrium Oxide (Y_2O_3) crystal is considered to be the most promising sesquioxide host because of its unique chemical and thermal stability. The Y_2O_3 host crystal is also one of the multifunctional materials that can give rise to many application areas owing to its fabulous capacity of incorporating the activated laser ions (Ming et al., 2018; Wang et al., 2018; Ju et al., 2020). The latest study has indicated that the Ce^{3+} doped Y_2O_3 crystals (Y_2O_3:Ce) exhibit dominant emission bands at around 380 nm and relatively low intensive band at 560 nm (Gieszczyk et al., 2019). The results further demonstrate the ideal applications of energy storage phosphors for Y_2O_3:Ce. The excellent advantages of Y_2O_3:Ce can also be evidenced by the effective use as various laser ceramics (Lupei et al., 2017).

It is well-known that the laser actions can be generally identified in the absorption and emission spectra of rare-earth doped materials. In order to explore the luminescent properties of Y_2O_3:Ce, Jia et al. (2001) had synthesized the Y_2O_3:Ce nanoparticles in experiments and measured the photoluminescence spectra at room temperature. Their results revealed that the strong emissions cover the ultraviolet band from 240 nm to 380 nm. To explain the emission lines of the spectra, Loitongbam et al. (2013) measured the luminescence intensities of Y_2O_3:Ce and found that the characteristic blue color emissions at 424 and 486 nm are originated from Ce^{3+} ion 5d (spectra terms) $\rightarrow$ 4f (spectra terms). An unexpected optical activity, including up and down conversions, for Y_2O_3:Ce crystal was firstly observed by Marin et al. (2013). Although the laser actions were established by a few studies, many researchers were motivated to probe the structural properties of Y_2O_3:Ce. The effect of doping Ce^{3+} ion into Y_2O_3 fibers was investigated by Zhu et al. (2008). They found that the obvious quenching of the luminescence occurred at Ce^{3+} concentration of 5%. By using the solid-state-reactive method, Liu et al. (2020) carried out a study on the structures of a series of Ce^{3+} doped Y_2O_3 ternary ceramics. The results demonstrated that the solubility of Ce^{3+} concentration at 4% could broaden emission spectra and lead to a large red-shift, which is attractive for the white light emitting. A recent research on the structural properties of Y_2O_3:Ce was conducted by Krutikova et al. (2020). The nanopowders were obtained by laser ablation and the X-ray diffraction (XRD) patterns of Y_2O_3:Ce crystal were reported. By looking at the investigations concerning Y_2O_3:Ce in the literatures, it can be concluded that the systematic electronic structures have not yet been explored, especially for the theoretical insights. Furthermore, the lacks of Y_2O_3:Ce microstructures constitute a problem to exploit its potential prospects in many applications.

In this paper, we have performed a systematic study on the stable structures and electronic properties for Y_2O_3 doped with Ce^{3+} system. By using the CALYPSO (Crystal structure AnaLYsis by Particle Swarm Optimization) structure search method (Wang et al., 2010, 2012; Li et al., 2014) combined with first-principle calculation, the low-lying energy structures of Y_2O_3:Ce are extensively searched. A large number of candidate structures are obtained and the ground state structure together with the first four metastable structures is analyzed in detail. Based on the obtained lowest energy structure of Y_2O_3:Ce, we thoroughly conduct a calculation of the electronic properties, which could provide powerful guidance for further experimental and theoretical studies.

COMPUTATIONAL DETAILS

We have carried out an unbiased structure search for Y_2O_3 doped with Ce^{3+} system based on the CALYPSO method (Wang et al., 2010, 2012; Li et al., 2014). The CALYPSO is able to successfully predict the stable structures only with given chemical composition of the system (Lu et al., 2013, 2017, 2018; Lu and Chen, 2018). The detailed method of CALYPSO has been reported in many papers (Ju et al., 2016, 2017, 2019a,b). In this work, the structure searches are performed for Y_2O_3 doped with Ce system at 80 atoms in one unit cell. The obtained low-lying energy structures are used to perform further geometric optimizations. We conduct the *ab initio* structural relaxations and electronic properties calculations in the framework of density functional theory (DFT) by using the local density approximation (LDA) exchange correlation functional, as implemented in the Vienna Ab Initio Simulation Package (VASP) (Kresse and Hafner, 1993; Kresse and Furthmuller, 1996; Perdew et al., 1996). Considering the strong f-electrons correlations within the heavy Ce^{3+} ion, an onsite Coulomb repulsion $U = 5.0$ eV is employed in the calculations (Herbst and Waston, 1978). We use the projector-augmented wave method to simulate the valence electron space of Ce, Y, and O atoms. The used electrons are $4f^15s^25p^65d^16s^2$, $4s^24p^64d^15s^2$, and $2s^22p^4$, respectively. Sufficiently fine Monkhorst-Pack k meshes and 500 eV cutoff energy have been chosen to make sure that the calculated enthalpy of each atom is <1 meV. By using a super cell approach, the phonon dispersion spectra are calculated in PHONOPY code (Atsushi et al., 1993). The electron localization function (ELF) (Becke and Edgecombe, 1990; Savin et al., 1992) analysis of Y_2O_3:Ce is performed and the results are depicted in the VESTA software (Momma and Izumi, 2011). The projected Crystal Orbital Hamilton Population (COHP) (Richard and Peter, 1993) are calculated by the LOBSTER code (Volker et al., 2011; Stefan et al., 2016).

RESULTS AND DISCUSSIONS

Crystal Structures

The stable structures for Y_2O_3:Ce system are favorably identified by using the method described in section Computational Details. On the basis of total energies from low to high, we have plotted the lowest-energy structure of Y_2O_3:Ce in **Figure 1**, together with the local $[CeO_6]^{9-}$ complex ligand. Noticeably, the ground

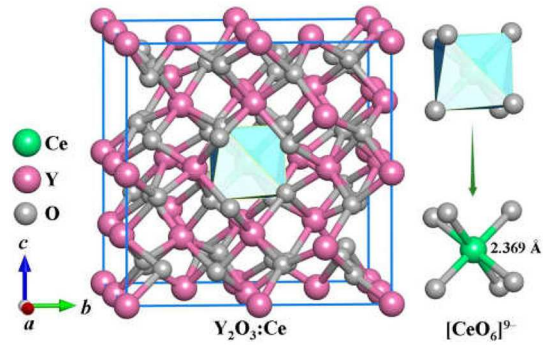

FIGURE 1 | The ground state structure of Y_2O_3:Ce.

TABLE 1 | Coordinates of all atoms for the ground state Y_2O_3:Ce.

Atom	*x*	*y*	*z*	Wyckoff site symmetry
Ce	0.50000	0.50000	0.50000	1b
Y1	0.50000	0	0	3d
Y4	0	0.50000	0.50000	3e
Y5	0	0	0	1a
Y8	1.21723	−0.00048	−0.24957	6f
Y9	0.78317	−0.50109	−0.24904	6f
Y10	0.28219	0.00104	0.25009	6f
Y11	0.72090	−0.50141	0.24728	6f
O1	0.64138	−0.12945	−0.09800	6f
O2	1.14358	−0.62871	0.40217	6f
O3	0.35267	−0.63253	0.60591	6f
O4	0.85797	−0.12919	0.09753	6f
O5	0.85966	0.12874	0.40167	6f
O6	0.35814	−0.37026	−0.09599	6f
O7	1.14102	−0.37007	0.09751	6f
O8	0.64188	0.12739	0.59868	6f

state structure of Y_2O_3:Ce possesses a novel structure with R-3 (No. 148) space group. To the best of our knowledge, the rhombohedral phase of Y_2O_3:Ce crystal is uncovered for the first time. This result indicates an interesting phase transition that the crystallographic symmetry of Y_2O_3 changes from cubic (Ia-3) to rhombohedral (R-3) when the impurity Ce^{3+} is doped into the host crystal. It is clearly seen from **Figure 1** that the host Y^{3+} ion can be naturally occupied by the impurity Ce^{3+} ion. Interestingly, the Wyckoff position of Ce^{3+} is 1b (0.5, 0.5, 0.5), suggesting that the ground state Y_2O_3:Ce is a standard cage-like structure. This result is different from that of Y_2O_3:Nd system (Ju et al., 2020). For reference, the coordinates of all atoms for the ground state Y_2O_3:Ce are summarized in **Table 1**. The estimated unit cell parameters and volume for Y_2O_3:Ce are a = b = c = 10.541 Å and 1171.371 Å (Han et al., 2019), respectively. These values are slightly smaller than those of pure Y_2O_3 but are comparable to the results reported by Kumar et al. (2017). As regard to the local structure, the Ce^{3+} ion is calculated to be 6-fold coordinated by O^{2-}, forming the $[CeO_6]^{9-}$ complex ligand. The cationic site symmetry of Ce^{3+} is C_{3i} with six equal Ce–O bonds of 2.369 Å. This bond length is similar with that of Y–O bonds because the effective radius of Ce^{3+} (1.03 Å) is very close to Y^{3+} (0.90 Å).

In the structure prediction, we adopt the chemical composition of Ce:Y: O = 1: 31: 48 to obtain the stable structures with nominal concentration of Ce^{3+}. In this sense, the impurity Ce^{3+} in Y_2O_3 crystal is equal to 3.125 at %. Apart from the ground state structure, the CALYPSO also identifies a large number of candidate isomers that can be useful to study the structural evolution of the Y_2O_3:Ce. **Figure 2** illustrates the first four metastable structures of Y_2O_3:Ce. The isomer (a) has the same R-3 space group as the lowest energy structure while the impurity Ce^{3+} ions are likely to substitute the Y^{3+} at the lattice vertexes. The Ce^{3+} ion of isomer (a) takes the 1a (0, 0, 0) position. It is evidenced that the calculated crystal lattice parameters (10.543 Å) are nearly same as those of lowest-energy structure. The group symmetry of isomer (b) is predicted to be P1 with a triclinic phase. The Wyckoff position of Ce^{3+} is predicted to be 1a (0.25, 0.75, 0.25). Calculated result reveals that the isomer (c) exhibits a monoclinic structure which belongs to P2 symmetry. The impurity Ce^{3+} ion occupies the 1b (0, 0.47157, 05) position. For the configuration of isomer (d), it is seen that the Ce^{3+} ions appear at the center sites of bottom and top in the crystal lattice. The isomer (d) is assigned to P1 group symmetry and is 0.27 eV energetically higher than ground state structure.

Although the X-ray powder diffraction (XRD) patterns of Y_2O_3:Ce crystals have been extensively studied, there appears to be inconsistencies of the spectra (Chien and Yu, 2008; Taibeche et al., 2016; Kumar et al., 2017). In order to clarify the crystal characters of the lowest-energy structure, we simulate the XRD patterns of Y_2O_3:Ce in the 2θ range of 15–65°. The result compared with experimental data is presented in **Figure 3**. It is evident that the calculated spectrum is in perfect agreement with the values measured by Kumar et al. (2017), demonstrating the validity of the lowest energy structure as well as the accuracy of our theoretical calculations. It should be pointed out that the simulated diffraction peak at 34° is ascribed to the (400) plane direction. This is accord with the result obtained by Taibeche et al. (2016) but different from the measured value proposed by Chien and Yu (2008). For comparison, the XRD patterns of the four isomers (a), (b), (c), and (d) are also provided in **Figure 3**. Although the overall distribution of the peaks in isomers is closely similar with each other, there are minor differences in the relative intensities. To evaluate the dynamical stability of Y_2O_3:Ce, the phonon spectrum within the Brillouin zone of ground state structure are calculated. **Figure 4** illustrates the phonon dispersion curves along the high-symmetry directions including F, Γ, and Z. Clearly, the overall values in **Figure 4** are positive and no virtual frequencies are observed in the full Brillouin zone. It is concluded that the rhombohedral phase structure of Y_2O_3:Ce crystal is dynamically stable.

Electronic Properties

To further elucidate the electronic properties of Y_2O_3:Ce crystal, we have performed a series of *ab initio* calculations including the

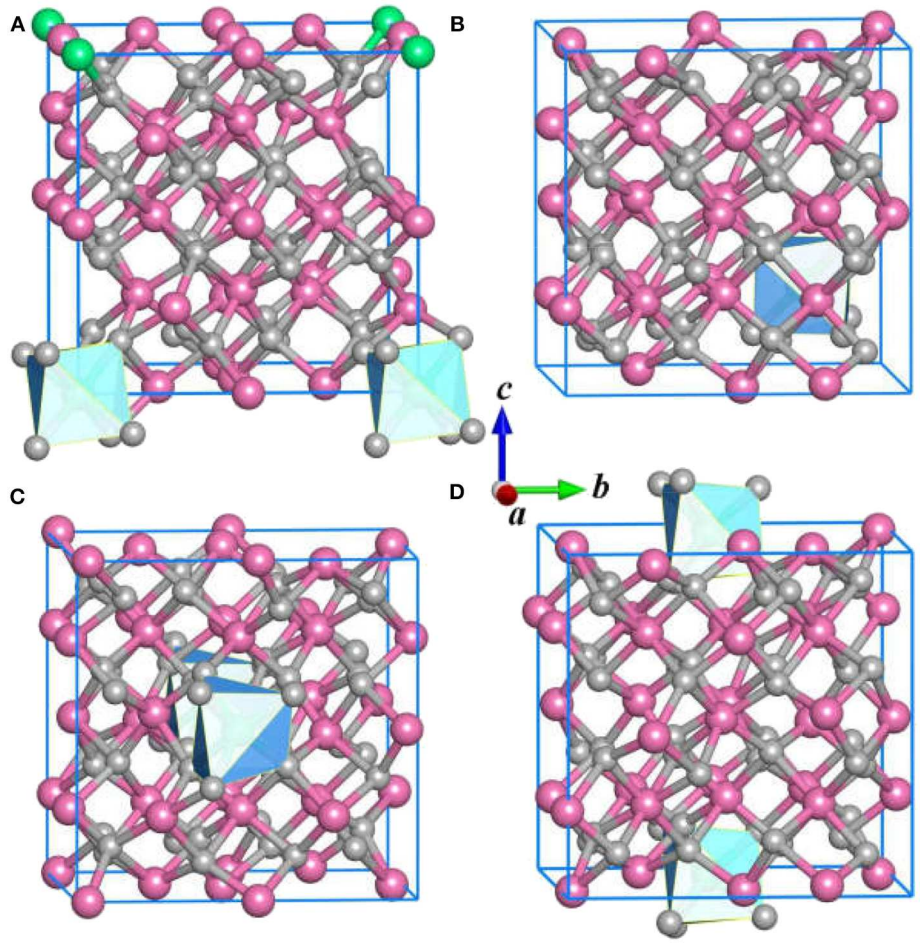

FIGURE 2 | The **(A–D)** isomers for Y_2O_3:Ce.

electronic band structures, total and partial electronic density of states and electron localization functions. The calculated band structure and density of states (DOS) are plotted together in **Figure 5**. Our calculated results show that both of the conduction band minimum and valence band maximum are identified at Γ site. The band structure is considered to be a typical of semiconductor with relatively flat top of the valence bands. According to the calculations, the band gap value of ground state Y_2O_3:Ce is equal to 4.20 eV directly at Γ point. This result is very close to the energy gap of Y_2O_3:Nd system (Ju et al., 2020) but significantly smaller than that of pure Y_2O_3 crystal (Wilk and Wallace, 2002). The direct band gap of 4.20 eV suggests a semiconductor character of the Y_2O_3:Ce. In addition to the electronic band gap, the electronic calculations of high-symmetry directions are in accordance with the above analysis based on phonon spectrum. In **Figure 5A**, we can clearly see that the band structures can be divided into three parts. The high conduction band is above 4.20 eV while the low valence band is below −0.17 eV. Interestingly, an extremely narrow valence band is observed just below the Fermi level. This result is greatly different with the band structures of pure Y_2O_3. The calculations show that the narrow valence band is caused by the electronic Alpha states. In contrast, the Beta electrons are not identified near the Fermi level. In order to explore the origins of the electronic bands, we further calculate the partial DOS including s, p, d and f states. The calculated DOS are depicted in **Figure 5B**. It can be clearly seen that the high conduction bands are mainly formed by d and p states. The p electrons are calculated to be the strongest state in the low valence bands. Moreover, the partial DOS of Y_2O_3:Ce reveals that the extremely narrow valence band near Fermi level is ascribed to the f orbital, which suggests that the impurity Ce^{3+} ion leads to a dramatic reduction of the band gap. In other words, it is concluded that the incorporation of the doped Ce^{3+} ion into Y_2O_3 host crystal results in an insulator to semiconductor transition.

To achieve foundational understanding of the bonding character and distribution of electrons of Y_2O_3:Ce crystal, we have carried out a calculation on the electron localization functions based on the ground state structure. The visually ELF of the structure and (100) plane are presented together in **Figure 6**. Obviously, the electrons near the cationic atoms are greatly localized with ELF values at ∼0.9 while the ELF values

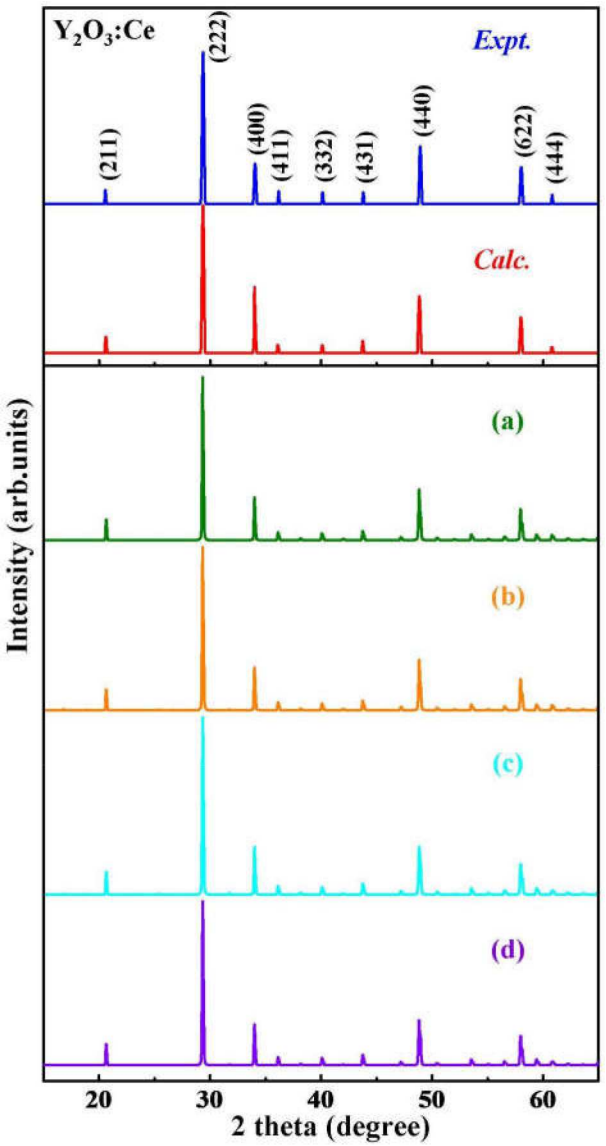

FIGURE 3 | The simulated XRD patterns for ground state Y_2O_3:Ce and isomers **(a–d)**, compared with measured spectra.

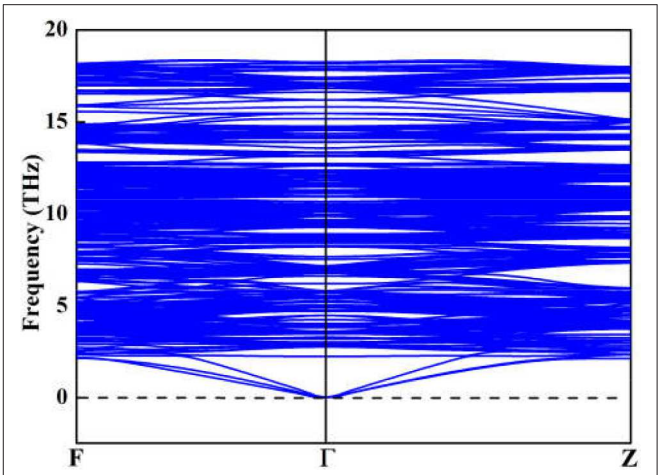

FIGURE 4 | Simulated phonon dispersions of the lowest energy structure for Y_2O_3:Ce.

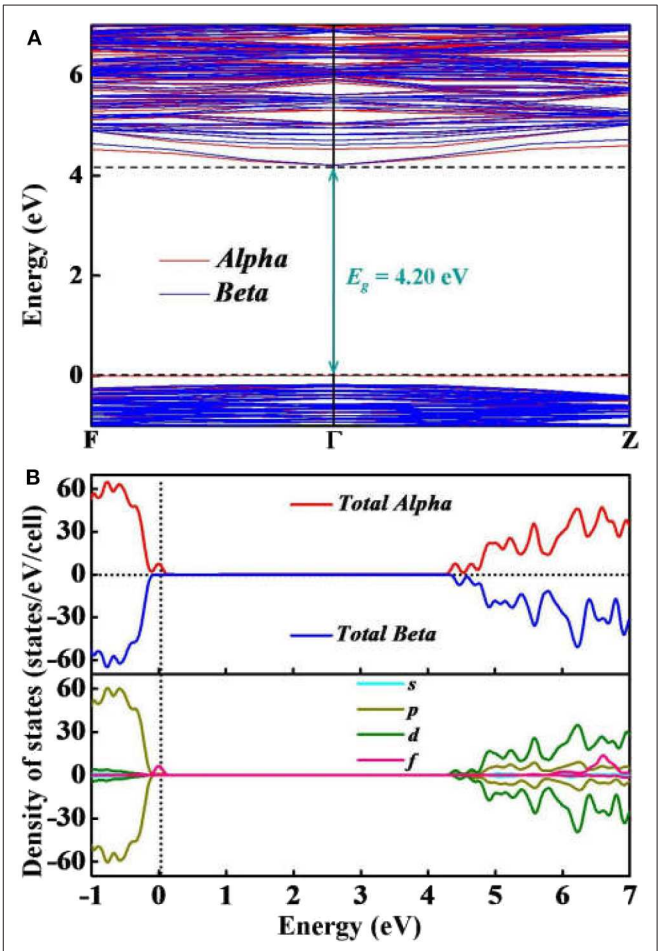

FIGURE 5 | Simulated **(A)** electronic bands and **(B)** total and partial DOS of Y_2O_3:Ce.

in the crystal lattice are nearly zero. This result indicates that the electrons localization on Ce and Y atoms broadens toward O atoms, forming a complete charge delocalization in the vicinity of O atoms. The strong ionic bonds are identified between Ce-O and Y-O. Furthermore, our calculations also show that the value of ELF at Ce atom is relatively larger than the ELF of Y atoms. This phenomenon can be explained as the remaining 4f (Masanori et al., 2020) electron of Ce^{3+} ion. It should be pointed out that there are strong charge localizations between O-O atoms, demonstrating the covalent bond of O atoms. To further quantitatively estimate the contribution of bonds between O atoms, we have presented the projected Crystal Orbital Hamilton

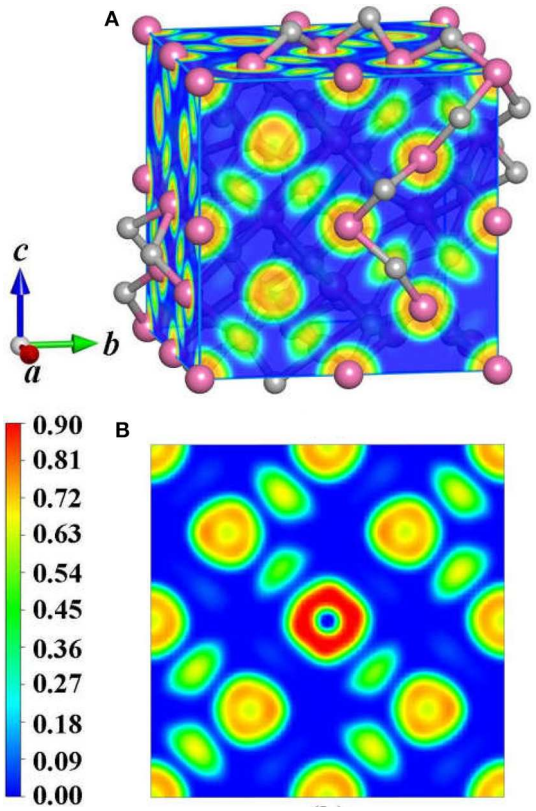

FIGURE 6 | ELF of the **(A)** structure and **(B)** <100> plane for Y_2O_3:Ce.

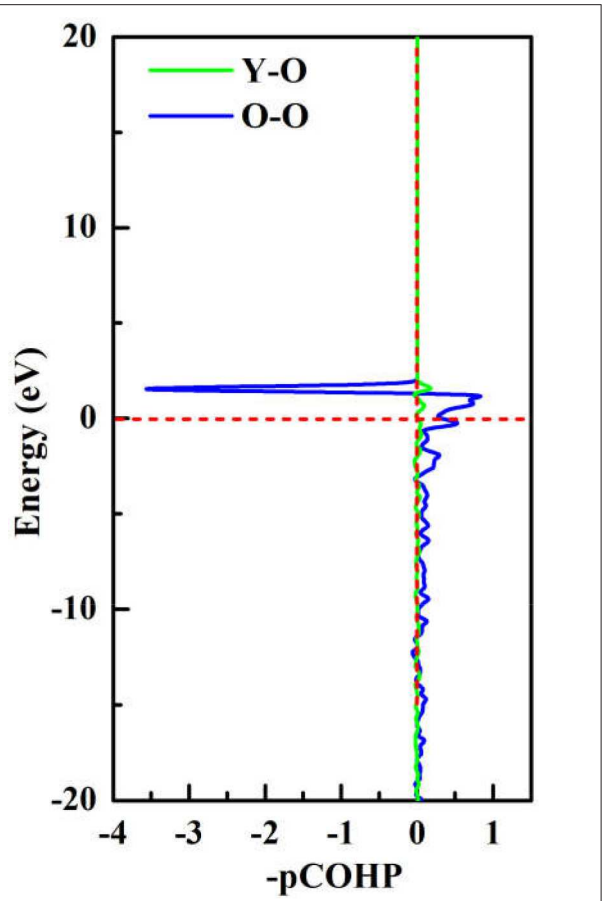

FIGURE 7 | The projected Crystal Orbital Hamilton Population (-pCOHP) curves for the O-O bonds in Y_2O_3:Ce.

Population (-pCOHP) curves for the O-O bonds in Y_2O_3:Ce. As shown in **Figure 7**, the strong bonding contributions of O-O bonds are evidenced. The bond features near the Fermi level can be ascribed to covalent. It is convinced that the excellent stability of Y_2O_3:Ce crystal is owing to the strong covalent bonds of O atoms.

CONCLUSION

To summarize, we have systematically reported the structural evolutions, doping site locations and electronic properties of Y_2O_3 crystal doped with Ce^{3+} ions. By using the CALYPSO method in conjunction with first-principles calculations, a novel stable phase with R-3 space group is identified for the first time. For the ground state structure, the doped Ce^{3+} can naturally occupy the central Y^{3+} site in the crystal lattice of Y_2O_3, forming a standard cage-like structure. The cationic site symmetry of Ce^{3+} is calculated to be C_{3i} with six equal Ce–O bonds. The first four candidate isomers present different doping sites for Ce^{3+}, which is helpful to investigate the structural evolution of Y_2O_3:Ce. By comparing the simulated XRD patterns with experimental data, we demonstrate the validity of the lowest energy structure. The dynamically stability of Y_2O_3:Ce crystal is carefully examined through the calculation of phonon dispersions. Our results of electronic band structures reveal that both of the conduction band minimum and valence band maximum are located at Γ site, leading to a band gap value of 4.20 eV. This band gap suggests a semiconductor character of Y_2O_3:Ce system. Interestingly, an extremely narrow valence band near Fermi level is observed in the band structure and the contribution of this band is assigned to f orbital. In addition, the calculated results of visually ELF show that the charge localizations between O-O atoms are dramatically strong, suggesting the covalent bond character of O atoms in the Y_2O_3:Ce crystal. These findings could provide important information of the microstructures of rare-earth doped laser materials.

DATA AVAILABILITY STATEMENT

All datasets generated for this study are included in the article/supplementary material.

AUTHOR CONTRIBUTIONS

MJ, JW, and CZ conceived the idea. MJ, JH, YJ, YC, WS, and SL performed the calculations. MJ, JH,

and WS wrote the manuscript. All authors reviewed the manuscript.

FUNDING

This work was financial supported in part by National Natural Science Foundation of China (Nos. 11904297, 11747139, and 11804031) and the Fundamental Research Funds for the Central Universities (SWU118055), the Scientific Research Project of Education Department of Hubei Province (No. Q20191301), the Open Research Projects of Wuhan Huada (No. NERCEL-OP2015001) and the Provincial Teaching Research Project in Hubei province of China (Grant No. 2017369).

REFERENCES

Atsushi, T., Fumiyasu, O., and Isao, T. (1993). First-principles calculations of the ferroelastic transition between rutile-type and $CaCl_2$-type SiO_2 at high pressures. *Phys. Rev. B* 78:134106.

Becke, A. D., and Edgecombe, K. E. (1990). A simple measure of electron localization in atomic and molecular systems. *J. Chem. Phys.* 92, 5397–5403. doi: 10.1063/1.458517

Chien, W. C., and Yu, Y. Y. (2008). Preparation of Y_2O_3:Ce^{3+} phosphors by homogeneous precipitation inside bicontinuous cubic phase. *Mater. Lett.* 62, 4217–4219. doi: 10.1016/j.matlet.2008.06.041

Gieszczyk, W., Bilski, P., Kłosowski, M., Mrozik, A., Zorenko, Yu., Zorenko, T., et al. (2019). Luminescent properties of undoped and Ce^{3+} doped crystals in Y_2O_3-Lu_2O_3-Al_2O_3 triple oxide system grown by micro-pulling-down method. *Opt. Mater.* 89, 408–413. doi: 10.1016/j.optmat.2019.01.023

Han, Z. K., Zhang, L., Liu, M., Maria, V. G. P., and Gao, Y. (2019). The structure of oxygen vacancies in the near-surface of reduced CeO_2 (111) under strain. *Front. Chem.* 7:436. doi: 10.3389/fchem.2019.00795

Herbst, J. F., and Waston, R. E. (1978). Relativistic calculations of 4f excitation energies in the rare-earth metals: further results. *Phys. Rev. B* 17, 3089–3098. doi: 10.1103/PhysRevB.17.3089

Jia, W., Wang, Y., Fernandez, F., Wang, X., Huang, S., and Yen, W. M. (2001). Photoluminescence of Ce^{3+},Tb^{3+}:Y_2O_3 nanoclusters embedded in SiO_2 sol-gel glasses. *Mater. Sci. Eng. C* 16, 55–58. doi: 10.1016/S0928-4931(01)00298-3

Ju, M., Lu, C., Yeung, Y., Kuang, X., Wang, J., and Zhu, Y. (2016). Structural evolutions and crystal field characterizations of Tm-doped $YAlO_3$: new theoretical insights. *ACS Appl. Mater. Interfaces* 8, 30422–30429. doi: 10.1021/acsami.6b09079

Ju, M., Sun, G., Kuang, X., Lu, C., Zhu, Y., and Yeung, Y. (2017). Theoretical investigation of the electronic structure and luminescence properties for NdxY1–x$Al_3(BO_3)$4 non-linear laser crystal. *J. Mater. Chem. C* 5, 7174–7181. doi: 10.1039/C7TC01911D

Ju, M., Xiao, Y., Sun, W., Lu, C., and Yeung, Y. (2020). In-depth determination of the microstructure and energy transition mechanism for Nd^{3+}-doped yttrium oxide laser crystals. *J. Phys. Chem. C* 124, 2113–2119. doi: 10.1021/acs.jpcc.9b10482

Ju, M., Xiao, Y., Zhong, M., Sun, W., Xia, X., Yeung, Y., et al. (2019b). New theoretical insights into the crystal-field splitting and transition mechanism for Nd^{3+}-doped $Y_3Al_5O_{12}$. *ACS Appl. Mater. Interfaces* 11, 10745–10750. doi: 10.1021/acsami.9b00973

Ju, M., Zhong, M., Lu, C., and Yeung, Y. (2019a). Deciphering the microstructure and energy-level splitting of Tm^{3+}-doped yttrium aluminum garnet. *Inorg. Chem.* 58, 1058–1066. doi: 10.1021/acs.inorgchem.8b02009

Kresse, G., and Furthmuller, J. (1996). Efficient iterative schemes for ab initio totalenergy calculations using a plane-wave basis set. *Phys. Rev. B* 54, 11169–11186. doi: 10.1103/PhysRevB.54.11169

Kresse, G., and Hafner, J. (1993). Ab initio molecular dynamics for liquid metals. *Phys. Rev. B* 47, 558–561. doi: 10.1103/PhysRevB.47.558

Krutikova, I., Ivanov, M., Murzakaev, A., and Nefedova, K. (2020). Laser-synthesized Ce^{3+} and Pr^{3+} doped Y_2O_3 nanoparticles and their characteristics. *Mater. Lett.* 265:127435. doi: 10.1016/j.matlet.2020.127435

Kumar, P., Nagpal, K., and Gupta, B. K. (2017). Unclonable security codes designed from multicolour luminescent lanthanide doped Y_2O_3 nanorods for anti-counterfeiting. *ACS Appl. Mater. Interfaces* 9, 14301–14308. doi: 10.1021/acsami.7b03353

Li, L., Hao, J., Liu, H., Li, Y., and Ma, Y. (2014). The metallization and superconductivity of dense hydrogen sulfide. *J. Chem. Phys.* 140:174712. doi: 10.1063/1.4874158

Lin, Y. C., Bettinelli, M., and Karlsson, M. (2019). Unraveling the mechanisms of thermal quenching of luminescence in Ce^{3+}−doped garnet phosphors. *Chem. Mater.* 31, 3851–3862. doi: 10.1021/acs.chemmater.8b05300

Liu, Y., Hu, S., Zhang, Y., Wang, Z., Zhou, G., and Wang, S. (2020). Crystal structure evolution and luminescence property of Ce^{3+}-doped Y_2O_3-Al_2O_3-Sc_2O_3 ternary ceramics. *J. Eur. Ceram. Soc.* 40, 840–846. doi: 10.1016/j.jeurceramsoc.2019.10.022

Loitongbam, R. S., Singh, W. R., Phaomei, G., and Singh, N. S. (2013). Blue and green emission from Ce^{3+} and Tb^{3+} co-doped Y_2O_3 nanoparticles. *J. Lumin.* 140, 95–102. doi: 10.1016/j.jlumin.2013.02.049

Lu, C., Amsler, M., and Chen, C. (2018). Unraveling the structure and bonding evolution of the newly discovered iron oxide FeO_2. *Phys. Rev. B* 98:054102. doi: 10.1103/PhysRevB.98.054102

Lu, C., and Chen, C. (2018). High-Pressure evolution of crystal bonding structures and properties of FeOOH. *J. Phys. Chem. Lett.* 9, 2181–2185. doi: 10.1021/acs.jpclett.8b00947

Lu, C., Li, Q., Ma, Y., and Chen, C. (2017). Extraordinary indentation strain stiffening produces superhard tungsten nitrides. *Phys. Rev. Lett.* 119:11550. doi: 10.1103/PhysRevLett.119.115503

Lu, C., Miao, M., and Ma, Y. (2013). Structural evolution of carbon dioxide under high pressure. *J. Am. Chem. Soc.* 135, 14167–14171. doi: 10.1021/ja404854x

Lupei, A., Lupei, V., and Hau, S. (2017). Vibronics in optical spectra of Yb^{3+} and Ce^{3+} in YAG and Y_2O_3 ceramics. *Opt. Mater.* 63, 143–152. doi: 10.1016/j.optmat.2016.06.024

Marin, R., Back, M., Mazzucco, N., Enrichi, F., Frattini, R., Benedetti, A., et al. (2013). Unexpected optical activity of cerium in Y_2O_3:Ce^{3+},Yb^{3+}, Er^{3+} up and down-conversion system. *Dalton Trans.* 42, 16837–16845. doi: 10.1039/C3DT51297E

Masanori, N., Akira, M., Daisuke, U., Yuki, M., Yosuke, G., Yoshikazu, M., et al. (2020). Flux growth and superconducting properties of (Ce,Pr)$OBiS_2$ single crystals. *Front. Chem.* 8:44. doi: 10.3389/fchem.2020.00044

Ming, C., Pei, M., Ren, X., Xie, N., Cai, Y., Qin, Y., et al. (2018). Improving luminescent penetrability by Tm^{3+}/Ce^{3+} doped Y_2O_3 nanocrystals for optical imaging. *Mater. Lett.* 218, 154–156. doi: 10.1016/j.matlet.2018.01.169

Momma, K., and Izumi, F. (2011). VESTA 3 for three-dimensional visualization of crystal, volumetric and morphology data. *J. Appl. Crystallogr.* 44, 1272–1276. doi: 10.1107/S0021889811038970

Perdew, J. P., Burke, K., and Ernzerhof, M. (1996). Generalized gradient approximation made simple. *Phys. Rev. Lett.* 77, 3865–3868. doi: 10.1103/PhysRevLett.77.3865

Richard, D., and Peter, E. B. (1993). Crystal Orbital Hamilton Populations (COHP). Energy-resolved visualization of chemical bonding in solids based on density-functional calculations. *J. Phys. Chem.* 97, 8617–8624. doi: 10.1021/j100135a014

Savin, A., Jepsen, O., Flad, J., Andersen, O. K., Preuss, H., and von Schnering, H. G. (1992). Electron localization in solid-state structures of the elements: the diamond structure. *Angew. Chem. Int. Ed. Engl.* 31, 187–188. doi: 10.1002/anie.199201871

Stefan, M., Volker, L. D., Andrei, L. T., and Richard, D. (2016). LOBSTER: a tool to extract chemical bonding from plane-wave based DFT. *J. Comput. Chem.* 37, 1030–1035. doi: 10.1002/jcc.24300

Taibeche, M., Guerbous, L., Boukerika, A., Kechouane, M., Nedjar, R., and Zergoug, T. (2016). Ab-initio simulations at the atomic scale of an exceptional

experimental photoluminescence signal observed in Ce^{3+}- doped Y_2O_3 sesquioxide system. *Opt*. 127, 10561–10568. doi: 10.1016/j.ijleo.2016.08.092

Volker, L. D., Andrei, L. T., and Richard, D. (2011). Crystal Orbital Hamilton Population (COHP) analysis as projected from plane-wave basis sets. *J. Phys. Chem. A* 115, 5461–5466. doi: 10.1021/jp202489s

Wang, N., He, J., Ye, K., Song, X., and L, T. (2018). Sol-gel synthesis and enhanced 1.54 μm emission in Y_2O_3:Yb^{3+}, Er^{3+} nanophosphors co-doped with Ce^{3+} ions. *Infrared Phys. Technol*. 93, 77–80. doi: 10.1016/j.infrared.2018.07.023

Wang, Y., Lv, J., Zhu, L., and Ma, Y. (2010). Crystal structure prediction via particleswarm optimization. *Phys. Rev. B* 82:094116. doi: 10.1103/PhysRevB.82.094116

Wang, Y., Lv, J., Zhu, L., and Ma, Y. (2012). CALYPSO: a method for crystal structure prediction. *Comput. Phys. Commun*. 183, 2063–2070. doi: 10.1016/j.cpc.2012.05.008

Wilk, G., and Wallace, R. M. (2002). Alternative gate dielectrics for microelectronics. *Mater. Res. Soc. Bull*. 27:3. doi: 10.1557/mrs2002.70

Zhu, L., Wang, X., Yu, G., Hou, X., Zhang, G., Sun, J., et al. (2008). Effect of Ce^{3+} doping and calcination on the photoluminescence of ZrO_2 (3% Y_2O_3) fibers. *Mater. Res. Bull*. 43, 1032–1037. doi: 10.1016/j.materresbull.2007.04.025

Conflict of Interest: The authors declare that the research was conducted in the absence of any commercial or financial relationships that could be construed as a potential conflict of interest.

frontiers in Materials

ORIGINAL RESEARCH
published: 16 June 2020
doi: 10.3389/fmats.2020.00124

Tailoring the Band Gap in Codoped GaN Nanosheet From First Principle Calculations

Changjiao Ke[1], *Chunling Tian*[1]* *and Yundan Gan*[2]

[1] School of Physical Science and Technology, Southwest University, Chongqing, China, [2] Xi'an Modern Chemistry Research Institute, Xi'an, China

To develop an efficient photocatalyst with intense visible light absorption and high charge mobility is important but still remains a problem. In this work, we have explored the electronic properties of C-monodoped, C-Ge, and C-Sn codoped GaN nanosheets by the hybrid density functional theory in order to find the excellent photocatalytic materials. Results indicate the monodoping of C introduces unoccupied impurity states inside the band gap that serve on recombination centers. Thus, the C monodoping is not suitable to ameliorate visible light absorption. Moreover, the C-Ge and C-Sn codoping not only successfully reduce the band gap of nanosheet GaN but also avoid the unoccupied impurity states. The charge-compensated C-Ge and C-Sn codoped GaN nanosheets are energetically favorable for hydrogen evolution but not insufficient to produce oxygen, indicating that they could serve as Z-scheme photocatalysts. In particular, the minimum defect formation energy of C-Ge is negative and lowest. The C-Ge codoped GaN system has dynamic stability. So, the C-Ge codoped nanosheet GaN is one of the most prospective candidates for the decomposition of hydrogen from water.

Keywords: photocatalysis, hybrid density functional, doped, band structural calculation, GaN nanosheet

OPEN ACCESS

Edited by:
Zhenxiang Cheng,
University of Wollongong, Australia

Reviewed by:
Guangzhao Wang,
Yangtze Normal University, China
Shakeel Ahmad Khandy,
National Taiwan University, Taiwan

***Correspondence:**
Chunling Tian
tclswn@163.com

Specialty section:
This article was submitted to Computational Materials Science, a section of the journal Frontiers in Materials

Received: *08 February 2020*
Accepted: *17 April 2020*
Published: *16 June 2020*

Citation:
Ke C, Tian C and Gan Y (2020) Tailoring the Band Gap in Codoped GaN Nanosheet From First Principle Calculations. Front. Mater. 7:124. doi: 10.3389/fmats.2020.00124

1. INTRODUCTION

Gallium nitride (GaN) has attracted considerable interest in recent years for its excellent photoelectric properties. With a large band gap (3.04 eV) (Bastos et al., 2018), GaN is widely used as short-wavelength light-emitting diodes (Ha et al., 2007) and room-temperature laser diodes (Feng et al., 2017). The conduction band edge of bulk GaN is at 0.5 eV higher than the redox potential of H^+/H_2, which implies that the GaN can decompose hydrogen from water (Maeda et al., 2005; Kida et al., 2006). Its wide band gap, however, makes GaN photochemically active only under UV light irradiation. In order to extend the visible light response of GaN, some efforts have been made based on band gap engineering strategies. It was found that Cr-O codoping significantly narrows the band gap of GaN, but this leads to an intermediate band entering the band gap (Pan et al., 2010), which increases the probability of carrier capture. Similar results were obtained for V-O codoped GaN (Meng et al., 2012).

According to the recent theoretical calculations (Freeman et al., 2006), the monolayer GaN has a honeycomb structure similar to that of graphene (Castro Neto et al., 2009), and boron nitride nanosheets (Golberg et al., 2010). These two-dimensional (2D) atomic-layer nanomaterials are interesting topics for their picturesque properties, which would have advantages over bulk structures in many cases (Onen et al., 2016). Particularly, the 2D GaN has a large specific surface area and shorter carrier migration distance etc., and it can remain in high-temperature

environments (Sun et al., 2017). The unique properties of nanosheets GaN motivate our research into whether a tunable band gap could be obtained via chemical modification. In this work, the C-monodoping and C-Ge and C-Sn codoping were used to modulate the band structure of GaN nanosheet. We focused our studies on the structure, electronic properties, and minimum defect formation energies of the doped GaN nanosheets.

2. COMPUTATIONAL METHOD

Our first-principles calculations were executed by using density functional theory (DFT) within generalized gradient approximation (GGA) (White and Bird, 1994) parameterized by Perdew, Burke, and Ernzerhof (PBE) (Ernzerhof and Scuseria, 1999), as realized in VASP code (Kresse and Furthmüller, 1996; Kresse and Joubert, 1999). Projector augmented wave (PAW) (Blöchl, 1994) potentials were employed to treat interactions between ions and valance electrons. The electron configuration of N ($2s^2p^3$), Ga ($3d^{10}4s^24p^1$), C ($2s^22p^2$), Ge ($3d^{10}4s^24p^2$), and Sn ($5s^25p^2$) were chosen to construct the potential function, respectively. All the calculations were carried out with a plan-wave cutoff energy of 550 eV. We adopted vacuum space of 20 Å along the z-direction in order to wipe out the interaction between the periodic images. All the atomic structure energy convergence tolerance for self-consistent iteration was set to 1.0×10^{-5} eV, and the convergence criteria force was set to 0.01 eVÅ^{-1}. The Brillouin zone integrations were approximated with a $9 \times 9 \times 1$ *k*-point (Monkhorst and Pack, 1976) for the GaN nanosheet structure relaxation and electronic properties calculations. The GGA-PBE algorithm will underrate the band gap value of the semiconductor. The accurate electronic structure was calculated by the Heyd-Scuseria-Ernzerhof (HSE06) (Heyd et al., 2003; Heyd and Scuseria, 2004) hybrid functional method. The HSE06 expression for the exchange-correlation energy was written a:

$$E_{XC}^{HSE} = \chi E_X^{SR}(\mu) + (1-\chi)E_X^{PBE,SR}(\mu) + E_X^{PBE,LR}(\mu) + E_C^{PBE} \quad (1)$$

The exchange-correlation energy includes the short- and long-ranged parts. Here, the SR is the short-range parts, and LR stands for the long-ranged. χ represents the mixing coefficient and is set to 0.25. μ indicates the screening parameter and is set to 0.2. In addition, the total density of states (TDOS) and the projected density of states (PDOS) are calculated by the tetrahedral method with Blöchl correction (Blöchl et al., 1994).

3. RESULTS AND DISCUSSION

3.1. Pure GaN Nanosheet

The GaN nanosheet is the (001) facet of the optimized bulk, which has a honeycomb graphite structure. This structure is shown in **Figures 1A,B**. The Ga-N bond length is 1.849 Å and is smaller than in the bulk GaN case (1.966 Å) (Sahin et al., 2009). Since the sp^2 bond is stronger than the sp^3 bond, the bond length in the GaN nanosheet becomes shorter. The **Figure 1C** displays the band structure of the GaN nanosheet with the band gap of 3.41 eV using the HSE06 functional. The VBM is located at the k point while the CBM is at the Γ point, which means that the GaN nanosheet is the indirect band gap semiconductor. According to the **Figure 1D**, the GaN nanosheet has non-magnetic semiconducting character, and the VBM and CBM are predominantly derived from N 2p, Ga 4p, and Ga 3d orbits. The hybridization between the N 2p, Ga 4p, and Ga 3d orbits are located at the bottom of the conduction band. The bond length d_{Ga-N}, lattice constant *a*, and band gaps calculated by the PBE and HSE06 functionals are given in **Table 1**. Our theoretical data have exhibited good agreement with previous studies (Maruska and Tietjen, 1969; Armstrong et al., 2005; Zeyan et al., 2008; Sahin et al., 2009; Xia et al., 2013; Bastos et al., 2018), which indicates that the calculation methods in this study are reasonable. It can be found that the PBE algorithm will underestimate the band gap of GaN nanosheet. Therefore, the HSE06 algorithm is adopted to study the electronic structures of the GGA-PBE optimized phases.

3.2. Monodoping in the GaN Nanosheet

In this section, we studied the effect of C doping on the electronic properties of the nanosheet GaN. For $GaN_{1-x}C_x$, the nanosheets (with x = 0.125) were modeled by replacing aneutral N atom (A site in **Figure 1A**) with a C atom in the 2×2×1 supercell of the GaN nanosheet. Because the charge number of the doping system is less than that of the pure system, we considered the spin-polarization effect in the calculation.

For the C modoped GaN nanosheet, the bond distance between the C atom and the nearest-neighboring Ga atom is 1.911 Å, which is close to the bond distance (1.849 Å) of Ga-N in nanosheet GaN. The minor difference may be explained by the ionic radius difference between C and N atom. The DOS and band structure of GaN nanosheets with the C doping presented in **Figures 2A,B**. For both C monodoped systems, the VBM is mainly contributed by mixing of the N 2p, C 2p, Ga 4p, and Ga 3d states, whereas the CBM is primarily contributed by the mixing of the between Ga 4p, N 2p, Ga 3d, and C 2p states. C dopant introduces the unoccupied impurity states on the spin down direction. The impurity state formed by a strong hybrid of C 2p and Ga 4p is very close to the conduction band of GaN. The generation of the impurity state may be due to the fact that the C and N are elements of the same cycle, and the p-orbital energy of C is thus higher than that of N. Electrons in the valence band can easily migrate to the conduction band through these impurity states. Although the band gaps for C doping GaN nanosheet decrease to 1.84 eV, the monodoped system has partially unoccupied impurity states at top of Fermi level. These impurity states can facilitate electron-hole recombination and have destructive influence on the photocatalytic activity. It indicates that C monodoped GaN nanosheet is not suitable for a visible light photocatalyst.

3.3. Codoping in the GaN Nanosheet

To overcome the unoccupied impurity states, the anion-cation passivated codoping was utilized to maintain the charge balance (Gai et al., 2009). In this section, we have discussed the influence of codoping C-Ge and C-Sn on the electronic properties of the supercell $2 \times 2 \times 1$ GaN nanosheet. The C atom substitutes

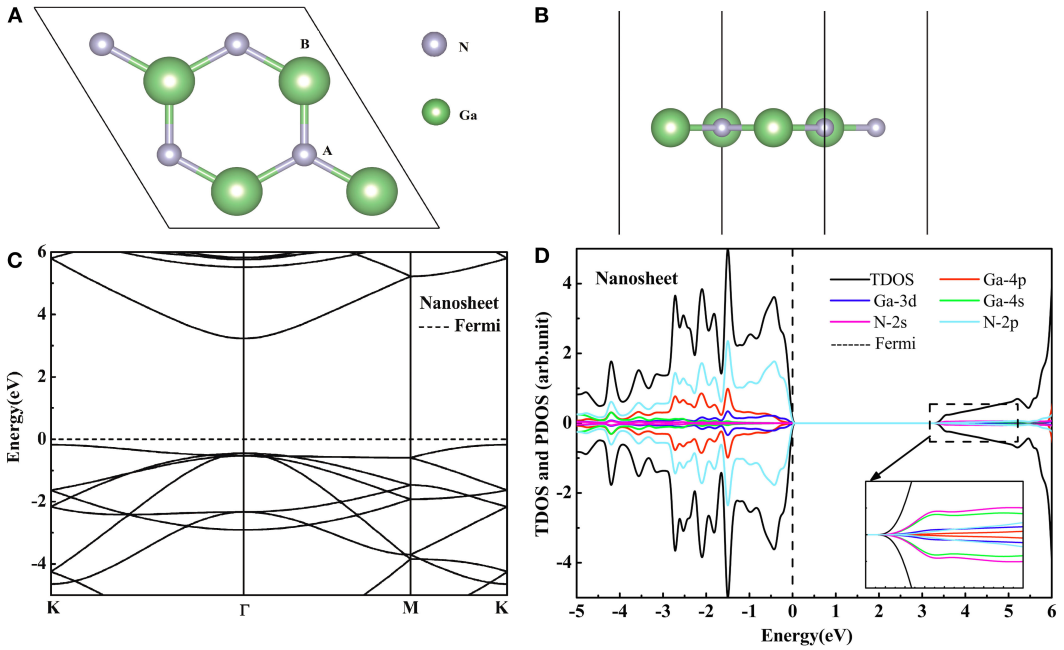

FIGURE 1 | The top **(A)** and side **(B)** views of GaN nanosheet. The HSE06 calculated band structure **(C)** and DOS **(D)** of the pure GaN nanosheet.

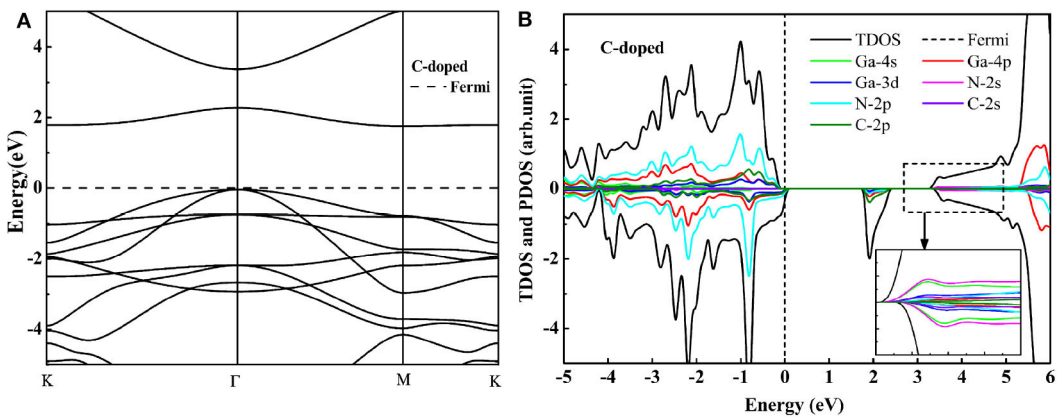

FIGURE 2 | The HSE06 calculated band structure **(A)** and DOS **(B)** of the C monodoped GaN nanosheet.

TABLE 1 | The obtained lattice constant *a*, bond length d_{Ga-N}, and band gap E_g with the PBE and HSE06 functional.

Structure		*a* (Å)	d_{Ga-N}	HSE06-E_g (eV)	PBE-E_g (eV)
Nanosheet	This work	3.202	1.849	3.41	2.44
	Other work	3.216 (Xia et al., 2013)	1.851 (Xia et al., 2013)	3.44 (Armstrong et al., 2005)	2.27 (Sahin et al., 2009)

the N atom (A site in **Figure 1A**), and the Ge (or Sn) atom substitutes the Ga atom (B site in **Figure 1A**), respectively. For C-Ge and C-Sn codoping, the N-Ge bond length is 1.829 Å, and the N-Sn bond distance is 2.00 Å, decreasing 0.02 Å, and increasing 0.151Å, respectively, with comparison with the N-Ga bond length (1.849 Å). The C-Ge bond length is 1.810 Å and the C-Sn bong length is 1.986 Å. The DOS and band structure for the C-Ge are plotted in **Figure 3**. According to the DOS, we found that the VBM is dominated by C 2p, Ga 4p, N 2p, and Ga 3d states, whereas the CBM is dominated by N 2s, Ge 4s, Ga 4s, and N 2p states. Since the band structures display that the VBM and CBM are located at the Γ point, the C-Ge system is the direct band gap semiconductor. The calculated band gap of C-Ge codoped GaN nanosheet is 1.83 eV. The

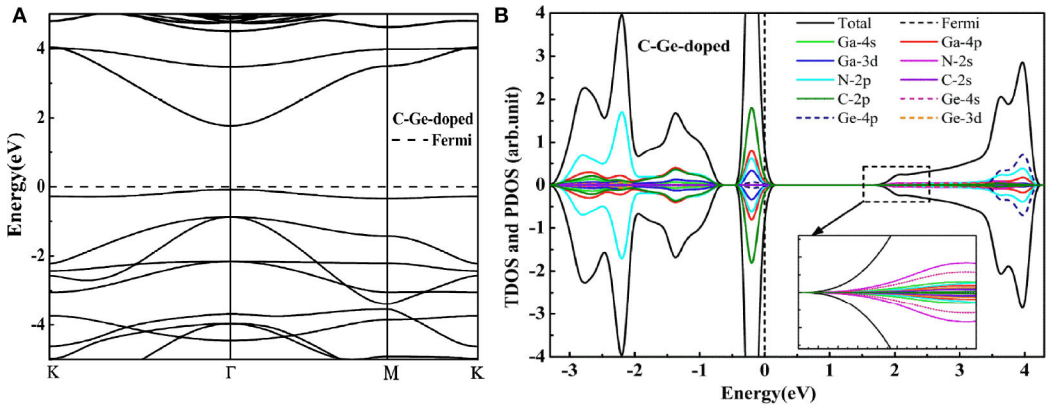

FIGURE 3 | The HSE06 calculated band structure **(A)** and DOS **(B)** of the C-Ge codoped GaN nanosheet.

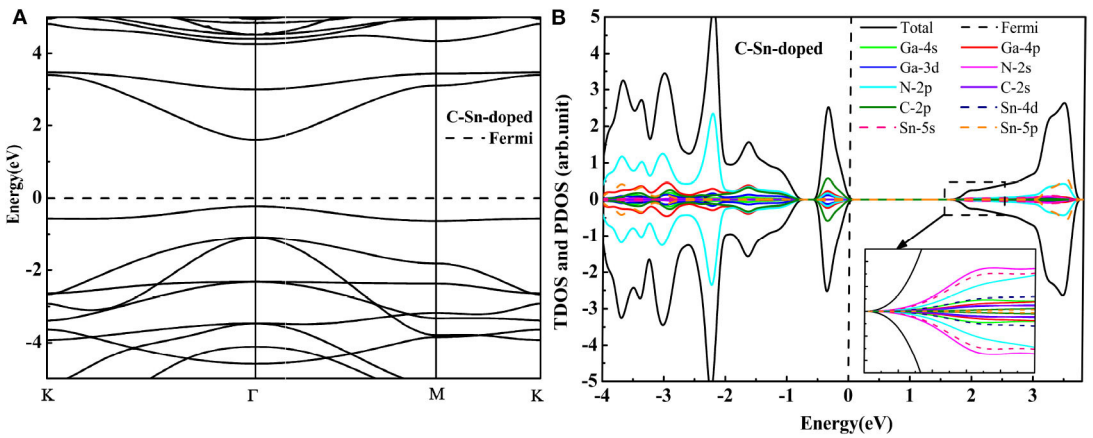

FIGURE 4 | The HSE06 calculated band structure **(A)** and DOS **(B)** of the C-Sn codoped GaN nanosheet.

DOS of C-Sn doping is plotted in **Figure 4B**. It indicates that the VBM is dominated by C 2p, Ga 4p, N 2p, and Ga 3d, whereas the CBM is dominated by Sn 5s, N 2p, Ga 4p, and Sn 4d. These configurations have strong hybridization at the top of the valence band and at the bottom the conduction band. According to **Figure 4A**, the calculated band gap of C-Sn codoped GaN nanosheet is 1.85 eV. The interesting phenomenon is that the impurity states are completely occupied for codoped GaN nanosheets.

As discussed above, those results indicate that the nanosheet GaN changes from an indirect band gap to a direct band gap by C-Ge and C-Sn codoping. The nanosheet GaN band gap decreases from 3.41 to 1.83 eV in the C-Ge codoping case and to 1.85 eV in the C-Sn codoping one. Smaller band gap values and a direct band gap are beneficial for excited state electronics, as they allow for greater ease with which to jump to the conduction band. At the same time, the smaller band gap value is favorable for moving the absorption spectrum to the visible light region. Therefore, the C-Ge and C-Sn codoped nanosheets GaN are likely to remarkable candidates for visible light photocatalyst.

3.4. Defect Formation Energy

We have calculated the defect formation energy (E_f) for evaluating the stability of doping system in each case. The defect formation energy is defined as (Van de Walle and Neugebauer, 2004; Castleton et al., 2006):

$$E_f = E(doped) - E(GaN) - \sum_i n_i \mu_i \tag{2}$$

Here, $E(doped)$ and $E(GaN)$ indicate the total energies of doped and pure nanosheet GaN, respectively. n_i represents the number of the atoms that has been added to (n_i>0) or removed from (n_i<0) the pure system for the construction doped nanosheet GaN, while μ_i is the chemical potential of the element i, and its value μ_i rests with the synthetic environment

$$\mu_{Ga} + \mu_N = \mu_{GaN(nanosheet)} \tag{3}$$

Here, $\mu_{GaN(nanosheet)}$ represents the chemical potential, which is equal to the energy of the unit cell. As the chemical potential of

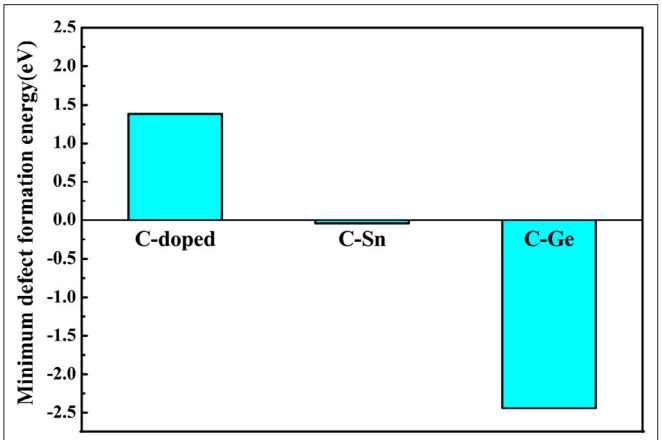

FIGURE 5 | The obtained minimum defect formation energies for monodoped and codoped GaN nanosheets.

Ga and N cannot exceed that of the Ga bulk $\mu_{Ga(bulk)}$ and N gas $\mu_{N(gas)}$, the following rules must be obeyed

$$\mu_{Ga}^{min} \leq \mu_{Ga} \leq \mu_{Ga(bulk)} \tag{4}$$

$$\mu_{N}^{min} \leq \mu_{N} \leq \mu_{N(gas)} \tag{5}$$

To form the nanosheet GaN naturally, the minima of μ_{Ga} and μ_N will satisfy

$$\mu_{Ga}^{min} = E(Ga_nN_n) - E(Ga_{n-1}N_n) \tag{6}$$

$$\mu_{N}^{min} = E(Ga_nN_n) - E(Ga_nN_{n-1}) \tag{7}$$

Here, $E(Ga_nN_n)$ is the total energy of perfect system with n primitive cells, $E(Ga_{n-1}N_n)$ the total energy with Ga defect, and $E(Ga_nN_{n-1})$ the total energy with N defect. We set the $\Delta\mu_{Ga}=\mu_{Ga} - \mu_{Ga(bulk)}$ and $\Delta\mu_N=\mu_N - \mu_{N(gas)}$. In this article, only the minimum defect formation energies of doped GaN nanosheets have been estimated; e.g., the defect formation energy take the minimum value when μ_{Ga} equals $\mu_{Ga(bulk)}$. The minimum formation energies for doping GaN nanosheets are shown in **Figure 5**, and the results are outlined in **Table 2**.

From the above discussion, we know that the minimum defect formation energy for the C monodoping is positive, which means that the C monodoping is more difficult to form because the electronegativity of C is less than that of N. The C-Ge and C-Sn codoping minimum defect formation energies are significantly lower than C monodoping. Importantly, the minimum defect formation energy of the C-Ge codoped is negative and lowest, which is greatly reduced by the opposite charge states of C-Ge atoms.

3.5. Band Edge Alignment

It is well-known that an excellent photocatalyst should not only have an appropriate band gap but also suitable band edge positions, i.e., The water reduction level and oxidation level must lie between the CBM and VBM in order to thermodynamically allow for both the hydrogen evolution reaction and oxygen evolution. On the basis of the band edge positions, some photocatalysts are suitable for only hydrogen evolution, and some photocatalysts are good for only oxygen evolution, which is called the Z-scheme photocatalysis system. Here, we have considered the situation of the standard water reduction level (−4.44 eV) and oxidation level (−5.67 eV) with respect to the vacuum level (Chakrapani et al., 2007). A large vacuum space has been used to calculate the absolute position of the band edge for quantitatively comparing with the water redox potentials. As the calculated vacuum level is a relative value, we have shifted the energy value of the CBM (VBM) for each system by subtracting this value to obtain the absolute band edge position.

TABLE 2 | The calculated band gaps (E_{gap}), minimum defect formation energies (E_f), and chemical potentials of N and Ga.

Structure	E_{gap} (eV)	E_f (eV)	$\Delta\mu_{Ga}$ (eV)	$\Delta\mu_N$ (eV)
C(x = 0.125)	1.84	1.39	−0.36	−0.36
C-Sn	1.85	0.55	−0.36	−0.36
C-Ge	1.83	−1.71	−0.36	−0.36

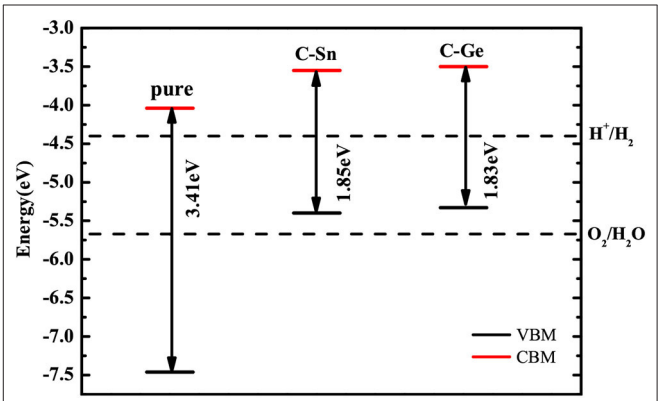

FIGURE 6 | The calculated VBM and CBM positions of pure and codoped GaN nanosheets with respect to the water redox potentials.

The calculated positions of the CBM and VBM of the pure and doped GaN nanosheets with respect to the standard hydrogen electrode potentials are indicated in **Figure 6**. Compared to the band edge potentials of pure GaN, both CB and VB edges of codoped systems are increased. The calculated CBM and VBM of C-Ge (C-Sn) codoped nanosheet are located at −3.50 eV (−3.55 eV) and −5.33 eV (−5.40 eV), respectively. The CBM of C-Ge (C-Sn) is 0.90 eV (0.85 eV) above the water reduction level, and the VBM of C-Ge (C-Sn) is 0.34 eV (0.27 eV) above the water oxidation level. Thus, the C-Sn and C-Ge codoped GaN nanosheets are energetically favorable for hydrogen evolution but not insufficient to produce oxygen, indicating that they could serve as Z-scheme photocatalysts.

3.6. Optical Properties

Optical properties play a critical role in evaluating the performance of photocatalysts in the visible light region. Thus,

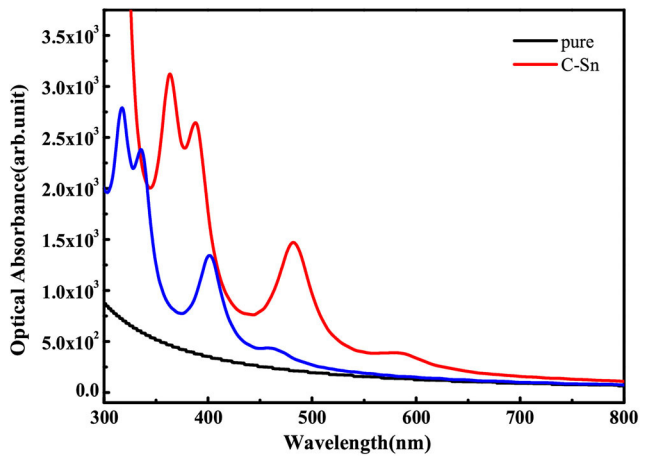

FIGURE 7 | The optical absorption spectra of pure and codoped GaN nanosheets.

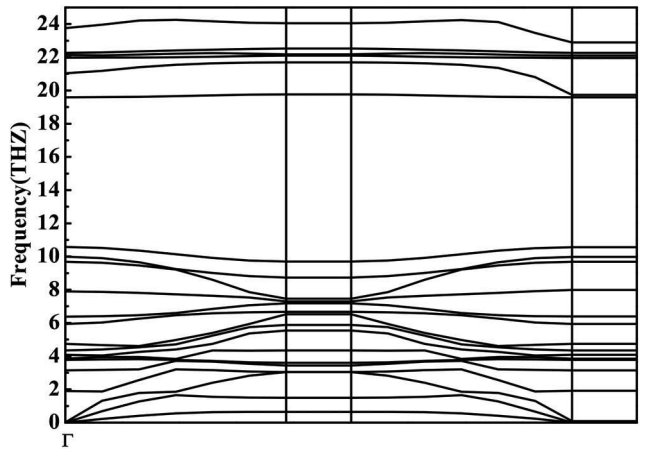

FIGURE 8 | Phonon dispersion for C-Ge codoped GaN nanosheet.

we have investigated the optical absorption spectra of the pure and codoped GaN nanosheets. The absorption coefficient $\alpha(\omega)$ satisfies the following relation (Onen et al., 2016)

$$\alpha(\omega) = \sqrt{2}\omega\sqrt{\sqrt{\varepsilon_1^2(\omega) + \varepsilon_2^2(\omega)} - \varepsilon_1(\omega)} \tag{8}$$

where $\varepsilon_1(\omega)$ is the real part that is obtained using the Kramers-Kronig transformation, and $\varepsilon_2(\omega)$ is the imaginary part, which has been calculated by summing over a large amount of empty states. **Figure 7** shows the obtained absorption coefficient of pure and codoped GaN nanosheets. It can be seen that the C-Sn and C-Ge codoped can harvest a longer wavelength of visible light spectrum compared to the pure GaN nanosheet for visible light photocatalysis, which can be attributed to the reasonable band gap reduction.

3.7. Dynamical Stability

Phonon calculations provide a criterion for the stability of one structure and indicate, through soft modes, structural instability (Ahmad Khandy et al., 2019; Xuan et al., 2019; Ahmad Khandy and Chai, 2020). We therefore calculated phonon dispersion curves for the codoped GaN nanosheet. The C-Ge codoping system was considered, as it has a negative formation energy and can be stably formed. **Figure 8** shows the phonon dispersion curves (PDCs) of C-Ge codoping system obtained using GGA scheme, which contains 24 phonon branches composed of Ga_3GeN_3C cell, including three acoustic modes and 21 optical modes. It is obvious from the figure that there is no virtual frequency in this doping system. It can therefore be concluded that the C-Ge codoped GaN system has dynamic stability.

4. CONCLUSIONS

The electronic properties of C monodoped, C-Ge, and C-Sn codoped GaN nanosheets have been investigated at the HSE06 level of theory. For C monodoping, the effective band gap values of the $GaN_{1-x}C_x$(x = 0.125) nanosheet can be decreased. However, the C monodoping will introduce the unoccupied impurity states, which leads to the decrease of carrier concentration. The band gap values for the C-Ge and C-Sn codoping GaN nanosheets are 1.83 and 1.85 eV, respectively. Narrow band gap semiconductors can absorb and utilize visible light, and semiconductors can thus be used in solar energy conversion and photocatalysis. The C-Ge and C-Sn codoping GaN nanosheets are direct band gap semiconductors, which make them more advantageous over other materials. Anionic (C) and cationic (Ge or Sn) compensated cooping, greatly reducing the minimum formation energy of doping. However, the minimum defect formation energy of the C-Ge codoping GaN nanosheet is the smallest. The C-Ge and C-Sn codoped systems may be a potential candidate for photocatalytic water splitting to generate hydrogen because of their appropriate band gap and band edge positions. More importantly, the result of the optical absorption spectral analysis shows that the C-Ge and C-Sn codoped GaN nanosheets absorb a longer wavelength of the visible light spectrum as compared to the pure GaN nanosheet. Those results imply that the C-Ge codoping GaN nanosheet could be promising candidate as a visible light photocatalyst for water splitting.

DATA AVAILABILITY STATEMENT

All datasets generated for this study are included in the article/supplementary material.

AUTHOR CONTRIBUTIONS

CK: acquisition, analysis, and interpretation of data for the work. CT: drafting the work or revising it critically for important intellectual content. All authors contributed to the article and approved the submitted version.

REFERENCES

Ahmad Khandy, S., and Chai, J.-D. (2020). Robust stability, half-metallic ferrimagnetism and thermoelectric properties of new quaternary Heusler material: a first principles approach. *J. Magn. Magn. Mater.* 502:166562. doi: 10.1016/j.jmmm.2020.166562

Ahmad Khandy, S., Islam, I., Gupta, D. C., Khenata, R., and Laref, A. (2019). Lattice dynamics, mechanical stability and electronic structure of Fe-based Heusler semiconductors. *Sci. Rep.* 9:1475. doi: 10.1038/s41598-018-37740-y

Armstrong, A., Arehart, A. R., Green, D., Mishra, U. K., and Ringel, S. A. (2005). Impact of deep levels on the electrical conductivity and luminescence of gallium nitride codoped with carbon and silicon. *J. Appl. Phys.* 98, 1145–1127. doi: 10.1063/1.2005379

Bastos, C. M. O., Sabino, F. P., Sipahi, G. M., and Da Silva, J. L. F. (2018). A comprehensive study of g-factors, elastic, structural and electronic properties of III-V semiconductors using hybrid-density functional theory. *J. Appl. Phys.* 123:065702. doi: 10.1063/1.5018325

Blöchl, P. E. (1994). Projector augmented-wave method. *Phys. Rev. B Condens. Matter* 50, 17953–17979. doi: 10.1103/PhysRevB.50.17953

Blöchl, P. E., Jepsen, O., and Andersen, O. K. (1994). Improved tetrahedron method for Brillouin-zone integrations. *Phys. Rev. B* 49, 16223–16233. doi: 10.1103/PhysRevB.49.16223

Castleton, C. W. M., Höglund, A., and Mirbt, S. (2006). Managing the supercell approximation for charged defects in semiconductors: finite-size scaling, charge correction factors, the band-gap problem, and the ab initio dielectric constant. *Phys. Rev. B* 73:035215. doi: 10.1103/PhysRevB.73.035215

Castro Neto, A. H., Guinea, F., Peres, N. M. R., Novoselov, K. S., and Geim, A. K. (2009). The electronic properties of graphene. *Rev. Mod. Phys.* 81, 109–162. doi: 10.1103/RevModPhys.81.109

Chakrapani, V., Angus, J. C., Anderson, A. B., Wolter, S. D., Stoner, B. R., and Sumanasekera, G. U. (2007). Charge transfer equilibria between diamond and an aqueous oxygen electrochemical redox couple. *Science* 318, 1424–1430. doi: 10.1126/science.1148841

Ernzerhof, M., and Scuseria, G. E. (1999). Assessment of the Perdew-Burke-Ernzerhof exchange-correlation functional. *J. Chem. Phys.* 110, 5029–5036. doi: 10.1063/1.478401

Feng, L., Zhao, D., Jiang, D., Liu, Z., Zhu, J., Ping, C., et al. (2017). Suppression of optical field leakage to GaN substrate in GaN-based green laser diode. *Superlatt. Microstruct.* 102, 484–489. doi: 10.1016/j.spmi.2017.01.012

Freeman, C. L., Claeyssens, F., Allan, N. L., Harding, J. H. (2006). Graphitic nanofilms as precursors to wurtzite films: theory. *Phys. Rev. Lett.* 96:066102. doi: 10.1103/PhysRevLett.96.066102

Gai, Y., Li, J., Li, S.-S., Xia, J.-B., and Wei, S.-H. (2009). Design of narrow-gap TiO_2: a passivated codoping approach for enhanced photoelectrochemical activity. *Phys. Rev. Lett.* 102:036402. doi: 10.1103/PhysRevLett.102.036402

Golberg, D., Bando, Y., Huang, Y., Terao, T., Mitome, M., Tang, C., et al. (2010). Boron nitride nanotubes and nanosheets. *ACS Nano* 4, 2979–2993. doi: 10.1021/nn1006495

Ha, G. Y., Park, T. Y., Kim, J. Y., Kim, D. J., Min, K. I., and Park, S. J. (2007). Improvement of reliability of GaN-based light-emitting diodes by selective wet etching with p-GaN. *IEEE Photon. Technol. Lett.* 19, 813–815. doi: 10.1109/LPT.2007.897291

Heyd, J., and Scuseria, G. E. (2004). Efficient hybrid density functional calculations in solids: assessment of the Heyd-Scuseria-Ernzerhof screened Coulomb hybrid functional. *J. Chem. Phys.* 121, 1187–1192. doi: 10.1063/1.1760074

Heyd, J., Scuseria, G. E., and Ernzerhof, M. (2003). Hybrid functionals based on a screened Coulomb potential. *J. Chem. Phys.* 118, 8207–8215. doi: 10.1063/1.1564060

Kida, T., Minami, Y., Guan, G., Nagano, M., Akiyama, M., Yoshida, A., et al. (2006). Photocatalytic activity of gallium nitride for producing hydrogen from water under light irradiation. *J. Mater. Sci.* 41, 3527–3534. doi: 10.1007/s10853-005-5655-8

Kresse, G., and Furthmüller, J. (1996). Efficient iterative schemes for ab initio total-energy calculations using a plane-wave basis set. *Phys. Rev. B* 54, 11169–11186. doi: 10.1103/PhysRevB.54.11169

Kresse, G., and Joubert, D. (1999). From ultrasoft pseudopotentials to the projector augmented-wave method. *Phys. Rev. B* 59, 1758–1775. doi: 10.1103/PhysRevB.59.1758

Maeda, K., Takata, T., Hara, M., Saito, N., Inoue, Y., Kobayashi, H., et al. (2005). GaN:ZnO solid solution as a photocatalyst for visible-light-driven overall water splitting. *J. Am. Chem. Soc.* 127, 8286–8287. doi: 10.1021/ja05 18777

Maruska, H. P., and Tietjen, J. J. (1969). The preparation and properties of vapor-deposited single-crystal-line GaN. *Appl. Phys. Lett.* 15, 327–329. doi: 10.1063/1.1652845

Meng, G., Ying, D., and BaiBiao, H. (2012). Tailoring the band gap of GaN codoped by VO for enhanced solar energy conversion from first-principles calculations. *Comput. Mater. Sci.* 54, 101–104. doi: 10.1016/j.commatsci.2011. 10.019

Monkhorst, H. J., and Pack, J. D. (1976). Special points for Brillouin-zone integrations. *Phys. Rev. B* 13, 5188–5192. doi: 10.1103/PhysRevB.13.5188

Onen, A., Kecik, D., Durgun, E., Ciraci, S. (2016). GaN: from three- to two-dimensional single-layer crystal and its multilayer van der Waals solids. *Phys. Rev. B* 93:085431. doi: 10.1103/PhysRevB.93.085431

Pan, H., Gu, B., Eres, G., Zhang, Z. (2010). Ab initio study on noncompensated CrO codoping of GaN for enhanced solar energy conversion. *J. Chem. Phys.* 132:104501. doi: 10.1063/1.3337919

Sahin, H., Cahangirov, S., Topsakal, M., Bekaroglu, E., Aktrk, E., Senger, R. T., et al. (2009). Monolayer honeycomb structures of group IV elements and III-V binary compounds. *Phys. Rev. B* 80:155453. doi: 10.1103/PhysRevB.80.155453

Sun, M., Chou, J. P., Yu, J., and Tang, W. (2017). Electronic properties of blue phosphorene/graphene and blue phosphorene/graphene-like gallium nitride heterostructures. *Phys. Chem. Chem. Phys.* 19:17324. doi: 10.1039/C7CP01852E

Van de Walle, C. G., and Neugebauer, J. (2004). First-principles calculations for defects and impurities: applications to III-nitrides. *J. Appl. Phys.* 95, 3851–3879. doi: 10.1063/1.1682673

White, J. A., and Bird, D. M. (1994). Implementation of gradient-corrected exchange-correlation potentials in Car-Parrinello total-energy calculations. *Phys. Rev. B* 50, 4954–4957. doi: 10.1103/PhysRevB.50.4954

Xia, C., Peng, Y., Wei, S., and Jia, Y. U. (2013). The feasibility of tunable p-type Mg doping in a GaN monolayer nanosheet. *Acta Mater.* 61, 7720–7725. doi: 10.1016/j.actamat.2013.09.010

Xuan, F., Chai, J.-D., and Su, H. (2019). Local density approximation for the short-range exchange free energy functional. *ACS Omega* 4, 7675–7683. doi: 10.1021/acsomega.9b00303

Zeyan, W., Baibiao, H., Lin, Y., Ying, D., Peng, W., Xiaoyan, Q., et al. (2008). Enhanced ferromagnetism and tunable saturation magnetization of Mn/C-codoped GaN nanostructures synthesized by carbothermal nitridation. *J. Am. Chem. Soc.* 130:16366. doi: 10.1021/ja807030v

Conflict of Interest: The authors declare that the research was conducted in the absence of any commercial or financial relationships that could be construed as a potential conflict of interest.

frontiers in Physics

ORIGINAL RESEARCH
published: 30 June 2020
doi: 10.3389/fphy.2020.00232

GGA and GGA Plus U Study of Half-Metallic Quaternary Heusler Compound CoCrScSn

Chuankun Zhang, Haiming Huang, Chengrui Wu, Zhanwu Zhu, Zedong He and Guoying Liu*

School of Science, Hubei University of Automotive Technology, Shiyan, China

The structural, mechanical, electronic, magnetic, and half-metallic properties of quaternary Heusler compound CoCrScSn are studied using the GGA and GGA + U method based on first-principles calculations. It is found that Type-I structure of CoCrScSn compound is the most stable, and its ground state is ferromagnetic. At the equilibrium lattice constant, the electronic structures obtained by GGA and GGA + U methods indicate that CoCrScSn compound have typical half-metal character. The results of elastic constants and half-metallic robustness show that the mechanical stability and half-metallicity of CoCrScSn can be well-maintained in the range of 6.2–6.9 Å under GGA and 5.7–6.4 Å under GGA + U, respectively. When CoCrScSn compound exhibits half-metallic properties, the total magnetic moment per molecular unit is 4.0 μ_B, which is in good agreement with the Slater-Pauling rule, and Cr atoms are the main source of molecular magnetic moment. All the aforementioned results indicate that quaternary Heusler compound CoCrScSn would be an ideal candidate in spintronics.

Keywords: heusler, half-metal, elastic constant, first-principles, spintronics

OPEN ACCESS

Edited by:
Xiaotian Wang,
Southwest University, China

Reviewed by:
Saadi Berri,
University Ferhat Abbas of Setif, Algeria
Jabbar M. Khalaf Al-Zyadi,
University of Basrah, Iraq
Fethallah Dahmane,
Centre Universitaire El-Wancharissi Tissemsilt, Algeria

****Correspondence:***
Chuankun Zhang
chknzhang@163.com

Specialty section:
This article was submitted to Computational Physics, a section of the journal Frontiers in Physics

Received: *26 April 2020*
Accepted: *28 May 2020*
Published: *30 June 2020*

Citation:
Zhang C, Huang H, Wu C, Zhu Z, He Z and Liu G (2020) GGA and GGA Plus U Study of Half-Metallic Quaternary Heusler Compound CoCrScSn. Front. Phys. 8:232. doi: 10.3389/fphy.2020.00232

INTRODUCTION

Spintronics, also known as magnetoelectronics, is a new discipline and technology that has developed rapidly since the 1990s [1, 2]. The information transport of traditional electronic devices mainly depends on the charge. Spintronics not only uses the charge transport, but also adds the spin and magnetic moment of the electron. Compared with traditional semiconductor electronic devices, spintronic devices have many advantages such as non-volatile, low power consumption and high integration. For spintronic materials, it is necessary to have higher electron polarizability and in this case, half-metallic magnetic materials become the best choice for spintronic applications. In the field of spintronics, half-metallic magnetic materials are widely used in spin diodes, spin valves, spin filters, and other devices due to their special electronic structure [3–5]. The most important feature of half-metallic magnetic materials is that the majority-spin (minority-spin) direction is metal property, and the minority-spin (majority-spin) direction is semiconductor or insulator property, leading to 100% spin polarization at the Fermi level [6, 7]. The unique electronic structure of half-metallic magnetic materials has become a research hotspot recently [8–10].

Heusler alloy compounds have always been one of the most important members of half-metallic magnetic materials. Since the first half-metallic magnetic material, ternary Heulser alloy NiMnSb [11] was predicted, researchers have paid great attention to the this kinds of compounds [12–25]. The crystal of Heusler compounds is generally cubic structure with four atoms. The four atoms occupy A(0,0,0), B(0.25,0.25,0.25), C(0.50, 0.50, 0.50), and D(0.75, 0.75, 0.75), respectively [26, 27].

According to the different ways of occupying atoms, Heusler compounds have derived many types of structures, including full-Heusler, half-Heuler, inverse-Heusler, and quaternary-Heusler, etc. There are many half-metallic magnetic materials in these different Heusler configurations, and they are widely concerned by researchers in experiments and theory [28–34].

In recent years, there are some reports about the CoCr-based quaternary Heusler compounds. In 2012, Gokoglu [35] found that quaternary Heusler compound NiCoCrGa displays a slightly disturbed half-metallic behavior with high-spin polarization ratio at Fermi level. In 2017, Xu et al. [36] found that the quaternary Heusler (Y, La, Lu)CoCr/FeMn(Al, Ga) containing rare earth elements has the characteristics of spin gapless semiconductors. In 2019, Wu et al. [37] found that the Curie temperature of CrCoScZ (Z = Si, Ge, Sn) based on mean field theory is higher than that of room temperature. Huang et al. [38] found that the bulk and surface states of CoCrScBi are half-metallic. In 2020, Khan et al. [39] studied the structural stability, band structure, density of states, magnetic and mechanical properties of CoCr-based quaternary Heusler compounds CoCrYZ (Z = Si, Ge, Ga, Al) and found all these materials possess half-metallic character.

Recent studies on quaternary Heusler compounds show that the Coulomb interaction of 3d electrons in transition metals has a significant effect on the electronic structure of alloys. Gao et al. [40] reveal that the half-metallicity is lost for both CoFeCrAl and CoFeCrGa but retentive for both CoFeCrSi and CoFeCrGe when the Coulomb interactions are considered. Paudel et al. [41] found the band gap width of CoFeZrGe, CoFeZrSb, and CoFeZrSi compounds under GGA + U changed a lot compared with that under GGA. Although CoCrScSn compound has been shown to have half-metallic behavior in previous studies [37], there has been no report on whether it has stable mechanical properties, nor on whether the Coulomb interactions between transition metal atoms in CoCrScSn affect its physical properties. Therefore, in order to reveal the effect of the coulomb interaction on the electronic structure of CoCrScSn, and also to understand its mechanical stability, so that CoCrScSn can be applied in spintronics. In this study, we perform a complete first-principles study of the ground state, mechanical, electronic, magnetic, and half-metallic properties of CoCrScSn compound based on the generalized gradient approximation (GGA) [42] with strong-correlated correction (GGA + U).

CALCULATION METHODS

In this study, the GGA and GGA + U as implemented in the Vienna ab-initio simulation package (VASP) package [43], was used to calculate the physical and mechanical properties of the CoCrScSn compound. The effective U(U_{eff}) values of 2.7 eV for Co, 2.0 eV for Cr, and 0.5 eV for Sc [44, 45] were selected, respectively, as these values provides correct description magnetic moment and electronic structure in the Heusler compounds [46]. For the self-consistent calculation, the plane wave cutoff energy was chosen to be 500 eV. A mesh of 9 × 9 × 9 Monkhorst-Pack k-point was used. The convergence tolerances were selected as the difference in total energy and the maximum force within 1.0×10^{-5} eV and 1.0×10^{-2} eV/atom, respectively.

TABLE 1 | Equilibrium lattice equilibrium constants (Å) and atomic positions for three different types of crystals.

Types	a	Co	Cr	Sc	Sn
Type-I	6.3848	3/4, 3/4, 3/4	1/4, 1/4, 1/4	1/2, 1/2, 1/2	0, 0, 0
Type-II	6.4172	3/4, 3/4, 3/4	1/2, 1/2, 1/2	1/4, 1/4, 1/4	0, 0, 0
Type-III	6.4705	3/4, 3/4, 3/4	0, 0, 0	1/2, 1/2, 1/2	1/4, 1/4, 1/4

TABLE 2 | Total energies (eV) of CoCrScSn compound in NM, FM, and AFM states.

Types	NM	FM	AFM
Type-I	−105.1269	−108.6031	−108.5538
Type-II	−101.0947	−105.3795	−105.0217
Type-III	−102.5495	−106.5999	−105.5016

RESULTS AND DISCUSSIONS

Structural Properties

According to the results of earlier research, quaternary Heusler compounds usually have three different structures depending on the positions occupied by the atoms. The three structures are defined as type-I, type-II, and type-III, respectively [47–50]. For CoCrScSn compound, the occupancy positions of Co, Cr, Sc, and Sn atoms are shown in **Table 1**. We must first determine which of the three structures is the most stable. Therefore, we are very concerned about the relationship between the total energy of the three structures and the lattice constant. Through structural optimization, we have obtained the equilibrium lattice constants of three structures of CoCrScSn compounds as shown in **Table 1**. **Table 2** shows the total energies of CoCrScSn compound in non-magnetic (NM), ferromagnetic (FM), and antiferromagnetic (AFM) states at the equilibrium structures. It can be seen that among these three structures, the energy of the ferromagnetic state with the type-I structure is the lowest, which means that the type-I structure of the CoCrScSn compound is the most stable, and the ground state of this stable structure is ferromagnetic. The next studies only consider the ferromagnetic type-I structure of CoCrScSn compound.

So far, there are no experimental reports about CoCrScSn compound. In order to test the possibility of synthesizing CoCrScSn compound, we performed a calculation of formation energy, which is calculated as follows:

$$E_f = E_{Tot} - E_{Co} - E_{Cr} - E_{Sc} - E_{Sn} \quad (1)$$

where E_{Tot} are the total energy of the CoCrScSn compound per formula unit at equilibrium lattice constants and E_{Co}, E_{Cr}, E_{Sc}, and E_{Sn} correspond to the total energy per atom for the Co, Cr, Sc, and Sn atoms, respectively. During calculation, Co, Cr, and Sc are taken as face-centered cubic structure (space group Fm-3m),

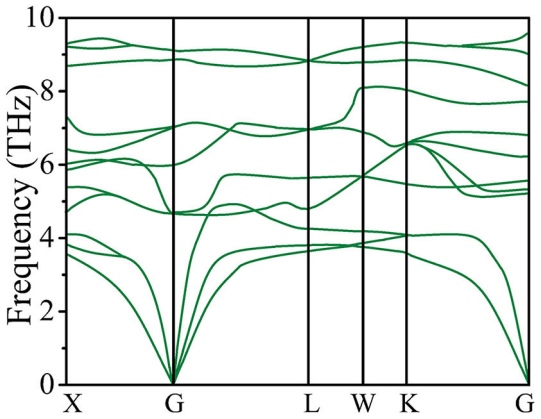

FIGURE 1 | Phonon dispersion curves of the CoCrScSn compound at equilibrium lattice constants.

Sn is taken as body-centered cubic structure (space group Im-3m). We use the ferromagnetic energy of the title compound as the E_{Tot} of formula (1) to obtain the formation energy of type-I, type-II, and type-III as −1.35, −0.55, and −0.85 eV, respectively. The negative values of the formation energy indicate that these three structures of CoCrScSn compounds are energetically stable and may be fabricated experimentally.

In order to examine the dynamical stability, the phonon dispersion curves of the type-I structure of CoCrScSn compound have been calculated and depicted in **Figure 1**. It is seen that the title compound have positive phonon frequency, which is an key indicator of the dynamical stability of the Heusle compound. There are no available experimental related to the quaternary Heusler compoud CoCrScSn to make a comparison with our data, and we are looking forward to the experimental synthesis of the title compound.

Mechanical Properties

The mechanical properties of cubic crystals are determined by three elastic constants, C_{11}, C_{12}, and C_{44}. The elastic constants C_{11}, C_{12}, and C_{44} at are obtained by calculating the strain as a function of total energy. Born and Huang criteria give that the mechanical stability of cubic crystals is determined by the following formula [51, 52]:

$$C_{11} - C_{12} > 0\ C_{44} > 0\ C_{11} + 2C_{12} > 0 \tag{2}$$

The elastic constants C_{11}, C_{12}, and C_{44} of CoCrScSn compound at equilibrium lattice constant were calculated to be 154.9 GPa, 61.5 GPa, and 62.7 GPa for GGA and 165.2 GPa, 70.3 GPa, and 74.2 GPa for GGA + U, respectively. As a comparison, we found that the C_{11} and C_{44} of CoCrScSn in this paper were larger than that of another similar compound CoCrScBi, while C_{12} was smaller than that of CoCrScBi [38].

$$B = \frac{C_{11} + 2C_{12}}{3} \tag{3}$$

$$G_V = \frac{C_{11} - C_{12} + 3C_{44}}{5} \tag{4}$$

$$G_R = \frac{5(C_{11} - C_{12})C_{44}}{4C_{44} + 3(C_{11} - C_{12})} \tag{5}$$

$$G = \frac{G_V + G_R}{2} \tag{6}$$

According to formula (3)–(6), the bulk modulus B and shear modulus G calculated are 92.63 GPa, 55.72 GPa for GGA, and 101.93 GPa, 62.02 GPa for GGA + U, respectively. The bulk modulus and shear modulus of CoCrScBi are reported as 127.03 GPa and 31.88 GPa, respectively. The bulk modulus of CoCrScSn is smaller than that of CoCrScBi, indicating that CoCrScSn is more prone to volume deformation than CoCrScBi. However, the larger shear modulus of CoCrScSn confirms its greater resistance to shear strain than CoCrScBi. The elastic constants obtained by using GGA and GGA + U all meet the elastic stability criteria and therefore, ferromagnetic type-I structure of CoCrScSn compound are mechanically stable.

As we all know, the physical properties of compounds will change with the change of crystal structure. The change of lattice constant of compounds under external pressure is one of the simplest ways to change the physical properties of compounds. Next, we study the mechanical stability of CoCrScSn compound when the lattice constant changes.

Under the uniform pressure P, the stress-strain coefficients will replace the elastic constants with the following expression:

$$B_{11} = C_{11} - P, B_{12} = C_{12} + P, B_{44} = C_{44} - P \tag{7}$$

Accordingly, the mechanical stability of CoCrScSn compound under uniform pressure is determined by the following formula [53, 54]:

$$B_{11} - B_{12} > 0, B_{11} + 2B_{12} > 0, B_{44} > 0 \tag{8}$$

That is

$$C_{11} - C_{12} - 2P > 0, C_{11} + 2C_{12} + P > 0, C_{44} - P > 0 \tag{9}$$

Figures 2A,B shows the change curve of the elastic modulus of CoCrScSn compound with the lattice constant under GGA and GGA + U, respectively. Under GGA, when the lattice constant of CoCrScSn compound is between 5.8 and 7.2 Å, C_{11}-C_{12}-2P, C_{11}+2C_{12}+P, and C_{44}-P are greater than zero, as shown in **Figure 2A**. This means that the mechanical properties of CoCrScSn compound in this lattice constant range are stable. One can see from **Figure 2A** that when the lattice constant is too large, it may cause negative values of C_{11}-C_{12}-2P, C_{11}+2C_{12}+P, and C_{44}-P. At this time, CoCrScSn compound will show unstable mechanical properties. This result is consistent with the fact that the interaction between atoms weakens and the stability is destroyed when the crystal expands. Under GGA + U, the

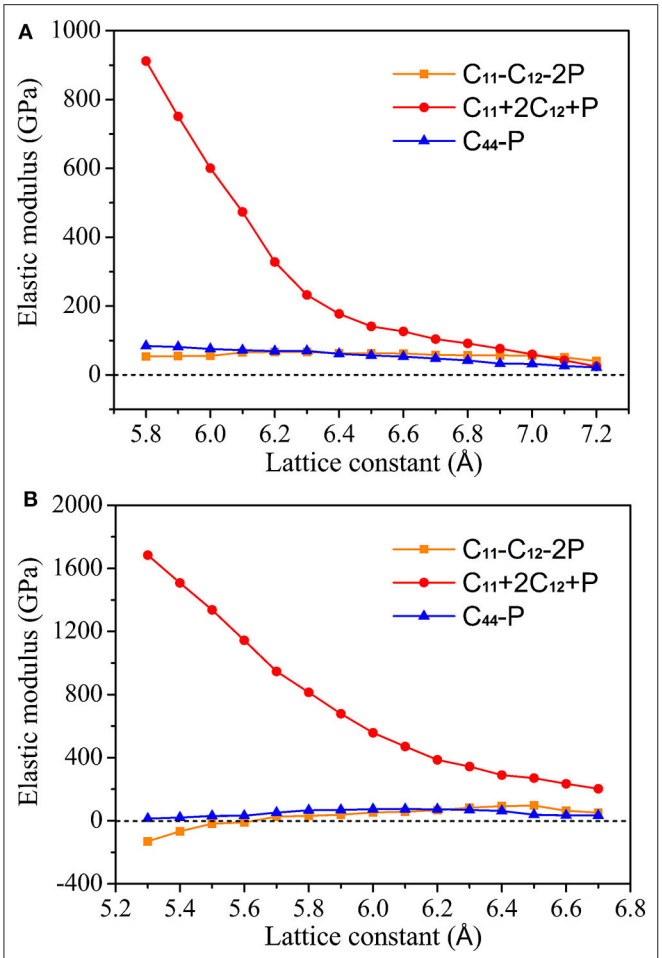

FIGURE 2 | Elastic modulus of CoCrScSn compound under different lattice constant. **(A)** GGA, **(B)** GGA + U.

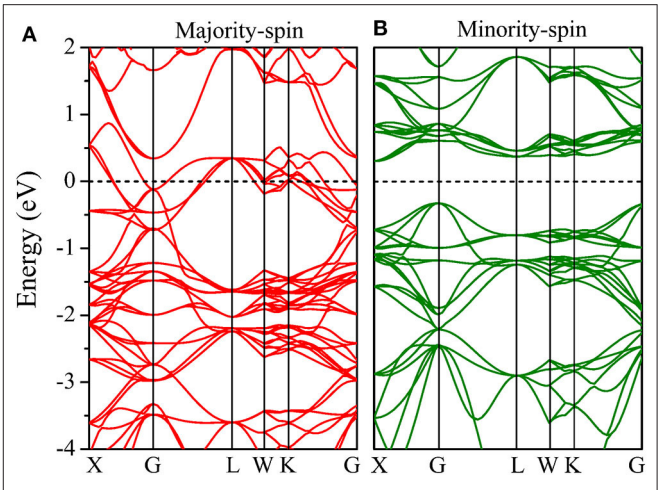

FIGURE 3 | Band structures of CoCrScSn compound under GGA. **(A)** Majority-spin, **(B)** minority-spin.

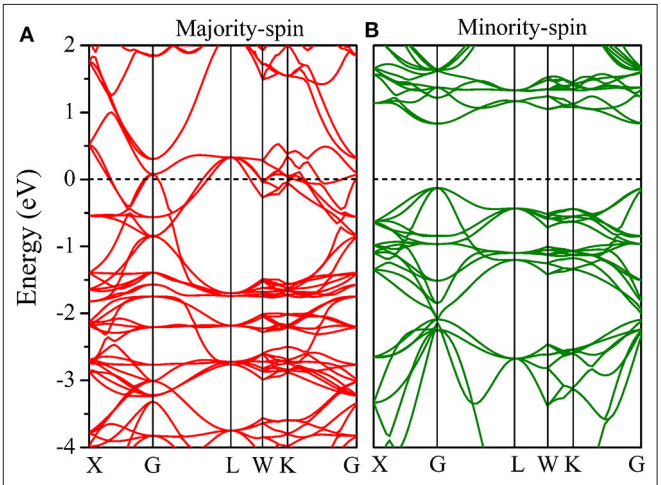

FIGURE 4 | Band structures of CoCrScSn compound under GGA + U. **(A)** Majority-spin, **(B)** minority-spin.

mechanical properties of CoCrScSn are stable in the range of 5.6–6.7 Å as shown in **Figure 2B**. When the lattice constant is lower than 5.6 Å, C_{11}-C_{12}-2P appears a negative value, and when the lattice constant is > 6.7 Å, C_{44}-P may be a negative value, both of which will make the mechanical properties of the CoCrScSn compound unstable.

Electronic Properties

We further calculated the band structures of the CoCrScSn compound under GGA and GGA + U, as shown in **Figures 3**, **4**, respectively. Under the cases of GGA and GGA + U, the majority-spin direction shows metal behavior, while minority-spin direction shows semiconductor behavior, which is a typical half-metal character. Furthermore, the band gap of minority-spin is an indirect under GGA, and direct (at the G point) under GGA + U. Under GGA and GGA + U, the minority-spin band gap of the title compound is 0.66 and 0.93 eV, respectively. The band gap considering Coulomb interaction is larger than that without Coulomb interaction. It shows that the Coulomb interaction has an obvious influence on the electronic structure of the CoCrScSn compound, so it is necessary to consider the Coulomb interaction when studying the electronic structure of the title compound.

Figure 5 shows the total and local density of states (DOSs) of CoCrScSn compound under GGA and GGA + U, respectively. Same as the result of the energy band structure, one spin direction is metallic, the other is semiconductor, and the title compound is a half-metal. By comparing the DOS distribution under GGA and GGA + U, it is clear that the shape of density of state in the two cases is roughly the same, but the local position is slightly different due to the Coulomb interaction. Obviously, the majority-spin below the Fermi level moves slightly to the low energy region, the minority-spin below the Fermi level moves toward the Fermi level, and the minority-spin above the Fermi level moves away from the Fermi level when the Coulomb interaction is considered.

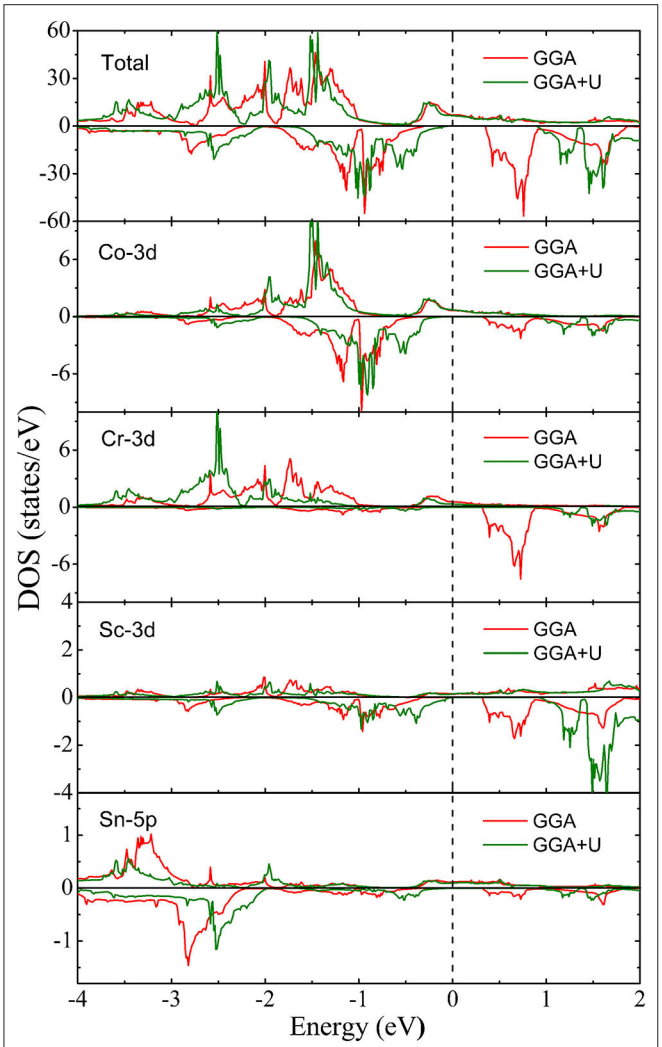

FIGURE 5 | Total and local density of states of CoCrScSn compound under GGA and GGA + U, respectively.

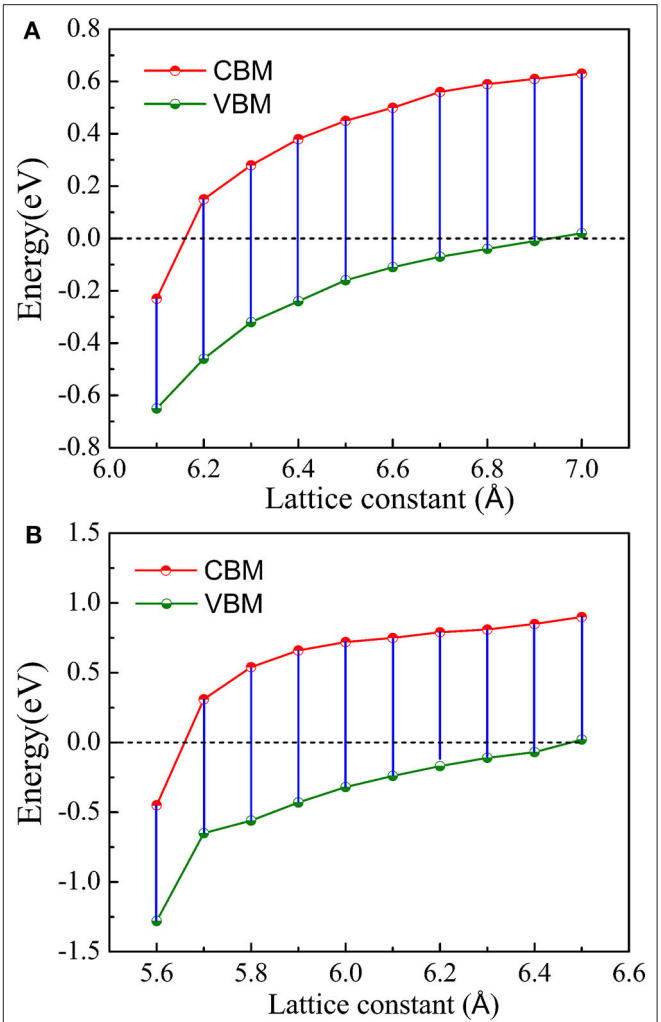

FIGURE 6 | Minority-spin CBM and VBM of CoCrScSn compound at different lattice constant. **(A)** GGA, **(B)** GGA + U.

The robustness of half-metallicity is a key factor for spintronic materials. For practical applications, it is particularly important whether the half-metallic properties can still exist under external pressure or strain. Next, we will study the stability of half-metallicity of CoCrScSn compound when the lattice constant changes. **Figure 6** shows the curve of the minority-spin band gap width with the lattice constant of the CoCrScSn compound under GGA and GGA + U. The results show that the majority-spin direction always shows the metallic property when the lattice constant changes, therefore, the half-metallic property is determined by the minority-spin band gap. That is to say, when there is a band gap in minority-spin, the title compound has half-metallic property, when there is no band gap, the half-metallicity will disappears.

Figure 6 shows that under GGA and GGA + U, the conduction band minimum (CBM) and valence band maximum (VBM) in minority-spin change with the lattice constant. It can be seen that within the lattice constants region of 6.2–6.9 Å, the CBM and VBM are located on the two sides of the Fermi level under GGA. At this time, the semiconductor character of minority-spin is obvious, the title compound has stable half-metallic property. When the lattice constant is lower than 6.2 Å or higher than 6.9 Å, the minority-spin band gap disappears and the half-metallicity disappears.

In the case of GGA + U, the CoCrScSn compound also has similar characteristics, but due to the influence of Coulomb interaction, the lattice constant of the compound maintaining the half-metallicity region is from 5.7 to 6.4 Å. Combined with the mechanical properties research, we can find that in the case of GGA, the mechanical and half-metallic properties of the CoCrScSn compound are very stable within the lattice constant range of 6.2–6.9 Å. In the case of GGA + U, the mechanical properties and half-metallic properties exist stably in the range of 5.7–6.4 Å.

Magnetic Properties

Slater and Pauling in two pioneering papers show that if a minority-spin electron is added to a magnetic compound, the total magnetic moment of the compound will be reduced by 1 μ_B. If a majority-spin electron is added, the total magnetic moment of the compound will be increased by 1 μ_B [55–57]. This behavior called Slater-Pauling (SP) rule has been studied not only in binary magnetic compounds [58], but also in half-metallic Heusler compounds. So far, people have summarized some SP relation between the total magnetic moment (M_t) and number of valence electrons (Z_t) of per molecular unit in half-metallic Heusler compounds, such as $M_t = Z_t$-18 [59], $M_t = Z_t$-24 [4], and $M_t = Z_t$-28 [57]. Some half-metallic quaternary Heusler compounds mainly satisfy the SP rule of $M_t = Z_t$-18 [60–63] and $M_t = Z_t$-24 [64–66].

In CoCrScSn compound, the number of valence electrons of Co, Cr, Sc and Sn atoms are nine, six, three, and four, respectively, so the Z_t is twenty two. The calculations of GGA and GGA + U show that the M_t at equilibrium lattice constant is 4.0 μ_B. Obviously, the M_t and Z_t are in accordance with the SP relation $M_t = Z_t$-18, and CoCrScSn compound conform to the typical characteristics of half-metallic Heusler compound.

Figure 7 shows the total and local magnetic moments of CoCrScSn compound at different lattice constants under GGA and GGA + U, respectively. From 6.2 to 6.9 Å under GGA and from 5.7 to 6.4 Å under GGA + U, the M_t is an integral value 4.0 μ_B. Within this lattice constant range, the CoCrScSn compound has stable half-metallic character. When the lattice constant under GGA is lower than 6.2 Å or higher than 6.9 Å, the M_t is no longer an integral value, and the half-metallicity of the CoCrScSn compound will disappear.

The same situation also occurs when considering the Coulomb interaction. If the lattice constant is < 5.7 Å or higher than 6.4 Å, the M_t does not meet the SP rule and the title compound will lose the half-metal character. It can be seen from the local magnetic moment distribution curve that Cr atom is the most important source of the magnetic properties of the title compound, and Co atom also contributes to the total magnetic moment, but the contribution degree is smaller than Cr atom. It seems that Sc and Sn atoms also have certain magnetic moments, but because Sc and Sn atoms are not magnetic themselves, they are induced magnetic moments due to the influence of Cr and Co atoms.

Higher Curie temperature is another key factor for the application of half-metallic magnetic materials in spintronics. Theoretically, the mean field approximation is often used to estimate the Curie temperature (T_c) of materials. The formula can be expressed as follows [37, 67]:

$$T_c = \frac{2\Delta E_{AFM-FM}}{3CK_B} \tag{10}$$

where ΔE_{AFM-FM} is the total energy difference between antiferromagnetic and ferromagnetic states. C is the amount of the magnetic ion, and k_B is Boltzmann constant. The Curie temperature calculated based on formula (6) for CoCrScSn is 762 K, which is slightly less than the previous theoretical research result.

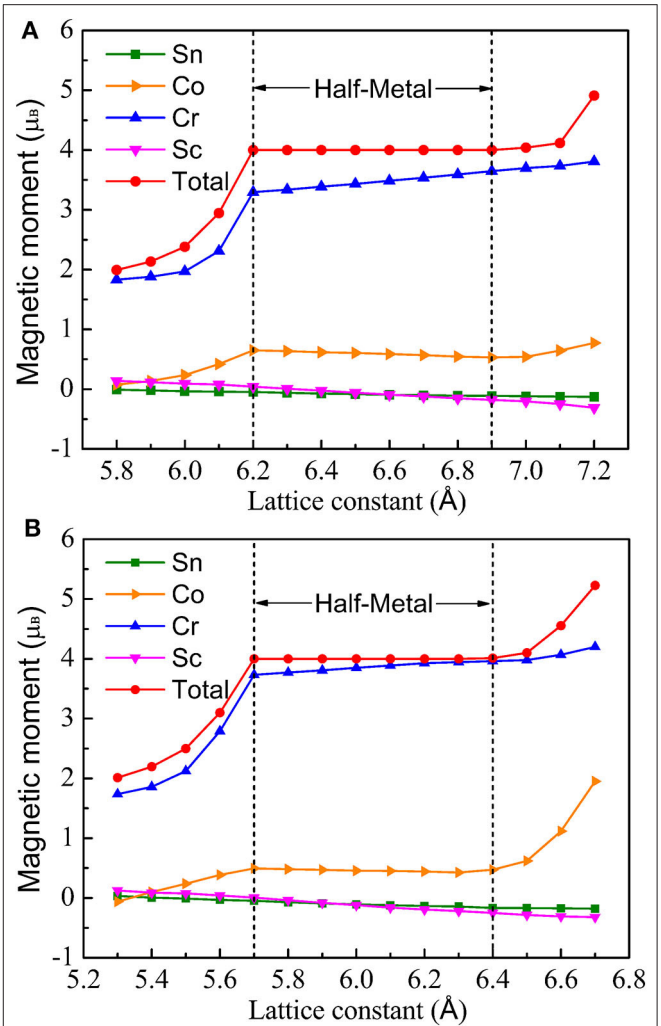

FIGURE 7 | Total and atomic magnetic moments of CoCrScSn compound at different lattice constant. **(A)** GGA, **(B)** GGA + U.

Furthermore, Wurmehl et al. [68] proposed a linear relation to estimate the Curie temperature of the half-metal Heusler compound by using the M_t, and the expression is [69]

$$T_c = 23 + 181M_t \tag{11}$$

The Curie temperature for CoCrScSn were estimated according to the model presented is 747K, which is very close to the result of mean field approximation. Although the theoretical estimate of the Curie temperature is often higher than the actual value, we conclude that the Curie temperature of CoCrScSn should be higher than room temperature, which make it interesting for technological applications in spintronics.

CONCLUSIONS

In this study, we focused on quaternary Heusler compound CoCrScSn, and showed a complete first-principles study on the structure, mechanical, electronic, magnetic, and half-metallic properties of this material. It was found that the type-I structure of quaternary Heusler compound CoCrScSn is the most stable, and the type-I structure has a stable ferromagnetic ground state. Elastic constant analysis shows that CoCrScSn compound have stable mechanical properties at the equilibrium lattice constant. The mechanical properties of CoCrScSn will change if the lattice constant changes. The further studies show that if the lattice constant can be maintained within the range of 5.8–7.2 Å under GGA, and 5.6–6.7 Å under GGA + U, the mechanical properties of CoCrScSn compound are also stable. At the equilibrium lattice constant, the electronic structure of CoCrScSn compound under GGA and GGA + U shows that it has obvious half-metal character. The half-metal robustness of the CoCrScSn compound can be maintained in the lattice constant range of 6.2–6.9 Å for GGA, 5.7–6.4 Å for GGA + U. At the equilibrium lattice constant, the molecular magnetic moment of the compound is an integer value of 4.0 μ_B. No matter how the lattice constant changes, as long as the compound has half-metallic character, the total magnetic moment of the CoCrScSn compound meets the Slater-Pauling rule. The mean field approximation shows that the Curie temperature is higher than room temperature, which makes the title compound a promising application in spintronics.

DATA AVAILABILITY STATEMENT

All datasets generated for this study are included in the article/supplementary material.

AUTHOR CONTRIBUTIONS

CZ designed the research. HH analyzed the data and results. CZ and HH performed the research and wrote the paper. CW checked the article grammar. ZH, ZZ, and GL contributed to the revisions. All authors contributed to the article and approved the submitted version.

FUNDING

This work was supported by the Natural Science Foundation of Hubei Province (No. 2017CFB740) and the Doctoral Scientific Research Foundation of Hubei University of Automotive Technology (No. BK201804).

REFERENCES

1. Wolf SA, Awschalom DD, Buhrman RA, Daughton JM, von Molnar S, Roukes ML, et al. Spintronics: a spin-based electronics vision for the future. *Science*. (2001) 294:1488–95. doi: 10.1126/science.1065389
2. Zutic I, Fabian J, Das Sarma S. Spintronics: fundamentals and applications, *Rev Mod Phys*. (2004) 76:323–410. doi: 10.1103/RevModPhys.76.323
3. Pickett WE, Moodera JS. Half Metallic Magnets. *Phys Today*. (2001) 54:39–44. doi: 10.1063/1.1381101
4. Galanakis I, Dederichs PH, Papanikolaou N. Slater-Pauling behavior and origin of the half metallicity of the full-Heusler alloys. *Phys Rev B*. (2002) 66:174429. doi: 10.1103/PhysRevB.66.174429
5. Song Y, Dai G. Spin filter and spin valve in ferromagnetic graphene. *Appl Phys Lett*. (2015) 106:223104. doi: 10.1063/1.4921668
6. Bhat TM, Gupta DC. Robust thermoelectric performance and high spin polarisation in CoMnTiAl and FeMnTiAl compounds. *RSC Adv*. (2016) 6:80302–9. doi: 10.1039/c6ra18934b
7. Gupta DC, Bhat IH. Magnetic, electronic, high-spin polarization and half-metallic properties of Ru_2VGe and Ru_2VSb Heusler alloys: An FP-LAPW study. *J Magn Magn Mater*. (2015) 374:209–13. doi: 10.1016/j.jmmm.2014.08.032
8. Addadi Z, Doumi B, Mokaddem A, Elkeurti A, Sayede A, Tadjer A, et al. Electronic and ferromagnetic properties of 3d(V)-doped (BaS) barium sulfide. *J Supercond Nov Magn*. (2017) 30:917–23. doi: 10.1007/s10948-016-3894-3
9. Dahmane F, Tadjer A, Doumia B, Mesria D, Aouragb H, Sayede A. First principles study of the electronic structures and magnetic properties of transition metal-doped cubic indium nitride. *Mater Sci Semicond Process*. (2014) 21:66–73. doi: 10.1016/j.mssp.2014.01.037
10. Huang HM, Cao ML, Jiang ZY, Xiong YC, Zhang X, Luo SJ, et al. High spin polarization in formamidinium transition metal iodides: first principles prediction of novel half-metals and spin gapless semiconductors. *Phys Chem Chem Phys*. (2019) 21:16213. doi: 10.1039/c9cp00958b
11. De Groot RA, Mueller FM, Van Engen PG, Buschow KHJ. New class of materials: half-metallic ferromagnets. *Phys Rev Lett*. (1983) 50:2024. doi: 10.1103/PhysRevLett.50.2024
12. Huang HM, Luo SJ, Yao KL. Half-metallicity and tetragonal distortion in semi-heusler alloy FeCrSe. *J Appl Phys*. (2014) 115:043713. doi: 10.1063/1.4863122
13. Han Y, Bouhemadou A, Khenata R, Cheng Z, Yang T, Wang X. Prediction of possible martensitic transformations in all-d-metal zinc-based heusler alloys from first-principles. *J Magn Magn Mater*. (2019) 471:49–55. doi: 10.1016/j.jmmm.2018.09.053
14. Chen Y, Chen S, Wang B, Wu B, Huang H, Qin X, et al. Half-Metallicity and magnetism of the quaternary Heusler compound $TiZrCoIn_{1-x}Ge_x$ from the first-principles calculations. *Appl Sci*. (2019) 9:620. doi: 10.3390/app9040620
15. Tan X, You J, Liu PF, Wang Y. Theoretical study of the electronic, magnetic, mechanical and thermodynamic properties of the spin gapless semiconductor CoFeMnSi. *Crystals*. (2019) 9:678. doi: 10.3390/cryst9120678
16. Li T, Wu Y, Han Y, Wang X. Tuning the topological nontrivial nature in a family of alkali-metal-based inverse heusler compounds: a first-principles study. *J Magn Magn Mater*. (2018) 463:44–9. doi: 10.1016/j.jmmm.2018.05.025
17. Feng L, Ma J, Yang Y, Lin T, Wang L. The electronic, magnetic, half-metallic and mechanical properties of the equiatomic quaternary heusler compounds FeRhCrSi and FePdCrSi: a first-principles study. *Appl Sci*. (2018) 8:2370. doi: 10.3390/app8122370
18. Sakon T, Yamasaki Y, Kodama H, Kanomata T, Nojiri H, Adachi Y. The characteristic properties of magnetostriction and magneto-volume effects of Ni_2MnGa-Type ferromagnetic heusler alloys. *Materials*. (2019) 12:3655. doi: 10.3390/ma12223655
19. Faleev SV, Ferrante Y, Jeong J, Samant MG, Jones B, Stuart P. Origin of the tetragonal ground state of Heusler compounds. *Phys Rev Appl*. (2017) 7:034022. doi: 10.1103/PhysRevApplied.7.034022
20. Wang XT, Dai XF, Wang LY, Liu XF, Wang WH, Wu GH, et al. Electronic structures and magnetism of Rh_3Z (Z=Al, Ga, In, Si, Ge, Sn, Pb, Sb) with DO_3 structures. *J Magn Magn Mater*. (2015) 378:16–23. doi: 10.1016/j.jmmm.2014.10.161
21. Dahmane F, Mesri D, Tadjer A, Khenata R, Benalia S, Djoudi L, et al. Electronic structure, magnetism and stability of Co_2CrX (X=Al, Ga, In) ab initio study. *Mod Phys Lett B*. (2016) 30:1550265. doi: 10.1142/S0217984915502656
22. Han YL, Wu MX, Kuang MQ, Yang T, Chen XB, Wang XT. All-d-metal equiatomic quaternary Heusler hypothetical alloys ZnCdTMn (T= Fe, Ru, Os, Rh, Ir, Ni, Pd, Pt): a first-principle investigation of electronic structures,

magnetism, and possible martensitic transformations. *Results Phys*. (2018) 11:1134–41. doi: 10.1016/j.rinp.2018.11.024
23. Li TZ, Khenata R, Cheng ZX, Chen H, Yuan HK, Yang T, et al. Martensitic transformation, electronic structure and magnetism in D03-ordered heusler Mn_3Z (Z=B, Al, Ga, Ge, Sb) alloys, *Acta Cryst*. (2018) B74:673–80. doi: 10.1107/S2052520618013525
24. Berri S. First-principles calculations to investigate the structural, electronic, and half-metallic properties of $Ti_2RhSn_{1-x}Si_x$, $Ti_2RhSn_{1-x}Ge_x$, and $Ti_2RhGe_{1-x}Si_x$(x=0, 0.25, 0.5, 0.75, and 1) quaternary heusler alloys. *J Supercond Nov Magn*. (2019) 32:2219–28. doi: 10.1007/s10948-018-4952-9
25. Khalaf Al-zyadi JM, Kadhim AA, Yao KL. Half-metallicity of the (001), (111) and (110) surfaces of CoRuMnSi and interface half-metallicity of CoRuMnSi/CdS. *RSC Adv*. (2018) 8:25653. doi: 10.1039/c8ra02918k
26. Huang H, Yang K, Zhao W, Zhou T, Yang X, Wu B. High-pressure-induced transition from ferromagnetic semiconductor to spin gapless semiconductor in quaternary heusler alloy VFeScZ (Z=Sb, As, P). *Appl Sci*. (2019) 9:2859. doi: 10.3390/app9142859
27. Jin Y, Kharel P, Lukashev P, Valloppilly S, Staten B, Herran J, et al. Magnetism and electronic structure of CoFeCrX (X= Si, Ge) heusler alloys. *J Appl Phys*. (2016) 120:053903. doi: 10.1063/1.4960350
28. Chen Z, Xu H, Gao Y, Wang X, Yang T. Site-Preference, electronic, magnetic, and half-metal properties of full-heusler Sc_2VGe and a discussion on the uniform strain and tetragonal deformation effects. *Crystals*. (2019) 9:445. doi: 10.3390/cryst9090445
29. Wang XT, Zhao WQ, Cheng ZX, Dai XF, Khenata R. Electronic, magnetic,half-metallic and mechanical properties of a new quaternary heusler compound ZrRhTiT1: Insights from first-principles studies. *Solid State Commun*. (2018) 269:125–30. doi: 10.1016/j.ssc.2017.10.021
30. Zhang HP, Liu WB, Lin TT, Wang WH, Liu GD. Phase stability and magnetic properties of Mn_3Z (Z=Al, Ga, In, Tl, Ge, Sn, Pb) heusler alloys. *Appl Sci*. (2019) 9:964. doi: 10.3390/app9050964
31. Pourebrahim G, Ahmadian F, Momeni P. Robust half-metallicity in quaternary heusler compounds KSrNZ (Z=O, S, and Se). *J Supercond Novel Magn*. (2019) 32:3305–14. doi: 10.1007/s10948-019-5098-0
32. Yousuf S, Gupta DC. Insight into half-metallicity, spin-polarization and mechanical properties of $L2_1$ structured MnY_2Z (Z=Al, Si, Ga, Ge, Sn, Sb) heusler alloys. *J Alloy Compd*. (2018) 735:1245–52. doi: 10.1016/j.jallcom.2017.11.239
33. Benea D, Gavrea R, Coldea M, Isnard O, Pop V. Half-metallic compensated ferrimagnetism in the Mn-Co-V-Al Heusler alloys. *J Magn Magn Mater*. (2019) 475:229–33. doi: 10.1016/j.jmmm.2018.11.115
34. Li Y, Liu GD, Wang XT, Liu EK, Xi XK, Wang WH, et al. First-principles study on electronic structure, magnetism and half-metallicity of the NbCoCrAl and NbRhCrAl compounds. *Results Phys*. (2017) 7:2248–54. doi: 10.1016/j.rinp.2017.06.047
35. Gökoglu G. Ab initio electronic structure of NiCoCrGa half-metallic quaternary heusler compound. *Solid State Sci*. (2012) 14:1273–6. doi: 10.1016/j.solidstatesciences.2012.07.013
36. Xu G, You Y, Gong Y, Liu E, Xu F, Wang W. Highly-dispersive spin gapless semiconductors in rare-earth-element contained quaternary heusler compounds. *J Phys D Appl Phys*. (2017) 50:105003. doi: 10.1088/1361-6463/aa57a3
37. Wu B, Huang H, Zhou G, Yang X, Li P, Feng Y. Half-metallic ferrimagnets behavior of a new quaternary Heusler alloy CrCoScZ (Z = Si, Ge, Sn). *Eur Phys J B*. (2019) 92:119. doi: 10.1140/epjb/e2019-90646-4
38. Huang HM, Jiang ZY, Hu YJ, Li W, Luo S. Effect of coulomb interaction on the electronic properties of bulk and surface of quaternary heusler CoCrScBi. *Solid State Sci*. (2019) 97:106018. doi: 10.1016/j.solidstatesciences.2019.106018
39. Khan MI, Arshad H, Rizwan M, Gillani SSA, Zafar M, Ahmed S, et al. Investigation of structural, electronic, magnetic and mechanical properties of a new series of equiatomic quaternary Heusler alloys CoYCrZ (Z=Si, Ge, Ga, Al): a DFT study. *J Alloy Comp*. (2020) 819:152964. doi: 10.1016/j.jallcom.2019.152964
40. Gao GY, Hu L, Yao KL, Luo B, Liu N. Large half-metallic gaps in the quaternary heusler alloys CoFeCrZ (Z=Al, Si, Ga, Ge): a first-principles study. *J Alloy Comp*. (2013) 551:539–43. doi: 10.1016/j.jallcom.2012.11.077
41. Paudel R, Zhu J. Structural, electronic, magnetic, elastic, and thermal properties of co-based equiatomic quaternary Heusler alloys. *J Magn Magn Mater*. (2018) 453:10–6. doi: 10.1016/j.jmmm.2017.12.103
42. Perdew JP, Burke K, Ernzerhof M. Generalized gradient approximation made simple. *Phys Rev Lett*. (1996) 77:3865–8. doi: 10.1103/PhysRevLett.77.3865
43. Kresse G, Furthmüller J. Efficiency of ab-initio total energy calculations for metals and semiconductors using a plane-wave basis set. *Comput Mater Sci*. (1996) 6:15–50. doi: 10.1016/0927-0256(96)00008-0
44. Rai DP, Thapa RK. An investigation of semiconducting behavior in the minority spin of Co_2CrZ (Z = Ga, Ge, As): LSDA and LSDA+U method. *J Alloy Comp*. (2012) 542:257–63. doi: 10.1016/j.jallcom.2012.07.059
45. Rai DP, Thapa RK. An abinitio study of the half-metallic properties of Co_2TGe (T=Sc,Ti,V,Cr,Mn,Fe): LSDA+U method. *J Korean Phys Soc*. (2013) 62:1652–60. doi: 10.3938/jkps.62.1652
46. Curtarolo S, Setyawan W, Hart GLW, Jahnatek M, Chepulskii RV, Taylor RH, et al. AFLOW: An automatic framework for high-throughput materials discovery. *Comput Mater Sci*. (2012) 58:218–26. doi: 10.1016/j.commatsci.2012.02.005
47. Idrissia S, Khalladia R, Zitib S, El Mekkaouia N, Mtouguia S, Labrimc H, et al. The electronic and magnetic proprieties of the rare earth-based quaternary heusler compound LuCoVGe. *Physica B Condens Matter*. (2019) 562:116–23. doi: 10.1016/j.physb.2019.03.018
48. Rani D, Bainsla L, Suresha KG, Alam A. Experimental and theoretical investigation on the possible half-metallic behaviour of equiatomic quaternary heusler alloys: CoRuMnGe and CoRuVZ (Z = Al, Ga). *J Magn Magn Mater*. (2019) 492:165662. doi: 10.1016/j.jmmm.2019.165662
49. Forozani G, Abadi AAM, Baizaee SM, Gharaati A. Structural, electronic and magnetic properties of CoZrIrSi quaternary heusler alloy: first-principles study. *J Alloy Comp*. (2020) 815:152449. doi: 10.1016/j.jallcom.2019.152449
50. Wei XP, Gao PF, Zhang YL. Investigations on gilbert damping, curie temperatures and thermoelectric properties in CoFeCrZ quaternary heusler alloys. *Curr Appl Phys*. (2020) 20:593–603. doi: 10.1016/j.cap.2020.02.007
51. Mehmood N, Ahmad R, Murtaza G. Ab initio investigations of structural, elastic, mechanical, electronic, magnetic, and optical properties of half-heusler compounds RhCrZ (Z=Si, Ge). *J Supercond Novel Magn*. (2017) 30:2481–8. doi: 10.1007/s10948-017-4051-3
52. Huang YC, Guo XF, Ma YL, Shao HB, Xiao ZB. Stabilities, electronic and elastic properties of $L1_2$-$Al_3(Sc_{1-x},Zr_x)$ with different Zr content: a first-principles study. *Physica B Condens Matter*. (2018) 548:27–33. doi: 10.1016/j.physb.2018.08.019
53. Allali D, Bouhemadou A, Zerarga F, Ghebouli MA, Bin-Omran S. Prediction study of the elastic and thermodynamic properties of the $SnMg_2O_4$, $SnZn_2O_4$ and $SnCd_2O_4$ spinel oxides. *Comput Mater Sci*. (2012) 60:217–23. doi: 10.1016/j.commatsci.2012.03.044
54. Gu JB, Wang CJ, Zhang WX, Sun B, Liu GQ, Liu DD, et al. High-pressure structure and elastic properties of tantalum single crystal: first principles investigation. *Chin Phys B*. (2016) 25:126103. doi: 10.1088/1674-1056/25/12/126103
55. Slater JC. The ferromagnetism of nickel. II. Temperature effects. *Phys Rev*. (1936) 49:931. doi: 10.1103/PhysRev.49.931
56. Pauling L. The nature of the interatomic forces in metals. *Phys Rev*. (1938) 54:899. doi: 10.1103/PhysRev.54.899
57. Skaftouros S, Özdogan K, Sașioglu E, Galanakis I. Generalized slater-pauling rule for the inverse heusler compounds. *Phys Rev B*. (2013) 87:024420. doi: 10.1103/PhysRevB.87.024420
58. Khalaf Al-zyadi JM, Samuel RM, Gao GY, Yao KL. The half-metallic characteristics of the (001) surface of zinc-blende TiTe. *J Magn Magn Mater*. (2013) 346:166–70. doi: 10.1016/j.jmmm.2013.07.032
59. Galanakis I, Dederichs PH, Papanikolaou N. Origin and properties of the gap in the half-ferromagnetic heusler alloys, *Phys Rev B*. (2002) 66:134428. doi: 10.1103/PhysRevB.66.134428
60. Berri S. Electronic structure and half-metallicity of the new heusler alloys PtZrTiAl, PdZrTiAl and Pt 0.5 Pd 0.5 ZrTiAl. *Chin J Phys*. (2017) 55:195–202. doi: 10.1016/j.cjph.2016.10.017
61. Berri S, Ibrir M, Maouche D, Attallah M. Robust half-metallic ferromagnet of quaternary heusler compounds ZrCoTiZ(Z =Si, Ge, Ga and Al). *Comput Condens Matter*. (2017) 1:26–31. doi: 10.1016/j.cocom.2014.10.003

62. Berri S, Ibrir M, Maouche D, Attallah M. First principles study of structural, electronic and magnetic propertiesof ZrFeTiAl, ZrFeTiSi, ZrFeTiGe and ZrNiTiAl. *J Magn Magn Mater*. (2014) 371:106–11. doi: 10.1016/j.jmmm.2014.07.033
63. Xie HH, Gao Q, Li L,Lei G, Mao GY, Hu XR, Deng JB. First-principles study of four quaternary heusler alloys ZrMnVZ and ZrCoFeZ (Z=Si, Ge). *Comput Mater Sci*. (2015) 103:52–5. doi: 10.1016/j.commatsci.2015.03.010
64. Berri S, Maouche D, Ibrir M, Zerarga F. A first-principle study of half-metallic ferrimagnetism in the CoFeTiSb quaternary heusler compound. *J Magn Magn Mater*. (2014) 354:65–9. doi: 10.1016/j.jmmm.2013.10.044
65. Berri S. First-principles study on half-metallic properties of the CoMnCrSb quaternary Heusler compound. *J Supercond Nov Magn*. (2016) 29:1309–15. 10.1007/s10948-016-3404-7
66. Khalaf Al-zyadi JM,Kadhim AA, Yao KL. Electronic and magnetic properties of the (001) surface of the CoNbMnSi heusler alloy: first-principles calculations. *J Electron Spectrosc Relat Phenom*. (2018) 226:17–21. doi: 10.1016/j.elspec.2018.04.005
67. Rostamia M, Afkania M, Torkamania MR, Kanjouri F. Bulk and surface DFT investigations of the electronic and magnetic properties of CsXNO (X=Mg, Ca and Sr) quaternary heusler alloys. *Mater Chem Phys*. (2020) 248:122923. doi: 10.1016/j.matchemphys.2020.122923
68. Wurmehl S, Fecher GH, Kandpal HC, Ksenofontov V, Felser C, Lin HJ, et al., Geometric, electronic, and magnetic structure of Co_2FeSi: Curie temperature and magnetic moment measurements and calculations. *Phys Rev B*. (2005) 72:184434. doi: 10.1103/PhysRevB.72.184434
69. Candan A, Ugur G, Charifi Z, Baaziz H, Ellialtioglu MR. Electronic structure and vibrational properties in cobalt-based full-Heusler compounds: a first principle study of Co_2MnX (X=Si, Ge, Al, Ga). *J Alloy Comp*. (2013) 560:215–22. doi: 10.1016/j.jallcom.2013.01.102

Conflict of Interest: The authors declare that the research was conducted in the absence of any commercial or financial relationships that could be construed as a potential conflict of interest.

frontiers in Chemistry

ORIGINAL RESEARCH
published: 10 July 2020
doi: 10.3389/fchem.2020.00526

Recent Insights Into Electronic Performance, Magnetism and Exchange Splittings in the Cr-substituted CaO

Bendouma Doumi[1,2], *Allel Mokaddem*[2,3], *Abdelkader Tadjer*[4] *and Adlane Sayede*[5]*

[1] *Department of Physics, Faculty of Sciences, Dr. Tahar Moulay University of Saida, Saida, Algeria,* [2] *Instrumentation and Advanced Materials Laboratory, University Center of Nour Bachir El-Bayadh, El-Bayadh, Algeria,* [3] *Technology Department, University Center of Nour Bachir El-Bayadh, El-Bayadh, Algeria,* [4] *Modelling and Simulation in Materials Science Laboratory, Physics Department, Djillali Liabes University of Sidi Bel-Abbes, Sidi Bel-Abbes, Algeria,* [5] *University of Artois, CNRS, Centrale Lille, Univ. Lille, UMR 8181 – UCCS – Unité de Catalyse et Chimie du Solide, Lens, France*

The first-principles computations of density functional theory are employed to characterize the structural properties, electronic structures, and ferromagnetism induced by Cr impurities in $Ca_{1-x}Cr_xO$ compounds at concentrations $x = 0.25$, 0.5, and 0.75. The dynamic stability is performed by the phonon spectra calculations. The structural parameters are computed by using Wu-Cohen generalized gradient approximation, while the electronic and magnetic properties are determined by the accurate Tran–Blaha-modified Becke–Johnson exchange potential. The crystal field, direct and indirect exchange splittings were investigated to determine the origin and stability of ferromagnetic state configuration. The $Ca_{1-x}Cr_xO$ systems have right half-metallicities, which are verified by the spin polarization of 100% and the integer values of total magnetic moments. The $Ca_{0.75}Cr_{0.25}O$, $Ca_{0.5}Cr_{0.5}O$, and $Ca_{0.25}Cr_{0.75}O$ are half-metallic ferromagnetic with flip-gaps of 1.495, 0.888, and 0.218 eV, respectively. Therefore, the $Ca_{1-x}Cr_xO$ materials are suitable candidates for possible applications of spin-injection in future semiconductors spintronics.

Keywords: first-principles calculations, electronic structures, ferromagnetism, exchange splittings, spintronics

OPEN ACCESS

Edited by:
Xiaotian Wang,
Southwest University, China

Reviewed by:
Yong Li,
Hangzhou Dianzi University, China
Liying Wang,
Tianjin University, China

****Correspondence:***
Adlane Sayede
adlane.sayede@univ-artois.fr

Specialty section:
This article was submitted to Theoretical and Computational Chemistry, a section of the journal Frontiers in Chemistry

Received: *04 April 2020*
Accepted: *22 May 2020*
Published: *10 July 2020*

Citation:
Doumi B, Mokaddem A, Tadjer A and Sayede A (2020) Recent Insights Into Electronic Performance, Magnetism and Exchange Splittings in the Cr-substituted CaO. Front. Chem. 8:526. doi: 10.3389/fchem.2020.00526

INTRODUCTION

In recent years, the exploitation of new materials for technological development has become an attractive area of research for the scientific community. Spintronics is a modern field emerging from quantum electronics relating to exploration and control of the electron spin; it is currently an important research topic because the spin-based devices have interesting multifunctional characteristics such as non-volatility, data-processing speed, higher integration densities (Elilarassi and Chandrasekaran, 2017; Rai et al., 2018). In the last years, the half-metal ferromagnetic (HMF) materials have attracted considerable interest due to their wide application in spintronic devices as magnetic sensors, tunnel junctions, and spin injection sources of electrons (Özdemir and Merdan, 2019). The diluted magnetic semiconductors (DMSs) are obtained from the III–V, II–VI, or IV–VI semiconductors doped with magnetic elements, inducing changes in their structural, electronic, and magnetic properties, which are related to the concentration of magnetic impurities. These materials have received a lot of attention for scientific research because they are promising

candidates for innovative applications in spintronics, as an example for non-volatile memories, optical switches, and magneto-optical devices (Ohno, 1998; Dietl et al., 2000; Wolf et al., 2001; Zuti et al., 2004; Sato et al., 2010; Kumar et al., 2014).

Alkaline earth chalcogenides are important materials with a wide technological application ranging from catalysis to microelectronics as well as in the area of electro- and photo-luminescent devices (Hakamata et al., 2005; Speziale et al., 2006; Murtaza et al., 2014). Among these compounds, the CaX (X = O, S, Se) has a closed-shell ionic environment, crystallizing in the rock-salt NaCl-type (B1) structure at ambient conditions (Doll et al., 1996; Mishra et al., 2012). Under high pressure, they undergo a first-order structural phase transition from the NaCl-type (B1) to the CsCl-type (B2) crystal structure (Luo et al., 1994; Doll et al., 1996; Dadsetani and Doosti, 2009; Mishra et al., 2012). The CaO calcium oxide can be a potential candidate as a DMS material according to several theoretical studies (Kenmochi et al., 2004; Kemmochi et al., 2005; An Dinh et al., 2006). Kenmochi et al. (2004) have studied a new class of DMSs based on CaO without transition metals, where the substituted CaO by C and N at the oxygen sites shows room-temperature ferromagnetism with half-metallic property. The ferromagnetism in C-doped CaO is explained by the exchange coupling constants, where it is induced by the strong hybridization between 2p states of carbon and 2p states of oxygen (An Dinh et al., 2006). Further, Kemmochi et al. (2005) have found that the stability of ferromagnetic state in the C-doped CaO is originated from the Zener's double-exchange mechanism.

In this study, we have investigated the structural parameters, electronic performance, magnetism, and exchange splittings of $Ca_{1-x}Cr_xO$ materials at various concentrations $x = 0$, 0.25, 0.5, and 0.75. The calculations are performed by the use of first-principle approaches of density functional theory (DFT) (Hohenberg and Kohn, 1964; Kohn and Sham, 1965) as implemented in the WIEN2k package (Blaha et al., 2001). The phonon spectra are used to verify the dynamic stability of $Ca_{1-x}Cr_xO$ materials. The exchange and correlation potential is evaluated by the generalized gradient approximation of Wu and Cohen (GGA-WC) (Wu and Cohen, 2006), and the Tran–Blaha-modified Becke–Johnson potential (TB-mBJ) (Tran and Blaha, 2009).

COMPUTATIONAL METHODS

The calculations of structural, electronic, and magnetic properties of $Ca_{1-x}Cr_xO$ are carried out using the WIEN2k code (Blaha et al., 2001) based on the first-principle computations of DFT and the full-potential linearized augmented plane-wave (FP-LAPW) method (Singh and Nordstrom, 2006). We have computed the structural parameters using GGA-WC approximation (Wu and Cohen, 2006), while the electronic and magnetic properties are determined by employing the TB-mBJ exchange potential (Becke and Johnson, 2006; Tran and Blaha, 2009). The phonon frequencies are determined by the phonopy code (Togo and Tanaka, 2015) based on the density functional perturbation theory (Giannozzi et al., 1991; Gonze and Lee, 1997). The phonon spectra are calculated using the WIEN2k and the phonopy packages to verify the dynamic stability of $Ca_{1-x}Cr_xO$ doping compounds.

The averages of Muffin-tin spheres radii are selected for Ca, Cr, and O atoms in condition that Muffin-tin spheres do not overlap. The cutoff of -6 Ry is utilized to separate between the valence and core states. The basic functions and the potentials are extended in combination of spherical harmonics around the atomic sites, that is to say, the atomic spheres with a cutoff $l_{max} = 10$, and in the interstitial region are extended into plane waves with a cutoff $R_{MT}k_{max} = 8$ (where R_{MT} is the average radius of the Muffin-tin spheres). We have expanded the charge density in Fourier up to $G_{max} = 14$ $(a.u.)^{-1}$, where G_{max} represents the largest vector in the Fourier expansion. The calculations were performed for structures of eight (8) atoms of $Ca_{1-x}Cr_xO$ at concentrations $x = 0$, 0.25, 0.5, and 0.75 such as CaO, $Ca_{0.75}Cr_{0.25}O$, $Ca_{0.5}Cr_{0.5}O$, and $Ca_{0.25}Cr_{0.75}O$ supercells. The integration of the Brillouin zone was carried out by the Monkhorst–Pack mesh (Monkhorst and Pack, 1976) using the special k-points of $(10 \times 10 \times 10)$ for CaO and $(5 \times 5 \times 5)$ for $Ca_{0.75}Cr_{0.25}O$, $Ca_{0.5}Cr_{0.5}O$, and $Ca_{0.25}Cr_{0.75}O$ compounds. The self-consistent is achieved when the total energy convergence condition was set to be 10^{-1} mRy.

RESULTS AND DISCUSSION

Structural Properties

Crystal Structures

The calcium oxide CaO is known as a wide-band gap II–VI semiconductor, crystallizing in rock-salt NaCl (B1) structure at ambient conditions (Doll et al., 1996; Mishra et al., 2012). The primitive unit cell of CaO contains two atoms such as the calcium (Ca) and the oxygen (O), which belong, respectively, to the main groups II and VI of the periodic table. Our study is based on the conventional NaCl structure of eight atoms of CaO such as Ca_4O_4, where the Ca is located at (0, 0, 0) position and the O atom at (0.5, 0.5, 0.5) with space group of $Fm\bar{3}m$ No. 225. The Ca_3CrO_4, $Ca_2Cr_2O_4$, and $CaCr_3O_4$ supercells are created by substituting one, two, and three Cr impurities at Ca sites, respectively. Consequently, we have obtained three supercells such as $Ca_{0.75}Cr_{0.25}O$ at concentration $x = 0.25$, $Ca_{0.5}Cr_{0.5}O$ at $x = 0.5$ and $Ca_{0.25}Cr_{0.75}O$ at $x = 0.75$. The $Ca_{0.75}Cr_{0.25}O$ and $Ca_{0.25}Cr_{0.75}O$ have cubic lattices with space group of $Pm\bar{3}m$ No 221, while the $Ca_{0.5}Cr_{0.5}O$ supercell has a tetragonal lattice with space group of *P4/mmm* No. 123. We have noticed that all symmetry operations have been considered in the initialization of structures of $Ca_{1-x}Cr_xO$ supercells for computations of different properties.

Structural Stability

The structural stability of the $Ca_{1-x}Cr_xO$ compounds in the ferromagnetic rock-salt NaCl (B1) structure is verified by computing the formation energies. The formation energies (E_{form}) of the $Ca_{4-y}Cr_yO_4$ materials are determined using the following expression (Bai et al., 2011; Doumi et al., 2015a):

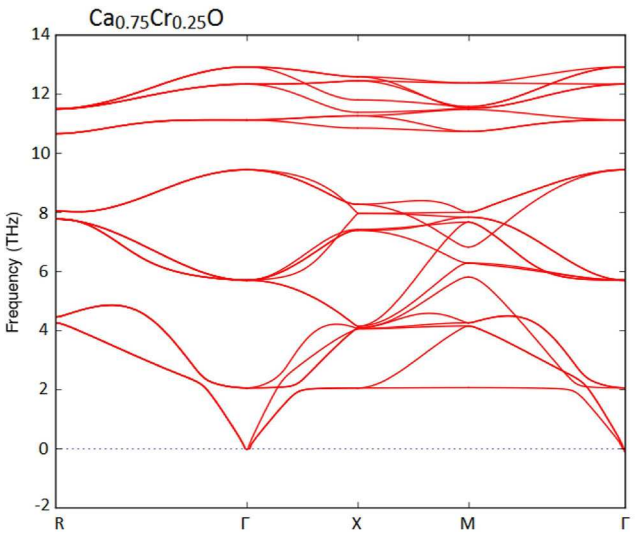

FIGURE 1 | Phonon spectra for $Ca_{0.75}Cr_{0.25}O$.

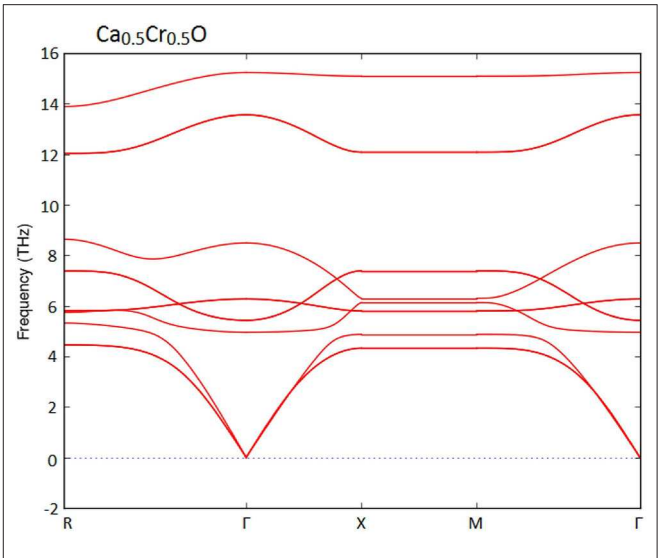

FIGURE 2 | Phonon spectra for $Ca_{0.5}Cr_{0.5}O$.

$$E_{\text{form}} = E_{\text{total}}(Ca_{4-y}Cr_yO_4) - \left(\frac{(4-y)\,E(\text{Ca})}{8}\right) - \left(\frac{y\,E(\text{Cr})}{8}\right) - \left(\frac{4\,E(\text{O})}{8}\right) \quad (1)$$

where $E_{\text{total}}(Ca_{4-y}Cr_yO_4)$ corresponds to the minimum total energy of $Ca_{4-y}Cr_yO_4$ per atom, and E(Ca), E(Cr), and E(O) refer to the minimum total energies per atom of bulks Ca, Cr, and O, respectively. The $y = 1$, 2, and 3 are the number of substituted Cr impurities in $Ca_{4-y}Cr_yO_4$ supercells. We have found that the formation energies are −5.99, −6.37, and −6.76 eV, respectively, for $Ca_{0.75}Cr_{0.25}O$, $Ca_{0.5}Cr_{0.5}O$, and $Ca_{0.25}Cr_{0.75}O$. Therefore, the negative values of formation energies suggest that these compounds are thermodynamically stable in the ferromagnetic rock-salt structure.

Furthermore, we have used the phonon spectra to demonstrate the dynamic stability of the $Ca_{1-x}Cr_xO$ doping compounds. The diagrams of phonon frequencies at high symmetry points in the Brillouin zone of $Ca_{0.75}Cr_{0.25}O$, $Ca_{0.5}Cr_{0.5}O$, and $Ca_{0.25}Cr_{0.75}O$ are shown by **Figures 1–3**, respectively. These figures depicted that all branches of phonons have positive frequencies, and there are no negative frequencies (Deng et al., 2019), confirming the dynamic stability of $Ca_{0.75}Cr_{0.25}O$, $Ca_{0.5}Cr_{0.5}O$, and $Ca_{0.25}Cr_{0.75}O$ compounds.

Equilibrium Structural Parameters

The variations of total energies as a function of volumes of $Ca_{1-x}Cr_xO$ compounds are fitted by Murnaghan (1944) equation of state to determine the equilibrium structural parameters. **Table 1** summarizes the lattice constants, the bulk modules, and their first derivatives with other experimental data (Mammone et al., 1981; Kaneko et al., 1982; Richet et al., 1988) and theoretical values (Tran et al., 2007; Wu et al., 2014; Cinthia et al., 2015; Fan et al., 2015; Nejatipour and Dadsetani, 2015; Santana et al., 2016; Yang et al., 2016; Salam, 2018) computed by the generalized gradient approximation of Perdew–Burke–Ernzerhof (GGA-PBE) (Perdew et al., 1996), revised GGA of Perdew–Burke–Ernzerhof (GGA-PBEsol) (Perdew et al., 2008) and the local density approximation (LDA) (Perdew and Zunger, 1981; Perdew and Wang, 1992).

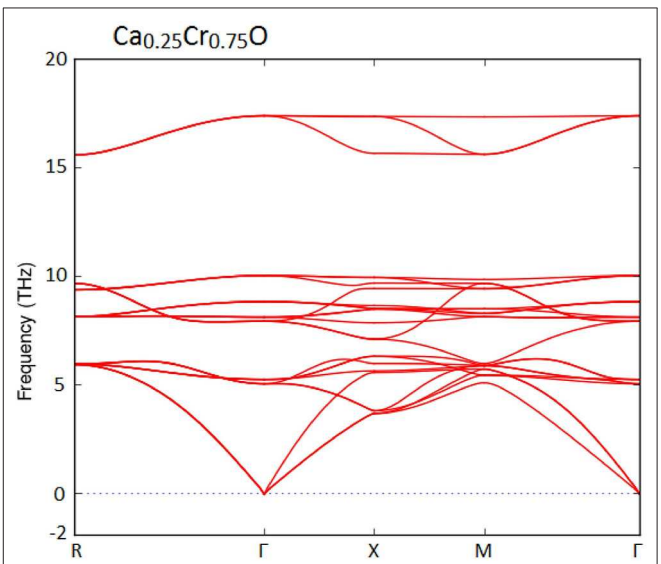

FIGURE 3 | Phonon spectra for $Ca_{0.25}Cr_{0.75}O$.

The results of lattice constants and bulk modulus of CaO are closed to theoretical values of Tran et al. (2007) and Fan et al. (2015) calculated with GGA-WC potential (Wu and Cohen, 2006). We see that there is a good agreement between our calculations and experimental results (Mammone et al., 1981; Kaneko et al., 1982; Richet et al., 1988) and theoretical value

TABLE 1 | Computed structural parameters such as lattice constants (*a*), bulk modules (*B*), and their pressure derivatives (*B′*) for $Ca_{1-x}Cr_xO$ materials at concentrations $x = 0$, 0.25, 0.5, and 0.75 with other experimental and theoretical data.

Material	*a* (Å)	*B* (GPa)	*B′*	Method	References
This work				Generalized gradient approximation of Wu and Cohen (GGA-WC)	
CaO	4.772	113.15	4.44		
$Ca_{0.75}Cr_{0.25}O$	4.660	126.40	4.63		
$Ca_{0.5}Cr_{0.5}O$	4.549	128.91	3.63		
$Ca_{0.25}Cr_{0.75}O$	4.415	133.23	3.75		
Other calculations					
CaO	4.812			Experimental	Kaneko et al., 1982
		111	4.2	Experimental	Richet et al., 1988
	4.8105	115	4.1	Experimental	Mammone et al., 1981
	4.777	116		GGA-WC	Tran et al., 2007
	4.77			GGA-WC	Fan et al., 2015
	4.841	105		Generalized gradient approximation of Perdew–Burke–Ernzerhof (GGA-PBE)	Tran et al., 2007
	4.81			GGA-PBE	Fan et al., 2015
	4.857			GGA-PBE	Wu et al., 2014
	4.843	107	4.2	GGA-PBE	Cinthia et al., 2015
	4.84			GGA-PBE	Nejatipour and Dadsetani, 2015
	4.834			GGA-PBE	Yang et al., 2016
	4.836	102.3	4.17	GGA-PBE	Salam, 2018
	4.77			Revised GGA of Perdew–Burke–Ernzerhof (GGA-PBEsol)	Fan et al., 2015
	4.719	129		Local density approximation (LDA)	Tran et al., 2007
	4.71			LDA	Fan et al., 2015
	4.734	119.54	4.23	LDA	Santana et al., 2016

found by GGA-PBE sol (Perdew et al., 2008). On the other hand, the obtained values of these parameters with GGA-WC (Wu and Cohen, 2006) are better than the calculations of Tran et al. (2007), Wu et al. (2014) Cinthia et al. (2015), Nejatipour and Dadsetani (2015), Yang et al. (2016), Salam (2018), Tran et al. (2007), Fan et al. (2015), and Santana et al. (2016) found, respectively, by GGA-PBE (Perdew et al., 1996) and LDA approximation (Perdew and Zunger, 1981; Perdew and Wang, 1992). The performance of GGA-WC approximation for predicting structural parameters is due to the fourth-order gradient expansion of exchange-correlation functional (Doumi et al., 2015b; Sajjad et al., 2015). For the $Ca_{1-x}Cr_xO$ doping compounds, the ionic radius of Cr is lower than that of Ca atom, leading to decrease in the lattice constant with increasing Cr concentration. Consequently, the bulk modulus of $Ca_{1-x}Cr_xO$ increases with increasing concentration of Cr. The $Ca_{1-x}Cr_xO$ doping compound becomes harder as the concentration of Cr increases.

Electronic Properties

Band Structures and Half-Metallicity

We have used the predicted structural parameters to characterize the electronic structures and the half-metallicity in $Ca_{1-x}Cr_xO$ compounds. The TB-mBJ potential is used to determine the electronic structures and accurate band gaps of $Ca_{1-x}Cr_xO$ compounds at concentration $x = 0$, 0.25, 0.5, and 0.75. The band structures of CaO, $Ca_{0.75}Cr_{0.25}O$, $Ca_{0.5}Cr_{0.5}O$, and $Ca_{0.25}Cr_{0.75}O$ are shown, respectively, by the **Figures 4**–**7**.

According to **Figure 4**, the CaO is a semiconductor because both majority and minority spins revealed the analogous band structures with indirect gaps. The CaO has an indirect gap($E^{\Gamma X}$) between the valence bands maximum and conduction bands minimum situated, respectively, at Γ and X high symmetry points. **Figures 5**–**7** demonstrate that the $Ca_{1-x}Cr_xO$ for all concentrations are metallic and semiconductors, respectively, for majority- and minority-spin bands. Consequently, the $Ca_{1-x}Cr_xO$ doping materials are half-metallic ferromagnets. The metallic character is due to localized partially filled 3d-Cr states of majority spins around Fermi level (E_F), which interact with carriers of valence states of host semiconductor. For minority spins, the $Ca_{1-x}Cr_xO$ doping systems keep a semiconductor behavior as CaO compound because the 3d-Cr empty minority-spin states arise in the bottom of conduction band minimum at Γ high symmetry point far than E_F. Thus, the gap nature shifted from indirect band gap for CaO to direct gap for $Ca_{1-x}Cr_xO$ doping systems.

The minority spins of $Ca_{1-x}Cr_xO$ systems are characterized by direct wide-band gaps called half-metallic ferromagnetic (HMF) gaps located at the Γ high symmetry point. The minimal energies that separate the Fermi level (zero eV), and the conduction band minimums determine the half-metallic (HM) gaps. **Table 2** shows the computed band gaps such as the direct HMF gaps

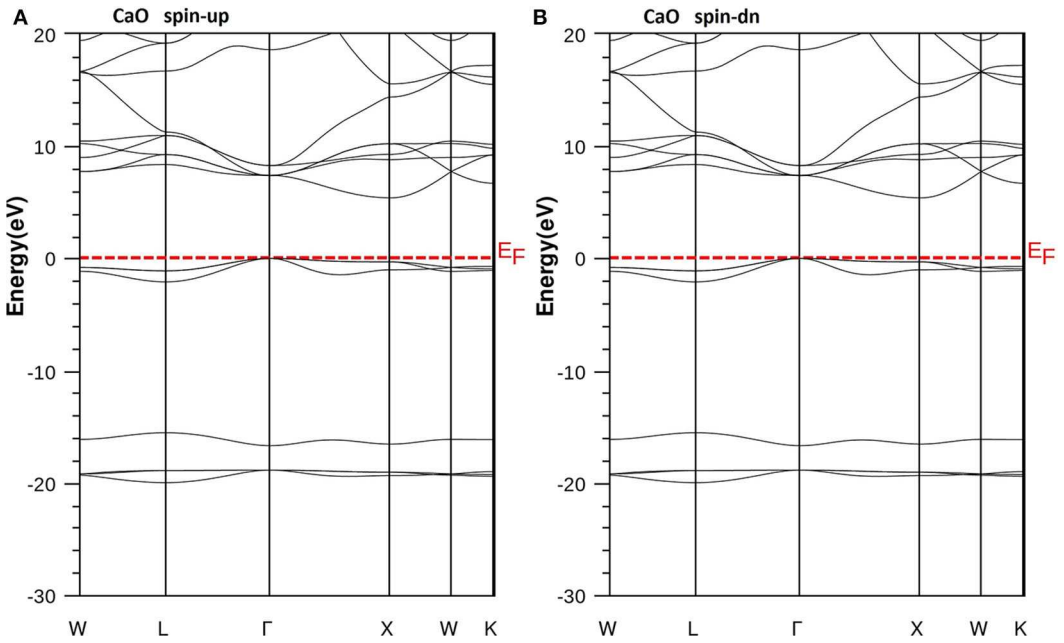

FIGURE 4 | Band structures of CaO. **(A)** Majority spins (*up*) and **(B)** minority spins (*dn*). The Fermi level is set to zero (*horizontal dotted line*).

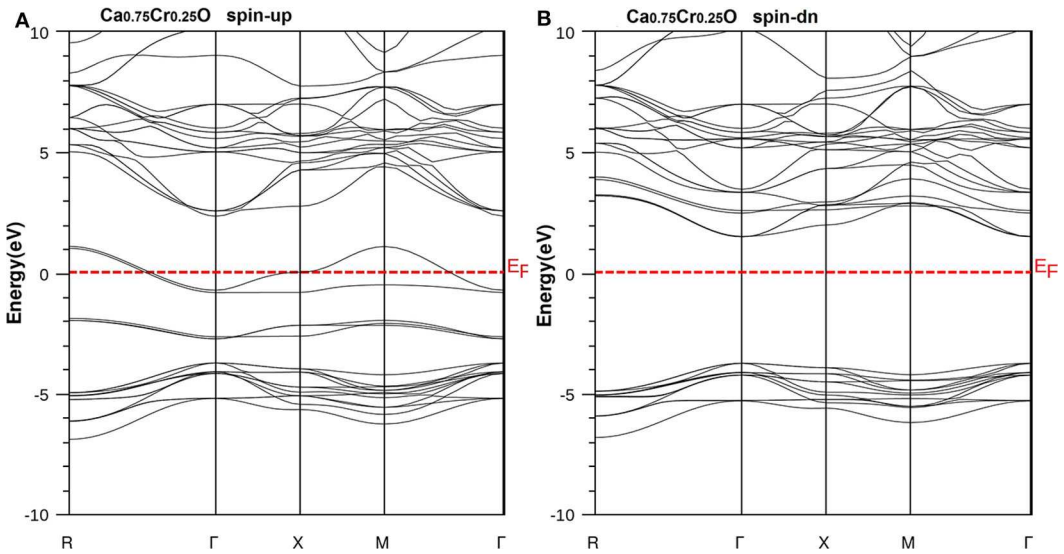

FIGURE 5 | Band structures of $Ca_{0.75}Cr_{0.25}O$. **(A)** Majority spins (*up*) and **(B)** minority spins (*dn*). The Fermi level is set to zero (*horizontal dotted line*).

(E_{HMF}) and HM gaps (E_{HM}) of $Ca_{0.75}Cr_{0.25}O$, $Ca_{0.5}Cr_{0.5}O$, and $Ca_{0.25}Cr_{0.75}O$, and the indirect gap ($E^{\Gamma X}$) of CaO with other theoretical (Fan et al., 2015; Nejatipour and Dadsetani, 2015; Yang et al., 2016; Tran and Blaha, 2017; Salam, 2018) and experimental data (Whited et al., 1973). The result of wide-indirect gap of 5.392 eV of CaO is in good agreement with recent calculated value of 5.35 eV of Tran and Blaha (2017) study using the same TB-mBJ potential (Becke and Johnson, 2006; Tran and Blaha, 2009), and it is better than the values ranging from 3.437 to 3.67 eV of Fan et al. (2015), Nejatipour and Dadsetani (2015), Yang et al. (2016), Tran and Blaha (2017), Salam (2018) found by the LDA (Perdew and Zunger, 1981; Perdew and Wang, 1992), GGA-WC (Wu and Cohen, 2006), GGA-PBE (Perdew et al., 1996), and GGA-PBEsol exchange potentials (Perdew et al., 2008). The TB-mBJ provides accurate gap for CaO because he is known for its performance in the calculation of electronic structures of insulators and semiconductors with respect to LDA and all forms of GGA approximations (Bhattacharjee and

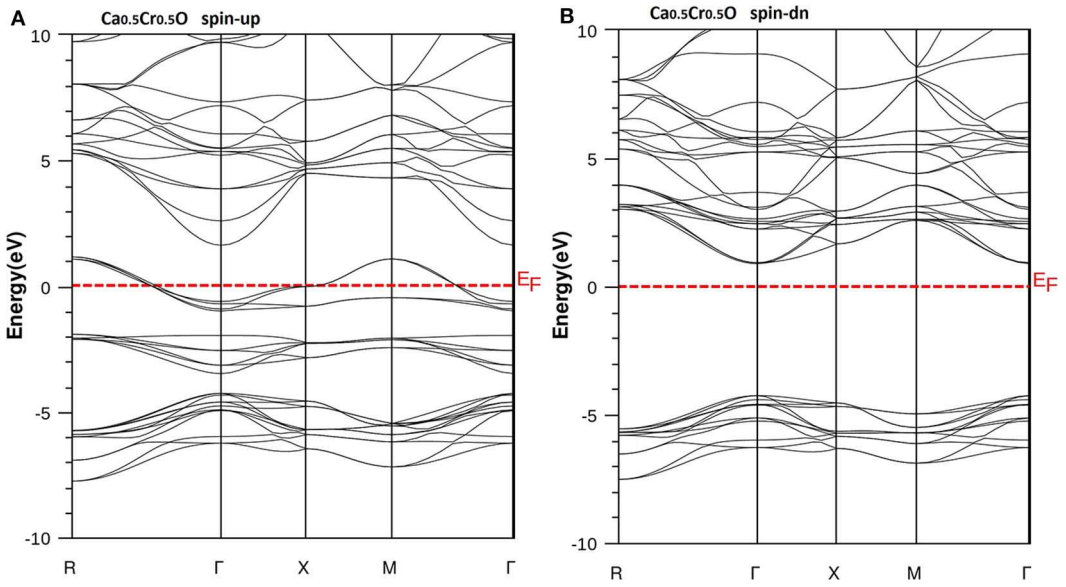

FIGURE 6 | Band structures of $Ca_{0.5}Cr_{0.5}O$. **(A)** Majority spins (*up*) and **(B)** minority spins (*dn*). The Fermi level is set to zero (*horizontal dotted line*).

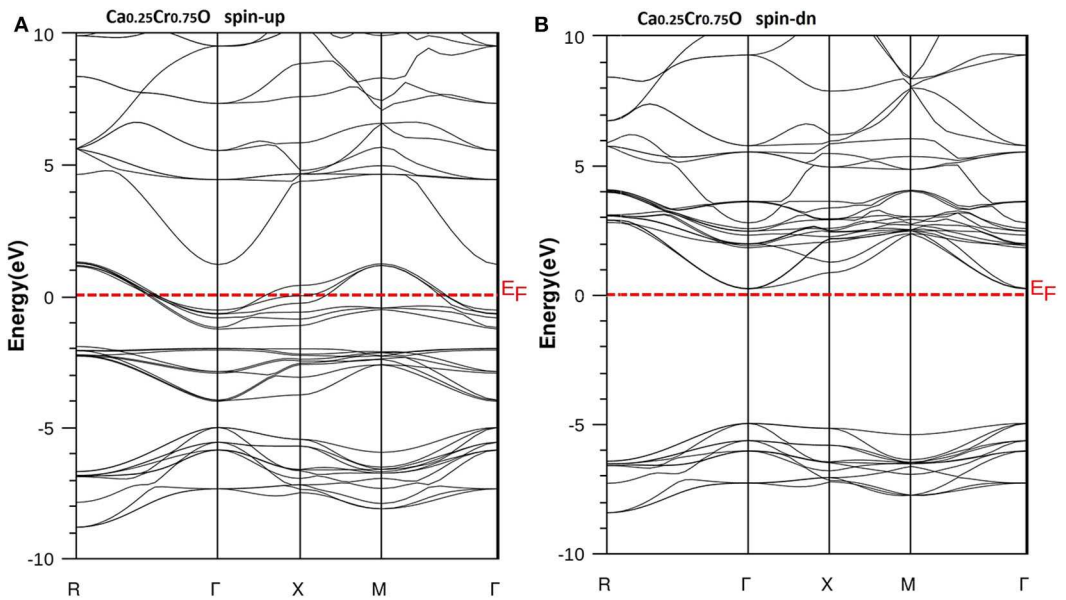

FIGURE 7 | Band structures of $Ca_{0.25}Cr_{0.75}O$. **(A)** Majority spins (*up*) and **(B)** minority spins (*dn*). The Fermi level is set to zero (*horizontal dotted line*).

Chattopadhyaya, 2017a,b; Chattopadhyaya and Bhattacharjee, 2017; Berriah et al., 2018).

Moreover, the half-metallic gap or flip-gap is an interesting performance for exploring the spin-injection for a half-metallic material in spintronics. The $Ca_{0.75}Cr_{0.25}O$, $Ca_{0.5}Cr_{0.5}O$, and $Ca_{0.25}Cr_{0.75}O$ compounds have the HM gaps of 1.495, 0.888, and 0.218 eV, respectively, situated between the conduction bands minimum (CBM) and E_F. The CBM moves toward E_F due to widening of 3d-Cr empty states at the bottom of conduction band, and hence, the HM gap decreases from $Ca_{0.75}Cr_{0.25}O$, $Ca_{0.5}Cr_{0.5}O$, to $Ca_{0.25}Cr_{0.75}O$. The HM gap behavior is maintained for different concentrations, meaning that the $Ca_{1-x}Cr_xO$ doping systems are right half-metallic materials.

Densities of States and Spin Polarization

In order to understand the origin of half-metallic feature induced by the substituting effect of Cr, we have plotted the total and partial densities of states (DOS) of Cr, Ca, and O atoms of $Ca_{1-x}Cr_xO$ compounds. **Figures 8–10** show, respectively, the DOS of $Ca_{0.75}Cr_{0.25}O$, $Ca_{0.5}Cr_{0.5}O$, and $Ca_{0.25}Cr_{0.75}O$. We

TABLE 2 | Computed band gaps such as indirect band gap ($E^{\Gamma x}$) for CaO, half-metallic ferromagnetic (HMF) gaps (E_{HMF}), and half-metallic (HM) gaps (E_{HM}) of minority-spin bands for $Ca_{1-x}Cr_xO$ at concentrations $x = 0.25$, 0.5, and 0.75 with other theoretical and experimental data.

Material	E_{HMF} (eV)	E_{HM} (eV)	$E^{\Gamma X}$ (eV)	Method	
This work					
CaO			5.392	Tran–Blaha-modified Becke–Johnson potential (TB-mBJ)	
$Ca_{0.75}Cr_{0.25}O$	5.242	1.495		TB-mBJ	
$Ca_{0.5}Cr_{0.5}O$	5.142	0.888		TB-mBJ	
$Ca_{0.25}Cr_{0.75}O$	5.195	0.218		TB-mBJ	
Other calculations					
CaO			3.53	GGA-WC	Fan et al., 2015
			3.647	GGA-PBE	Fan et al., 2015
			3.669	GGA-PBE	Nejatipour and Dadsetani, 2015
			3.65	GGA-PBE	Yang et al., 2016
			3.658	GGA-PBE	Salam, 2018
			3.67	GGA-PBE	Tran and Blaha, 2017
			3.518	GGA-PBEsol	Fan et al., 2015
			3.437	LDA	Fan et al., 2015
			3.49	LDA	Tran and Blaha, 2017
			5.35	TB-mBJ	Tran and Blaha, 2017
			7.00	Experimental	Whited et al., 1973

clearly see that all compounds are metallic for majority spin and semiconductors for minority spin, where their bonding, non-bonding, and anti-bonding states are distinguished from each other by the contributions of the DOS formed by different orbitals of each Ca, O, and Cr atoms.

The partial DOS of **Figures 8–10B** revealed that the 3d-Cr states are splitted into the low-lying t_{2g} and high-lying e_g states owing to the effect of octahedral crystal field created by neighboring oxygen (O) ions. For both minority and majority spins, the bonding states are mainly contributed by the p-O states and by the small p-Ca and 3d-Cr states in the ranges of −6.5 to −4, −7.5 to −4.5, and −8.25 to −5.25 eV, respectively, for $Ca_{0.75}Cr_{0.25}O$, $Ca_{0.5}Cr_{0.5}O$, and $Ca_{0.25}Cr_{0.75}O$. For the majority spins of $Ca_{1-x}Cr_xO$, the non-bonding states are principally dominated by the t_{2g}-(3d-Cr) fully filled levels that hybridize largely with p-O orbitals, while the anti-bonding states are mostly contributed by the hybridization of the e_g-(3d-Cr) levels and p-O states around E_F. However, the upper part of valence bands of majority spins is originated from both t_{2g}-(3d-Cr) non-bonding states and e_g-(3d-Cr) anti-bonding states, which extend strongly in the gap owing to broadening of 3d-Cr levels around E_F.

Furthermore, the upper part of valence bands of minority spins are formed by the bonding states originated from the p-O orbitals, which are centered at −5.25, −6, and −6.75 eV for $Ca_{0.75}Cr_{0.25}O$, $Ca_{0.5}Cr_{0.5}O$, and $Ca_{0.25}Cr_{0.75}O$, respectively. The bottom of conduction band is generated predominantly by the 3d-Cr empty anti-bonding states, which move to lower energies toward Fermi level from $Ca_{0.75}Cr_{0.25}O$, $Ca_{0.5}Cr_{0.5}O$, to $Ca_{0.25}Cr_{0.75}O$ with increasing Cr concentration. Therefore, the distinguish half-metallic ferromagnetic and half-metallic gaps are created around E_F in minority spins for $Ca_{0.75}Cr_{0.25}O$, $Ca_{0.5}Cr_{0.5}O$, and $Ca_{0.25}Cr_{0.75}O$ materials.

The spin-polarized material is known by its spin polarization of electronic structures, which is an important factor for characterizing a half-metal. The polarization (P) of half-metal compound results from the different contributions of numbers of DOS around E_F. It is determined from the following expression (Soulen et al., 1998; Wang et al., 2017):

$$P = \frac{\left|N\uparrow(E_F) - N\downarrow(E_F)\right|}{\left|N\uparrow(E_F) + N\downarrow(E_F)\right|} \quad (2)$$

where $N\uparrow(E_F)$ and $N\downarrow(E_F)$ indicate, respectively, the DOS of majority and minority spins at E_F. From **Figures 8–10A**, the density of states $N\downarrow(E_F)$ equals zero because the DOS do not cross E_F, leading to a spin polarization of 100%. Therefore, the $Ca_{1-x}Cr_xO$ compounds appear to be suitable candidates for possible spin-injection in spintronics applications.

Magnetic Properties

Magnetic Moments

The spin-polarized electronic structures show an asymmetric character, indicating that the $Ca_{1-x}Cr_xO$ compounds are magnetic in nature. The magnetism is induced by the magnetic spins arising from the localized 3d-Cr majority-spin states around E_F. The Cr impurity contributes two electrons to host carriers of valence bands, resulting in Cr^{+2} ion. Thus, the 3d-Cr states become partially filled with four electrons. Therefore, the magnetism is originated from the four itinerant electrons of Cr^{+2} ions in $Ca_{1-x}Cr_xO$ doping materials.

From the DOS of majority spins, one can see that the non-bonding states enclose three low-lying t_{2g} levels, which are completely occupied by three electrons. In contrast, the two high-lying e_g states have an anti-bonding nature, which are partially occupied by one electron because they are crossed by Fermi level in the middle. According to the Hund's rule, the 3d-Cr states generate a total magnetic moment of 4 μ_B per Cr ion. Consequently, the $Ca_{0.75}Cr_{0.25}O$, $Ca_{0.5}Cr_{0.5}O$, and $Ca_{0.25}Cr_{0.75}O$ compounds have total magnetic moments of 4, 8, and 12 μ_B, respectively, for one, two, and three Cr doping impurities.

The calculated total and partial magnetic moments of Ca, Cr, and O atoms and in the interstitial sites for $Ca_{0.75}Cr_{0.25}O$, $Ca_{0.5}Cr_{0.5}O$, and $Ca_{0.25}Cr_{0.75}O$ are given in **Table 3**. The total magnetic moment per Cr atom is an integer number of 4 μ_B. It is a typical feature of half-metallic materials (Wang et al., 2017; Zhang et al., 2017). All compounds have negative partial magnetic moments for O atoms, revealing that carriers of host valence bands enclosing p-O states interact anti-ferromagnetically with 3d-Cr states. Besides, the positive partial magnetic moments of Cr and Ca atoms describe the ferromagnetic interaction between Cr and Ca magnetic spins.

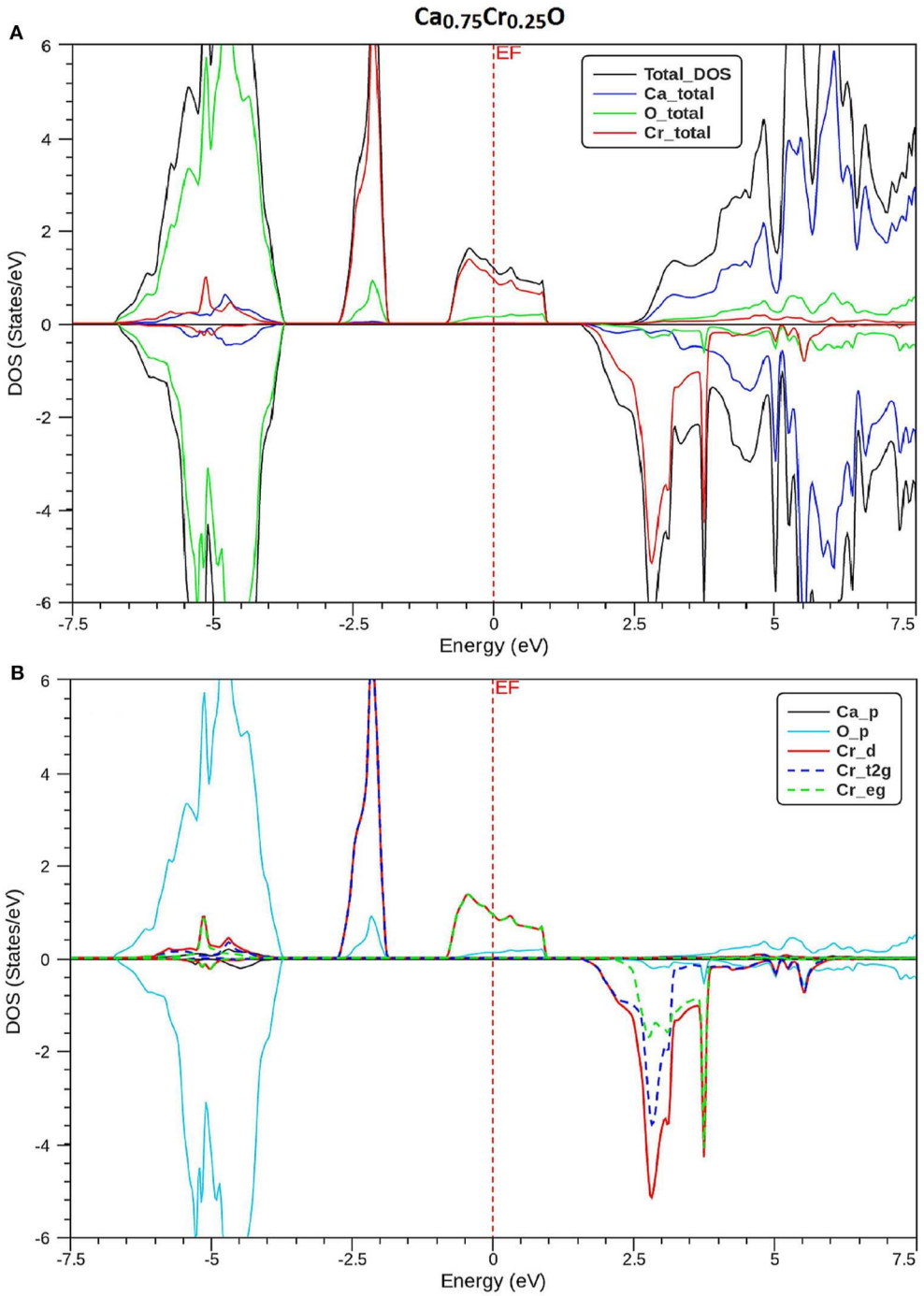

FIGURE 8 | Spin-polarized total and partial densities of states (DOS) of $Ca_{0.75}Cr_{0.25}O$. The Fermi level is set to zero (*vertical dotted line*). **(A)** Total DOS of Ca, Cr, and O and **(B)** Partial DOS of p-Ca, p-O, d-Cr, t2g_d-Cr, and eg_d-Cr.

Exchange Splitting Mechanisms

The ferromagnetism is created from the localized electrons of t_{2g} and e_{2g} of 3d-Cr states mediated by holes, where the empty holes of e_g states occur at the top of valence band and generate an acceptor hole type carrier hybridizing with carriers of host valence band (Doumi et al., 2013). The degenerate 3d-Cr into t_{2g} and e_{2g} is due to crystal field generated from the electrostatic environment of surrounding oxygen (O) ions, where the 3d-Cr majority-spin levels contain four unpaired electrons (Noor et al., 2018). According to the Hund's rule, this kind of process mediates magnetism in $Ca_{1-x}Cr_xO$ materials (Yaqoob et al., 2019). It is understood that both exchange splitting of 3d-Cr states and

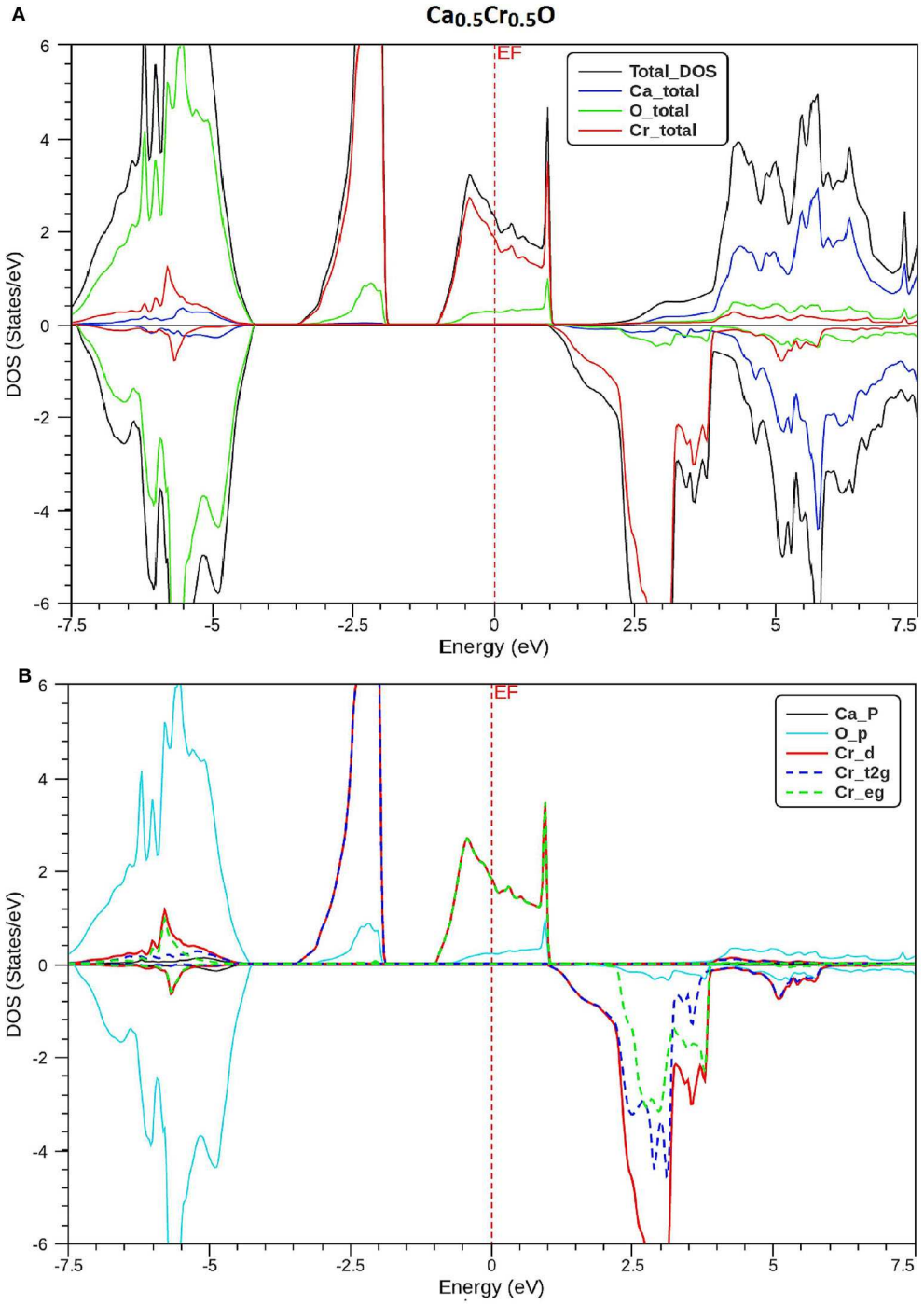

FIGURE 9 | Spin-polarized total and partial densities of states (DOS) of $Ca_{0.5}Cr_{0.5}O$. The Fermi level is set to zero (*vertical dotted line*). **(A)** Total DOS of Ca, Cr, and O and **(B)** DOS of p-Ca, p-O, d-Cr, t2g_d-Cr, and eg_d-Cr.

crystal field take part in the contribution of ferromagnetism in $Ca_{1-x}Cr_xO$ doping materials.

The magnitude of crystal field energy (ΔE_{CF}) is defined as a difference between E_{eg} and E_{t2g} energies of e_g and t_{2g} states $\left(\Delta E_{CF} = E_{eg} - E_{t2g}\right)$. The direct exchange splitting energy $\Delta_x(d) = d\downarrow - d\uparrow$ is determined from the separation between the empty d-Cr ($d\downarrow$) minority-spin and occupied d-Cr ($d\uparrow$) majority-spin peaks. Another factor is used to determine the magnitude of ferromagnetism such as the indirect $\Delta_x(pd) = E_v^{\downarrow} - E_v^{\uparrow}$ exchange splitting resulted from the energy difference

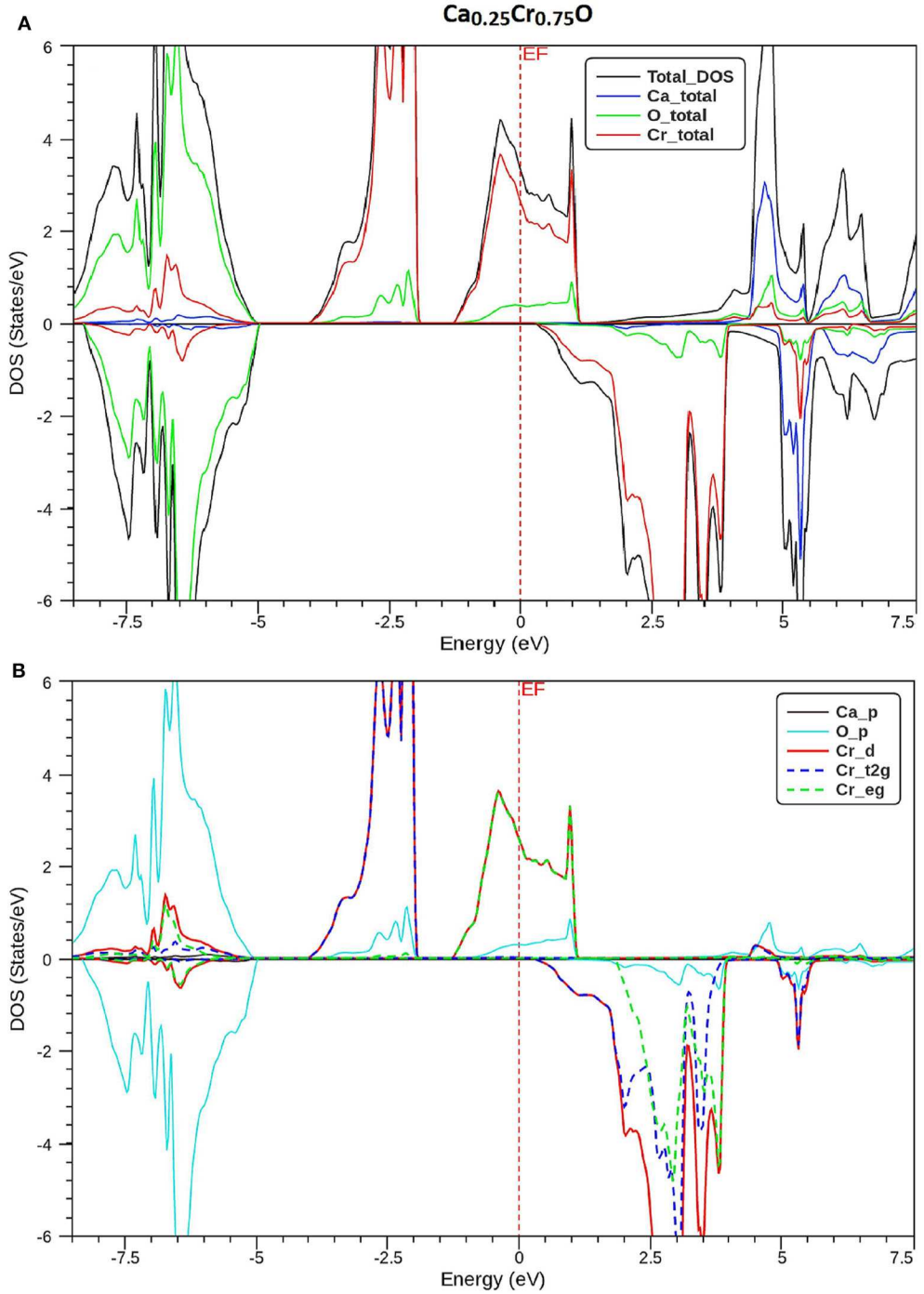

FIGURE 10 | Spin-polarized total and partial densities of states (DOS) of $Ca_{0.25}Cr_{0.75}O$. The Fermi level is set to zero (*vertical dotted line*). **(A)** Total DOS of Ca, Cr, and O and **(B)** Partial DOS of p-Ca, p-O, d-Cr, t2g_d-Cr, and eg_d-Cr.

between $E_v^{\downarrow}$ and $E_v^{\uparrow}$ valence band maximums of minority- and majority-spin channels, respectively.

The values of ΔE_{CF}, $\Delta_x(d)$, and$\Delta_x(pd)$ exchange splitting are shown in **Table 4**. The obtained values of (ΔE_{CF} and $\Delta_x(d)$) are (1.71 and 4.98 eV), (2.97 and 4.90 eV), and (1.74 and 5.17 eV), revealing that the direct exchange splittings are more dominated compared to the crystal field splittings. Therefore, the ferromagnetism state is mainly favored by the contribution of direct exchange splitting mechanism than that of crystal field (Amin et al., 2018). Besides, the partial magnetic moment of Cr increases from 3.652 μ_B for $Ca_{0.75}Cr_{0.25}O$, 7.203 μ_B for $Ca_{0.5}Cr_{0.5}O$, to 10.541 μ_B for $Ca_{0.25}Cr_{0.75}O$ with decreasing

TABLE 3 | Computed total and partial magnetic moments of the relevant Cr, Ca, and O atoms and in the interstitial sites (in Bohr magneton μ_B) for $Ca_{1-x}Cr_xO$ at concentrations $x = 0.25$, 0.5, and 0.75.

Material	Total	Cr	Ca	O	Interstitial
$Ca_{0.75}Cr_{0.25}O$	4	3.652	0.009	−0.075	0.414
$Ca_{0.5}Cr_{0.5}O$	8	7.203	0.011	−0.049	0.835
$Ca_{0.25}Cr_{0.75}O$	12	10.541	0.009	−0.059	1.391

TABLE 4 | Computed energies of crystal field ΔE_{CF}, direct $\Delta_x(d)$, and indirect $\Delta_x(pd)$exchange splittings for $Ca_{1-x}Cr_xO$ at concentrations $x = 0.25$, 0.5, and 0.75.

Material	ΔE_{CF} (eV)	Δ_x(d) (eV)	Δ_x(pd) (eV)
$Ca_{0.75}Cr_{0.25}O$	1.71	4.98	−3.75
$Ca_{0.5}Cr_{0.5}O$	2.97	4.90	−4.25
$Ca_{0.25}Cr_{0.75}O$	1.74	5.17	−4.97

TABLE 5 | Computed conduction band-edge ΔE_c(eV) and valence band-edge ΔE_v(eV) spin-splittings, and sp-d exchange constants $N_0\alpha$ and $N_0\beta$ for $Ca_{1-x}Cr_xO$ at concentrations $x = 0.25$, 0.5, and 0.75.

Material	ΔE_c (eV)	ΔE_v (eV)	$N_0\alpha$	$N_0\beta$
$Ca_{0.75}Cr_{0.25}O$	−0.858	−3.030	−1.716	−6.060
$Ca_{0.5}Cr_{0.5}O$	−0.741	−3.643	−0.741	−3.643
$Ca_{0.25}Cr_{0.75}O$	−0.972	−4.431	−0.648	−2.954

$\Delta_x(pd)$, meaning that magnetic moment of Cr is directly related to the indirect exchange splitting. On the other hand, the attraction nature of spin-polarized electrons is measured from the indirect exchange splitting (Verma et al., 2011; Mahmood et al., 2016, 2018). The indirect exchange splittings $\Delta_x(pd)$ have negative values because the valence band maximums of minority-spins are situated at lower energies with respect to the valence band maximums of majority-spins. This means that the minority-spins have more attractive (negative) potential than that of majority-spins, leading to perfectly localized magnetic states. Consequently, the ferromagnetism is preferred in the $Ca_{1-x}Cr_xO$ compounds. In the DMS based on III–V and II–VI semiconductors doped with transition metals, when the d states of magnetic dopants are partially occupied (Sato and Katayama-Yoshida, 2002; Sato et al., 2003a,b), the stability of ferromagnetism is described by the double-exchange mechanism (Akai, 1998). According to this rule, the anti-bonding states of partially filled 3d-Cr atoms associated with double-exchange mechanism stabilize the ferromagnetic state configuration in $Ca_{1-x}Cr_xO$.

The magnitudes of valence and conduction band edge splitting are measured by the two sp-d exchange constants $N_0\alpha$ and $N_0\beta$. The $N_0\alpha$ parameter determines the s-d exchange interaction between the s carriers of conduction bands and d-Cr levels, while the $N_0\beta$ describes the p-d exchange coupling between the p states of carriers of valence bands and d-Cr levels. We have used the mean field theory (Sanvito et al., 2001; Raebiger et al., 2004) to calculate the exchange constants of $Ca_{1-x}Cr_xO$ compounds given by the following relations.

$$N_0\alpha = \frac{\Delta E_c}{x\langle s\rangle} \tag{3}$$

$$N_0\beta = \frac{\Delta E_v}{x\langle s\rangle} \tag{4}$$

The $\Delta E_v = E_v^{\downarrow} - E_v^{\uparrow}$ and $\Delta E_c = E_c^{\downarrow} - E_c^{\uparrow}$ difference energies correspond, respectively, to the valence band-edge and conduction band-edge spin-splittings at Γ high symmetry point. The $\langle s\rangle$ and x are the half total magnetic moment per Cr and the concentration of Cr, respectively (Sanvito et al., 2001). The calculated ΔE_v, ΔE_c, $N_0\alpha$, and $N_0\beta$ are summarized in **Table 5**. Yaqoob et al. (2019) have predicted that the negative values of $N_0\alpha$ and $N_0\beta$ are due to the quantum confinement effect or structural symmetry changes that modify the coupling of different states. For $Ca_{1-x}Cr_xO$ materials, the negative values of $N_0\alpha$ and $N_0\beta$ describe the anti-ferromagnetic coupling between the valence and conduction bands and the 3d states of magnetic Cr atoms.

CONCLUSIONS

We have characterized the structural properties, the spin-polarized electronic structures, and ferromagnetic performance induced by the Cr impurities in $Ca_{1-x}Cr_xO$ compounds at concentrations $x = 0$, 0.25, 0.5, and 0.75. The $Ca_{1-x}Cr_xO$ doping materials are dynamically stable due to their positive phonon frequencies. The structural parameters and indirect gap of CaO are very significant with respect to the recent calculations found by GGA-WC and TB-mBJ. For $Ca_{1-x}Cr_xO$, the lattice constant decreases with increasing Cr concentration, leading to the increase in bulk modulus, where the sizes of the ionic radii of Ca and Cr atoms are the factors determining these changes. The $Ca_{1-x}Cr_xO$ systems have a half-metallic ferromagnetic feature, where the ferromagnetism is favored by the large contribution of direct exchange splitting than that of the crystal field. The analysis of magnetic properties shows that both double-exchange and p-d exchange mechanisms participate to stabilize ferromagnetic state configuration. The half-metallic ferromagnets $Ca_{1-x}Cr_xO$ compounds maintain a half-metal gap feature for all concentrations with spin polarization of 100%, making them suitable spin-injection candidates for possible exploration in semiconductors spintronics.

DATA AVAILABILITY STATEMENT

All datasets presented in this study are included in the article/supplementary material.

AUTHOR CONTRIBUTIONS

With the submission of this manuscript, all authors declare that the manuscript is original. All authors of this research

paper have contributed to this manuscript. All authors of this paper have read and approved the final version submitted. The contents of this manuscript have not been copyrighted or published previously. The contents of this manuscript are not now under consideration for publication elsewhere.

REFERENCES

Akai, H. (1998). Ferromagnetism and its stability in the diluted magnetic semiconductor (In, Mn) As. *Phys. Rev. Lett.* 81, 3002–3005. doi: 10.1103/PhysRevLett.81.3002

Amin, B., Majid, F., Saddique, M. B., Haq, B. U., Laref, A., Alrebdi, T. A., et al. (2018). Physical properties of half-metallic $AMnO_3$ (A= Mg, Ca) oxides via ab initio calculations. *Comp. Mater. Sci.* 146, 248–254. doi: 10.1016/j.commatsci.2018.01.033

An Dinh, V., Toyoda, M., Sato, K., and Katayama-Yoshida, H. (2006). Exchange interaction and Tc in alkaline-earth-metal-oxide-basedDMS without magnetic impurities: first principle pseudo-SIC and monte carlo calculation. *J. Phys. Soc. Jpn.* 75:093705. doi: 10.1143/JPSJ.75.093705

Bai, J., Raulot, J.-M., Zhang, Y., Esling, C., Zhao, X., and Zuo, L. (2011). The effects of alloying element Co on Ni–Mn–Ga ferromagnetic shape memory alloys from first-principles calculations. *Appl. Phys. Lett.* 98:164103. doi: 10.1063/1.3582239

Becke, A. D., and Johnson, E. R. (2006). A simple effective potential for exchange. *J. Chem. Phys.* 124:221101. doi: 10.1063/1.2213970

Berriah, K., Doumi, B., Mokaddem, A., Elkeurti, M., Sayede, A., Tadjer, A., et al. (2018). Theoretical investigation of electronic performance, half-metallicity, and magnetic properties of Cr-substituted BaTe. *J. Comput. Electron.* 17, 909–919. doi: 10.1007/s10825-018-1192-y

Bhattacharjee, R., and Chattopadhyaya, S. (2017a). Effects of barium (Ba) doping on structural, electronic and optical properties of binary strontium chalcogenide semiconductor compounds-A theoretical investigation using DFT based FP-LAPW approach. *Mater. Chem. Phys.* 199, 295–312. doi: 10.1016/j.matchemphys.2017.06.057

Bhattacharjee, R., and Chattopadhyaya, S. (2017b). Effects of doping of calcium atom (s) on structural, electronic and optical properties of binary strontium chalcogenides-A theoretical investigation using DFT based FP-LAPW methodology. *Solid State Sci.* 71, 92–110. doi: 10.1016/j.solidstatesciences.2017.06.010

Blaha, P., Schwarz, K., Madsen, G. K., Kvasnicka, D., and Luitz, J. (2001). *In WIEN2k, An Augmented Plane Wave + Local Orbitals Program for Calculating Crystal Properties*. ed K. Schwarz (Wien: Techn. Universitaet Wien).

Chattopadhyaya, S., and Bhattacharjee, R. (2017). Theoretical study of structural, electronic and optical properties of $Ba_xPb_{1-x}S$, $Ba_xPb_{1-x}Se$ and $Ba_xPb_{1-x}Te$ ternary alloys using FP-LAPW approach. *J. Alloy. Compd.* 694, 1348–1364. doi: 10.1016/j.jallcom.2016.10.096

Cinthia, A. J., Priyanga, G. S., Rajeswarapalanichamy, R., and Iyakutti, K. (2015). Structural, electronic and mechanical properties of alkaline earth metal oxides MO (M= Be, Mg, Ca, Sr, Ba). *J. Phys. Chem. Solids* 79, 23–42. doi: 10.1016/j.jpcs.2014.10.021

Dadsetani, M., and Doosti, H. (2009). The linear optical properties for NaCl phase of calcium mono chalcogenides by density functional theory. *Comp. Mater. Sci.* 45, 315–320. doi: 10.1016/j.commatsci.2008.10.003

Deng, J., Liu, N., Guo, J., and Chen, X. (2019). Large spin gaps in the half-metals MN_4 (M= Mn, Fe, Co) with N_2 dimers. *Phys. Rev. B* 99:184409. doi: 10.1103/PhysRevB.99.184409

Dietl, T., Ohno, H., Matsukura, F., Cibert, J., and Ferrand, E. D. (2000). Zener model description of ferromagnetism in zinc-blende magnetic semiconductors. *Science* 287, 1019–1022. doi: 10.1126/science.287.5455.1019

Doll, K., Dolg, M., and Stoll, H. (1996). Correlation effects in MgO and CaO: cohesive energies and lattice constants. *Phys. Rev. B* 54:13529. doi: 10.1103/PhysRevB.54.13529

Doumi, B., Mokaddem, A., Ishak-Boushaki, M., and Bensaid, D. (2015a). First-principle investigation of magnetic and electronic properties of vanadium-and chromium-doped cubic aluminum phosphide. *Mat. Sci. Semicon. Proc.* 32, 166–171. doi: 10.1016/j.mssp.2015.01.014

Doumi, B., Mokaddem, A., Sayede, A., Dahmane, F., Mogulkoc, Y., and Tadjer, A. (2015b). First-principles investigations on ferromagnetic behaviour of $Be_{1-x}V_xZ$ (Z= S, Se and Te)(x= 0.25). *Superlattice Microst.* 88, 139–149. doi: 10.1016/j.spmi.2015.09.008

Doumi, B., Tadjer, A., Dahmane, F., Mesri, D., and Aourag, H. (2013). Investigations of structural, electronic, and half-metallic ferromagnetic properties in $(Al, Ga, In)_{1-x}M_xN$ (M= Fe, Mn) diluted magnetic semiconductors. *J. Supercond. Novel. Magn.* 26, 515–525 doi: 10.1007/s10948-012-1808-6

Elilarassi, R., and Chandrasekaran, G. (2017). Optical, electrical and ferromagnetic studies of ZnO: Fe diluted magnetic semiconductor nanoparticles for spintronic applications. *Spectrochim. Acta A* 186, 120–131. doi: 10.1016/j.saa.2017.05.065

Fan, Q., Chai, C., Wei, Q., Yang, Y., Qiao, L., Zhao, Y., et al. (2015). Mechanical and electronic properties of $Ca_{1-x}Mg_xO$ alloys. *Mat. Sci. Semicon. Proc.* 40, 676–684. doi: 10.1016/j.mssp.2015.07.035

Giannozzi, P., De Gironcoli, S., Pavone, P., and Baroni, S. (1991). Ab initio calculation of phonon dispersions in semiconductors. *Phys. Rev. B* 43:7231. doi: 10.1103/PhysRevB.43.7231

Gonze, X., and Lee, C. (1997). Dynamical matrices, Born effective charges, dielectric permittivity tensors, and interatomic force constants from density-functional perturbation theory. *Phys. Rev. B* 55:10355. doi: 10.1103/PhysRevB.55.10355

Hakamata, S., Ehara, M., Kominami, H., Nakanishi, Y., and Hatanaka, Y. (2005). Preparation of CaS: Cu, F thin-film electroluminescent devices with an emission including purple region. *Appl. Surf. Sci.* 244, 469–472. doi: 10.1016/j.apsusc.2004.10.104

Hohenberg, P., and Kohn, W. (1964). Inhomogeneous electron gas. *Phys. Rev.* 136:B864. doi: 10.1103/PhysRev.136.B864

Kaneko, Y., Morimoto, K., and Koda, T. (1982). Optical properties of alkaline-earth chalcogenides. I. Single crystal growth and infrared reflection spectra due to optical phonons. *J. Phys. Soc. Jpn.* 51, 2247–2254. doi: 10.1143/JPSJ.51.2247

Kemmochi, K., Seike, M., Sato, K., Yanase, A., and Katayama-Yoshida, H. (2005). New class of high-TC diluted ferromagnetic semiconductors based on CaO without transition metal elements. *J. Supercond.* 18, 37–40. doi: 10.1007/s10948-005-2147-7

Kenmochi, K., Seike, M., Sato, K., Yanase, A., and Katayama-Yoshida, H. (2004). New class of diluted ferromagnetic semiconductors based on CaO without transition metal elements. *Jpn. J. Appl. Phys.* 43, L934–L936. doi: 10.1143/JJAP.43.L934

Kohn, W., and Sham, L. J. (1965). Self-consistent equations including exchange and correlation effects. *Phys. Rev.* 140, A1133–A1138. doi: 10.1103/PhysRev.140.A1133

Kumar, S., Negi, N., Katyal, S., Sharma, P., and Sharma, V. (2014). Structural, morphological and magnetic analysis of Cd–Co–S dilute magnetic semiconductor nanofilms. *J. Magn. Magn. Mater.* 367, 1–8. doi: 10.1016/j.jmmm.2014.04.065

Luo, H., Greene, R. G., Ghandehari, K., Li, T., and Ruoff, A. L. (1994). Structural phase transformations and the equations of state of calcium chalcogenides at high pressure. *Phys. Rev. B* 50, 16232–16237. doi: 10.1103/PhysRevB.50.16232

Mahmood, Q., Alay-E-Abbas, S., Hassan, M., and Noor, N. (2016). First-principles evaluation of Co-doped ZnS and ZnSe ferromagnetic semiconductors. *J. Alloy. Compd.* 688, 899–907. doi: 10.1016/j.jallcom.2016.07.302

Mahmood, Q., Ali, S., Hassan, M., and Laref, A. (2018). First principles study of ferromagnetism, optical and thermoelectric behaviours of AVO_3 (A= Ca, Sr, Ba) perovskites. *Mater. Chem. Phys.* 211, 428–437. doi: 10.1016/j.matchemphys.2018.03.019

Mammone, J., Mao, H., and Bell, P. (1981). Equations of state of CaO under static pressure conditions. *Geophys. Res. Lett.* 8, 140–142. doi: 10.1029/GL008i002p00140

Mishra, M., Sharma, G., Kothari, R., Vijay, Y., and Sharma, B. (2012). Electronic structure of CaX (X= O, S, Se) compounds using Compton spectroscopy. *Comp. Mater. Sci.* 51, 340–346. doi: 10.1016/j.commatsci.2011.07.015

Monkhorst, H. J., and Pack, J. D. (1976). Special points for Brillonin-zone integrations. *Phys. Rev. B* 13, 5188–5192. doi: 10.1103/PhysRevB.13.5188

Murnaghan, F. (1944). The compressibility of media under extreme pressures. *Proc. Natl. Acad. Sci. U.S.A.* 30,244–247. doi: 10.1073/pnas.30.9.244

Murtaza, G., Khenata, R., Safeer, A., Alahmed, Z., and Omran, S. B. (2014). Shift of band gap from indirect to direct and optical response of CaO by doping S, Se, Te. *Comp. Mater. Sci.* 91, 43–49. doi: 10.1016/j.commatsci.2014.04.039

Nejatipour, H., and Dadsetani, M. (2015). Excitonic effects in the optical properties of alkaline earth chalcogenides from first-principles calculations. *Phys. Scripta.* 90:085802. doi: 10.1088/0031-8949/90/8/085802

Noor, N., Saddique, M. B., Haq, B. U., Laref, A., and Rashid, M. (2018). Investigations of half-metallic ferromagnetism and thermoelectric properties of cubic $XCrO_3$ (X= Ca, Sr, Ba) compounds via first-principles approaches. *Phys. Lett. A* 382, 3095–3102. doi: 10.1016/j.physleta.2018.07.045

Ohno, H. (1998). Making nonmagnetic semiconductors ferromagnetic. *Science* 281, 951–956. doi: 10.1126/science.281.5379.951

Özdemir, E. G., and Merdan, Z. (2019). First-principles calculations on half-metal ferromagnetic results of VZrAs and VZrSb half-heusler compounds and $Al_{1-x}M_xAs$ (M= Co, Fe and x= 0.0625, 0.125, 0.25) diluted magnetic semiconductors. *J. Alloy. Compd.* 807:151656. doi: 10.1016/j.jallcom.2019.151656

Perdew, J. P., Burke, K., and Ernzerhof, M. (1996). Generalized gradient approximation made simple. *Phys. Rev. Lett.* 77, 3865–3868. doi: 10.1103/PhysRevLett.77.3865

Perdew, J. P., Ruzsinszky, A., Csonka, G. I., Vydrov, O. A., Scuseria, G. E., Constantin, L. A., et al. (2008). Restoring the density-gradient expansion for exchange in solids and surfaces. *Phys. Rev. Lett.* 100:136406. doi: 10.1103/PhysRevLett.100.136406

Perdew, J. P., and Wang, Y. (1992). Accurate and simple analytic representation of the electron-gas correlation energy. *Phys. Rev. B* 45, 13244–13249. doi: 10.1103/PhysRevB.45.13244

Perdew, J. P., and Zunger, A. (1981). Self-interaction correction to density-functional approximations for many-electron systems. *Phys. Rev. B* 23, 5048–5079. doi: 10.1103/PhysRevB.23.5048

Raebiger, H., Ayuela, A., and Nieminen, R. (2004). Intrinsic hole localization mechanism in magnetic semiconductors. *J. Phys-Condens. Mat.* 16, L457–L462. doi: 10.1088/0953-8984/16/41/L05

Rai, D., Laref, A., Shankar, A., Sakhya, A. P., Khenata, R., and Thapa, R. (2018). Spin-induced transition metal (TM) doped SnO_2 a dilute magnetic semiconductor (DMS): a first principles study. *J. Phys. Chem. Solids* 120, 104–108. doi: 10.1016/j.jpcs.2018.04.006

Richet, P., Mao, H. K., and Bell, P. M. (1988). Static compression and equation of state of CaO to 1.35 Mbar. *J. Geophys. Res.* 93, 15279–15288. doi: 10.1029/JB093iB12p15279

Sajjad, M., Manzoor, S., Zhang, H., Noor, N., Alay-E-Abbas, S., Shaukat, A., et al. (2015). The half-metallic ferromagnetism character in $Be_{1-x}V_xY$ (Y= Se and Te) alloys: an ab-initio study. *J. Magn. Magn. Mater.* 379, 63–73. doi: 10.1016/j.jmmm.2014.11.004

Salam, M. M. A. (2018). Theoretical study of CaO, CaS and CaSe via first-principles calculations. *Results Phys.* 10, 934–945. doi: 10.1016/j.rinp.2018.07.042

Santana, J. A., Krogel, J. T., Kent, P. R., and Reboredo, F. A. (2016). Cohesive energy and structural parameters of binary oxides of groups IIA and IIIB from diffusion quantum Monte Carlo. *J. Chem. Phys.* 144:174707. doi: 10.1063/1.4947569

Sanvito, S., Ordejón, P., and Hill, N. A. (2001). First-principles study of the origin and nature of ferromagnetism in $Ga_{1-x}Mn_xAs$. *Phys. Rev. B* 63:165206. doi: 10.1103/PhysRevB.63.165206

Sato, K., Bergqvist, L., Kudrnovsk,ý, J., Dederichs, P. H., Eriksson, O., Turek, I., et al. (2010). First-principles theory of dilute magnetic semiconductors. *Rev. Mod. Phys.* 82, 1633–1690. doi: 10.1103/RevModPhys.82.1633

Sato, K., Dederichs, P., Araki, K., and Katayama-Yoshida, H. (2003a). Ab initio materials design and Curie temperature of GaN-based ferromagnetic semiconductors. *Phys. Status Solidi*, 2855–2859. doi: 10.1002/pssc.200303289

Sato, K., and Katayama-Yoshida, H. (2002). First principles materials design for semiconductor spintronics. *Semicond. Sci. Tech.* 17, 367–376. doi: 10.1088/0268-1242/17/4/309

Sato, K., Katayama-Yoshida, H., and Dederichs, P. (2003b). Curie temperatures of III–V diluted magnetic semiconductors calculated from first-principles in mean field approximation. *J. Supercond.* 16, 31–35. doi: 10.1023/A:1023264113451

Singh, D. J., and Nordstrom, L. (2006). *Planewaves, Pseudopotentials, and the LAPW Method*. New York, NY: Springer Science and Business Media.

Soulen, R., Byers, J., Osofsky, M., Nadgorny, B., Ambrose, T., Cheng, S., et al. (1998). Measuring the spin polarization of a metal with a superconducting point contact. *Science* 282, 85–88. doi: 10.1126/science.282.5386.85

Speziale, S., Shieh, S. R., and Duffy, T. S. (2006). High-pressure elasticity of calcium oxide: a comparison between Brillouin spectroscopy and radial X-ray diffraction. *J. Geophys. Res.* 111:B02203. doi: 10.1029/2005JB003823

Togo, A., and Tanaka, I. (2015). First principles phonon calculations in materials science. *Scripta Mater.* 108, 1–5. doi: 10.1016/j.scriptamat.2015.07.021

Tran, F., and Blaha, P. (2009). Accurate band gaps of semiconductors and insulators with a semilocal exchange-correlation potential. *Phys. Rev. Lett.* 102:226401. doi: 10.1103/PhysRevLett.102.226401

Tran, F., and Blaha, P. (2017). Importance of the kinetic energy density for band gap calculations in solids with density functional theory. *J. Phys. Chem. A* 121, 3318–3325. doi: 10.1021/acs.jpca.7b02882

Tran, F., Laskowski, R., Blaha, P., and Schwarz, K. (2007). Performance on molecules, surfaces, and solids of the Wu-Cohen GGA exchange-correlation energy functional. *Phys. Rev. B* 75:115131. doi: 10.1103/PhysRevB.75.115131

Verma, U., Sharma, S., Devi, N., Bisht, P., and Rajaram, P. (2011). Spin-polarized structural, electronic and magnetic properties of diluted magnetic semiconductors $Cd_{1-x}Mn_xTe$ in zinc blende phase. *J. Magn. Magn. Mater.* 323, 394–399. doi: 10.1016/j.jmmm.2010.09.016

Wang, X., Khachai, H., Khenata, R., Yuan, H., Wang, L., Wang, W., et al. (2017). Structural, electronic, magnetic, half-metallic, mechanical, and thermodynamic properties of the quaternary Heusler compound FeCrRuSi: a first-principles study. *Sci. Rep. Uk* 7:16183. doi: 10.1038/s41598-017-16324-2

Whited, R., Flaten, C. J., and Walker, W. (1973). Exciton thermoreflectance of MgO and CaO. *Solid. State. Commun.* 13, 1903–1905. doi: 10.1016/0038-1098(73)90754-0

Wolf, S., Awschalom, D., Buhrman, R., Daughton, J., Von Molnar, S., Roukes, M., et al. (2001). Spintronics: a spin-based electronics vision for the future. *Science* 294, 1488–1495. doi: 10.1126/science.1065389

Wu, X., Liu, L., Li, W., Wang, R., and Liu, Q. (2014). Effect of temperature on elastic constants, generalized stacking fault energy and dislocation cores in MgO and CaO. *Comp. Cond. Matter.* 1, 38–44. doi: 10.1016/j.cocom.2014.10.005

Wu, Z., and Cohen, R. E. (2006). More accurate generalized gradient approximation for solids. *Phys. Rev. B* 73:235116. doi: 10.1103/PhysRevB.73.235116

Yang, X., Wang, Y., Yan, H., and Chen, Y. (2016). Effects of epitaxial strains on spontaneous polarizations and band gaps of alkaline-earth-metal oxides MO (M= Mg, Ca, Sr, Ba). *Comp. Mater. Sci.* 121, 61–66. doi: 10.1016/j.commatsci.2016.04.021

Yaqoob, N., Sabir, B., Murtaza, G., Khalil, R. M. A., Muhammad, N., and Laref, A. (2019). Structural, electronic, magnetic, optical and thermoelectric response of half-metallic AMnTe2 (A= Li, Na, K): an ab-initio calculations. *Physica B* 574:311656. doi: 10.1016/j.physb.2019.08.033

Zhang, L., Wang, X., and Cheng, Z. (2017). Electronic, magnetic, mechanical, half-metallic and highly dispersive zero-gap half-metallic properties of rare-earth-element-based quaternary Heusler compounds. *J. Alloy. Compd.* 718, 63–74. doi: 10.1016/j.jallcom.2017.05.116

Zuti, I., Fabian, J., and Sarma, S. D. (2004). Spintronics: fundamentals and application. *Rev. Mod. Phys.* 76, 323–410. doi: 10.1103/RevModPhys.76.323

Conflict of Interest: The authors declare that the research was conducted in the absence of any commercial or financial relationships that could be construed as a potential conflict of interest.

frontiers in Chemistry

ORIGINAL RESEARCH
published: 17 July 2020
doi: 10.3389/fchem.2020.00558

Computational Insights Into the Electronic Structure and Magnetic Properties of Rhombohedral Type Half-Metal $GdMnO_3$ With Multiple Dirac-Like Band Crossings

Yu Chang[1,2], *Sung-Ryong Moon*[2]*, *Xin Wang*[1,2]*, *Rabah Khenata*[3]*, *H. Khachai*[4] and *Minquan Kuang*[5]*

[1] Tonghua Normal University, Tonghua, China, [2] Department of Electronic Engineering, Wonkwang University, Iksan, South Korea, [3] Laboratoire de Physique Quantique de La Matiere et de Modelisation Mathematique (LPQ3M), Université de Mascara, Mascara, Algeria, [4] Laboratoire D'etude des Materiaux & Instrumentations Optiques, Physics Department, Djillali Liabès University of Sidi Bel-Abbès, Sidi Bel Abbès, Algeria, [5] School of Physical Science and Technology, Southwest University, Chongqing, China

OPEN ACCESS

Edited by:
Gokhan Surucu,
Middle East Technical University, Turkey

Reviewed by:
Şule Uğur,
Ğazi University, Turkey
Hamza Yaşar Ocak,
Dumlupinar University, Turkey

***Correspondence:**
Sung-Ryong Moon
srmoon@wku.ac.kr
Xin Wang
dlcrystal622@wku.ac.kr
Rabah Khenata
rkhenata@univ_mascara.dz
Minquan Kuang
mqkuang@swu.edu.cn

Specialty section:
This article was submitted to Theoretical and Computational Chemistry, a section of the journal Frontiers in Chemistry

Received: 29 April 2020
Accepted: 02 June 2020
Published: 17 July 2020

Citation:
Chang Y, Moon S-R, Wang X, Khenata R, Khachai H and Kuang M (2020) Computational Insights Into the Electronic Structure and Magnetic Properties of Rhombohedral Type Half-Metal $GdMnO_3$ With Multiple Dirac-Like Band Crossings. Front. Chem. 8:558. doi: 10.3389/fchem.2020.00558

In spintronics, half-metallic materials (HMMs) with Dirac-like cones exhibit interesting physical properties such as massless Dirac fermions and full spin polarization. We combined first-principles calculations with the quasi-harmonic Debye model, and we proposed that the rhombohedral $GdMnO_3$ is an HMM with multiple linear band crossings. The physical properties of $GdMnO_3$ were studied thoroughly. Moreover, the changes of multiple linear band crossings and 100% spin polarization under spin-orbit coupling as well as the electron and hole doping were also investigated. It is noted that such spin-polarized HMMs with linear band crossings are still very rare in two-dimensional and three-dimensional materials.

Keywords: half-metal, spintronics, DFT, electronic structures, rhombohedral, spin-polarization

Different from traditional electronics, spintronics mainly use spin rather than charge as a carrier for transmitting and processing information (Awschalom and Flatté, 2007), greatly improving the performance and effectively reducing the power consumption of electronic devices. The field of spintronics has developed rapidly in recent years, but it still faces many challenges, such as long distance spin transport, spin-polarized carrier generation and injection, and spin manipulation and detection. In response to these problems, scientists have proposed a series of spintronic materials such as spin gapless semiconductors (SGS) (Wang, 2008, 2017; Wang et al., 2010, 2016, 2017, 2018; Han et al., 2018), zero-gap half-metals (HMs) (Du et al., 2013), Dirac HMs (Ishizuka and Motome, 2012; He et al., 2016; Liu et al., 2017; Zhang et al., 2017), dilute magnetic semiconductors (DMS) (Furdyna, 1988), and bipolar Magnetic Semiconductor (BMS) (Li et al., 2012).

Currently, the new generation of spintronics also faces a problem of achieving zero-energy consumption and ultra-high speed for electronic transmission. Dirac-type half-metallic materials are excellent candidates for achieving these goals because they have the advantages of having massless Dirac fermions and high spin polarization. The first Dirac half-metal (DHMs) was theoretically verified in triangular ferromagnet (Ishizuka and Motome, 2012). Since then, research on DHMs has mainly focused on two-dimensional materials (He et al., 2016; Liu et al., 2017). Very recently, a three-dimensional material, MnF_3 with multiple Dirac cones near the Fermi level was predicted by Jiao et al. (2017). Compared to the materials with a single-Dirac-cone DHM, materials with multiple Dirac band dispersions can exhibit higher carrier transmission efficiency and stronger

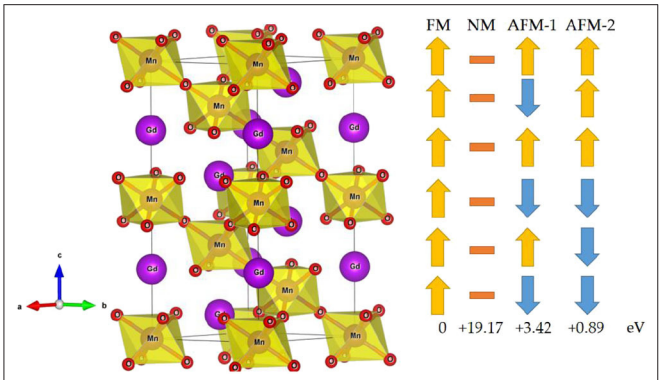

FIGURE 1 | (Left) Crystal structures of the $R\bar{3}c$-type $GdMnO_3$ material with hexagonal structure; **(Right)** four magnetic structures, i.e., FM, NM, and two AFM structures (labeled as AFM-1, and AFM-2).

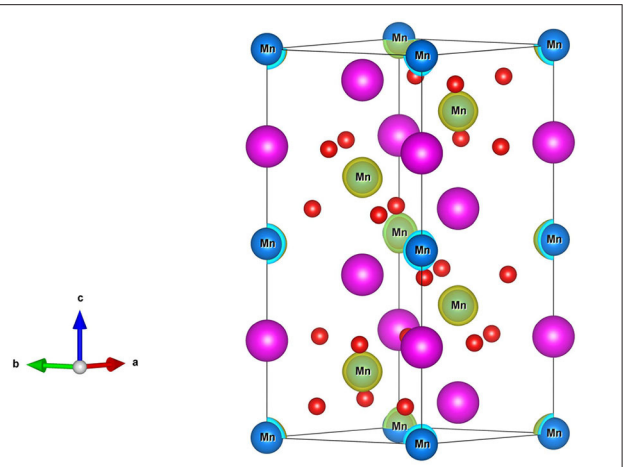

FIGURE 2 | Spin-density of $GdMnO_3$ obtained by the DFT+U method.

non-linear electromagnetic response. Subsequently, $LaMnO_3$ (Ma et al., 2018) with the $R\bar{3}c$ type structure was proposed by Du's group in 2018 to display complete spin-polarization and multiple Dirac cones around the Fermi level.

Unfortunately, the types and number of DHMs is extremely limited. Therefore, it is necessary to design more HMMs with Dirac-like band crossings and 100% spin polarization. In this work, we will study the electronic structures, magnetism, and thermodynamic properties of the $R\bar{3}c$ type $GdMnO_3$ using first-principles calculations incorporating the quasi-harmonic Debye model (QDM). Furthermore, the spin-orbit coupling, and the electron and hole doping effects were taken into consideration to examine the stability of the electronic structure. A more detailed description of the Computational Methods is provided in the **Supplementary Information**.

The $R\bar{3}c$-type $GdMnO_3$ crystal structure with hexagonal setting is shown in **Figure 1** (Left). The $GdMnO_3$ crystal structure belongs to space group number 167 and the optimized equilibrium lattice parameters for the FM state are a = b = 5.63 Å and c = 13.17 Å. The six Mn atoms have four types of magnetic orderings, namely, FM, NM, AFM-1, and AFM-*2*. As shown in **Figure 1** (Right), the spin orderings of the six Mn are ↑↑↑↑↑↑, ↑↓↑↓↑↓, and ↑↑↑↓↓↓ respectively, for FM, AFM-1 and AFM-*2* configurations. By fully relaxing the crystal structures of $GdMnO_3$ and checking the magnetic structures of this $GdMnO_3$. From **Figure 1** (Right), one can conclude that the most stable magnetic phase is the FM phase due to its lowest total energy. The calculated total magnetic moment of this material under FM and equilibrium lattice constant is 24 μ_B per unit cell, and arises mainly from the Mn atoms (the spin density of $GdMnO_3$ is given in **Figure 2**), with the atomic magnetic moment of each Mn atom of ∼4.4 μ_B.

Figure 3 shows the spin-polarized band structures of $GdMnO_3$ obtained by DFT+U calculations. To accurately describe the electronic structures of $GdMnO_3$, the on-site Coulomb interaction U and exchange interaction J were set to 10.1 and 0.88 eV, respectively, for Mn-3*d* based on reference (Ma et al., 2018). An examination of the band structure shows that while the band gap (∼4.73 eV) and the half-metallic band gap (∼0.75 eV) is found in the spin-down channel, the bands in the spin-up channel show metallic properties, suggesting that $GdMnO_3$ is a half-metallic material (Anjami et al., 2017; Jiao et al., 2017; Ma et al., 2018). Normally, a large energy gap (difference between the energies of the highest occupied and lowest unoccupied in the spin-down channel) and a half-metallic band gap (difference between the energies of highest occupied and the Fermi level in the spin-down channel) are considered to be evidence of robust half-metallic behaviors.

Interestingly, in the spin-up channel, there are some Dirac-like band crossings that are very close to the Fermi level. In **Figure 3**, we used yellow squares to highlight the regions of the Dirac-like crossing points near the Fermi level. Clearly, three Dirac-like crossing points are present along the M–Γ path, two Dirac-like crossing points are present along the Γ-K path, one Dirac-like crossing point is located at the A high symmetry point, and a Dirac-like crossing point is found along the A–H path.

Figure 4 shows the TDOS and PDOS of $GdMnO_3$ in both spin directions obtained using the DFT+U method. Spin polarization (%) is a highly important parameter and can be expressed as Jiao et al. (2017): $P = \frac{|N\uparrow(E_f)-N\downarrow(E_f)|}{|N\uparrow(E_f)+N\downarrow(E_f)|} \times 100$ where $N \uparrow (E_f)$ and $N \downarrow (E_f)$. Here, $N \uparrow (E_f)$ is the number of the spin-up states and $N \uparrow (E_f)$ is the number of the spin-down states. An examination of **Figure 4A** shows that the *P*-value of $GdMnO_3$ is 100%, indicating that $GdMnO_3$ can be selected for using in future spintronic devices.

An examination of **Figure 4B** shows a clear energy gap in the vicinity of the Fermi level in the spin-down channel; however, the spin-up electrons show metallic behavior. For the spin-up channel, the density of states primarily arises from the *d* states of the Mn atoms and the *p* states of O atoms. It is important to note that the DOS peak at approximately −7 eV (7 eV) of the spin-down channel (spin-up channel) is induced due to the strong spin splitting (Qin et al., 2017; Han et al., 2019) of the Mn atoms. At the same time, the nearly symmetrical DOS of O in both spin directions suggest that the atomic magnetic moments of O can be ignored.

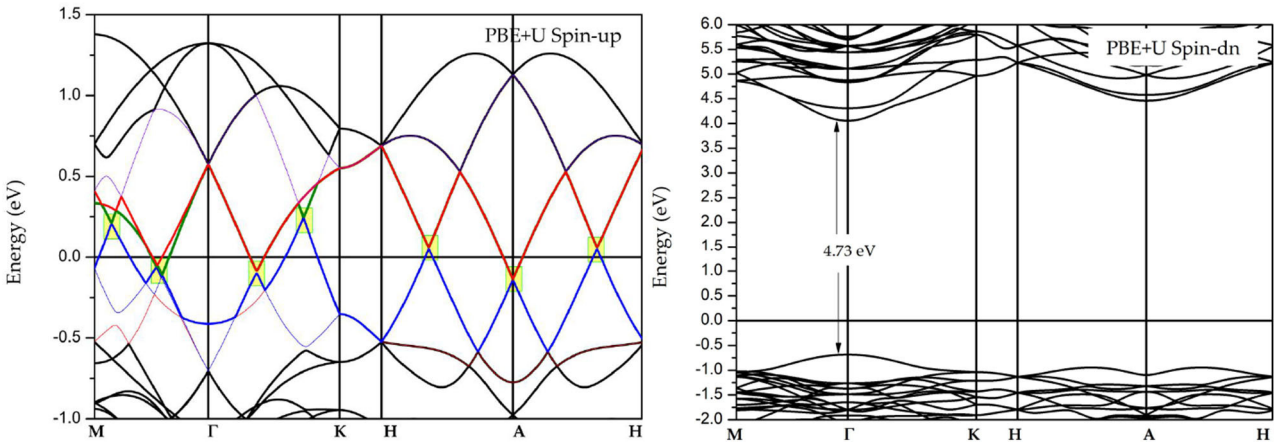

FIGURE 3 | Spin-polarized band structure of $GdMnO_3$ obtained by the DFT+U method.

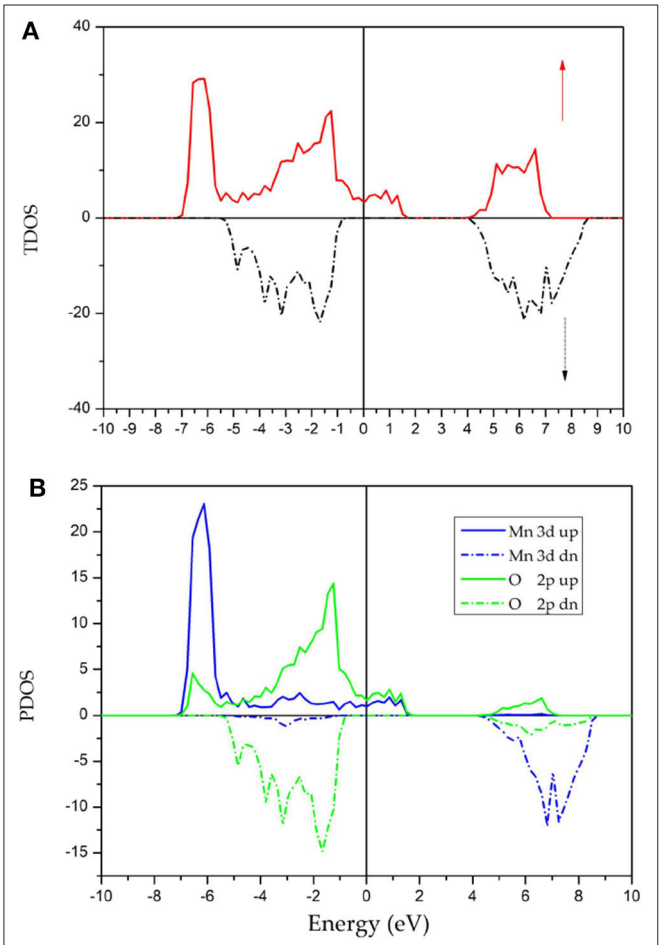

FIGURE 4 | Calculated TDOS **(A)** and PDOS **(B)** of $GdMnO_3$ obtained using the DFT+U method.

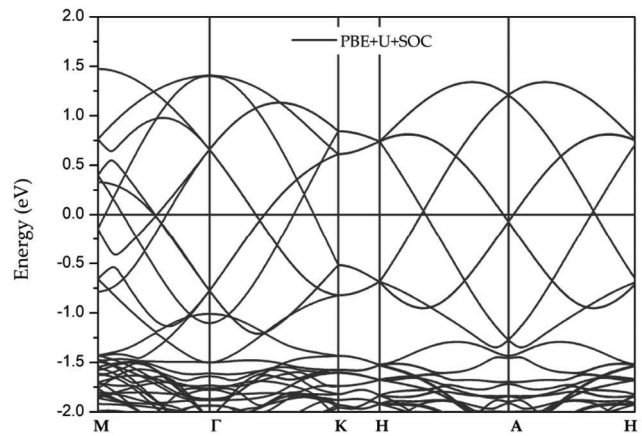

FIGURE 5 | Band structures of $GdMnO_3$ obtained using the DFT+U+SOC method.

Because the $GdMnO_3$ system contains heavy atoms, the effect of the spin-orbit coupling (SOC) should be discussed in this work. **Figure 5** shows the band structures of $GdMnO_3$ obtained by DFT+U+SOC calculations. It is observed that the Dirac-like band crossings is still present when the SOC is taken into account, namely, the conduction and valence bands are still degenerate. Due to the robustness with respect to the SOC effect, $GdMnO_3$ features long spin coherence which is helpful for spintronic applications.

It is well-known that electron and hole doping may influence the stability of the electronic structure around the Fermi level. Therefore, in this work, we will study the effect of electron and hole doping on the band structure. The doping concentration of each atom is 0.025 carrier, and the obtained band structures under the electron doping and under hole doping are shown in **Figures 6A–D**, respectively. An examination of these figures shows that electron doping will increase the energy of the Fermi level, while hole doping will decrease the Fermi level energy. Both electron and hole doping have no obvious effect on the Dirac-like band crossings and half-metallic states (see **Figures 6A,C**) with the exception of changing the location of the Dirac-like band

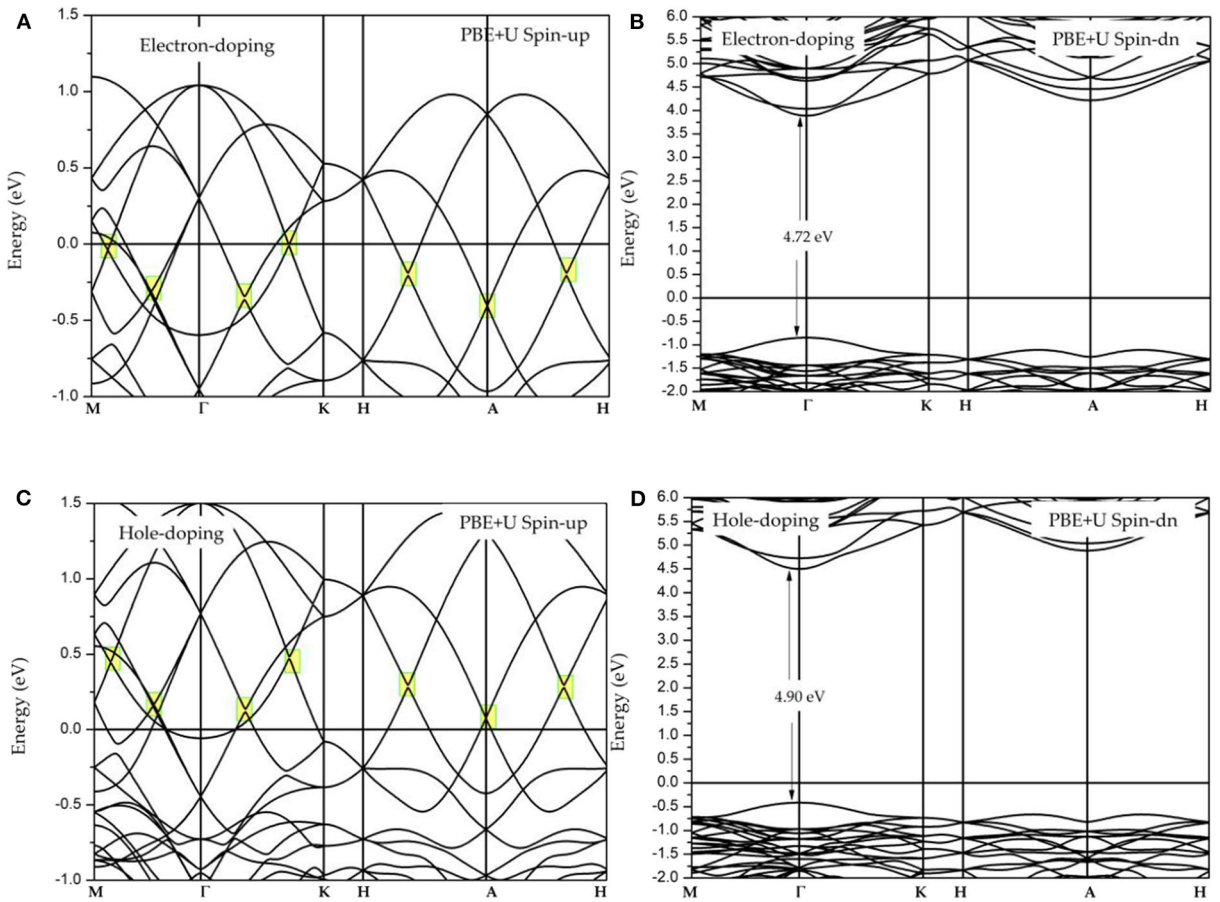

FIGURE 6 | (A,B) Spin-polarized band structures of $GdMnO_3$ under electron doping; **(C,D)** spin-polarized band structures of $GdMnO_3$ under hole doping.

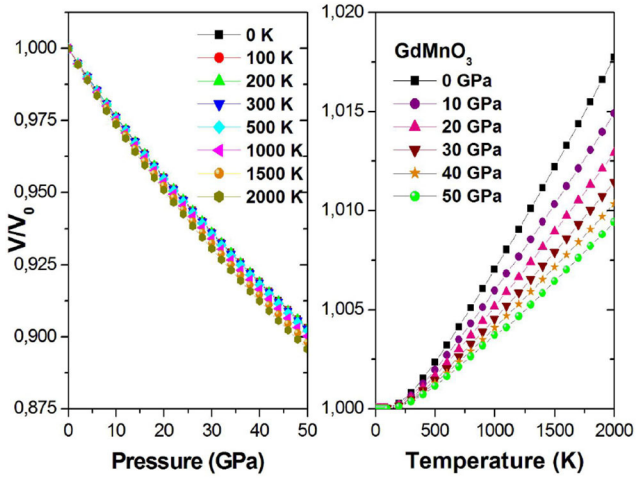

FIGURE 7 | V/V_0 ratio as a function of the pressure (temperature) at different given temperatures (pressures).

crossing points. The carrier concentration, can be adjusted by use of a gate voltage (Thelander et al., 2004).

Then, we calculated some thermodynamic parameters to understand the thermodynamic behavior of $GdMnO_3$ under high temperature and high pressure limits. As mentioned in the Computational method section, in this work, QDM is used to investigate the thermodynamic properties, and the investigated temperature and pressure regions were 0–2,000 K and 0–50 GPa, respectively.

Figure 7 shows the relationship between the V/V_0 rate of change and temperature and pressure, where V_0 is the initial volume and V is the final volume for a given pressure. In **Figure 7** (Left), we can clearly find that for a given fixed temperature, the rate V/V_0 decreases with increasing pressure. This is a negative correlation; in other words, the slope is negative. As observed from **Figure 7** (Right), the V/V_0 rate and temperature are positively correlated.

The relationships between α_V on the one hand and pressure and temperature on the other hand are shown in **Figure 8**. For a fixed pressure, with increasing temperature, α_V increases first sharply and then slowly. This may be due to the higher pressure limiting the rise of α_V. **Figure 8** (Right) shows that for a constant temperature, although the increase in the pressure will gradually decrease α_V, for higher temperature, the increase in the

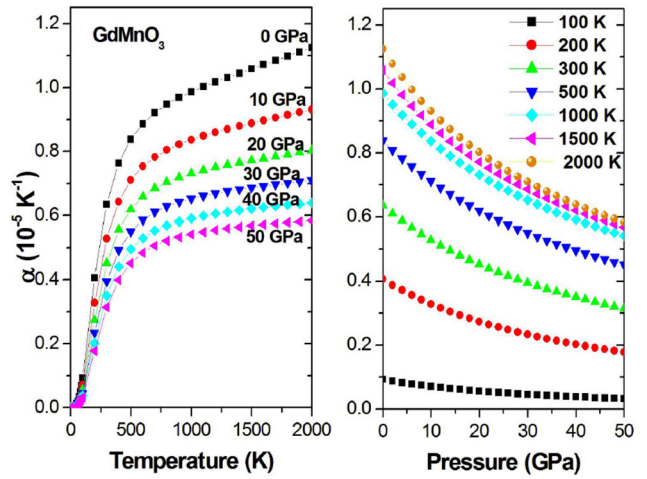

FIGURE 8 | α_V as a function of the temperature (pressure) at different given pressures (temperatures).

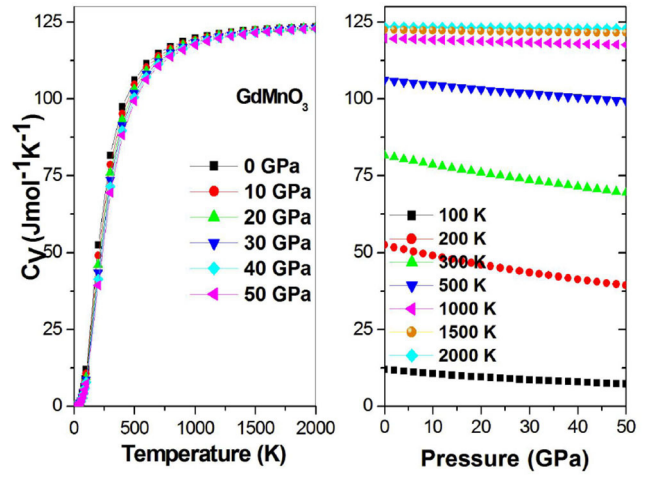

FIGURE 10 | Heat capacity C_V as a function of the temperature (pressure) at different given pressures (temperatures).

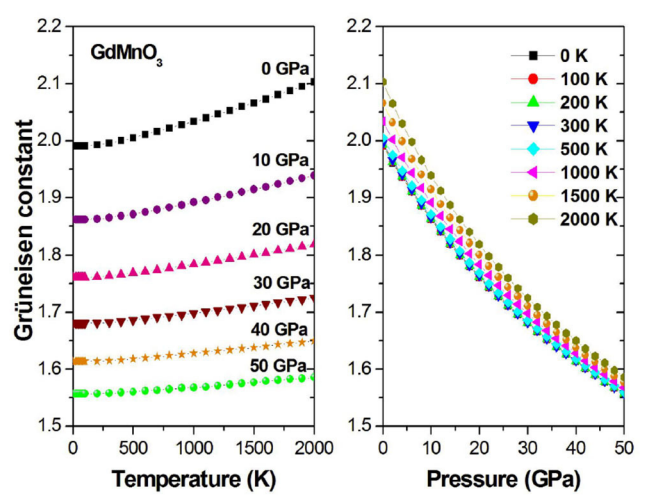

FIGURE 9 | Grüneisen constant γ as a function of the temperature (pressure) at different given pressures (temperatures).

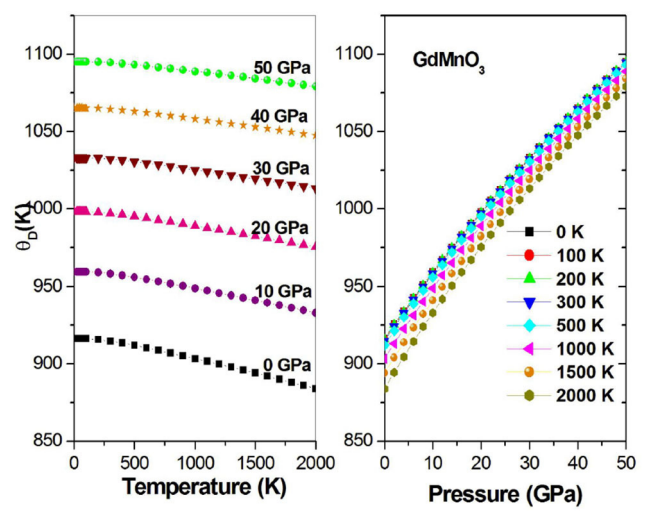

FIGURE 11 | Debye temperature θ_p as a function of the temperature (pressure) at different given pressures (temperatures).

pressure will only increase the initial value of α_V without affecting the trend.

Using the Grüneisen parameter (γ) to predict the thermodynamic properties of the material at high temperatures and pressures, we can evaluate the effect of the crystal anharmonicity. **Figure 9** shows the relationship between γ on the one hand and the pressure and temperature on the other hand, and it is observed that with increasing temperature or decreasing pressure, the pressure/temperature relationship increases accordingly.

Figure 10 shows that the heat capacity of $GdMnO_3$ shows a close to cubic dependence on the temperature (T^3) at low temperatures, suggesting that lattice vibrations will increase with increasing temperature. Moreover, the high temperature value is constant, as stated by the Dulong-Petti limit, indicating that the thermal energy at high temperature excites all phonon modes. The increase in the absolute pressure increase is a negative effect and will stop lattice vibrations.

Figure 11 shows the Debye temperature and its relation to the temperature at fixed pressures and the Debye temperature and its relationship to the pressure at fixed temperatures. The value of θ_p has a negative quasi-linear relationship with temperature and a positive quasi-linear relationship with pressure.

In this study, a new material, perovskite $R\bar{3}c$ type $GdMnO_3$, with half-metallic behavior and multiple linear band crossing was examined and its electronic, magnetic, and thermodynamic properties were investigated via first-principles and QDM calculations. In this work, different magnetic structures were considered, namely, FM, NM, AFM-1, and AFM-2. We found

that FM is the most stable due to its lowest total energy. The SOC effect has a weak effect on the electronic structure and therefore this material may have the potential for long spin coherence for long-range spin transport. The effects of electron and hole doping were also included in this calculation. We found the properties of half-metallicity and multiple linear band crossings are highly robust against electron and hole doping.

DATA AVAILABILITY STATEMENT

The raw data supporting the conclusions of this article will be made available by the authors, without undue reservation.

AUTHOR CONTRIBUTIONS

YC: software, methodology, and writing. S-RM: supervisor. XW, RK, and HK: reviewing and editing. MK: conceptualization. All authors contributed to the article and approved the submitted version.

SUPPLEMENTARY MATERIAL

The Supplementary Material for this article can be found online at: https://www.frontiersin.org/articles/10.3389/fchem.2020.00558/full#supplementary-material

REFERENCES

Anjami, A., Boochani, A., Elahi, S. M., and Akbari, H. (2017). Ab-initio study of mechanical, half-metallic and optical properties of Mn_2ZrX (X= Ge, Si) compounds. *Results Phys.* 7, 3522–3529. doi: 10.1016/j.rinp.2017.09.008

Awschalom, D. D., and Flatté, M. E. (2007). Challenges for semiconductor spintronics. *Nat. phys.* 3, 153–159. doi: 10.1038/nphys551

Du, Y., Xu, G. Z., Zhang, X. M., Liu, Z., Yu, S., Liu, E., et al. (2013). Crossover of magnetoresistance in the zero-gap half-metallic Heusler alloy Fe_2CoSi. *EPL* 103:37011. doi: 10.1209/0295-5075/103/37011

Furdyna, J. K. (1988). Diluted magnetic semiconductors. *J. Appl. Phys.* 64, R29–R64. doi: 10.1063/1.341700

Han, Y., Chen, Z., Kuang, M., Liu, Z., Wang, X., and Wang, X. (2019). 171 Scandium-based full Heusler compounds: A comprehensive study of competition between XA and $L2_1$ atomic ordering. *Results Phys.* 12, 435–446. doi: 10.1016/j.rinp.2018.11.079

Han, Y., Khenata, R., Li, T., Wang, L., and Wang, X. (2018). Search for a new member of parabolic-like spin-gapless semiconductors: the case of diamond-like quaternary compound $CuMn_2InSe_4$. *Results Phys.* 10, 301–303. doi: 10.1016/j.rinp.2018.06.031

He, J., Ma, S., Lyu, P., and Nachtigall, P. (2016). Unusual Dirac half-metallicity with intrinsic ferromagnetism in vanadium trihalide monolayers. *J. Mater. Chem. C.* 4, 2518–2526. doi: 10.1039/C6TC00409A

Ishizuka, H., and Motome, Y. (2012). Dirac half-metal in a triangular ferrimagnet. *Phys. Rev. Lett.* 109:237207. doi: 10.1103/PhysRevLett.109.237207

Jiao, Y., Ma, F., Zhang, C., Bell, J., Sanvito, S., and Du, A. (2017). First-principles prediction of spin-polarized multiple Dirac rings in manganese fluoride. *Phys. Rev. Lett.* 119:016403. doi: 10.1103/PhysRevLett.119.016403

Li, X., Wu, X., Li, Z., Yang, J., and Hou, J. G. (2012). Bipolar magnetic semiconductors: a new class of spintronics materials. *Nanoscale* 4, 5680–5685. doi: 10.1039/c2nr31743e

Liu, Z., Liu, J., and Zhao, J. (2017). YN_2 monolayer: novel p-state Dirac half metal for high-speed spintronics. *Nano Res.* 10, 1972–1979. doi: 10.1007/s12274-016-1384-3

Ma, F., Jiao, Y., Jiang, Z., and Du, A. (2018). Rhombohedral lanthanum manganite: a new class of dirac half-metal with promising potential in spintronics. *ACS Appl. Mater. Interfaces* 10, 36088–36093. doi: 10.1021/acsami.8b09349

Qin, G., Wu, W., Hu, S., Tao, Y., Yan, X., Jing, C., et al. (2017). Effect of swap disorder on the physical properties of the quaternary heusler alloy PdMnTiAl: a first-principles study. *IUCrJ* 4, 506–511. doi: 10.1107/S205225251700745X

Thelander, C., Bjork, M. T., Larsson, M. W., Hansen, A. E., Wallenberg, L. R., and Samuelson, L. (2004). Electron transport in InAs nanowires and heterostructure nonowire devices. *Solid State Commun.* 131:573. doi: 10.1016/j.ssc.2004.05.033

Wang, X., Cheng, Z., Liu, G., Dai, X., Khenata, R., Wang, L., et al. (2017). Rare earth-based quaternary Heusler compounds MCoVZ (M= Lu, Y; Z= Si, Ge) with tunable band characteristics for potential spintronic applications. *IUCrJ* 4, 758–768. doi: 10.1107/S2052252517013264

Wang, X., Cheng, Z., Wang, J., Wang, X.-L., and Liu, G. D. (2016). Recent advances in the Heusler based spin-gapless semiconductors. *J. Mater. Chem. C.* 4, 7176–7192. doi: 10.1039/C6TC01343K

Wang, X., Li, T., Cheng, Z., Wang, X.-L., and Chen, H. (2018). Recent advances in Dirac spin-gapless semiconductors. *Appl. Phys. Rev.* 5:041103. doi: 10.1063/1.5042604

Wang, X. L. (2008). Proposal for a new class of materials: spin gapless semiconductors. *Phys. Rev. Lett.* 100:156404. doi: 10.1103/PhysRevLett.100.156404

Wang, X. L. (2017). Dirac spin-gapless semiconductors: promising platforms for massless and dissipationless spintronics and new (quantum) anomalous spin Hall effects. *Natl. Sci. Rev.* 4, 252–257. doi: 10.1093/nsr/nww069

Wang, X. L., Dou, S. X., and Zhang, C. (2010). Zero-gap materials for future spintronics, electronics and optics. *NPG Asia Mater.* 2, 31–38. doi: 10.1038/asiamat.2010.7

Zhang, S., Zhang, C., Zhang, S., Ji, W., Li, P., Wang, P., et al. (2017). Intrinsic Dirac half-metal and quantum anomalous Hall phase in a hexagonal metal-oxide lattice. *Phys. Rev. B.* 96:205433. doi: 10.1103/PhysRevB.96.205433

Conflict of Interest: The authors declare that the research was conducted in the absence of any commercial or financial relationships that could be construed as a potential conflict of interest.

frontiers in Chemistry

ORIGINAL RESEARCH
published: 14 August 2020
doi: 10.3389/fchem.2020.00704

The Tetragonal Monoxide of Platinum: A New Platform for Investigating Nodal-Line and Nodal-Point Semimetallic Behavior

Yang Li[1,2]*, *Jihong Xia*[2] and *Vipul Srivastava*[3]

[1] Faculty of Mechanical and Electrical Engineering, Kunming University of Science and Technology, Kunming, China, [2] Department of Physics, Chongqing University of Arts and Sciences, Chongqing, China, [3] Department of Physics, School of Chemical Engineering and Physical Sciences, Lovely Professional University, Phagwara, India

The search for new topological materials that are realistic to synthesize has attracted increasing attention. In this study, we systematically investigated the electronic, mechanical, and topological semimetallic properties, as well as the interesting surface states, of the tetragonal monoxide of platinum, which is realistic to synthesize, via a first-principles approach. Our calculated results indicate that PtO is a novel topological semimetal with double nodal lines in the $k_z = 0$ plane and a pair of triple topological nodal points along the A'-M-A directions. Obvious surface states, including Fermi arc and drum-head-like surfaces, could be found around nodal points and nodal lines. The dynamic and mechanical stabilities of $P4_2/mmc$-type PtO were examined in detail via calculation of the phonon dispersion and determination of elastic constants, respectively. Some other mechanical properties, including the bulk modulus, Young's modulus, shear modulus, Poisson's ratio, and Pugh's index, were considered in this study. $P4_2/mmc$-type PtO provides a good research platform for investigation of novel behaviors that combine mechanical properties and rich topological elements.

Keywords: double nodal lines, fermi arc and drum-head-like surface states, triple point, DFT, phonon dispersion, mechanical behaviors

OPEN ACCESS

Edited by:
Zhenxiang Cheng,
University of Wollongong, Australia

Reviewed by:
Junjie He,
University of Bremen, Germany
Yong-Chun Gao,
North China University of Science and Technology, China

***Correspondence:**
Yang Li
liyang@cqwu.edu.cn;
liyang_physics@126.com

Specialty section:
This article was submitted to Theoretical and Computational Chemistry, a section of the journal Frontiers in Chemistry

Received: *19 June 2020*
Accepted: *08 July 2020*
Published: *14 August 2020*

Citation:
Li Y, Xia J and Srivastava V (2020) The Tetragonal Monoxide of Platinum: A New Platform for Investigating Nodal-Line and Nodal-Point Semimetallic Behavior. Front. Chem. 8:704. doi: 10.3389/fchem.2020.00704

INTRODUCTION

As rising stars in the topological material family, topological semimetals (Fang et al., 2012, 2016; Chiu and Schnyder, 2014; Yan and Felser, 2017; Gao et al., 2019), whose band crossing points form 0-D nodal point, 1-D nodal line, or 2-D nodal surface states in momentum space, have recently attracted extensive attention. Topological nodal point semimetals (Hosur et al., 2012; Zyuzin and Burkov, 2012; Hosur and Qi, 2013; Vazifeh and Franz, 2013; Liu et al., 2014; Lundgren et al., 2014; Kobayashi and Sato, 2015; Miransky and Shovkovy, 2015; Xu et al., 2015a; Young and Kane, 2015) enjoy 0-D nodal points in momentum space. Topological nodal line semimetals (Cai et al., 2018; Chen et al., 2018; Gao et al., 2018; Zhou et al., 2018; He et al., 2019; Jin et al., 2019a; Pham et al., 2019; Yi et al., 2019; Zou et al., 2019; Zhao et al., 2020) host 1-D topological nodal lines in momentum space via band crossing along a line in momentum space. Topological nodal surface semimetals (Wu et al., 2018; Zhang et al., 2018; Fu et al., 2019a; Qie et al., 2019; Yang et al., 2020) host 2-D nodal surface states that are composed of continuous band crossing points.

In addition, topological semimetals exhibit many types of band crossing points based on degeneracy. Weyl and Dirac semimetals feature 2-fold and 4-fold degenerate 0-D band crossing points, respectively. In detail, Weyl semimetals (Hosur et al., 2012; Zyuzin and Burkov, 2012; Hosur and Qi, 2013; Vazifeh and Franz, 2013; Lundgren et al., 2014; Yan and Felser, 2017) have nodal points that are protected by inversion (P) or time-reversal symmetries (T). Dirac semimetals (Liu et al., 2014; Lundgren et al., 2014; Kobayashi and Sato, 2015; Miransky and Shovkovy, 2015; Young and Kane, 2015) host quadruple degenerate nodal points that are protected by crystalline symmetry. Furthermore, topological semimetals with 3-, 6-, and 8-fold degenerate band crossing points have been considered (Weng et al., 2016a,b; Cai et al., 2018; Kumar et al., 2020) by researchers. Of these, triply degenerate nodal point-type semimetals (Weng et al., 2016a,b) are well-studied due to their novel topological elements and related surface states. Triple nodal points can appear both in isolation and at nodal line connections.

Many topological semimetals that are realistic to synthesize and have various types of band crossing points have been proposed. Unfortunately, these band crossing points are usually disturbed by other trivial bands near the Fermi level, which covers novel physics behaviors from the band crossing points. Hence, to search for topological behaviors of topological semimetals with rich topological elements, it is necessary to find topological semimetals with clean band structures near the Fermi level. Thus far, there are few potential clean topological semimetals with more than one topological element. This greatly impedes further investigation of realistic topological semimetals with rich topological elements.

In this work, we focus on an old realistic material, tetragonal PtO with ICSD IDs[1] 164290 and 26599. In 1941, Moore Jr and Pauling (Moore Pauling, 1941) synthesized PdO and PtO by the method of Shriner and Adams, involving fusing palladous chloride and potassium nitrate, and platinous oxide by a similar method. Based on previous powder photographic X-ray data, the tetragonal crystal PtO (Moore Pauling, 1941) exhibits a $P4_2/mmc$ type structure with lattice constants $a = b = 3.04 \pm 0.03$ and $c = 5.34 \pm 0.05$Å. In this paper, we use a first-principles analysis to investigate its electronic and mechanical properties, as well as its phase stability, systematically. We report its interesting 0-D and 1-D topological elements and the related surface states.

COMPUTATIONAL DETAILS

First-principles calculations were performed using the Vienna *ab initio* simulation package (VASP) (Hafner, 2007) with density functional theory (DFT) (Lejaeghere et al., 2016). The generalized gradient approximation (GGA) (Perdew et al., 1996) of the Perdew–Burke–Ernzerhof (PBE) functional (Ernzerhof and Scuseria, 1999) was selected for the exchange-correlation potential. The projector augmented wave (PAW) (Kresse and Joubert, 1999) pseudo-potential was employed with a cutoff energy of 600 eV for plane-wave expansions. The energy and force convergence criteria were set to 10^{-6} eV per atom and 0.0005 eV/Å, respectively. The surface states were obtained using the Wannier-tools package (Villanova and Park, 2018). The phonon dispersion of $2 \times 2 \times 2$ supercell of PtO monolayer was checked based on density functional perturbation theory (DFPT).

[1] Available online at: https://www.materialsproject.org/materials/mp-7947/.

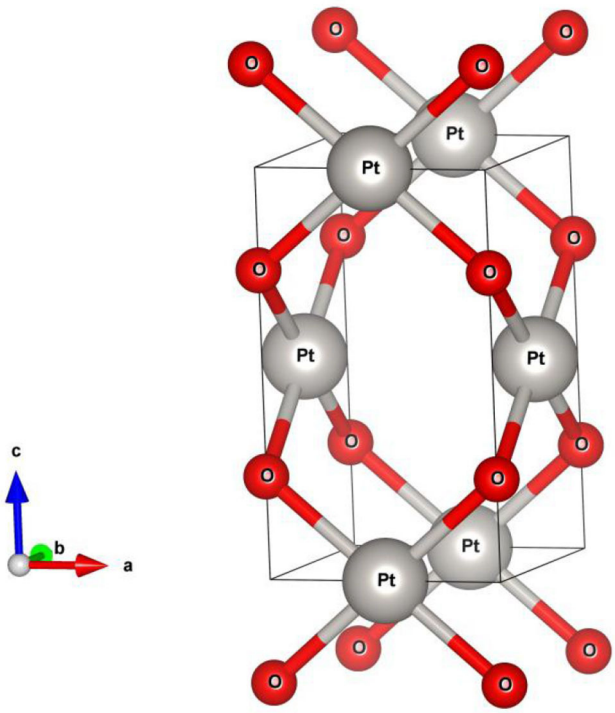

FIGURE 1 | Crystal model of tetragonal PtO.

RESULTS AND DISCUSSION

Structural Model and Dynamic Stability

PtO (Moore Pauling, 1941) crystallizes in a tetragonal structure (as shown in **Figure 1**) with space group $P4_2/mmc$ (no. 131). The minimum energy approach was used for structural optimization. The PtO primitive cell contains two O and two Pt atoms. The atomic positions and equilibrium lattice constants were determined after complete relaxation. The resulting lattice constants are $a = b = 3.15$ and $c = 5.37$Å, and are in a good agreement with the experimental data. In their relaxed atomic positions, the Pt and O atoms occupy the 2c (0.0, 0.5, 0.0) and 2e (0.0, 0.0, 0.25) Wyckoff sites, respectively. We would like to point out that the results of current study will retain if the experimental lattice constants are selected, as shown in **Figure S1**.

Based on the 3-D bulk Brillouin zone (BZ) selected in **Figure 2**, the phonon dispersion (Sultana et al., 2018; Abutalib, 2019; Ding et al., 2019; Fu et al., 2019b; Han et al., 2019; Jia et al., 2019) was determined in order to examine the dynamic stability of tetragonal PtO. It is well-known that materials are dynamically stable when no imaginary phonon modes exist in their phonon dispersion curves. **Figure 3** shows the

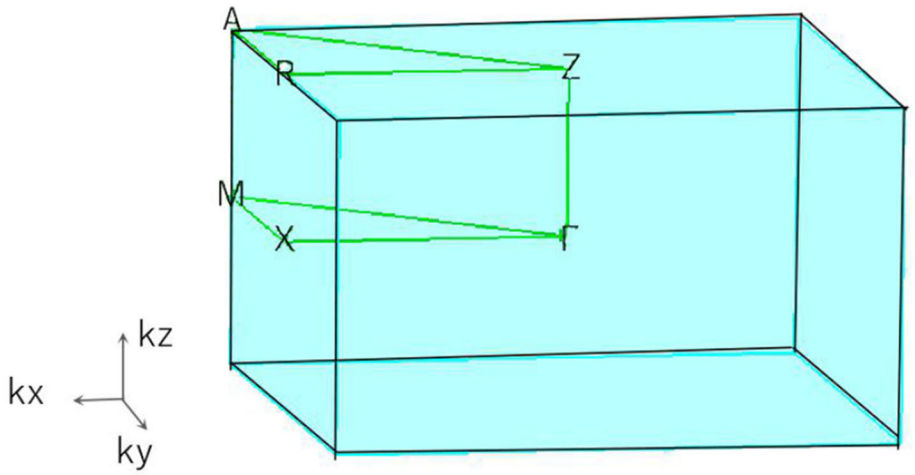

FIGURE 2 | The 3-D bulk Brillouin zone (BZ) of tetragonal PtO.

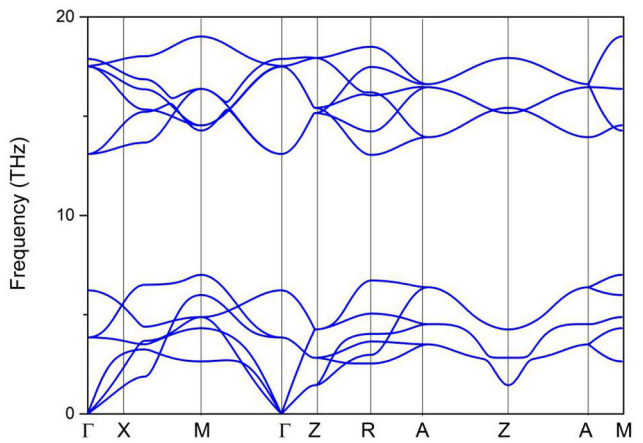

FIGURE 3 | Phonon dispersion of tetragonal PtO along the Γ-X-M-Γ-Z-R-A-Z-A-M directions.

TABLE 1 | Calculated PtO elastic constants.

C_{11} (GPa)	C_{12} (GPa)	C_{13} (GPa)	C_{33} (GPa)	C_{44} (GPa)	C_{66} (GPa)
232.61	130.02	169.23	315.41	22.83	38.40

calculated phonon dispersion along the Γ-X-M-Γ-Z-R-A-Z-A-M directions. Since only positive frequencies appear in **Figure 3**, PtO is a dynamically stable material.

Mechanical Properties and Mechanical Stability

By analyzing the elastic constants, we can obtain information about the mechanical stability of PtO. In this paper, we use the energy-strain method to compute six independent elastic constants. The results are shown in **Table 1**.

TABLE 2 | Elastic behaviors of tetragonal crystal PtO.

B	*G*	*E*	*v*	*B/G*
185.62	38.83	108.90	0.402	4.780

Tetragonal PtO has six independent elastic constants, C_{11}, C_{12}, C_{13}, C_{33}, C_{44}, and C_{66}. We can use the Born–Huang criteria (see criteria i, ii, and iii) to test the mechanical stability of tetragonal PtO:

Criteria (i) $C_{11} > |C_{12}|$;
Criteria (ii) $2C_{13}^2 < C_{33}(C_{11} + C_{12})$; and
Criteria (iii) $C_{44} > 0$.

The Born–Huang criteria indicate that PtO is mechanically stable. Other useful mechanical parameters, including the bulk modulus (B), shear modulus (G), Young's modulus (E), Poisson's ratio (v), and Pugh's index (B/G) are shown in **Table 2**.

The critical value B/G that is used to distinguish between brittle and ductile crystals is 1.75. Obviously, PtO is in hand elastically ductile. Moreover, the critical value of v that distinguishes between the ionic and covalent chemical band natures is ∼0.25. The chemical bonds in a PtO tetragonal crystal are mainly ionic. We use the ELATE program to determine the directional dependence anisotropy of PtO on the Young's modulus, shear modulus, and Possion's ratio in **Figures 4–6**, respectively. The elastic anisotropy of PtO can be determined from these figures. This is quite important for future practical applications of this material.

Topological Elements and Novel Surface States

Without considering the spin–orbit coupling effect, the band structure of PtO at its equilibrium lattice constants along

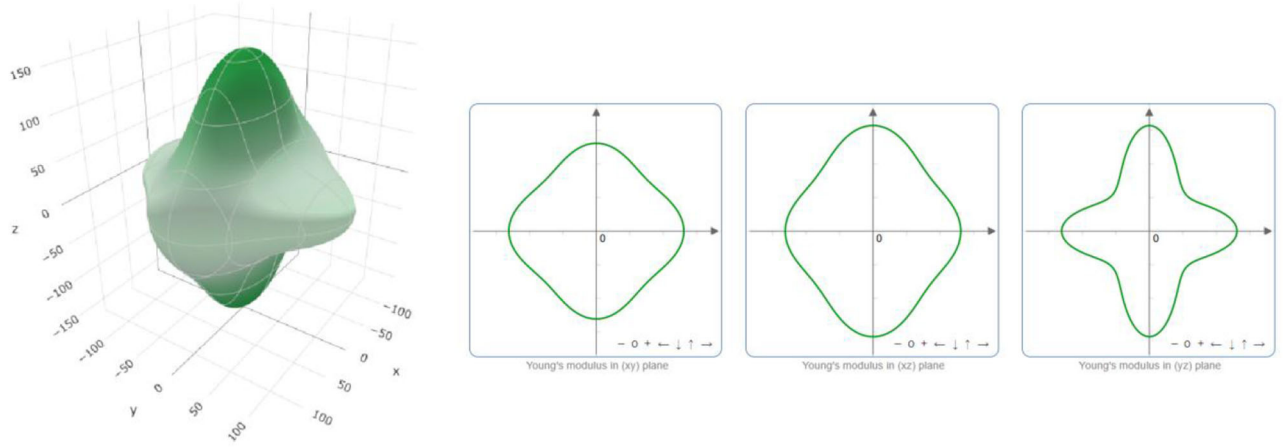

FIGURE 4 | Directional dependence of the Young's modulus.

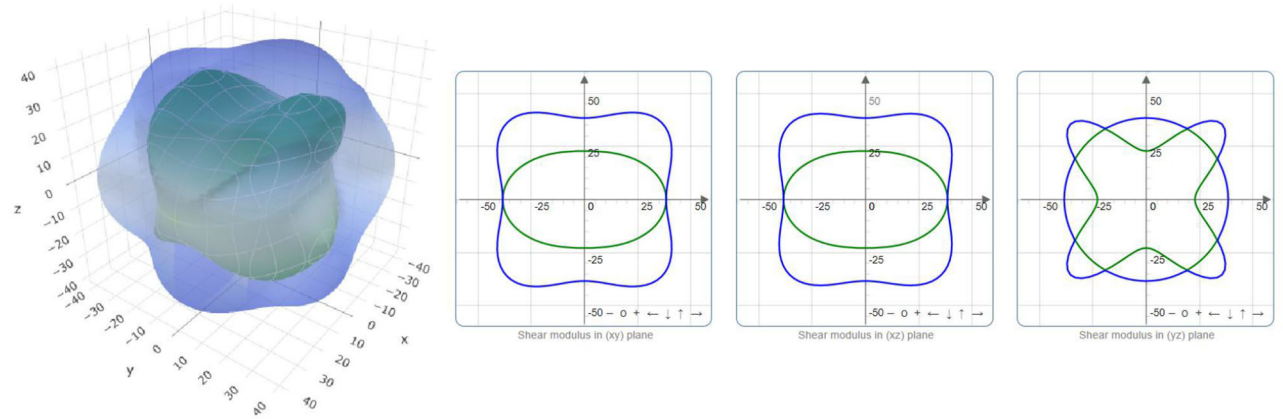

FIGURE 5 | Directional dependence of the shear modulus: blue and green indicate the maximum and minimum values, respectively.

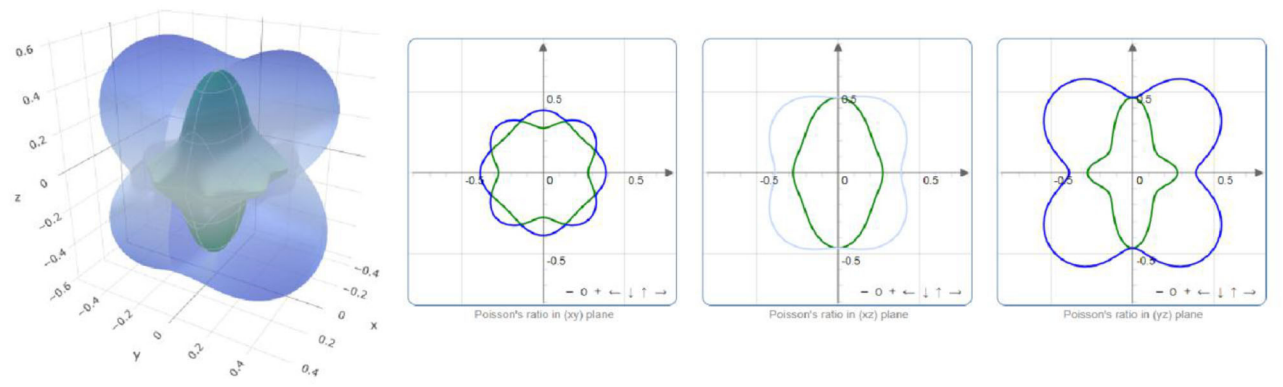

FIGURE 6 | Directional dependence of Poisson's ratio: blue and green indicate the maximum and minimum values, respectively.

the Γ-X-M-Γ-Z-R-A-Z-A-M directions was calculated using the GGA method, and the result is given in **Figure 7**. PtO is a typical semimetal (Wang et al., 2020a,b; Yalameha and Nourbakhsh, 2020) with clean band crossing points, These band-crossing points are located around the Fermi level and far from other trivial bands. Interestingly, these band crossing points

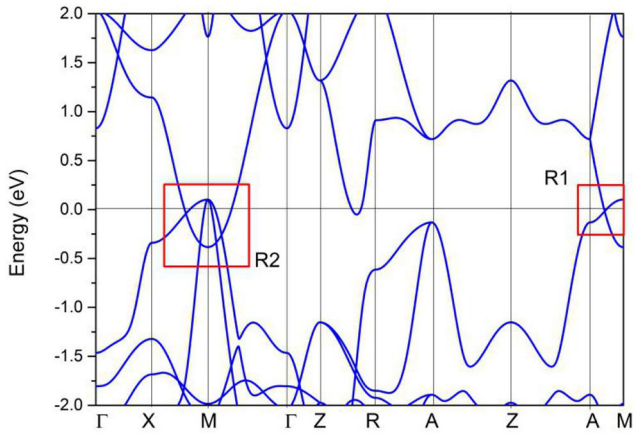

FIGURE 7 | Calculated band structure of PtO along the Γ-X-M-Γ-Z-R-A-Z-A-M directions, as determined using the GGA method.

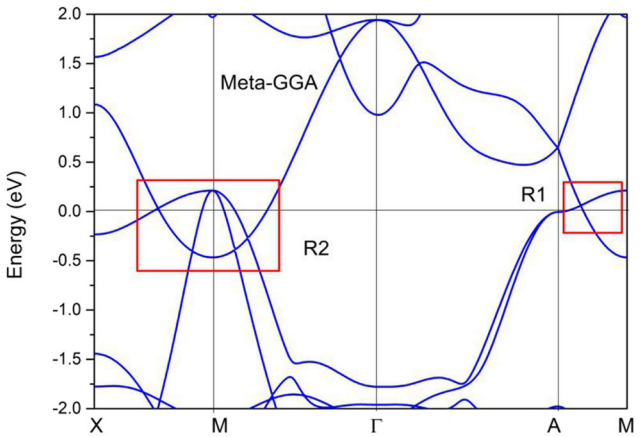

FIGURE 8 | Calculated band structure of PtO along the X-M-Γ-A-M directions, as determined using the TPSS-meta-GGA method.

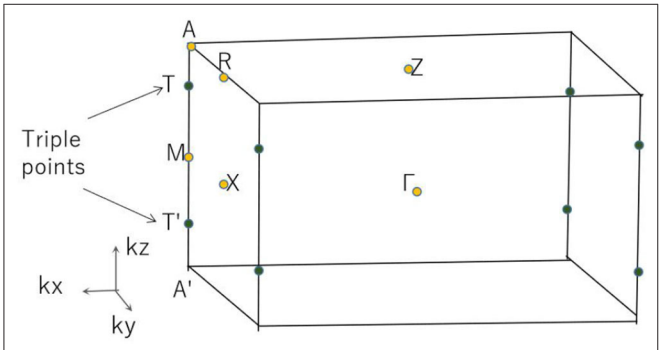

FIGURE 9 | Triple nodal point positions (highlighted as green balls).

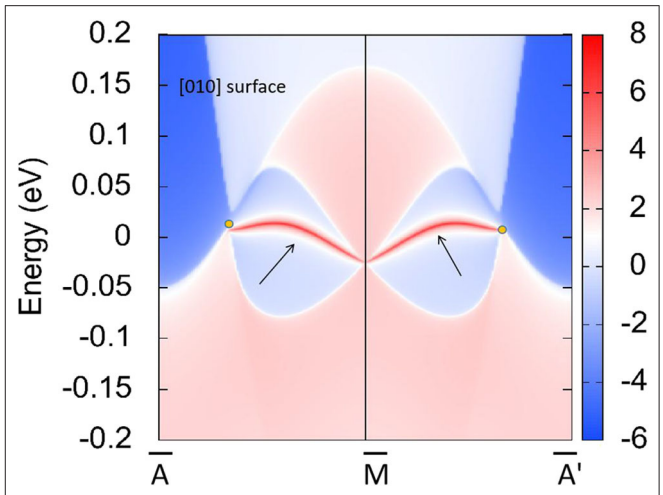

FIGURE 10 | Projected spectrum on the (010) PtO tetragonal crystal surface. The band crossing points are marked as yellow balls and the Fermi arc surface states are highlighted using black arrows.

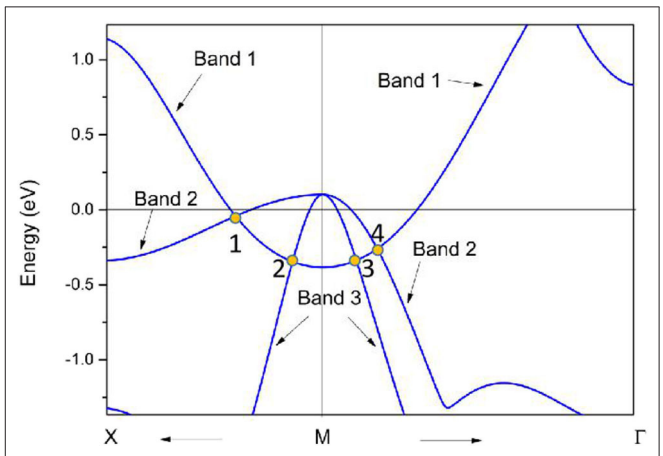

FIGURE 11 | Calculated PtO band structure along the X-M-Γ directions, as determined using the GGA method. The band crossing points, labeled 1, 2, 3, and 4, are marked by yellow balls.

are concentrated mainly in the R1 and R2 regions. We will discuss each band crossing point in R1 and R2. To confirm the band crossing points near the Fermi level further, one type of meta-GGA method, Tao–Perdew–Staroverov–Scuseria (TPSS) (Sun et al., 2011), was selected to prove the occurrence of the band crossing points in the R1 and R2 regions. The PtO band structure along the X-M-Γ-A-M directions as determined via the TPSS-meta-GGA method is shown in **Figure 8**. Obviously, the band crossing points in both regions are retained.

In R1, we can see that the band crossing point along the A-M direction induces a pair of triple nodal points. Symmetry analysis (with the help of Quantum ESPRESSO) shows that the two bands (conduction and valence bands), respectively, belong to irreducible representations Γ_2 and Γ_2 of the C_{4v} symmetry for the A-M path (in R1). This pair of triple nodal points is generated by one non-degenerate band and one doubly degenerate band. The triple nodal point locations are given

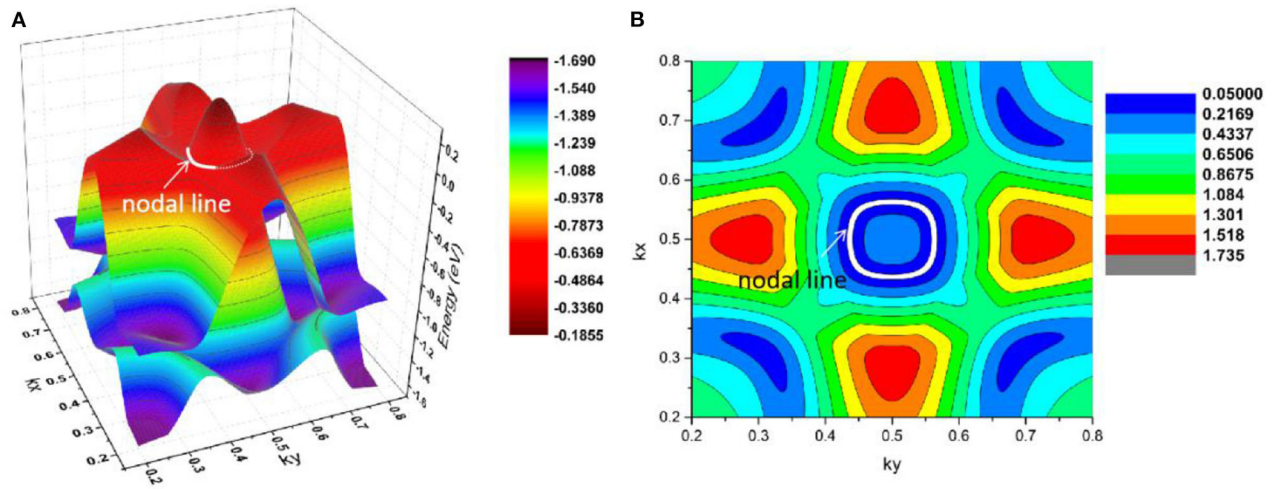

FIGURE 12 | M-point-centered **(A)** 3-D and **(B)** 2-D plots of bands 1 and 3 in the $k_z = 0$ plane in R2. The white line indicates the nodal line in this plane.

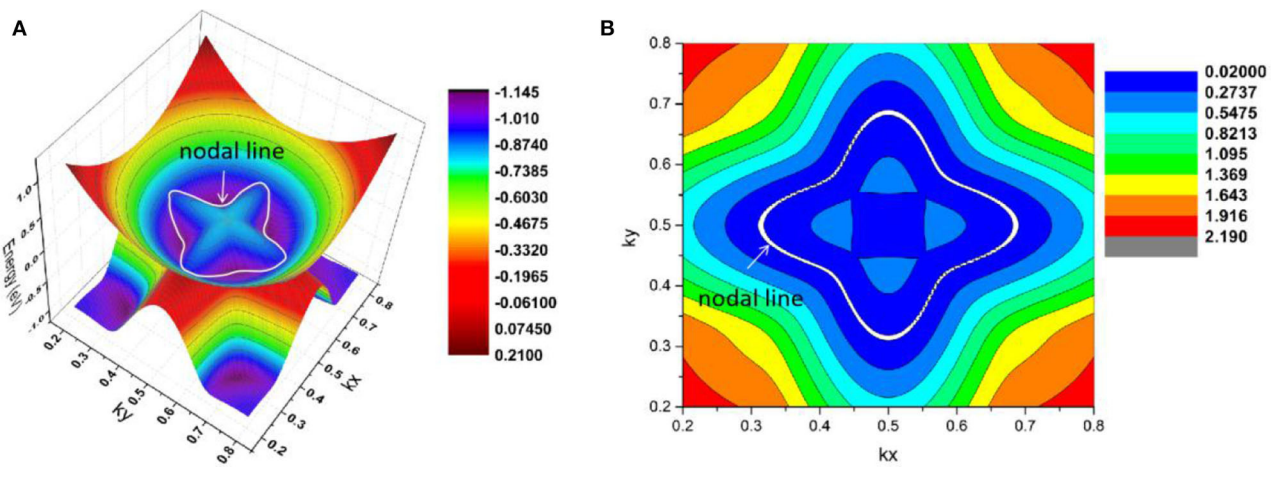

FIGURE 13 | M-point-centered **(A)** 3-D and **(B)** 2-D plots of bands 1 and 2 in the $k_z = 0$ plane in R2. The nodal line is marked as a white line.

in **Figure 9**. The Fermi arc surface state (Xu et al., 2015b; Jin et al., 2019b, 2020) can be seen as strong evidence for the appearance of triple nodal points. In **Figure 10**, we show the projected spectrum on the (010) PtO tetragonal crystal surface. The triple nodal points are highlighted as yellow balls and the obvious Fermi arc non-trivial surface states, which are located inside the band crossing points and marked by black arrows, are near the Fermi level.

As shown in **Figure 11**, there are four band crossing points along the X-M-Γ directions and near the Fermi level in R2. Band crossing points 1 and 4 are generated by crossing bands 1 and 2. However, band crossing points 2 and 3 are formed by overlaps between bands 1 and 3. Since PtO hosts both *P* and *T* symmetries, these four band crossing points along the X-M-Γ directions in the $k_z = 0$ plane cannot be treated as isolated points (Gao et al., 2018; He et al., 2019; Zhao et al., 2020). To further verify that these four band crossing points in R2 belong to nodal lines, 3-D and 2-D plots of bands 1 and 3 in the $k_z = 0$ plane are given in **Figure 12**. One M-point-centered closed nodal line, marked as a white line, occurs in the $k_z = 0$ plane. Similarly, the 3-D and 2-D plots of bands 1 and 2 in the $k_z = 0$ plane are shown in **Figure 13**. The other M-point-centered nodal line with a closed shape appears in the $k_z = 0$ plane. However, these two closed nodal lines exhibit different shapes and sizes, and are located at different energies. The closed nodal line shown in **Figure 13** is larger than that in **Figure 12**. An overall illustration of the M-point-centered double closed nodal lines in the $k_z = 0$ plane is shown in **Figure 14**.

Typically, drum-head-like surface states that originate from the bulk band crossing points can be observed (Zhou et al., 2018; Yi et al., 2019). To further prove this argument, the spectrum is projected on the (001) PtO tetragonal

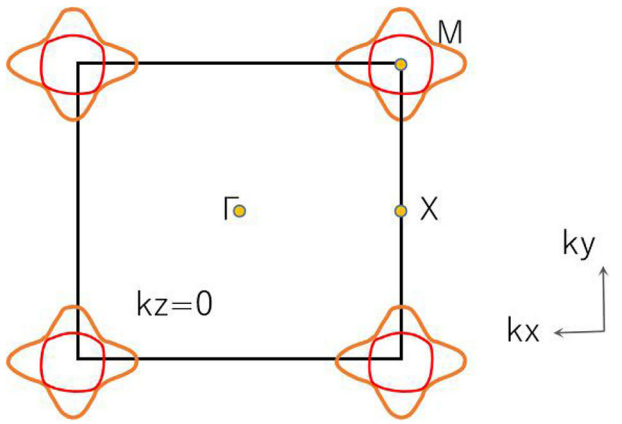

FIGURE 14 | Illustration of M-point-centered double closed nodal lines in the $k_z = 0$ plane. Double nodal lines are marked using different colors.

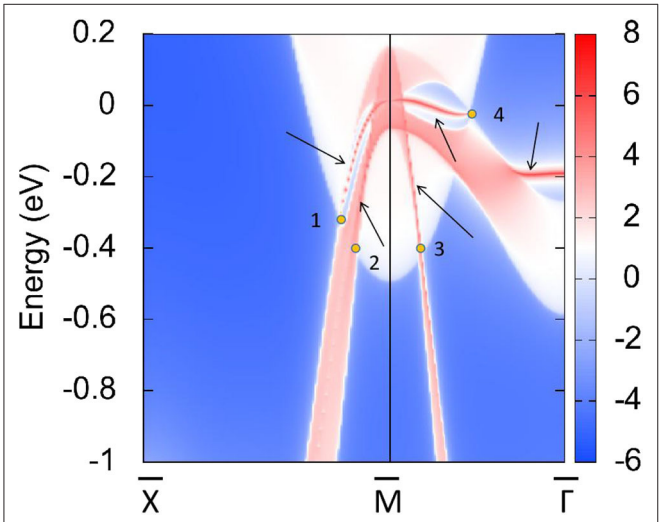

FIGURE 15 | Projected spectrum on the (001) PtO tetragonal crystal surface. Band crossing points 1, 2, 3, and 4 are marked as yellow balls and the drum-head-like surface states are highlighted using black arrows.

crystal surface in **Figure 15**. The drum-head-like surface states clearly appear outside and inside band crossing points 1, 2, 3, and 4.

CONCLUSIONS

In summary, we have systematically used first-principles calculations to study the electronic, mechanical, and topological properties of tetragonal phase PtO, which is a realistic material. PtO is an excellent topological semimetal with pairs of triple nodal points and double closed nodal lines in the $k_z = 0$ plane when the spin–orbit coupling effect is ignored. The 0-D triple nodal points and 1-D closed nodal lines are further confirmed by the exotic Fermi arc surface states and drum-head-like surface states, respectively. The mechanical properties and phonon dispersion of this material allowed us to determine that PtO is mechanically stable, elastically ductile, and dynamically stable. These results demonstrate that PtO is an interesting material, which can be used to achieve experimental detection of nodal points and nodal lines or to further practical applications.

DATA AVAILABILITY STATEMENT

All datasets generated for this study are included in the article/**Supplementary Material**.

AUTHOR CONTRIBUTIONS

YL: software, supervision, and conceptualization. JX and VS: reviewing and editing. All authors contributed to the article and approved the submitted version.

FUNDING

This work is supported by the first batch of post-doctoral research fund projects in Yunnan Province (Serial No. 9), the Science and Technology Research Program of Chongqing Municipal Education Commission (Grant No. KJQN201801346), and the Chongqing University of Arts and Sciences Foundation (Grant No. Z2011Rcyj05).

SUPPLEMENTARY MATERIAL

The Supplementary Material for this article can be found online at: https://www.frontiersin.org/articles/10.3389/fchem.2020.00704/full#supplementary-material

REFERENCES

Abutalib, M. M. (2019). A DFT based prediction of a new 2D zirconium disulfide Pmmm-ZrS_2 monolayer: A quasi direct band gap semiconductor. *Res. Phys.* 12, 903–907. doi: 10.1016/j.rinp.2018.10.028

Cai, J., Xie, Y., Chang, P., Kim, H., and Chen, Y. (2018). Nodal-chain network, intersecting nodal rings and triple points coexisting in nonsymmorphic Ba_3Si_4. *Phys. Chem. Chem. Phys.* 20, 21177–21183. doi: 10.1039/C8CP02810A

Chen, H., Zhang, S., Jiang, W., Zhang, C., Guo, H., Liu, Z., et al. (2018). Prediction of two-dimensional nodal-line semimetals in a carbon nitride covalent network. *J. Mater. Chem. C* 6, 11252–11259. doi: 10.1039/C8TA02555J

Chiu, C. K., and Schnyder, A. P. (2014). Classification of reflection-symmetry-protected topological semimetals and nodal superconductors. *Phys. Rev. B* 90:205136. doi: 10.1103/PhysRevB.90.205136

Ding, G., Hu, Y., Li, D., and Wang, X. (2019). A comparative study of thermoelectric properties between bulk and monolayer SnSe. *Res. Phys.* 15:102631. doi: 10.1016/j.rinp.2019.102631

Ernzerhof, M., and Scuseria, G. E. (1999). Assessment of the Perdew–Burke–Ernzerhof exchange-correlation functional. *J. Chem. Phys.* 110, 5029–5036. doi: 10.1063/1.478401

Fang, C., Gilbert, M. J., Dai, X., and Bernevig, B. A. (2012). Multi-Weyl topological semimetals stabilized by point group

symmetry. *Phys. Rev. Lett.* 108:266802. doi: 10.1103/PhysRevLett.108.266802

Fang, C., Lu, L., Liu, J., and Fu, L. (2016). Topological semimetals with helicoid surface states. *Nat. Phys.* 12, 936–941. doi: 10.1038/nphys3782

Fu, B. B., Yi, C. J., Zhang, T. T., Caputo, M., Ma, J. Z., Gao, X., et al. (2019a). Dirac nodal surfaces and nodal lines in ZrSiS. *Sci. Adv.* 5:eaau6459. doi: 10.1126/sciadv.aau6459

Fu, J., Song, T., Liang, X., and Zhao, G. (2019b). Composition dependence of phonon and thermodynamic properties of the ternary AlGaN mixed crystal. *Res. Phys.* 14:102505. doi: 10.1016/j.rinp.2019.102505

Gao, H., Venderbos, J. W., Kim, Y., and Rappe, A. M. (2019). Topological semimetals from first-principles. *Ann. Rev. Mater. Res.* 49, 153–183. doi: 10.1146/annurev-matsci-070218-010049

Gao, Y., Xie, Y., Chen, Y., Gu, J., and Chen, Z. (2018). Spindle nodal chain in three-dimensional α' boron. *Phys. Chem. Chem. Phys.* 20, 23500–23506. doi: 10.1039/C8CP03874K

Hafner, J. (2007). Materials simulations using VASP—a quantum perspective to materials science. *Comp. Phys. Commun.* 177, 6–13. doi: 10.1016/j.cpc.2007.02.045

Han, Y., Wu, M., Feng, Y., Cheng, Z., Lin, T., Yang, T., et al. (2019). Competition between cubic and tetragonal phases in all-d-metal Heusler alloys, $X_{2-x}Mn_{1+x}V$ (X = Pd, Ni, Pt, Ag, Au, Ir, Co; x = 1, 0): a new potential direction of the Heusler family. *IUCrJ* 6, 465–472. doi: 10.1107/S2052252519004007

He, T., Zhang, X., Meng, W., Jin, L., Dai, X., and Liu, G. (2019). Topological nodal lines and nodal points in the antiferromagnetic material β-Fe_2PO_5. *J. Mater. Chem. C* 7, 12657–12663. doi: 10.1039/C9TC04046C

Hosur, P., Parameswaran, S. A., and Vishwanath, A. (2012). Charge transport in Weyl semimetals. *Phys. Rev. Lett.* 108:046602. doi: 10.1103/PhysRevLett.108.046602

Hosur, P., and Qi, X. (2013). Recent developments in transport phenomena in Weyl semimetals. *Comptes Rendus Phys.* 14, 857–870. doi: 10.1016/j.crhy.2013.10.010

Jia, K., Yang, C., Wang, M., Ma, X., and Yi, Y. (2019). First-principles insight on elastic, electronic, and thermoelectric transport properties of BAgX (X =Ti, Zr, Hf). *Res. Phys.* 15:102563. doi: 10.1016/j.rinp.2019.102563

Jin, L., Zhang, X., Dai, X., Liu, H., Chen, G., and Liu, G. (2019b). Centrosymmetric Li_2NaN: a superior topological electronic material with critical-type triply degenerate nodal points. *J. Mater. Chem. C* 7, 1316–1320. doi: 10.1039/C8TC05930F

Jin, L., Zhang, X., He, T., Meng, W., Dai, X., and Liu, G. (2019a). Topological nodal line state in superconducting NaAlSi compound. *J. Mater. Chem. C* 7, 10694–10699. doi: 10.1039/C9TC03464A

Jin, L., Zhang, X., He, T., Meng, W., Dai, X., and Liu, G. (2020). Electronic structure, doping effect and topological signature in realistic intermetallics $Li_{3-x}Na_xM$ (x = 3, 2, 1, 0; M = N, P, As, Sb, Bi). *Phys. Chem. Chem. Phys.* 22, 5847–5854. doi: 10.1039/C9CP06033B

Kobayashi, S., and Sato, M. (2015). Topological superconductivity in Dirac semimetals. *Phys. Rev. Lett.* 115:187001. doi: 10.1103/PhysRevLett.115.187001

Kresse, G., and Joubert, D. (1999). From ultrasoft pseudopotentials to the projector augmented-wave method. *Phys. Rev. B* 59:1758. doi: 10.1103/PhysRevB.59.1758

Kumar, N., Yao, M., Nayak, J., Vergniory, M. G., Bannies, J., Wang, Z., et al. (2020). Signatures of sixfold Degenerate Exotic Fermions in a superconducting Metal $PdSb_2$. *Adv. Mater.* 32:1906046. doi: 10.1002/adma.201906046

Lejaeghere, K., Bihlmayer, G., Björkman, T., Blaha, P., Blügel, S., Blum, V., et al. (2016). Reproducibility in density functional theory calculations of solids. *Science* 351:aad3000. doi: 10.1126/science.aad3000

Liu, Z. K., Zhou, B., Zhang, Y., Wang, Z. J., Weng, H. M., Prabhakaran, D., et al. (2014). Discovery of a three-dimensional topological Dirac semimetal, Na_3Bi. *Science* 343, 864–867. doi: 10.1126/science.1245085

Lundgren, R., Laurell, P., and Fiete, G. A. (2014). Thermoelectric properties of Weyl and Dirac semimetals. *Phys. Rev. B* 90:165115. doi: 10.1103/PhysRevB.90.165115

Miransky, V. A., and Shovkovy, I. A. (2015). Quantum field theory in a magnetic field: from quantum chromodynamics to graphene and Dirac semimetals. *Phys. Rep.* 576, 1–209. doi: 10.1016/j.physrep.2015.02.003

Moore and Pauling, 1941∼Moore, W. J. Jr, and Pauling, L. (1941). The crystal structures of the tetragonal monoxides of lead, tin, palladium, and platinum. *J. Am. Chem. Soc.* 63, 1392–1394. doi: 10.1021/ja01850a074

Perdew, J. P., Burke, K., and Ernzerhof, M. (1996). Generalized gradient approximation made simple. *Phys. Rev. Lett.* 77:3865. doi: 10.1103/PhysRevLett.77.3865

Pham, A., Klose, F., and Li, S. (2019). Robust topological nodal lines in halide carbides. *Phys. Chem. Chem. Phys.* 21, 20262–20268. doi: 10.1039/C9CP04330F

Qie, Y., Liu, J., Wang, S., Sun, Q., and Jena, P. (2019). Tetragonal C_{24}: a topological nodal-surface semimetal with potential as an anode material for sodium ion batteries. *J. Mater. Chem. A* 7, 5733–5739. doi: 10.1039/C8TA11276B

Sultana, F., Uddin, M. M., Ali, M. A., Hossain, M. M., Naqib, S. H., and Islam, A. K. M. A. (2018). First principles study of M_2InC (M = Zr, Hf and Ta) MAX phases: the effect of M atomic species. *Res. Phys.* 11, 869–876. doi: 10.1016/j.rinp.2018.10.044

Sun, J., Marsman, M., Csonka, G. I., Ruzsinszky, A., Hao, P., Kim, Y. S., et al. (2011). Self-consistent meta-generalized gradient approximation within the projector-augmented-wave method. *Phys. Rev. B* 84:035117. doi: 10.1103/PhysRevB.84.035117

Vazifeh, M. M., and Franz, M. (2013). Electromagnetic response of Weyl semimetals. *Phys. Rev. Lett.* 111:027201. doi: 10.1103/PhysRevLett.111.027201

Villanova, J. W., and Park, K. (2018). Magnetic field induced Weyl semimetal from Wannier-function-based tight-binding model. *Phys. Rev. B* 98:075123. doi: 10.1103/PhysRevB.98.075123

Wang, X., Ding, G., Cheng, Z., Surucu, G., Wang, X. L., and Yang, T. (2020a). Novel topological nodal lines and exotic drum-head-like surface states in synthesized CsCl-type binary alloy TiOs. *J. Adv. Res.* 22, 137–144. doi: 10.1016/j.jare.2019.12.001

Wang, X., Ding, G., Cheng, Z., Surucu, G., Wang, X. L., and Yang, T. (2020b). Rich topological nodal line bulk states together with drum-head-like surface states in NaAlGe with anti-PbFCl type structure. *J. Adv. Res.* 23, 95–100. doi: 10.1016/j.jare.2020.01.017

Weng, H., Fang, C., Fang, Z., and Dai, X. (2016a). Topological semimetals with triply degenerate nodal points in θ-phase tantalum nitride. *Phys. Rev. B* 93:241202. doi: 10.1103/PhysRevB.93.241202

Weng, H., Fang, C., Fang, Z., and Dai, X. (2016b). Coexistence of Weyl fermion and massless triply degenerate nodal points. *Phys. Rev. B* 94:165201. doi: 10.1103/PhysRevB.94.165201

Wu, W., Liu, Y., Li, S., Zhong, C., Yu, Z. M., Sheng, X. L., et al. (2018). Nodal surface semimetals: theory and material realization. *Phys. Rev. B* 97, 115125. doi: 10.1103/PhysRevB.97.115125

Xu, S. Y., Belopolski, I., Alidoust, N., Neupane, M., Bian, G., Zhang, C., et al. (2015a). Discovery of a Weyl fermion semimetal and topological fermi arcs. *Science* 349, 613–617. doi: 10.1126/science.aaa9297

Xu, S. Y., Liu, C., Kushwaha, S. K., Sankar, R., Krizan, J. W., Belopolski, I., et al. (2015b). Observation of Fermi arc surface states in a topological metal. *Science* 347, 294–298. doi: 10.1126/science.1256742

Yalameha, S., and Nourbakhsh, Z. (2020). Coexistence of type-I and critical-type nodal line states in intermetallic compounds ScM (M = Cu, Ag, Au). *J. Phys. Condensed Matter* 32:295502. doi: 10.1088/1361-648X/ab80f4

Yan, B., and Felser, C. (2017). Topological materials: weyl semimetals. *Ann. Rev. Condensed Matter Phys.* 8, 337–354. doi: 10.1146/annurev-conmatphys-031016-025458

Yang, T., Khenata, R., and Wang, X. (2020). Predicted remarkably topological nodal surface states in $P6_3/m$ type Sr_3WN_3 from first-principles. *Res. Phys.* 17:103026. doi: 10.1016/j.rinp.2020.103026

Yi, X., Li, W. Q., Li, Z. H., Zhou, P., Ma, Z., and Sun, L. Z. (2019). Topological dual double node-line semimetals NaAlSi(Ge) and their potential as cathode material for sodium ion batteries. *J. Mater. Chem. C* 7, 15375–15381. doi: 10.1039/C9TC04096J

Young, S. M., and Kane, C. L. (2015). Dirac semimetals in two dimensions. *Phys. Rev. Lett.* 115:126803. doi: 10.1103/PhysRevLett.115.126803

Zhang, X., Yu, Z. M., Zhu, Z., Wu, W., Wang, S. S., Sheng, X. L., et al. (2018). Nodal loop and nodal surface states in the Ti_3Al family of materials. *Phy. Rev. B* 97:235150. doi: 10.1103/PhysRevB.97.235150

Zhao, Z., Zhang, Z., and Guo, W. (2020). A family of all sp2-bonded carbon allotropes of topological semimetals with strain-robust nodal-lines. *J. Mater. Chem. C* 8, 1548–1555. doi: 10.1039/C9TC05470G

Zhou, P., Ma, Z., and Sun, L. Z. (2018). Coexistence of open and closed type nodal line topological semimetals in two dimensional B_2C. *J. Mater. Chem. C* 6, 1206–1214. doi: 10.1039/C7TC05095J

Zou, Z. C., Zhou, P., Ma, Z., and Sun, L. Z. (2019). Strong anisotropic nodal lines in the TiBe family. *Phys. Chem. Chem. Phys.* 21, 8402–8407. doi: 10.1039/C9CP00508K

Zyuzin, A. A., and Burkov, A. A. (2012). Topological response in Weyl semimetals and the chiral anomaly. *Phys. Rev. B* 86:115133. doi: 10.1103/PhysRevB.86.115133

Conflict of Interest: The authors declare that the research was conducted in the absence of any commercial or financial relationships that could be construed as a potential conflict of interest.

frontiers in Chemistry

ORIGINAL RESEARCH
published: 26 August 2020
doi: 10.3389/fchem.2020.00727

Cubic Hafnium Nitride: A Novel Topological Semimetal Hosting a 0-Dimensional (0-D) Nodal Point and a 1-D Topological Nodal Ring

Yang Li[1,2]* *and Jihong Xia*[1]*

[1] Department of Physics, Chongqing University of Arts and Sciences, Chongqing, China, [2] Faculty of Mechanical and Electrical Engineering, Kunming University of Science and Technology, Kunming, China

Very recently, topological semimetals with nontrivial band crossing and associated topological surface states have received widespread attention. Various types of topological semimetals, including nodal point semimetals, nodal line semimetals, and nodal surface semimetals, have been predicted from first principles. In absence of spin-orbit coupling (SOC) effect, we propose that cubic-type hafnium nitride (HfN) with a $Pm\bar{3}m$ space group is a novel topological semimetal hosting a rare 0-D triple nodal point and a 1-D topological nodal ring. More importantly, the interesting 0-D and 1-D topological states all occur near the Fermi level, and these topological states are not disturbed by other extraneous bands. When the SOC effect is taken into consideration, 0-D triple nodal point was gapped and a new 0-D topological element, namely, Dirac point appears along Γ-R path. Finally, the dynamical and mechanical stabilities of this semimetal and its associated mechanical properties are discussed in order to provide a reference for future investigations. Our work promises that HfN can serve as a superior topological semimetal with high stability, excellent mechanical properties, and rich topological states.

Keywords: topological nodal ring, triple point, density functional theory, phonon dispersion, mechanical behaviors

OPEN ACCESS

Edited by:
Xiaotian Wang,
Southwest University, China

Reviewed by:
Jiangchao Han,
Beihang University, China
Yongmao Cai,
Northeast Electric Power University, China

***Correspondence:**
Yang Li
liyang@cqwu.edu.cn;
liyang_physics@126.com
Jihong Xia
jhxia@cqwu.edu.cn;
jhxia1010@126.com

Specialty section:
This article was submitted to Theoretical and Computational Chemistry, a section of the journal Frontiers in Chemistry

Received: *19 June 2020*
Accepted: *14 July 2020*
Published: *26 August 2020*

Citation:
Li Y and Xia J (2020) Cubic Hafnium Nitride: A Novel Topological Semimetal Hosting a 0-Dimensional (0-D) Nodal Point and a 1-D Topological Nodal Ring. Front. Chem. 8:727. doi: 10.3389/fchem.2020.00727

INTRODUCTION

After the discovery of topological insulators (Zhang et al., 2009; Hasan and Kane, 2010; Yu et al., 2010; Qi and Zhang, 2011; Rechtsman et al., 2013), topological semimetals (Jiang et al., 2015; Fang et al., 2016; Chang et al., 2017; Yan and Felser, 2017; Gao et al., 2019) with topological band inversion and exotic topological boundary states have attracted widespread attention. To date, many types of topological semimetals have been proposed, including topological nodal point semimetals (Liu et al., 2013, 2019; Li et al., 2014; Xu et al., 2014, 2016, 2020; Dvorak and Wu, 2015; Cheng et al., 2017; Zhong et al., 2017; Gao et al., 2019; Zhang et al., 2019), topological nodal line semimetals (Cai et al., 2018; Chen et al., 2018; Gao et al., 2018; Zhou et al., 2018; He et al., 2019; Jin et al., 2019a; Pham et al., 2019; Yi et al., 2019; Zou et al., 2019; Zhao et al., 2020), and topological nodal surface semimetals (Qie et al., 2019; Yang and Zhang, 2020).

For nodal point semimetals, the most studied members among them are Weyl and Dirac semimetals. Weyl semimetals (Hosur and Qi, 2013; Soluyanov et al., 2015; Zheng et al., 2016; Lin et al., 2017; Zhang M. et al., 2018; Bedoyapinto et al., 2020; Geishendorf et al., 2020; Thakur et al., 2020) possess twofold degenerate 0-D Weyl nodes, which are protected by inversion (P) or

time-reversal (T) symmetries. However, Dirac semimetals (Chen et al., 2015; Gong et al., 2017; Yuan et al., 2017; Zhang X. et al., 2018; Jing and Heine, 2019) host quadruple-degenerate 0-D Dirac points, and these massless Dirac points are protected by the crystalline symmetry. In addition to the Weyl and Dirac semimetals generated by twofold- or quadruple-degenerate nodal points, topological nodal point semimetals with triple-degenerate 0-D nodal points have also become a new focus of research due to their novel topological states and related physics properties. Among inversion-asymmetric and centrosymmetric systems, some members are proposed to be triple point-type semimetals (He et al., 2017; Lv et al., 2017).

Moreover, topological nodal line semimetals (Cai et al., 2018; Chen et al., 2018; Zhou et al., 2018; Pham et al., 2019; Yi et al., 2019) possess 1-D topological elements, which are formed by band crossing along a line in momentum space. Compared to the topological nodal point semimetals with 0-D topological elements, topological nodal line semimetals feature more subtypes due to the fact that the 1-D line can deform into many different geometries. Topological nodal ring semimetals with a 1-D nodal loop in momentum space form one well-known type of topological nodal line semimetal. Topological nodal ring semimetals have emerged as a hot research topic very recently because these topological materials have intriguing electronic band behaviors and interesting drum-head-like surface states.

Topological materials are suitable for a range of potential applications, such as superconductivity (Das et al., 2012), chemical sensors (Schoop et al., 2018), and thermoelectricity (Sung et al., 2014). However, the candidates for such topological semimetals that possess more than one topological element are quite limited, which greatly restricts further investigations into those topological semimetals with rich topological elements. We would like to point out that materials with CsCl-type enjoy many interesting properties, such as simple in crystal structure, easy of synthesis and high phase stability, and thus, CsCl-type materials are a good target for searching for now functional materials. In this study, we propose, from first principles, that cubic (CsCl type) hafnium nitride (HfN), which is a phase-stable material, can serve as an interesting topological semimetal exhibiting both 0-D and 1-D topological elements. Furthermore, these topological elements all appear around the Fermi level. We hope the 0-D and 1-D topological elements, as well as the nontrivial surface states in cubic HfN, will soon be confirmed experimentally.

COMPUTATIONAL DETAILS

All atomic and electronic structure calculations were performed by means of the Vienna *Ab initio* Simulation Package (VASP) (Sun et al., 2003) within the generalized gradient approximation (Perdew et al., 1996) using the Perdew–Burke–Ernzerhof (PBE) exchange-correlation functional. The projector augmented wave (PAW) (Perdew et al., 1998) pseudo-potential was employed with a cutoff energy of 600 eV for plane-wave expansions. The whole Brillouin zone is sampled with the Γ- centered k mesh of 11 × 11 × 11. The convergence criteria for energy and force were set at 10^{-6} eV per atom and 0.0005 eV/Å, respectively. The surface states of HfN were investigated in this study on a basis of a slab model built by WannierTools package (http://www.wanniertools.com) (Mostofi et al., 2008), according to the method of maximally localized Wannier functions. The value of NSlab, i.e., Number of slabs for slab band was set as 20 in this work.

RESULTS AND DISCUSSION

Cubic phase HfN with space group $Pm\bar{3}m$ and ICSD: 183420[1] was chosen for this study. The crystal structure of HfN was optimized and is shown in **Figure 1A**. The optimized lattice constants are a = b = c = 2.803 Å, which are in good agreement with the calculated results shown in the materials project database[1] (a = b = c = 2.816 Å). Subsequently, we will study the electronic structure, topological elements, and surface states using the lattice constants obtained from the crystal structure.

The 3-D bulk Brillouin zone (BZ) is shown in **Figure 1B**. Based on the 3-D BZ, the phonon dispersion was determined in order to examine the dynamical stability of cubic HfN material with this space group. It is noted that materials are dynamically stable when there exist no imaginary phonon modes in their phonon dispersion curves. The phonon dispersion obtained along the Γ-X-M-Γ-R-X direction is shown in **Figure 2**. The absence of a negative frequency in the figure confirms the dynamical stability of the HfN material.

Because HfN is a cubic system, the mechanical behavior of HfN can be achieved using three elastic constants: C_{11}, C_{12}, and C_{44}. The results for these are as follows: C_{11} = 551.16 GPa, C_{12} = 92.96 GPa, and C_{44} = 24.31 GPa. The mechanical stability of cubic HfN can be examined based on the Born–Huang criteria as follows:

$$\text{Criterion 1}: C_{11} - C_{12} > 0;$$
$$\text{Criterion 2}: C_{11} + 2C_{12} > 0;$$
$$\text{Criterion 3}: C_{44} > 0.$$

HfN is mechanically stable based on the above-mentioned Born–Huang criteria. Some other important mechanical parameters can also be obtained, such as the bulk modulus (B = 245.68 GPa), shear modulus (G = 72.03 GPa), Poisson's ratio (ν = 0.366), and Pugh's index (B/G = 3.41), based on C_{11}, C_{12}, and C_{44}. B/G and ν are normally used to examine the brittleness and ductility of materials, with critical values of 1.75 and 0.26, respectively. For HfN, it is elastically ductile. Furthermore, the value of ν is also used to examine the nature of the chemical bonds of materials, with a critical value of 0.25; a value of ν greater (or less) than 0.25 implies an ionic (or covalent) nature. The chemical bonds of HfN are mainly ionic.

The calculated anisotropy parameter A value of 0.106 deviates from unity, reflecting the fact that HfN is elastically anisotropic. Furthermore, the directional-dependence anisotropy of Young's modulus, the shear modulus, and Poisson's ratio for HfN were obtained by means of the ELATE (Gaillac et al., 2016) program,

[1]https://www.materialsproject.org/materials/mp-1001834/

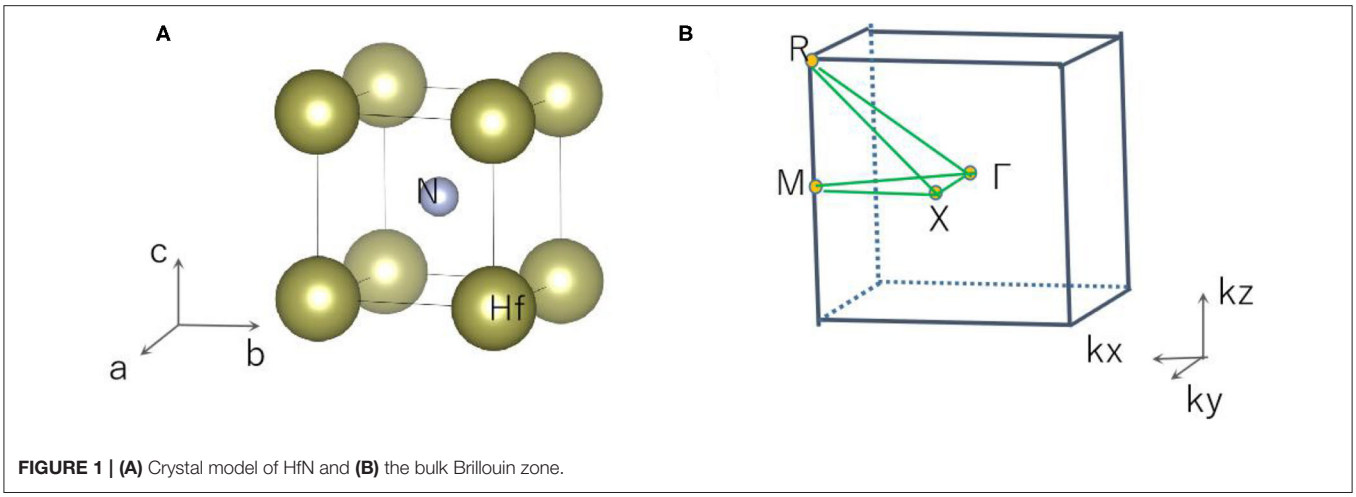

FIGURE 1 | (A) Crystal model of HfN and **(B)** the bulk Brillouin zone.

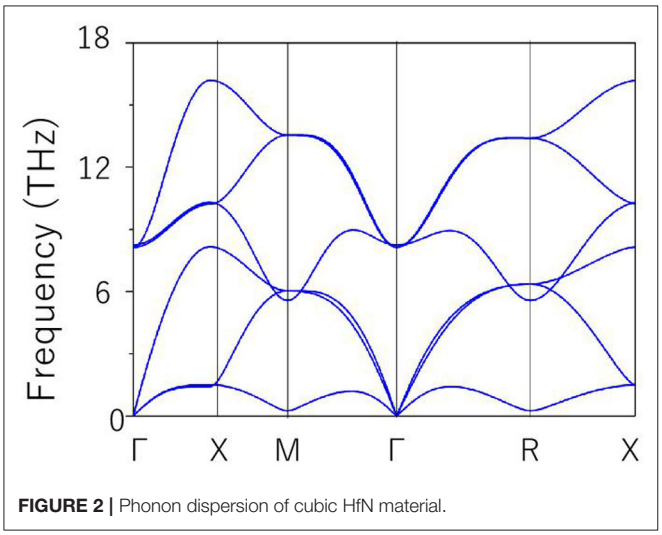

FIGURE 2 | Phonon dispersion of cubic HfN material.

as shown in **Figures S1–S3**, respectively. Young's modulus, the shear modulus, and Poisson's ratio in **Figures S1–S3** all show obvious anisotropy. We would like to point out that the mechanical anisotropy of HfN is very important for its practical applications.

Based on the values of the equilibrium lattice constants obtained, we studied the electronic band structures of cubic HfN. The Γ-X-M-Γ-R-X high symmetry points (**Figure 1B**) in the first BZ were selected to describe the band structure of HfN. Using the generalized gradient approximation (GGA) method, the calculated band structure is shown in **Figure 3A**. When the spin-orbit coupling effect is ignored, we can see that HfN manifests a semimetallic band structure with conduction and valence bands overlapping each other. Interestingly, one can see that HfN possesses several band crossing points located close to the Fermi energy. We divided these band crossing points into two parts, i.e., regions R1 and R2, and we discuss these in detail separately. Before discussing the band crossing points in regions R1 and R2, the state-of-the-art Heyd–Scuseria–Ernzerhof (HSE) 06 method (Heyd and Scuseria, 2004), which can be seen as a better way of describing the band crossing points than the GGA method, was also selected to further prove the occurrence of the band crossing points in regions R1 and R2. The results of the calculated band structure of HfN with HSE 06 along the X-M-Γ-R directions are shown in **Figure 3B**.

First, we study the band crossing point in region R2, which indicates a band crossing point at the Γ point. This band crossing point was generated by one non-degenerate band and one doubly degenerate band. That is to say, this band crossing point is a triple nodal point, as shown in **Figures 3A,B**.

Next, we discuss the band crossing points along the X-M-Γ directions in region R1. Here, one can see that there are two band crossing points in total, generated by the crossing of two non-degenerate bands. Because this cubic HfN system possesses both P and T symmetries, both band crossing points in this system cannot be regarded as isolated points. Normally, both points should reside on the nodal line. To further verify that these two band crossing points in region R1 belong to a nodal line, a 3-D plot of both bands in the $k_z = 0$ plane is shown in **Figure 3C**. One can see that there is a closed nodal line, i.e., nodal ring, in the $k_z = 0$ plane, and the two band crossing points in region R1 belong to the closed nodal line (marked as a white ring). To confirm the shape of the closed nodal line in the $kz = 0$ plane, we show the 2-D plot of both bands in the $k_z = 0$ plane in **Figure 3D**. A near-ring shape can be seen in this figure. It is well-known that the nodal ring (Wang et al., 2020) can be classified into three types: type I, type II, and a hybrid type, according to the degree of tilting of the band crossing points in the nodal ring. Type I (or II) nodal rings are formed only by type I (or II) band crossing points, while the hybrid rings simultaneously host type I and type II band crossing points [more details about the three types of nodal ring can be found in (Wang et al., 2020)]. As shown in **Figure 3C**, the nodal ring in the $k_z = 0$ plane belongs to type I.

Figure 4 shows the HfN (001) surface state without the effect of SOC, which clearly shows that topological surface states can be found around the triple nodal point at the points marked by the arrows. However, the surface state near the nodal ring is only faintly visible inside the projected topological nodal ring (see the arrow along the direction).

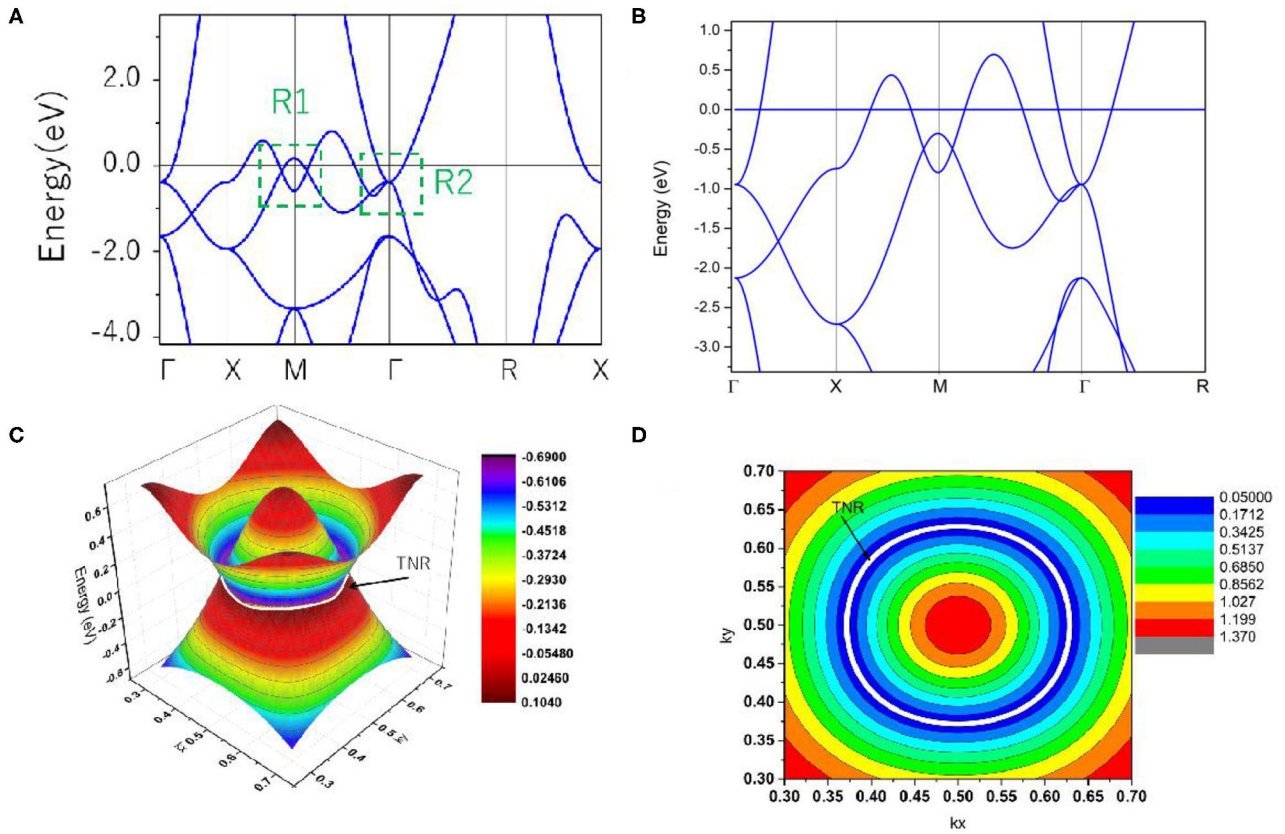

FIGURE 3 | (A) Band structure of HfN via the GGA method; **(B)** Band structure of HfN via the HSE 06 method; **(C)** 3-D plot of both bands in the $k_z = 0$ plane in region R1; **(D)** 2-D plot of both bands in the $k_z = 0$ plane in region R1.

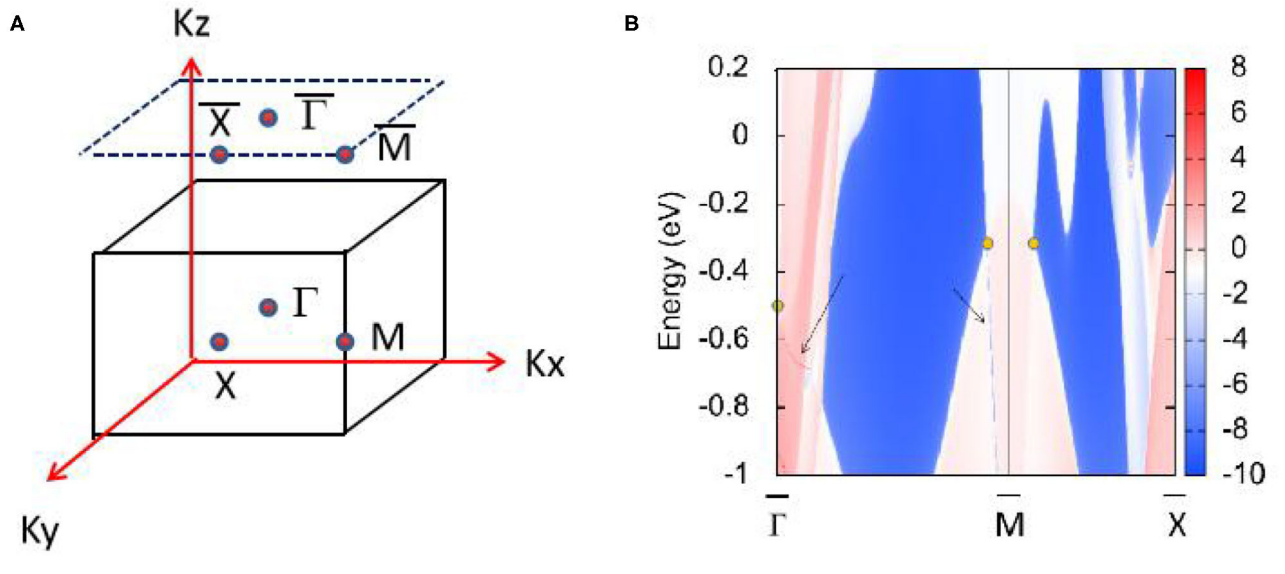

FIGURE 4 | (A) (0 0 1) surface Brillouin zone of HfN; **(B)** Projection spectrum on the (001) surface state of HfN near the 1-D nodal ring and 0-D triple nodal point. The band crossing points are highlighted by yellow circles and the surface states are marked by black arrows.

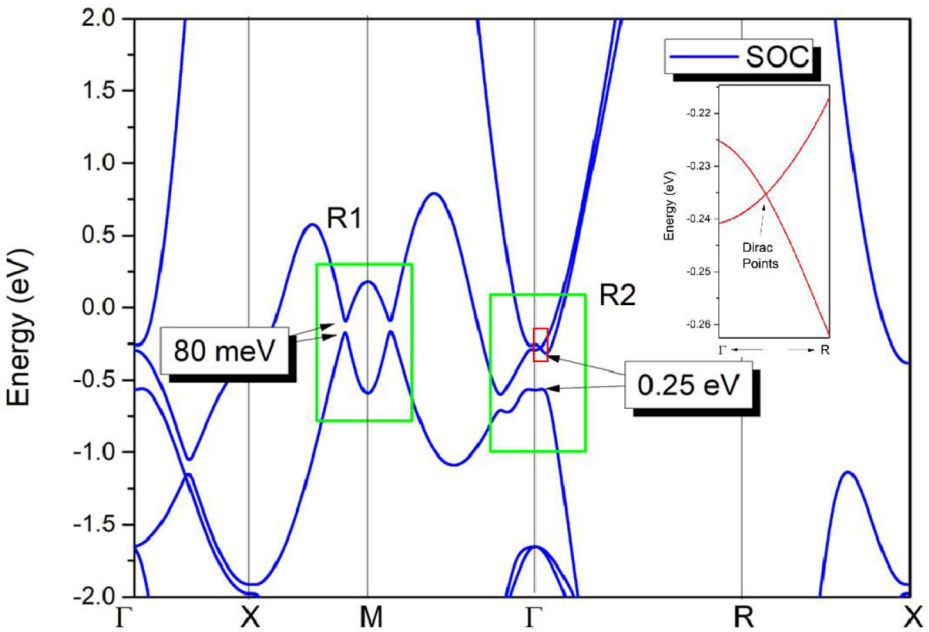

FIGURE 5 | Band structure of HfN via the GGA method; The SOC effect was taken into consideration during the calculation. Insert figure: Enlarged band structure of HfN along Γ-R direction.

In the final, the effect of SOC on the electronic structure has been discussed and results are given in **Figure 5**. At the Γ point, an energy band gap of 0.25 eV can be found, reflecting that the triple nodal point is gapped under SOC. However, along Γ-R direction, two bands now cross with each other at−0.235 eV below the Fermi level. In this cubic HfN, the time-reversal and inversion symmetries retain, thus each band is twofold degenerate when the SOC is taken into consideration. This band-crossing point at −0.235 eV along Γ-R direction (see the insert figure in **Figure 5**) is a Dirac point with fourfold degeneracy. We would like to point out that similar triple nodal point - Dirac point transition can also be observed in TiB_2 (Zhang et al., 2017) and Li_2NaN (Jin et al., 2019b) materials.

In R1, two band crossing points are also gapped due to the SOC effect. The SOC gaps are calculated to be ∼80 meV, as shown in **Figure 5**. We would like to point out that most nodal lines proposed so far will be gapped under the effect of SOC. The SOC-induced gaps in HfN are comparable with those in typical nodal line semimetals, such as Cu_3NPd (Yu et al., 2015) (60–100 meV), CaAgBi (Yamakage et al., 2016) (80–140 meV), and $BaSn_2$ (Huang et al., 2016) (60–160 meV).

CONCLUSIONS

In this study, we report that cubic HfN is a newly designed topological semimetal with rich topological elements, i.e., 0-D and 1-D band crossing points. When the spin-orbit coupling (SOC) effect is ignored, near the Fermi level, HfN possesses a triple nodal point at the Γ point and a nodal ring in the $k_z = 0$ plane. The topological surface states around the 0-D and 1-D band crossing points were determined. When the SOC effect is taken into consideration, 0-D triple nodal point disappears, however, new topological signature, i.e., 0-D Dirac point occurs along Γ-R direction. The computational results also suggest that cubic HfN possesses mechanical stability, dynamical stability, elastic ductility, and anisotropy. Our investigation has revealed that HfN is a good topological semimetal with rich topological elements, high stability, and important mechanical properties.

DATA AVAILABILITY STATEMENT

All datasets generated for this study are included in the article/**Supplementary Material**.

AUTHOR CONTRIBUTIONS

YL: software, methodology, writing, and supervisor. JX: reviewing. All authors contributed to the article and approved the submitted version.

FUNDING

This work was supported by the first batch of postdoctoral research fund research projects in Yunnan Province (Serial No. 9), the Science and Technology Research Program of Chongqing Municipal Education Commission (Grant No. KJQN201801346), and the Chongqing University of Arts and Sciences Foundation (Grant No. Z2011Rcyj05).

SUPPLEMENTARY MATERIAL

The Supplementary Material for this article can be found online at: https://www.frontiersin.org/articles/10.3389/fchem.2020.00727/full#supplementary-material

REFERENCES

Bedoyapinto, A., Pandeya, A. K., Liu, D., Deniz, H., Chang, K., Tan, H., et al. (2020). Realization of epitaxial NbP and TaP weyl semimetal thin films. *ACS Nano*. 14, 4405–4413. doi: 10.1021/acsnano.9b09997

Cai, J., Xie, Y., Chang, P., Kim, H., and Chen, Y. (2018). Nodal-chain network, intersecting nodal rings and triple points coexisting in nonsymmorphic Ba_3Si_4. *Phys. Chem. Chem. Phys.* 20, 21177–21183. doi: 10.1039/C8CP02810A

Chang, T., Xu, S., Sanchez, D., Tsai, W., Huang, S., Chang, G., et al. (2017). Type-II symmetry-protected topological dirac semimetals. *Phys. Rev. Lett.* 119, 026404. doi: 10.1103/PhysRevLett.119.026404

Chen, H., Zhang, S., Jiang, W., Zhang, C., Guo, H., Liu, Z., et al. (2018). Prediction of two-dimensional nodal-line semimetals in a carbon nitride covalent network. *J. Mater. Chem. C* 6, 11252–11259. doi: 10.1039/C8TA02555J

Chen, Z., Zhang, C., Zou, Y., Zhang, E., Yang, L., Hong, M., et al. (2015). Scalable growth of high mobility dirac semimetal Cd_3As_2 microbelts. *Nano Lett.* 15, 5830–5834. doi: 10.1021/acs.nanolett.5b01885

Cheng, T., Lang, H., Li, Z., Liu, Z., and Liu, Z. (2017). Anisotropic carrier mobility in two-dimensional materials with tilted Dirac cones: theory and application. *Phys. Chem. Chem. Phys.* 19, 23942–23950. doi: 10.1039/C7CP03736H

Das, A., Ronen, Y., Most, Y., Oreg, Y., Heiblum, M., and Shtrikman, H. (2012). Zero-bias peaks and splitting in an Al–InAs nanowire topological superconductor as a signature of Majorana fermions. *Nat. Phys.* 8, 887–895. doi: 10.1038/nphys2479

Dvorak, M., and Wu, Z. (2015). Dirac point movement and topological phase transition in patterned graphene. *Nanoscale* 7, 3645–3650. doi: 10.1039/C4NR06454B

Fang, C., Lu, L., Liu, J., and Fu, L. (2016). Topological semimetals with helicoid surface states. *Nat. Phys.* 12, 936–941. doi: 10.1038/nphys3782

Gaillac, R., Pullumbi, P., and Coudert, F. (2016). ELATE: an open-source online application for analysis and visualization of elastic tensors. *J. Phys. Cond. Matter.* 28:275201. doi: 10.1088/0953-8984/28/27/275201

Gao, H., Venderbos, J. W., Kim, Y., and Rappe, A. M. (2019). Topological Semimetals from first-principles. *Annu. Rev. Mater. Res.* 49, 153–183. doi: 10.1146/annurev-matsci-070218-010049

Gao, Y., Xie, Y., Chen, Y., Gu, J., and Chen, Z. (2018). Spindle nodal chain in three-dimensional α' boron. *Phys. Chem. Chem. Phys.* 20, 23500–23506. doi: 10.1039/C8CP03874K

Geishendorf, K., Vir, P., Shekhar, C., Felser, C., Facio, J. I., Den Brink, J. V., et al. (2020). Signatures of the magnetic entropy in the thermopower signals in nanoribbons of the magnetic weyl semimetal $Co_3Sn_2S_2$. *Nano Lett.* 20, 300–305. doi: 10.1021/acs.nanolett.9b03822

Gong, P., Deng, B., Huang, L., Hu, L., Wang, W., Liu, D., et al. (2017). Robust and pristine topological dirac semimetal phase in pressured two-dimensional black phosphorus. *J. Phys. Chem. C* 121, 20931–20936. doi: 10.1021/acs.jpcc.7b08926

Hasan, M. Z., and Kane, C. L. (2010). Colloquium: topological insulators. *Rev. Mod. Phys.* 82, 3045–3067. doi: 10.1103/RevModPhys.82.3045

He, J. B., Chen, D., Zhu, W. L., Zhang, S., Zhao, L., Ren, Z., et al. (2017). Magnetotransport properties of the triply degenerate node topological semimetal tungsten carbide. *Phys. Rev. B* 95:195165. doi: 10.1103/PhysRevB.95.195165

He, T., Zhang, X., Meng, W., Jin, L., Dai, X., and Liu, G. (2019). Topological nodal lines and nodal points in the antiferromagnetic material β-Fe_2PO_5. *J. Mater. Chem. C* 7, 12657–12663. doi: 10.1039/C9TC04046C

Heyd, J., and Scuseria, G. E. (2004). Efficient hybrid density functional calculations in solids: assessment of the Heyd–Scuseria–Ernzerhof screened Coulomb hybrid functional. *J. Chem. Phys.* 121, 1187–1192. doi: 10.1063/1.1760074

Hosur, P., and Qi, X. (2013). Recent developments in transport phenomena in Weyl semimetals. *Comp Rend Phys.* 14, 857–870. doi: 10.1016/j.crhy.2013.10.010

Huang, H., Liu, J., Vanderbilt, D., and Duan, W. (2016). Topological nodal-line semiemtals in alkaline-earth stannides, germanides, and silicides, *Phys. Rev. B* 93:201114. doi: 10.1103/PhysRevB.93.201114

Jiang, Q., Jiang, H., Liu, H., Sun, Q., and Xie, X. C. (2015). Topological imbert-fedorov shift in weyl semimetals. *Phys. Rev. Lett.* 115, 156602. doi: 10.1103/PhysRevLett.115.156602

Jin, L., Zhang, X., Dai, X., Liu, H., Chen, G., and Liu, G. (2019b). Cemtrosymmetric Li2NaN: a superior topological electronic material with critical-type triply degenerate nodal points. *J. Mater. Chem. C* 7, 1316–1320. doi: 10.1039/C8TC05930F

Jin, L., Zhang, X., He, T., Meng, W., Dai, X., and Liu, G. (2019a). Topological nodal line state in superconducting NaAlSi compound. *J. Mater. Chem. C* 7, 10694–10699. doi: 10.1039/C9TC03464A

Jing, Y., and Heine, T. (2019). Two-dimensional kagome lattices made of hetero triangulenes are dirac semimetals or single-band semiconductors. *J. Am. Chem. Soc.* 141, 743–747. doi: 10.1021/jacs.8b09900

Li, X., Dai, Y., Ma, Y., and Huang, B. (2014). Electronic and magnetic properties of honeycomb transition metal monolayers: first-principles insights. *Phys. Chem. Chem. Phys.* 16, 13383–13389. doi: 10.1039/C4CP01512F

Lin, C., Arafune, R., Liu, R., Yoshimura, M., Feng, B., Kawahara, K., et al. (2017). Visualizing type-II weyl points in tungsten ditelluride by quasiparticle interference. *ACS Nano* 11, 11459–11465. doi: 10.1021/acsnano.7b06179

Liu, Z., Feng, W., Xin, H., Gao, Y., Liu, P., Yao, Y., et al. (2019). Two-dimensional spin–valley-coupled Dirac semimetals in functionalized SbAs monolayers. *Mater. Horizons* 6, 781–787. doi: 10.1039/C8MH01588K

Liu, Z., Wang, J., and Li, J. (2013). Dirac cones in two-dimensional systems: from hexagonal to square lattices. *Phys. Chem. Chem. Phys.* 15, 18855–18862. doi: 10.1039/c3cp53257g

Lv, B. Q., Feng, Z., Xu, Q., Gao, X., Ma, J., Kong, L., et al. (2017). Observation of three-component fermions in the topological semimetal molybdenum phosphide. *Nature* 546, 627–631. doi: 10.1038/nature22390

Mostofi, A. A., Yates, J. R., Lee, Y., Souza, I., Vanderbilt, D., and Marzari, N. (2008). Wannier90: a tool for obtaining maximally-localised Wannier functions. *Comput. Phys. Commun.* 178, 685–699. doi: 10.1016/j.cpc.2007.11.016

Perdew, J. P., Burke, K., and Ernzerhof, M. (1996). Generalized gradient approximation made simple. *Phys. Rev. Lett.* 77:3865. doi: 10.1103/PhysRevLett.77.3865

Perdew, J. P., Burke, K., and Ernzerhof, M. (1998). Perdew, burke, and ernzerhof reply. *Phys. Rev. Lett.* 80:891. doi: 10.1103/PhysRevLett.80.891

Pham, A., Klose, F., and Li, S. (2019). Robust topological nodal lines in halide carbides. *Phys. Chem. Chem. Phys.* 21, 20262–20268. doi: 10.1039/C9CP04330F

Qi, X., and Zhang, S. (2011). Topological insulators and superconductors. *Rev. Mod. Phys.* 83, 1057–1110. doi: 10.1103/RevModPhys.83.1057

Qie, Y., Liu, J., Wang, S., Sun, Q., and Jena, P. (2019). Tetragonal C_{24}: a topological nodal-surface semimetal with potential as an anode material for sodium ion batteries. *J. Mater. Chem. A* 7, 5733–5739. doi: 10.1039/C8TA11276B

Rechtsman, M. C., Zeuner, J. M., Plotnik, Y., Lumer, Y., Podolsky, D. K., Dreisow, F., et al. (2013). Photonic Floquet topological insulators. *Nature* 496, 196–200. doi: 10.1038/nature12066

Schoop, L. M., Pielnhofer, F., and Lotsch, B. V. (2018). Chemical principles of topological semimetals. *Chem. Mater.* 30, 3155–3176. doi: 10.1021/acs.chemmater.7b05133

Soluyanov, A. A., Gresch, D., Wang, Z., Wu, Q., Troyer, M., Dai, X., et al. (2015). Type-II Weyl semimetals. *Nature* 527, 495–498. doi: 10.1038/nature15768

Sun, G., Kurti, J., Rajczy, P., Kertesz, M., Hafner, J., and Kresse, G. (2003). Performance of the Vienna *ab initio* simulation package (VASP) in chemical applications. *J. Mol. Struct. Theochem.* 624, 37–45. doi: 10.1016/S0166-1280(02)00733-9

Sung, J. H., Heo, H., Hwang, I., Lim, M., Lee, D., Kang, K., et al. (2014). Atomic layer-by-layer thermoelectric conversion in topological insulator bismuth/antimony tellurides. *Nano Lett.* 14, 4030–4035. doi: 10.1021/nl501468k

Thakur, G. S., Vir, P., Guin, S. N., Shekhar, C., Weihrich, R., Sun, Y., et al. (2020). Intrinsic anomalous hall effect in Ni-substituted magnetic weyl semimetal $Co_3Sn_2S_2$. *Chem. Mater.* 32, 1612–1617. doi: 10.1021/acs.chemmater.9b05009

Wang, X., Cheng, Z., Zhang, G., Kuang, M., Wang, X.-L., and Chen, H. (2020). Strain tuning of closed topological nodal lines and opposite pockets in quasi-two-dimensional α-phase $FeSi_2$. *Phys. Chem. Chem. Phys.* 22, 13650–13658. doi: 10.1039/D0CP02334E

Xu, L., Du, A., and Kou, L. (2016). Hydrogenated borophene as a stable two-dimensional Dirac material with an ultrahigh Fermi velocity. *Phys. Chem. Chem. Phys.* 18, 27284–27289. doi: 10.1039/C6CP05405F

Xu, L., Wang, R., Miao, M., Wei, X., Chen, Y., Yan, H., et al. (2014). Two dimensional Dirac carbon allotropes from graphene. *Nanoscale* 6, 1113–1118. doi: 10.1039/C3NR04463G

Xu, S., Chen, Z., Zhao, Y., Zhang, X., Xu, H., and Yang, X. (2020). Realizing graphene-like Dirac cones in triangular boron sheets by chemical functionalization. *J. Mater. Chem. C* 8, 2798–2805. doi: 10.1039/C9TC06464H

Yamakage, A., Tamakawa, Y., Tanaka, Y., and Okamoto, Y. (2016). Line-node Dirac semiemtal and topological insulating phase in noncentrosymmetric pnictides CaAgX (X = P, As), *J. Phys. Soc. Jpn.* 85:013708. doi: 10.7566/JPSJ.85.013708

Yan, B., and Felser, C. (2017). Topological materials: weyl semimetals. *Ann Rev Conden Matt Phys.* 8, 337–354. doi: 10.1146/annurev-conmatphys-031016-025458

Yang, T., and Zhang, X. (2020). Nearly flat nodal surface states in pseudo-one-dimensional molybdenum monochalcogenides $X(MoS)_3$ (X = K, Rb, Cs). *J. Mater. Chem. C*, doi: 10.1039/D0TC01978J

Yi, X., Li, W. Q., Li, Z. H., Zhou, P., Ma, Z., and Sun, L. Z. (2019). Topological dual double node-line semimetals NaAlSi(Ge) and their potential as cathode material for sodium ion batteries. *J. Mater. Chem. C* 7, 15375–15381. doi: 10.1039/C9TC04096J

Yu, R., Weng, H., Fang, Z., Dai, X., and Hu, X. (2015). Topological nodal-line semimetal and Dirac semiemtal state in antiperovskite Cu_3PdN, *Phys. Rev. B* 115:036807. doi: 10.1103/PhysRevLett.115.036807

Yu, R., Zhang, W., Zhang, H., Zhang, S., Dai, X., and Fang, Z. (2010). Quantized anomalous hall effect in magnetic topological insulators. *Science* 329, 61–64. doi: 10.1126/science.1187485

Yuan, X., Cheng, P., Zhang, L., Zhang, C., Wang, J., Liu, Y., et al. (2017). Direct observation of landau level resonance and mass generation in dirac semimetal Cd_3As_2 thin films. *Nano Lett.* 17, 2211–2219. doi: 10.1021/acs.nanolett.6b04778

Zhang, B., Li, Y., Zhang, C., and Wang, J. (2019). Two-dimensional ZrB_2C_2 with multiple tunable Dirac states. *Phys. Chem. Chem. Phys.* 21, 24212–24217. doi: 10.1039/C9CP04913D

Zhang, H., Liu, C., Qi, X., Dai, X., Fang, Z., and Zhang, S. (2009). Topological insulators in Bi_2Se_3, Bi_2Te_3 and Sb_2Te_3 with a single Dirac cone on the surface. *Nat. Phys.* 5, 438–442. doi: 10.1038/nphys1270

Zhang, M., Yang, Z. C., and Wang, G. (2018). Coexistence of type-I and type-II weyl points in the weyl-semimetal OsC_2. *J. Phys. Chem. C* 122, 3533–3538. doi: 10.1021/acs.jpcc.8b00920

Zhang, X., Liu, Q., Xu, Q., Dai, X., and Zunger, A. (2018). Topological insulators versus topological dirac semimetals in honeycomb compounds. *J. Am. Chem. Soc.* 140, 13687–13694. doi: 10.1021/jacs.8b06652

Zhang,X., Yu, Z., Sheng, X., and Yang, H., Yang, S. (2017). Coexistance of four-band nodal rings and triply degenerate nodal points in centrosymmetric metal diborides. *Phys. Rev. B* 95:235116. doi: 10.1103/PhysRevB.95.235116

Zhao, Z., Zhang, Z., and Guo, W. (2020). A family of all sp2-bonded carbon allotropes of topological semimetals with strain-robust nodal-lines. *J. Mater. Chem. C* 8, 1548–1555. doi: 10.1039/C9TC05470G

Zheng, H., Xu, S., Bian, G., Guo, C., Chang, G., Sanchez, D. S., et al. (2016). Atomic-scale visualization of quantum interference on a weyl semimetal surface by scanning tunneling microscopy. *ACS Nano* 10, 1378–1385. doi: 10.1021/acsnano.5b06807

Zhong, C., Chen, Y., Xie, Y., Sun, Y., and Zhang, S. B. (2017). Semi-Dirac semimetal in silicene oxide. *Phys. Chem. Chem. Phys.* 19, 3820–3825. doi: 10.1039/C6CP08439G

Zhou, P., Ma, Z., and Sun, L. Z. (2018). Coexistence of open and closed type nodal line topological semimetals in two dimensional B_2C. *J. Mater. Chem. C* 6, 1206–1214. doi: 10.1039/C7TC05095J

Zou, Z. C., Zhou, P., Ma, Z., and Sun, L. Z. (2019). Strong anisotropic nodal lines in the TiBe family. *Phys. Chem. Chem. Phys.* 21, 8402–8407. doi: 10.1039/C9CP00508K

Conflict of Interest: The authors declare that the research was conducted in the absence of any commercial or financial relationships that could be construed as a potential conflict of interest.

frontiers in Chemistry

ORIGINAL RESEARCH
published: 26 August 2020
doi: 10.3389/fchem.2020.00722

Weyl Fermions in VI_3 Monolayer

Taoyuan Jia, Weizhen Meng, Haopeng Zhang, Chunhai Liu, Xuefang Dai, Xiaoming Zhang and Guodong Liu**

School of Material Sciences and Engineering, Hebei University of Technology, Tianjin, China

We report the presence of a Weyl fermion in VI_3 monolayer. The material shows a sandwich-like hexagonal structure and stable phonon spectrum. It has a half-metal band structure, where only the bands in one spin channel cross the Fermi level. There are three pairs of Weyl points slightly below the Fermi level in spin-up channel. The Weyl points show a clean band structure and are characterized by clear Fermi arcs edge state. The effects of spin-orbit coupling, electron correlation, and lattice strain on the electronic band structure were investigated. We find that the half-metallicity and Weyl points are robust against these perturbations. Our work suggests VI_3 monolayer is an excellent Weyl half-metal.

Keywords: topological semimetal, 2D materials, first-principles calculations, half-metal, Weyl state

OPEN ACCESS

Edited by:
Gokhan Surucu, Middle East Technical University, Turkey

Reviewed by:
Wenbo Mi, Tianjin University, China
Zhipeng Hou, South China Normal University, China

****Correspondence:***
Xiaoming Zhang
zhangxiaoming87@hebut.edu.cn
Guodong Liu
gdliu1978@126.com

Specialty section:
This article was submitted to Theoretical and Computational Chemistry, a section of the journal Frontiers in Chemistry

Received: *30 June 2020*
Accepted: *14 July 2020*
Published: *26 August 2020*

Citation:
Jia T, Meng W, Zhang H, Liu C, Dai X, Zhang X and Liu G (2020) Weyl Fermions in VI_3 Monolayer. Front. Chem. 8:722. doi: 10.3389/fchem.2020.00722

INTRODUCTION

In recent years, Weyl semimetals (WSMs) have attracted extensive research attentions (Wan et al., 2011; Lv et al., 2015; Shekhar et al., 2015; Soluyanov et al., 2015; Sun et al., 2015; Weng et al., 2015; Deng et al., 2016; Koepernik et al., 2016; Wu et al., 2016; Kumar et al., 2017). In a WSM, at least one of the time reversal and inversion symmetry is broken. The crossing points, namely, Weyl nodes, appear in pairs with different chirality (Ruan et al., 2016a,b). Such chiral anomaly can induce interesting transport properties such as anomalous Hall effect and negative magnetoresistance (Liu et al., 2013; Son and Spivak, 2013; Liu and Vanderbilt, 2014; Hirayama et al., 2015; Huang et al., 2015). Besides, Weyl nodes can be classified into two categories, namely, types I and II, according to the tilt degree of band crossing. Type I WSMs with traditional band dispersion follow the Lorentz symmetry (Wan et al., 2011; Lv et al., 2015; Shekhar et al., 2015; Sun et al., 2015; Weng et al., 2015). However, for type II WSMs (Soluyanov et al., 2015; Deng et al., 2016; Koepernik et al., 2016; Wu et al., 2016; Kumar et al., 2017), the Weyl cones are completely tilted. The tilted Weyl cones can cause the coexistence of electron-like pocket and hole-like pocket at the same energy level. As the results, type II WSMs have different physical phenomena from type I ones, including modified anomalous Hall conductivity, direction-dependent chiral anomaly, and momentum space Klein tunneling (Koshino, 2016; O'Brien et al., 2016; Yu et al., 2016; Zyuzin and Tiwari, 2016).

Up to now, a large number of WSMs have been reported, and some of which have been confirmed in experiments such as TaAs (Lv et al., 2015), NbP (Shekhar et al., 2015), and NbAs (Yang et al., 2019). These examples are all three-dimensional (3D) non-magnetic materials. Recently, WSMs in two-dimensional (2D) materials and magnetic materials have received increasing interests. For 2D WSMs, the interest arises from the promising applications in spintronic

nanodevices (You et al., 2019). For magnetic WSMs, the interest comes from the novel interplay between the non-trivial band topology and the magnetic ordering (Xu et al., 2011; Kübler and Felser, 2016; Wang et al., 2016; Chen et al., 2019; He et al., 2019; Jin et al., 2020; Meng et al., 2020a,b,c). Recently, the VI_3 material (Kong et al., 2019; Tian et al., 2019; Huang et al., 2020; Long et al., 2020; Zhang et al., 2020), both in 3D and 2D, has attracted great attention. The 3D VI_3 material is a ferromagnetic insulator, which is a layered material (Kong et al., 2019). In addition, 3D VI_3 compound has a R3 phase at room temperature, and experimental evidence suggests that it may undergo a structure phase transition at 78 K (Huang et al., 2020). Importantly, 2D VI_3 had been proved by Long et al. (2020) to be a ferromagnetic half-metal and provides an excellent candidate material for electronic devices. In this work, we report that VI_3 monolayer is an excellent 2D WSM. We have systematically investigated the stability, magnetism, and band topology of VI_3 monolayer. We find VI_3 monolayer is dynamically stable and naturally has the ferromagnetic ordering. The band structure suggests VI_3 monolayer is a half-metal, which holds fully spin-polarized conducting electrons. Especially, there exists a band crossing near the Fermi level, which forms three pairs of Weyl fermions in the spin-up band structure. We have further investigated the effects of spin-orbit coupling (SOC), electron correlation, and lattice strain on the electronic band structure. In addition, the non-trivial edge states for the Weyl points are clearly identified. These results suggest VI_3 monolayer can serve as a good platform to investigate Weyl states in 2D.

COMPUTATIONAL METHODS AND DETAILS

The first-principles calculations in this work are performed by using the Vienna *ab initio* Simulation Package (Blochl, 1994; Kresse and Joubert, 1999). The exchange-correlation potential is adopted by the generalized gradient approximation (GGA) of Perdew–Burke–Ernzerhof functional (Perdew et al., 1996). For the crystal structure of VI_3 monolayer, we built a vacuum with the thickness >18 Å to avoid potential interactions between layers. The cutoff energy is set as 500 eV. The Brillouin zone is sampled by a Monkhorst–Pack k-mesh with size of 15 × 15 × 1. To account for the Coulomb interaction, the GGA + U method is applied during our calculations (Anisimov et al., 1991). For the V-3d orbitals, the *U* value is chosen as 3eV. The phonon spectra are calculated by using the PHONOPY code (Togo et al., 2008).

RESULTS AND DISCUSSION

Before studying the structure and electronic band of the monolayer VI_3, we want to point out that the layered compound VI_3 has already been synthesized by chemical vapor transport method experimentally. The specific synthesis process can be

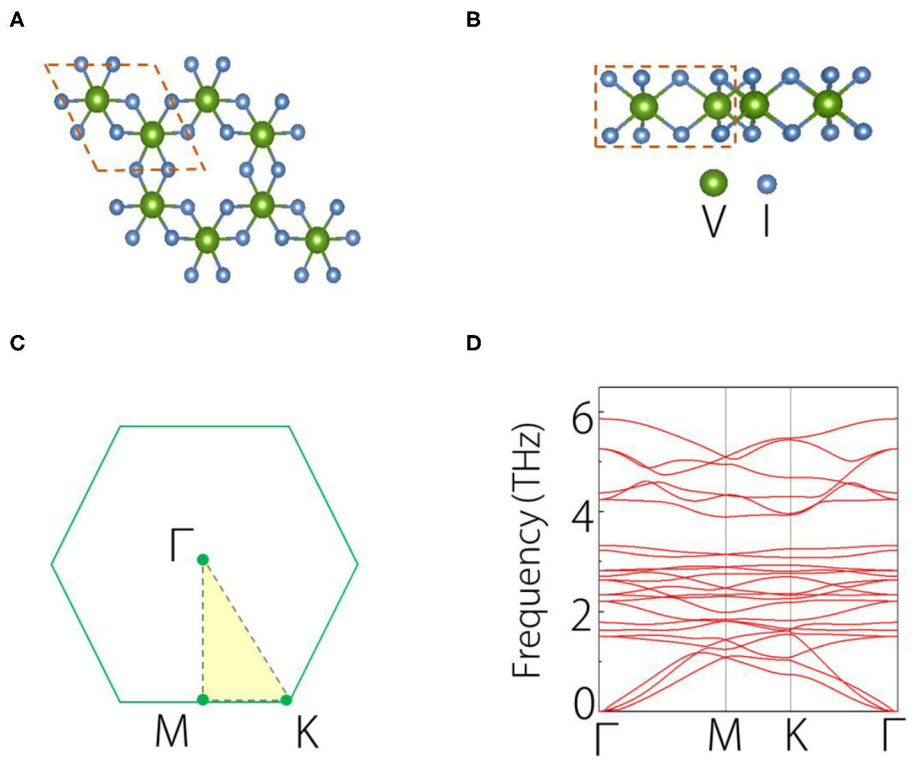

FIGURE 1 | (A) Top view and **(B)** side views of VI_3 monolayer, the dotted line circles the primitive cell. **(C)** Brillouin zone for VI_3 monolayer. **(D)** Calculated phonon spectrum of VI_3 monolayer.

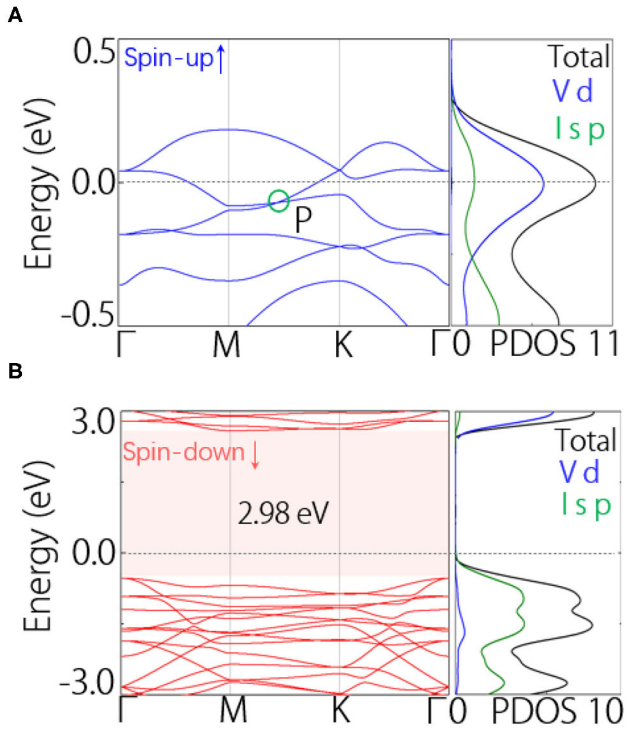

FIGURE 2 | (A) Spin-up and **(B)** spin-down band structures of VI_3 monolayer without SOC. In **(A,B)**, the total and projected density of states (PDOS) are also shown.

found in Kong et al. (2019). In addition, monolayer VI_3 is very promising to be exfoliated from its bulk phase (Miro et al., 2014).

Next, we study the structure of single-layer VI_3. **Figures 1A,B** show the top and side views of the geometric structure of VI_3 monolayer. **Figure 1C** shows the Brillouin zone (BZ) of monolayer VI3. In the structure, each V atom bonds with six I atoms, forming the hexagonal structure. From the side view, we can observe that the material has a triple-layered form, with one V layer sandwiched by two I layers. The circled regions in (A) and (B) show the unit cell of VI_3 monolayer, which contains two V atoms and six I atoms. The Cr_2C compound shows a hexagonal structure with space group *P3M1*. The lattice constant of VI_3 monolayer is $a = b = 7.13$ Å. The bond length of V-I is 2.80 Å, and that of I-I is 4.13 Å. These values are very close to the reported results of He et al. (2016). We have calculated the phonon spectrum of VI_3 monolayer, as displayed in **Figure 1D**. We find no negative frequency phonons in all the highly symmetric k paths. This suggests that the VI_3 monolayer can be stable.

Before studying the band structure of VI_3 monolayer, we first verify its magnetic ground state. In VI_3 monolayer, the magnetic moments are mainly contributed by the 3d transition element V. Here, we consider three potential magnetization directions of V moment, including [001], [010], and [100]. Our calculation results show that the [001] magnetization direction has the lowest energy. Then, in the [001] direction, we considered four magnetic configurations including ferromagnet (FM), Néel antiferromagnet (AFM), stripe AFM, and zigzag AFM. Our calculation results show that the energy of FM is lower than that of other magnetic structures in VI_3 monolayer. The total magnetic moment is 4 μ_B per unit cell, which is almost contributed by the V atoms. In addition, we have calculated the exchange energy ΔE of VI_3 monolayer, which is approximately 28 meV. Then, we can estimate the Curie temperature (T_c) according to the following equation:

$$k_B T_c = 2\Delta/(3C) \quad (1)$$

In (1), the parameter "C" represents the number of magnetic atoms in unit cell, and "k_B" represents the Boltzmann constant. We calculated that the Curie temperature T_c value of VI_3 monolayer is 106 K, which is comparable with the Monte Carlo simulations (98 K) (He et al., 2016).

Here, we discuss the electronic band structure of VI_3 monolayer. At first, we did not consider SOC in the calculations. The band structures are shown in **Figures 2A,B**. In the spin-up band structure, we find one band crosses the Fermi level, manifesting a metallic signature (**Figure 2A**). In the spin-down band structure, we can find a band gap around the Fermi level, manifesting the insulating signature (**Figure 2B**). Therefore, VI_3 monolayer is in fact a half-metal. In particular, the half-metal gap is about 2.98 eV (**Figure 2B**), which is much layer than previously reported half-metals in 2D including YN_2 (1.35eV) (Liu et al., 2017) and Na_2C (0.77eV) monolayer (Ji et al., 2018). In the spin-up band structure, we notice there shows a band crossing point (P) in the M–K path, slightly below the Fermi level (**Figure 2B**). By checking the density of states, we find the states near the Fermi level mostly come from the *d* orbitals of V atom.

Figure 3A shows the orbital-projected band structure near the crossing point P. We can observe the band inversion of the two bands, suggesting the non-trivial band topology in VI_3 monolayer. Then we take into account the SOC effect in the calculation. The comparison of band structure between SOC and without SOC is shown in **Figures 3B,C**. We can find that the band crossing retains under SOC, even though its position has slightly changed. Without SOC, the crossing point locates at 0.04 eV below the Fermi level; under SOC, it locates at 0.08 eV below the Fermi level. Because the band crossing happens in two bands, the band crossing in fact forms Weyl points. To be noted, in VI_3 monolayer, the time reversal is broken, but the inversion symmetry is retained; hence, the Weyl points are time-reversal–breaking Weyl points.

In **Figure 3D**, we show the 3D plotting of band structure near the Weyl point. We can find that the Weyl cone is titled. Because of the preserved inversion symmetry, there are in total three pairs of such Weyl points in the system. From the symmetry analysis, the Weyl points in monolayer VI_3 are protected by the C_{3v} symmetry. It is worth noticing that Weyl points have many special physical phenomena, such as modified anomalous Hall conductivity, direction-dependent chiral anomaly, momentum space Klein tunneling (Koshino, 2016; O'Brien et al., 2016; Yu et al., 2016; Zyuzin and Tiwari, 2016). However, the Weyl fermions have been rarely found in 2D materials. Therefore,

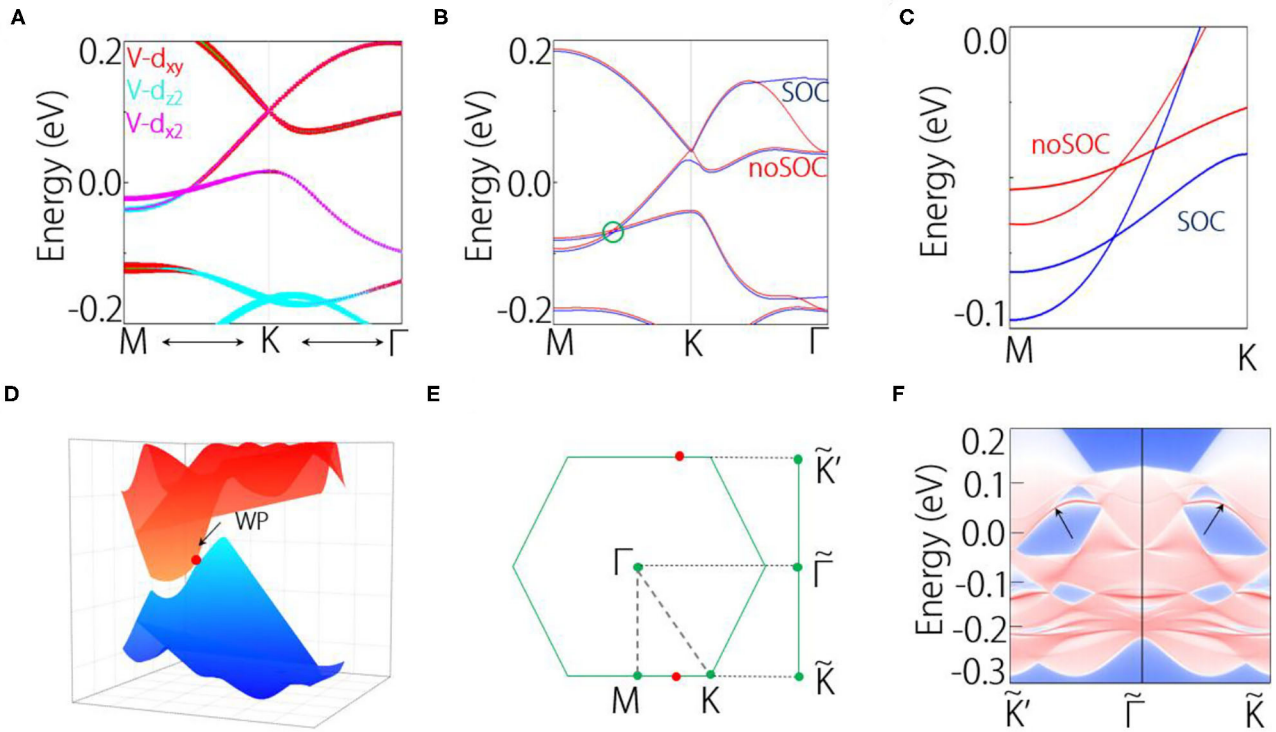

FIGURE 3 | (A) Orbital-projected band structure near the crossing point P. **(B,C)** Comparison of band structure between SOC and without SOC, where **(C)** is the enlarged band structure. **(D)** 3D band dispersions near the Weyl point. **(E)** 2D Brillouin zone and its projection to the edge. **(F)** Edge states of VI_3 monolayer.

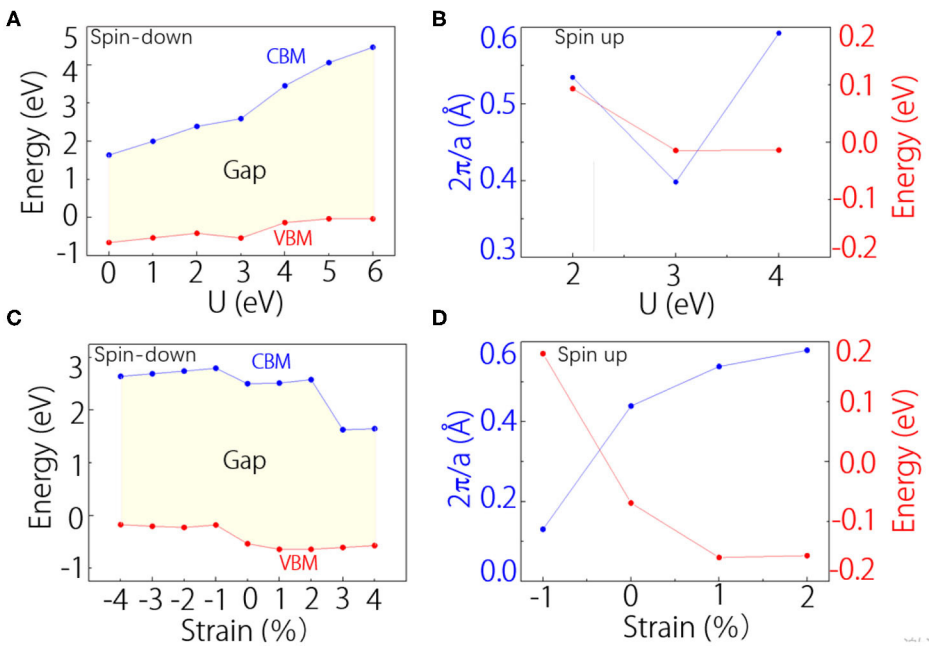

FIGURE 4 | (A) The curves of the valence band maximum (VBM) and the conduction band minimum (CBM) under different *U*-values in the spin-down channel. The shadowed area shows the band gap. **(B)** The position of Weyl points under different *U*-values. **(C,D)** Similar with **(A,B)**, but for the changes under different stains.

the VI_3 monolayer reported here can be a good platform to study the Weyl fermions in 2D. In addition, in **Figure 3E**, the orbital projection is performed on (010) surface, we have also identified the Fermi arc edge states of the Weyl points, as shown

in **Figure 3F**. This further verifies the non-trivial band topology in VI_3 monolayer.

Finally, we discuss the effects of electron correlation and lattice strain on the half-metal band structure and the Weyl points. In **Figure 4A**, we show the positions of the conduction band minimum and the valence band maximum with shifting the *U*-values of V atom from 0 to 6 eV. The results show that VI_3 monolayer is always a ferromagnetic half-metal, and the spin-down band gap will increase with increasing the *U*-values. For the Weyl points, we find they can exist when *U*-values are at 2–4 eV. **Figure 4B** shows the positions of the Weyl points at different *U*-values. Similarly, in **Figures 4C,D**, we show the strain effects on the half-metal band structure and the Weyl points. We can find that the half-metal band structure can retain from 4% compressive stain to 4% tensile strain (**Figure 4C**). Meanwhile, as shown in **Figure 4D**, we find the Weyl points can exist from 1% compressive stain to 2% tensile strain (**Figure 4D**). These results show that the half-metal band structure and the Weyl points are in some degree robust against electron correlation effects and lattice strain.

SUMMARY

We have reported the Weyl fermion in 2D VI_3 monolayer. The phonon spectrum suggests VI_3 monolayer is dynamically stable. We have verified that VI_3 monolayer has the ferromagnetic ground state. In the ground state, we find VI_3 monolayer has a half-metal band structure with the half-metallic gap as large as 2.98 eV; thus, the conducting electrons can be fully spin-polarized. Very interestingly, VI_3 monolayer shows three pairs of Weyl points near the Fermi level, locating in the spin-up band structure. Importantly, the three pairs of Weyl points show clear Fermi arcs on the edge. Moreover, we verify that the half-metal band structure and the Weyl points in VI_3 monolayer are robust against proper electron correlation effects and lattice strain. These properties make VI_3 monolayer have promising applications in spintronic nanodevices.

DATA AVAILABILITY STATEMENT

The raw data supporting the conclusions of this article will be made available by the authors, without undue reservation.

AUTHOR CONTRIBUTIONS

This project was conceived by XZ and GL. TJ, HZ, and CL completed theoretical model and first principles calculations with the help from XZ and XD. TJ and WM performed the data analysis and designed the manuscript with the assistances from XZ and GL. This manuscript was written by TJ and XZ with important inputs from GL and XD. This project was supervised by GL. All authors discussed the results and commented on the manuscript.

FUNDING

This work was supported by Nature Science Foundation of Hebei Province (Nos. E2019202107 and E2019202222), National Natural Science Foundation of China (Grants No. 11904074). XZ acknowledges the financial support from Young Elite Scientists Sponsorship Program by Tianjin.

REFERENCES

Anisimov, V. I., Zaanen, J., and Andersen, O. K. (1991). Band theory and mott insulators: Hubbard U instead of stoner I. *Phys. Rev. B* 44:943. doi: 10.1103/PhysRevB.44.943

Blochl, P. E. (1994). Projector augmented-wave method. *Phys. Rev. B* 50:17953. doi: 10.1103/PhysRevB.50.17953

Chen, C., Yu, Z. M., Li, S., Chen, Z., Sheng, X. L., and Yang, S. A. (2019). Weyl-loop half-metal in Li_2 (FeO_3) $_2$. *Phys. Rev. B* 99:075131. doi: 10.1103/PhysRevB.99.075131

Deng, K., Wan, G. L., Deng, P., Zhang, K. N., Ding, E. Y., Yan, M. Z., et al. (2016). Experimental observation of topological Fermi arcs in type-II Weyl semimetal $MoTe_2$. *Nat. Phys.* 12, 1105–1110. doi: 10.1038/nphys3871

He, J. J., Ma, S. Y., Lyu, P., and Nachtigall, P. (2016). Unusual Dirac half-metallicity with intrinsic ferromagnetism in vanadium trihalide monolayers. *J. Mater. Chem. C* 4, 2518–2526. doi: 10.1039/C6TC00409A

He, T. L., Zhang, X. M., Meng, W. Z., Jin, L., Dai, X. F., and Liu, G. D. (2019). Topological nodal lines and nodal points in the antiferromagnetic material β-Fe_2PO_5. *J. Mater. Chem. C* 7, 12657–12663. doi: 10.1039/C9TC04046C

Hirayama, M., Okugawa, R., Ishibashi, S., Murakami, S., and Miyake, T. (2015). Weyl node and spin texture in trigonal tellurium and selenium. *Phys. Rev. Lett.* 114:206401. doi: 10.1103/PhysRevLett.114.206401

Huang, C. X., Wu, F., Yu, S. L., Jena, P., and Kan, E. (2020). Discovery of twin orbital-order phases in ferromagnetic semiconducting VI3 monolayer. *Phys. Chem. Phys.* 22, 512–517. doi: 10.1039/C9CP05643B

Huang, X., Zhao, L., Long, Y., Wang, P., Chen, D., Yang, Z., et al. (2015). Observation of the chiral-anomaly-induced negative magnetoresistance in 3D Weyl semimetal TaAs. *Phys. Rev. X* 5:031023. doi: 10.1103/PhysRevX.5.031023

Ji, W. X., Zhang, B. M., Zhang, S. F., Zhang, C. W., Ding, M., Wang, P., et al. (2018). Na_2C monolayer: a novel 2*p* Dirac half-metal with multiple symmetry-protected Dirac cones. *Nanoscale* 10, 13645–13651. doi: 10.1039/C8NR02761G

Jin, L., Zhang, X. M., He, T. L., Meng, W. Z., Dai, X. F., and Liu, G. D. (2020). Ferromagnetic two-dimensional metal-chlorides MCl (M= Sc, Y, and La): candidates for Weyl nodal line semimetals with small spin-orbit coupling gaps. *App. Sur. Sci.* 520:146376. doi: 10.1016/j.apsusc.2020.146376

Koepernik, K., Kasinathan, D., Efremov, D. V., Khim, S., Borisenko, S., Buchner,. B., et al. (2016). $TaIrTe_4$: a ternary type-II Weyl semimetal. *Phys. Rev. B* 93:201101. doi: 10.1103/PhysRevB.93.201101

Kong, T., Stolze, K., Timmons, E. I., Tao, J., Ni, D., Guo, S., et al. (2019). VI3-a new layered ferromagnetic semiconductor. *Adv Mater.* 31:1808074. doi: 10.1002/adma.201808074

Koshino, M. (2016). Cyclotron resonance of figure-of-eight orbits in a type-II Weyl semimetal. *Phys. Rev. B* 94:035202. doi: 10.1103/PhysRevB.94.035202

Kresse, G., and Joubert, D. (1999). From ultrasoft pseudopotentials to the projector augmentedwave method. *Phys. Rev. B* 59:1758. doi: 10.1103/PhysRevB.59.1758

Kübler, J., and Felser, C. (2016). Non-collinear antiferromagnets and the anomalous Hall effect. *Europhys. Lett.* 114:47005. doi: 10.1209/0295-5075/114/47005

Kumar, N., Sun, Y., Xu, N., Manna, K., Yao, M. Y., Suss, V., et al. (2017). Extremely high magnetoresistance and conductivity in the type-II Weyl semimetals WP_2 and MoP_2. *Nat. Commun.* 8:1642. doi: 10.1038/s41467-017-01758-z

Liu, C. X., Ye, P., and Qi, X. L. (2013). Chiral gauge field and axial anomaly in a Weyl semimetal. *Phys. Rev. B* 87:235306. doi: 10.1103/PhysRevB.87.235306

Liu, Z. F., Liu, J. Y., and Zhao, J. J. (2017). YN_2 monolayer: novel p-state Dirac half metal for high-speed spintronics. *Nano Res.* 10, 1972–1979. doi: 10.1007/s12274-016-1384-3

Liu,. J., and Vanderbilt, D. (2014). Weyl semimetals from noncentrosymmetric topological insulators. *Phys. Rev. B* 90:155316. doi: 10.1103/PhysRevB.90.155316

Long, C., Wang, T., Jin, H., Wang, H., and Dai, Y. (2020). Stacking-independent ferromagnetism in Bilayer VI3 with Half-metallic characteristic. *J. Phys. Chem. Lett.* 11, 2158–2164. doi: 10.1021/acs.jpclett.0c00065

Lv, B. Q., Weng, H. M., Fu, B. B., Wang, X. P., Miao, H., Ma, J., et al. (2015). Experimental discovery of Weyl semimetal TaAs. *Phys. Rev. X* 5:031013. doi: 10.1103/PhysRevX.5.031013

Meng, W. Z., Zhang, X. M., He, T. L., Dai, X. F., Jin, L., and Liu, G. D. (2020b). Crystal Structures, electronic structures and topological signatures in equiatomic TT'X compounds (T = Sc, Zr, Hf; T' = Co, Pt, Pd, Ir, Rh; X = Al, Ga, Sn). *J. Phy. Chem. C* 124, 7378–7385. doi: 10.1021/acs.jpcc.0c00303

Meng, W. Z., Zhang, X. M., He, T. L., Dai, X. F., Jin, L., Liu, Y., et al. (2020a). Ternary compound HfCuP: An excellent Weyl semimetal with the coexistence of type-I and type-II Weyl nodes. *J. Adv. Res.* 24, 523–528. doi: 10.1016/j.jare.2020.05.026

Meng, W. Z., Zhang, X. M., Liu, Y., Dai, X. F., and Liu, G. D. (2020c). Lorentz-violating type-II Dirac fermions in full-Heusler compounds XMg2Ag (X=Pr, Nd, Sm). *New J. Phys.* 22:073061. doi: 10.1088/1367-2630/ab9d55

Miro, P., Audiffred, M., and Heine, T. (2014). An atlas of two-dimensional materials. *Chem. Soc. Rev.* 43, 6537–6554. doi: 10.1039/C4CS00102H

O'Brien, T. E., Diez, M., and Beenakker, C. W. J. (2016). Magnetic breakdown and Klein tunneling in a type-II Weyl semimetal. *Phys. Rev. Lett.* 116:236401. doi: 10.1103/PhysRevLett.116.236401

Perdew, J. P., Burke, K., and Ernzerhof, M. (1996). Generalized gradient approximation made simple. *Phys. Rev. Lett.* 77:3865. doi: 10.1103/PhysRevLett.77.3865

Ruan, J., Jian, S. K., Yao, H., Zhang, H., Zhang, S. C., and Xing, D. (2016a). Symmetry-protected ideal 14 Weyl semimetal in HgTe-class materials. *Nat. Commun.* 7:11136. doi: 10.1038/ncomms11136

Ruan, J., Jian, S. K., Zhang, D., Yao, H., Zhang, H., Zhang, S. C., et al. (2016b). Ideal Weyl Semimetals in the Chalcopyrites $CuTlSe_2$, $AgTlTe_2$, $AuTlTe_2$, and ZnPbAs2. *Phys. Rev. Lett.* 116:226801. doi: 10.1103/PhysRevLett.116.226801

Shekhar, C., Nayak, A. K., Sun, Y., Schmidt, M., Nicklas, M., Leermakers, I., et al. (2015). Extremely large magnetoresistance and ultrahigh mobility in the topological Weyl semimetal candidate NbP. *Nat. Phys.* 11, 645–649. doi: 10.1038/nphys3372

Soluyanov, A. A., Gresch, D., Wang, Z. J., Wu, Q. S., Troyer, M., Dai, X., et al. (2015). Type-II Weyl semimetals. *Nature* 527, 495–498. doi: 10.1038/nature15768

Son, D. T., and Spivak, B. Z. (2013). Chiral anomaly and classical negative magnetoresistance of Weyl metals. *Phys. Rev. B* 88:104412. doi: 10.1103/PhysRevB.88.104412

Sun, Y., Wu, S. C., and Yan, B. H. (2015). Topological surface states and Fermi arcs of the noncentrosymmetric Weyl semimetals TaAs, TaP, NbAs, and NbP. *Phys. Rev. B* 92:115428. doi: 10.1103/PhysRevB.92.115428

Tian, S. J., Zhang, J. F., Li, C. H., Ying, T. P., Li, S. Y., Zhang, X., et al. (2019). Ferromagnetic van der Waals crystal VI_3. *J. Am. Chem. Soc.* 141, 5326–5333. doi: 10.1021/jacs.8b13584

Togo, A., Oba, F., and Tanaka, I. (2008). First-principles calculations of the ferroelastic transition between rutile-type and $CaCl_2$-Type SiO_2 at high pressures. *Phys. Rev. B* 78:134106. doi: 10.1103/PhysRevB.78.134106

Wan, X., Turner, A. M., Vishwanath, A., and Savrasov, S. Y. (2011). Topological semimetal and Fermi-arc surface states in the electronic structure of pyrochlore iridates. *Phys. Rev. B* 83:205101. doi: 10.1103/PhysRevB.83.205101

Wang, Z. J., Vergniory, M. G., Kushwaha, S., Hirschberger, M., Chulkov, E. V., Ernst, A., et al. (2016). Time-reversal-breaking weyl fermions in magnetic heusler alloys. *Phys. Rev. Lett.* 117:236401. doi: 10.1103/PhysRevLett.117.236401

Weng, H. M., Fang, C., Fang, Z., Bernevig, B. A., and Dai, X. (2015). Weyl semimetal phase in noncentrosymmetric transition-metal monophosphides. *Phys. Rev. X* 5:011029. doi: 10.1103/PhysRevX.5.011029

Wu, Y., Mou, D. X., Jo, N. H., Sun, K. W., Huang, L. N., Bud'ko, S. L., et al. (2016). Observation of Fermi arcs in the type-II Weyl semimetal candidate WTe2. *Phys. Rev. B* 94:121113. doi: 10.1103/PhysRevB.94.121113

Xu, G., Weng, H. M., Wang, Z. J., Dai, X., and Fang, Z. (2011). Chern $HALL effect in $HgCr_2Se_4$. *Phys. Rev. Lett.* 107:186806. doi: 10.1103/PhysRevLett.107.186806

Yang, H. F., Yang, L. X., Liu, Z. K., Sun, Y., Chen, C., Peng, H., et al. (2019). Topological Lifshitz transitions and Fermi arc manipulation in Weyl semimetal NbAs. *Nat. Commu.* 10:3478. doi: 10.1038/s41467-019-11491-4

You, J. Y., Chen, C., Zhang, Z., Sheng, X. L., Yang, S. Y. A., and Su, G. (2019). Two-dimensionalWeyl half-semimetal and tunable quantum anomalous Hall effect. *Phys. Rev. B* 100:64408. doi: 10.1103/PhysRevB.100.064408

Yu, Z. M., Yao, Y., and Yang, S. Y. A. (2016). Predicted unusual magnetoresponse in type-II Weyl semimetals. *Phys. Rev. Lett.* 117:077202. doi: 10.1103/PhysRevLett.117.077202

Zhang, F., Mi, W., and Wang, X. (2020). Spin-dependent electronic structure and magnetic anisotropy of 2D ferromagnetic Janus $Cr_2I_3X_3$ (X = Br, Cl) monolayers. *Adv. Electron. Mater.* 6:1900778. doi: 10.1002/aelm.201900778

Zyuzin, A. A., and Tiwari, R. P. (2016). Intrinsic anomalous Hall effect in type-II Weyl semimetals. *JETP Lett.* 103, 717–722. doi: 10.1134/S002136401611014X

Conflict of Interest: The authors declare that the research was conducted in the absence of any commercial or financial relationships that could be construed as a potential conflict of interest.

frontiers in Chemistry

ORIGINAL RESEARCH
published: 11 September 2020
doi: 10.3389/fchem.2020.00604

Formation of a Key Intermediate Complex Species in Catalytic Hydrolysis of NH_3BH_3 by Bimetal Clusters: Metal-Dihydride and Boron-Multihydroxy

W. J. Yan [1,2], Y. F. Zheng [1], T. W. Zhou [1], G. Z. Wang [3], D. D. Wang [1] and H. K. Yuan [1]**

[1] School of Physical Science and Technology, Southwest University, Chongqing, China, [2] School of Mechatronics and Information Engineering, Chongqing College of Humanities, Science & Technology, Chongqing, China, [3] School of Electronic Information Engineering, Yangtze Normal University, Chongqing, China

OPEN ACCESS

Edited by:
Gokhan Surucu,
Middle East Technical University, Turkey

Reviewed by:
Baihai Li,
University of Electronic Science and Technology of China, China
Xueling Lei,
Jiangxi Normal University, China

***Correspondence:**
G. Z. Wang
wangyan6930@yznu.edu.cn
H. K. Yuan
yhk10@swu.edu.cn

Specialty section:
This article was submitted to Theoretical and Computational Chemistry, a section of the journal Frontiers in Chemistry

Received: 13 May 2020
Accepted: 10 June 2020
Published: 11 September 2020

Citation:
Yan WJ, Zheng YF, Zhou TW, Wang GZ, Wang DD and Yuan HK (2020) Formation of a Key Intermediate Complex Species in Catalytic Hydrolysis of NH_3BH_3 by Bimetal Clusters: Metal-Dihydride and Boron-Multihydroxy. Front. Chem. 8:604. doi: 10.3389/fchem.2020.00604

The hydrolysis of AB (AB, NH_3BH_3) with the help of transition metal catalysts has been identified as one of the promising strategies for the dehydrogenation in numerous experiments. Although great progress has been achieved in experiments, evaluation of the B-N bond cleavage channel as well as the hydrogen transfer channel has not been performed to gain a deep understanding of the kinetic route. Based on the density functional theory (DFT) calculation, we presented a clear mechanistic study on the hydrolytic reaction of AB by choosing the smallest NiCu cluster as a catalyst model. Two attacking types of water molecules were considered for the hydrolytic reaction of AB: stepwise and simultaneous adsorption on the catalyst. The Ni and Cu metal atoms play the distinctive roles in catalytic activity, i.e., Ni atom takes reactions for the H_2O decomposition with the formation of $[OH]^-$ group whereas Cu atom takes reactions for the hydride transfer with the formation of metal-dihydride complex. The formation of Cu-dihydride and B-multihydroxy complex is the prerequisite for the effectively hydrolytic dehydrogenation of AB. By analyzing the maximum barrier height of the pathways which determines the kinetic rates, we found that the hydride hydrogen transferring rather than the N-B bond breaking is responsible to the experimentally measured activation energy barrier.

Keywords: DMol^3, first-principal calculation, bimetal clusters, catalytic, DFT

1. INTRODUCTION

Among many practical hydrogen storage materials, ammonia-borane (AB, NH_3BH_3) is believed to be an attractive solid hydrogen storage candidate owing to its high hydrogen content, nontoxic, excellent solubility, and stability in water (Peng and Chen, 2008; Hamilton et al., 2009; Staubitz et al., 2010; Jiang and Xu, 2011; Sanyal et al., 2011; Thorne et al., 2011; Lu and Xu, 2012; Xi et al., 2012). To enhance the kinetics of the hydrogen release for its on-board applications, intensive efforts have been made in solid state by thermolysis dehydrogenation (Demirci and Miele, 2009; Hamilton et al., 2009) and in solution by hydrolysis and methanolysis dehydrogenation (Xu and Chandra, 2007; Umegaki et al., 2009; Chua et al., 2011). In the absence of suitable catalysts, the

thermal/hydrolytic decomposition to generate the hydrogen is a very slow process and it has to undergo several step reactions at very high temperature (Hu et al., 1978; Matus et al., 2007; Stowe et al., 2007; Huang and Autrey, 2012), which seriously restricts the development of AB as a promising hydrogen storage material. In the perspective of hydrolysis dehydrogenation, finding high active and low-cost catalysts to make AB completely release its hydrogen under moderate conditions is a key point for this system.

Up to now, there has been a steady growth in a number of publications dealing with the catalytic hydrolysis of AB to generate the hydrogen at low temperature (Jiang and Xu, 2011; Patel and Miotello, 2015). Originally, noble metal catalysts such as Au (Chandra and Xu, 2007), Pt (Chandra and Xu, 2006a, 2007; Mohajeri et al., 2007; Chen et al., 2014), Pd (Chandra and Xu, 2007; Metin et al., 2011; Kılıç et al., 2012), Rh (Chandra and Xu, 2006a, 2007; Zahmakiran and Özkar, 2009; Karahan et al., 2012), Ru (Chandra and Xu, 2007; Rachiero et al., 2011a; Can and Metin, 2012; Liang et al., 2012; Zhou Q. et al., 2016), and Ir (Wang et al., 2017b) were extensively explored, although their expensive costs are the dominate disadvantage for the potential applicability. Along with the development of cheaper catalysts without the loss of highly efficient, nanoparticle based on more abundant first-row transition metals Fe (Xu and Chandra, 2006; Yan J. M. et al., 2008; Dinç et al., 2012), Co (Xu and Chandra, 2006; Demirci and Miele, 2010; Yan et al., 2010b; Metin and Özkar, 2011; Li et al., 2017), Ni (Xu and Chandra, 2006; Kalidindi et al., 2008a; Yan et al., 2009; Metin et al., 2010; Metin and Özkar, 2011; Li et al., 2017; Wang et al., 2017a), and Cu (Xu and Chandra, 2006; Kalidindi et al., 2008a,b; Zahmakiran et al., 2010) have also been tentatively studied, however, they have only moderate catalysis and lack the desiring stability in the hydrolysis conditions. To get over the challenges of cost expensiveness of the noble metal as well as the catalytic limitation of transition metal, the modulation of the noble metal content by alloying with first-row transition metal was considered as a feasible solution, because their active sites could be maintained and their active capabilities could be improved in alloying catalysts. As one expected, most bimetallic catalysts such as Cu(Fe, Ni, Ru) (Rachiero et al., 2011b; Lu et al., 2013, 2014; Zhang et al., 2016), (Pd, Au, Ru)Co (Yan et al., 2010a; Chen et al., 2011; Sun et al., 2011; Lu et al., 2012; Wang et al., 2012), (Au, Ag, Pt, Ru)Ni (Chen et al., 2007, 2012; Yao C. F. et al., 2008; Jiang et al., 2010), and (Ni, Cu)Pd (Çiftci and Metin, 2014; Güngörmez and Metin, 2015) have been reported to exhibit the better performance than the monometal catalysts for the hydrogen generation from the hydrolysis of AB. It was deduced that the formations of the heterometallic bonds can adjust the bonding (molecular) orbitals of catalyst surface atoms to reactant with AB and H_2O molecules. This can stabilize the reaction intermediates and lead to the improvement of catalytic activity on AB for hydrogen generation (Lu et al., 2013). The behind reason is attributed to the synergistic effect between the heterometallic atoms that originates from the electronic effect (such as the adjustment of *d*-band level or charge transfers) and the structural morphology (such as the formation of core-shell or mixing structures).

By measuring the composition of hydrolytic products in the presence of various transition metal-based catalysts (Yao C. F. et al., 2008; Rachiero et al., 2011b; Chou et al., 2012; Liu et al., 2012; Komova et al., 2016), it was confirmed that 1 mole of AB is hydrolyzed to give nearly 1 mole of NH_4^+ ions and 3 moles of H_2 gas. For example, Yao C. F. et al. (2008) have chemically identified that the gaseous product is exclusively H_2 molecules and the soluble product is NH_4^+ ions. Based on NMR experiment, Rachiero et al. (2011b) have demonstrated that the initial product $B(OH)_4^-$ is adsorbed over the catalyst surface without B-N adducts or intermediates desorbing. Consequently, the overall hydrolysis reaction of AB can be described as $NH_3BH_3+3H_2O\xrightarrow{\text{catalyst}}\text{catalyst}\cdot NH_3+B(OH)_3+3H_2\uparrow$, which was readily confirmed by the composition of reaction products using the x-ray diffraction analysis (Mohajeri et al., 2007; Brockman et al., 2010; Chou et al., 2012; Liu et al., 2012; Komova et al., 2016). The NH_3 and $B(OH)_3$ are being dissolved in water as described by a well known acid-base equilibrium $NH_3+H_2O\leftrightarrow NH_4^++OH^-$ and $B(OH)_3+OH^-\leftrightarrow B(OH)_4^-\leftrightarrow BO_2^-+2H_2O$ (Brockman et al., 2010; Komova et al., 2016). These final products suggest that one portion of H_2 molecule is generated through the H-O bond breaking in H_2O and the other is generated through the H-B bond breaking in AB, and NH_3 molecule is formed by B-N bond cleavage. In addition, the observations of these experiments are consistent with the Langmuir-Hinshelwood mechanism for the heterogeneous catalysis (Basu et al., 2010; Rakap and Özkar, 2010), i.e., AB and H_2O adsorb over the catalytic surface to be hydrolyzed upon the formation of the final by-product $B(OH)_4^-$. Although great progress has been achieved in the experiments for the fast and complete H_2 release, evaluations of the B-N bond cleavage channel and the hydrogen transfer channel have not been performed to gain a deep understanding of the kinetic route, to suggest a methodological scheme which properly describes these reactions, and to find out crucial step to tune the reactions for future application in H_2 storage. In our opinion, this is a substantial gap in this field of research.

By using the density functional theory (DFT) calculations, herein, we investigate the reaction pathways of H_2 release from the hydrolytic AB and examine the catalytic roles of small NiCu clusters. Experimentally, NiCu bimetallic nanoparticles have been successfully fabricated and the catalytic activity was evaluated in the hydrolytic dehydrogeneration of AB (Lu et al., 2014; Zhang et al., 2016). The results shown that NiCu bimetallic nanoparticles exhibit the excellent catalytic activity and the low activation energy barriers owning to the charge transfer between Cu and Ni atoms (Lu et al., 2014; Zhang et al., 2016). Since the dehydrogenation reaction of AB involves an ionic recombination of hydridic $H^{\delta-}$ and protic $H^{\delta+}$, the positively Ni atom would play an attractive role to interact with the $[OH]^-$ group by hydrolyzing H_2O while the negatively Cu atom would act as an agent to accept the hydrolyzed H^+ ion. Considering the dissociation of NH_3 molecule from AB in the experiments, we naturally deduce the hydrolytic dehydrogenation of AB that the hydridic H(B) atoms from $-BH_3$ edge of AB would like to interact with the protic H(O) atoms from H_2O, aggregating and forming

three H_2 molecules. Firstly and importantly, validation of the aforementioned rules and trends is crucial and necessary from the electronic structure. Secondly, the potential energy surfaces on the reaction channels describe the heights of activation energy barriers and thermodynamic stabilities, which can be used to compare with the experimental measurement. Finally, our results are important in developing the evidence-based experimental requirements for the safe handling of this hydride in everyday laboratory and industrial practice. In what follows, we will firstly describe the computational methodology used in the work in section 2, and then present our results and discussions in section 3. Finally, a summary is given in section 4.

2. METHODS

Our calculations have been performed by using the Density Functional Theory (DFT) based DMol^3 code (Delley, 2000), where the Perdew-Wang (PW91) exchange-correlation potential (Becke, 1988; Perdew and Wang, 1992) to the generalized gradient approximation (GGA) (White and Bird, 1994) was adopted. The double numerical basis sets with the *p*-polarization function (DNP), all electrons treated as the valance electrons, and the thermal corrections were employed in the calculations for the equilibrium geometries of all molecular species, i.e., the reactant-complex (R), transition states (TS), intermediates (IM), and products (P). The DNP basis set is quite a bit better than Gaussian 6-31G** basis set under the accurate level, and the former one is more effective than the latter one (Hirshfeld, 1977; Wu et al., 2013). The harmonic vibrational frequencies were determined at the same level to confirm whether the optimized structures are local minima (no imaginary frequency) or transition states (one imaginary frequency) and to evaluate the zero-point vibrational energy. To obtain the TS, linear synchronous transit (LST) and quadratic synchronous transit (QST) methods were firstly utilized to execute an extensive search, and then the TS optimization has been done with the eigenvector-following methods, following which the TS confirmation was performed to produce a refined reaction path based on LST or QST (Peng and Schlegel, 1993; Peng et al., 1996; Ayala and Schlegel, 1997). The convergence criterions were set to 2×10^{-5} Ha for the maximum energy change, 4×10^{-3} Ha/Å for the maximum force, 5×10^{-3} Å for the maximum atomic displacement, respectively. The activation energy barrier (E_{act}) determines whether or not the reactions take place spontaneously and reach to the final state without the extra-energy absorbed from the outside. It was calculated as the energy difference between the initial reactants and the highest transition state of a whole reaction pathway, i.e., $E_{act} = E_{HTS}$-E_{React}. The energy values hereafter are enthalpy except for specially mentioned. The zero-point energy and enthalpy corrections have not been considered, because the corrections always reduce the values in a small magnitude (Zhou T. et al., 2016).

For free AB, we found that the bond-lengths of B-N, B-H, and N-H bonds are 1.66, 1.22, 1.02 Å, respectively, which are in good agreement with the experimental measurements (Thorne et al., 2011) and theoretical values under more precise calculations (Gaussian-B3LYP/6-311+g*) (Zhou T. et al., 2016). Thus, we have a high degree of confidence in our structural configurations. To validate our method in calculating the dehydrogenation dynamics, we have calculated the dehydrogenation pathways of AB without (**Figures 1A,B**) and with (**Figures 1C,D**) the help of Cu_2 catalyst by using the DMol^3 and Gaussian methods. From **Figure 1**, we noted that the DMol^3 method (BPW91/DNP) gives a similar variational trend as the Gaussian method does (Zhou T. et al., 2016). Although the IM states and TS states under the former calculations are higher in energy than under the latter calculations, both methods report the same energy orderings of these states. Typically, the highest energy barrier (the decisive reaction step) (1.953 eV) and the exoergic energy (0.162 eV) of the whole reaction path are well reproduced by DMol^3 method. Furthermore, the Van der Waals correction (Bučko et al., 2010) has been taken into account (BPW91/DNP/OBS) for the benchmark calculations, however, the results (red lines) shown that it does not present the superiority. Therefore, the following calculations were performed within the DMol-BPW91/DNP method.

3. RESULTS

3.1. Synergistic Adsorption of H_2O and AB Molecules on NiCu Dimer

The initial interactions between the reactants (AB and H_2O) and catalyst (NiCu dimer) can be demonstrated by the energetically most favorable configurations shown in **Figure 2**. Although the AB hydrolysis reaction is complex in nature and it involves multistep mechanism, the configuration of the pre-equilibrium complex AB (reactants adsorbed on catalyst) is very important for the following reactions. By examining the possible adsorption styles of AB on NiCu dimer, including: $-BH_3$ ($-NH_3$) edge solely linked with Cu (Ni) atom; $-BH_3$ and $-NH_3$ edges synchronously linked with Cu and Ni atoms (and *vice versa*); B and N atoms directly linked with Cu (Ni) atom, we found that the configuration within $-BH_3$ edge approaching Ni atom is the most stable (R0). It is similar to the structure IM31 we proposed in previous literature (Zhou T. et al., 2016). The reason that $-BH_3$ edge prefers to bond with Ni atom instead of Cu atom can be understood from the Lewis base and acid reactions (Roach et al., 2009; Reber et al., 2010; Li et al., 2013). Since the overall negatively charged $-BH_3$ fragment [specifically for the hydridic H(B) donors] can be regarded as the Lewis base, it would like to interact with the positively charged Ni atom that can be regarded as the Lewis acid. In **Figure 2**, the highest occupied molecular orbital (HOMO), the lowest unoccupied molecular orbital (LUMO), and Mulliken atomic charges are presented on each structural configuration. From the point of view of the frontier orbital theory (Li and Evans, 1995), the LUMO/LUMO+1 site serves as the Lewis acid which will accept electrons readily, while the HOMO site serves as the Lewis base which will donate electrons. Consequently, $-BH_3$ edge would like to interact with Ni atom, because HOMO (LUMO) charge distribution is primarily localized around the $-BH_3$ fragment of AB molecule (Ni site of NiCu dimer).

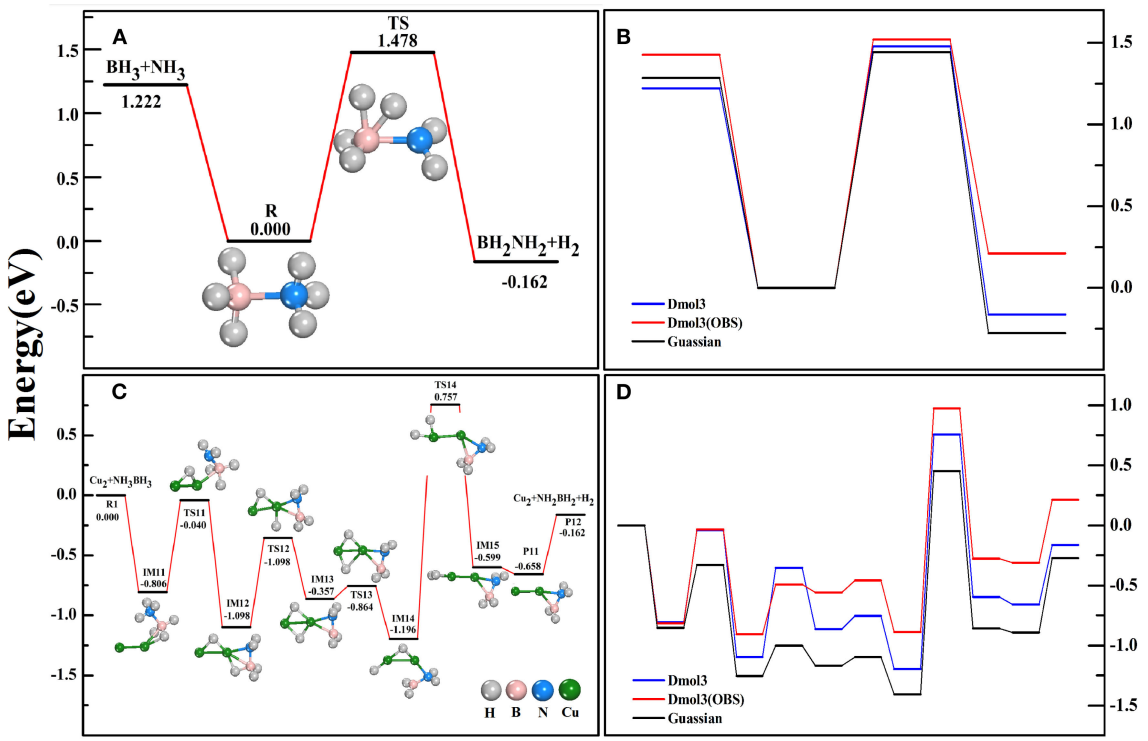

FIGURE 1 | The reaction pathways of AB dehydrogenation without **(A)** and with **(C)** the catalyst Cu_2 dimer. The comparison of counterpart reactions in Gaussian and DMol^3 software **(B,D)**.

By inspecting the changes of bond-lengths between the adsorbed AB (R0) and the free AB, we found that two H-B bonds near Ni atom are elongated by 0.048 Å while one H-B bond far from Ni atom is compressed by 0.011 Å. The B-N bond is also compressed by 0.027 Å. There are the negligible changes for two of H-N bond-lengths on $-NH_3$ edge whereas the other H-N bond is stretched by 0.025Å. Since Ni/Cu atoms are positively/negatively charged in NiCu dimer, they would like to present the moderate interactions with different hydrogen species because the former/latter one is the hydridic-hydrogen/protic-hydrogen acceptor. After the adsorption, the hydridic H(B) atoms donate their partial electrons to Ni atom, resulting in H(B) atoms in the less negatively charged state (-0.178 e$\rightarrow -0.057$ e). Meanwhile, the Ni atom back donates its electrons to B and Cu atoms, resulting in B atom in the less positively charged state (0.194 e$\rightarrow$0.023 e) and Cu atom in the more negatively charged state (-0.038 e$\rightarrow -0.270$ e). Note that the drawing force of Ni atom on its neighboring H(B) atoms has stretched the B-H bond-lengths. These activated H(B) atoms are then being ready for the subsequent dehydrogenation reactions owning to the formation of the agostic-bonds [B-H(B)$\cdots$Ni] (Brookhart et al., 2007; Zins et al., 2015).

In the hydrolysis reaction process, it has been proposed that AB molecule firstly diffuses onto the catalyst surface and forms an activated intermediate. Upon the attack of a water molecule, the intermediate of AB molecule is dissociated to release H_2 (Chandra and Xu, 2006a,b; Xu and Chandra, 2006; Lu et al., 2013). Consequently, H_2O molecule should to adsorb on the AB-NiCu complex. Note that the adsorption of H_2O molecules plays a negligible role on the bond-lengths and bond-angles of AB fragment (R1 and R22 in **Figure 2**). For one H_2O adsorption in R1 configuration, one protic H(O) atom is bonded with both Ni and Cu atoms, stretching the corresponding H-O bond by 0.045 Å. If O atom is bonded with Ni atom, it is 0.183 eV higher in energy. For two H_2O adsorption in R22 configuration, O atom of the second H_2O with the lone-pair electrons will nucleophilically attack the well-defined electrophilic Ni site, because O atom tends to donate its lone-pair electrons to the LUMO and/or LUMO+1 orbitals around the Ni site (R1). Relative to O atom in free H_2O, we found that the O atom of the O-bonded H_2O in R22 losses 0.031 electrons (-0.489 e$\rightarrow -0.458$ e) while the O atom of the H-bonded H_2O acquires 0.019 electrons (-0.489 e$\rightarrow -0.548$ e). Although the R1 and R22 configurations present the negligible differences in bond-lengths and Mulliken charges, their HOMO (LUMO) charge distributions are significantly different. Previously, the investigation has proposed that the HOMO (LUMO) distributions can be used as a fine guidance to determine the sub-reaction pathway (Li et al., 2013). Here, the HOMO (LUMO) differences between R1 (one H_2O adsorption) and R22 (two H_2O adsorption) suggest that the stepwise and simultaneous H_2O attacking would give rise to different reaction pathways.

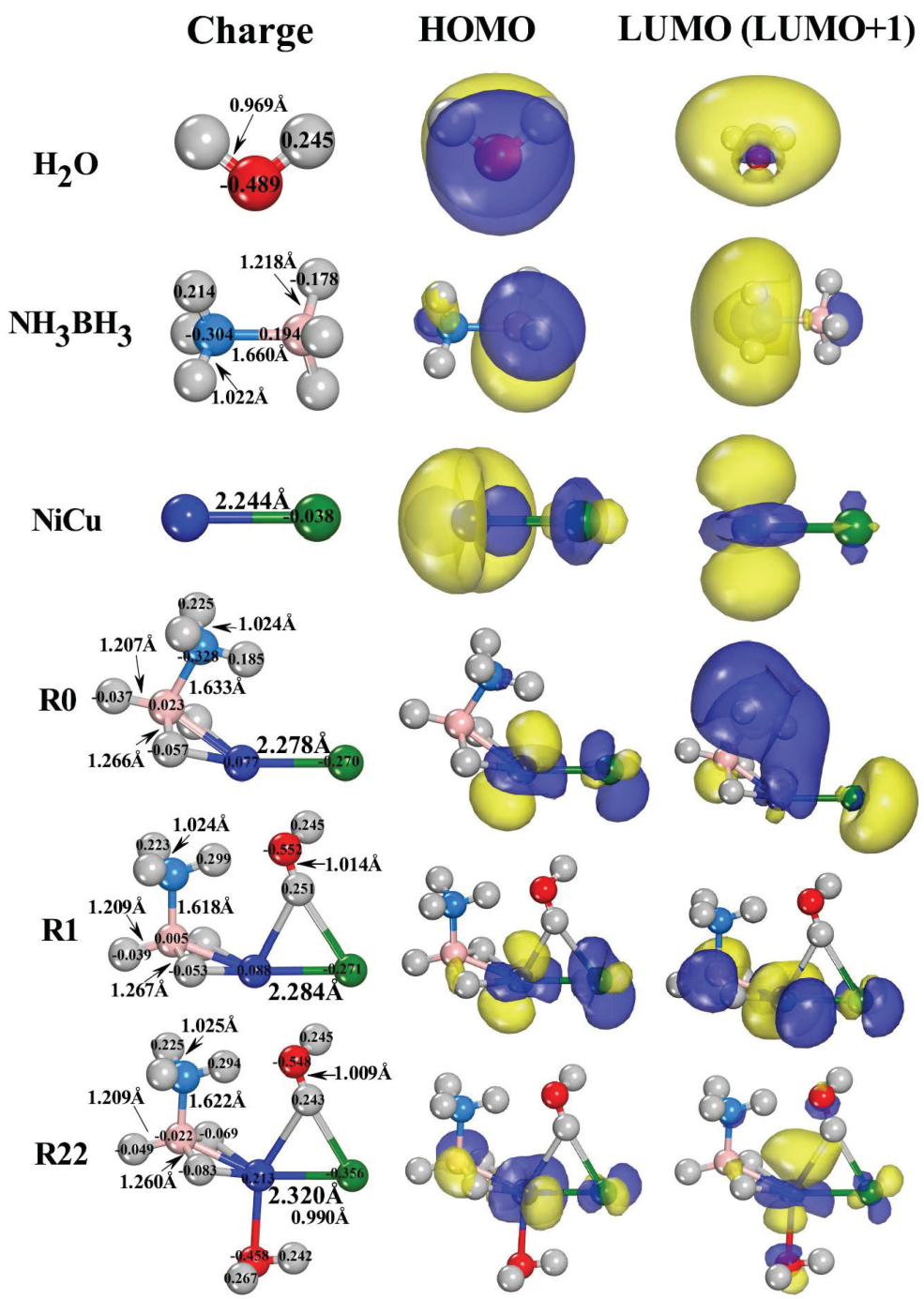

FIGURE 2 | The bond-length (in Å), Mulliken population charges (in e), as well as the schematic diagram of the frontier molecular orbitals (HOMO, LUMO/LUMO+1) for the energetically favorable reactant structures.

3.2. The Hydrolysis of AB Catalyzed by NiCu Dimer via the Stepwise H_2O Attack

In **Figures 3A–C**, we shown two preferential reaction pathways (path1 and path2) for the hydrolytic dehydrogenation of AB molecule catalyzed by NiCu dimer. These reactions undergo the stepwise attacks of H_2O molecules, named as H_2O^{st}, H_2O^{nd}, H_2O^{rd}. The energies of R, IM, TS, P, together with their structural configurations were illustrated on each step. For the R1 reactant-complex that H_2O^{st} and AB molecules are simultaneously adsorbed on NiCu dimer (**Figure 3A**), it situates at an energy level of 1.587 eV below the initial reactants AB+H_2O^{st}+NiCu. In the next reaction step, the cationic Ni atom would like to

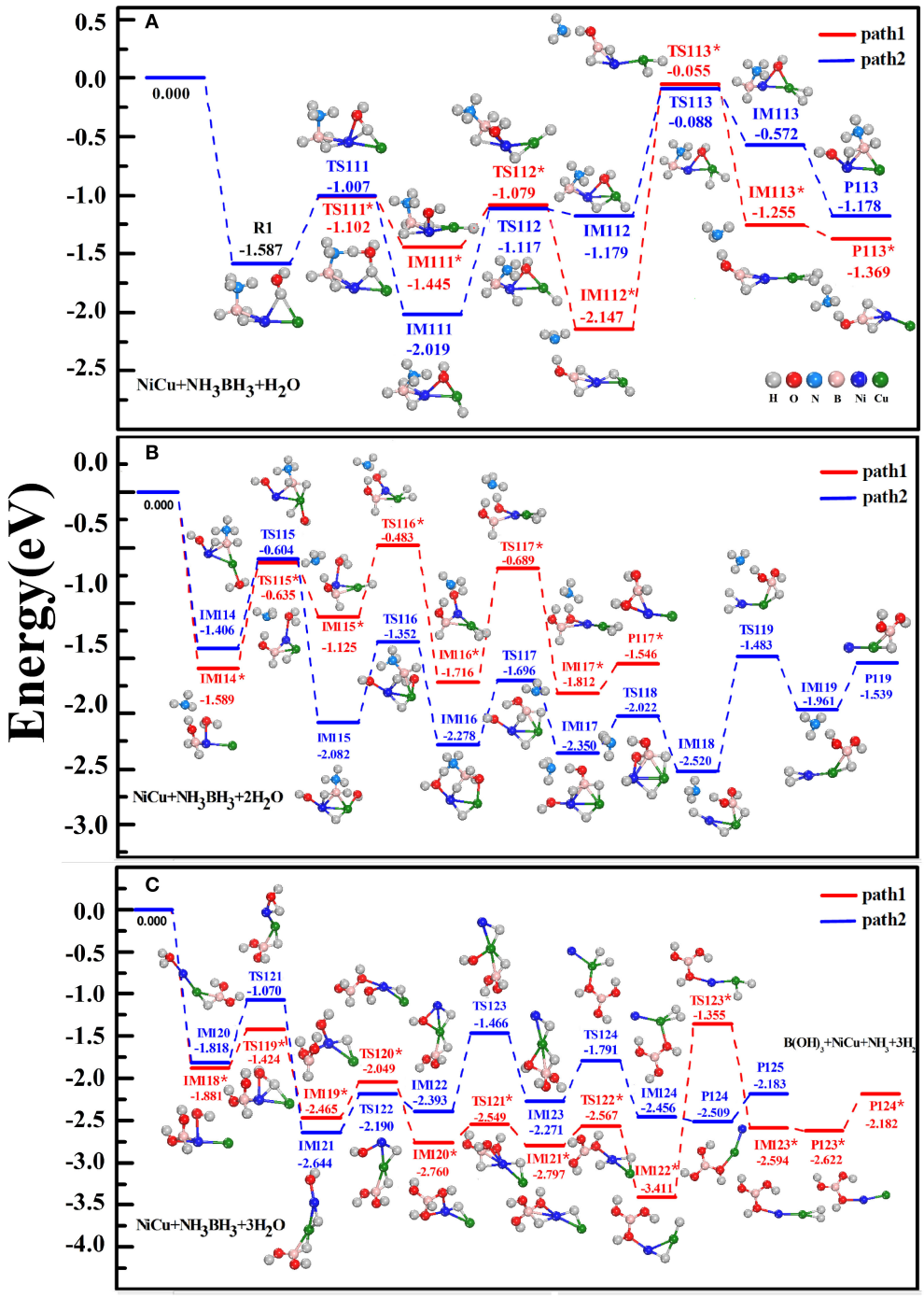

FIGURE 3 | Schematic energy profiles of hydrogen production from the catalytic hydrolysis of AB in the presence of NiCu dimer. The stepwise attacks involving three H_2O molecules, named as H_2O^{st}, H_2O^{nd}, H_2O^{rd}, are sequentially considered in **(A–C)**. The reactant, transition state, intermediate state, and product are denoted by R1, TS, IM, P, respectively.

interact with the nucleophilic [$-OH^{st}$] but the anionic Cu atom would like to interact with the protic H(O) acceptor. Under the synergistical roles of Ni and Cu atoms, the H_2O^{st} molecule is decomposed into one hydrogen atom H(O) and one hydroxy group [$-OH^{st}$] in IM111* or IM111 state. In terms of the reaction principle for the bond activation, [$-OH^{st}$] group will attack the positively charged B atom. If the O atom of [$-OH^{st}$] hydroxy is close enough to the B atom, the stronger interactions between O and B atoms than between N and B atoms will split the B-N bond via the activation energy barrier of the TS112* state

(1.445–1.079 = 0.366 eV), i.e., $-NH_3$ is dissociated from BH_3-NH_3 fragment in IM112* state by releasing the energy of 2.147–1.079 = 1.068 eV. Previously, Banu et al. (2015) have found that when the H_2O molecule directly interacts with BH_3-NH_3 fragment yet without TM catalyst, the breaking of B-N bond at the assistant of [-OH] group needs to cross a very high energy barrier of 1.19 eV, and the counterpart TS state is even 0.91 eV above the separated reactants AB+H_2O. Clearly, the present of NiCu dimer can significantly reduce the activation energy barrier during the hydrolytic AB. If the O-B interaction doesn't play the role this time, the O atom maintains its interactions with Ni and Cu atom in IM112 state (presenting a three-membered Ni-O-Cu ring). Whichever the reaction it happens, one H(B) atom of AB is somewhat activated by Ni atom and being ready to adsorb on Cu atom, because the corresponding H-B bond in IM112* is elongated by 0.169 Å (elongated by 0.056Å in IM112) with respect to 1.218 Å of free AB. Following the IM112* or IM112 state, H(O) and H(B) atoms on Cu atom move close to each other to form a Cu-dihydride complex in IM113* state or IM113 state. Ultimately, the $H_2{}^{(st)}$ molecule is released from the first-step-product P113* ([OH]·BH_2·NiCu+NH_3+H_2) or product P113 ([OH]·NiCu·NH_3BH_2+H_2), which releases the energy of 0.114 or 0.606 eV.

Apart from the above dehydrogenation pathways, we have considered other reaction routes from the R1 reactants: the first dissociation of H(B) atom and then H(O) atom; the stepwise dissociations of H(N) and H(O) atoms. However, these reaction routes have not any superiority with respect to the path1 and path2. For example, the reaction that one H(B) atom in R1 is activated and interacted with Cu atom has to go across a very high energy barrier (1.146 eV). It is 0.789 eV higher in energy than IM111* state. There are the possibilities that the released H_2 molecule is comprised of H(B) and H(N) atoms from AB fragment, which is analogous to what we have proposed in Zhou T. et al. (2016). Nevertheless, our primary goal is to explore the reaction mechanism that the hydrolytic dehydrogenation is happening with the assistant of H_2O. Consequently, these routes have been discarded owning to no dissociation of H(O) atom from H_2O. As a mater of fact, Shevlin et al. (2011) have indicated that the dehydrogenation via the combination of the protic atoms from the N-moiety and the hydridic atoms from the B-moiety is energetically unfavored for the metal amidoboranes MNH_2BH_3. In addition, another possible pathway could follow the IM111* or IM111 states: (i) One H(N) atom transfers to [–OH] group to produce the adsorbed H_2O and BH_3-NH_2 fragment once again; (ii) One H(O) atom is dissociated from the H_2O and then shifted to Cu atom, forming the Cu-dihydride complex and [–OH] group; (iii) The B-N bond of BH_3-NH_2 fragment is broken by [–OH] group, yielding the NH_2 and H_2 products. However, the B-N bond has an obvious contraction as one H(N) atom was migrated from $-NH_3$ edge after the first step reaction. It will be of ever-increasing difficulty to break the B-N bond by [–OH] group. Typically and importantly, the released product of NH_2 in this pathway does not agree with the experimental product of NH_3 (Yao C. F. et al., 2008; Rachiero et al., 2011b; Chou et al., 2012; Liu et al., 2012).

For the adsorption of the second H_2O^{nd} on the first-step-products, both Ni and Cu atoms are considered as the tentatively adsorbing sites. Our calculations demonstrate that the Ni site is 0.176 eV lower in energy than the Cu site in adsorbing O atom for the product P113*, whereas it reverses for the product P113. In **Figure 3B**, we show the subsequent reactions that the first-step-products are attacked by the H_2O^{nd}. The crucial reaction steps for the path1 are follows: (i) One of two hydridic H(B) atoms in IM114* is activated by the Lewis acid of Ni atom, and then it is optimally adsorbed on Cu atom in the formation of Cu-monohydride complex in IM115*; (ii) The protic H(O) atom and [-OH^{nd}] of the H_2O^{nd} are synergistically activated by Cu and Ni atoms, and then this protic H(O) atom shifts to Cu atom yielding the Cu-dihydride complex in IM116*; (iii) The [-OH^{nd}] group moves close to B atom to form the B-dihydroxy and Cu-dihydride fragments in IM117*, which is followed by the releasing of $H_2{}^{(nd)}$ molecule (the second-step-products P117*). For the successive reactions along the path2, there presents a thermodynamically downhill trend from IM114 to IM118 as well as from TS115 to TS118, revealing that these reactions would take place spontaneously due to their overall exothermic processes. In analogous with the dehydrogenation mechanism involving the H_2O^{st} attack, three critical processes can be clearly concerned for the H_2O^{nd} attack: (i) The protic H(O) atom is somewhat activated by Ni atom and then it links with both Ni and Cu atoms in IM115; (ii) The [-OH^{nd}] group breaks the N-B bond and dissociate $-NH_3$ fragment through IM116 to IM117; (iii) The B-dihydroxy and Ni-dihydride complex comes into being through IM118 to IM119, from which $H_2{}^{(nd)}$ is subsequently liberated (second-step-products P119). Generally speaking, since each energy barrier can be crossed at the available energies provided by the exothermic reaction, the overall reactions are thermodynamically feasible for either path1 or path2. Nevertheless, P119 state is the predomination state, because each IM state together with the counterpart TS state in path2 lies lower in energy than that in path1.

After the adsorption of the third H_2O^{rd} on the second-step-products (**Figure 3C**), IM118* and IM120 states come into being, respectively. Again, Ni atom serves as the activation site for dissociating H(O) atom from H_2O^{rd}, and its neighboring Cu atom serves as the attractive site for adsorbing H(O) atom. The last H(B) atom is gradually transferred to Cu atom to form the Cu-dihydride fragment. It is synchronously/succesively accompanied by the shifting of [-OH^{rd}] group from Ni atom to B atom (forming the B-trihydroxy fragment) and by the releasing of $H_2{}^{(rd)}$ molecule. All IM and TS states are accessible for proceeding the dehydrogenation reactions. Viewing the pathway as a whole, we found that TS113* and TS113 states are only 0.055 and 0.088 eV lower in energy than the initial reactants. Since they present the highest energy barriers, these states are the rate determining barriers of the overall dehydrogenation processes. Nevertheless, it is nothing to be worried about this requirement, because the foregoing reactions are overall exothermic process and TS113* and TS113 states can be overcome. Ultimately, the hydrolytic dehydrogenation reaction is completed, $NH_3BH_3+3H_2O \xrightarrow{NiCu}$

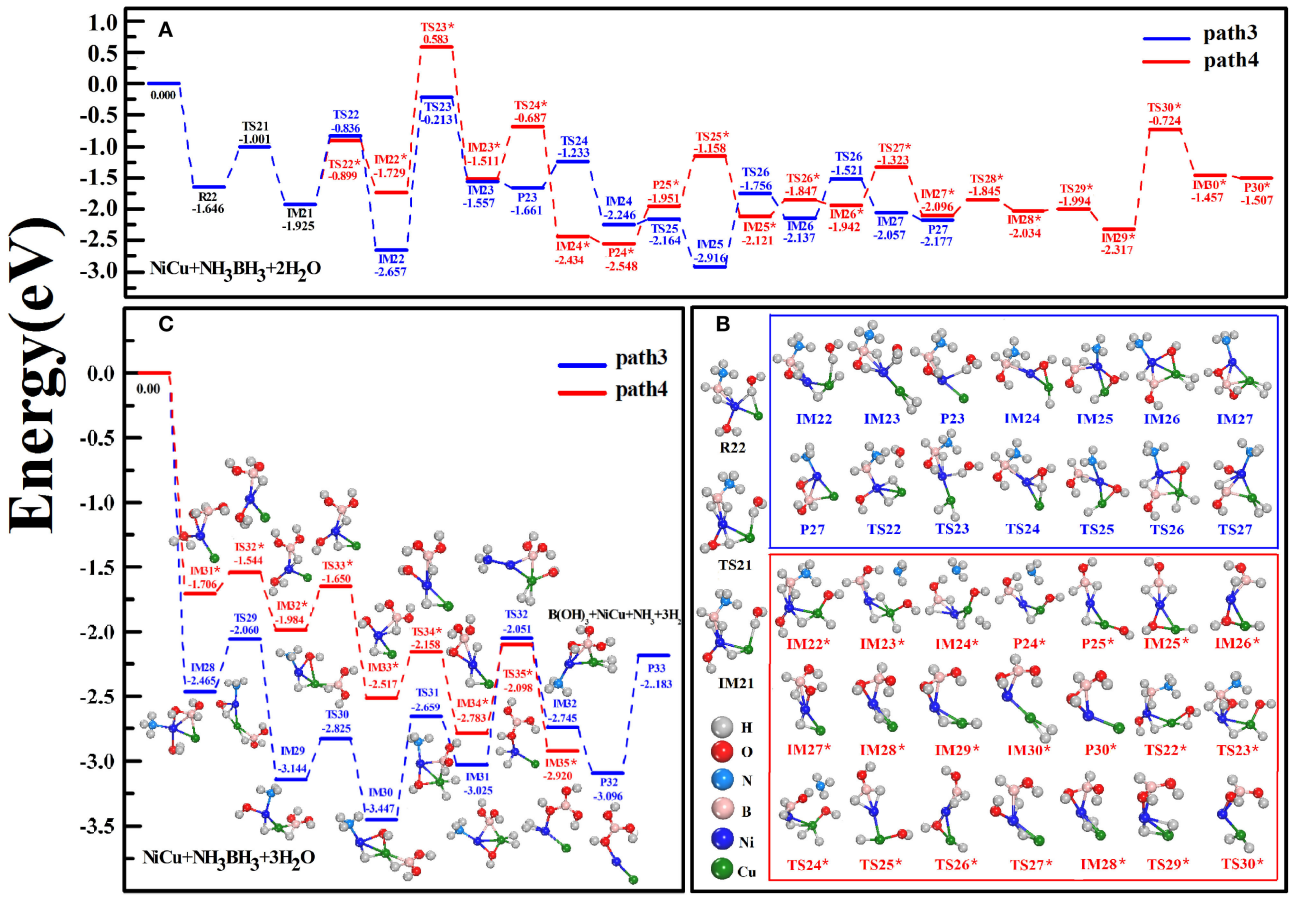

FIGURE 4 | Schematic energy profiles of catalytic hydrolysis of AB involving the simultaneous H_2O attacks **(A)**. The hydrolysis AB is simultaneously attacked by $H_2O^{(1)}$ and $H_2O^{(2)}$ **(B)** and subsequently attacked by $H_2O^{(3)}$ **(C)**.

$NiCu{\cdot}NH_3{+}B(OH)_3{+}3H_2\uparrow$, which is catalyzed by the NiCu dimer and orderly attacked by three H_2O molecules. We can conclude that *the formation of Cu-dihydride* and *B-multihydroxy fragments in IM states is crucial for the hydrolytic dehydrogenation, and both metal atoms are acted as the catalytic sites for breaking the H-O bond of H_2O and N-B bond of NH_3BH_3*.

3.3. The Hydrolysis of AB Catalyzed by NiCu Dimer via the Simultaneous H_2O Attack

For the hydrolytic AB via the simultaneous adsorption of a few H_2O molecules, we considered the reaction case: AB is simultaneously attacked by $H_2O^{(1)}$ and $H_2O^{(2)}$ and subsequently attacked by $H_2O^{(3)}$. In the configuration of R22 reactant (**Figure 4B**), $H_2O^{(1)}$ with O atom is attached to Ni atom while $H_2O^{(2)}$ with H atom is bridged with Cu and Ni atoms. From R22 to IM22 states along the path3, one H-O bond of $H_2O^{(1)}$ and one H-B bond of AB are successively broken. Then, H(O) and H(B) atoms are bonded with Cu atom to generate the Cu-dihydride complex and $[-OH]^{(1)}$ group, following which the B-monohydroxy complex (IM22) comes into being. In this situation, N-B bond-length is elongated by 0.050 Å with respect to 1.622 Å in R22. For the subsequent reaction from IM22 to IM23, $H_2O^{(2)}$ is shifted from Cu site to Ni site. After releasing the first $H_2^{(st)}$ in P23, several steps related to the atomic transfers are crucial: (i) One H(O) atom of $H_2O^{(2)}$ is dissociated and subsequently bonded with Cu atom (IM24), yielding $[-OH]^{(2)}$ group that is ready to break the N-B bond of AB (IM25); (ii) One H(B) atom gradually moves to Cu atom to generate the Cu-dihydride (IM26), which is the prerequisite in releasing the second $H_2^{(nd)}$ (P27); (iii) The adsorption site of $[-OH]^{(2)}$ is adjusted to connect with B atom (TS27), which contributes to the B-dihydroxy fragments (IM27). Thus, above reactions can be described as: $NH_3BH_3{+}2H_2O \xrightarrow{NiCu} NiCu{\cdot}NH_3\cdots HB(OH)_2{+}2H_2\uparrow$. When $H_2O^{(3)}$ is adsorbed on the resulting product P27 (**Figure 4C**), analogously, one H(O) atom of $H_2O^{(3)}$ and the last H(B) atom are gradually transferred to Cu atom (from IM29 to IM31). It is followed by the movement of $[-OH]^{(3)}$ group to B site, again yielding the Cu-dihydride and B-trihydroxy

complex (IM32). Then, the releases of NH_3 and H_2[(rd)] via P32 and P33 states can be achieved. Finally, we complete the experimental reactions in an overall exothermic and barrierless pathway, $NH_3BH_3+3H_2O \xrightarrow{NiCu} NH_3+NiCu{\cdot}B(OH)_3+3H_2\uparrow$. On the whole, the key mechanism of the path3 is that H(O) and H(B) atoms are alternately dissociated from H_2O and AB molecules, successively yielding Cu-dihydride and B-multihydroxy complexes in IM states.

Unlike the dehydrogenation mechanism of the path3, we consider the reaction path 4 that two H(O) atoms are firstly detached from $H_2O^{(1)}$ and $H_2O^{(2)}$ (IM22*) and then H(B)

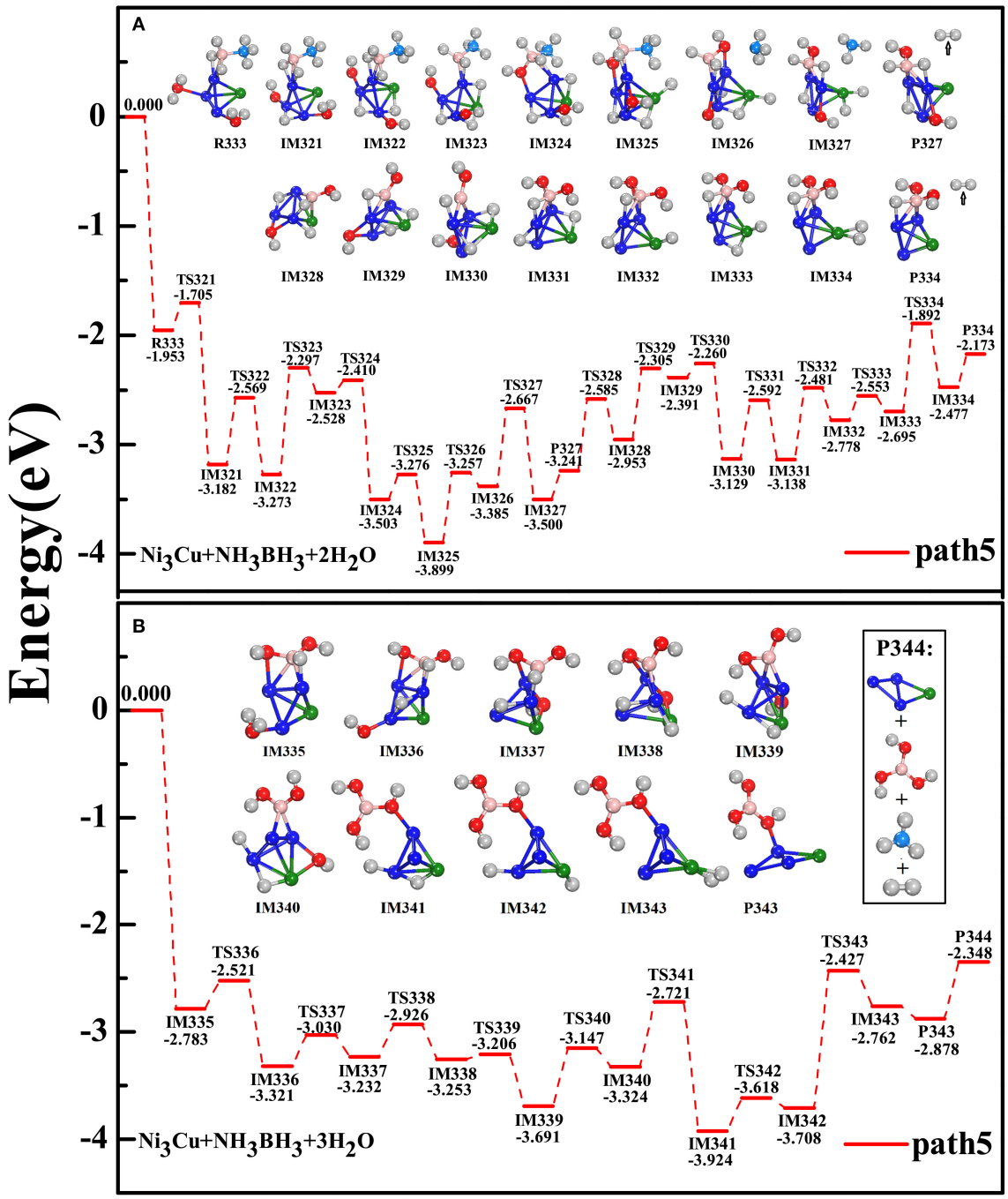

FIGURE 5 | Similar to that of **Figure 4** but for the catalyst of Ni_3Cu tetramer: **(A)** hydrolysis of AB simultaneously attacked by $H_2O^{(1)}$ and $H_2O^{(2)}$; **(B)** subsequently attacked by the third $H_2O^{(3)}$.

atoms are departed from AB molecule (IM24*). However, high energy barrier of 1.729–0.583 = 1.146 eV is encountered at TS23* state when $[-OH]^{(1)}$ group acts as an attacker to dissociate $-NH_3$ fragment (IM23*). Although this reaction step is thermodynamically unfeasible, to verify our findings that the hydrolytic dehydrogenation reaction undergoes via the specific intermediate states, we continue the reactions irrespective of TS23* state. To one's expectation, the formations of the Cu-dihydride complexes (IM24*, IM30*, and IM35*) together with the B-multihydroxy complexes (IM23*, IM27*, IM34*) can be clearly discerned from the sequential steps in **Figures 4B,C**. Experimentally, the activation energy for the catalytic hydrolysis of AB dehydrogenation has been conjectured to be the step reaction of B-N bond breaking (Xu and Chandra, 2006; Chandra and Xu, 2007), where an apparent value was estimated around 0.4 eV for CuNi catalysts (Lu et al., 2014; Zhang et al., 2016). Our E_{act} = 0.58 eV determined by the highest energy barrier of the reaction path4 at TS113* state is approach to these experimental activation energies. Here, we found that the hydride transfer is responsible for the rate-determining step for all pathways we studied.

3.4. The Hydrolysis of AB Catalyzed by Ni_3Cu Cluster via the Simultaneous H_2O Attack

Since the tetrahedral structure is the block-unit for constructing large metal nanoclusters, Ni_3Cu tetrahedron cluster is treated as an ideal model to underline the catalysis effect on the hydrolytic dehydrogenation of AB. Importantly, experimental synthesizing has shown the Cu@Ni core-shell structure, where Ni atoms are on the structural surface and as the active sites (Lu et al., 2014; Zhang et al., 2016). After considering the different adsorption styles, i.e., -BH_3 fragment (or -NH_3 fragment) is adjacent to Ni atom (or Cu atom) as well as $H_2O^{(1)}$ and $H_2O^{(2)}$ molecules are attached on various metal sites, we found that R333 configuration is the most favorable adsorption style (**Figure 5**). Although the reaction steps are more and complex in the present of Ni_3Cu cluster, according to the criterion of the dehydrogenation that the reactions should follow the pathway in an exothermic, overall barrierless, and the minimum energy profile, we found that the accessible pathway for the catalytic dehydrogenation by Ni_3Cu cluster is exactly identical to that by NiCu dimer. The subsequent reaction steps are following: the alternation of the breaking of three H-O bonds from three H_2O molecules (IM321, IM322, IM336) with the breaking of three B-H bonds from AB molecule (IM323, IM328, IM338); the dissociation of NH_3 from AB molecule (IM326); the adjustment of the adsorbing sites of H(O) and H(B) atoms and [-OH] groups to yield the metal-dihydride and B-multioxhydryl fragment (IM327, IM334, IM343); the liberation of three H_2 molecules through three intermediate products (P327, P334, P343); the recovery of Ni_3Cu catalyst after the complete reactions (P344). Throughout all procedures of the path5, the hydrolytic dehydrogenation process is feasible both in kinetics and thermodynamics: $NH_3BH_3+3H_2O \xrightarrow{Ni_3Cu} Ni_3Cu{\cdot}NH_3BH_3\cdots(H_2O)_3 \rightarrow Ni_3Cu{\cdot}NH_3+B(OH)_3+3H_2\uparrow$.

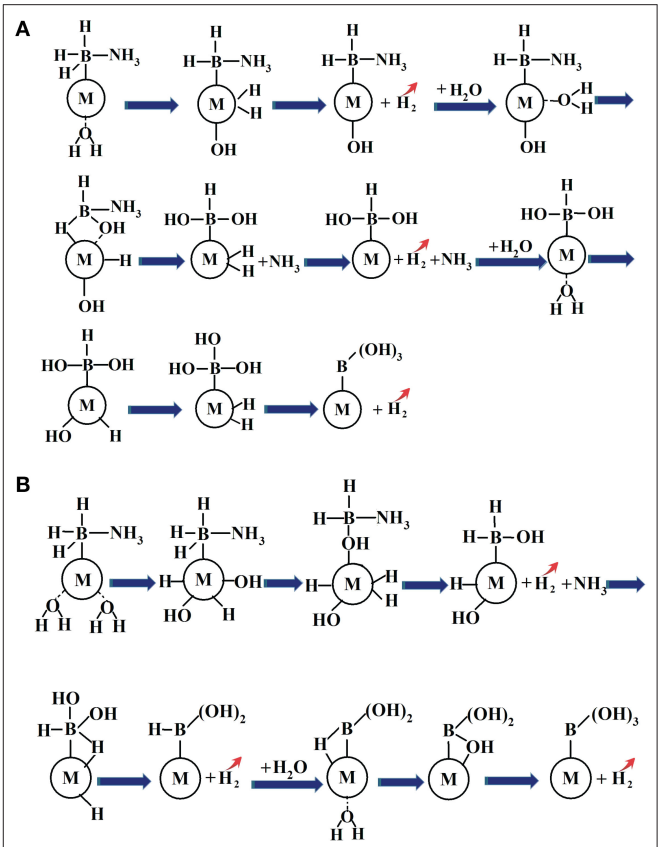

FIGURE 6 | The proposed schematic representation of hydrolytic AB for hydrogen generation in the presence of metal catalyst: **(A)** hydrolysis of AB catalyzed by metal catalyst via the stepwise H_2O attack; **(B)** hydrolysis of AB by metal catalyst via the simultaneous H_2O attack.

4. CONCLUSIONS

A novel reaction strategy to the prediction of the dehydrogenation sequences for catalytic hydrolysis of AB by NiCu bimetal catalyst has been developed, $NH_3BH_3+3H_2O \xrightarrow{NiCu} NiCu{\cdot}NH_3+B(OH)_3+3H_2\uparrow$, and the plausible mechanisms were analyzed under a molecular level by using the density functional theory method. Our proposed catalytic hydrolysis of AB for the hydrogen generation are illustrated in **Figure 6**.

The driving force behind the formations of NH_3 and H_2 is the development of [-OH] group and Cu-dihydride complex species after the H_2O participation. The former resultant attack the B-N bond to dissociate NH_3 and the latter resultant is the prerequisite toward the H_2 elimination. The activation energy barrier for the hydrolytic AB is most likely caused by the hydride transfer from H(B) to metal atom rather than the B-N bond breaking. The formation of heterometallic NiCu bonds and the charge transfers might be the key factor to tune the frontier molecular orbitals of the catalyst surface atom, which play the decisive role to react with the molecules (AB and H_2O) and to stabilize the possible intermediate states, leading to the improved catalytic activity

and selectivity in comparison with those of the corresponding monometallic counterparts.

DATA AVAILABILITY STATEMENT

All datasets generated for this study are included in the article/supplementary material.

AUTHOR CONTRIBUTIONS

WY, YZ, and TZ: software and writing-original draft preparation. GW: software, writing-original draft preparation, and methodology. DW: writing-reviewing and editing. HY: software, writing-original draft preparation, methodology, writing-reviewing and editing, and conceptualization. All authors contributed to the article and approved the submitted version.

FUNDING

This work was supported by the National Natural Science Foundation of China (11574253), the Natural Science Foundation of Chongqing (CSTC-2017jcyjBX0035), and the Postgraduates' Research and Innovation Project of Chongqing (CYS18088).

REFERENCES

Ayala, P. Y., and Schlegel, H. B. (1997). A combined method for determining reaction paths, minima, and transition state geometries. *J. Chem. Phys.* 107, 375–384. doi: 10.1063/1.474398

Banu, T., Debnath, T., Ash, T., and Das, A. K. (2015). Hydrolysis of ammonia borane and metal amidoboranes: a comparative study. *J. Chem. Phys.* 143, 194305–194305. doi: 10.1063/1.4935933

Basu, S., Zheng, Y., Varma, A., Delgass, W. N., and Gore, J. P. (2010). Catalytic hydrolysis of ammonia borane: intrinsic parameter estimation and validation. *J. Power Sources* 195, 1957–1963. doi: 10.1016/j.jpowsour.2009.10.070

Becke, A. D. (1988). Density-functional exchange-energy approximation with correct asymptotic behavior. *Phys. Rev. A* 38, 3098–3100. doi: 10.1103/PhysRevA.38.3098

Brockman, A., Zheng, Y., and Gore, J. (2010). A study of catalytic hydrolysi s of concentrated ammonia borane solution. *Int. J. Hydrogen Energy* 35, 7350–7356. doi: 10.1016/j.ijhydene.2010.04.172

Brookhart, M., Green, M. L. H., and Parkin, G. (2007). Agostic interactions in transition metal compounds. *Proc. Natl. Acad. Sci. U.S.A.* 104, 6908–6914. doi: 10.1073/pnas.0610747104

Bučko, T., Hafner, J., Lebègue, S., and Angyan, J. G. (2010). Improved description of the structure of molecular and layered crystals: ab initio DFT calculations with van der Waals corrections. *J. Phys. Chem. A* 114, 11814–11824. doi: 10.1021/jp106469x

Can, H., and Metin, Ö. (2012). A facile synthesis of nearly monodisperse ruthenium nanoparticles and their catalysis in the hydrolytic dehydrogenation of ammonia borane for chemical hydrogen storage. *Appl. Catal. B Environ.* 125, 304–310. doi: 10.1016/j.apcatb.2012.05.048

Chandra, M., and Xu, Q. (2006a). A high-performance hydrogen generation system: transition metal-catalyzed dissociation and hydrolysis of ammonia-borane. *J. Power Sources* 156, 190–194. doi: 10.1016/j.jpowsour.2005.05.043

Chandra, M., and Xu, Q. (2006b). Dissociation and hydrolysis of ammoniaeborane with solid acids and carbon dioxide: an efficient hydrogen generation system. *J. Power Sources* 159, 855–860. doi: 10.1016/j.jpowsour.2005.12.033

Chandra, M., and Xu, Q. (2007). Room temperature hydrogen generation from aqueous ammonia-borane using noble metal nanoclusters as highly active catalysts. *J. Power Sources* 168, 135–142. doi: 10.1016/j.jpowsour.2007.03.015

Chen, F., Ma, H., Li, Y., and Chen, J. (2007). $Ni_{1-x}Pt_x$ ($x = 0$–0.12) hollow spheres as catalysts for hydrogen generation from ammonia borane. *Inorg. Chem.* 46, 788–794. doi: 10.1021/ic061712e

Chen, G., Desinan, S., Nechache, R., Rosei, R., Rosei, F., and Ma, D. (2011). Bifunctional catalytic/magnetic Ni@Ru core-shell nanoparticles. *Chem. Commun.* 47, 6308–6310. doi: 10.1039/c1cc10619h

Chen, G., Desinan, S., Rosei, R., Rosei, F., and Ma, D. (2012). Synthesis of Ni-Ru alloy nanoparticles and their high catalytic activity in dehydrogenation of ammonia borane. *Chem. Eur. J.* 18, 7925–7930. doi: 10.1002/chem.201200292

Chen, W., Ji, J., Feng, X., Duan, X., Qian, G., Li, P., et al. (2014). Mechanistic insight into size-dependent activity and durability in Pt/CNT catalyzed hydrolytic dehydrogenation of ammonia borane. *J. Am. Chem. Soc.* 136, 16736–16739. doi: 10.1021/ja509778y

Chou, C., Lee, D., and Chen, B. (2012). Hydrogen production from hydrolysis of ammonia borane with limited water supply. *Int. J. Hydrogen Energy* 37, 15681–15690. doi: 10.1016/j.ijhydene.2012.05.108

Chua, Y. S., Chen, P., Wu, G., and Xiong, Z. (2011). Development of amidoboranes for hydrogen storage. *Chem. Commun.* 47, 5116–5129. doi: 10.1039/C0CC05511E

Çiftci, N. S., and Metin, Ö. (2014). Monodisperse nickel-palladium alloy nanoparticles supported on reduced graphene oxide as highly efficient catalysts for the hydrolytic dehydrogenation of ammonia borane. *Int. J. Hydrogen Energy* 39, 18863–18870. doi: 10.1016/j.ijhydene.2014.09.060

Delley, B. (2000). From molecules to solids with the $DMol^3$ approach. *J. Chem. Phys.* 113, 7756–7764. doi: 10.1063/1.1316015

Demirci, U. B., and Miele, P. (2009). Sodium borohydride versus ammonia borane, in hydrogen storage and direct fuel cell applications. *Energy Environ. Sci.* 2, 627–637. doi: 10.1039/B900595A

Demirci, U. B., and Miele, P. (2010). Hydrolysis of solid ammonia borane. *J. Power Sources* 195, 4030–4035. doi: 10.1016/j.jpowsour.2010.01.002

Dinç, M., Metin, Ö., and Özkar, S. (2012). Water soluble polymer stabilized iron(0) nanoclusters: a cost-effective and magnetically recoverable catalyst in hydrogen generation from the hydrolysis of sodium borohydride and ammonia borane. *Catal. Today* 183, 10–16. doi: 10.1016/j.cattod.2011.05.007

Güngörmez, K., and Metin, Ö. (2015). Composition-controlled catalysis of reduced graphene oxide supported CuPd alloy nanoparticles in the hydrolytic dehydrogenation of ammonia borane. *Appl. Catal. A* 494, 22–28. doi: 10.1016/j.apcata.2015.01.020

Hamilton, C. W., Baker, R. T., Staubitz, A., and Manners, I. (2009). B-N compounds for chemical hydrogen storage. *Chem. Soc. Rev.* 38, 279–293. doi: 10.1039/b800312m

Hirshfeld, F. L. (1977). Bonded-atom fragments for describing molecular charge densities. *Theor. Chem. ACC.* 44, 129–138. doi: 10.1007/BF00549096

Hu, M. G., Geanangel, R. A., and Wendlandt, W. W. (1978). The thermal decomposition of ammonia borane. *Thermochim Acta* 23, 249–255. doi: 10.1016/0040-6031(78)85066-7

Huang, Z., and Autrey, T. (2012). Boron-nitrogen-hydrogen (BNH) compounds: recent developments in hydrogen storage, applications in hydrogenation and catalysis, and new syntheses. *Energy Environ. Sci.* 5, 9257–9268. doi: 10.1039/c2ee23039a

Jiang, H., and Xu, Q. (2011). Catalytic hydrolysis of ammonia borane for chemical hydrogen storage. *Catal. Today* 170, 56–63. doi: 10.1016/j.cattod.2010.09.019

Jiang, H. L., Umegaki, T., Akita, T., Zhang, X. B., Haruta, M., and Xu, Q. (2010). Bimetallic Au-Ni nanoparticles embedded in SiO_2 nanospheres: synergetic catalysis in hydrolytic dehydrogenation of ammonia borane. *Chem. Eur. J.* 16, 3132–3137. doi: 10.1002/chem.200902829

Kalidindi, S. B., Indirani, M., and Jagirdar, B. R. (2008a). First row transition metal ion-assisted ammoniaeborane hydrolysis for hydrogen generation. *Inorg. Chem.* 47, 7424–7429. doi: 10.1021/ic800805r

Kalidindi, S. B., Sanyal, U., and Jagirdar, B. R. (2008b). Nanostructured Cu and $Cu@Cu_2O$ core shell catalysts for hydrogen generation from ammonia-borane. *Phys. Chem. Chem. Phys.* 10, 5870–5874. doi: 10.1039/B805726E

Karahan, S., Zahmakiran, M., and Özkar, S. (2012). A facile one-step synthesis of polymer supported rhodium nanoparticles in organic medium and their catalytic performance in the dehydrogenation of ammonia-borane. *Chem. Commun.* 48, 1180–1182. doi: 10.1039/C1CC15864C

Kılıç, B., Şencanlı, S., and Metin, Ö. (2012). Hydrolytic dehydrogenation of ammonia borane catalyzed by reduced graphene oxide supported monodisperse palladium nanoparticles: high activity and detailed reaction kinetics. *J. Mol. Catal. A-Chem.* 361, 104–110. doi: 10.1016/j.molcata.2012.05.008

Komova, O. V., Kayl, N. L., Odegova, G. V., Netskina, O. V., and Simagina, V. I. (2016). Destabilization of NH_3BH_3 by water during hydrothermolysis as a key factor in the high hydrogen evolution rates. *Int. J. Hydrogen Energy* 41, 17484-17495. doi: 10.1016/j.ijhydene.2016.07.163

Li, F., Sun, L. X., Zhao, J. J., Xu, F., Zhou, H. Y., Zhang, Q. M., et al. (2013). Mechanisms of H_2 generation for metal doped Al_{16} M (M = Mg and Bi) clusters in water. *Int. J. Hydrogen Energy* 38, 6930–6937. doi: 10.1016/j.ijhydene.2013.03.076

Li, Y., and Evans, J. N. S. (1995). The fukui function: a key concept linking frontier molecular orbital theory and the hard-soft-acid-base principle. *J. Am. Chem. Soc.* 117, 7756–7759. doi: 10.1021/ja00134a021

Li, Z., He, T., Liu, L., Chen, W. D., Zhang, M., Wu, G.T., et al. (2017). Covalent triazine framework supported non-noble metal nanoparticles with superior activity for catalytic hydrolysis of ammonia borane: from mechanistic study to catalyst design. *Chem. Sci.* 8, 781–788. doi: 10.1039/C6SC02456D

Liang, H. Y., Chen, G. Z., Desinan, S., Rosei, R., Rosei, F., and Ma, D. L. (2012). In situ facile synthesis of ruthenium nanocluster catalyst supported on carbon black for hydrogen generation from the hydrolysis of ammoniaeborane. *Int. J. Hydrogen Energy* 37, 17921–17927. doi: 10.1016/j.ijhydene.2012.09.026

Liu, C., Wu, Y., Chou, C., Chen, B., Hsueh, C., Ku, J., et al. (2012). Hydrogen generated from hydrolysis of ammonia borane using cobalt and ruthenium based catalysts. *Int. J. Hydrogen Energy* 37, 2950–2959. doi: 10.1016/j.ijhydene.2011.05.022

Lu, Z. H., Jiang, H. L., Yadav, M., Aranishi, K., and Xu, Q. (2012). Synergistic catalysis of Au-Co@SiO2 nanospheres in hydrolytic dehydrogenation of ammonia borane for chemical hydrogen storage. *J. Mater. Chem.* 22, 5065–5071. doi: 10.1039/c2jm14787d

Lu, Z. H., Li, J., Feng, G., Yao, Q., Zhang, F., Zhou, R., et al. (2014). Synergistic catalysis of MCM-41 immobilized Cu-Ni nanoparticles in hydrolytic dehydrogeneration of ammonia borane. *Int. J. Hydrogen Energy* 39, 13389–13395. doi: 10.1016/j.ijhydene.2014.04.086

Lu, Z. H., Li, J., Zhu, A., Yao, Q., Huang, W., Zhou,R., et al. (2013). Catalytic hydrolysis of ammonia borane via magnetically recyclable copper iron nanoparticles for chemical hydrogen storage. *Int. J. Hydrogen Energy* 38, 5330–5337. doi: 10.1016/j.ijhydene.2013.02.076

Lu, Z. H., and Xu, Q. (2012). Recent progress in boron- and nitrogen-based chemical hydrogen storage. *Funct. Mater. Lett.* 5, 1230001–1230009. doi: 10.1142/S1793604712300010

Matus, M. H., Anderson, K. D., Camaioni, D. M., Autrey, S. T., and Dixon, D. A. (2007). Reliable predictions of the thermochemistry of boron-nitrogen hydrogen storage compounds: $B_xN_xH_y$, $x = 2$, 3. *J. Phys. Chem. A* 111, 4411–4421. doi: 10.1021/jp070931y

Metin, O., Duman, S., Dinc, M., and Ozkar, S. (2011). Oleylamine-stabilized palladium(0) nanoclusters as highly active heterogeneous catalyst for the dehydrogenation of ammonia borane. *J. Phys. Chem. C* 115, 10736–10743. doi: 10.1021/jp201906n

Metin, Ö., Mazumder, V., Özkar, S., and Sun, S. (2010). Monodisperse nickel nanoparticles and their catalysis in hydrolytic dehydrogenation of ammonia borane. *J. Am. Chem. Soc.* 132, 1468–1469. doi: 10.1021/ja909243z

Metin, Ö., and Özkar, S. (2011). Water soluble nickel(0) and cobalt(0) nanoclusters stabilized by poly(4-styrenesulfonic acid-comaleic acid): highly active, durable and cost effective catalysts in hydrogen generation from the hydrolysis of ammonia borane. *Int. J. Hydrogen Energy* 36, 1424–1432. doi: 10.1016/j.ijhydene.2010.10.070

Mohajeri, N., Ali, T., and Adebiyi, O. (2007). Hydrolytic cleavage of ammonia-borane complex for hydrogen production. *J. Power Sources* 167, 482–485. doi: 10.1016/j.jpowsour.2007.02.059

Patel, N., and Miotello, A. (2015). Progress in Co-B related catalyst for hydrogen production by hydrolysis of boron-hydrides: a review and the perspectives to substitute noble metals. *Int. J. Hydrogen Energy* 40, 1429–1464. doi: 10.1016/j.ijhydene.2014.11.052

Peng, B., and Chen, J. (2008). Ammonia borane as an efficient and lightweight hydrogen storage medium. *Energy Environ. Sci.* 1, 479–483. doi: 10.1039/B809243P

Peng, C., Ayala, P. Y., Schlegel, H. B., and Frisch, M. J. (1996). Using redundant internal coordinates to optimize equilibrium geometries and transition states. *J. Comput. Chem.* 17, 49–56. doi: 10.1002/(sici)1096-987x(19960115)17:1<49::aid-jcc5>3.0.co;2-0

Peng, C., and Schlegel, H. B. (1993). Combining Synchronous Transit and Quasi-Newton Methods to Find Transition States. *Isr. J. Chem.* 33, 449–454. doi: 10.1002/ijch.199300051

Perdew, J. P., and Wang, Y. (1992). Accurate and simple analytic representation of the electron-gas correlation energy. *Phys. Rev. B* 45, 13244–132499. doi: 10.1103/PhysRevB.45.13244

Rachiero, G. P., Demirci, U. B., and Miele, P. (2011a). Facile synthesis by polyol method of a ruthenium catalyst supported on γ-$Al_2O_3$for hydrolytic dehydrogenation of ammonia borane. *Catal. Today* 170, 85–92. doi: 10.1016/j.cattod.2011.01.040

Rachiero, G. P., Demirci, U. B., and Miele, P. (2011b). Bimetallic RuCo and RuCu catalysts supported on γ-AlO. A comparative study of their activity in hydrolysis of ammonia-borane. *Int. J. Hydrogen Energy* 36, 7051–7065. doi: 10.1016/j.ijhydene.2011.03.009

Rakap, M., and Özkar, S. (2010). Zeolite confined palladium (0) nanoclusters as effective and reusable catalyst for hydrogen generation from the hydrolysis of ammonia-borane. *Int. J. Hydrogen Energy* 35, 1305–1312. doi: 10.1016/j.ijhydene.2009.11.056

Reber, A. C., Khanna, S. N., Roach, P. J., Woodward, W. H., and Castleman, A. W. (2010). Reactivity of aluminum cluster anions with water: origins of reactivity and mechanisms for H_2 release. *J. Phys. Chem. A* 114,6071–6081. doi: 10.1021/jp911136s

Roach, P. J., Woodward, W. H., Castleman, A. W., Reber, A. C., and Khanna, S. N. (2009). Complementary active sites cause size-selective reactivity of aluminum cluster anions with water. *Science* 323, 492–495. doi: 10.1126/science.1165884

Sanyal, U., Demirci, U. B., Jagirdar, B. R., and Miele, P. (2011). Hydrolysis of ammonia borane as a hydrogen source: fundamental issues and potential solutions towards implementation. *ChemSusChem*. 4, 1731–1739. doi: 10.1002/cssc.201100318

Shevlin, S. A., Kerkeni, B., and Guo, Z. X. (2011). Dehydrogenation mechanisms and thermodynamics of MNH_2BH_3 (M = Li, Na) metal amidoboranes as predicted from first principles. *Phys. Chem. Chem. Phys.* 13, 7649–1659. doi: 10.1039/c0cp02213f

Staubitz, A., Robertson, A. P. M., and Manners, I. (2010). Ammonia-Borane and related compounds as dihydrogen sources. *Chem. Rev.* 110, 4079–4124. doi: 10.1021/cr100088b

Stowe, A. C., Shaw, W. J., Linehan, J. C., Benjamin, S., and Autrey, T. (2007). In situ solid state ^{11}B MAS-NMR studies of the thermal decomposition of ammonia borane: mechanistic studies of the hydrogen release pathways from a solid state hydrogen storage material. *Phys. Chem. Chem. Phys.* 9, 1831–1836. doi: 10.1039/b617781f

Sun, D., Mazumder, V., Metin, O., and Sun, S. (2011). Catalytic hydrolysis of ammonia borane via cobalt palladium nanoparticles. *ACS Nano* 5, 6458–6464. doi: 10.1021/nn2016666

Thorne, L. R., Suenram, R. D., and Lovas, F. J. (2011). Microwave spectrum, torsional barrier, and structure of BH_3NH_3. *J. Chem. Phys.* 78, 167–171. doi: 10.1063/1.444528

Umegaki, T., Yan, J. M., Zhang, X. B., Shioyama, H., Kuriyama, N., and Xu,Q. (2009). Boron- and nitrogen-based chemical hydrogen storage materials. *Int. J. Hydrogen Energy* 34, 2303–2311. doi: 10.1016/j.ijhydene.2009.01.002

Wang, C. L., Tuninetti, J., Wang, Z., Zhang, C., Ciganda, R., Salmon, L., et al. (2017a). Hydrolysis of ammonia-borane over Ni/ZIF-8 nanocatalyst: high efficiency, mechanism, and controlled hydrogen release. *J. Am. Chem. Soc.* 139, 11610–11615. doi: 10.1021/jacs.7b06859

Wang, J., Qin, Y. L., Liu, X., and Zhang, X. B. (2012). *In situ* synthesis of magnetically recyclable graphene-supported Pd@Co coreshell nanoparticles as efficient catalysts for hydrolytic dehydrogenation of ammonia borane. *J. Mater. Chem.* 22, 12468–12470. doi: 10.1039/C2JM32229C

Wang, W. H., Tang, H. P., Lu, W. D., Li, Y., Bao, M., and Himeda, Y. (2017b). Mechanistic insights into the catalytic hydrolysis of ammonia borane with proton-responsive iridium complexes: an experimental and theoretical study. *ChemCatChem* 9, 3191–3196. doi: 10.1002/cctc.201700325

White, J. A., and Bird, D. M. (1994). Implementation of gradient-corrected exchange-correlation potentials in Car-Parrinello totalenergy calculations. *Phys. Rev. B* 50, 4954–4957. doi: 10.1103/PhysRevB.50.4954

Wu, Z., Xu, L., Zhang, W., Ma, Y., Yuan, Q., Jin, Y., et al. (2013). Structure sensitivity of low-temperature NO decomposition on Au surfaces. *J. Catal.* 304, 112–122. doi: 10.1016/j.jcat.2013.04.013

Xi, P., Chen, F., Xie, G., Ma, C., Liu, H., Shao, C., et al. (2012). Surfactant free RGO/Pd nanocomposites as highly active heterogeneous catalysts for the hydrolytic dehydrogenation of ammonia borane for chemical hydrogen storage. *Nanoscale* 4, 5597–5601. doi: 10.1039/c2nr31010d

Xu, Q., and Chandra, M. (2006). Catalytic activities of non-noble metals for hydrogen generation from aqueous ammonia-borane at room temperature. *J. Power Sources* 163, 364–370. doi: 10.1016/j.jpowsour.2006.09.043

Xu, Q., and Chandra, M. (2007). A portable hydrogen generation system: catalytic hydrolysis of ammonia-borane. *J. Alloy Compd.* 446, 729–732. doi: 10.1016/j.jallcom.2007.01.040

Yan, J. M., Zhang, X. B., Akita, T., Haruta, M., and Xu, Q. (2010a). One-step seeding growth of magnetically recyclable Au@Co core-shell nanoparticles: highly efficient catalyst for hydrolytic dehydrogenation of ammonia borane. *J. Am. Chem. Soc.* 132, 5326–5327. doi: 10.1021/ja910513h

Yan, J. M., Zhang, X. B., Han, S., Shioyama, H., and Xu, Q. (2008). Iron-nanoparticle-catalyzed hydrolytic dehydrogenation of ammonia borane for chemical hydrogen storage. *Angew. Chem. Int. Ed.* 47, 2287–2289. doi: 10.1002/anie.200704943

Yan, J. M., Zhang, X. B., Han, S., Shioyama, H., and Xu, Q. (2009). Synthesis of longtime water/air-stable Ni nanoparticles and their high catalytic activity for hydrolysis of ammoniaeborane for hydrogen generation. *Inorg. Chem.* 48, 7389–7393. doi: 10.1021/ic900921m

Yan, J. M., Zhang, X. B., Shioyama, H., and Xu, Q. (2010b). Room temperature hydrolytic dehydrogenation of ammonia borane catalyzed by Co nanoparticles. *J. Power Sources* 195, 1091–1094. doi: 10.1016/j.jpowsour.2009.08.067

Yao, C. F., Zhuang, L., Cao, Y. L., Ai, X. P., and Yang, H. X. (2008). Hydrogen release from hydrolysis of borazane on Pt-and Ni-based alloy catalysts. *Int. J. Hydrogen Energy* 3, 2462–2467. doi: 10.1016/j.ijhydene.2008.02.028

Zahmakiran, M., Durap, F., and Özkar, S. (2010). Zeolite confined copper (0) nanoclusters as cost-effective and reusable catalyst in hydrogen generation from the hydrolysis of ammonia-borane. *Int. J. Hydrogen Energy* 35, 187–197. doi: 10.1016/j.ijhydene.2009.10.055

Zahmakiran, M., and Özkar, S. (2009). Zeolite framework stabilized rhodium (0) nanoclusters catalyst for the hydrolysis of ammonia-borane in air: outstanding catalytic activity, reusability and lifetime. *Appl. Catal. B-Environ.* 89, 104–110. doi: 10.1016/j.apcatb.2008.12.004

Zhang, J., Li, H., Zhang, H., Zhu, Y., and Mi, G. (2016). Porously hierarchical Cu@Ni cubic-cage microstructure: Very active and durable catalyst for hydrolytically liberating H_2 gas from ammonia borane. *Renew. Energy* 99, 1038–1045. doi: 10.1016/j.renene.2016.07.066

Zhou, Q., Yang, H., and Xu, C. (2016). Nanoporous Ru as highly efficient catalyst for hydrolysis of ammonia borane. *Int. J. Hydrogen Energy* 41, 12714–12721. doi: 10.1016/j.ijhydene.2016.05.128

Zhou, T., Wang, G., Cui, H., Yuan, H., Kuang, A., Tian, C. L., et al. (2016). A novel dehydrogenation style of NH_3BH_3 by catalyst of transition metal clusters. *Int. J. Hydrogen Energy* 41, 11746–11760. doi: 10.1016/j.ijhydene.2015.12.201

Zins, E. L., Silvi, B., and Alikhani, M. E. (2015). Activation of C-H and B-H bonds through agostic bonding: an ELF/QTAIM insight. *Phys. Chem. Chem. Phys.* 17, 9258–9281. doi: 10.1039/C4CP05728G

Conflict of Interest: The authors declare that the research was conducted in the absence of any commercial or financial relationships that could be construed as a potential conflict of interest.

frontiers in Chemistry

ORIGINAL RESEARCH
published: 23 September 2020
doi: 10.3389/fchem.2020.585753

Pure Zirconium: Type II Nodal Line and Nodal Surface States

Li Zhang[1]* *and Kai Wang*[2,3]*

[1] Changchun Institute of Technology, Changchun, China, [2] Engineering Research Center (ERC), Harbin Medical University, Harbin, China, [3] Nanoscience and Technology Center, The Fourth Medical College of Harbin Medical University, Harbin, China

Type II nodal line states have novel properties, such as direction-reliant chiral anomalies and high anisotropic negative magneto-resistance. These type II nodal line states have been widely investigated. Compared to nodal line materials, there are far fewer proposed nodal surface materials, and furthermore, a very recent challenge is to find a realistic material that co-exhibits both nodal line and nodal surface states. In this manuscript, we present the study of the electronic and topological states of pure zirconium within the density functional theory. We found that pure Zr is an interesting material that rarely exhibits both the type II nodal line state (in $k_z = 0$ plane) and nodal surface state (in $k_z = \pi$ plane). The nontrivial topological states are explained based on the orbital-resolved band structures. Our study shows that pure Zr can serve as a new platform to investigate the interplay between the nodal line state and the nodal surface state.

Keywords: pure Zr, nodal line state, nodal surface state, electronics structures, first-principle prediction

OPEN ACCESS

Edited by:
Zhenxiang Cheng,
University of Wollongong, Australia

Reviewed by:
Yang Li,
Kunming University of Science and Technology, China
Yong Li,
Hangzhou Dianzi University, China

***Correspondence:**
Li Zhang
dbcy9999@163.com
Kai Wang
wangkai@hrbmu.edu.cn

Specialty section:
This article was submitted to Theoretical and Computational Chemistry, a section of the journal Frontiers in Chemistry

Received: *21 July 2020*
Accepted: *17 August 2020*
Published: *23 September 2020*

Citation:
Zhang L and Wang K (2020) Pure Zirconium: Type II Nodal Line and Nodal Surface States. Front. Chem. 8:585753. doi: 10.3389/fchem.2020.585753

INTRODUCTION

Topological semimetals and topological metals (Fang et al., 2016; Yan and Felser, 2017; Schoop et al., 2018; Zhou et al., 2018; Gao et al., 2019; Hu et al., 2019; Klemenz et al., 2019; Pham et al., 2019; Xie et al., 2019; Yi et al., 2019) have been widely investigated because they can be regarded as good candidates for use in the areas of spintronics and quantum computers. Weyl and Dirac materials (Ouyang et al., 2016; Zhong et al., 2016; Zhou et al., 2016; Liu et al., 2017; Fu et al., 2018; Meng et al., 2019, 2020a; Zhang et al., 2020), which host 2-fold and fourfold degenerate band-crossing points, have been explored in real materials and their exotic properties have been confirmed in experiments. Moving forward, a series of three-dimension materials, with 1D and 2D band crossing points, have been predicted to be nodal line semimetals/metals (Phillips and Aji, 2014; Gan et al., 2017; Jin et al., 2017, 2019, 2020; Lu et al., 2017; Yang et al., 2017; Chen et al., 2018; Gao et al., 2018; Liu et al., 2018) and nodal surface semimetals/metals (Wu et al., 2018; Zhang et al., 2018; Wang et al., 2020), respectively.

Moreover, topological semimetals/metals can also be classified by the tilting degree of the fermion cone. Hence, Weyl materials can be roughly divided into two main categories, namely, type I Weyl semimetals/metals (Osterhoudt et al., 2019) where the two bands have opposite velocities and type II Weyl materials (Soluyanov et al., 2015; Ma et al., 2019) where the two bands have the same velocity. Type II Weyl materials are expected to exhibit many interesting features (Koepernik et al., 2016; Yu et al., 2016; Sharma et al., 2017), such as signals in magneto-oscillations, anisotropic chiral anomalies, and an unusual magneto-response.

Besides the two types of Weyl materials, a third type exists, named hybrid Weyl materials (Alisultanov, 2018), in which one Weyl point is type I while the other one is type II. Similar to Weyl materials, nodal line materials are composed of numerous band crossing points and they can

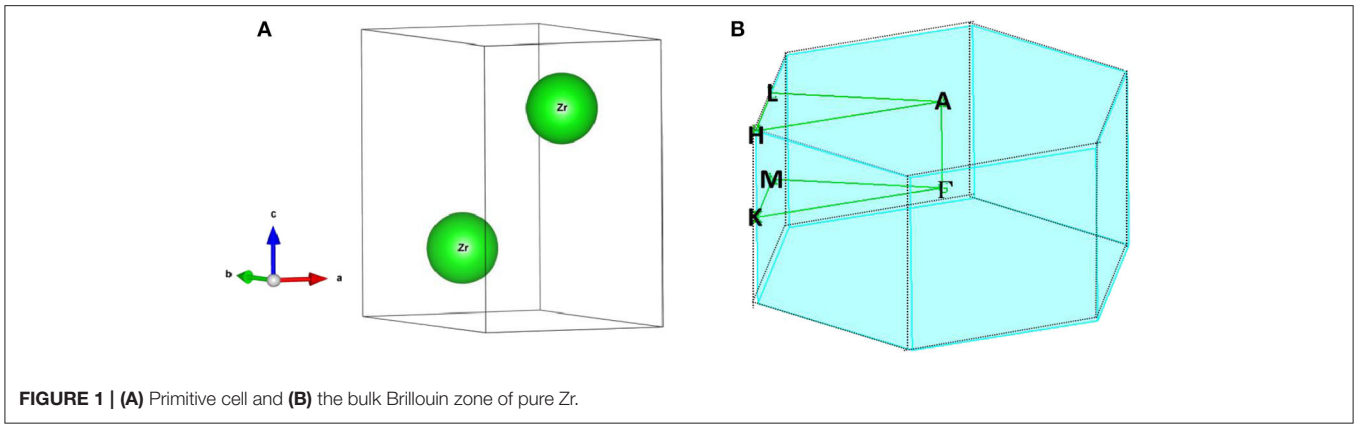

FIGURE 1 | (A) Primitive cell and **(B)** the bulk Brillouin zone of pure Zr.

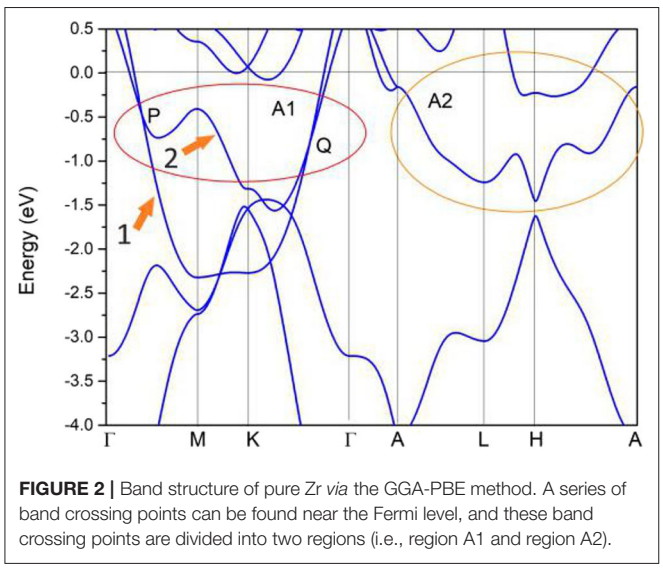

FIGURE 2 | Band structure of pure Zr *via* the GGA-PBE method. A series of band crossing points can be found near the Fermi level, and these band crossing points are divided into two regions (i.e., region A1 and region A2).

also be classified as type I, type II, and hybrid types on the basis of the band dispersion around the band crossing points.

Nodal surface materials have been proposed in some 3D materials with different families, such as the Ti_3Al family (Zhang et al., 2018), $BaVS_3$ family (Liang et al., 2016), and $HfIr_3B_4$ (Wang et al., 2020). The predicted nodal surface materials are far fewer, compared to nodal line and nodal point materials. What is more, up to now, there has been no experimental verification of nodal surface materials. Noted that the nodal surface properties can be predicted among magnetic materials due to the bands for each spin channel can be effectively seen as a spinless system with a chosen spin polarization axis. Therefore, nodal surface materials can be seen as good candidates for using in spintronic.

In this manuscript, we aim to present a first-principle study of the electronic structures and the topological signatures of a new metal (i.e., pure Zr) co-featuring the type II nodal line state and the nodal surface state. Importantly, $P6_3/mmc$ Zr is a realistic material and its experimental lattice constants are a = b = 3.232 Å; c = 5.147 Å, respectively (Wyckoff, 1963). Our results provide a realistic material platform for exploring the fundamental physics of type II nodal line and nodal surface states, and their hybridization.

COMPUTATIONAL DETAILS

We performed this study by the following main steps: (i) We investigated the most stable configuration by volume optimization and calculation of lattice parameters for $P6_3/mmc$ Zr, (ii) We computed band structures, including the 2D band structure along Γ-M-K-Γ-A-L-H-A high-symmetry points and the orbital-resolved band structures. These two investigations were completed with the Vienna ab initio Simulation Package (Sun et al., 2003). Volume optimizations and lattice parameter estimations were carried out with the generalized gradient approximation (GGA) (Perdew et al., 1996) of the Perdew–Burke–Ernzerhof (PBE) functional (Perdew et al., 1998). The cutoff energy was set as 600 eV. The Brillouin zone was sampled by a Monkhorst–Pack *k*-mesh with a size of 11 × 11 × 6. The self-consistent field convergence for the total energy and the force variation were set as 1×10^{-6} eV and 0.00001 eV·Å^{-1}, respectively.

Experimentally, Zr is a realistic material and it naturally shares a hexagonal phase, with 194 space group numbers, a $P6_3/mmc$ space group, and a series of ICSDs (such as 653524, 653525, 653528, 653529)[1]. The crystal structure of Zr was fully relaxed before the band-structure calculation. The crystal model as well as the atomic positions were determined and are shown in **Figure 1A**. From this, one can see that this crystal model contains two Zr atoms; one located at the (0.6666, 0.3333, 0.75) position, and the other located at the (0.3333, 0.6666, 0.25) position. The achieved optimized lattice constants are a = b = 3.234 Å; c = 5.161 Å, respectively, which are in good agreement with the experimental ones (Wyckoff, 1963). The calculated electronic density of states of Zr is shown in Figure S1, the metallic properties of Zr can be observed due to a large peak appears around the Fermi level.

[1] Available online at: https://materialsproject.org/materials/mp-131/

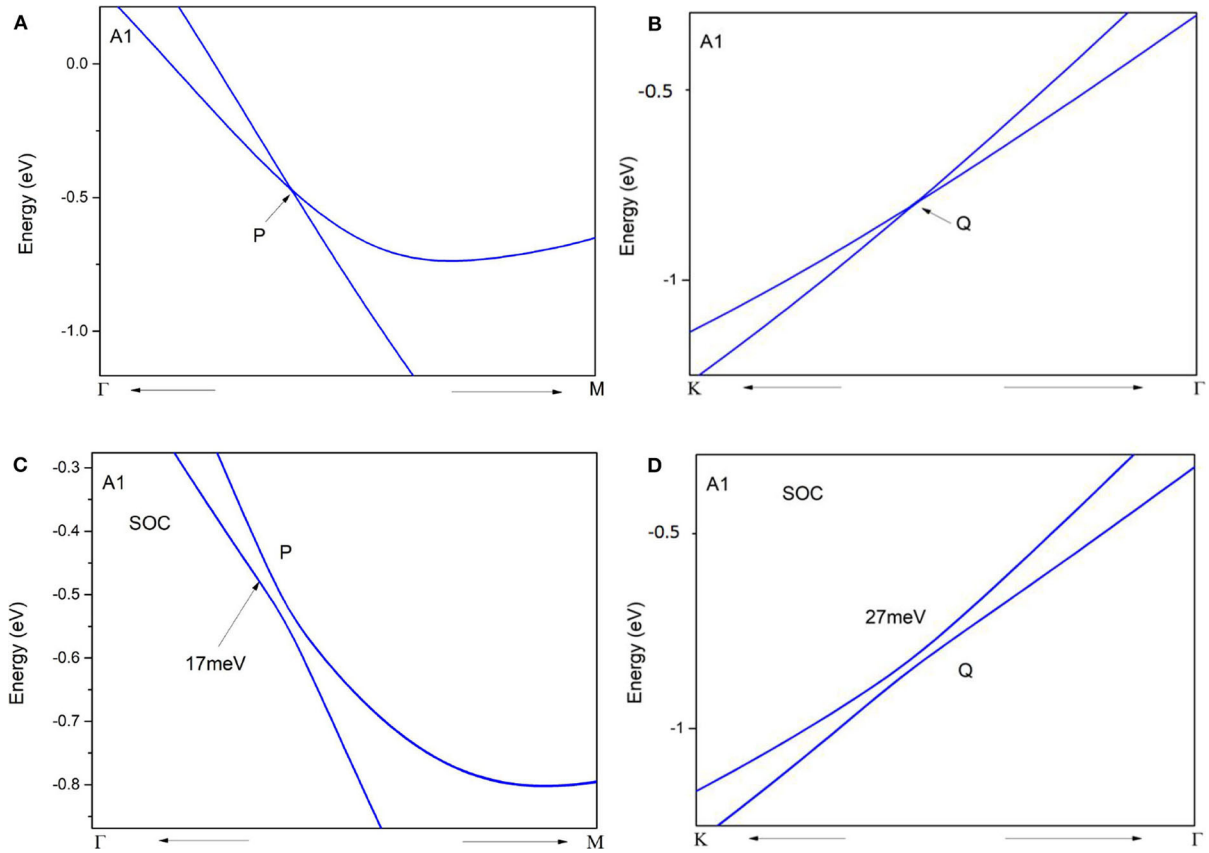

FIGURE 3 | Enlarged band structures of pure Zr *via* the GGA-PBE method along Γ-M **(A,C)** and M-K **(B,D)** paths, respectively. The band structures calculated in **(A–D)** do not have spin–orbit coupling (have spin–orbit coupling).

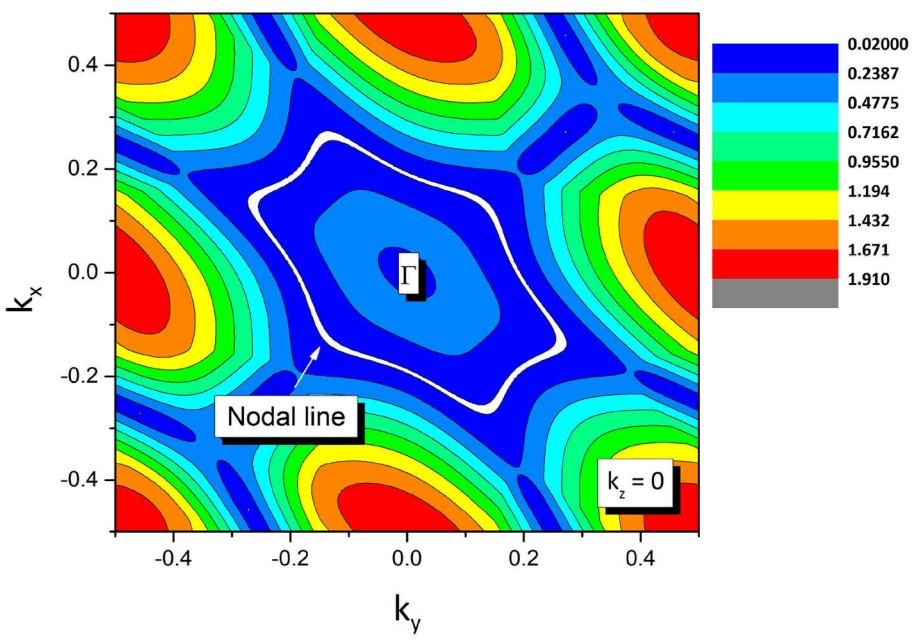

FIGURE 4 | The shape of the nodal line at the $k_z = 0$ plane. The Γ-centered nodal line is marked as a white line.

RESULTS AND DISCUSSION

We first consider the electronic band structure of pure Zr in the absence of spin-orbit coupling. The GGA-PBE result for the band structure along Γ-M-K-Γ-A-L-H-A high-symmetry points (see **Figure 1B**) is exhibited in **Figure 2**. From this figure, one can see the metallic behavior of this material with some obvious band crossing points. These band crossing points are formed by the overlapping between band 1 (labeled as 1) and band 2 (labeled as 2). These two bands belong to the irreducible representations A_1 and B_2 of the C_{2v} symmetry. Furthermore, these band crossing points are mainly located at two regions, named as A1 and A2, respectively. In **Figure S2**, the band structure of Zr metal under experimental lattice constants is also computed via GGA method and one can see that these band-crossing points are still retained.

In the A1 region, two band crossing points (i.e., P and Q) can be found along the Γ-M and M-K paths, respectively. All of these band crossing points are located quite close to the Fermi level. Because the pure Zr system enjoys spatial inversion and time reversal symmetries, the P and Q band crossing points belong to a nodal line instead of isolated points (Jin et al., 2019). Moreover, the Γ-M and M-K paths are situated in the mirror-invariant plane $k_z = 0$, which can protect a nodal line.

The enlarged band structures (in the absence of spin-orbital coupling) around P and Q band crossing points are given in

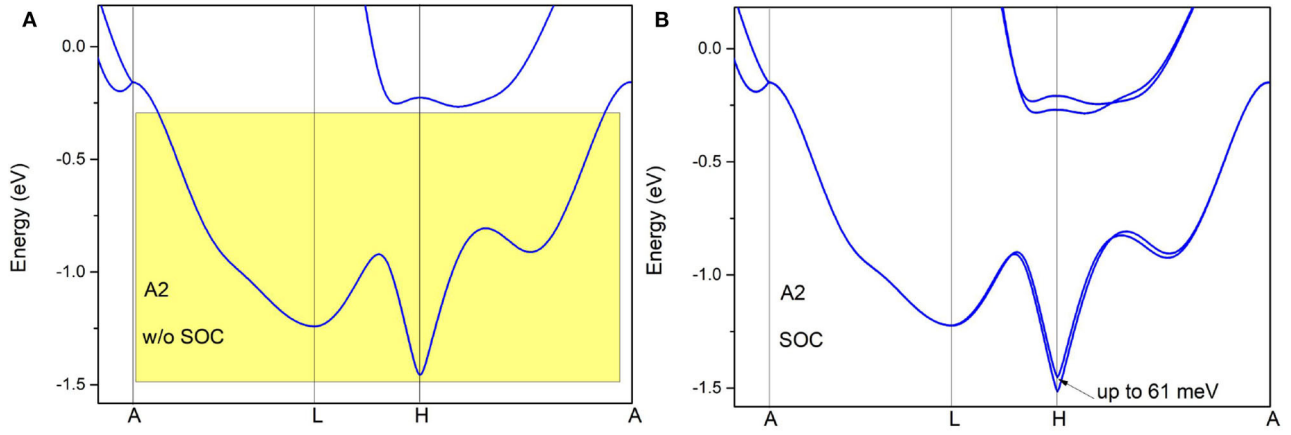

FIGURE 5 | Band structures of pure Zr *via* the GGA-PBE method along A-L-H-A paths. The band structures calculated in **(A,B)** are without spin–orbit coupling (with spin–orbit coupling).

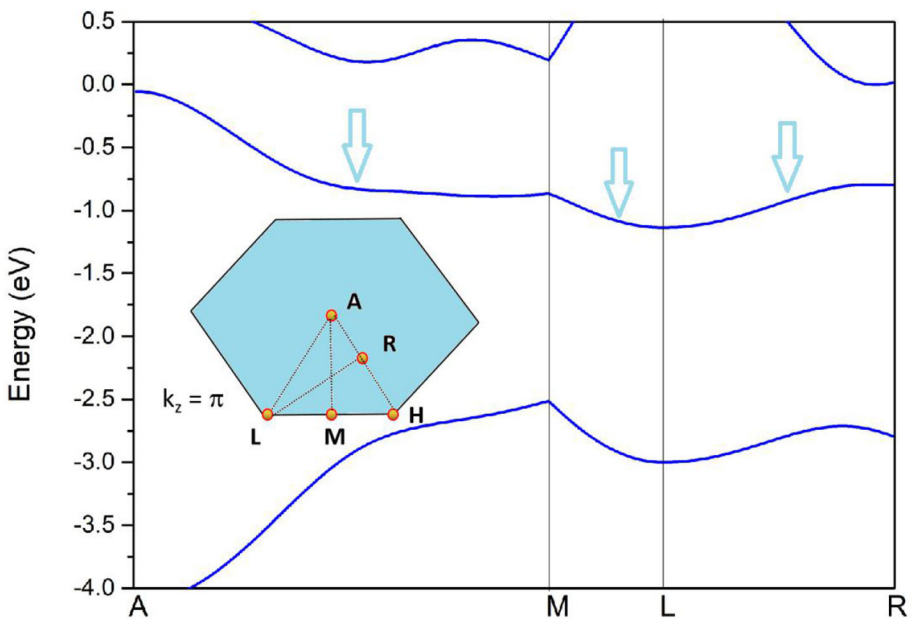

FIGURE 6 | Band structures of pure Zr *via* the GGA-PBE method along A-M-L-R paths. The insert figure is selected k-paths at the $k_z = \pi$ plane.

Figures 3A,B, respectively. Around these band crossing points, the band structures host a large linear energy region (see **Figures 3A,B**). Based on the slopes of the involved bands in crystal momentum space around the band crossing points P and Q, one can see that they belong to type II. To determine whether P and Q band crossing points are isolated nodal points or belong to a nodal line, the shape of the nodal line at the $k_z = 0$ plane is exhibited in **Figure 4**. From this figure, a Γ-centered nodal line (highlighted by the white line) can be obviously observed at the $k_z = 0$ plane.

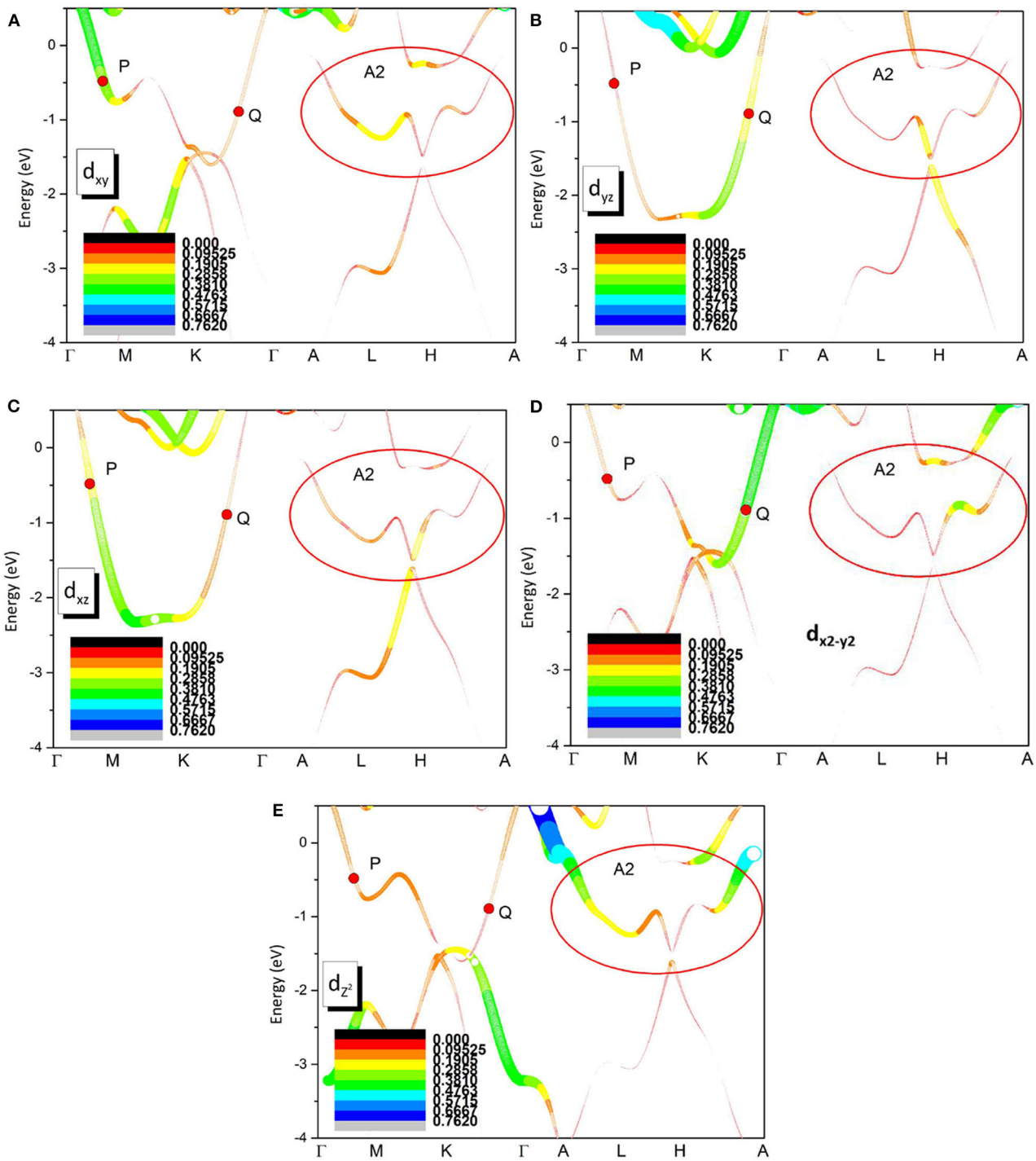

FIGURE 7 | Orbital resolved band structures of pure Zr *via* the GGA-PBE method along A-M-L-R paths. **(A–E)** are for Zr-d_{xy}, Zr-d_{yz}, Zr-d_{xz}, Zr-, Zr- orbitals, respectively.

One should note that the nodal line state is protected by two independent mechanisms for Zr system: one is the spatial inversion and the time reversal symmetries; the other one is mirror symmetry M_z, because the two crossing bands have opposite mirror eigenvalues. Therefore, the nodal line state in the Zr system is robust because Zr hosts two kinds of symmetry-protected mechanisms. That is, if we break only one kind of symmetry protection, the nodal line state will be retained. The same symmetry protection mechanism has also been reported in previous work, such as TiB_2 with the type I nodal line state (Zhang et al., 2017).

The SOC effect was also taken into consideration in the Zr system in region A1, and the calculated band structures around P and Q band crossing points are given in **Figures 3C,D**, respectively. From these figures, one can see that the SOC-induced gaps around P and Q are ∼17 and ∼27 meV, respectively. We noted that these opened gaps around the band crossing points are indeed small and these values of Zr are smaller than the values of some previously proposed nodal line materials (Meng et al., 2020b), such as Cu_3NPd (60–100 meV), CaAgBi (80–140 meV), $BaSn_2$ (60–160 meV).

The band structure of pure Zr along A-L-H-A paths is given without SOC in **Figure 5A**. In region A2, there are two bands linearly crossing at the A point, and they then become degenerate in plane $k_z = \pi$ forming a nodal surface. The nodal surface state is essential because it can be indicated by symmetry (i.e., the non-symmorphic S_{2z} and the time reversal symmetries T). Consider the twofold screw rotation S_{2z} in pure Zr, S_{2z} *(x,y,z)→(-x,-y,z+1/2)*. In the $k_z = \pi$ plane, each k point is invariant under $S_{2z}T$. Because $(S_{2z}T)^2 = T_{001} =$ on plane $k_z = \pi$, the bands on this plane have a Kramer-like degeneracy. A nodal surface can be also understood as a result of Kramer degeneracy.

To further confirm the nodal surface state in the $k_z = \pi$ plane, the band structure along the A-M-L-R paths (see the insert figure in **Figure 6**) is given in **Figure 6**. From it, one can see that the two bands are also degenerated with each other in this plane, which results in a nodal surface state in plane $k_z = \pi$. The effect of spin–orbit coupling (SOC) on the electronic structure is examined and the results of band structure along A-L-H-A (with SOC) are given in **Figure 5B**. The values of the SOC-induced gaps along A-L-H-A directions are up to 61 meV. The gaps in Zr are smaller than those in some topological materials (Meng et al., 2020b), such as Cu_3NPd (60–100 meV), and $BaSn_2$ (60–160 meV).

Finally, the orbital-resolved band structures of Zr-d_{xy}, Zr-d_{yz}, Zr-d_{xz}, Zr-$d_{x^2-y^2}$, Zr-d_{z^2} orbitals are given in **Figure 7**. One can see that band 1 (see **Figure 2**) is mainly coming from the hybridization between the Zr-d_{yz} and Zr-d_{xz} orbitals. However, band 2 forms the hybridization among Zr-d_{xy}, Zr-$d_{x^2-y^2}$, Zr-d_{z^2} orbitals. In the A1 region, as shown in **Figure 7**, the band crossing point P is mainly coming from Zr-d_{xz} and Zr-d_{xy} orbitals, however, the band crossing point Q is mainly arising from the Zr-d_{yz} and Zr-$d_{x^2-y^2}$ orbitals. In region A2, the band crossing points of the surface states ($k_z = \pi$ plane) are dominated by the Zr-d_{z^2} orbital, however, the contribution of other orbitals of Zr atom cannot be ignored.

CONCLUSIONS

In conclusion, based on symmetry analysis and first-principle calculations, we have shown a realistic material, pure Zr, which features a type II nodal line state at the $k_z = 0$ plane and a nodal surface state at the $k_z = \pi$ plane when the SOC effect is ignored. The nodal line state at the $k_z = 0$ plane is protected by the spatial inversion, time reversal, and horizontal mirror symmetries. The nodal surface state at the $k_z = \pi$ plane is protected by the screw rotation and time reversal symmetries. The effect of SOC on the topological nodal line and nodal surface states was tested and the SOC-induced band gaps for both A1 and A2 regions were found to be smaller than 61 meV.

The orbital-resolved band structures of Zr-d_{xy}, Zr-d_{yz}, Zr-d_{xz}, Zr-$d_{x^2-y^2}$, Zr-d_{z^2} orbitals for the pure Zr system were exhibited. In region A1, the point P is mainly coming from Zr-d_{xz} and Zr-d_{xy} orbitals, however, the point Q is mainly arising from the Zr-d_{yz} and Zr-$d_{x^2-y^2}$ orbitals. In region A2, the surface states ($k_z = \pi$ plane) are dominated by the Zr-d_{z^2} orbital, however, the contribution of other orbitals of the Zr atom cannot be ignored.

DATA AVAILABILITY STATEMENT

All datasets generated for this study are included in the article/**Supplementary Material**.

AUTHOR CONTRIBUTIONS

LZ: conceptualization, methodology, software, formal analysis, data curation, and writing. KW: investigation, funding, and project administration. All authors contributed to the article and approved the submitted version.

FUNDING

This work was supported by National Natural Science Foundation of China (grant number: 81601541), National Natural Science Foundation of Heilongjiang Province (grant number: LH2020H067), Topic Foundation of Changchun Institute of Technology (grant number: 320200040), and Young People Foundation of Changchun Institute of Technology (grant number: 320200033).

SUPPLEMENTARY MATERIAL

The Supplementary Material for this article can be found online at: https://www.frontiersin.org/articles/10.3389/fchem.2020.585753/full#supplementary-material

REFERENCES

Alisultanov, Z. Z. (2018). Hybrid Weyl semimetal under crossed electric and magnetic fields: field tuning of spectrum type. *Phys. Lett. A* 382, 3211–3215. doi: 10.1016/j.physleta.2018.08.028

Chen, H., Zhang, S., Jiang, W., Zhang, C., Guo, H., Liu, Z., et al. (2018). Prediction of two-dimensional nodal-line semimetals in a carbon nitride covalent network. *J. Mater. Chem.* 6, 11252–11259. doi: 10.1039/C8TA02555J

Fang, C., Lu, L., Liu, J., and Fu, L. (2016). Topological semimetals with helicoid surface states. *Nat. Phys.* 12, 936–941. doi: 10.1038/nphys3782

Fu, C., Guin, S. N., Watzman, S. J., Li, G., Liu, E., Kumar, N., et al. (2018). Large Nernst power factor over a broad temperature range in polycrystalline Weyl semimetal NbP. *Energy Environ. Sci.* 11, 2813–2820. doi: 10.1039/C8EE02077A

Gan, L., Wang, R., Jin, Y. J., Ling, D. B., Zhao, J., Xu, W. P., et al. (2017). Emergence of topological nodal loops in alkaline-earth hexaborides XB_6 (X = Ca, Sr, and Ba) under pressure. *Phys. Chem. Chem. Phys.* 19, 8210–8215. doi: 10.1039/C6CP08421D

Gao, H., Venderbos, J. W., Kim, Y., and Rappe, A. M. (2019). Topological semimetals from first-principles. *Ann. Rev. Mater. Res.* 49, 153–183. doi: 10.1146/annurev-matsci-070218-010049

Gao, Y., Xie, Y., Chen, Y., Gu, J., and Chen, Z. (2018). Spindle nodal chain in three-dimensional α' boron. *Phys. Chem. Chem. Phys.* 20, 23500–23506. doi: 10.1039/C8CP03874K

Hu, J., Xu, S., Ni, N., and Mao, Z. (2019). Electronic transport and quantum oscillation of topological semimetals. *Ann. Rev. Mater. Res.* 49, 207–252. doi: 10.1146/annurev-matsci-070218-010023

Jin, L., Zhang, X., He, T., Meng, W., Dai, X., and Liu, G. (2019). Topological nodal line state in superconducting NaAlSi compound. *J. Mater. Chem. C* 7, 10694–10699. doi: 10.1039/C9TC03464A

Jin, L., Zhang, X., He, T., Meng, W., Dai, X., and Liu, G. (2020). Electronic structure, doping effect and topological signature in realistic intermetallics $Li_{3-x}Na_xM$ (x = 3, 2, 1, 0; M = N, P, As, Sb, Bi). *Phys. Chem. Chem. Phys.* 22, 5847–5854. doi: 10.1039/C9CP06033B

Jin, Y. J., Wang, R., Zhao, J., Du, Y., Zheng, C., Gan, L., et al. (2017). The prediction of a family group of two-dimensional node-line semimetals. *Nanoscale* 9, 13112–13118. doi: 10.1039/C7NR03520A

Klemenz, S., Lei, S., and Schoop, L. M. (2019). Topological semimetals in square-net materials. *Ann. Rev. Mater. Res.* 49, 185–206. doi: 10.1146/annurev-matsci-070218-010114

Koepernik, K., Kasinathan, D., Efremov, D. V., Khim, S., Borisenko, S. V., Buchner, B., et al. (2016). $TaIrTe_4$: a ternary type-II Weyl semimetal. *Phys. Rev. B* 93:201101. doi: 10.1103/PhysRevB.93.201101

Liang, Q., Zhou, J., Yu, R., Wang, Z., and Weng, H. (2016). Node-surface and node-line fermions from nonsymmorphic lattice symmetries. *Phys. Rev. B* 93:085427. doi: 10.1103/PhysRevB.93.085427

Liu, J., Li, X., Wang, Q., Kawazoe, Y., and Jena, P. (2018). A new 3D Dirac nodal-line semi-metallic graphene monolith for lithium ion battery anode materials. *J. Mater. Chem.* 6, 13816–13824. doi: 10.1039/C8TA04428G

Liu, P., Zhou, L., Tretiak, S., and Wu, L. (2017). Two-dimensional hexagonal M3C2 (M = Zn, Cd and Hg) monolayers: novel quantum spin Hall insulators and Dirac cone materials. *J. Mater. Chem. C* 5, 9181–9187. doi: 10.1039/C7TC02739G

Lu, J., Luo, W., Li, X., Yang, S., Cao, J., Gong, X., et al. (2017). Two-dimensional node-line semimetals in a honeycomb-kagome lattice. *Chin. Phys. Lett.* 34:057302. doi: 10.1088/0256-307X/34/5/057302

Ma, J., Gu, Q., Liu, Y., Lai, J., Yu, P., Zhuo, X., et al. (2019). Nonlinear photoresponse of type-II Weyl semimetals. *Nat. Mater.* 18, 476–481. doi: 10.1038/s41563-019-0296-5

Meng, L., Li, Y., Wu, J., Zhao, L., and Zhong, J. (2020a). A type of novel Weyl semimetal candidate: layered transition metal monochalcogenides Mo_2XY (X, Y = S, Se, Te, X ≠ Y). *Nanoscale* 12, 4602–4611. doi: 10.1039/C9NR09123H

Meng, L., Wu, J., Zhong, J., and Romer, R. A. (2019). A type of robust superlattice type-I Weyl semimetal with four Weyl nodes. *Nanoscale* 11, 18358–18366. doi: 10.1039/C9NR04551A

Meng, W., Zhang, X., He, T., Jin, L., and Liu, G. (2020b). Multiple fermionic states with clear nontrivial surface signature in CsCl-type compound eras. *Comput. Mater. Sci.* 183:109815. doi: 10.1016/j.commatsci.2020.109815

Osterhoudt, G., Diebel, L. K., Gray, M., Yang, X., Stanco, J., Huang, X., et al. (2019). Colossal mid-infrared bulk photovoltaic effect in a type-I Weyl semimetal. *Nat. Mater.* 18, 471–475. doi: 10.1038/s41563-019-0297-4

Ouyang, T., Xiao, H., Tang, C., Hu, M., and Zhong, J. (2016). Anisotropic thermal transport in Weyl semimetal TaAs: a first principles calculation. *Phys. Chem. Chem. Phys.* 18, 16709–16714. doi: 10.1039/C6CP02935C

Perdew, J. P., Burke, K., and Ernzerhof, M. (1996). Generalized gradient approximation made simple. *Phys. Rev. Lett.* 77:3865. doi: 10.1103/PhysRevLett.77.3865

Perdew, J. P., Burke, K., and Ernzerhof, M. (1998). Perdew, Burke, and Ernzerhof reply. *Phys. Rev. Lett.* 80:891. doi: 10.1103/PhysRevLett.80.891

Pham, A., Klose, F., and Li, S. (2019). Robust topological nodal lines in halide carbides. *Phys. Chem. Chem. Phys.* 21, 20262–20268. doi: 10.1039/C9CP04330F

Phillips, M. R., and Aji, V. (2014). Tunable line node semimetals. *Phys. Rev. B* 90:115111. doi: 10.1103/PhysRevB.90.115111

Schoop, L. M., Pielnhofer, F., and Lotsch, B. V. (2018). Chemical principles of topological semimetals. *Chem. Mater.* 30, 3155–3176. doi: 10.1021/acs.chemmater.7b05133

Sharma, G., Goswami, P., and Tewari, S. (2017). Chiral anomaly and longitudinal magnetotransport in type-II Weyl semimetals. *Phys. Rev. B* 96:045112. doi: 10.1103/PhysRevB.96.045112

Soluyanov, A. A., Gresch, D., Wang, Z., Wu, Q., Troyer, M., Dai, X., et al. (2015). Type-II Weyl semimetals. *Nature* 527, 495–498. doi: 10.1038/nature 15768

Sun, G., Kurti, J., Rajczy, P., Kertesz, M., Hafner, J., and Kresse, G. (2003). Performance of the Vienna ab initio simulation package (VASP) in chemical applications. *J. Mol. Struct-Theochem.* 624, 37–45. doi: 10.1016/S0166-1280(02)00733-9

Wang, X., Cheng, Z., Zhang, G., Wang, B., Wang, X., and Chen, H. (2020). Rich novel zero-dimensional (0D), 1D, and 2D topological elements predicted in the P63/m type ternary boride $HfIr_3B_4$. *Nanoscale* 12:8314. doi: 10.1039/D0NR00635A

Wu, W., Liu, Y., Li, S., Zhong, C., Yu, Z., Sheng, X., et al. (2018). Nodal surface semimetals: theory and material realization. *Phys. Rev. B* 97:115125. doi: 10.1103/PhysRevB.97.115125

Wyckoff, R. W. G. (1963). *New York Hexagonal Closest Packed, Hcp, Structure Crystal Structures*. 2nd ed. (New York, NY: Interscience Publishers), 7–83.

Xie, H., Qie, Y., Imran, M., and Sun, Q. (2019). Topological semimetal porous carbon as a high-performance anode for Li-ion batteries. *J. Mater. Chem. A*, 7, 14253–14259. doi: 10.1039/C9TA03587G

Yan, B., and Felser, C. (2017). Topological materials: weyl semimetals. *Ann. Rev. Condensed Matter Phys.* 8, 337–354. doi: 10.1146/annurev-conmatphys-031016-025458

Yang, B., Zhang, X., and Zhao, M. (2017). Dirac node lines in two-dimensional Lieb lattices. *Nanoscale* 9, 8740–8746. doi: 10.1039/C7NR00411G

Yi, X., Li, W. Q., Li, Z. H., Zhou, P., Ma, Z., and Sun, L. Z. (2019). Topological dual double node-line semimetals NaAlSi(Ge) and their potential as cathode material for sodium ion batteries. *J. Mater. Chem. C* 7, 15375–15381. doi: 10.1039/C9TC04096J

Yu, Z., Yao, Y., and Yang, S. A. (2016). Predicted unusual magnetoresponse in type-II weyl semimetals. *Phys. Rev. Lett.* 117:077202. doi: 10.1103/PhysRevLett.117.077202

Zhang, M., Zhang, S., Wang, P., and Zhang, C. (2020). Emergence of a spin-valley Dirac semimetal in a strained group-VA monolayer. *Nanoscale* 12, 3950–3957. doi: 10.1039/C9NR09545D

Zhang, X., Yu, Z., Sheng, X., Yang, H. Y., and Yang, S. A. (2017). Coexistence of four-band nodal rings and triply degenerate nodal points in centrosymmetric metal diborides. *Phys. Rev. B* 95:235116. doi: 10.1103/PhysRevB.95.2 35116

Zhang, X., Yu, Z., Zhu, Z., Wu, W., Wang, S., Sheng, X., et al. (2018). Nodal loop and nodal surface states in the Ti3Al family of materials. *Phys. Rev. B* 97:235150. doi: 10.1103/PhysRevB.97.235150

Zhong, C., Chen, Y., Xie, Y., Yang, S. A., Cohen, M. L., and Zhang, S. B. (2016). Towards three-dimensional Weyl-surface semimetals in graphene networks. *Nanoscale* 8, 7232–7239. doi: 10.1039/C6NR00882H

Zhou, P., Ma, Z., and Sun, L. Z. (2018). Coexistence of open and closed type nodal line topological semimetals in two dimensional B2C. *J. Mater. Chem. C*, 6, 1206–1214. doi: 10.1039/C7TC05095J

Zhou, T., Zhang, C., Zhang, H., Xiu, F., and Yang, Z. (2016). Enhanced thermoelectric properties of the Dirac semimetal Cd_3As_2. *Inorg. Chem. Front.* 3, 1637–1643. doi: 10.1039/C6QI00383D

Conflict of Interest: The authors declare that the research was conducted in the absence of any commercial or financial relationships that could be construed as a potential conflict of interest.

frontiers in Materials

ORIGINAL RESEARCH
published: 24 September 2020
doi: 10.3389/fmats.2020.00262

Hypothetical $P6_3/mmc$-Type $CsCrCl_3$ Ferromagnet: Half-Metallic Property and Nodal Surface State

Yang Li[1,2]*

[1] Faculty of Mechanical and Electrical Engineering, Kunming University of Science and Technology, Kunming, China,
[2] Department of Physics, Chongqing University of Arts and Sciences, Chongqing, China

This work focuses on the electronic, magnetic, and half-metallic behaviors and interesting surface state of a hypothetical $CsCrCl_3$ ferromagnet with a $P6_3/mmc$ space group, investigated using the spin-polarized generalized gradient approach (GGA) and spin-polarized GGA plus Hubbard U correction within the framework of density functional theory. The calculated total magnetic moment of $P6_3/mmc$ $CsCrCl_3$ is ∼7.397 μ_B, and the main contribution to the total magnetism is from the Cr atoms. Based on the obtained spin-polarized band structures, we confirm that this hypothetical $CsCrCl_3$ ferromagnet is a half-metal with 100% spin-polarization. Without spin-orbit coupling, i.e., when the spin and orbit degrees of freedom are dependent, we found an interesting nodal surface state at the $k_z = \pi$ plane due to the $P6_3/mmc$ type lattice structure having a twofold screw axis S_{2z}. Our study provides strong evidence that a protected nodal surface state can be achieved in magnetic materials.

Keywords: DFT, half-metallic materials, band gap, nodal surface properties, electronic structure

OPEN ACCESS

Edited by:
Zhenxiang Cheng,
University of Wollongong, Australia

Reviewed by:
Biao Wang,
Southwest University, China
Guangqian Ding,
Chongqing University of Posts and Telecommunications, China
Xiaoming Zhang,
Hebei University of Technology, China

***Correspondence:**
Yang Li
liyang@cqwu.edu.cn;
liyang_physics@126.com

Specialty section:
This article was submitted to Computational Materials Science, a section of the journal Frontiers in Materials

Received: *06 June 2020*
Accepted: *17 July 2020*
Published: *24 September 2020*

Citation:
Li Y (2020) Hypothetical $P6_3/mmc$-Type $CsCrCl_3$ Ferromagnet: Half-Metallic Property and Nodal Surface State. Front. Mater. 7:262. doi: 10.3389/fmats.2020.00262

INTRODUCTION

The search for half-metallic materials (De Groot et al., 1983; Pickett and Moodera, 2001; Elfimov et al., 2002; Kusakabe et al., 2004; Zhang et al., 2018) with 100% spin-polarization (P) (Žutic et al., 2004) is a hot research topic in next-generation spintronics (Li and Yang, 2016). Half-metallic materials (Ding and Wang, 2016; Hu et al., 2017; Wang et al., 2017; Wu et al., 2017; Bhattacharyya et al., 2018; Du et al., 2019; Huang et al., 2019; Wang et al., 2019; Zhang et al., 2019) are so called owing to their unique electronic band structures in both spin channels: the bands in one spin channel exhibit a metallic property, whereas those in the other spin channel have semiconducting or insulating behaviors. Therefore, based on the formula: $P = \frac{n\uparrow(E_F)-n\downarrow(E_F)}{n\uparrow(E_F)+n\downarrow(E_F)} \times 100\%$, where ($n \uparrow (E_F)$ and $n \downarrow (E_F)$ are the spin-up density of states (DOS) and the spin-down DOS at the Fermi level (E_F), respectively, the half-metallic materials should have 100% P in theory. Notably, half-metallic materials are good spin injectors into semiconductors, with maximum efficiency in spintronics devices. Various families of materials, including Heusler alloys (Kandpal et al., 2007; Wang et al., 2015; Cui et al., 2019; Han et al., 2019; Singh and Gupta, 2019), metallic oxides (Szotek et al., 2004), perovskite compounds (Li et al., 2015), wurtzite compounds (Wu et al., 2006), nanowires (Li et al., 2017), nanoribbons (Son et al., 2006), and some two-dimensional (2D) monolayers (Gao et al., 2016; Ashton et al., 2017; Feng et al., 2018; Liu et al., 2019), have been predicted to be half-metallic materials. Half-metals can be used for pure spin generation and injection. To develop practicable spintronic devices using half-metals, the spin-flip (half-metallic gap) should be wide enough to prevent thermally agitated spin-flip transition and preserve half-metallicity.

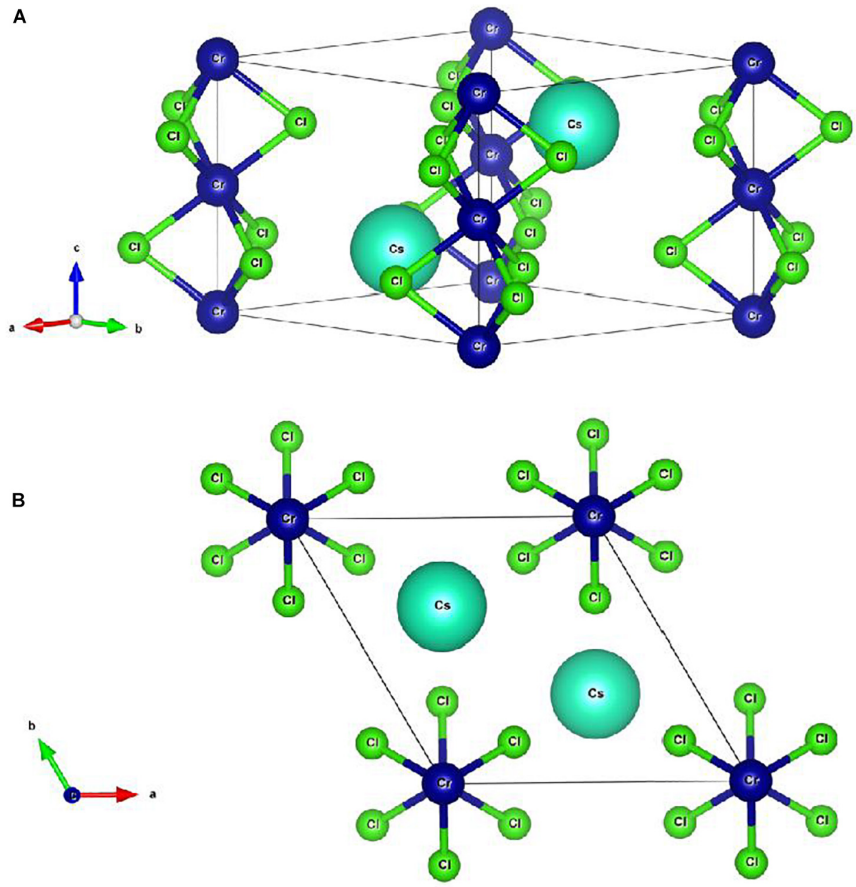

FIGURE 1 | Crystal model of $CsCrCl_3$ from different perspectives **(A,B)**.

Wu et al. (2018) proposed a new class of topological bulk materials, 3D nodal surface semimetals. They are topological materials with 2D nodal surface states, which are different from topological semimetals with a 0D nodal point (Soluyanov et al., 2015; Young and Kane, 2015; Kumar et al., 2017; Jin K. et al., 2019) and 1D nodal line (Chen et al., 2018; Liu et al., 2018; Zhou et al., 2018; He et al., 2019; Jin L. et al., 2019; Pham et al., 2019; Yan et al., 2019; Yi et al., 2019; Zou et al., 2019; Zhao et al., 2020). To date, only a few nodal surface semimetals (Wu et al., 2018) have been the subject of theoretical investigations. Nodal surface semimetals have a 2D nodal surface state composed of numerous band-crossing points. That is, each point on the surface is an intersection point between the two bands, and its dispersion is linear along the surface normal direction. Coarse-grained quasiparticles excited from a nodal surface effectively behave as 1D massless Dirac fermions along the surface normal direction and may show novel physical behaviors.

In this work, we use density functional theory (DFT) calculations to systematically investigate the electronic, magnetic, and half-metallic properties of the hypothetical $CsCrCl_3$ ferromagnet, as well as a topological nodal surface signature, with respect to its potential applications in next-generation spintronics and electronics devices. We predict that the hypothetical $CsCrCl_3$ ferromagnet is a novel material co-featuring a half-metallic property and nodal surface state at the $k_z = \pi$ plane. The formation energy of the ferromagnetic type $CsCrCl_3$ with $P6_3/mmc$ space group and 194 space

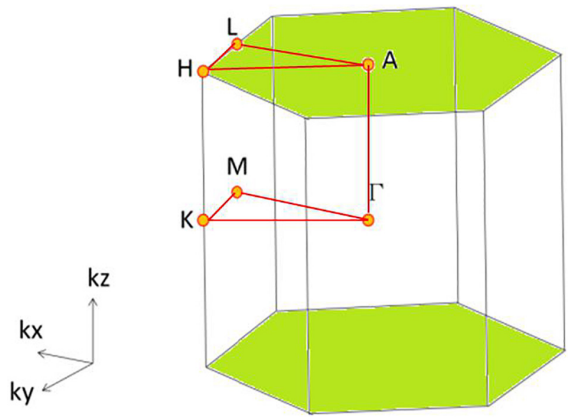

FIGURE 2 | Selected high-symmetry points in the first Brillouin zone. The $k_z = \pi$ plane is shown in green.

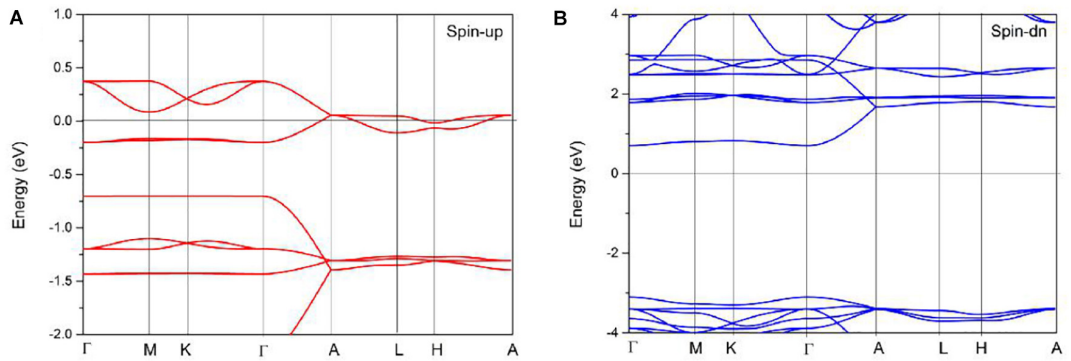

FIGURE 3 | Spin-polarized band structures of $CsCrCl_3$ system via GGA method. **(A)** for spin-up and **(B)** for spin-down.

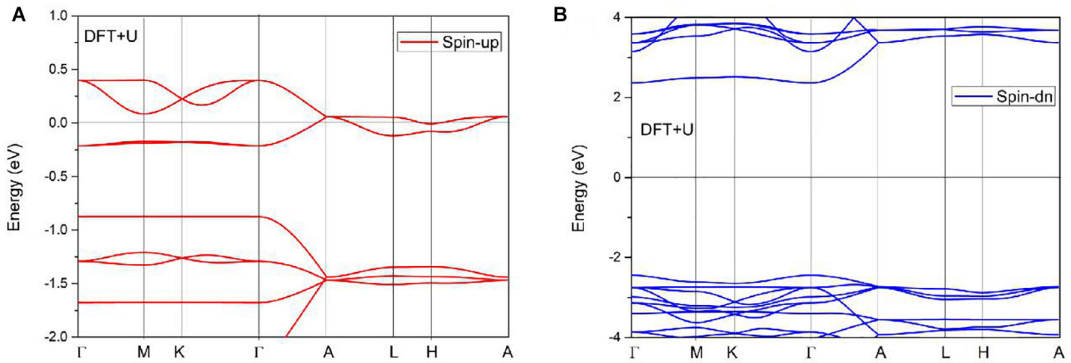

FIGURE 4 | Spin-polarized band structures of $CsCrCl_3$ system via DFT + *U* method. **(A)** for spin-up and **(B)** for spin-down.

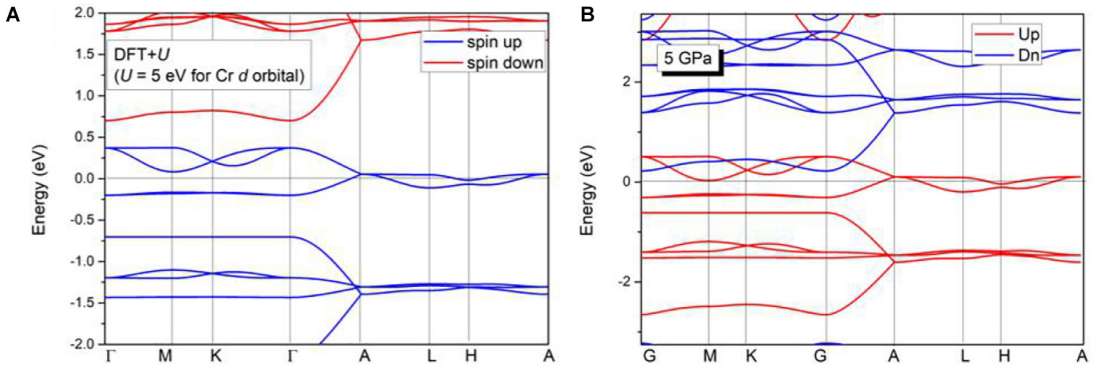

FIGURE 5 | Spin-polarized band structures of $CsCrCl_3$ system with DFT + *U* method **(A)** and with uniform strain **(B)**, respectively.

number was calculated to be -1.736 eV in https://www.materialsproject.org/materials/mp-570326/, indicating that this hexagonal ferromagnet is theoretically stable.

COMPUTATIONAL DETAILS

All atomic and electronic structure calculations were performed using the Vienna *ab initio* simulation package (Sun et al., 2003) with generalized gradient approximation (GGA) (Perdew et al., 1996) using the Perdew–Burke–Ernzerhof (Perdew et al., 1998) exchange-correlation functional. The projector augmented wave pseudo-potential was employed, with a cutoff energy of 600 eV for plane-wave expansions and a Monkhorst–Pack special $5 \times 5 \times 9$ k-point mesh. The convergence criteria for energy and force were set to 10^{-6} eV per atom and 0.0005 eV/Å, respectively. For the $CsCrCl_3$ material, we considered strong correlation effects in the transition-metal Cr atoms. The Hubbard

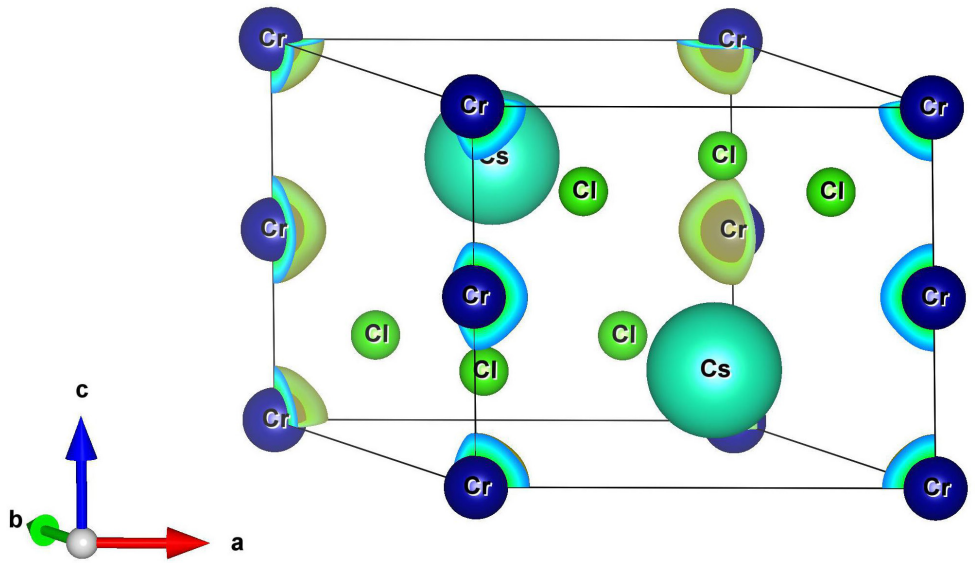

FIGURE 6 | Spin-density for the $CsCrCl_3$ ferromagnet.

U correction was also used in the rotationally invariant DFT + *U* approach to further confirm the band structure.

RESULTS AND DISCUSSION

The crystal structure of $CsCrCl_3$ from different perspectives is given in **Figures 1A,B**, respectively. $CsCrCl_3$ has a $BaVS_3$ type hexagonal structure, with a $P6_3/mmc$ space group and a space number of 194. As shown in **Figure 1**, the Cr atoms are surrounded by octahedrons of Cl atoms, which form 1D chains along the *z*-axis and share common faces. These chains are arranged in a trigonal lattice in the *x*-*y* plane, with Cs atoms inserted between the chains. We fully optimized the crystal model (**Figure 1**), and the obtained equilibrium lattice constants for the $CsCrCl_3$ ferromagnet were a = b = 7.40130 Å and c = 6.1870 Å. Our calculated results were in good agreement with those in the materials project database[1] (a = b = 7.395 Å, c = 6.173 Å) and topological materials database[2] (a = b = 7.249 Å, c = 6.228 Å).

Based on the obtained equilibrium lattice constants, we studied the electronic band structures of the $CsCrCl_3$ ferromagnet. The Γ-M-K-Γ-A-L-H-A high-symmetry points (**Figure 2**) in the first Brillouin zone were selected to describe the spin-polarized band structures of the $CsCrCl_3$ ferromagnet. The spin-up and spin-down band structures were calculated using the GGA method and the results are shown in **Figures 3A,B**, respectively. One can see that the spin-up electronic bands and the E_F overlapped with each other, reflecting the metallic property. For the spin-down channel, a clear band gap appeared, indicating the semiconducting behavior. Moreover, the values of the band gap and half-metallic gap (Guo et al., 2016; Wang et al., 2016) were calculated to be 3.78 and 0.7 eV, respectively, indicating that the half-metallic state of the $CsCrCl_3$ system is very robust. To properly account for the strong correlation effects in the transition-metal Cr atoms, a Hubbard *U* correction was adopted in the rotationally invariant DFT + *U* approach. In **Figure 4**, the spin-polarized band structures obtained via the DFT + *U* method (*U* = 3 eV for Cr-*d* orbitals) are shown. One can see that the half-metallic state for this $CsCrCl_3$ system was retained. That is, the metallic state and semiconducting state, in the spin-up and spin-down directions, respectively, could still be observed. However, the band gap and the half-metallic band gap in the spin-down channel increased to values of 4.496 and 2.375 eV, respectively.

Furthermore, we would like to point out that the half-metallic states of the $CsCrCl_3$ ferromagnet are very robust to the Hubbard *U* correction and the uniform strain. In **Figure 5**, the band structures of the $CsCrCl_3$ ferromagnet with *U* = 5 eV for Cr-*d* orbitals and with 5 GPa uniform strain, respectively, are given. One can see that the $CsCrCl_3$ ferromagnet still hosts half-metallic properties under the above-mentioned situations.

The primitive cell of the $CsCrCl_3$ ferromagnet contained eight atoms, i.e., two Cr atoms, two Cs atoms, and six Cl atoms. The total magnetic moment for this system was 7.397 μ_B, and the atomic magnetic moments of Cr atoms (~3.693 μ_B) dominated the total magnetism. To further examine the magnetism of this system, the spin-density in both spin channels was determined (**Figure 6**). The spin-density was mainly located around the Cr atoms, indicating that they have large atomic magnetic moments.

[1]https://www.materialsproject.org/materials/mp-570326/
[2]https://www.topologicalquantumchemistry.org/#/detail/36132

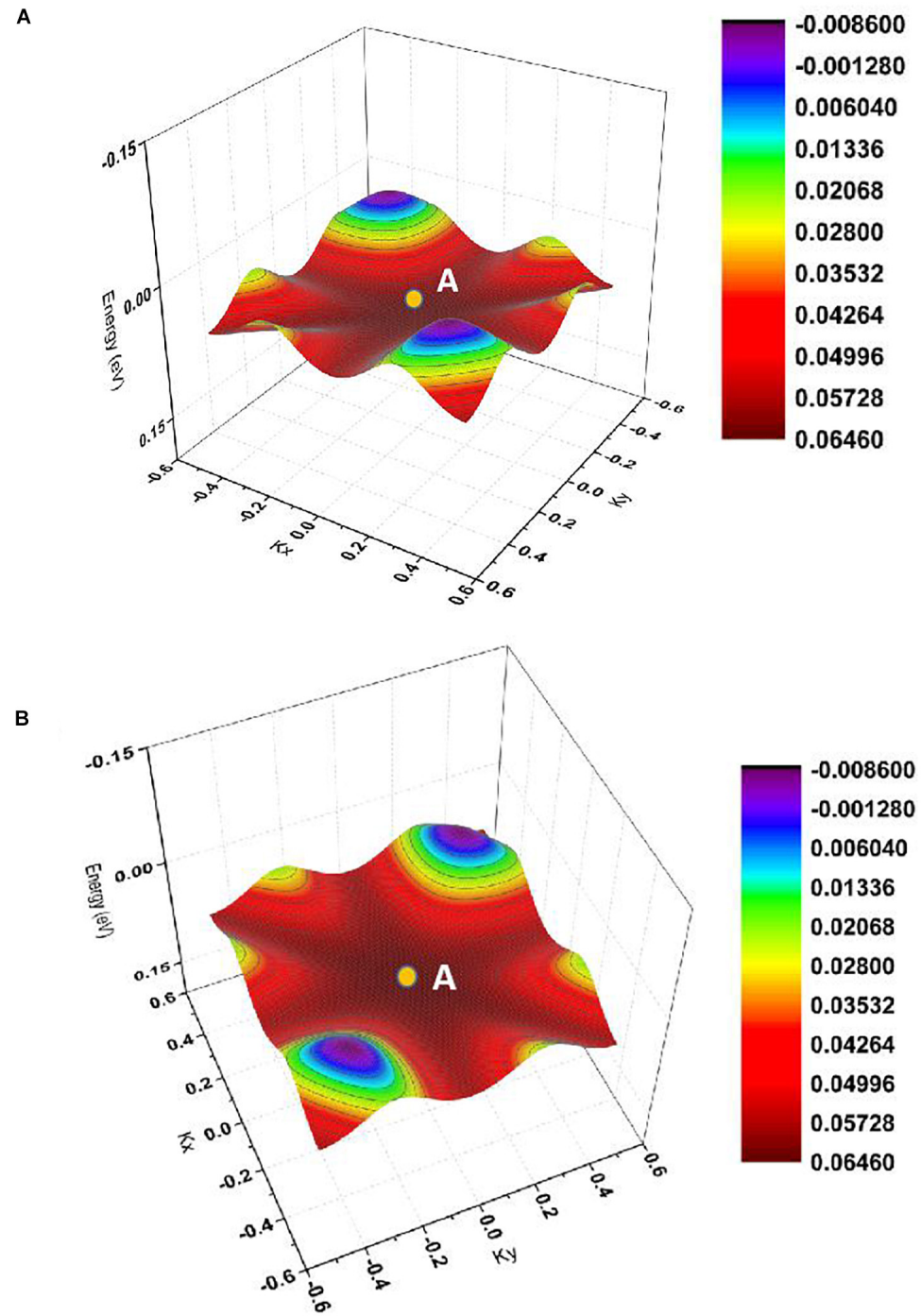

FIGURE 7 | A-point centered 3D band structures of $CsCrCl_3$ ferromagnet at $k_z = \pi$ plane in spin-up channel (without SOC effect). **(A,B)** are from different view sides.

The contributions of other atoms, including Cs and Cl atoms, to the total magnetism were almost negligible.

Note that the spin-orbit coupling (SOC) effect was not considered in this work. Without SOC, the spin and orbit degrees of freedom are independent; therefore, the spin degree and the orbit degree can be regarded as different subspaces (Wu et al., 2018). With a selected spin-polarization axis, the spin-up and spin-down directions are decoupled; therefore, the bands for each spin species can be effectively seen as for a spin-free system. Thus, the protected nodal surface state can be realized in one spin of a ferromagnet when the SOC effect is neglected. As shown in **Figure 3**, along the A-L-H-A direction, two bands (in the range

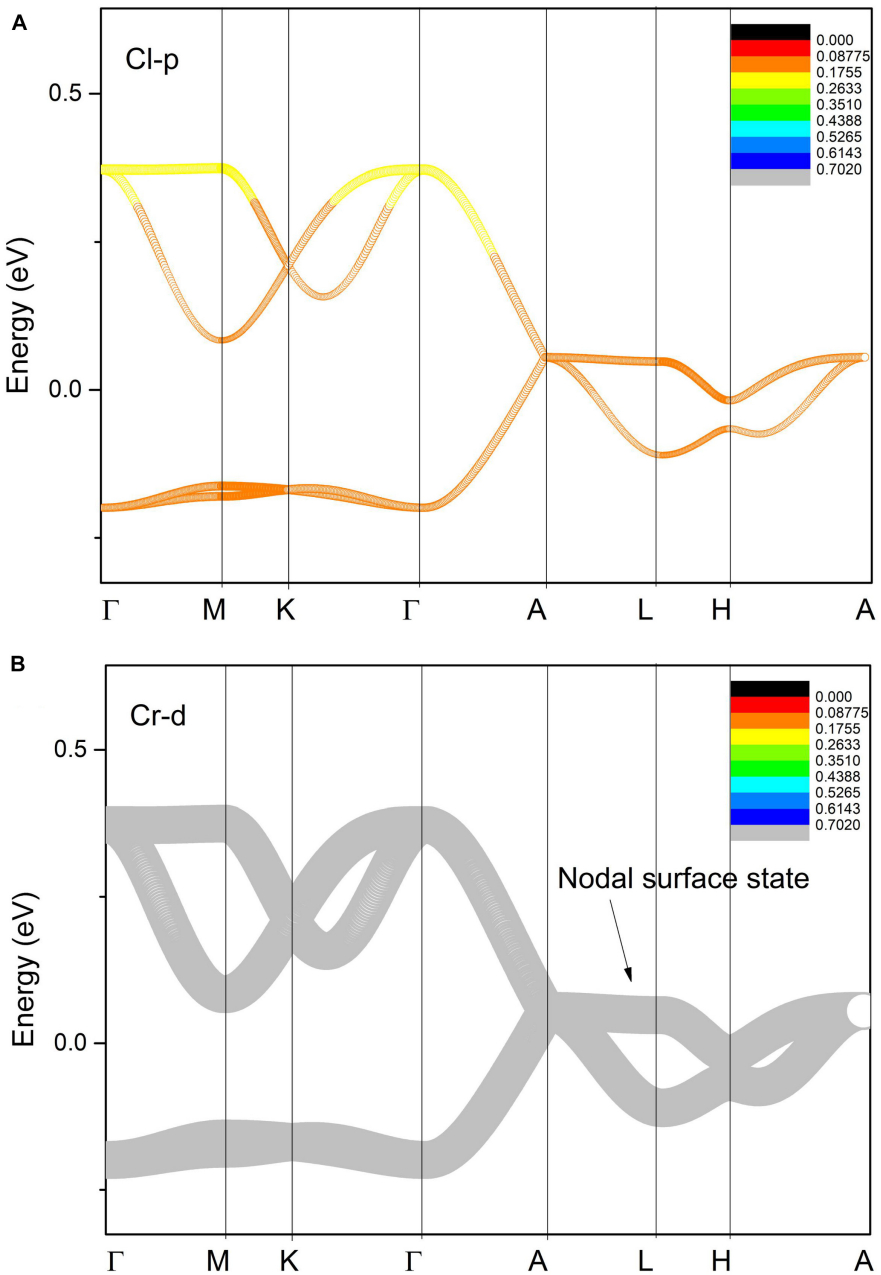

FIGURE 8 | Orbital-resolved band structures of Cl-*p* **(A)** and Cr-*d* **(B)** orbitals of $CsCrCl_3$ in the spin-up channel. The nodal surface state, formed by the crossing of two bands near the E_F, is highlighted by an arrow along the A-L-H-A direction.

of -0.1 to 0.1 eV) were totally degenerate with each other. The lattice structure of the $CsCrCl_3$ ferromagnetic system features a 2-fold screw axis S_{2z}. As discussed by Wu et al. (2018), a nodal surface state (at the $k_z = \pi$ plane) must occur in the ferromagnetic material if the crystal structure of the ferromagnetic material hosts a 2-fold screw axis S_{2z}. To further investigate whether there was a nodal surface state in this $CsCrCl_3$ system, the 3D band structure (A-point-centered) in the spin-up channel was examined from different perspectives. In **Figures 7A,B**, one can see that a nodal surface state existed in the $k_z = \pi$ plane near the E_F. Furthermore, one can see that the nodal surface state (at the $k_z = \pi$ plane and in the spin-up channel) was relatively flat in energy, that is, the energy variation was less than 0.2 eV. Finally, in **Figure 8**, the calculated orbital-resolved band structures of the Cl-*p* and Cr-*d* orbitals states are shown. The orbital-resolved band structure of the Cs-s orbitals is not shown, as it had little effect on the nodal surface state near the E_F in the spin-up channel. The main contribution to the nodal surface state was from the Cr-*d* orbits; however, the contribution of the Cl-*p* orbitals was not negligible.

CONCLUSION

In conclusion, in this study, a hypothetical $CsCrCl_3$ ferromagnetic system with a $P6_3/mmc$ space group and a space number of 197 was investigated in detail with respect to its electronic structures, magnetism, half-metallic behavior, and topological signature via DFT and DFT + U. We predict that the $CsCrCl_3$ ferromagnet is an excellent half-metal with a large band gap and a half-metallic gap. Moreover, this $CsCrCl_3$ ferromagnet has a nodal surface state (at the $k_z = \pi$ plane) in the spin-up channel when the SOC effect is not taken into consideration. The nodal surface state in the spin-up channel is due to the $P6_3/mmc$ lattice structure, which features a twofold screw axis S_{2z}. Based on the spin-density and the orbital-resolved band structure, we confirmed that the main contribution to the total magnetism and the surface state near the E_F was from the Cr-d orbitals. It is hoped that our theoretical work will inspire further research to explore the half-metallic behaviors and the nodal surface states of many other materials in the future.

DATA AVAILABILITY STATEMENT

All datasets presented in this study are included in the article/supplementary material.

AUTHOR CONTRIBUTIONS

The author confirms being the sole contributor of this work and has approved it for publication.

FUNDING

This work was supported by the first batch of post-doctoral research fund research projects in Yunnan Province (Serial No. 9), the Science and Technology Research Program of Chongqing Municipal Education Commission (Grant No. KJQN201801346), and the Chongqing University of Arts and Sciences Foundation (Grant No. Z2011Rcyj05).

REFERENCES

Ashton, M., Gluhovic, D., Sinnott, S. B., Guo, J., Stewart, D., and Hennig, R. G. (2017). Two-dimensional intrinsic half-metals with large spin gaps. *Nano Lett.* 17, 5251–5257. doi: 10.1021/acs.nanolett.7b01367

Bhattacharyya, G., Choudhuri, I., and Pathak, B. (2018). High Curie temperature and half-metallicity in an atomically thin main group-based boron phosphide system: long range ferromagnetism. *Phys. Chem. Chem. Phys.* 20, 22877–22889. doi: 10.1039/c8cp03440k

Chen, H., Zhang, S., Jiang, W., Zhang, C., Guo, H., Liu, Z., et al. (2018). Prediction of two-dimensional nodal-line semimetals in a carbon nitride covalent network. *J. Mater. Chem. A* 6, 11252–11259. doi: 10.1039/c8ta02555j

Cui, Z., Wu, B., Ruan, X., Zhou, Q., Liu, Z., Fu, X., et al. (2019). Enhancing the half-metallicity of equiatomic quaternary Heusler compound CoFeCrGe via atomic doping. *Results Phys.* 15:102533. doi: 10.1016/j.rinp.2019.102533

De Groot, R., Mueller, F. M., Van Engen, P. G., and Buschow, K. H. (1983). New class of materials: half-metallic ferromagnets. *Phys. Rev. Lett.* 50, 2024–2027. doi: 10.1103/physrevlett.50.2024

Ding, Y., and Wang, Y. (2016). Enhanced piezoelectricity and half-metallicity of fluorinated AlN nanosheets and nanoribbons: a first-principles study. *J. Mater. Chem. C* 4, 1517–1526. doi: 10.1039/c5tc03910j

Du, Y., Bu, H., Ji, C., Zhang, X., Li, C., and Fang, X. (2019). Tunable magnetic and half-metallic properties of the two-dimensional electron gas in LaAlO3/SrTiO3(111) heterostructures. *Phys. Chem. Chem. Phys.* 21, 18170–18178. doi: 10.1039/c9cp00746f

Elfimov, I. S., Yunoki, S., and Sawatzky, G. A. (2002). Possible path to a new class of ferromagnetic and half-metallic ferromagnetic materials. *Phys. Rev. Lett.* 89:216403.

Feng, Y., Wu, X., Han, J., and Gao, G. (2018). Robust half-metallicities and perfect spin transport properties in 2D transition metal dichlorides. *J. Mater. Chem. C* 6, 4087–4094. doi: 10.1039/c8tc00443a

Gao, G., Ding, G., Li, J., Yao, K., Wu, M., and Qian, M. (2016). Monolayer MXenes: promising half-metals and spin gapless semiconductors. *Nanoscale* 8, 8986–8994. doi: 10.1039/c6nr01333c

Guo, R., Liu, G., Wang, X., Rozale, H., Wang, L., Khenata, R., et al. (2016). First-principles study on quaternary Heusler compounds ZrFeVZ (Z = Al, Ga, In) with large spin-flip gap. *RSC Adv.* 6, 109394–109400. doi: 10.1039/c6ra18873g

Han, Y., Chen, Z., Kuang, M., Liu, Z., Wang, X., and Wang, X. (2019). 171 Scandium-based full Heusler compounds: a comprehensive study of competition between XA and L21 atomic ordering. *Results Phys.* 12, 435–446. doi: 10.1016/j.rinp.2018.11.079

He, T., Zhang, X., Meng, W., Jin, L., Dai, X., and Liu, G. (2019). Topological nodal lines and nodal points in the antiferromagnetic material β-Fe2PO5. *J. Mater. Chem. C* 7, 12657–12663. doi: 10.1039/c9tc04046c

Hu, R., Zhang, Z. H., and Fan, Z. Q. (2017). BN nanoflake quantum-dot arrays: structural stability, and electronic and half-metallic properties. *Phys. Chem. Chem. Phys.* 19, 20137–20146. doi: 10.1039/c7cp02391j

Huang, H. M., Cao, M., Jiang, Z., Xiong, Y., Zhang, X., Luo, S., et al. (2019). High spin polarization in formamidinium transition metal iodides: first principles prediction of novel half-metals and spin gapless semiconductors. *Phys. Chem. Chem. Phys.* 21, 16213–16222. doi: 10.1039/c9cp00958b

Jin, K., Huang, H., Wang, Z., and Liu, F. (2019). A 2D nonsymmorphic Dirac semimetal in a chemically modified group-VA monolayer with a black phosphorene structure. *Nanoscale* 11, 7256–7262. doi: 10.1039/c9nr00906j

Jin, L., Zhang, X., He, T., Meng, W., Dai, X., and Liu, G. (2019). Topological nodal line state in superconducting NaAlSi compound. *J. Mater. Chem. C* 7, 10694–10699. doi: 10.1039/c9tc03464a

Kandpal, H. C., Fecher, G. H., and Felser, C. (2007). Calculated electronic and magnetic properties of the half-metallic, transition metal based Heusler compounds. *J. Phys. D Appl. Phys.* 40, 1507–1523. doi: 10.1088/0022-3727/40/6/s01

Kumar, N., Sun, Y., Xu, N., Manna, K., Yao, M., Suss, V., et al. (2017). Extremely high magnetoresistance and conductivity in the type-II Weyl semimetals WP2 and MoP2. *Nat. Commun.* 8, 1–8.

Kusakabe, K., Geshi, M., Tsukamoto, H., and Suzuki, N. (2004). New half-metallic materials with an alkaline earth element. *J. Phys. Condens. Matter.* 16:S5639.

Li, M., Retuerto, M., Deng, Z., Stephens, P. W., Croft, M., Huang, Q., et al. (2015). Giant magnetoresistance in the half-metallic double-perovskite ferrimagnet Mn2FeReO6. *Angew. Chem.* 54, 12069–12073. doi: 10.1002/anie.201506456

Li, X., Lv, H., Dai, J., Ma, L., Zeng, X. C., Wu, X., et al. (2017). Half-metallicity in one-dimensional metal trihydride molecular nanowires. *J. Am. Chem. Soc.* 139, 6290–6293. doi: 10.1021/jacs.7b01369

Li, X., and Yang, J. (2016). First-principles design of spintronics materials. *Natl. Sci. Rev.* 3, 365–381. doi: 10.1093/nsr/nww026

Liu, J., Li, X., Wang, Q., Kawazoe, Y., and Jena, P. (2018). A new 3D Dirac nodal-line semi-metallic graphene monolith for lithium ion battery anode materials. *J. Mater. Chem.* 6, 13816–13824. doi: 10.1039/c8ta04428g

Liu, Y., Guo, S., Yu, J., and Zhong, H. (2019). Large magnetoresistance and perfect spin filter effect in Fe doped SnS2 half-metallic monolayers: a first principles study. *Phys. Lett. A* 383, 674–679. doi: 10.1016/j.physleta.2019.01.008

Perdew, J. P., Burke, K., and Ernzerhof, M. (1996). Generalized gradient approximation made simple. *Phys. Rev. Lett.* 77:3865. doi: 10.1103/physrevlett.77.3865

Perdew, J. P., Burke, K., and Ernzerhof, M. (1998). Perdew, burke, and ernzerhof reply. *Phys. Rev. Lett.* 80:891. doi: 10.1103/physrevlett.80.891

Pham, A., Klose, F., and Li, S. (2019). Robust topological nodal lines in halide carbides. *Phys. Chem. Chem. Phys.* 21, 20262–20268. doi: 10.1039/c9cp04330f

Pickett, W. E., and Moodera, J. S. (2001). Half metallic magnets. *Phys. Today* 54, 39–44. doi: 10.1063/1.1381101

Singh, S., and Gupta, D. C. (2019). Lanthanum based quaternary Heusler alloys LaCoCrX (X = Al, Ga): hunt for half-metallicity and high thermoelectric efficiency. *Results Phys.* 13:102300. doi: 10.1016/j.rinp.2019.102300

Soluyanov, A. A., Gresch, D., Wang, Z., Wu, Q., Troyer, M., Dai, X., et al. (2015). Type-II Weyl semimetals. *Nature* 527, 495–498.

Son, Y., Cohen, M. L., and Louie, S. G. (2006). Half-metallic graphene nanoribbons. *Nature* 444, 347–349. doi: 10.1038/nature05180

Sun, G., Kurti, J., Rajczy, P., Kertesz, M., Hafner, J., and Kresse, G. (2003). Performance of the Vienna ab initio simulation package (VASP) in chemical applications. *J. Mol. Struct. Theochem.* 624, 37–45. doi: 10.1016/s0166-1280(02)00733-9

Szotek, Z., Temmerman, W. M., Svane, A., Petit, L., Stocks, G. M., and Winter, H. (2004). Half-metallic transition metal oxides. *J. Magn. Magn. Mater.* 272-276, 1816–1817. doi: 10.1016/j.jmmm.2003.12.818

Wang, X., Cheng, Z., Liu, G., Dai, X., Khenata, R., Wang, L., et al. (2017). Rare earth-based quaternary Heusler compounds MCoVZ (M = Lu, Y; Z = Si, Ge) with tunable band characteristics for potential spintronic applications. *IUCrJ* 4, 758–768. doi: 10.1107/s2052252517013264

Wang, X., Cheng, Z., Wang, J., Wang, L., Yu, Z., Fang, C., et al. (2016). Origin of the half-metallic band-gap in newly designed quaternary Heusler compounds ZrVTiZ (Z = Al, Ga). *RSC Adv.* 6, 57041–57047. doi: 10.1039/c6ra08600d

Wang, X., Dai, X. F., Wang, L., Liu, X., Wang, W., Wu, G. H., et al. (2015). Electronic structures and magnetism of Rh3Z (Z = Al, Ga, In, Si, Ge, Sn, Pb, Sb) with DO3 structures. *J. Magn. Magn. Mater.* 378, 16–23. doi: 10.1016/j.jmmm.2014.10.161

Wang, X., Ding, G., Cheng, Z., Yuan, H., Wang, X., Yang, T., et al. (2019). R3c-type LnNiO3 (Ln = La, Ce, Nd, Pm, Gd, Tb, Dy, Ho, Er, Lu) half-metals with multiple Dirac cones: a potential class of advanced spintronic materials. *IUCrJ* 6, 990–995. doi: 10.1107/s2052252519012570

Wu, R. Q., Peng, G., Liu, L., and Feng, Y. P. (2006). Wurtzite NiO: a potential half-metal for wide gap semiconductors. *Appl. Phys. Lett.* 89:082504. doi: 10.1063/1.2335970

Wu, W., Liu, Y., Li, S., Zhong, C., Yu, Z., Sheng, X., et al. (2018). Nodal surface semimetals: theory and material realization. *Phys. Rev. B* 97:115125.

Wu, X., Han, J., Feng, Y., Li, G. Q., Wang, C., Ding, G., et al. (2017). Half-metals and half-semiconductors in a transition metal doped SnSe2 monolayer: a first-principles study. *RSC Adv.* 7, 44499–44504. doi: 10.1039/c7ra07648g

Yan, L., Liu, P., Bo, T., Zhang, J., Tang, M., Xiao, Y., et al. (2019). Emergence of superconductivity in a Dirac nodal-line Cu2Si monolayer: ab initio calculations. *J. Mater. Chem. C* 7, 10926–10932. doi: 10.1039/c9tc03740c

Yi, X., Li, W. Q., Li, Z. H., Zhou, P., Ma, Z., and Sun, L. Z. (2019). Topological dual double node-line semimetals NaAlSi(Ge) and their potential as cathode material for sodium ion batteries. *J. Mater. Chem. C* 7, 15375–15381. doi: 10.1039/c9tc04096j

Young, S. M., and Kane, C. L. (2015). Dirac semimetals in two dimensions. *Phys. Rev. Lett.* 115, 126803–126803.

Zhang, M., Zhang, C., Wang, P., and Li, S. (2018). Prediction of high-temperature Chern insulator with half-metallic edge states in asymmetry-functionalized stanene. *Nanoscale* 10, 20226–20233. doi: 10.1039/c8nr07503d

Zhang, Y., Liu, Z. H., Wu, Z., and Ma, X. Q. (2019). Prediction of fully compensated ferrimagnetic spin-gapless semiconducting FeMnGa/Al/In half Heusler alloys. *IUCrJ* 6, 610–618. doi: 10.1107/s2052252519005062

Zhao, Z., Zhang, Z., and Guo, W. (2020). A family of all sp2-bonded carbon allotropes of topological semimetals with strain-robust nodal-lines. *J. Mater. Chem. C* 8, 1548–1555. doi: 10.1039/c9tc05470g

Zhou, P., Ma, Z., and Sun, L. Z. (2018). Coexistence of open and closed type nodal line topological semimetals in two dimensional B2C. *J. Mater. Chem. C* 6, 1206–1214. doi: 10.1039/c7tc05095j

Zou, Z. C., Zhou, P., Ma, Z., and Sun, L. Z. (2019). Strong anisotropic nodal lines in the TiBe family. *Phys. Chem. Chem. Phys.* 21, 8402–8407. doi: 10.1039/c9cp00508k

Žutic, I., Fabian, J., and Sarma, S. D. (2004). Spintronics: fundamentals and applications. *Rev. Mod. Phys.* 76, 323–410.

Conflict of Interest: The author declares that the research was conducted in the absence of any commercial or financial relationships that could be construed as a potential conflict of interest.

frontiers in Physics

ORIGINAL RESEARCH
published: 25 September 2020
doi: 10.3389/fphy.2020.587419

Tunable Magnetic Anisotropy and Dzyaloshinskii-Moriya Interaction in an Ultrathin van der Waals Fe_3GeTe_2/In_2Se_3 Heterostructure

Dong Chen[1,2], *Wei Sun*[1], *Hang Li*[1], *Jianli Wang*[1,3]* *and Yuanxu Wang*[1]*

[1] Institute for Computational Materials Science, School of Physics and Electronics, Henan University, Kaifeng, China, [2] College of Physics and Electronic Engineering, Xinyang Normal University, Xinyang, China, [3] Institute for Superconducting and Electronic Materials, Australian Institute of Innovative Materials, University of Wollongong, Wollongong, NSW, Australia

The promise of future spintronic devices with nanoscale dimension, high-density, and low-energy consumption motivates the search for van der Waals heterostructure that stabilize topologically protected whirling spin textures such as magnetic skyrmions and domain walls. To translate these compelling features into practical devices, a key challenge lies in achieving effective manipulation of the magnetic anisotropy energy and the Dzyaloshinskii-Moriya (DM) interaction, the two key parameters that determine skyrmions. Through the first-principles calculation, we demonstrate that the polarization-induced broken inversion symmetry in the two-dimensional Fe_3GeTe_2/In_2Se_3 multiferroic heterostructure does cause an interfacial DM interaction. The strong spin-orbit coupling triggers the magnetic anisotropy of the Fe_3GeTe_2/In_2Se_3 heterostructure. The magnetic anisotropy and the DM interaction in Fe_3GeTe_2 can be well-controlled by the ferroelectric polarization of In_2Se_3. This work paves the way toward the spintronic devices based on van der Waals heterostructures.

Keywords: first-principles, multiferroic heterostructure, Dzyaloshinskii-Moriya interaction, magnetic anistropy, density of states

PACS: 63.20.dk, 74.78.Fk, 85.75.-d, 75.30.Gw

OPEN ACCESS

Edited by:
Xiaotian Wang,
Southwest University, China

Reviewed by:
Fang Hong,
Institute of Physics Chinese Academy of Science, China
Changping Yang,
Hubei University, China

***Correspondence:**
Jianli Wang
jianli@uow.edu.au
Yuanxu Wang
wangyx@henu.edu.cn

Specialty section:
This article was submitted to Computational Physics, a section of the journal Frontiers in Physics

Received: *01 August 2020*
Accepted: *19 August 2020*
Published: *25 September 2020*

Citation:
Chen D, Sun W, Li H, Wang J and Wang Y (2020) Tunable Magnetic Anisotropy and Dzyaloshinskii-Moriya Interaction in an Ultrathin van der Waals Fe_3GeTe_2/In_2Se_3 Heterostructure. Front. Phys. 8:587419. doi: 10.3389/fphy.2020.587419

INTRODUCTION

Two-dimensional (2D) van der Waals (vdW) materials have many novel properties compared to their three-dimensional (3D) counterparts, such as topology, spin frustration, and magnetic skyrmion [1]. The vdW bulks can be cleaved/exfoliated down to the monolayer limit with their structural integrities and chemical stabilities retained [2], which brings great convenience to the building of heterostructures (HSs). When cleaved, the specific surface area of the vdW material greatly increases, which is suitable to be tuned by many kinds of experimental stimuli. These advantages would provide completely new platforms with all magnetic atoms participating in the magnetoelectric coupling, and largely reshape the landscape of 2D vdW multiferroics [3, 4]. Inspired by the new physical picture of 2D materials, exploring the atom-thick vdW HS is the frontier of current spintronics research. The Dzyaloshinskii-Moriya (DM) interaction has recently received a lot of attention due to new findings on the magnetic skyrmions, spin waves, and chiral domain walls [5–8]. Magnetic skyrmion and domain wall are the smallest components that can be used in the next-generation magnetic race-track memories [9]. A critical constant of DM interaction $D_C = \sqrt{\frac{JK}{\pi}}$ is defined to evaluate the stability of the skyrmions [10], where J and

K are the exchange coupling and magnetic anisotropy, respectively. The DM interaction and the magnetic anisotropy manipulated in 2D HS will greatly improve the practical applications of spintronic devices.

The coupling between ferroelectricity and ferromagnetism allows the control of spin via electric field or the control of charge via magnetic field, which leads to multifunctional performance of spintronic devices [11]. Thesore, the co-existence of these two ferroic orders in 2D materials is very attractive. The single-phase multiferroics are extremely rare because ferroelectricity arising from the off-center cations requires empty *d*-orbitals, while ferromagnetism usually results from partially occupied *d*-orbitals [12]. Scientists have built various heterostructures from the ferroelectric (FE) and ferromagnetic (FM) materials. Not only the coexistence of ferroelectricity and ferromagnetism, but also the magnetoelectric couplings were achieved in these HSs [1, 4, 12]. Since the first prediction of 2D FE hydroxyl-decorated graphene in 2013, more and more 2D FE materials have been discovered, e.g., SnSe, SnS, GeS, Bi_2O_2Se, and Bi_2O_2Te (in-plane FE) [13, 14], as well as MoS_2, $CuInP_2S_6$, In_2Se_3, and MXenes (perpendicular FE) [13, 15]. The mechanisms involved in these in-plane and perpendicular polarizations are the polar functional groups, the hopping of halogen adatoms, or polar phonon modes [11]. In recent years, dozens of 2D ferromagnets have been found experimentally or predicted theoretically [14, 16]. The emerging of more novel 2D vdW ferroelectric materials and 2D vdW magnetic compounds indicates an enhanced probability to form multiferroic HSs.

The bulk Fe_3GeTe_2 (FGT) belongs to 2D vdW magnetic materials with a layered hexagonal lattice, where the weakly bonded Fe_3Ge layers are sandwiched between two Te slabs. As a strongly correlated itinerant ferromagnet, FGT contains two inequivalent Fe coordinates: the Fe1 atoms form a hexagonal net, while the Fe2 atoms are bonded covalently with Ge. This compound has many excellent properties, for example: a mixed valence state $(Fe^{2+})(Fe^{3+})_2(Ge^{4-})(Te^{2-})_2$ [17], a [001] oriented easy axis [18], and a FM configuration down to the monolayer regime [19, 20]. In particular, FGT can be easily exfoliated along the [001] direction due to the weak vdW interaction [19]. Recently, Yi et al. [21] have demonstrated a new phase of FGT (namely a competing AFM configuration) and the FM slabs become AFM order below 152 K. Nevertheless, Tian et al. [22] reported that the AFM configuration originates from the movement of pinned magnetic domain walls. The above-mentioned arguments indicate that the fundamental properties of FGT are still under development. The experimentally confirmed 2D vdW ferromagnets are mainly focused on three materials: CrI_3, $Cr_2Ge_2Te_6$, and Fe_3GeTe_2 [23–25]. Even though the Curie temperature (T_C) of 230 K [17] is below (but not too far below) the room temperature, FGT show a much higher T_C than the CrI_3 ($T_C = 61$ K) and $Cr_2Ge_2Te_6$ ($T_C = 61$ K) bulks [26, 27]. The combination of high T_C and the above-mentioned properties makes FGT a promising candidate for exploring itinerant ferromagnetism in a truly 2D form.

Having the FM part at hand, we now investigate the FE part of our multiferroic HS. As an all-known fact, the perpendicular polarization is usually more important than the in-plane one because the perpendicular polarization can effectively penetrate the FM layers in a FE/FM HS, thus manipulating the magnetism of the FM slabs. The 2D vdW materials with perpendicular polarization are relatively rare, which is mainly due to the fact that incomplete screening of surface charges induced depolarization field opposes the spontaneous polarization of the vdW materials, thereby suppressing the ferroelectricity. Recently, In_2Se_3 has been widely used in spintronic devices for memory and logic applications. Ding et al. [28] have reported that α-In_2Se_3 is a room-temperature FE material (down to the stable single-layer regime) with intrinsic in-plane and controllable perpendicular polarizations, which may open avenues for developing new concepts of magnetoelectric devices.

Very recently, Huang et al. [29] have investigated the effect of asymmetric interfacial coupling on the FE stability of 2D Fe_3GeTe_2/In_2Se_3 HS through the first-principles calculation, but some important physical properties such as the MAE and DM interaction are not included in their work. Besides, a large hole doping induced magnetic anisotropy reduction is demonstrated in $Fe_{3-x}GeTe_2$ layered structure [30]. They also found the sharp decrease in magnetic anisotropy energy (MAE) caused by the change of electronic structure. Nevertheless, the reason for the change of electronic structure, hence the change of MAE is still unclear. Motivated by recent developments, we now study the DM interaction and magnetic anisotropy manipulated by a ferroelectric polarization in a truly 2D form. Control the magnetism of 2D materials, as well as modulate the magnetic order and electronic spin are of great importance in novel spintronic devices since they have smaller size and lower energy consumption compared with traditional electronic devices. We have first demonstrated the reversible control the DM interaction and MAE by the FE polarization in the Fe_3GeTe_2/In_2Se_3 HS, as well as its underlying mechanisms. A magnetoelectric coupling is expected in our FE/FM HSs, opening up the possibility to control the magnetic skyrmions by the FE-polarization.

MODELS AND METHODS

The freestanding FGT monolayer is composed of two Fe1 layers, two Te layers and one mixed layer of Ge and Fe2 atoms, as shown in **Figure 1A**. The Fe atoms in the FGT monolayer can be divided into two inequivalent Fe1 and Fe2 atoms with the valence states of $(Te^{2-})(Fe1^{3+})/(Ge^{4-})(Fe2^{2+})/(Te^{2-})(Fe1^{3+})$ [31]. Excitingly, the exfoliation of mono-layer or few- layer Fe_3GeTe_2 has been experimentally achieved by Fei et al. [32] and Deng et al. [2]. Due to the relatively strong FE polarization, we choose In_2Se_3 as the substrate with its most stable structure [28] [see **Figure 1B**]. **Figure 1C** shows the coefficients of the DM interaction. Besides, the perpendicular FE polarization of the In_2Se_3 quintuple layers (QLs) can be easily reversed through several kinetic pathways given in Ding et al. [28]. In this work, four In_2Se_3 QLs are applied to form a substrate because the magnitude of the FE polarization reaches its maximum value at the thickness of 3 or 4 QLs [28]. Huang et al. [29] found that the energy difference between the up-polarization and down-polarization became a constant when the thickness of In_2Se_3 is more than 4 QLs. This result proven

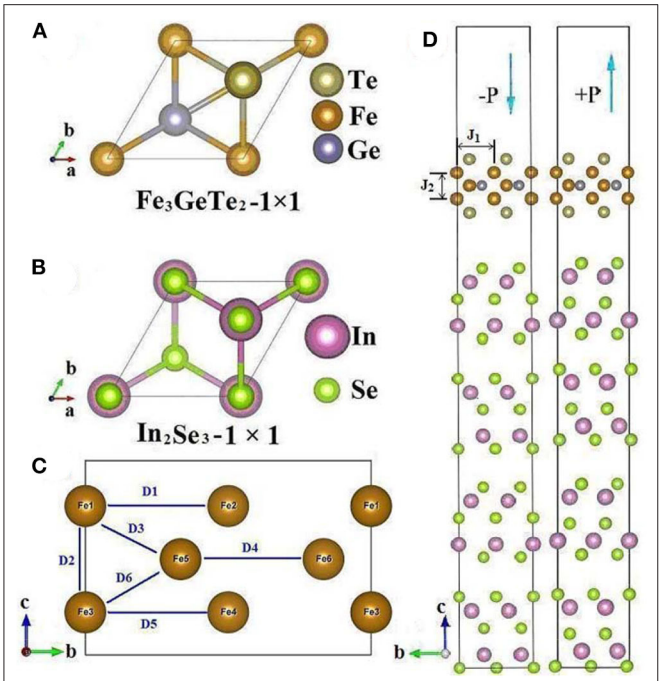

FIGURE 1 | The crystal structures of the van der Waals Fe_3GeTe_2/In_2Se_3 HS. The top view of the bulk Fe_3GeTe_2 **(A)** and In_2Se_3 compounds **(B)**; the side view of the coefficients of Dzyaloshinskii-Moriya (DM) interaction in the Fe_3GeTe_2 monolayer, only the Fe atoms are shown in the structure **(C)**; and the side view of the Fe_3GeTe_2/In_2Se_3 HSs with the ferroelectric polarization directed downward (–*P*) and upward (+*P*) **(D)**. These two HSs are built along the (001) direction within the $\sqrt{2} \times \sqrt{2}$ in-plane supercells.

that our In_2Se_3 substrate is thick enough to get reliable results. The unit cell is chosen to be equal to that of ferromagnetic Fe_3GeTe_2 with the experimental lattice parameters *a, b* that also commensurate to the In_2Se_3 layers. In order to comprehensively describe the AFM configuration, we build a $\sqrt{2} \times \sqrt{2}$ supercell with the *x-y* planes of FGT and In_2Se_3 changed from rhombus to rectangular, as shown in **Figure 1D**. Our HSs have idealized hard interfaces without any defects or adsorbates. More importantly, the calculation methods and detailed parameters are given in the **Supplementary Information**.

RESULTS AND DISCUSSIONS

As it can be seen in **Table 1**, the lattice constants of the FGT monolayer agree well with the experimental data ($a = 0.4050$ nm, $b = 0.7014$ nm) [33]. Our calculated magnetic moments of the freestanding FGT monolayer are also in agreement with the experimental data ($m_1 = 2.18\ \mu_B$, $m_2 = 1.54\ \mu_B$) [34], which partially proved that our results are reliable. The lattice mismatch between FGT and In_2Se_3 is only 1.2% for both *a* and *b* axes, which indicates that these two materials can form heterostructures perfectly. It is worth noting that 2D FGT retains its FM configuration not only in the freestanding state, but also in the heterostructures. The orientation of the FE polarization has

TABLE 1 | The calculated lattice parameters *a, b,* the magnetic order, the energy difference between the FM order and the lowest-energy AFM order ($\Delta E = E_{FM} - E_{AFM}$), the magnetic moments m_1, m_2 of the two inequivalent Fe atoms, the net magnetization *M*, the magnetic anisotropy energy (MAE) per Fe atom, the exchange parameters J_1 and J_2 of the freestanding Fe_3GeTe_2 monolayer and the FGT/In_2Se_3 HS.

Properties	Freestanding Fe_3GeTe_2	–*P* HS	+*P* HS
a/nm	0.4057	0.4091	0.4089
b/nm	0.7047	0.7078	0.7083
Order	FM	FM	FM
ΔE/meV	−65.79	−76.70	−75.22
m_1/μ_B	2.61	2.62	2.61
m_2/μ_B	1.58	1.58	1.62
M/μ_B	13.09	13.10	13.21
J_1/meV	10.68	10.74	10.57
J_2/meV	−7.45	−85.95	−84.57
MAE/meV per Fe	0.39	0.28	0.69

little effect on the magnetic moments and magnetic order of the FGT/In_2Se_3 HS.

Our calculated exchange parameters J_1 and J_2 are shown in **Figure 1C**, which are in general agreement with Deng's results (J_1 =5.79 meV, J_2 = −6.48 meV) [2]. Although the in-plane exchange interaction J_1 is AFM, it is much weaker when compared to the FM interaction between the Fe1 and Fe2 atoms [2]. Hence the FM configuration can be retained in the freestanding FGT monolayer. When coupled with the In_2Se_3 substrate, J_2 increases quickly. The sign of the exchange parameter for the FGT/In_2Se_3 HS, found positive for J_1 and negative for J_2, while J_2 is predominantly stronger than J_1. The parameter J_2 is strong and negative so as to stabilize the FM order of the FGT/In_2Se_3 HS.

The MAE is calculated as the total energy difference between the HS with in-plane and perpendicular magnetization axes, which can be written as [35]

$$MAE = E_{100} - E_{001} \quad (1)$$

To obtain the MAE, we consider the SOC effect in our calculation. The calculated MAE is 0.39 meV per Fe atom, indicating strong easy axis anisotropy in the freestanding FGT monolayer. Our result is in good agreement with the data obtained by Zhuang et al. [19] (0.52 meV per Fe atom). The significant MAE exhibited by the freestanding FGT monolayer, which caused by strong SOC, suggests that the 2D FGT has potential for applications in magnetic data storage applications [19]. The FGT monolayer shows a perpendicular magnetic anisotropy in all cases involved, which agrees well with the experimental data of the bulk FGT [17]. The MAE of the HS is reduced by 28% and enhanced by 77% in the down-polarization and the up-polarization directions, respectively. Our calculated average orbital moment of Fe1 and Fe2 is ∼0.08 μ_B, which is much smaller than that of an isolated Fe^{2+} ion (2 μ_B) according to Hund's rule. The relatively sizable value of 0.08 μ_B shows that orbital magnetic moment is not completely quenched and

hence causing the strong SOC and a large MAE [19]. Therefore, we conclude that the strength of SOC is enhanced by the $+P$ polarization, leading to the enhancement of MAE.

Figure 2 shows the spin-resolved total and partial DOS of the fully relaxed FGT monolayer, in which the Fermi level (E_F) is set as zero. According to **Figure 2A**, we find that our system is metallic with several high peaks in the valence band (VB). The VB is mainly contributed by the non-localized Fe-3d, Ge-4p, and Te-5p states, while the Fe-3p, Ge-4s, and Te-5s states are small and negligible. The DOS just below the Fermi level is mainly contributed by the majority spin state of Te-4p, as well as the majority and minority states of Fe-3d. We observe the stronger Fe-Te hybridization and weaker Fe-Ge interaction mainly in the -4.5 — -2, eV and -5.5 — -4 eV region, respectively. According to the Stoner criterion [36], $I{\cdot}N(E_F){>}1$ reflects the itinerant ferromagnetism of the material, where $N(E_F)$ is the spin-averaged DOS at the E_F and I is the Stoner parameter [19]. From **Figure 2B**, our calculated value of $I{\cdot}N(E_F)$ is 2.05, which reflects an itinerant ferromagnetic nature of the FGT monolayer. This is in agreement with the results given in Zhuang et al. [19]. Moreover, the ferromagnetic order of the freestanding FGT monolayer has also been confirmed in **Table 1**.

Figure 3 shows the total DOS (TDOS) and partial DOS (PDOS) of the Fe_3GeTe_2/In_2Se_3 HS for the $-P$ case, which is useful in understanding the specific contributions of different atomic orbitals. We can see less TDOS near the E_F in the freestanding FGT monolayer. When combined with the In_2Se_3 substrate, the TDOS near the E_F increases dramatically, inducing a sizable DOS at the Fermi level. Namely, the metallicity is much better in the Fe_3GeTe_2/In_2Se_3 HSs than in the freestanding FGT monolayer. This novel feature is quite different from the case when the anisotropic SOC plays a decisive role in stabilizing the FM configuration in another famous 2D material CrI_3 [37]. In the CrI_3 monolayer, a spin gap at the center of the Brillouin zone can be found below the Curie temperature. The spin-up and spin-down DOSs are asymmetric, indicating significant spin polarization of our HS system. The spin polarizability can be defined as: $SP_F = [N(E_F)_\alpha\text{-}N(E_F)_\beta]/[N(E_F)_\alpha + N(E_F)_\beta] \times 100\%$, where $N(E_F)_\alpha$ and $N(E_F)_\beta$ are the DOS at Fermi level for the spin-up and spin-down channels, respectively [38]. The SP_F of the freestanding FGT monolayer, the $-P$ HS, and the $+P$ HS are 34.01, 35.57, and 29.69%, respectively. This indicates a much weaken quantum confinement effect in our HS system than in the strained FGT nanoribbons (SP_F = 45–85.6%) shown in Han et al. [38].

To further explore the difference between the two inequivalent Fe atoms, we show the PDOS of Fe1 and Fe2 in **Figures 3B,C**, respectively. Remarkably our HS system presents a metallic character, strictly confined in the FGT layer. The metallic FGT layer exhibits ferromagnetism, with a magnetic moment of 2.2 μ_B/Fe atom. Both the majority and minority spin states of the five split 3d orbitals are non-zero states near the E_F. They mainly assemble between -4 to 1 eV, while the smaller spin-down states are around -3 to -0.5 eV, which produces large magnetic moments in Fe1 atoms. For the Fe2 atoms, there are more spin-down states between -3.5 to -0.5 eV than for Fe1 atoms, which compensate the difference between spin-up and spin-down states. This causes the Fe2 atoms to have lower magnetic moments than Fe1. In the VB region, the contribution of Fe atoms at the E_F is mainly due to the Fe1 d_{xy}, d_{yz}, d_{xz}, and $d_{x^2-y^2}^2$ orbitals as well as the Fe2 d_{xz}, $d_{x^2-y^2}^2$, and $d_{z^2}^2$ orbitals (d_{xy} and d_{yz} orbitals are almost degenerated). The rest of the orbitals are either too small or too far from the Fermi level. In the CB region, the Fe-3d PDOS is mainly contributed by the spin-down channels. The TDOS shown in **Figures 3A**, **4A** and the PDOS shown in **Figures 3B,C**, **4B,C** are quite similar, especially in the valence band region.

It is also shown in **Figures 3D,E**, **4D,E** that the Fe and Te atoms contributing to the DOS near E_F, but Fe1 does more than others [39]. Contrastingly, the Ge atoms, which can hardly be seen near the E_F, play a less significant role in the FGT/In_2Se_3 HS. In **Figures 3F–I**, **4F–I**, we can see that the upper VB is dominated by the states of selenium atoms and a slight contribution of indium atoms, while the lower VB and the CB are the results of strong hybridization of In and Se. The DOSs of the Layer 1 to Layer 4 are almost alike, but the $-P$ DOS and $+P$ DOS gradually move to the high energy and low energy regions, respectively. This is mainly due to the change of electric potential induced by polarization discontinuity. We found that all the insulating In_2Se_3 layers have little effects on the magnetic properties of our HSs. For the Fe1 and Fe2 atoms, we find essentially the same features with minor changes in the hybridization peaks when the FE-P reverses. The very similar DOS for both the $\pm P$ cases indicating the almost unchanged magnetic properties of the FGT/In_2Se_3 HSs. It is worthy of note that the DOS of FGT layer given by Huang et al. [29] is also metallic, and our DOS is in topological resemblance with the DOS shown in Huang et al. [29].

Figure 5 illustrates the charge density difference of the ferromagnetic Fe_3GeTe_2/In_2Se_3 HS for both the $\pm P$ cases. We only show the charge of the FGT/In_2Se_3 interface (not the whole HS) because the charge transfer mainly occurs near the interface. Here, the yellow (blue) region represents charge accumulation (depletion). For the $-P$ case, there is obvious charge transfer between the Te-Se atoms than between the Te-Fe atoms. This reflects the importance of Te orbitals in bridging the exchange-coupling between the Fe atoms, which agrees well with the DOS result. For the $+P$ case, the charge redistribution at the FGT/In_2Se_3 interface are less obvious. This is mainly due to the fact that the positive FE polarization leads to an increment of the distance between the FGT layer and the In_2Se_3 substrate, hence greatly reducing the interfacial charge transfer. **Figure 5** reveals three features: (1) Fe1 and Fe2 atoms are non-equivalent; (2) when the FE-P reverses, the charge transfer of the Fe atoms is mainly along the z-axis, implying the importance of dz^2 electrons that give rise to the inter- and intra-layer FM order; (3) The very little charge transfer of Fe leads to almost unchanged magnetic moments of the Fe1 and Fe2 atoms.

On the one hand, 2D vdW ferromagnetic materials with the FM orders are of great scientific interesting and technological importance for the next-generation storage devices. On the other hand, the DM interaction plays a key role in stabilizing the chiral domain walls and magnetic skyrmions in magnetic thin films with broken inversion symmetry. Therefore, it is important

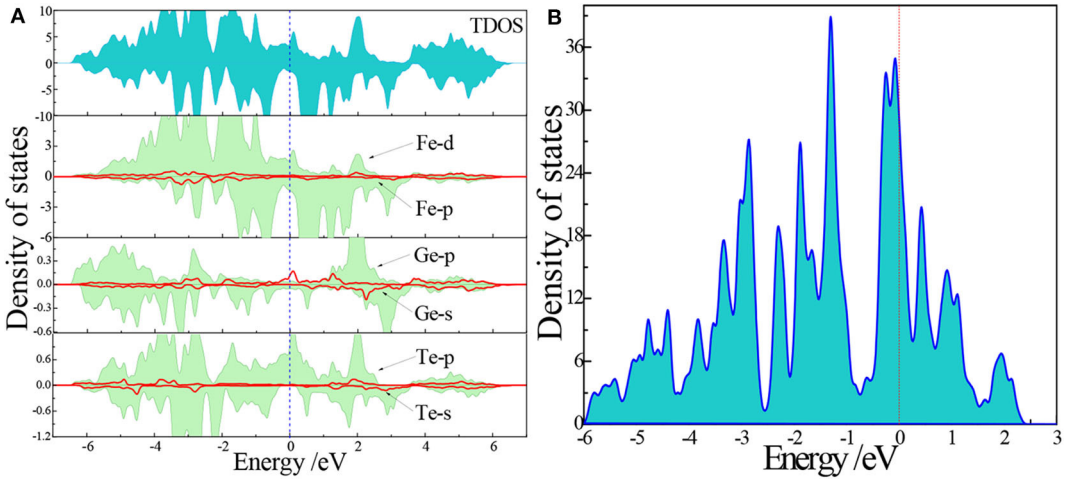

FIGURE 2 | The spin-polarized total/partial DOS **(A)** and the spin-averaged total DOS **(B)** of the freestanding Fe_3GeTe_2 monolayer.

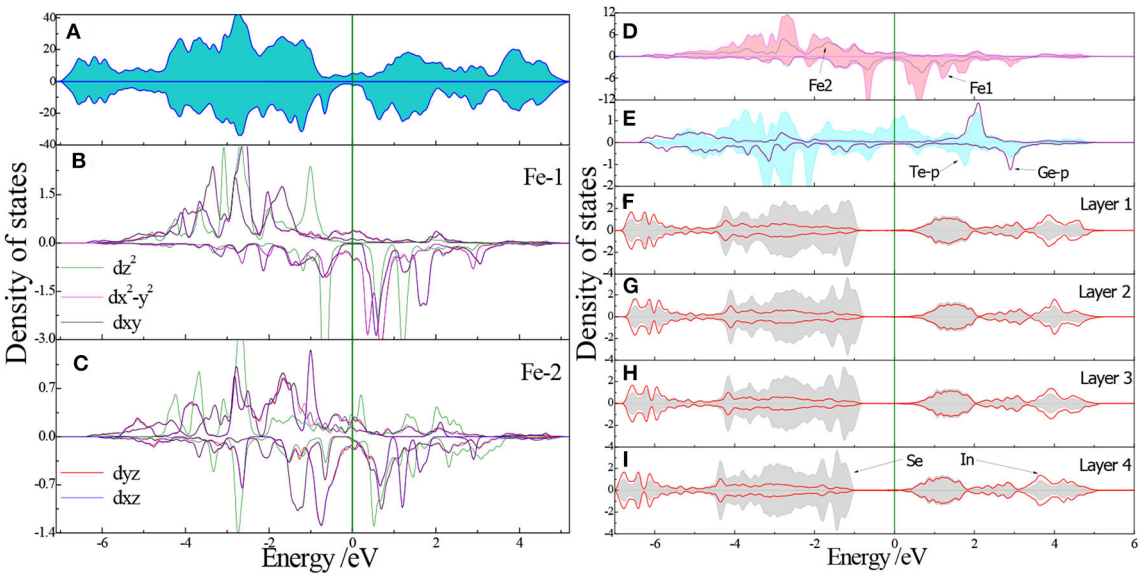

FIGURE 3 | Total DOS of the Fe_3GeTe_2/In_2Se_3 HS for the *–P* case **(A)**; the partial DOS of the five 3d orbitals for the four Fe1 **(B)**; and two Fe2 atoms **(C)**; the DOS of the inequivalent Fe1 and Fe2 atoms **(D)**; the DOS of Te-5p and Ge-4p states **(E)**; the layer-resolved DOS of the In_2Se_3 layers **(F–I)**.

to control the DM interaction in 2D vdW materials with their FM orders unchanged. In order to obtain the coefficients of DM interaction, we have built a 2 × 2 × 1 supercell of our FGT/In_2Se_3 HS containing 24 Fe atoms. As shown in **Figure 1C**, the coefficients D (D_1, D_2, D_3, D_4, D_5, and D_6) can be obtained by mapping different spin configurations on the Hamiltonian H given in equation (1) [40]. For our rectangular HS along the z-axis, the D_x and D_y will cancel each other out due to the C_{3v} symmetry of Fe atoms. Here only the D_z is calculated for simplicity. We first set all the spins along the z-axis, and then change the spins of two neighbors Fe positions 1 and 2 ($\boldsymbol{S}_1$ and $\boldsymbol{S}_2$) into four configurations: (i) $\boldsymbol{S}_1$ = (0, S, 0), $\boldsymbol{S}_2$ = (0, 0, S); (ii) $\boldsymbol{S}_1$ = (0, S, 0), $\boldsymbol{S}_2$ = (0, 0, –S); (iii) $\boldsymbol{S}_1$ = (0, –S, 0), $\boldsymbol{S}_2$ = (0, 0, S); (iv) $\boldsymbol{S}_1$ = (0, –S, 0), $\boldsymbol{S}_2$ = (0, 0, –S); where S represents the magnetic moment of Fe [41]. These energies of the four spin states are described as E_1, E_2, E_3, and E_4. Then, the coefficient D can be determined by $D = (E_1+E_4-E_2-E_3)/(4S^2)$ [41]. There are a large number of literatures calculate the coefficients of the DM interaction using VASP [42–44]. Although the coefficients are very small, these works confirm the accuracy of the VASP results. In this work, only the DM interactions between the nearest-neighboring Fe ions are considered.

To validate the plausible mechanism of ferroelectrically-driven DM interaction, we performed first-principles calculation on the FGT/In_2Se_3 HS (see **Supplementary Information** for

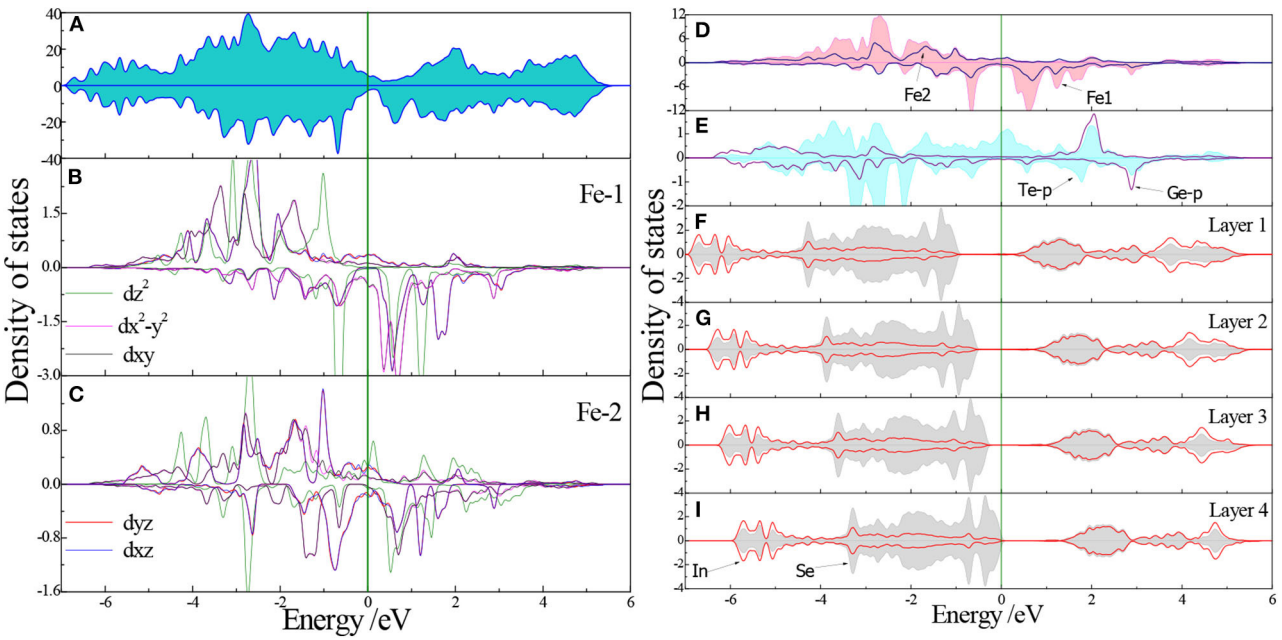

FIGURE 4 | Total DOS of the Fe_3GeTe_2/In_2Se_3 HS for the $+P$ case **(A)**; the partial DOS of the five 3d orbitals for the four Fe1 **(B)**; and two Fe2 atoms **(C)**; the DOS of the inequivalent Fe1 and Fe2 atoms **(D)**; the DOS of Te-5p and Ge-4p states **(E)**; the layer-resolved DOS of the In_2Se_3 layers **(F–I)**.

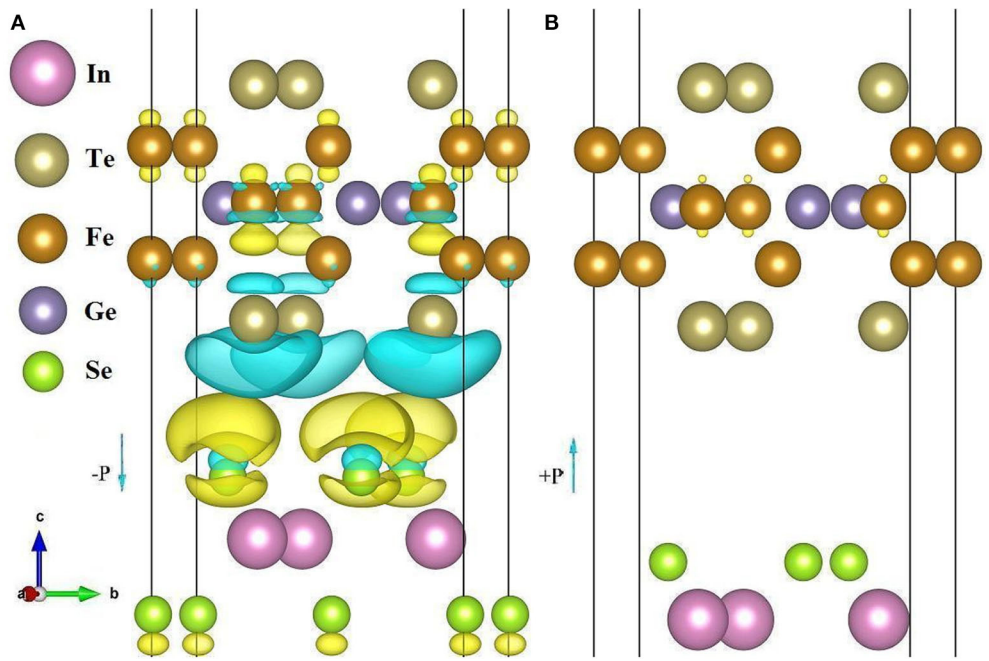

FIGURE 5 | Charge density difference of the Fe_3GeTe_2/In_2Se_3 heterostructure for the $-P$ **(A)** and $+P$ cases **(B)**. The isosurface value is set to be 0.00035 e/bohr^3.

details). The coefficients of the DM interaction D_1-D_6 for first-nearest neighbors are listed in **Table 2**, resulting in a magnitude D of −0.0224 (−0.0185) meV for the HS at the $-P$ ($+P$) case, that is about two orders of magnitude smaller than the exchange parameter J_1. When the FE polarization changes from $+P$ to $-P$, the D_2 and D_3 change from positive to negative, and other coefficients D_1, D_4, D_5, D_6, and D [D=(D_1+D_4+D_5)/3] vary −24, 102, −92, −65, and −58%, respectively. This indicates that the FE polarization effects on the in-plane D_1, D_6 and hence the average D is moderate. These DM interaction energies

TABLE 2 | The coefficients of the DM interaction on the FGT/In_2Se_3 HS for both the $\pm P$ cases.

	D_1/meV	D_2/meV	D_3/meV	D_4/meV	D_5/meV	D_6/meV	D/meV
$-P$	−0.0307	−0.0022	−0.0072	0.0092	−0.0458	−0.0138	−0.0224
$+P$	−0.0232	0.0025	0.0079	0.0186	−0.0034	−0.0047	−0.0093

may be result of the broken inversion symmetry and the strong SOC effect [45, 46]. Our FGT/In_2Se_3 HS has the polarization-dependent DM interaction, which can be used in skyrmion-based racetrack memory. Although our results are small, there are many ways to enhance the DM interaction in experiments. For example, one way is enhancing the spin-orbit coupling [47], and doping of heavy atoms is another way [48]. Using criticality analysis, Tan et al. [20] have demonstrated that the coupling length between vdW layers in Fe_3GeTe_2 is estimated to be 5 layers. Wu et al. [45] have confirmed that the increasing of the thickness of FGT up to 4–60 layers will lead to greatly enhanced DM interaction. In short, we have demonstrated that the strong SOC in the In_2Se_3 layers does induce an interfacial DM interaction at the interface with FGT, and have achieved the robust manipulation of DM interaction in the Fe_3GeTe_2/In_2Se_3 heterostructure. Enhancing the DM interaction through the above-mentioned schemes can make our results more valuable in potential application of spintronics.

CONCLUSION

In this work, the vdW material In_2Se_3 with both in-plane and perpendicular spontaneous polarization and the vdW ferromagnetic compound Fe_3GeTe_2 are used to form a two-dimensional artificial 2D heterostructure. Through the first-principles calculation, we have demonstrated the magnetoelectric coupling in the two-dimensional Fe_3GeTe_2/In_2Se_3 system. This ferroelectric polarization of In_2Se_3 can manipulate the magnetic anisotropy and the DM interaction in Fe_3GeTe_2. When the FE polarization is switched from $-P$ to $+P$, the DM interaction of the heterostructure varies moderately, which is affected by the strong spin-orbit coupling. Through the reorientation of the polarization, we also realized the robust control of DM interaction which originates from the broken inversion symmetry. The spin polarizations shown in the density of states reflect spin-polarized states in the FGT/In_2Se_3 system, which are important in spintronic devices. We hope that our results can promote the research on the spintronic devices with low power consumption, non-volatile, and high-speed.

DATA AVAILABILITY STATEMENT

All datasets generated for this study are included in the article/**Supplementary Material**.

AUTHOR CONTRIBUTIONS

JW and YW conceived the idea. DC, WS, and HL performed the calculations. DC and WS wrote the manuscript. All authors reviewed the manuscript.

FUNDING

This work was supported by the National Natural Science Foundation of China under research (Nos. 51571083 and 11674083), as well as the Key Scientific and Technological Projects in Henan Province (No. 162102210169) and the Key Projects of the Higher Education Institutions of Henan Province (No. 16A140033).

SUPPLEMENTARY MATERIAL

The Supplementary Material for this article can be found online at: https://www.frontiersin.org/articles/10.3389/fphy.2020.587419/full#supplementary-material

REFERENCES

1. Jiang Z, Wang P, Xing JP, Jiang X, Zhao JJ. Screening and design of novel 2D ferromagnetic materials with high Curie temperature above room temperature. *ACS Appl Mater Interfaces*. (2018) **10**:39032–9. doi: 10.1021/acsami.8b14037
2. Deng Y, Yu Y, Song Y, Zhang J, Wang NZ, Sun Z, et al. Gate-tunable room-temperature ferromagnetism in two-dimensional Fe_3GeTe_2. *Nature*. (2018) **563**:94–9. doi: 10.1038/s41586-018-0626-9
3. Sun W, Wang WX, Chen D, Cheng ZX, Jia TT, Wang YX. Giant magnetoelectric coupling and two-dimensional electron gas regulated by polarization in $BiFeO_3/LaFeO_3$ heterostructures. *J Phys Chem C*. (2019) **123**:16393–9. doi: 10.1021/acs.jpcc.9b04499
4. Sun W, Wang WX, Chen D, Zhang GB, Cheng ZX, Wang YX. First-principles investigation on tunable electronic properties and magnetism by polarization in $PbTiO_3/BiFeO_3$ 2D ferroelectric heterostructures. *J Mater Chem C*. (2019) **7**:463–73. doi: 10.1039/C8TC04987D
5. Ding B, Li Z, Xu G, Li H, Hou Z, Liu E, et al. Observation of magnetic skyrmion bubbles in a van der Waals ferromagnet Fe_3GeTe_2. *Nano Lett*. (2020) **20**:868–73. doi: 10.1021/acs.nanolett.9b03453
6. Di K, Zhang VL, Lim HS, Ng SC, Kuok MH, Qiu XP, et al. Asymmetric spin-wave dispersion due to dzyaloshinskii-moriya interaction in an ultrathin Pt/CoFeB film. *Appl Phys Lett*. (2015) **106**:052403. doi: 10.1063/1.4907173
7. Fert A, Reyren N, Cros V. Magnetic skyrmions: advances in physics and potential applications. *Nat Rev Mater*. (2017) **2**:17031. doi: 10.1038/natrevmats.2017.31
8. Dzyaloshinsky I. A thermodynamic theory of "weak" ferromagnetism of antiferromagnetis. *J Phys Chem Solids*. (1958) **4**:241–55. doi: 10.1016/0022-3697(58)90076-3
9. Parkin S, Yang SH. Memory on the racetrack. *Nat Nanotechnol*. (2015) **10**:195–8. doi: 10.1038/nnano.2015.41
10. Wang L, Feng Q, Kim Y, Kim R, Lee KH, Pollard SD, et al. Ferroelectrically tunable magnetic skyrmions in ultrathin oxide heterostructures. *Nat Mater*. (2018) **17**:1087–94. doi: 10.1038/s41563-018-0204-4
11. Zhang J, Lin L, Zhang Y, Wu M, Yakobson BI, Dong S. Type-II multiferroic $Hf_2VC_2F_2$ mxene monolayer wih high transiton temperature. *J Am Chem Soc*. (2018) **140**:9768–73. doi: 10.1021/jacs.8b06475
12. Gong C, Kim EM, Wang Y, Lee G, Zhang X. Multiferroicity in atomic van der Waals heterostructures. *Nat Commun*. (2019) **10**:2657. doi: 10.1038/s41467-019-10693-0

13. Wu MH, Jena P. The rise of two-dimensional van der Waals ferroelectrics. *WIREs Comput Mol Sci.* (2018) **8**:e1365. doi: 10.1002/wcms.1365
14. Yin HB, Liu C, Zheng GP, Wang YX, Ren FZ. Ab initio simulation studies on the room-temperature ferroelectricity in two-dimensional β-phase GeS. *Appl Phys Lett.* (2019) **114**:192903. doi: 10.1063/1.5097425
15. Liu FC, You L, Seyler KL, Li X, Yu P, Lin J, et al. Room-temperature ferroelectricity in $CuInP_2S_6$ ultrathin flakes. *Nat Commun.* (2016) **7**:12357. doi: 10.1038/ncomms12357
16. Burch KS, Mandrus D, Park JG. Magnetism in two-dimensional van der Waals materials. *Nature.* (2018) **563**:47–52. doi: 10.1038/s41586-018-0631-z
17. Deiseroth H, Aleksandrov K, Reiner C, Kienle L, Kremer RK. Fe_3GeTe_2 and Ni_3GeTe_2-two new layered transition-metal compounds: crystal structures, HRTEM investigations, and magnetic and electrical properties. *Eur J Inorg Chem.* (2006) **8**:1561–7. doi: 10.1002/ejic.200501020
18. Johansen Ø, Risinggard V, Sudbø A, Linder J, Brataas A. Current control of magnetism in two-dimensional Fe_3GeTe_2. *Phys Rev Lett.* (2019) 122:217203. doi: 10.1103/PhysRevLett.122.217203
19. Zhuang HL, Kent PRC, Hennig RG. Strong anisotropy and magnetostriction in the two-dimensional stoner ferromagnet Fe_3GeTe_2. *Phys Rev B.* (2016) **93**:134407. doi: 10.1103/PhysRevB.93.134407
20. Tan C, Lee J, Jung SG, Park T, Albarakati S, Partridge J, et al. Hard magnetic properties in nanoflake van der Waals Fe_3GeTe_2. *Nat Commun.* (2018) **9**:1554. doi: 10.1038/s41467-018-04018-w
21. Yi J, Zhuang H, Zou Q, Wu Z, Cao G, Tang S, et al. Competing antiferromagnetism in a quasi-2D itinerant ferromagnet: Fe_3GeTe_2. *2D Mater.* (2017) 4:011005. doi: 10.1088/2053-1583/4/1/011005
22. Tian CK, Wang C, Ji W, Wang JC, Xia TL, Wang L, et al. Domain wall pinning and hard magnetic phase in Co-doped bulk single crystalline Fe_3GeTe_2. *Phys Rev B.* (2019) **99**:184428. doi: 10.1103/PhysRevB.99.184428
23. Albarakati S, Tan C, Chen ZJ, Partridge JG, Zheng G, Farrar L, et al. Antisymmetric magnetoresistance in van der Waals Fe_3GeTe_2/graphite/Fe_3GeTe_2 trilayer heterostructrues. *Sci Adv.* (2019) 5:eeaw0409. doi: 10.1126/sciadv.aaw0409
24. Song T, Cai X, Tu MWY, Zhang X, Huang B, Wilson NP, et al. Giant tunneling magnetoresistance in spin-filter van der Waals heterostructures. *Science.* (2018) **360**:1214–8. doi: 10.1126/science.aar4851
25. Jiang S, Shan J, Mak KF. Electric-field switching of two-dimensional van der Waals magnets. *Nat Mater.* (2018) **17**:406–10. doi: 10.1038/s41563-018-0040-6
26. McGuire MA, Dixit H, Cooper VR, Sales BC. Coupling of crystal structure and magnetism in the layered, ferromagnetic insulator CrI_3. *Chem Mater.* (2015) **27**:612–20. doi: 10.1021/cm504242t
27. Lohmann M, Su T, Niu B, Hou Y, Alghamdi M, Aldosary M, et al. Probing magnetism in insulating $Cr_2Ge_2Te_6$ by induced anomalous Hall effect in Pt. *Nano Lett.* (2019) **19**:2397–403. doi: 10.1021/acs.nanolett.8b05121
28. Ding W, Zhu J, Wang Z, Gao Y, Xiao D, Gu Y, et al. Prediction of intrinsic two-dimensional ferroelectrics in In_2Se_3 and other III_2-VI_3 van der Waals materials. *Nat Commun.* (2017) **8**:14956. doi: 10.1038/ncomms14956
29. Huang XK, Li GN, Chen C, Nie X, Jiang XP, Liu JM. Interfacial coupling induced critical thickness for the ferroelectric bistability of two-dimensional ferromagnet/ferroelectric van der Waals heterostructure. *Phys Rev B.* (2019) **100**:235445. doi: 10.1103/PhysRevB.100.235445
30. Park SY, Kim DS, Liu Y, Hwang J, Kim Y, Kim W, et al. Controlling the magnetic anisotropy of the van der Waals ferromagnet Fe_3GeTe_2 through hole doping. *Nano Lett.* (2020) **20**:95–100. doi: 10.1021/acs.nanolett.9b03316
31. Zhao YH, Gu JX, Chen ZF. Oxygen evolution reaction on 2D ferromagnetic Fe_3GeTe_2: boosting the reactivity by the self-reduction of surface hydroxyl. *Adv Funct Mater.* (2019) **29**:1904782. doi: 10.1002/adfm.201904782
32. Fei Z, Huang B, Malinowski P, Wang W, Song T, Sanchez J, et al. Two-dimensional itinerant ferromagnetism in atomically thin Fe_3GeTe_2. *Nat Mater.* (2018) **17**:778–82. doi: 10.1038/s41563-018-0149-7
33. Kim D, Park S, Lee J, Yoon J, Joo S, Kim T, et al. Antiferromagnetic coupling of van der Waals ferromagnetic Fe_3GeTe_2. *Nanotechnology.* (2019) **30**:245701. doi: 10.1088/1361-6528/ab0a37
34. May AF, Calder S, Cantoni C, Cao H, McGuire MA. Magnetic structure and phase stability of the van der Waals bonded ferromagnet $Fe_{3-x}GeTe_2$. *Phys Rev B.* (2016) **93**:014411. doi: 10.1103/PhysRevB.93.014411
35. Lee M, Choi H, Chung YC. Ferroelectric control of magnetic anisotropy of FePt/$BaTiO_3$ magnetoelectric heterojunction: a density functional theory study. *J Appl Phys.* (2013) 113:17C729. doi: 10.1063/1.4800499
36. Stoner EC. Collective electron ferromagnetism. *Proc R Soc Lond A.* (1938) **165**:372–414. doi: 10.1098/rspa.1938.0066
37. Chen L, Chung JH, Chen T, Duan C, Schneidewind A, Radelytskyi I, et al. Magnetic anisotropy in ferromagnetic CrI_3. *Phys Rev B.* (2020) **101**:134418. doi: 10.1103/PhysRevB.101.134418
38. Han JN, Fan ZQ, Zhang ZH. Structure stability, magneto-electronic properties, and modulation effects of Fe_3GeTe_2 nanoribbons. *Acta Phys Sin.* (2019) 68:208502. doi: 10.7498/aps.68.20191103
39. Duan DD, Jin S, Liu N, Shen S, Lin Z, Li K, et al. Tuning magnetic properties in quasi-two-dimensional ferromagnetic $Fe_{3-y}Ge_{1-x}As_xTe_2 (0 \leq x \leq 0.85)$. *Mater Res Express.* (2017) 4:036103. doi: 10.1088/2053-1591/aa63b5
40. Cheng Y, Yu SS, Zhu ML, Hwang J, Yang FY. Evidence of the topological hall effect in Pt/antiferromagnetic insulator bilayers. *Phys Rev Lett.* (2019) **123**:237206. doi: 10.1103/PhysRevLett.123.237206
41. Xiang HJ, Kan EJ, Wei SH, Whangbo MH, Gong XG. Predicting the spin-lattice order of frustrated systems from first principles. *Phys Rev B.* (2011) **84**:224429. doi: 10.1103/PhysRevB.84.224429
42. Ma X, Yu G, Tang C, Li X, He H, Shi J, et al. Interfacial Dzyaloshinskii-Moriya interaction: effect of 5d band filling and correlation with spin mixing conductance. *Phys Rev Lett.* (2018) **120**:157204. doi: 10.1103/PhysRevLett.120.157204
43. Luo HB, Zhang HB, Liu JP. Strong hopping induced dzyaloshinskii-moriya interaction and skyrmions in elemental cobalt. *NPJ Comput Mater.* (2019) **5**:50. doi: 10.1038/s41524-019-0187-y
44. Beutier G, Collins SP, Dimitrova OV, Dmitrienko VE, Katsnelson MI, Kvashnin YO, et al. Band filling control of the dzyaloshinskii-moriya interaction in weakly ferromagnetic insulators. *Phys Rev Lett.* (2017) **119**:167201. doi: 10.1103/PhysRevLett.119.167201
45. Wu Y, Zhang S, Yin G, Zhang J, Wang W, Zhu Y, et al. Néel-type skyrmion in WTe_2/Fe_3GeTe_2 van der Waals heterostructure. *Nat Commun.* (2020) **11**:3860. doi: 10.1038/s41467-020-17566-x
46. Yang H, Chen G, Cotta AAC, N'Diaye AT, Nikolaev SA, Soares EA, et al. Significant dzyaloshinskii-moriya interaction at graphene-ferromagnet interfaces due to the rashba effect. *Nat Mater.* (2018) 17:605–609. doi: 10.1038/s41563-018-0079-4
47. Moriya T. Anisotropic superexchange interaction and weak ferromagnetism. *Phys Rev.* (1960) **120**:91–8. doi: 10.1103/PhysRev.120.91
48. Li W, Jin C, Che R, Wei W, Lin L, Zhang L, set al. Emergence of skyrmions from rich parent phases in the molybdenum nitrides. *Phys Rev B.* (2016) **93**:060409R. doi: 10.1103/PhysRevB.93.060409

Conflict of Interest: The authors declare that the research was conducted in the absence of any commercial or financial relationships that could be construed as a potential conflict of interest.

frontiers in Chemistry

ORIGINAL RESEARCH
published: 08 October 2020
doi: 10.3389/fchem.2020.594411

First-Principles Study on the Magnetoelectric and Optical Properties of Novel Magnetic Semiconductor Li(Mg, Cr)P With Decoupled Spin and Charge Doping

Ting Chen, Nan Wu, Yue Li, Yuting Cui, Shoubing Ding and Zhimin Wu**

Chongqing Key Laboratory of Photoelectric Functional Materials, College of Physics and Electronic Engineering, Chongqing Normal University, Chongqing, China

The electronic structures, magnetic and optical properties of $Li_{1\pm y}(Mg_{1-x}Cr_x)$ P (x, y = 0.125) are calculated by using the first principles method based on density functional theory. We find that the incorporation of Cr causes the strong hybridization between Li-2s, P-2p, and Cr-3d orbitals, resulting in a spin-polarized impurity band and forming stronger Cr-P polar covalent bonds. $Li(Mg_{0.875}Cr_{0.125})P$ becomes half-metallic ferromagnetism. The properties of the doped systems can be regulated by Li off-stoichiometry. When Li is deficient, the narrower impurity band and stronger *p-d* orbital hybridization enhance the half-metallicity. While the half-metallicity disappears, the band gap becomes wider, and the conductivity decreases for Li excess system, but its magnetic moments increase. Comparing optical properties show that the imaginary part of dielectric and complex refractive index function and optical absorption spectrum all have a new peak in the low energy region after Cr doping, and the new peaks are significantly enhanced when Li is deficient. The absorption range of low frequency electromagnetic wave is enlarged, and the energy loss functions show obvious red-shift effect for the doped systems. The results indicate that the properties of Li(Mg,Cr)P can be controlled by Cr doping and Li off-stoichiometry independently, which will benefit potential spintronics applications.

Keywords: Cr doped LiMgP, electronic structure, ferromagnetism, optical properties, first-principles calculations

PACS: 31.15.A-, 71.15.Nc, 71.20.-b, 85.75.-d

OPEN ACCESS

Edited by:
Xiaotian Wang,
Southwest University, China

Reviewed by:
Zhifeng Liu,
Inner Mongolia University, China
Cai Cheng,
Sichuan Normal University, China
Li Li,
Chongqing University of Posts and Telecommunications, China

****Correspondence:***
Shoubing Ding
shoubingding@cqnu.edu.cn
Zhimin Wu
zmwu@cqnu.edu.cn

Specialty section:
This article was submitted to Theoretical and Computational Chemistry, a section of the journal Frontiers in Chemistry

Received: *13 August 2020*
Accepted: *07 September 2020*
Published: *08 October 2020*

Citation:
Chen T, Wu N, Li Y, Cui Y, Ding S and Wu Z (2020) First-Principles Study on the Magnetoelectric and Optical Properties of Novel Magnetic Semiconductor Li(Mg, Cr)P With Decoupled Spin and Charge Doping. Front. Chem. 8:594411. doi: 10.3389/fchem.2020.594411

INTRODUCTION

Diluted magnetic semiconductors (DMS) combine the charge freedom and spin freedom of the electrons in the same matrix and have both advantages of semiconductor and magnetic materials. Although a lot of studies have been carried out for the traditional DMS (Wolf et al., 2001; Zutic et al., 2004; Jungwirth et al., 2006; Dietl, 2010), there are still some obstacles that need to be solved. Firstly, for II-V-based diluted magnetic semiconductors, only local magnetic moments are introduced by replacing equivalent metal ions with Mn. The antiferromagnetic super-exchange interaction between local magnetic moments makes them have different magnetic behaviors at different magnetic ion concentration and temperature. Secondly, for III-V-based diluted magnetic semiconductors, due to the non-equivalent substitution of doping, the solubility of the magnetic

ions is limited and only metastable film materials can be formed (Ohno, 1998), which results in the specimens only available as thin films and sensitive to preparation methods and annealing treatments. The coupled spin and charge is an obstacle not only for fundamental understanding of ferromagnetic mechanism but also for effective improvement of controllable Curie temperature (Potashnik et al., 2001; Han et al., 2019).

These challenges have attracted great attention for finding a series of new generation DMS materials. Mašek et al. (2007) and Deng et al. (2011) firstly through theory and experiment, respectively, discovered a kind of new diluted magnetic semiconductor Li(Zn,Mn)As based on I-II-V groups. In the system, the spin is introduced by injecting Mn^{2+} in the site of Zn^{2+}, and the equivalent doping makes the system has higher Mn solubility. The carrier concentration can be controlled by changing the content of Li, making Li(Zn,Mn)As has higher Curie temperature (T_c) than (Ga,Mn)As. Following this, Wang et al. (2014) synthesized $Li_{1.1}(Zn_{1-x}Cr_x)As$, resulting in a ferromagnetic ordering below T_C ~218 K, nearer to the room temperature. However, one shortcoming of Mn-doped and Cr-doped LiZnAs is the using of the toxic element Arsenic. The transition metal doped LiZnP (Tao et al., 2017) and LiZnN (Cui et al., 2019) show that the magnetic moments come mainly from the TM-3d orbitals. Kacimi et al. (2014) calculated the structurel, electronic and optical properties of 96 I–II–V and I–III–IV compound semiconductors by using first-principles theory and found that LiMgP is a direct gap semiconductor with wider band gap, which is conducive to obtaining the new DMS materials with better properties through Cr doping.

In this work, the electronic structures, magnetic and optical properties of $Li_{1\pm y}(Mg_{1-x}Cr_x)P$ (x, y = 0, 0.125) are calculated by using the first principles method based on density functional theory. We find that the Cr doped systems exhibit half-metallic ferromagnetism. The electrical, magnetic and optical properties of Li(Mg,Cr)P can be controlled by Cr doping and Li off-stoichiometry independently, which will benefit potential spintronics applications.

COMPUTATIONAL DETAILS

LiMgP is an antifluorite structure (space group $F\bar{4}3$ m) with the lattice constant a = b = c = 6.005 Å (Kuriyama et al., 1998). The anion P is cubic close packed, the cations Mg and Li fill the gaps in the tetrahedral, and the coordination numbers of anions and cations are 4 and 8, respectively. LiMgP can be made from high temperature solid reaction between Li, Mg, and P (Kuriyama et al., 1998). LiMgP tetrahedral lattice can be viewed as a zinc blende MgP binary compound, filled with Li atoms at tetrahedral interstitial sites near P. LiMgP is a wide-gap semiconductor with a direct forbidden band gap of 2.43 eV (Kuriyama et al., 1998). To our calculations, a 2 × 1 × 1 (24 atoms) supercell of ZB-type LiMgP is constructed containing 8 Li, 8 Mg and 8 P atoms, as shown in **Figure 1A**. For the doping system, the model is constructed by replacing one Mg atom in the supercell with one Cr atom, and the doping concentration is 12.5% (**Figure 1B**). Besides, to study the effect of Li off-stoichiometry on the properties of Li(Mg,Cr)P, the models of Li vacancy and excess systems also are constructed by removing or

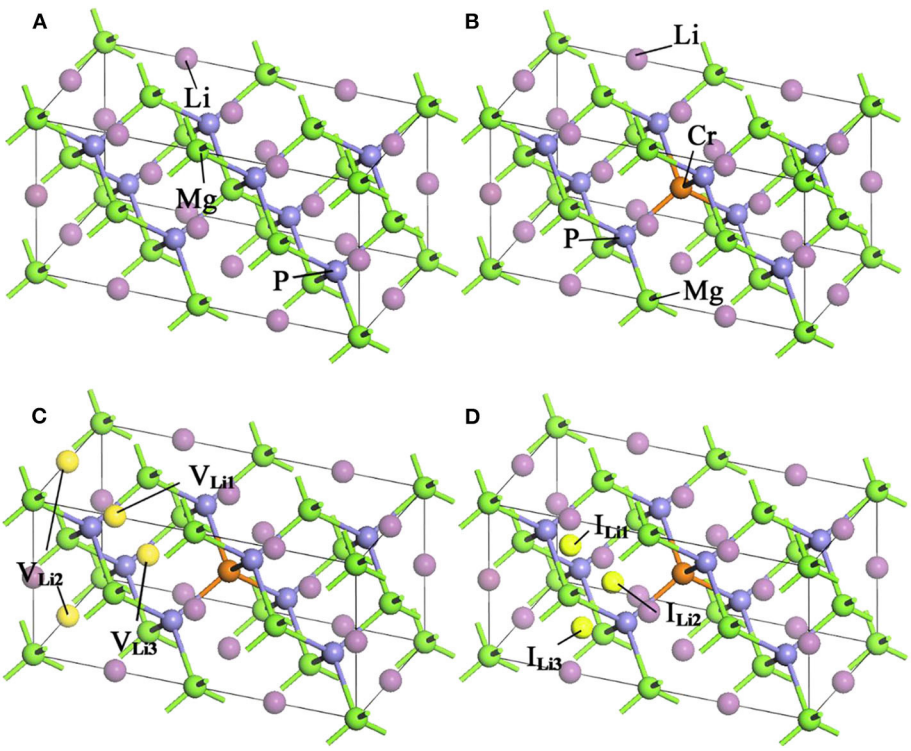

FIGURE 1 | Supercell structures of $Li_{1\pm y}(Mg_{1-x}Cr_x)P$: **(A)** LiMgP, **(B)** $Li(Mg_{0.875}Cr_{0.125})P$, **(C)** $Li_{0.875}(Mg_{0.875}Cr_{0.125})P$, and **(D)** $Li_{1.125}(Mg_{0.875}Cr_{0.125})P$.

adding a Li atom. The different symmetry vacancy and interstitial sites (V_{Li1}, V_{Li2}, V_{Li3}, and I_{Li1}, I_{Li2}, I_{Li3}) have been designated in **Figures 1C,D**, respectively.

The first-principles calculations are carried out with the Cambridge Serial Total Energy Package (CASTEP) code based on the density functional theory (DFT) method (Payne et al., 1992; Segall et al., 2002). The periodic boundary condition is applied in all calculations, and the generalized gradient approximation (GGA) in Perdew Burke Ernzerhof (PBE) (Perdew et al., 1996) is performed to deal with the electronic exchange-correlation potential energy. In order to reduce the number of the plane wave basis vector groups, the plane-wave ultrasoft pseudo potential (USPP) method (Vanderbilt, 1990) is implemented to describe the interaction between ionic core and valence electrons. The valence electronic configurations for Li, Mg, P, and Cr are Li:$2s^1$, Mg:$2p^6 3s^2$, P:$3s^2 3p^3$, and Cr: $3d^5 4s^1$, respectively. Single-particle Kohn-sham wave functions are expanded using the plane-wave with a cut-off energy of 400 eV. Sampling of the irreducible edge of the Brillouin zone is performed using the regular Monkhorst-Pack grid (Monkhorst and Pack, 1976) with a k-point mesh of 5 × 5 × 5. The self-consistent convergence accuracy is set at 2.0×10^{-6} eV/atom.

RESULTS AND DISCUSSION

Structure Optimization of $Li_{1\pm y}(Mg_{1-x}Cr_x)P$

To study the magnetoelectric and optical properties of novel magnetic semiconductor Li(Mg,Cr)P, the geometric structure of the original LiMgP supercell is firstly optimized by local Density Approximation (LDA) and General Gradient Approximation (GGA), respectively. The obtained lattice constant, band gaps and total energies are listed in **Table 1**, and compared with experimental data (Kuriyama et al., 1998). It can be found that the results obtained using the GGA reach a better agreement with the experimental data than those calculated using the LDA. As a consequence, it is more suitable to adopt GGA for the following calculations of Li(Mg,Cr)P. Besides, the geometric structures of the doping systems are also optimized with different symmetry vacancy and interstitial sites. The corresponding lattice constants, total energies and formation energies are shown in **Table 2**. We can find that the formation energies of V_{Li1} and I_{Li1} sites are the smallest, indicating that the doping systems of V_{Li1} and I_{Li1} sites are the most stable structures in the corresponding Li off-stoichiometry system, respectively.

TABLE 1 | The calculated lattice constants, band gaps and total energies of LiMgP with LDA and GGA.

LiMgP	*a*(Å)	*b*(Å)	*c*(Å)	Band gap(E_g)/eV	Total energy/eV
Experiment value (Kuriyama et al., 1998)	6.005	6.005	12.010	2.43	–
LDA	5.904	5.904	11.811	1.365	−10,754.55
GGA	6.030	6.030	12.061	1.533	−10,766.57

Electronic Structure of $Li_{1\pm y}(Mg_{1-x}Cr_x)P$

The spin polarized band structures of $Li_{1\pm y}(Mg_{1-x}Cr_x)P$ are shown in **Figure 2**. The insets are enlarged views of the vicinity of the Fermi energy level. We can find in **Figures 2A,B** that both the valence band maxima and the conduction band minima are at the high symmetry Γ point of Brillouin-zone, indicating that LiMgP is a direct gap semiconductor. The band structures of majority-spin and minority-spin are symmetrical completely, implying that the system has no net magnetic moments. The calculated band gap for LiMgP is 1.533 eV (shown in **Table 3**), which is smaller than the experimental result of 2.43 eV (Kuriyama et al., 1998). This is not surprising as the underestimation of the band gap is due to the generic nature of the density functional theory (Perdew and Levy, 1983; Godby et al., 1988). Nevertheless, this has no effect on the investigation of the electronics structure and relevant properties for Cr doped LiMgP systems (Shang et al., 2004).

As shown in **Figures 2C,D**, when Cr doped, the conduction band minima occur at the Γ point, while the valence band maxima are located around the Z point, in the Brillouin Zone. This result indicates that the material transforms into an indirect semiconductor. The band gap of $Li(Mg_{0.875}Cr_{0.125})P$ is 2.544 eV (**Table 3**), which obviously increases compared with that of LiMgP. This is because ten new spin impurity levels are emerged in band gap after doping Cr. Among them, each of the majority-spin and minority-spin bands has five impurity levels. The majority-spin impurity bands slightly cross the Femi level, demonstrating that the majority-spin bands exhibit metallic properties. While the minority-spin bands reveal still semi-conductive natures, making $Li(Mg_{0.875}Cr_{0.125})P$ system become a half-metallic material with 100% spin-polarized ratio of conduction electron. The spin-flip band gap is 0.767 eV, which are much larger than many other 3d-transition-metal-element-based materials (Guo et al., 2016). Usually, the larger spin-flip band gap, the more robust half-metallic behavior to lattice deformation and temperature (Guo et al., 2016). So the Cr doped LiMgP compounds reported in this work can be regarded as the good candidates for spintronics devices due to their large spin-flip gaps and robust half-metallicity.

$Li_{0.875}(Mg_{0.875}Cr_{0.125})P$ is also an indirect band gap semiconductor with the band gap of 2.531 eV (as show in

TABLE 2 | The lattice constants, total energies and formation energies of $Li_{1\pm y}(Mg_{1-x}Cr_x)P$.

Structure cell	lattice constants (Å)			Total energy(eV)	Formation energy(eV)
	a	*b*	*c*		
$Li(Mg_{0.875}Cr_{0.125})P$	6.005	6.005	12.010	−10,445.25	−6.569
$Li_{0.875}(Mg_{0.875}Cr_{0.125})P$-1	5.999	5.999	11.885	−12,067.47	−3.513
$Li_{0.875}(Mg_{0.875}Cr_{0.125})P$-2	5.990	6.005	11.912	−12,067.18	−3.221
$Li_{0.875}(Mg_{0.875}Cr_{0.125})P$-3	5.986	5.986	11.919	−12,067.19	−3.234
$Li_{1.125}(Mg_{0.875}Cr_{0.125})P$-1	6.038	6.0378	12.025	−12,448.96	−8.911
$Li_{1.125}(Mg_{0.875}Cr_{0.125})P$-2	6.035	6.043	12.039	−12,448.71	−8.659
$Li_{1.125}(Mg_{0.875}Cr_{0.125})P$-3	6.036	6.042	12.039	−12,448.71	−8.659

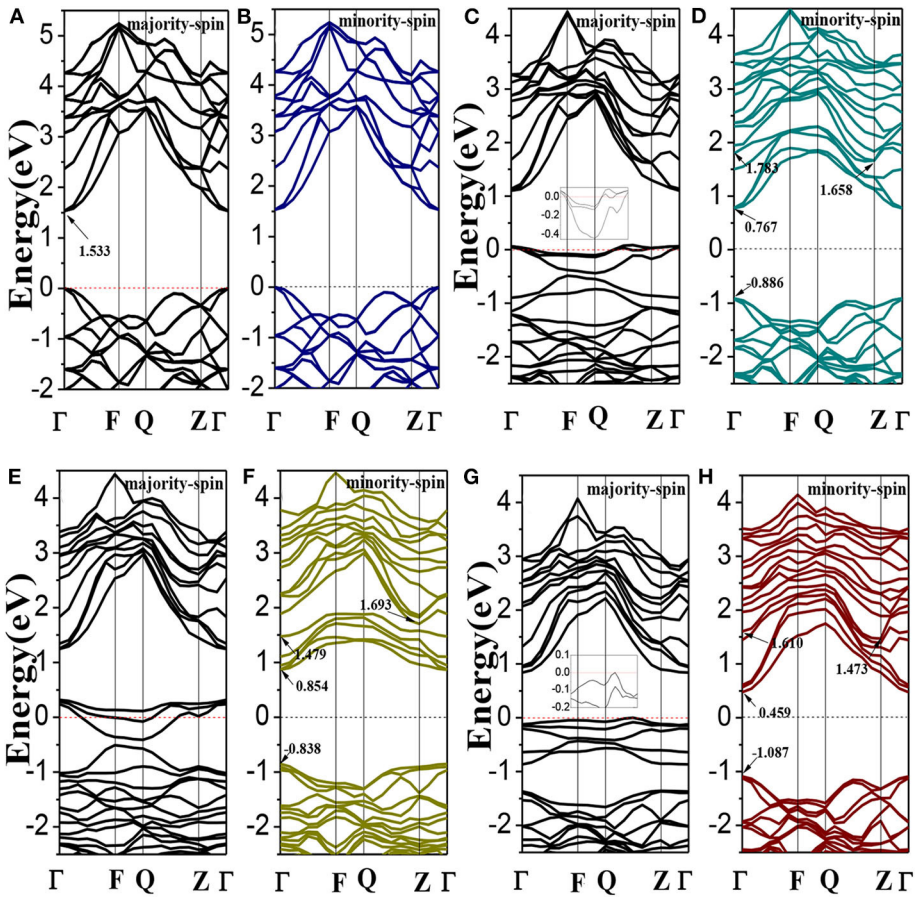

FIGURE 2 | The band structures of $Li_{1\pm y}(Mg_{1-x}Cr_x)P$: **(A,B)** LiMgP, **(C,D)** $Li(Mg_{0.875}Cr_{0.125})P$, **(E,F)** $Li_{0.875}(Mg_{0.875}Cr_{0.125})P$, and **(G,H)** $Li_{1.125}(Mg_{0.875}Cr_{0.125})P$. Inset: enlarged views of the vicinity of the Fermi energy level.

TABLE 3 | The band gaps, impurity band widths, half-metallic gap and magnetic moments of $Li_{1\pm y}(Mg_{1-x}Cr_x)P$.

$Li_{1\pm y}(Mg_{1-x}Cr_x)P$	Band gap(E_g)/eV	Impurity band width/eV	half-metallic gap/eV	Magnetic moment/μ_B
LiMgP	1.533	–	–	0
$Li(Mg_{0.875}Cr_{0.125})P$	2.544	1.016	0.767	4.08
$Li_{0.875}(Mg_{0.875}Cr_{0.125})P$	2.531	0.625	0.854	2.98
$Li_{1.125}(Mg_{0.875}Cr_{0.125})P$	2.560	1.151	–	4.90

Figures 2E,F). Three majority-spin impurity bands cross the Fermi level exhibiting a metallic nature, while the minority-spin impurity bands are above the Fermi level, resulting in that the Li vacancy system also exhibits a half-metallic nature. The spin-flip band gap of $Li_{0.875}(Mg_{0.875}Cr_{0.125})P$ is 0.854eV, and the half-metallicity is enhanced obviously when Li is deficient. Li excess system is also an indirect band gap semiconductor with the band gap of 2.560 eV. However, neither of the majority-spin and minority-spin impurity bands crosses the Fermi level. Therefore, $Li_{1.125}(Mg_{0.875}Cr_{0.125})P$ change back to semiconducting nature again.

The calculated total and partial density of states (DOS) for $Li_{1\pm y}(Mg_{1-x}Cr_x)P$ are shown in **Figure 3**. For pure LiMgP, we can find that there are two peaks in the valence band of TDOS (1 and 2 in **Figure 3A**). Peak 1 is mainly contributed by the electrons of Mg-3s and P-3p states and peak 2 mainly contains the electrons of Li-2s, Mg-2p, and P-3p states. The conduction band is mainly composed of the electrons of Li-2s, Mg-2p, and Mg-3s, and the Mg-2p states. The states of spin-up and spin-down are well-symmetry, revealing that pure LiMgP has no net magnetic moment. For Cr doped system, Li-2s, P-3p, and Cr-3d orbitals hybridize near the Fermi energy (**Figure 3B**), resulting in that the t_{2g} and e_g energy levels of Cr-3*d* state are separated from each other, and the t_{2g} energy level is pushed toward the Fermi level, induce $Li(Mg_{0.875}Cr_{0.125})P$ to become half-metallic ferromagnetism. When Li is deficient, the electrons of P-3p and Cr-3d states have the stronger p-d orbitals hybridization (**Figure 3C**). The t_{2g} levels are pushed up even further, making its occupation states reduce from three to one, which causes that the spin-flip band gap of $Li_{0.875}(Mg_{0.875}Cr_{0.125})P$ increases. When Li is excess, only a weak hybridization of p-d orbitals appears near

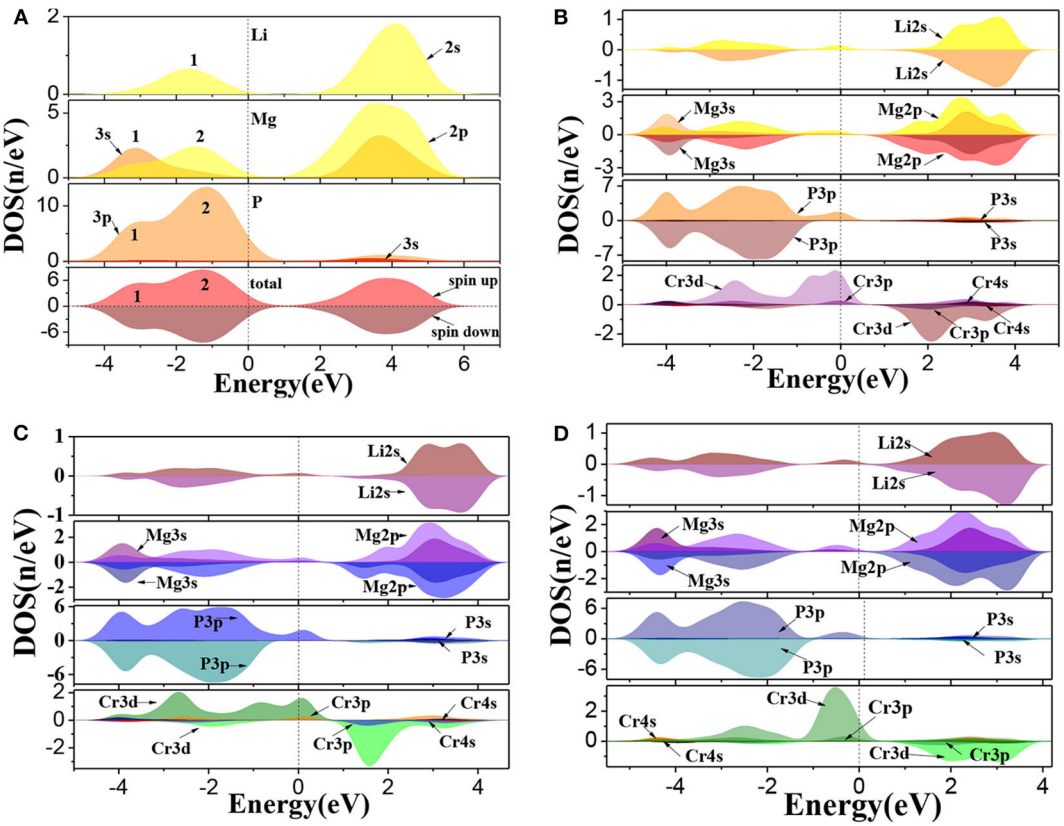

FIGURE 3 | The density of states of $Li_{1\pm y}(Mg_{1-x}Cr_x)P$: **(A)** LiMgP, **(B)** $Li(Mg_{0.875}Cr_{0.125})P$, **(C)** $Li_{0.875}(Mg_{0.875}Cr_{0.125})P$, and **(D)** $Li_{1.125}(Mg_{0.875}Cr_{0.125})P$.

the Fermi energy, and the t_{2g} levels is completely occupied by electrons. The half-metallicity disappears.

Moreover, the net magnetic moment is also calculated by integrating the occupied states below the Fermi energy and shown in **Table 3**. The obtained net magnetic moments are 4.08 μ_B, 2.98 μ_B, and 4.90 μ_B for the Cr doped, Li vacancy, and l Li excess system, respectively. The result indicates that the impurity band width and the net magnetic moments increase with the increasing of Li concentration.

Figure 4 shows the plots of charge density difference for $Li_{1\pm y}(Mg_{1-x}Cr_x)P$. For pure LiMgP (**Figure 4a**), the electron cloud of the P atom close to the Mg atom is denser. The second orbital of the P atom is polarized, and the electrons move inward. The Mg and P atoms form polarized covalent bonds. When Cr doped (**Figure 4b**), the P atoms gain more electrons from Cr atoms than the Mg atoms, indicating that the Cr-P polarized covalent bonds are stronger than that those of the Mg-P, which can be attributed to the strong hybridization between Li-2*s*, P-2p, and Cr-3d orbitals. When Li is deficient, the charge density between Li and P atoms becomes weaker, meanwhile, the charge density between Cr and P atoms turn stronger, indicating that P atoms cannot gain electrons from Li atoms, so the more charges need to be gained from Cr atoms. It can be seen in **Figure 4d** that P atoms can gain more electrons from Li atoms, resulting in that the charge loss of Cr atoms becomes less and the Cr-P polar covalent bonds become weaker for Li excess system.

Optical Properties of $Li_{1\pm y}(Mg_{1-x}Cr_x)P$

To further investigate the effects of Cr doping and Li off-stoichiometry on properties of $Li_{1\pm y}(Mg_{1-x}Cr_x)P$, the imaginary part of dielectric functions, complex refractive index functions, optical absorption spectra and energy loss spectra are also calculated and shown in **Figure 5**. We can find from **Figure 5A** that there is a dielectric peak at $E = 4.27$ eV, corresponding to the direct transition of P-3p in valence bands to Li-2s, Mg-3s, and Mg-2p states in conduction bands. It is worth noting that a new peak occurs in the low energy region and the peak at $E = 4.27$ eV reduces after Cr doping. Moreover, we also find that the new peak is significantly enhanced when Li is deficient, but when Li is excess the new peak disappears, and the main peak moves slightly toward the low energy region. The refractive index for pure LiMgP is 2.571 (**Figure 5B**). In the lower energy ($E<1.82$ eV) and higher energy ($E>11.54$ eV) region, the imaginary part of the complex refractive index function is zero, and the real part is a constant, indicating that the absorption of LiMgP is limit to a certain frequency range. Similarly to the dielectric functions, there are also new peaks in the low energy region of complex refractive index functions after Cr doping, implying that the absorption range of low frequency electromagnetic wave is enlarged for the doped systems. It can be seen in **Figure 5C** that a new peak of the optical absorption spectrum also appears in the low energy region after Cr doping, the main peak of absorption spectrum moves slightly toward

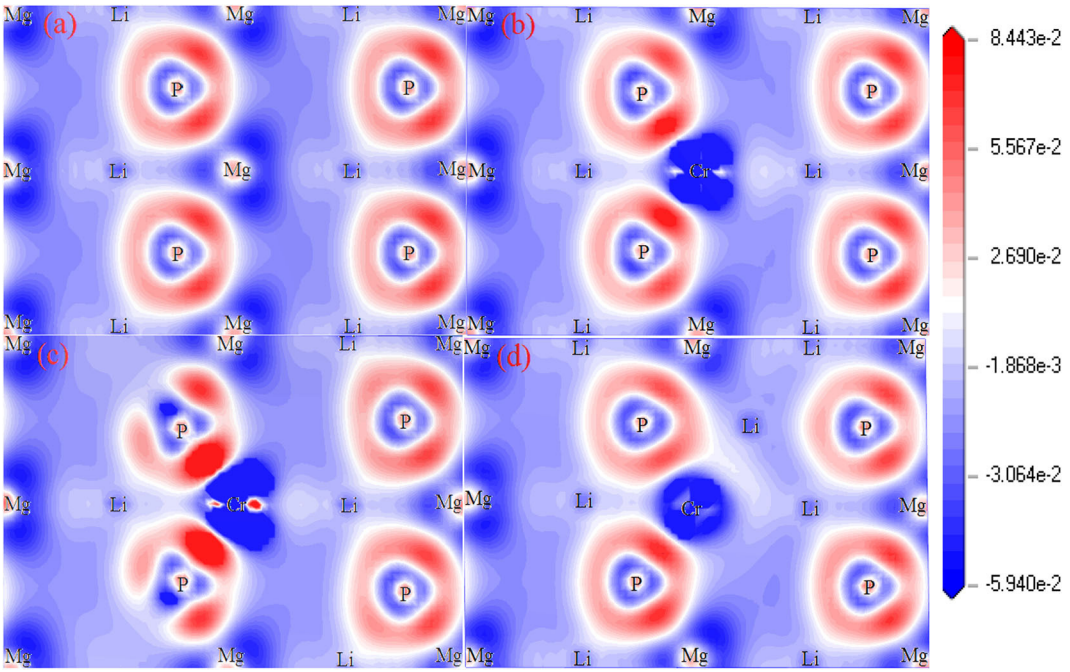

FIGURE 4 | The charge density difference of $Li_{1\pm y}(Mg_{1-x}Cr_x)P$: **(a)** LiMgP, **(b)** $Li(Mg_{0.875}Cr_{0.125})P$, **(c)** $Li_{0.875}(Mg_{0.875}Cr_{0.125})P$, and **(d)** $Li_{1.125}(Mg_{0.875}Cr_{0.125})$.

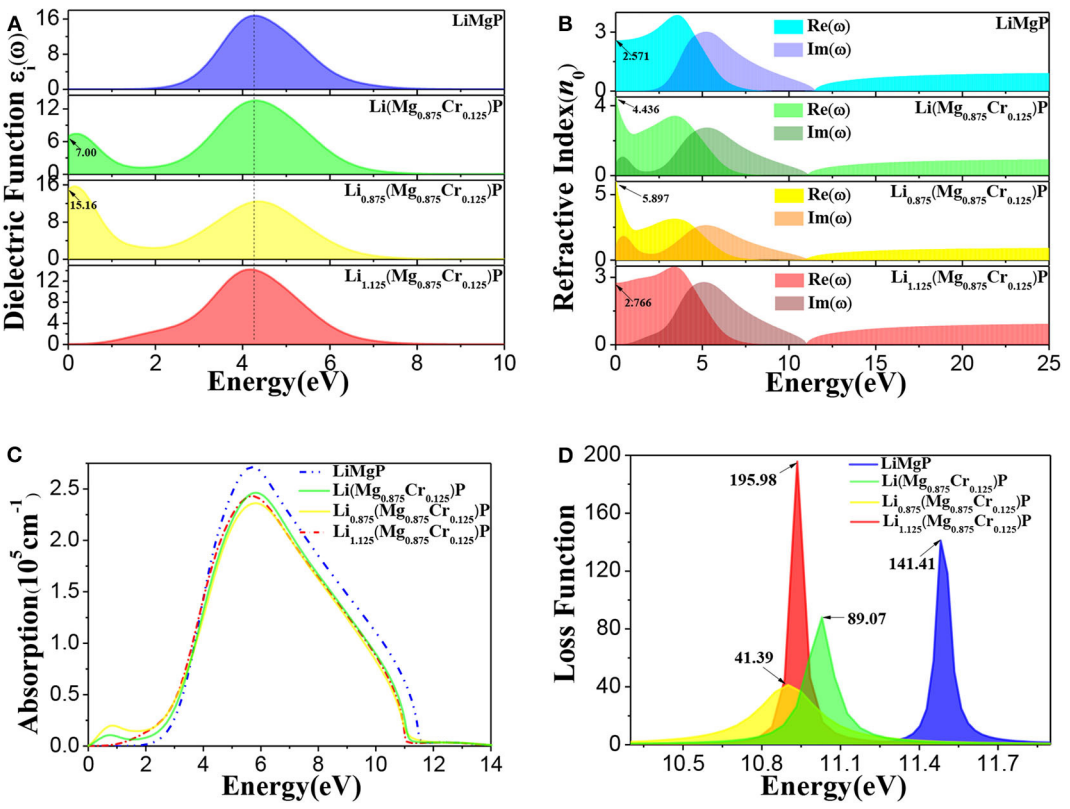

FIGURE 5 | The optical properties of $Li_{1\pm y}(Mg_{1-x}Cr_x)P$: **(A)** imaginary part of dielectric functions, **(B)** complex refractive index functions, **(C)** optical absorption spectra, **(D)** energy loss spectra.

the low energy region, demonstrating again that the absorption of low frequency electromagnetic wave is enhanced. As shown in **Figure 5D**, the energy loss functions also move obviously toward the low energy region, implying the red-shift effect for the doped systems. The energy loss for $Li(Mg_{0.875}Cr_{0.125})P$, $Li_{0.875}(Mg_{0.875}Cr_{0.125})P$, and $Li_{1.125}(Mg_{0.875}Cr_{0.125})P$ are about 63%, 29% and 138% of that for LiMgP, respectively.

SUMMARY

The electronic structures, magnetic and optical properties of $Li_{1\pm y}(Mg_{1-x}Cr_x)P$ (x, y = 0, 0.125) are calculated by using the first principles method based on density functional theory. We find that the Cr doped systems exhibit the half-metallic ferromagnetism. Due to the Cr doping, sp-d orbitals hybridization leads to spin-polarized impurity bands and form stronger Cr-P polar covalent bonds. Moreover, we also find that the properties of the doped systems can be regulated by Li off-stoichiometry. The impurity band width and the net magnetic moment increase with the increasing of Li concentration, but the half-metallicity and the conductivity decrease. When Li is excess, the p-d orbitals hybridization obviously becomes weaker and the half-metallicity disappears. Comparing optical properties shows that the imaginary part of dielectric, the complex refractive index function and the optical absorption spectrum all have a new peak in the low energy region after Cr doping, and the new peaks are significantly enhanced when Li is deficient. The absorption range of low frequency electromagnetic wave is enlarged, and the energy loss functions show obvious red-shift effect for the doped systems. The results indicate that the properties of Li(Mg,Cr)P can be controlled by Cr doping and Li off-stoichiometry independently, which will benefit potential spintronics applications.

DATA AVAILABILITY STATEMENT

The raw data supporting the conclusions of this article will be made available by the authors, without undue reservation.

AUTHOR CONTRIBUTIONS

All authors listed have made a substantial, direct and intellectual contribution to the work, and approved it for publication.

FUNDING

The work described in this paper was supported by Chongqing Natural Science Foundation of China (Grant No. cstc2019jcyj-msxmX0251).

REFERENCES

Cui, Y., Zhu, J. G., Tao, H. L., Liu, S. M., Lv, Y. Z., He, M., et al. (2019). Magnetic properties of diluted magnetic semiconductors Li(Zn,TM)N with decoupled charge and spin doping (TM: V, Cr, Mn, Fe, Co and Ni). *Comp. Mater. Sci.* 158, 260–264. doi: 10.1016/j.commatsci.2018.11.022

Deng, Z., Jin, C. Q., Liu, Q. Q., Wang, X. C., Zhu, J. L., Feng, S. M., et al. (2011). Li(Zn,Mn)As as a new generation ferromagnet based on a I-II-V semiconductor. *Nat. Commun.* 2:422. doi: 10.1038/ncomms1425

Dietl, T. (2010). A ten-year perspective on dilute magnetic semiconductors and oxides. *Nat. Mater.* 9, 965–974. doi: 10.1038/nmat2898

Godby, R. W., Schluter, M., and Sham, L. J. (1988). Self-energy operators and exchange-correlation potentials in semiconductors. *Phys. Rev. B* 37, 10159–10175. doi: 10.1103/PhysRevB.37.10159

Guo, R. K., Liu, G. D., Wang, X. T., Rozale, H., Wang, L. Y., Khenata, R., et al. (2016). First-principles study on quaternary Heusler compounds ZrFeVZ (Z = Al, Ga, In) with large spin-flip gap. *RSC Adv.* 6, 109394–109400. doi: 10.1039/C6RA18873G

Han, W., Chen, B. J., Gu, B., Zhao, G. Q., Yu, S., Wang, X. C., et al. (2019). Li(Cd,Mn)P: a new cadmium based diluted ferromagnetic semiconductor with independent spin & charge doping. *Sci. Rep.* 9:7490. doi: 10.1038/s41598-019-43754-x

Jungwirth, T., Sinova, J., Masek, J., Kucera, J., and MacDonald, A. H. (2006). Theory of ferromagnetic (III,Mn)V semiconductors. *Rev. Mod. Phys.* 78, 809–864. doi: 10.1103/RevModPhys.78.809

Kacimi, S., Mehnane, H., and Zaoui, A. (2014). I-II-V and I-III-IV half-Heusler compounds for optoelectronic applications: comparative ab initio study. *J. Alloy. Compd.* 587, 451–458. doi: 10.1016/j.jallcom.2013.10.046

Kuriyama, K., Kushida, T., and Taguchi, R. (1998). Optical band gap of the ordered filled-tetrahedral semiconductor LiMgP. *Solid State Commun.* 108, 429–432. doi: 10.1016/S0038-1098(98)00384-6

Mašek, J., Kudrnovsky, J., Maca, F., Gallagher, B. L., Campion, R. P., Gregory, D. H., et al. (2007). Dilute moment n-type ferromagnetic semiconductor Li(Zn,Mn)As. *Phys. Rev. Lett.* 98:067202. doi: 10.1103/PhysRevLett.98.067202

Monkhorst, H. J., and Pack, J. D. (1976). Special points for brillouin-zone integrations. *Phys. Rev. B* 13, 5188–5192. doi: 10.1103/PhysRevB.13.5188

Ohno, H. (1998). Making nonmagnetic semiconductors ferromagnetic. *Science* 281, 951–956. doi: 10.1126/science.281.5379.951

Payne, M. C., Teter, M. P., Allan, D. C., Arias, T. A., and Joannopoulos, J. D. (1992). Iterative minimization techniques for abinitio total-energy calculations molecular dynamics and conjugate gradients. *Rev. Mod. Phys.* 64, 1045–1097. doi: 10.1103/RevModPhys.64.1045

Perdew, J. P., Burke, K., and Ernzerhof, M. (1996). Generalized gradient approximation made simple. *Phys. Rev. Lett.* 77, 3865–3868. doi: 10.1103/PhysRevLett.77.3865

Perdew, J. P., and Levy, M. (1983). Physical content of the exact Kohn-Sham orbital energies band gaps and derivative discontinuities. *Phys. Rev. Lett.* 51, 1884–1887. doi: 10.1103/PhysRevLett.51.1884

Potashnik, S. J., Ku, K. C., Chun, S. H., Berry, J. J., Samarth, N., and Schiffer, P. (2001). Effects of annealing time on defect-controlled ferromagnetism in $Ga_{1-x}Mn_xAs$. *Appl. Phys. Lett.* 79, 1495–1497. doi: 10.1063/1.1398619

Segall, M. D., Lindan, P. J. D., Probert, M. J., Pickard, C. J., Hasnip, P. J., Clark, S. J., et al. (2002). First-principles simulation: ideas, illustrations and the CASTEP code. *J. Phys. Condens. Mat.* 14, 2717–2744. doi: 10.1088/0953-8984/14/11/301

Shang, G., Peacock, P. W., and Robertson, J. (2004). Stability and band offsets of nitrogenated high-dielectric-constant gate oxides. *Appl. Phys. Lett.* 84:106. doi: 10.1063/1.1638896

Tao, H. L., Wang, M. X., Zhang, Z. H., He, M., and Song, B. (2017). Effects of transition metal (TM = V, Cr, Mn, Fe, Co, and Ni) elements on magnetic mechanism of LiZnP with decoupled charge and spin doping. *J. Supercond. Nov. Magn.* 30, 2823–2828. doi: 10.1007/s10948-017-4037-1

Vanderbilt, D. (1990). Soft self-consistent pseudopotentials in a generalized eigenvalue formalism. *Phys. Rev. B* 41, 7892–7895. doi: 10.1103/PhysRevB.41.7892

Wang, Q., Man, H. Y., Ding, C., Gong, X., Guo, S. L., Jin, H. K., et al. (2014). $Li_{1.1}(Zn_{1-x}Cr_x)As$: Cr doped I-II-V diluted magnetic semiconductors in bulk form. *J. Appl. Phys.* 115:083917. doi: 10.1063/1.4867299

Wolf, S. A., Awschalom, D. D., Buhrman, R. A., Daughton, J. M., von Molnar, S., Roukes, M. L., et al. (2001). Spintronics: A spin-based electronics vision for the future. *Science* 294, 1488–1495. doi: 10.1126/science.1065389

Zutic, I., Fabian, J., and Das Sarma, S. (2004). Spintronics: fundamentals and applications. *Rev. Mod. Phys.* 76, 323–410. doi: 10.1103/RevModPhys.76.323

Conflict of Interest: The authors declare that the research was conducted in the absence of any commercial or financial relationships that could be construed as a potential conflict of interest.

frontiers in Chemistry

ORIGINAL RESEARCH
published: 05 November 2020
doi: 10.3389/fchem.2020.609118

Realization of Opened and Closed Nodal Lines and Four- and Three-fold Degenerate Nodal Points in XPt (X = Sc, Y, La) Intermetallic Compound: A Computational Modeling Study

*Heju Xu**

College of Science, North China University of Science and Technology, Tangshan, China

Realizing rich topological elements in topological materials has attracted increasing attention in the fields of chemistry, physics, and materials science. Topological semimetals/metals are classified into three main types: nodal-point, nodal-line, and nodal-surface types with zero-, one-, and two-dimensional topological elements, respectively. This study reports that XPt (X = Sc, Y, La) intermetallic compounds are topological metals with opened and closed nodal lines, and triply degenerate nodal points (TNPs) when the spin–orbit coupling (SOC) is ignored. Based on the calculated phonon dispersions, one can find that ScPt and YPt are dynamically stable whereas LaPt is not. When SOC is added, the one-dimensional nodal line and zero-dimensional TNPs disappear. Interestingly, a new zero-dimensional topological element, that is, Dirac points with 4-fold degenerate isolated band crossings with linear band dispersion appear. The proposed materials can be considered a good platform to realize zero- and one-dimensional topological elements in a single compound and to study the relationship between zero- and one-dimensional topological elements.

Keywords: 4-fold degenerate nodal point, triply degenerate nodal point (TNP), spin-orbit coupling (SOC), topological element, phonon dispersion

OPEN ACCESS

Edited by:
Xiaotian Wang,
Southwest University, China

Reviewed by:
Jiangchao Han,
Beihang University, China
Xiaoming Zhang,
Hebei University of Technology, China

***Correspondence:**
Heju Xu
xuheju@ncst.edu.cn

Specialty section:
This article was submitted to Theoretical and Computational Chemistry, a section of the journal Frontiers in Chemistry

Received: *22 September 2020*
Accepted: *12 October 2020*
Published: *05 November 2020*

Citation:
Xu H (2020) Realization of Opened and Closed Nodal Lines and Four- and Three-fold Degenerate Nodal Points in XPt (X = Sc, Y, La) Intermetallic Compound: A Computational Modeling Study. Front. Chem. 8:609118. doi: 10.3389/fchem.2020.609118

INTRODUCTION

In the last decade, with the discovery of topological insulators (Cava et al., 2013; Kou et al., 2013; Zhao et al., 2013; Shen and Cha, 2014; Wang et al., 2014; Luo et al., 2015; Zhou et al., 2015; Liu et al., 2016; Chen et al., 2017a; Loïc and Izmaylov, 2017; Pan et al., 2017; Pielnhofer et al., 2017; Politano et al., 2017; Andrey et al., 2018; Hu et al., 2018, 2019; Gao et al., 2019; Mal et al., 2019; Qiao et al., 2019; Narimani et al., 2020), topologically non-trivial materials have attracted significant interest in the chemistry, physics, and materials science communities. Recently, studies have increasingly focused on topological semimetals/metals (Bin et al., 2018; Chenguang et al., 2018; Zhou et al., 2018; He et al., 2019, 2020; Jin et al., 2019a, 2020b; Li et al., 2019; Qie et al., 2019; Xie et al., 2019; Yi et al., 2019; Zhong et al., 2019; Ma and Sun, 2020; Meng et al., 2020b; Wang et al., 2020a,c,d; Yang and Zhang, 2020; Zhang et al., 2020; Zhao et al., 2020) with non-trivial band topology. For example, in 2018, Schoop et al. (2018) described the key features of the electronic structures of topological semimetals/metals and how these structures can be realized based on chemical principles.

Topological semimetals/metals can be roughly classified into three main parts: nodal-point (Chen et al., 2015; Yuan et al., 2017; Zhang et al., 2017a,c, 2018c; Jing and Heine, 2018; Ma et al., 2018; Tsipas et al., 2018; Khoury et al., 2019), nodal-line (Chang et al., 2016; Liu et al., 2018b; Guo et al., 2019; Sankar et al., 2019; Tang et al., 2019; Xu et al., 2019; Zhang et al., 2019; Jin et al., 2020a; Kirby et al., 2020; Zhou et al., 2020), and nodal-surface (Türker and Sergej, 2018; Wu et al., 2018; Zhang et al., 2018b,d; Fu et al., 2019; Yang et al., 2019b, 2020; Chen et al., 2020; Wang et al., 2020e; Xiao et al., 2020) semimetals/metals enjoying zero-, one-, and two-dimensional topological elements, respectively. The main examples of nodal-point semimetals/metals are Weyl and Dirac semimetals/metals with 2- and 4-fold degenerate band-crossing points with linear dispersion. In addition, 3-, 6-, and 8-fold (Cano and Vergniory, 2016; Lu et al., 2016; Weng et al., 2016b) band degenerates also exist. Among them, nodal-point semimetals/metals with 3-fold band degenerates [i.e., triply degenerate nodal point (TNP)] are of importance owing to their special properties. Many investigations have been conducted to predict and confirm new TNP semimetals/metals (Weng et al., 2016a; Xia and Li, 2017; Zhang et al., 2017b,d; Guo et al., 2018; Owerre, 2018; Jin et al., 2019b; Yang et al., 2019a). For example, in 2019, Jin et al. (2019b) reported that centrosymmetric Li_2NaN is a topological material with critical-type TNPs. A critical-type TNP is an interesting topological metal phase that lies between type-I and type-II TNPs. In 2018, Guo et al. (2018) proposed that YRh_6Ge_4, $LaRh_6Ge_4$, and $LuRh_6Ge_4$ are TNP materials, and what is more, Zhu et al. (2020) performed transport measurements and confirmed TNP fermions in YRh_6Ge_4. In 2019, Yang et al. (2019a) experimentally demonstrated TNP as well as double Fermi arc surface states in a three-dimensional phononic crystal.

Nodal-line semimetals/metals with one-dimensional topological elements may show various forms according to the shape of the nodal lines, such as nodal link (Yan et al., 2017), nodal chain (Yan et al., 2018), nodal box (Sheng et al., 2017), nodal ring (Zhang et al., 2018a; Wang et al., 2020b), nodal knot (Bi et al., 2017; Lee et al., 2018), and nodal net (Feng et al., 2018). For example, in 2018, Zhou et al. (2018) proposed that two-dimensional B_2C hosts opened and closed nodal-line states based on first-principles calculation. In 2020, Yi et al. (2019) predicted that NaAlGe and NaAlSi nodal-line materials would be good cathode materials for sodium ion batteries. In 2020, Wang et al. (2020d) proposed that a two-dimensional Nb_3GeTe_6 monolayer is a topological nodal-line material with a nearly flat nodal line around the Fermi level and that it led to a remarkable thermoelectric power factor platform. In 2018, Liu et al. (2018a) proposed that graphene monolith, a three-dimensional nodal-line semimetal, is a candidate lithium ion battery anode material. In 2019, Yan et al. (2019) proposed that the Cu_2Si monolayer is a topological material with possible superconductivity and nodal-line fermions.

The electronic structure, dynamical stability, and topological signatures of ScPt, YPt, and LaPt, a cubic-type family of materials with $Pm\bar{3}m$ space group are investigated in the present study. This study shows that opened and closed nodal lines and 3-fold degenerate nodal-point states can be realized in ScPt, LaPt, and LuPt when the spin-orbit coupling is ignored. Moreover, the effect of spin-orbit coupling on the topological signatures of these systems is also considered. A 3- to 4-fold degenerate nodal-point transition can be found in these systems when spin-orbit coupling is added.

MATERIALS

The topological signatures of cubic-type ScPt, YPt, and LaPt are investigated. As an example, **Figure 1A** shows the structural model of cubic ScPt. This primitive ScPt cell contains one Sc atom and one Pt atom at the (0.5, 0.5, 0.5) and (0, 0, 0) sites, respectively. Using first-principles calculation, the structural models of ScPt, YPt, and LaPt are fully optimized; **Table 1** lists the calculated results.

The phonon dispersions of cubic-type ScPt, YPt, and LaPt are calculated using the force-constants method with Phonopy code (Togo and Tanaka, 2015). For these three compounds, $2 \times 2 \times 2$ supercells are built to calculate the phonon dispersions. The considered high-symmetry points are Γ-X-M-Γ-R-X, as shown in **Figure 1B**. **Figures 1C**, **2A** exhibit the calculated phonon dispersions of ScPt and YPt; one can find that ScPt and YPt are dynamically stable owing to the absence of the imaginary frequency (Han et al., 2019; Wu et al., 2019). However, the obtained phonon dispersion shown in **Figure 2B** indicates that LaPt is not dynamically stable.

COMPUTATIONAL METHODS

In this study, first-principles calculations are used, and the generalized gradient approximation (GGA) (Perdew et al., 1996) of the Perdew–Burke–Ernzerhof (PBE) (Perdew et al., 1998) functional is adopted for the exchange-correlation potential. In the calculations, the cutoff energy is set as 600 eV, and the Brillouin zone is sampled using a Monkhorst-Pack *k*-mesh with a size of $9 \times 9 \times 9$. To ensure good convergence, the calculations continue until the energy deviation is $<10^{-6}$ eV/atom. The atomic positions and lattice constants of the structures were totally relaxed until all the force components were smaller than 10^{-3} eV/Å.

RESULTS AND DISCUSSION

First, the physical natures of ScPt, YPt, and LaPt are determined. **Figures 1D**, **3A,C**, respectively, show the band structures of ScPt, YPt, and LaPt along the R-X-M-R-Γ paths. The spin–orbit coupling (SOC) is not added for the band structures in these figures; the effect of SOC on the electronic structures of these compounds will be discussed later in this paper. These three figures show that the bands and the Fermi level overlap each other, indicating common metallic behaviors.

Moreover, some obvious band crossings are seen around the Fermi level, namely, point A along the R-X path, point B along the X-M path, and point C along the M-R path. A careful study of these three band-crossing points indicates that points A and B are doubly degenerate band-crossing points,

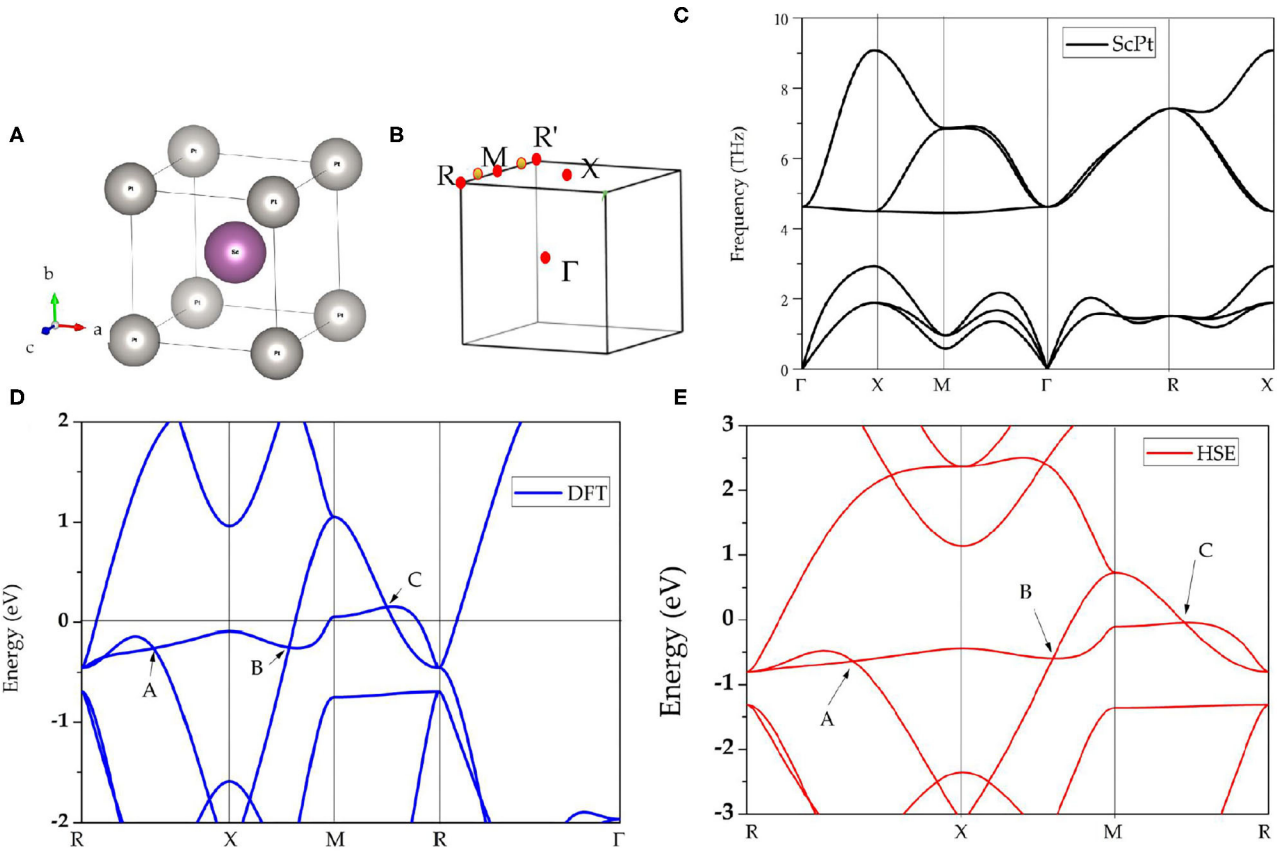

FIGURE 1 | (A) Crystal structures of cubic ScPt; **(B)** Brillouin zone and the considered high-symmetry points Γ-X-M-Γ-R-X; **(C)** calculated phonon dispersion of cubic ScPt at its optimized lattice constant; **(D)** calculated band structure of cubic ScPt with PBE method, where **(A–C)** indicate the band-crossing points around the Fermi level; and **(E)** calculated band structure of ScPt with Heyd–Scuseria–Ernzerhof (HSE) screened hybrid functional.

TABLE 1 | Optimized lattice constants for ScPt, YPt, and LaPt.

Compounds	a (Å)	b (Å)	c (Å)
ScPt	3.283	3.283	3.283
YPt	3.488	3.488	3.488
LaPt	3.659	3.659	3.659

whereas point C is a 3-fold degenerate band-crossing point formed by a doubly degenerate band and a non-degenerate band. Apart from these three clear band-crossing points, the band structure near the Fermi level is very clean; therefore, these three points dominate the topological signatures of these compounds. For clarity, hereafter, ScPt is used as an example to investigate the band topology considering that the band structures of ScPt, YPt, and LaPt are almost the same near the Fermi level.

Figure 1E shows the band structure of ScPt with the revised Heyd–Scuseria–Ernzerhof (HSE) (Heyd and Scuseria, 2004) screened hybrid functional. The HSE method is well-known to be accurate for describing the band gap of topological materials. In particular, for some *d*-orbital-dominated systems, the GGA method cannot provide a fair evaluation of the band gap around the Fermi level. **Figures 1D,E** show that the band-crossing points A, B, and C are still maintained under the HSE method; this confirms that the GGA method is suitable for investigating the electronic structure of the ScPt system.

In addition to SOC, the ScPt system enjoys time reversal (T) and spatial inversion (P) symmetries. Basically, doubly degenerate band crossings like points A and B should not be isolated (Weng et al., 2016b; Zhang et al., 2018b). Instead, they should belong to one type of nodal structure; they most commonly belong to a nodal-line structure. As shown in **Figures 1D**, **3A,C**, two bands cross each other and form two band-crossing points A and B along the R-X and X-M paths. Symmetry analysis shows that these two bands belong to irreducible representations A_{1g} and A_{2u} of D_{4h} symmetry, respectively.

Figure 4A shows the X-centered 3D band dispersion of the $k_z = \pi$ plane. The two above-mentioned bands form a closed nodal line in the $k_z = \pi$ plane (highlighted by a white line), and points A and B belong to this closed nodal line. The crystal symmetry of the ScPt cubic system implies three closed nodal lines in the $k_{x/y/z} = \pi$ planes. The nodal lines are located in the mirror-invariant plane, and they protect the mirror symmetry $M_{x,y,z}$. As

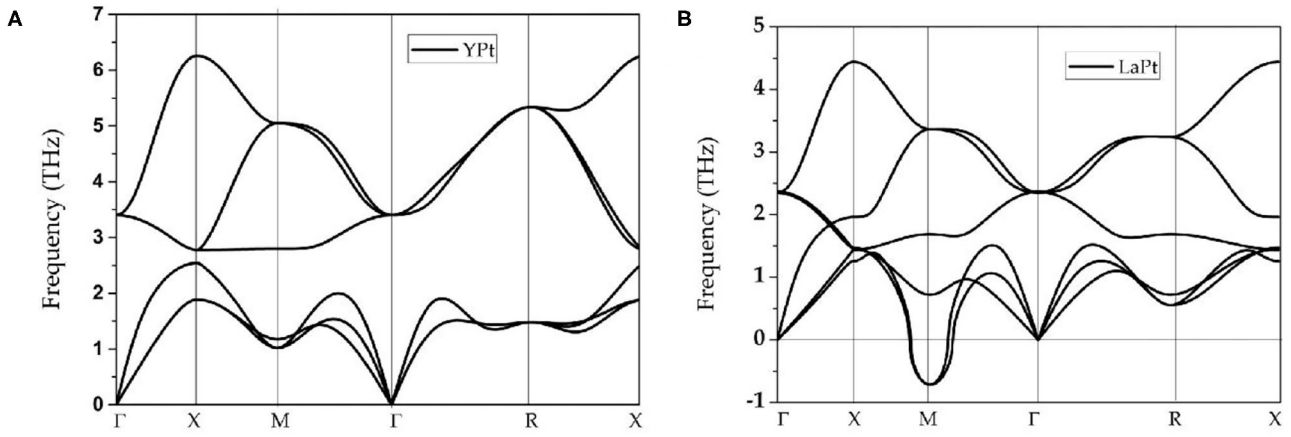

FIGURE 2 | (A,B) Calculated phonon dispersion of cubic YPt and LaPt, respectively, at their optimized lattice constants. The phonon dispersions of both intermetallic compounds are obtained using the force-constants method with Phonopy code.

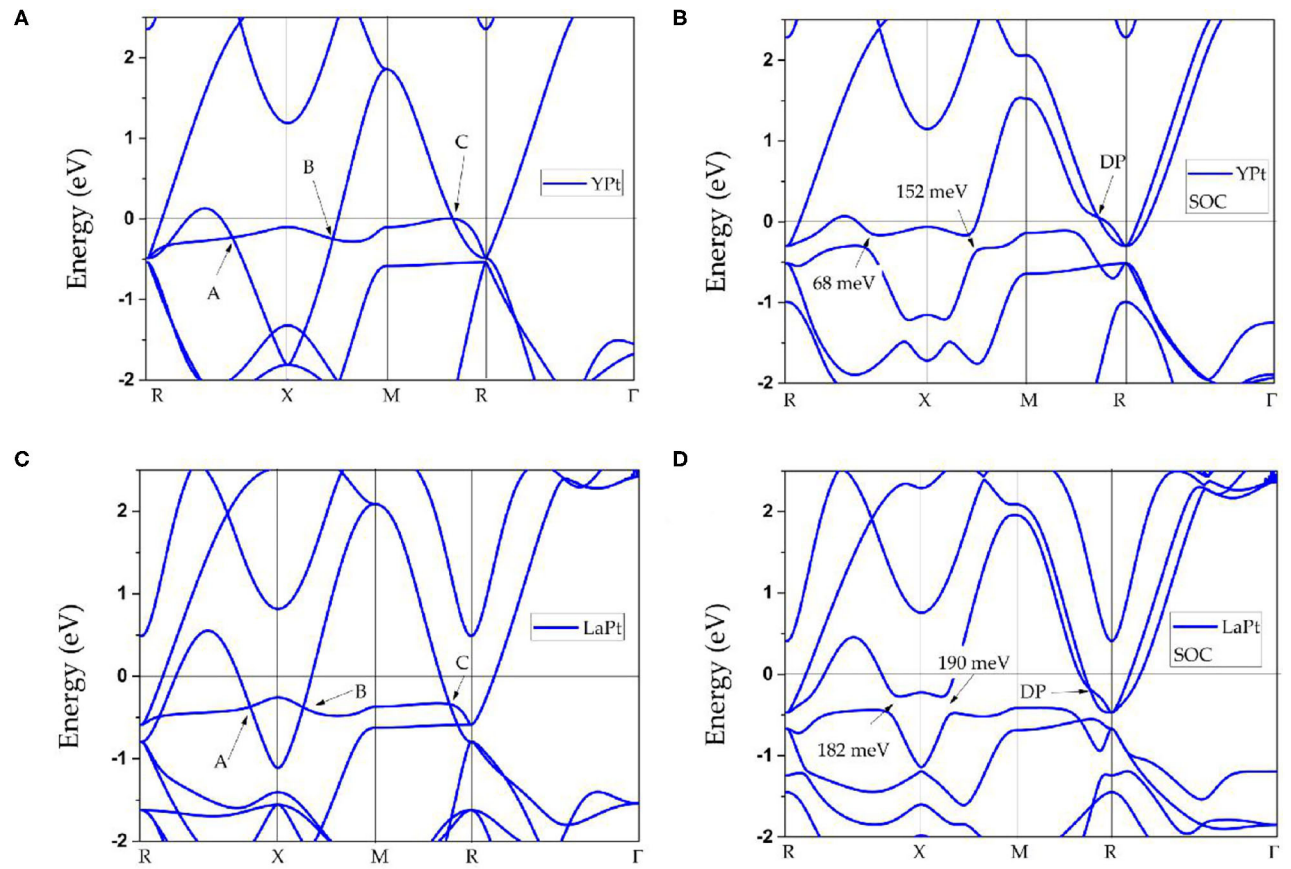

FIGURE 3 | (A–D) Calculated band structures of cubic YPt and LaPt with their optimized lattice constants. The spin–orbit coupling effect is neglected for **(A,C)** and added for **(B,D)**.

an example, **Figure 4B** shows the shape of the X-centered closed nodal line in the $k_z = \pi$ plane.

Figure 4C shows the R-centered 3D band dispersion in the $k_z = \pi$ plane; here, TNPs are indicated by green balls. As shown in **Figures 1D**, **3A,C**, the band-crossing point C is formed by a 2-fold degenerate band and a non-degenerate band along the M-R path. This 2-fold degenerate band can be seen as two independent bands that are completely degenerated along the whole M-R path.

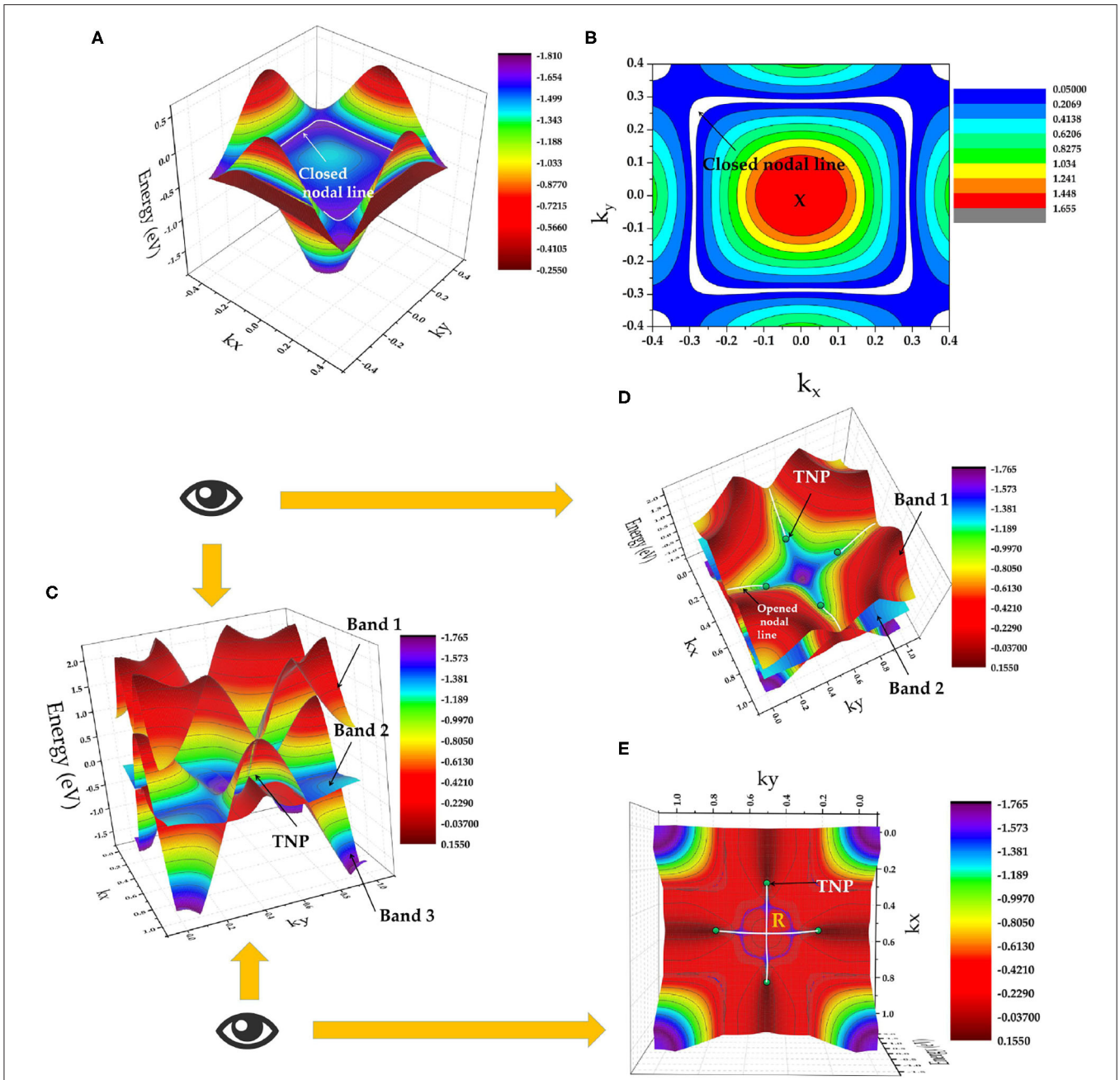

FIGURE 4 | (A) X-centered 3D band dispersion in the $k_z = \pi$ plane; **(B)** shape of closed X-nodal line in the $k_z = \pi$ plane (nodal line is indicated by white lines and marked by arrows); **(C)** R-centered 3D band dispersion in the $k_z = \pi$ plane, where TNPs and bands 1, 2, and 3 are marked by arrows; **(D)** top view of **(C)**; and **(E)** bottom view of **(C)**. The TNPs and the opened nodal lines (formed by degenerate bands 1 and 2) are indicated by green balls and white lines, respectively.

Therefore, this 2-fold degenerate band (named as band 1 and band 2) should contain a series of band-crossing points along the whole M-R path and form an opened nodal line along the M-R path. To clearly present the opened nodal lines and the TNPs in ScPt, **Figures 4D,E**, respectively, show top and bottom views of **Figure 4C**. These figures clearly show the opened nodal lines formed from bands 1 and 2 along the R-M path as well as the TNPs. Therefore, ScPt, YPt, and LaPt are topological metals that co-exhibit opened and closed nodal lines when the spin-orbit coupling is ignored. Based on the above-mentioned results, the ScPt family of materials is a good platform to study the relationship of closed and opened nodal lines.

Moreover, band-crossing point C along the M-R path is a TNP. Normally, TNP can not only occur in isolation but also

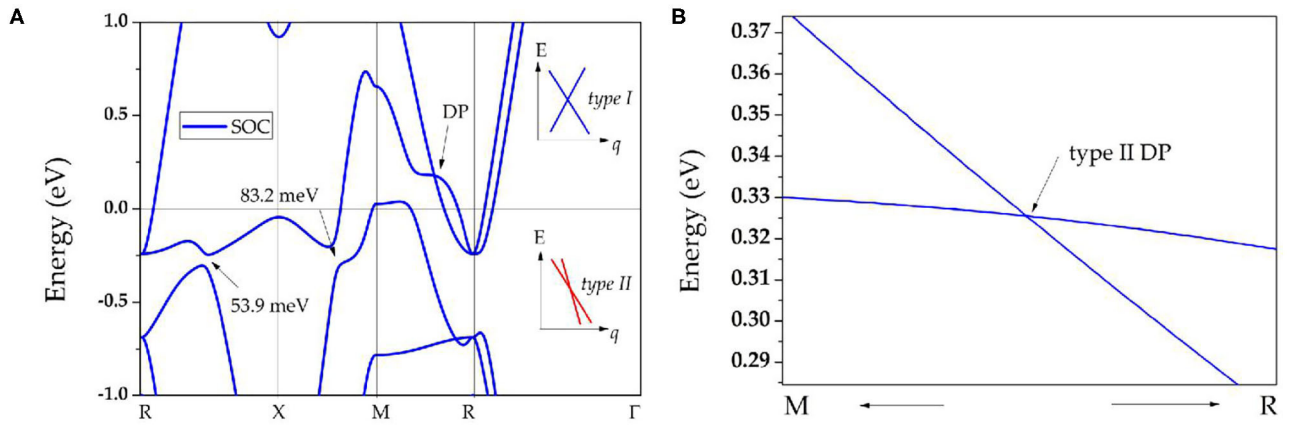

FIGURE 5 | (A) Band structure of ScPt with spin–orbit coupling; the insets show schematics of types I and II nodal points, indicated by blue and red lines, respectively; for type I nodal points, they are conventional type band dispersion, however, for type II nodal points, they enjoy a tilted band dispersion; **(B)** enlarged band structure of ScPt along the M-R path slightly above the Fermi level.

be linked by nodal lines in the momentum space. One pair of TNPs exists in ScPt, YPt, and LaPt. **Figure 1B** shows a schematic of the pair of TNPs (indicated by yellow balls) along the R-M-R′ path. As shown in **Figure 4C**, the TNPs are located at the crossing of band 3 (non-degenerate band) and bands 1 and 2 (2-fold degenerate band). Therefore, ScPt is concluded to have one-dimensional topological elements, namely, opened and closed nodal lines (in the $k_{x/y/z} = \pi$ plane) and a zero-dimensional topological element, namely, TNP, along the R-M-R′ path when the spin-orbit coupling is ignored. Therefore, ScPt, LaPt, and YPt are excellent target materials for studying the entanglement between nodal-line and nodal-point fermions.

Finally, the effect of SOC on the band structures of ScPt, YPt, and LaPt is investigated. The corresponding results are shown in **Figures 5A**, **3B,D**, respectively. The gaps induced by SOC for band-crossing points A and B are 53.9 and 83.2 meV, 68 and 152 meV, and 182 and 190 meV for ScPt, YPt, and LaPt, respectively. In comparison, the gaps induced by SOC in the well-known nodal-line materials Cu_2NPd (Yu et al., 2015), CaAgBi (Chen et al., 2017b), and $BaSn_2$ (Huang et al., 2016) are 60–100 meV, 80–140 meV, and 60–160 meV, respectively. Therefore, ScPt and YPt are comparable to these reference materials.

Moreover, **Figures 5B**, **3B,D** show that the TNPs disappear in ScPt, YPt, and LaPt systems. However, a new topological signature reveals a nodal point with linear band dispersion around the Fermi level. When the SOC effect was considered, each band was doubly degenerate. Therefore, the newly occurring nodal point along the along R-M path should be a Dirac nodal point (DP) with 4-fold degeneracy. Specifically, a pair of DPs with 4-fold degeneracy is found along the R-M-R′ path. Notably, similar SOC-induced TNP–DP transitions have also been reported in ErAs (Meng et al., 2020a), TiB_2 (Zhang et al., 2017d), and Li_2NaN (Jin et al., 2019b) topological materials. However, unlike the type-I DP predicted for ErAs, this is a type-II DP that may show strong anisotropy (Zhang et al., 2018b).

SUMMARY

In summary, cubic-type ScPt, YPt, and LaPt are shown to be newly designed topological materials through the use of density functional theory. ScPt and YPt are dynamically stable whereas LaPt is not. Without SOC, XPt (X = Sc, Y, La) metals show closed and opened nodal-line states and one pair of TNPs. With SOC, the TNPs (along the R-M-R′ path) change to type-II DPs and the nodal-line states in $k_{x/y/z} = \pi$ planes are gapped. A series of interesting topological signatures has been predicted in XPt (X = Sc, Y, La), and it is hoped that these proposed topological elements can be confirmed through experiments in the future.

DATA AVAILABILITY STATEMENT

The original contributions presented in the study are included in the article/supplementary materials, further inquiries can be directed to the corresponding author/s.

AUTHOR CONTRIBUTIONS

The author confirms being the sole contributor of this work and has approved it for publication.

FUNDING

This work was funded by the Science and Technology Research Project of Hebei Province Colleges and Universities (Grant No. QN2020113) and Tangshan Applied Basic Research Project (Grant No. 19130227g).

REFERENCES

Andrey, V., Sánchez-Barriga, J., Maria, B., Carolien, C., Joke, H., and Anna, S. (2018). Can surface reactivity of mixed crystals be predicted from their counterparts? A case study of $(Bi_{1-x}Sb_x)_2Te_3$ topological insulators. *J. Mater. Chem. C* 6, 8941–8949. doi: 10.1039/C8TC02235F

Bi, R., Yan, Z., Lu, L., and Wang, Z. (2017). Nodal-knot semimetals. *Phys. Rev. B* 96:201305. doi: 10.1103/PhysRevB.96.201305

Bin, Q., Tang, F., Ruan, Y. R., Yong, F., and Han, Z. D. (2018). Extremely large magnetoresistance in the nonmagnetic semimetal YBi. *J. Mater. Chem. C* 6, 10020–10029. doi: 10.1039/C8TC02839G

Cano, J., and Vergniory, M. G. (2016). Beyond dirac and Weyl fermions: unconventional quasiparticles in conventional crystals. *Science* 353:aaf5037. doi: 10.1126/science.aaf5037

Cava, R. J., Ji, H., Fuccillo, M. K., Gibson, Q. D., and Hor, Y. S. (2013). Crystal structure and chemistry of topological insulators. *J. Mater. Chem. C* 1, 3176–3189. doi: 10.1039/c3tc30186a

Chang, G., Xu, S. Y., Zheng, H., Singh, B., Hsu, C. H., and Bian, G. (2016). Room-temperature magnetic topological Weyl fermion and nodal line semimetal states in half-metallic Heusler Co_2TiX (X= Si, Ge, or Sn). *Sci. Rep.* 6:38839. doi: 10.1038/srep38839

Chen, C., Wang, S. S., Liu, L., Yu, Z. M., and Yang, S. A. (2017b). Ternary wurtzite CaAgBi materials family: A playground for essential and accidental, type-I and type-II Dirac fermions. *Phys. Rev. Mater.* 1:044201. doi: 10.1103/PhysRevMaterials.1.044201

Chen, K. X., Lyu, S. S., Luo, Z. Y., Fu, Y. X., Heng, Y., and Mo, D. C. (2017a). Theoretical design of a new family of two-dimensional topological insulators. *Phys. Chem. Chem. Phys.*19, 7481–7485. doi: 10.1039/C6CP08670E

Chen, S. Z., Li, S., Chen, Y., and Duan, W. (2020). Nodal flexible-surface semimetals: case of carbon nanotube networks. *Nano Lett.* 20:5400. doi: 10.1021/acs.nanolett.0c01786

Chen, Z., Zhang, C., Zhou, Y., Zhang, E., Yang, L., Hong, M., et al. (2015). Scalable growth of high mobility dirac semimetal Cd_3As_2 microbelts. *Nano Lett.* 15, 5830–5834. doi: 10.1021/acs.nanolett.5b01885

Chenguang, F., Narayan, G. S., June, W. S., Guowei, L., Enke, L., and Nitesh, K. (2018). Large Nernst power factor over a broad temperature range in polycrystalline Weyl semimetal NbP. *Energy Environ. Sci.* 11, 2813–2820. doi: 10.1039/C8EE02077A

Feng, X., Yue, C., Song, Z., Wu, Q. S., and Wen, B. (2018). Topological dirac nodal-net fermions in AlB_2-type TiB_2 and ZrB_2. *Phys. Rev. Mater.* 2:014202. doi: 10.1103/PhysRevMaterials.2.014202

Fu, B.-B., Yi, C., Zhang, T., Caputo, M., Ma, Z., Gao, X., et al. (2019). Dirac nodal surfaces and nodal lines in ZrSiS. *Sci. Adv.* 5:eaau6459. doi: 10.1126/sciadv.aau6459

Gao, L., Sun, J., Sethi, G., Zhang, Y., Du, S., and Liu, F. (2019). Orbital design of topological insulators from two-dimensional semiconductors. *Nanoscale* 11, 22743–22747. doi: 10.1039/C9NR06859G

Guo, L., Chen, T. W., Chen, C., Chen, L., Zhang, Y., and Gao, G. Y. (2019). Electronic transport evidence for topological nodal-line semimetals of ZrGeSe single crystals. *ACS Appl. Electr. Mater.* 1, 869–876. doi: 10.1021/acsaelm.9b00061

Guo, P. J., Yang, H. C., Liu, K., and Lu, Z. Y. (2018). Triply degenerate nodal points in RRh_6Ge_4 (R = Y, La, Lu). *Phys. Rev. B* 98:045134. doi: 10.1103/PhysRevB.98.045134

Han, Y., Wu, M., Feng, Y., Cheng, Z. X., and Wang, X. T. (2019). Competition between cubic and tetragonal phases in all-d-metal Heusler alloys, $X_{2-x}Mn_{1+x}V$ (X = Pd, Ni, Pt, Ag, Au, Ir, Co; x= 1, 0): a new potential direction of the Heusler family. *IUCrJ* 6, 465–472. doi: 10.1107/S2052252519004007

He, T., Zhang, X., Liu, Y., Dai, X., Liu, G., Liu, Z., et al. (2020). Ferromagnetic hybrid nodal loop and switchable type-I and type-II Weyl fermions in two dimensions. *Phys. Rev. B* 102:075133. doi: 10.1103/PhysRevB.102.075133

He, T., Zhang, X., Meng, W., Jin, L., Dai, X., and Liu, G. (2019). Topological nodal lines and nodal points in the antiferromagnetic material β-Fe_2PO_5. *J. Mater. Chem. C* 7, 12657–12663. doi: 10.1039/C9TC04046C

Heyd, J., and Scuseria, G. (2004). Efficient hybrid density functional calculations in solids: Assessment of the Heyd–Scuseria–Ernzerhof screened Coulomb hybrid functional. *J. Chem. Phys.* 121, 1187–1192. doi: 10.1063/1.1760074

Hu, X., Pang, Z., Chen, X., Ren, M., and Li, P. (2018). Two-dimensional topological insulators of Pb/Sb honeycombs on a Ge (111) semiconductor surface. *RSC Adv.* 8, 34999–35004. doi: 10.1039/C8RA06316H

Hu, X. K., Pang, Z. X., Zhang, C. W., Wang, P. J., Li, P., and Ji, W. X. (2019). A two-dimensional robust topological insulator with coexisting ferroelectric and valley polarization. *J. Mater. Chem. C* 7, 9406–9412. doi: 10.1039/C8TC06252H

Huang, H., Liu, J., Vanderbilt, D., and Duan, W. (2016). Topological nodal-line semimetals in alkaline-earth stannides, germanides, and silicides. *Phys. Rev. B* 93:201114. doi: 10.1103/PhysRevB.93.201114

Jin, L., Zhang, X., Dai, X., Liu, H., Chen, G., and Liu, G. (2019b). Centrosymmetric Li_2NaN: a superior topological electronic material with critical-type triply degenerate nodal points. *J. Mater. Chem. C* 7, 1316–1320. doi: 10.1039/C8TC05930F

Jin, L., Zhang, X., He, T., Meng, W., and Liu, G. (2020a). Ferromagnetic two-dimensional metal-chlorides MCl (M= Sc, Y, and La): candidates for Weyl nodal line semimetals with small spin-orbit coupling gaps. *Appl. Surf. Sci.* 520:146376. doi: 10.1016/j.apsusc.2020.146376

Jin, L., Zhang, X., Liu, Y., Dai, X., Shen, X., and Wang, L. (2020b). Two-dimensional Weyl nodal-line semimetal in a d^0 ferromagnetic K_2N monolayer with a high Curie temperature. *Phys. Rev. B* 102:125118. doi: 10.1103/PhysRevB.102.125118

Jin, L., Zhang, X. M., Dai, X. F., Wang, L. Y., and Liu, G. D. (2019a). Screening topological materials with a CsCl-type structure in crystallographic databases. *IUCrJ* 6, 688–694. doi: 10.1107/S2052252519007383

Jing, Y., and Heine, T. (2018). Two-dimensional kagome lattices made of hetero triangulenes are Dirac semimetals or single-band semiconductors. *J. Am. Chem. Soc.* 141, 743–747. doi: 10.1021/jacs.8b09900

Khoury, J. F., Rettie, A. J. E., Khan, M. A., Ghimire, N. J., and Kanatzidis, M. G. (2019). A new three-dimensional subsulfide Ir2In8S with Dirac semimetal behavior. *J. Am. Chem. Soc.* 141, 19130–19137. doi: 10.1021/jacs.9b10147

Kirby, R. J., Ferrenti, A., Weinberg, C., Klemenz, S., and Schoop, L. M. (2020). Transient drude response dominates near-infrared pump–probe reflectivity in nodal-line semimetals ZrSiS and ZrSiSe. *J. Phys. Chem. Lett.* 11, 6105–6111. doi: 10.1021/acs.jpclett.0c01377

Kou, L., Yan, B., Hu, F., Wu, S. C., Wehling, T. O., and Felser, C. (2013). Graphene-based topological insulator with an intrinsic bulk band gap above room temperature. *Nano Lett.* 13, 6251–6255. doi: 10.1021/nl4037214

Lee, C. H., Li, G., Liu, Y., Tai, T., Thomale, R., and Zhang, X. (2018). Tidal surface states as fingerprints of non-hermitian nodal knot metals. *arXiv [Preprint] arXiv:*1812.02011

Li, G., Xu, Q., Shi, W. J., Fu, C., and Felser, C. (2019). Surface states in bulk single crystal of topological semimetal $Co_3Sn_2S_2$ toward water oxidation. *Sci. Adv.* 5:eaaw9867. doi: 10.1126/sciadv.aaw9867

Liu, C., Zhang, H., Sun, Z., Ding, K., and Jie, J. (2016). Topological insulator Bi_2Se_3 nanowire/Si heterostructure photodetectors with ultrahigh responsivity and broadband response. *J. Mater. Chem. C* 4, 5648–5655. doi: 10.1039/C6TC01083K

Liu, J., Li, X., Wang, Q., Kawazoe, Y., and Jena, P. (2018a). A new 3D Dirac nodal-line semi-metallic graphene monolith for lithium ion battery anode materials. *J. Mater. Chem. A* 6, 13816–13824. doi: 10.1039/C8TA04428G

Liu, Z., Xin, H., Fu, L., Liu, Y., Song, T., and Cui, X. (2018b). All-silicon topological semimetals with closed nodal line. *J. Phys. Chem. Lett.* 10, 244–250. doi: 10.1021/acs.jpclett.8b03345

Loïc, J., and Izmaylov, A. F. (2017). Molecular "topological insulators": a case study of electron transfer in the bis (methylene) adamantyl carbocation. *Chem. Commun.* 53, 7365–7368. doi: 10.1039/C7CC02275A

Lu, L., Fang, C., Fu, L., Johnson, S. G., Joannopoulos, J. D., and Solja, I. M. (2016). Symmetry-protected topological photonic crystal in three dimensions. *Nat. Phys.* 12, 337–340. doi: 10.1038/nphys3611

Luo, L., Zheng, K., Zhang, T., Liu, Y. H., Yu, Y., and Lu, R. (2015). Optoelectronic characteristics of a near infrared light photodetector based on a topological insulator Sb_2Te_3 film. *J. Mater. Chem. C* 3, 9154–9160. doi: 10.1039/C5TC01772F

Ma, H., Chen, P., Li, B., Li, J., Ai, R., Zhang, Z., et al. (2018). Thickness-tunable synthesis of ultrathin type-II Dirac semimetal $PtTe_2$ single crystals and their thickness-dependent electronic properties. *Nano Lett.* 18, 3523–3529. doi: 10.1021/acs.nanolett.8b00583

Ma, L., and Sun, Q. (2020). A topological semimetal Li_2CrN_2 sheet as a promising hydrogen storage material. *Nanoscale* 12, 12106–12113. doi: 10.1039/D0NR02180F

Mal, P., Bera, G., Turpu, G. R., Srivastava, S. K., and Das, P. (2019). Vibrational spectra of $Pb_2Bi_2Te_3$, $PbBi_2Te_4$, and $PbBi_4Te_7$ topological insulators: temperature-dependent Raman and theoretical insights from DFT simulations. *Phys. Chem. Chem. Phys.* 21, 15030–15039. doi: 10.1039/C9CP01494B

Meng, W., Zhang, X., He, T., Jin, L., and Liu, G. (2020a). Multiple fermionic states with clear nontrivial surface signature in CsCl-type compound ErAs. *Comput. Mater. Sci.* 183:109815. doi: 10.1016/j.commatsci.2020.109815

Meng, W., Zhang, X., He, T., Jin, L., and Liu, G. (2020b). Ternary compound HfCuP: An excellent Weyl semimetal with the coexistence of type-I and type-II Weyl nodes. *J. Adv. Res.* 24:523. doi: 10.1016/j.jare.2020.05.026

Narimani, M., Shahram, Y., and Zahra, N. (2020). High thermoelectric efficiency of LaX (X = Sb, Bi) two dimensional topological insulators. *J. Phys. Conden. Matter.* 32:255501. doi: 10.1088/1361-648X/ab6046

Owerre, S. A. (2018). Magnonic triply-degenerate nodal points. *Europhys. Lett.* 120:57002. doi: 10.1209/0295-5075/120/57002

Pan, Z., Xue, L., and Sun, L. (2017). Large gap two dimensional topological insulators: the bilayer triangular lattice TlM (M = N, P, As, Sb). *J. Mater. Chem. C* 5, 4268–4274. doi: 10.1039/C7TC00634A

Perdew, J. P., Burke, K., and Ernzerhof, M. (1996). Generalized gradient approximation made simple. *Phys. Rev. Lett.* 77:3865. doi: 10.1103/PhysRevLett.77.3865

Perdew, J. P., Burke, K., and Ernzerhof, M. (1998). Perdew, burke, and ernzerhof reply. *Phys. Rev. Lett.* 80:891. doi: 10.1103/PhysRevLett.80.891

Pielnhofer, F., Menshchikova, T. V., Rusinov, I. P., Zeugner, A., Sklyadneva, I. Y., and Heid, R. (2017). Designing 3D topological insulators by 2D-Xene (X = Ge, Sn) sheet functionalization in GaGeTe-type structures. *J. Mater. Chem. C* 5, 4752–4762. doi: 10.1039/C7TC00390K

Politano, A., Vitiello, M. S., Viti, L., Boukhvalov, D. W., and Chiarello, G. (2017). The role of surface chemical reactivity in the stability of electronic nanodevices based on two-dimensional materials "beyond graphene" and topological insulators. *FlatChem* 1, 60–64. doi: 10.1016/j.flatc.2016.11.003

Qiao, J., Chuang, M. Y., Lan, J. C., Lin, Y. Y., Sung, W. H., and Fan, R. (2019). Two-photon absorption within layered Bi_2Te_3 topological insulators and the role of nonlinear transmittance therein. *J. Mater. Chem. C* 7, 7027–7034. doi: 10.1039/C9TC01885A

Qie, Y., Liu, J., Wang, S., Sun, Q., and Jena, P. (2019). Tetragonal C_{24}, a topological nodal-surface semimetal with potential as an anode material for sodium ion batteries. *J. Mater. Chem. A* 7, 5733–5739. doi: 10.1039/C8TA11276B

Sankar, R., Muthuselvam, I. P., Babu, K. R., Murugan, G. S., and Chou, F. C. (2019). Crystal growth and magnetic properties of topological nodal-line semimetal gdsbte with antiferromagnetic spin ordering. *Inorg. Chem.* 58, 11730–11737. doi: 10.1021/acs.inorgchem.9b01698

Schoop, L. M., Pielnhofer, F., and Lotsch, B. V. (2018). Chemical principles of topological semimetals. *Chem. Mater.* 30, 3155–3176. doi: 10.1021/acs.chemmater.7b05133

Shen, J., and Cha, J. J. (2014). Topological crystalline insulator nanostructures. *Nanoscale* 6, 14133–14140. doi: 10.1039/C4NR05124F

Sheng, X. L., Yu, Z. M., Yu, R., Weng, H., and Yang, S. A. (2017). d orbital topological insulator and semimetal in the antifluorite Cu_2S family: contrasting spin Helicities, nodal box, and hybrid surface states. *J. Phys. Chem. Lett.* 8, 3506–3511. doi: 10.1021/acs.jpclett.7b01390

Tang, M., Shen, H., Qie, Y., Xie, H., and Sun, Q. (2019). Edge-state-enhanced CO_2 electroreduction on topological nodal-line semimetal Cu_2Si nanoribbons. *J. Phys. Chem. C* 123, 2837–2842. doi: 10.1021/acs.jpcc.8b08871

Togo, A., and Tanaka, I. (2015). First principles phonon calculations in materials science. *Scr. Mater.* 108, 1–5. doi: 10.1016/j.scriptamat.2015.07.021

Tsipas, P., Tsoutsou, D., Fragkos, S., Sant, R., Alvarez, C., and Okuno, H. (2018). Massless dirac fermions in $ZrTe_2$ semimetal grown on InAs (111) by van der Waals epitaxy. *ACS Nano* 12, 1696–1703. doi: 10.1021/acsnano.7b08350

Türker, O., and Sergej, M. (2018). Weyl nodal surfaces. *Phys. Rev. B* 97:075120. doi: 10.1103/PhysRevB.97.075120

Wang, A., Zhang, X., and Zhao, M. (2014). Topological insulator states in a honeycomb lattice of s-triazines. *Nanoscale* 6, 11157–11162. doi: 10.1039/C4NR02707H

Wang, X., Cheng, Z., Zhang, G., Wang, B., Wang, X. L., and Chen, H. (2020c). Rich novel zero-dimensional (0D), 1D, and 2D topological elements predicted in the $P6_3/m$ type ternary boride $HfIr_3B_4$. *Nanoscale* 12, 8314–8319. doi: 10.1039/D0NR00635A

Wang, X., Ding, G., Khandy, S., Cheng, Z., Zhang, G., Wang, X., et al. (2020d). Unique topological nodal line states and associated exceptional thermoelectric power factor platform in Nb_3GeTe_6 monolayer and bulk. *Nanoscale* 12, 16910–16916. doi: 10.1039/D0NR03704D

Wang, X., Zhou, F., and Chen, H. (2020e). Organic-inorganic hybrid coordination polymer $C_3H_9CdCl_3N$ co-exhibiting superior Dirac point and nodal surface states. *Results Phys.* 17:103159. doi: 10.1016/j.rinp.2020.103159

Wang, X. T., Ding, G., Cheng, Z. X., Surucu, G., and Yang, T. (2020a). Novel topological nodal lines and exotic drum-head-like surface states in synthesized CsCl-type binary alloy TiOs. *J. Adv. Res.* 22, 137–144. doi: 10.1016/j.jare.2019.12.001

Wang, X. T., Ding, G., Cheng, Z. X., Wang, X. L., and Yang, T. (2020b). Intersecting nodal rings in orthorhombic-type $BaLi_2Sn$ compound. *J. Mater. Chem. C* 8, 5461–5466. doi: 10.1039/D0TC00504E

Weng, H., Fang, C., Fang, Z., and Dai, X. (2016a). Coexistence of Weyl fermion and massless triply degenerate nodal points. *Phys. Rev. B* 94:165201. doi: 10.1103/PhysRevB.94.165201

Weng, H., Fang, C., Fang, Z., and Dai, X. (2016b). Topological semimetals with triply degenerate nodal points in θ-phase tantalum nitride. *Phys. Rev. B* 93:241202. doi: 10.1103/PhysRevB.93.241202

Wu, M., Han, Y., Bouhemadou, A., Cheng, Z., and Wang, X. (2019). Site preference and tetragonal distortion in palladium-rich Heusler alloys. *IUCrJ* 6, 218–225. doi: 10.1107/S2052252518017578

Wu, W., Liu, Y., Li, S., Zhong, C., Yu, Z. M., and Sheng, X. L. (2018). Nodal surface semimetals: Theory and material realization. *Phys. Rev. B* 97:115125. doi: 10.1103/PhysRevB.97.115125

Xia, Y., and Li, G. (2017). Triply degenerate nodal points and topological phase transitions in $NaCu_3Te_2$. *Phys. Rev. B* 96:241204. doi: 10.1103/PhysRevB.96.241204

Xiao, M., Ye, L., Qiu, C., He, H., Liu, Z., and Fan, S. (2020). Experimental demonstration of acoustic semimetal with topologically charged nodal surface. *Sci. Adv.* 6:eaav2360. doi: 10.1126/sciadv.aav2360

Xie, H., Qie, Y., Imran, M., and Sun, Q. (2019). Topological semimetal porous carbon as a high-performance anode for Li-ion batteries. *J. Mater. Chem. A* 7, 14253–14259. doi: 10.1039/C9TA03587G

Xu, S. G., Zheng, B., Xu, H., and Yang, X. B. (2019). Ideal nodal line semimetal in a two-dimensional boron bilayer. *J. Phys. Chem. C* 123, 4977–4983. doi: 10.1021/acs.jpcc.8b12385

Yan, L., Liu, P. F., Bo, T., Zhang, J., Tang, M. H., and Xiao, Y. G. (2019). Emergence of superconductivity in a Dirac nodal-line Cu_2Si monolayer: ab initio calculations. *J. Mater. Chem. C* 7, 10926–10932. doi: 10.1039/C9TC03740C

Yan, Q., Liu, R., Yan, Z., Liu, B., Chen, H., Wang, Z., et al. (2018). Experimental discovery of nodal chains. *Nat. Phys.* 14, 461–464. doi: 10.1038/s41567-017-0041-4

Yan, Z., Bi, R., Shen, H., Lu, L., Zhang, S. C., and Wang, Z. (2017). Nodal-link semimetals. *Phys. Rev. B* 96:041103. doi: 10.1103/PhysRevB.96.041103

Yang, T., Khenata, R., and Wang, X. (2020). Predicted remarkably topological nodal surface states in $P6_3/m$ type Sr_3WN_3 from first-principles. *Results Phys.* 17:103026. doi: 10.1016/j.rinp.2020.103026

Yang, T., and Zhang, X. (2020). Nearly flat nodal surface states in pseudo-one-dimensional molybdenum monochalcogenides $X(MoS)_3$ (X = K, Rb, and Cs). *J. Mater. Chem. C* 8, 9046–9054. doi: 10.1039/D0TC01978J

Yang, Y., Sun, H. X., Xia, J. P., Xue, H., Gao, Z., Ge, Y., et al. (2019a). Topological triply degenerate point with double Fermi arcs. *Nat. Phys.* 15, 645–649. doi: 10.1038/s41567-019-0502-z

Yang, Y., Xia, J. P., Sun, H. X., Ge, Y., and Zhang, B. (2019b). Observation of a topological nodal surface and its surface-state arcs in an artificial acoustic crystal. *Nat. Commun.* 10, 1–7. doi: 10.1038/s41467-019-13258-3

Yi, X., Li, W., Li, Z., Zjou, P., Ma, Z., and Sun, L. (2019). Topological dual double node-line semimetals NaAlSi (Ge) and their potential as cathode material for sodium ion batteries. *J. Mater. Chem. C* 7, 15375–15381. doi: 10.1039/C9TC04096J

Yu, R., Weng, H., Fang, Z., Dai, X., and Hu, X. (2015). Topological node-line semimetal and Dirac semimetal state in antiperovskite Cu_3PdN. *Phys. Rev. Lett.* 115:036807. doi: 10.1103/PhysRevLett.115.036807

Yuan, X., Cheng, P., Zhang, L., Zhang, C., and Xiu, F. (2017). Direct observation of Landau level resonance and mass generation in dirac semimetal Cd_3As_2 thin films. *Nano Lett.* 17, 2211–2219. doi: 10.1021/acs.nanolett.6b04778

Zhang, C., Zhang, E., Wang, W., Liu, Y., Chen, Z. G., and Lu, S. (2017a). Room-temperature chiral charge pumping in dirac semimetals. *Nat. Commun.* 8, 1–9. doi: 10.1038/ncomms13741

Zhang, L., Zhang, S., Ji, W., Zhang, C., Li, P., Wang, P., et al. (2018a). Discovery of a novel spin-polarized nodal ring in a two-dimensional HK lattice. *Nanoscale* 10, 20748–20753. doi: 10.1039/C8NR05383A

Zhang, M. H., Zhang, S. F., Wang, P. J., and Zhang, C. W. (2020). Emergence of a spin-valley Dirac semimetal in a strained group-VA monolayer. *Nanoscale* 12, 3950–3957. doi: 10.1039/C9NR09545D

Zhang, T. T., Yu, Z. M., Guo, W., Shi, D., Zhang, G., and Yao, Y. (2017b). From type-II triply degenerate nodal points and three-band nodal rings to type-II Dirac points in centrosymmetric zirconium oxide. *J. Phys. Chem. Lett.* 8, 5792–5797. doi: 10.1021/acs.jpclett.7b02642

Zhang, X., Fu, B., Jin, L., Dai, X., and Yao, Y. (2019). Topological nodal line electrides: realization of an ideal nodal line state nearly immune from spin–orbit coupling. *J. Phys. Chem. C* 123, 25871–25876. doi: 10.1021/acs.jpcc.9b08446

Zhang, X., Jin, L., Dai, X., and Liu, G. (2017c). Topological type-II nodal line semimetal and Dirac semimetal state in stable kagome compound Mg_3Bi_2. *J. Phys. Chem. Lett.* 8, 4814–4819. doi: 10.1021/acs.jpclett.7b02129

Zhang, X., Jin, L., Dai, X., and Liu, G. (2018b). Highly anisotropic type-II nodal line state in pure titanium metal. *Appl. Phys. Lett.* 112:122403. doi: 10.1063/1.5023320

Zhang, X., Liu, Q., Xu, Q., Dai, X., and Zunger, A. (2018c). Topological insulators versus topological Dirac semimetals in honeycomb compounds. *J. Am. Chem. Soc.* 140, 13687–13694. doi: 10.1021/jacs.8b06652

Zhang, X., Yu, Z., Sheng, X., Yang, H., and Yang, S. A. (2017d). Coexistence of four-band nodal rings and triply degenerate nodal points in centrosymmetric metal diborides. *Phys. Rev. B* 95:235116. doi: 10.1103/PhysRevB.95.235116

Zhang, X., Yu, Z. M., Zhu, Z., Wu, W., and Yang, S. A. (2018d). Nodal loop and nodal surface states in the Ti 3 Al family of materials. *Phys. Rev. B* 97:235150. doi: 10.1103/PhysRevB.97.235150

Zhao, M., Dong, W., and Wang, A. (2013). Two-dimensional carbon topological insulators superior to graphene. *Sci. Rep.* 3:3532. doi: 10.1038/srep03532

Zhao, Z., Zhang, Z., and Guo, W. (2020). A family of all sp 2-bonded carbon allotropes of topological semimetals with strain-robust nodal-lines. *J. Mater. Chem. C* 8, 1548–1555. doi: 10.1039/C9TC05470G

Zhong, C., Wu, W., He, J., Ding, G., Liu, Y., and Li, D. (2019). Two-dimensional honeycomb borophene oxide: strong anisotropy and nodal loop transformation. *Nanoscale* 11, 2468–2475. doi: 10.1039/C8NR08729F

Zhou, P., Ma, Z., and Sun, L. (2018). Coexistence of open and closed type nodal line topological semimetals in two dimensional B_2C. *J. Mater. Chem. C* 6, 1206–1214. doi: 10.1039/C7TC05095J

Zhou, Q., Wang, J., Chwee, T. S., Wu, G., Wang, X., and Ye, Q. (2015). Topological insulators based on 2D shape-persistent organic ligand complexes. *Nanoscale* 7, 727–735. doi: 10.1039/C4NR05247A

Zhou, T., Tong, M., Xie, X., Yu, Y., Zhu, X., Wang, Z. Y., et al. (2020). Quantum transport signatures of a close candidate for a type II nodal-line semimetal. *J. Phys. Chem. Lett.* 11, 6475–6481. doi: 10.1021/acs.jpclett.0c01726

Zhu, Y., Gui, X., Wang, Y., Graf, D., Xie, W., Hu, J., et al. (2020). Evidence from transport measurements for YRh_6Ge_4 being a triply degenerate nodal semimetal. *Phys. Rev. B* 101:035133. doi: 10.1103/PhysRevB.101.035133

Conflict of Interest: The author declares that the research was conducted in the absence of any commercial or financial relationships that could be construed as a potential conflict of interest.

The handling editor declared a past co-authorship with one of the authors, HX.

frontiers in Chemistry

ORIGINAL RESEARCH
published: 19 November 2020
doi: 10.3389/fchem.2020.608398

Hexagonal Zr_3X (X = Al, Ga, In) Metals: High Dynamic Stability, Nodal Loop, and Perfect Nodal Surface States

*Heju Xu, Hailong Xi and Yong-Chun Gao**

College of Science, North China University of Science and Technology, Tangshan, China

In recent years, topological semimetals/metals, including nodal point, nodal line, and nodal surface semimetals/metals, have been studied extensively because of their potential applications in spintronics and quantum computers. In this study, we predict a family of materials, Zr_3X (X = Al, Ga, In), hosting the nodal loop and nodal surface states in the absence of spin–orbit coupling. Remarkably, the energy variation of the nodal loop and nodal surface states in Zr_3X are very small, and these topological signatures lie very close to the Fermi level. When the effect of spin–orbit coupling is considered, the nodal loop and nodal surface states exhibit small energy gaps (<25 and 35 meV, respectively) that are suitable observables that reflect the spin-orbit coupling response of these topological signatures and can be detected in experiments. Moreover, these compounds are dynamically stable, and they consequently form potential material platforms to study nodal loop and nodal surface semimetals.

Keywords: nodal loop states, nodal surface states, first-principles, electronic structures, spin-orbit-coupling

OPEN ACCESS

Edited by:
Zhenxiang Cheng,
University of Wollongong, Australia

Reviewed by:
Songtao Li,
North China Electric Power University, China
Yajiu Zhang,
Guangzhou University, China

****Correspondence:***
Yong-Chun Gao
gaoyc1963@ncst.edu.cn

Specialty section:
This article was submitted to Theoretical and Computational Chemistry, a section of the journal Frontiers in Chemistry

Received: *20 September 2020*
Accepted: *30 September 2020*
Published: *19 November 2020*

Citation:
Xu H, Xi H and Gao Y-C (2020) Hexagonal Zr_3X (X = Al, Ga, In) Metals: High Dynamic Stability, Nodal Loop, and Perfect Nodal Surface States. Front. Chem. 8:608398. doi: 10.3389/fchem.2020.608398

INTRODUCTION

The exploration of non-trivial topologies in crystalline solids has attracted significant attention from chemists, physicists, and material scientists (Kong and Cui, 2011; Cava et al., 2013; Banik et al., 2018; Zhang et al., 2018a; Tang et al., 2019). The main features of these topological solids are enclosed in their electronic-band structures. Initially, research was conducted in the context of the insulating state (Zhang et al., 2011; Li et al., 2012; Peng et al., 2012; Rasche et al., 2013; Wang et al., 2013; Kambe et al., 2014; Chang et al., 2015; Walsh et al., 2017; Barton et al., 2019; Zeugner et al., 2019), and the concept of band topology has now been extended to the metallic and semi-metallic states (Bradlyn et al., 2017; Bernevig et al., 2018; Schoop et al., 2018; Zhou et al., 2018; Gao et al., 2019; Hu et al., 2019; Klemenz et al., 2020; Wang et al., 2020b,c; Zhao Z. et al., 2020) as well.

The dimensionality of band-crossings is a criterion used to classify topological semimetals/metals. The most famous topological semimetals/metals with zero-dimensional band-crossings, i.e., zero-dimensional nodal points, are Dirac semimetals/metals (Chen et al., 2015, 2020; Bradlyn et al., 2017; Zhong et al., 2017; Jing and Heine, 2018; Liu et al., 2018b; Zhang et al., 2018b; Khoury et al., 2019; Wang et al., 2020f; Xu et al., 2020) and Weyl semimetals/metals

(Peng et al., 2016; Lin et al., 2017; Fu et al., 2018; Zhang et al., 2018c; Zhou et al., 2019; Gupta et al., 2020; Jia et al., 2020; Liu et al., 2020; Meng L. et al., 2020; Zhao B. et al., 2020). We selected Weyl semimetals/metals as examples here because there exists a band-crossing of the valance band and conduction band at an isolated nodal point in the momentum space of these solids. Particularly, around this isolated nodal point, the quasiparticle acts similarly to the behavior of Weyl fermions, which are particles of considerable interest in high-energy physics. We summarize some recent studies on Weyl materials as follows: (i) Zhao and Ma (2020) stated that hexagonal MnO ferromagnet is a magnetic Weyl semimetal with spin-gapless state; (ii) Meng W. et al. (2020b) predicted that HfCuP compound is a newly designed Weyl semimetal with different types of Weyl nodes; and (iii) Jia et al. (2020) reported that the VI_3 monolayer hosts a Weyl fermion and 100% spin-polarization. Furthermore, under the protection from certain crystalline symmetries, two Weyl points of opposite chirality can be stable at the same point, forming a Dirac point.

In the case of three-dimensional materials, besides the zero-dimensional nodal point metals/semimetals, in principle, there should exist one-dimensional and two-dimensional band-crossing metals/semimetals as well. For three-dimensional materials with one-dimensional band-crossings, some members, named as nodal line/loop semimetal/metals, have garnered considerable attention owing to their rich properties. Based on the shape of the nodal lines, they may host various forms, such as nodal link (Yan et al., 2017), nodal chains (Bzdušek et al., 2016), nodal boxes (Sheng et al., 2017), nodal ring (Wang et al., 2020d), nodal knot (Bi et al., 2017), and nodal net (Feng et al., 2018; Wang et al., 2018). So far, numerous types of nodal-line semimetals/metals have been predicted (He et al., 2019, 2020; Jin et al., 2019a,b, 2020a,c; Zhang et al., 2019; Meng W. et al., 2020a; Wang et al., 2020a,e; Zhou et al., 2020), and it is assumed that the node-line states have interesting characteristics in terms of their electronic, transport, and magnetic properties.

Zhong et al. (2016) had first observed topological semimetals/metals with two-dimensional band-crossings, i.e., nodal surface states. However, investigations into nodal surface semimetals/metals are very rare (Wu et al., 2018), and the energy variation of the nodal surface state is great.

If one material hosts two or more types of band-crossings, it can be considered a good platform to investigate the relationship among different topological signatures. Very recently, tetragonal PtO was proposed by Li et al. (2020b) as an effective material to study the one-dimensional nodal line and zero-dimensional nodal point states. Furthermore, Li and Xia (2020) predicted that cubic HfN is a topological material that co-exhibits nodal line and nodal loop states.

Motivated by the above-mentioned information and based on the first principles, we report a new family of topological materials, Zr_3X (X = Al, Ga, In) with one-dimensional nodal loop and two-dimensional nodal surface states. The progress in

TABLE 1 | Optimized lattice constants for Zr_3X compounds.

Compounds	a (Å)	b (Å)	c (Å)
Zr_3Al	6.202	6.202	5.371
Zr_3Ga	6.166	6.166	5.052
Zr_3In	6.325	6.325	5.221

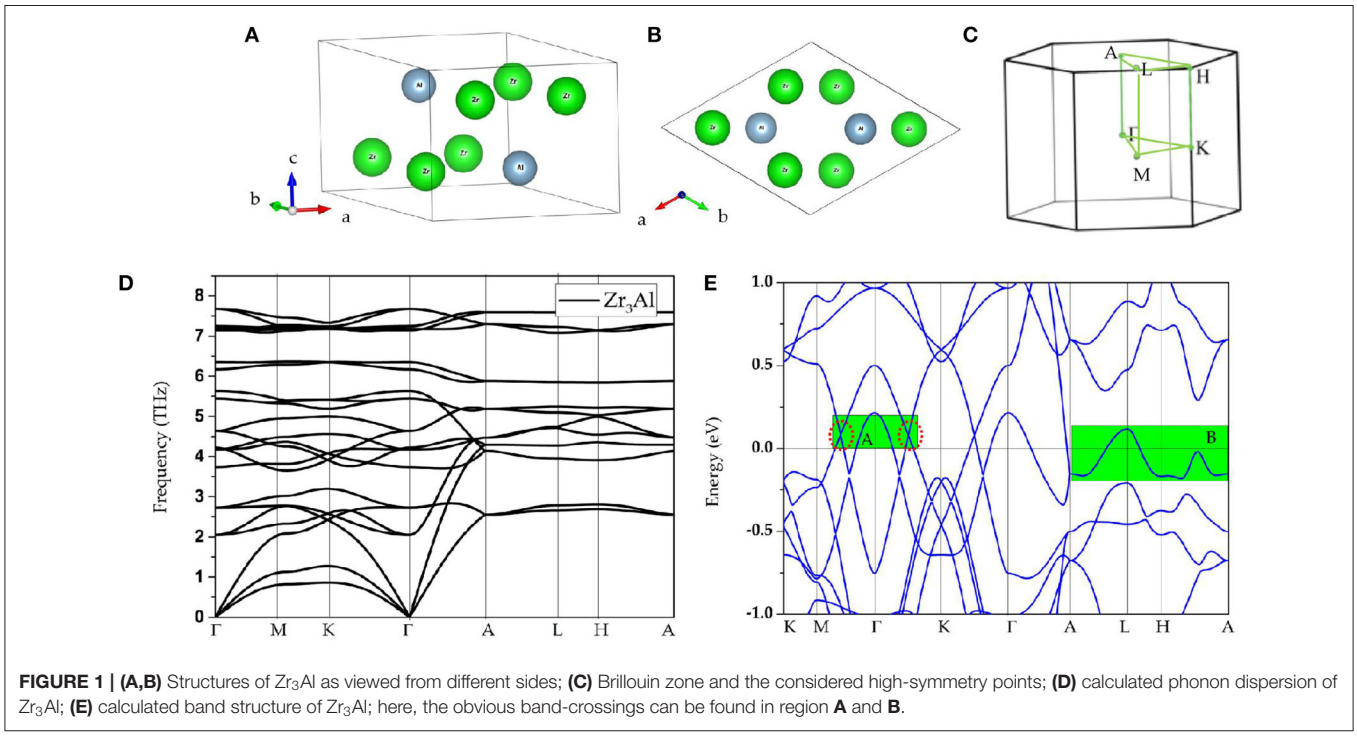

FIGURE 1 | (A,B) Structures of Zr_3Al as viewed from different sides; **(C)** Brillouin zone and the considered high-symmetry points; **(D)** calculated phonon dispersion of Zr_3Al; **(E)** calculated band structure of Zr_3Al; here, the obvious band-crossings can be found in region **A** and **B**.

the field of nodal line/surface states, including the conceptual development, the character and classification of these nodal structures, and the material realization, can be found in Wang et al. (2019). Moreover, the dynamical stable as well as the effect of spin-orbit coupling on the electronic structures of these materials are discussed in detail.

MATERIALS

In this study, we have focused on the hexagonal type Zr_3X (X = Al, Ga, In). As an example, the primitive cell structure of hexagonal $P6_3/mmc$ type Zr_3Al from different sides are shown in **Figures 1A,B**. From the figures, it is evident that Zr_3X has eight atoms, namely, two X atoms and six Zr atoms. The structures of Zr_3X have been totally relaxed with the help of first principles. The equilibrium lattice parameters of Zr_3X (X = Al, Ga, In) have been computed via minimizing the crystal total energy calculated for different values of lattice constant by means of Murnaghan's equation of state (EOS) (Murnaghan, 1944). The achieved lattice constants for these compounds are shown in **Table 1**.

Based on the Brillouin zone and considered high-symmetry points Γ-M-K-Γ-A-L-H-A (as shown in **Figure 1C**), dynamic stability was examined for these three compounds according to the calculated phonon dispersions, and the results are given in **Figures 1D, 2A,B**, respectively. These Zr_3X compounds are obviously dynamically stable due to the absence of the imaginary frequency (Han et al., 2019; Wu et al., 2019; Li et al., 2020a). These materials are therefore proposed to be experimental platforms to study topological semimetals/metals.

COMPUTATIONAL METHODS

In this study, calculations have been carried out using the Vienna ab initio simulation package (VASP) (Kresse and Furthmüller, 1996) based on the first-principles density functional theory (DFT), and the generalized gradient approximation (GGA) (Perdew et al., 1996) of Perdew–Burke–Ernzerhof (PBE) (Perdew et al., 1998) functional is adopted for the exchange-correlation potential. During the calculations, the cutoff energy is set as 600 eV, and the Brillouin zone is sampled by the Monkhorst–Pack *k*-mesh with a size of 6 × 6 × 6. Furthermore, we set the energy/force convergence criteria as 10^{-6} eV/10^{-3} eV.

RESULTS AND DISCUSSION

Observing the calculated band structure of Zr_3Al in **Figure 1E**, we find that Zr_3Al is a metal in which the bands and the Fermi level overlap. In addition to the metallic property, we find that there are several band-crossings near the Fermi level. These band-crossings are mainly located in two regions, named

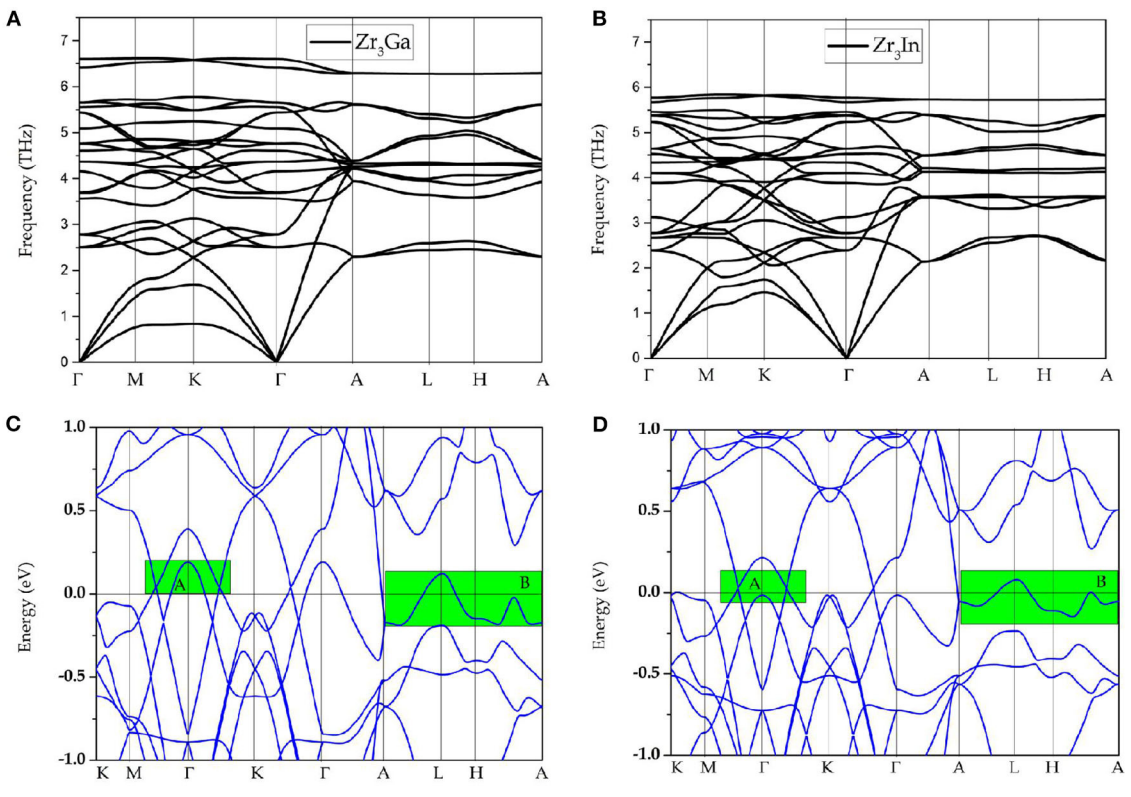

FIGURE 2 | (A,B) Phonon dispersions of Zr_3Ga and Zr_3In, respectively; **(C,D)** calculated band structures of Zr_3Ga and Zr_3In, respectively; here, band-crossings around the Fermi level are highlighted by green rectangles.

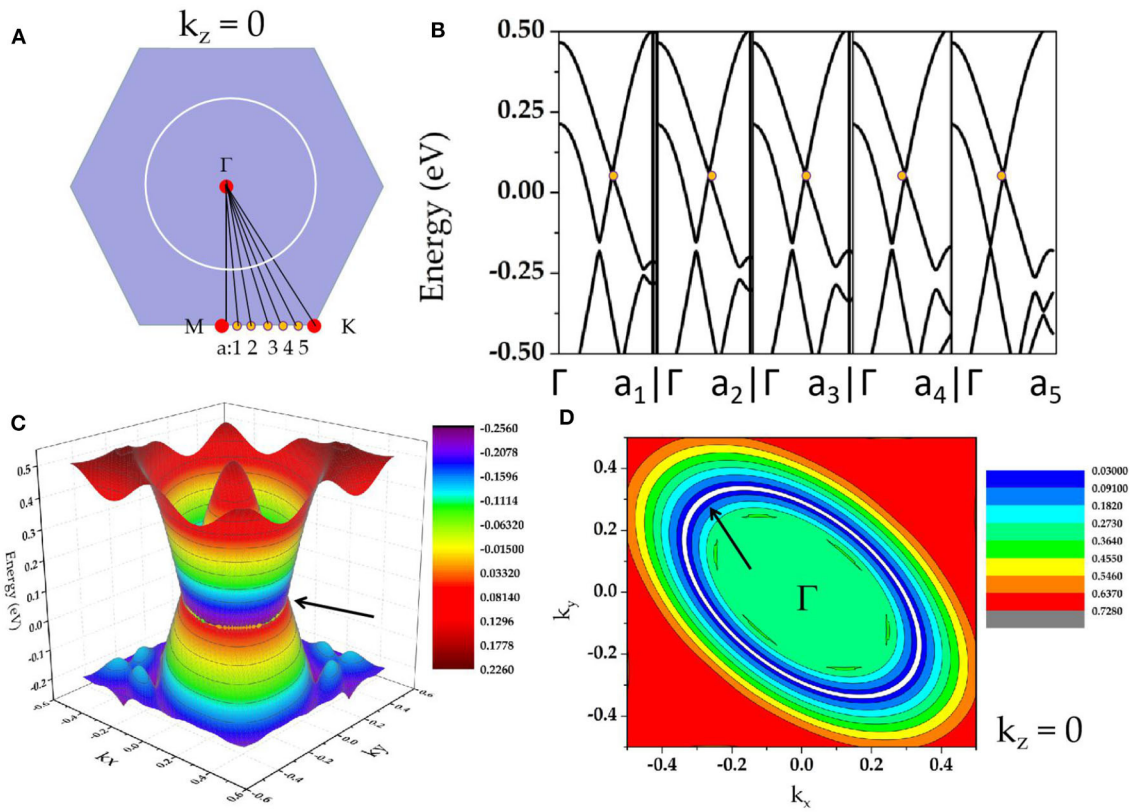

FIGURE 3 | (A) Considered paths Γ-Q (Q = M, a_1, a_2, a_3, a_4, a_5, K) in the $k_z = 0$ plane; **(B)** calculated band structures along Γ-a_1, Γ-a_2, Γ-a_3, Γ-a_4, Γ-a_5 paths; **(C)** Γ-centered three-dimensional band dispersion in region A of the $k_z = 0$ plane; **(D)** shape of Γ-nodal line in region A of the $k_z = 0$ plane (the nodal line is shown as white lines and marked by arrows).

as region A and region B, which have been highlighted by green backgrounds. Similar properties are observed in Zr_3Ga and Zr_3In, as shown in **Figures 2C,D**, respectively.

In **Figures 1E, 2C,D**, one may notice that the band structures for these Zr_3X compounds are approximately the same; hence, in the following discussion, Zr_3Al was selected as an example with which to study the band topology of Zr_3X compounds. As an example, the band structural of Zr_3Al via GGA+U (U = 4 eV for Zr-d orbitals) is given in **Supplementary Figure 1**. One can find that the band topology of Zr_3Al is still kept under GGA+U method.

In **Figure 1E**, we find that the band-crossings in region A and region B are quite close to the Fermi level. Specifically, the band-crossings in region A are along M-Γ-K paths, and the band-crossings in region B are along A-L-H-A paths. These band-crossings in both the regions may thus dominate the main features of Zr_3Al.

As shown in **Supplementary Figure 1**, in region A, we observe two obvious band-crossings; one is along M-Γ, and the other one is along Γ-K. Zr_3Al is a system with inversion P and time-reversal T symmetries; thus, the two band-crossings along M-Γ-K paths cannot be isolated points (Xu et al., 2017; Fu et al., 2019) on the plane $k_z = 0$. To determine that the two band-crossings in region A belong to a nodal loop on the plane $k_z = 0$, we selected Γ-a_1, Γ-a_2, Γ-a_3, Γ-a_4, and Γ-a_5 paths (see **Figure 3A**) to further calculate the band structures of Zr_3Al (a_1, a_2, a_3, a_4, and a_5 are equally spaced between M and K). The calculated band structures are shown in **Figure 3B**, and we find that band-crossings (marked as yellow circles) appear along Γ-a_1, Γ-a_2, Γ-a_3, Γ-a_4, and Γ-a_5 paths, implying that a nodal loop should occur on the plane $k_z = 0$. The Γ-centered three-dimensional band dispersion in region A of the $k_z = 0$ plane and the shape of Γ-nodal line in region A are shown in **Figures 3C,D**, respectively. As shown in **Figures 3B,C**, these band-crossings in region A host very little energy variation. That is, Zr_3X materials can be seen as exceedingly flat in energy, which may exhibit special properties that have exceptional applications. For example, very recently, Wang et al. (2020e) proposed that a nearly flat nodal line around the Fermi level will induce an exceptional thermoelectric power factor in the Nb_3GeTe_6 monolayer. Moreover, as shown in **Figure 3B**, we find that all the band crossing points on the plane $k_z = 0$ are type I (Liu et al., 2018a; see **Supplementary Figure 2**); this nodal line is thus type I.

In region B, one can see that there are degenerate bands along the A-L-H-A direction. This indicates that the bands in the plane $k_z = \pi$ are doubly degenerate, reflecting a nodal surface state that appeared in the plane $k_z = \pi$. To further confirm that the two bands are degenerated in $k_z = \pi$ plane,

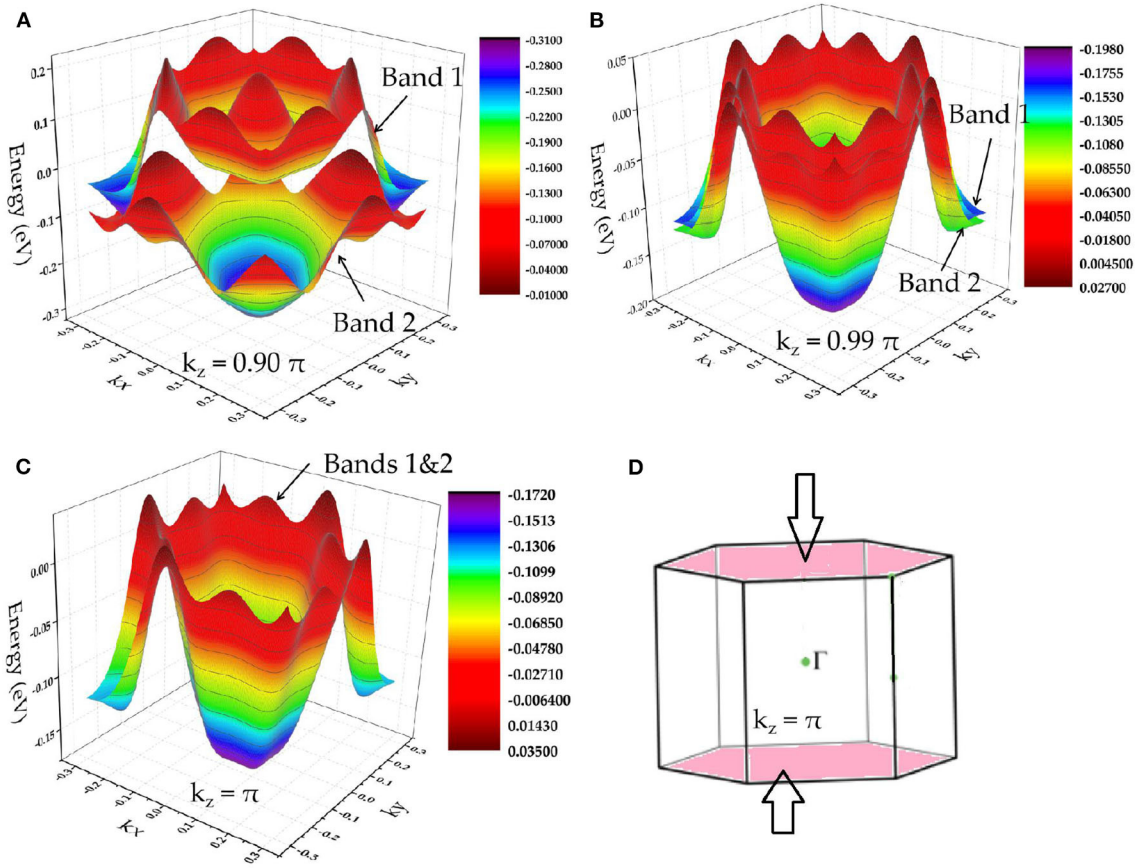

FIGURE 4 | (A–C) A-centered three-dimensional band dispersion in region B of the planes $k_z = 0.90\ \pi$, $k_z = 0.99\ \pi$, and $k_z = \pi$, respectively; **(D)** schematic diagram indicating the nodal surface state in the $k_z = \pi$ plane.

we show the A-centered three-dimensional band dispersion in region B of the planes $k_z = 0.90\ \pi$, $k_z = 0.99\ \pi$, and $k_z = \pi$ in **Figures 4A–C**, respectively. In **Figure 4C**, the two bands are obviously totally degenerate, leading to a new topological signature, i.e., nodal surface state, in the $k_z = \pi$ plane (as shown in **Figure 4D**). Furthermore, as shown in **Figure 4C**, the energy variation of the nodal surface state is very small (range from −0.15 to 0.05 eV). Similar to the situation of the nearly flat nodal line state in the $k_z = 0$ plane, the small energy variation of the nodal surface state in the $k_z = \pi$ plane may benefit the future experimental investigations.

Finally, we discuss the electronic-band structure in the presence of spin–orbit coupling. The corresponding calculations results are shown in **Figure 5**. We find that Zr_3Al is an excellent topological material whose band structure shows marked signatures (energy gaps) induced by the spin–orbit coupling effect (Fang et al., 2015). The spin–orbit coupling effect induces energy gaps of 23.05 and 20.08 meV (see **Figure 5A**) in region A. Furthermore, the band-crossings in region B have open energy gaps of 19.56 meV resulting from the spin–orbit coupling effect (see **Figure 5B**). The band structures of Zr_3Ga and Zr_3In with the effect of spin–orbit coupling are also exhibited in **Figures 5C,D**, respectively. The open energy gaps observed in these topological signatures, exhibited by Zr_3X metal (X = Al, Ga, In), are very small compared to the other well-known topological semimetals/metals (Fang et al., 2016). A detailed collection of SOC gaps of typical nodal line materials can be found in the Supplementary Information of (Jin et al., 2020b).

SUMMARY

In summary, the topological band structures of Zr_3X (X = Al, Ga, In) have been studied via DFT calculations in this study. Neglecting spin-orbit coupling, there is a nodal loop in the $k_z = 0$ plane and nodal surface state in the $k_z = \pi$ plane. The rich topological signatures are quite near to the Fermi level, which can be detected experimentally. Remarkably, the loop is nearly flat and the nodal surface features small energy variation. These above-mentioned topological signatures are not sensitive to the effect of spin–orbit coupling. Further, these compounds are proved to be dynamically stable based on the calculated phonon dispersions and host simple and clear band structures. It

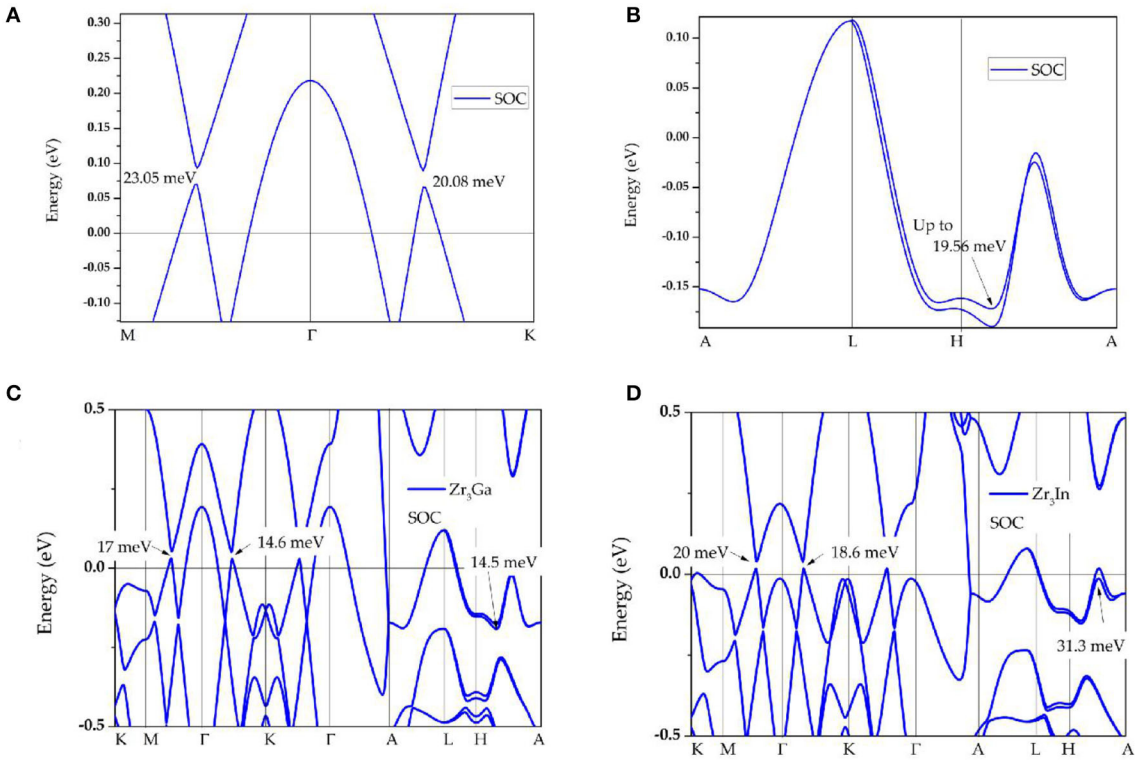

FIGURE 5 | (A,B) Band structures of Zr_3Al in the presence of spin–orbit coupling in region **A** and **B**, respectively; **(C,D)** band structures of Zr_3Ga and Zr_3In in the presence of spin–orbit coupling effect.

is expected that these non-trivial band-crossings can be experimentally observed via angle-resolved photoemission spectroscopy (ARPES).

DATA AVAILABILITY STATEMENT

The original contributions generated for the study are included in the article/**Supplementary Materials**, further inquiries can be directed to the corresponding author/s.

AUTHOR CONTRIBUTIONS

HXu: investigation and writing-original draft. Y-CG: supervision. HXu and Y-CG: formal analysis. HXi: methodology. All authors contributed to the article and approved the submitted version.

FUNDING

This study has been funded by the Science and Technology Research Project of Hebei Province Colleges and Universities (Grant No. QN2020113), and Tangshan Applied Basic Research Project (Grant No. 19130227g).

SUPPLEMENTARY MATERIAL

The Supplementary Material for this article can be found online at: https://www.frontiersin.org/articles/10.3389/fchem.2020.608398/full#supplementary-material

REFERENCES

Banik, A., Roychowdhury, S., and Biswas, K. (2018). The journey of tin chalcogenides towards high-performance thermoelectrics and topological materials. *Chem. Commun.* 54, 6573–6590. doi: 10.1039/C8CC02230E

Barton, A. T., Walsh, L. A., Smyth, C. M., Qin, X., Addou, R., Cormier, C., et al. (2019). Impact of etch processes on the chemistry and surface states of the topological insulator Bi2Se3. *ACS Appl. Mater. Interfaces* 11, 32144–32150. doi: 10.1021/acsami.9b10625

Bernevig, A., Weng, H., Fang, Z., and Dai, X. (2018). Recent progress in the study of topological semimetals. *J. Phys. Soc. Jpn.* 87:041001. doi: 10.7566/JPSJ.87.041001

Bi, R., Yan, Z., Lu, L., and Wang, Z. (2017). Nodal-knot semimetals. *Phys. Rev. B* 96:201305. doi: 10.1103/PhysRevB.96.201305

Bradlyn, B., Elcoro, L., Cano, J., Vergniory, M. G., Wang, Z., Felser, C., et al. (2017). Topological quantum chemistry. *Nature* 547, 298–305. doi: 10.1038/nature23268

Bzdušek, T., Wu, Q., Rüegg, A., Sigrist, M., and Soluyanov, A. A. (2016). Nodal-chain metals. *Nature* 538, 75–78. doi: 10.1038/nature19099

Cava, R. J., Ji, H., Fuccillo, M. K., Gibson, Q. D., and Hor, Y. S. (2013). Crystal structure and chemistry of topological insulators. *J. Mater. Chem. C* 1, 3176–3189. doi: 10.1039/c3tc30186a

Chang, C. Z., Zhao, W., Kim, D. Y., Zhang, H., Assaf, B. A., Heiman, D., et al. (2015). High-precision realization of robust quantum anomalous Hall state in a hard ferromagnetic topological insulator. *Nat. Mater.* 14, 473–477. doi: 10.1038/nmat4204

Chen, X., Chen, W., Yu, S., Xu, S., Rong, X., Huang, P., et al. (2020). Designing Dirac semimetals with a honeycomb Na_3Bi-lattice via isovalent cation substitution. *J. Mater. Chem.* C 8, 1257–1264. doi: 10.1039/C9TC05352B

Chen, Z. G., Zhang, C., Zou, Y., Zhang, E., Yang, L., Hong, M., et al. (2015). Scalable growth of high mobility dirac semimetal Cd_3As_2 microbelts. *Nano Lett.* 15, 5830–5834. doi: 10.1021/acs.nanolett.5b01885

Fang, C., Chen, Y., Kee, H. Y., and Fu, L. (2015). Topological nodal line semimetals with and without spin-orbital coupling. *Phys. Rev. B* 92:081201. doi: 10.1103/PhysRevB.92.081201

Fang, C., Weng, H., Dai, X., and Fang, Z. (2016). Topological nodal line semimetals. *Chin. Phys. B* 25:117106. doi: 10.1088/1674-1056/25/11/117106

Feng, X., Yue, C., Song, Z., Wu, Q., and Wen, B. (2018). Topological Dirac nodal-net fermions in AlB_2-type TiB_2 and ZrB_2. *Phys. Rev. Mater.* 2:014202. doi: 10.1103/PhysRevMaterials.2.014202

Fu, B. B., Yi, C. J., Zhang, T. T., Caputo, M., Ma, J. Z., Gao, X., et al. (2019). Dirac nodal surfaces and nodal lines in ZrSiS. *Sci. Adv.* 5:eaau6459. doi: 10.1126/sciadv.aau6459

Fu, C., Guin, S. N., Watzman, S. J., Li, G., Liu, E., Kumar, N., et al. (2018). Large Nernst power factor over a broad temperature range in polycrystalline Weyl semimetal NbP. *Energy Environ. Sci.* 11, 2813–2820. doi: 10.1039/C8EE02077A

Gao, H., Venderbos, J. W., Kim, Y., and Rappe, A. M. (2019). Topological semimetals from first principles. *Ann. Rev. Mater. Res.* 49, 153–183. doi: 10.1146/annurev-matsci-070218-010049

Gupta, U., Rajamathi, C. R., Kumar, N., Li, G., Sun, Y., Shekhar, C., et al. (2020). Effect of magnetic field on the hydrogen evolution activity using non-magnetic Weyl semimetal catalysts. *Dalton Trans.* 49, 3398–3402. doi: 10.1039/D0DT00050G

Han, Y., Wu, M., Feng, Y., Cheng, Z., Lin, T., Yang, T., et al. (2019). Competition between cubic and tetragonal phases in all-d-metal Heusler alloys, $X_{2--x}Mn_{1+x}V$ (X = Pd, Ni, Pt, Ag, Au, Ir, Co; x= 1, 0) a new potential direction of the Heusler family. *IUCrJ* 6, 465–472. doi: 10.1107/S2052252519004007

He, T., Zhang, X., Liu, Y., Dai, X., Liu, G., Yu, Z. M., et al. (2020). Ferromagnetic hybrid nodal loop and switchable type-I and type-II Weyl fermions in two dimensions. *Phys. Rev. B* 102:075133. doi: 10.1103/PhysRevB.102.075133

He, T., Zhang, X., Meng, W., Jin, L., Dai, X., and Liu, G. (2019). Topological nodal lines and nodal points in the antiferromagnetic material β-Fe_2PO_5. *J. Mater. Chem. C* 7, 12657–12663. doi: 10.1039/C9TC04046C

Hu, J., Xu, S. Y., Ni, N., and Mao, Z. (2019). Transport of topological semimetals. *Annu. Rev. Mater. Res.* 49, 207–252. doi: 10.1146/annurev-matsci-070218-010023

Jia, T., Meng, W., Zhang, H., Liu, C., Dai, X., Zhang, X., et al. (2020). Type-II Weyl state in VI_3 monolayer. *Front. Chem.* 8:722. doi: 10.3389/fchem.2020.00722

Jin, L., Zhang, X., He, T., Meng, W., Dai, X., and Liu, G. (2019b). Topological nodal line state in superconducting NaAlSi compound. *J. Mater. Chem. C* 7, 10694–10699. doi: 10.1039/C9TC03464A

Jin, L., Zhang, X., He, T., Meng, W., Dai, X., and Liu, G. (2020a). Electronic structure, doping effect and topological signature in realistic intermetallics $Li_{3--x}Na_xM$ (x = 3, 2, 1, 0; M= N, P, As, Sb, Bi). *Phys. Chem. Chem. Phys.* 22, 5847–5854. doi: 10.1039/C9CP06033B

Jin, L., Zhang, X., He, T., Meng, W., Dai, X., and Liu, G. (2020b). Ferromagnetic two-dimensional metal-chlorides MCl (M= Sc, Y., and La) candidates for Weyl nodal line semimetals with small spin-orbit coupling gaps. *Appl. Surface Sci.* 520:146376. doi: 10.1016/j.apsusc.2020.146376

Jin, L., Zhang, X., Liu, Y., Dai, X., Shen, X., Wang, L., et al. (2020c). Two-dimensional Weyl nodal-line semimetal in a d^0 ferromagnetic K_2N monolayer with a high Curie temperature. *Phys. Rev. B* 102:125118. doi: 10.1103/PhysRevB.102.125118

Jin, L., Zhang, X. M., Dai, X. F., Wang, L. Y., Liu, H. Y., and Liu, G. D. (2019a). Screening topological materials with a CsCl-type structure in crystallographic databases. *IUCrJ* 6, 688–694. doi: 10.1107/S2052252519007383

Jing, Y., and Heine, T. (2018). Two-dimensional kagome lattices made of hetero triangulenes are Dirac semimetals or single-band semiconductors. *J. Am. Chem. Soc.* 141, 743–747. doi: 10.1021/jacs.8b09900

Kambe, T., Sakamoto, R., Kusamoto, T., Pal, T., Fukui, N., Hoshiko, K., et al. (2014). Redox control and high conductivity of nickel bis (dithiolene) complex π-nanosheet: a potential organic two-dimensional topological insulator. *J. Am. Chem. Soc.* 136, 14357–14360. doi: 10.1021/ja507619d

Khoury, J. F., Rettie, A. J., Khan, M. A., Ghimire, N. J., Robredo, I., Pfluger, J. E., et al. (2019). A new three-dimensional subsulfide Ir_2In_8S with Dirac semimetal behavior. *J. Am. Chem. Soc.* 141, 19130–19137. doi: 10.1021/jacs.9b10147

Klemenz, S., Hay, A. K., Teicher, S. M., Topp, A., Cano, J., and Schoop, L. M. (2020). The role of delocalized chemical bonding in square-net-based topological semimetals. *J. Am. Chem. Soc.* 142, 6350–6359. doi: 10.1021/jacs.0c01227

Kong, D., and Cui, Y. (2011). Opportunities in chemistry and materials science for topological insulators and their nanostructures. *Nat. Chem.* 3, 845–849. doi: 10.1038/nchem.1171

Kresse, G., and Furthmüller, J. (1996). Efficient iterative schemes for ab initio total-energy calculations using a plane-wave basis set. *Phys. Rev. B* 54:11169. doi: 10.1103/PhysRevB.54.11169

Li, H., Cao, J., Zheng, W., Chen, Y., Wu, D., Dang, W., et al. (2012). Controlled synthesis of topological insulator nanoplate arrays on mica. *J. Am. Chem. Soc.* 134, 6132–6135. doi: 10.1021/ja3021395

Li, Y., and Xia, J. (2020). Cubic hafnium nitride: a novel topological semimetal hosting a 0-Dimensional (0-D) triple nodal point and a 1-D topological nodal ring. *Front. Chem.* 8:727. doi: 10.3389/fchem.2020.00727

Li, Y., Xia, J., Khenata, R., and Kuang, M. (2020a). Insight into the topological nodal line metal YB_2 with large linear energy range: a first-principles study. *Materials* 13:3841. doi: 10.3390/ma13173841

Li, Y., Xia, J., and Srivastava, V. (2020b). The tetragonal monoxide of platinum: a new platform for investigating nodal-line and nodal-point semimetallic behavior. *Front. Chem.* 8:704. doi: 10.3389/fchem.2020.00704

Lin, C. L., Arafune, R., Liu, R. Y., Yoshimura, M., Feng, B., Kawahara, K., et al. (2017). Visualizing type-II Weyl points in tungsten ditelluride by quasiparticle interference. *ACS Nano* 11, 11459–11465. doi: 10.1021/acsnano.7b06179

Liu, G., Jin, L., Dai, X., Chen, G., and Zhang, X. (2018a). Topological phase with a critical-type nodal line state in intermetallic CaPd. *Phys. Rev. B* 98:075157. doi: 10.1103/PhysRevB.98.075157

Liu, G. D., Zhai, X., Meng, H. Y., Lin, Q., Huang, Y., Zhao, C. J., et al. (2018b). Dirac semimetals based tunable narrowband absorber at terahertz frequencies. *Opt. Exp.* 26, 11471–11480. doi: 10.1364/OE.26.011471

Liu, J., Cheng, L., Zhao, D., Chen, X., Sun, H., Zhu, J. X., et al. (2020). Quenching of the relaxation pathway in the Weyl semimetal TaAs. *Phys. Rev. B* 102:064307. doi: 10.1103/PhysRevB.102.064307

Meng, L., Li, Y., Wu, J., Zhao, L., and Zhong, J. (2020). A type of novel Weyl semimetal candidate: layered transition metal monochalcogenides Mo_2XY (X, Y = S, Se, Te, X$\neq$ Y). *Nanoscale* 12, 4602–4611. doi: 10.1039/C9NR09123H

Meng, W., Zhang, X., Dai, X., and Liu, G. (2020a). IrSi as a superior electronic material with novel topological properties and nice compatibility with semiconductor Si. *Phys. Status Solidi–Rapid Res. Lett.* 14:2000178. doi: 10.1002/pssr.202000178

Meng, W., Zhang, X., He, T., Jin, L., Dai, X., Liu, Y., et al. (2020b). Ternary compound HfCuP: An excellent Weyl semimetal with the coexistence of type-I and type-II Weyl nodes. *J. Adv. Res.* 24, 523–528. doi: 10.1016/j.jare.2020.05.026

Murnaghan, F. D. (1944). The compressibility of media under extreme pressures. *Proc. Natl. Acad. Sci. U.S.A.* 30:244. doi: 10.1073/pnas.30.9.244

Peng, B., Zhang, H., Shao, H., Lu, H., Zhang, D. W., and Zhu, H. (2016). High thermoelectric performance of Weyl semimetal TaAs. *Nano Energy* 30, 225–234. doi: 10.1016/j.nanoen.2016.10.016

Peng, H., Dang, W., Cao, J., Chen, Y., Wu, D., Zheng, W., et al. (2012). Topological insulator nanostructures for near-infrared transparent flexible electrodes. *Nat. Chem.* 4, 281–286. doi: 10.1038/nchem.1277

Perdew, J. P., Burke, K., and Ernzerhof, M. (1996). Generalized gradient approximation made simple. *Phys. Rev. Lett.* 77:3865. doi: 10.1103/PhysRevLett.77.3865

Perdew, J. P., Burke, K., and Ernzerhof, M. (1998). Perdew, burke, and ernzerhof reply. *Phys. Rev. Lett.* 80:891. doi: 10.1103/PhysRevLett.80.891

Rasche, B., Isaeva, A., Ruck, M., Borisenko, S., Zabolotnyy, V., Büchner, B., et al. (2013). Stacked topological insulator built from bismuth-based graphene sheet analogues. *Nat. Mater.* 12, 422–425. doi: 10.1038/nmat3570

Schoop, L. M., Pielnhofer, F., and Lotsch, B. V. (2018). Chemical principles of topological semimetals. *Chem. Mater.* 30, 3155–3176. doi: 10.1021/acs.chemmater.7b05133

Sheng, X. L., Yu, Z. M., Yu, R., Weng, H., and Yang, S. (2017). A. d orbital topological insulator and semimetal in the antifluorite Cu_2S family: contrasting spin Helicities, nodal box, and hybrid surface states. *J. Phys. Chem. Lett.* 8, 3506–3511. doi: 10.1021/acs.jpclett.7b01390

Tang, F., Po, H. C., Vishwanath, A., and Wan, X. (2019). Comprehensive search for topological materials using symmetry indicators. *Nature* 566, 486–489. doi: 10.1038/s41586-019-0937-5

Walsh, L. A., Smyth, C. M., Barton, A. T., Wang, Q., Che, Z., Yue, R., et al. (2017). Interface chemistry of contact metals and ferromagnets on the topological insulator Bi2Se3. *J. Phys. Chem. C* 121, 23551–23563. doi: 10.1021/acs.jpcc.7b08480

Wang, J. T., Nie, S., Weng, H., Kawazoe, Y., and Chen, C. (2018). Topological nodal-net semimetal in a graphene network structure. *Phys. Rev. Lett.* 120:026402. doi: 10.1103/PhysRevLett.120.026402

Wang, S. S., Wu, W. K., and Yang, S. Y. (2019). Progress on topological nodal line and nodal surface. *Acta Phys. Sinica* 68:227101. doi: 10.7498/aps.68.20191538

Wang, X., Cheng, Z., Zhang, G., Wang, B., Wang, X. L., and Chen, H. (2020a). Rich novel zero-dimensional (0D), 1D, and 2D topological elements predicted in the $P6_3/m$ type ternary boride $HfIr_3B_4$. *Nanoscale* 12, 8314–8319. doi: 10.1039/D0NR00635A

Wang, X., Ding, G., Cheng, Z., Surucu, G., Wang, X. L., and Yang, T. (2020b). Novel topological nodal lines and exotic drum-head-like surface states in synthesized CsCl-type binary alloy TiOs. *J. Adv. Res.* 22, 137–144. doi: 10.1016/j.jare.2019.12.001

Wang, X., Ding, G., Cheng, Z., Surucu, G., Wang, X. L., and Yang, T. (2020c). Rich topological nodal line bulk states together with drum-head-like surface states in NaAlGe with anti-PbFCl type structure. *J. Adv. Res.* 23, 95–100. doi: 10.1016/j.jare.2020.01.017

Wang, X., Ding, G., Cheng, Z., Wang, X. L., Zhang, G., and Yang, T. (2020d). Intersecting nodal rings in orthorhombic-type $BaLi_2Sn$ compound. *J. Mater. Chem. C* 8, 5461–5466. doi: 10.1039/D0TC00504E

Wang, X., Ding, G., Khandy, S. A., Cheng, Z., Zhang, G., Wang, X. L., et al. (2020e). Unique topological nodal line states and associated exceptional thermoelectric power factor platform in Nb_3GeTe_6 monolayer and bulk. *Nanoscale* 12, 16910–16916. doi: 10.1039/D0NR03704D

Wang, X., Zhou, F., and Chen, H. (2020f). Organic-inorganic hybrid coordination polymer $C_3H_9CdCl_3N$ co-exhibiting superior Dirac point and nodal surface states. *Results Phys.* 17:103159. doi: 10.1016/j.rinp.2020.103159

Wang, Z. F., Su, N., and Liu, F. (2013). Prediction of a two-dimensional organic topological insulator. *Nano Lett.* 13, 2842–2845. doi: 10.1021/nl401147u

Wu, M., Han, Y., Bouhemadou, A., Cheng, Z., Khenata, R., Kuang, M., et al. (2019). Site preference and tetragonal distortion in palladium-rich Heusler alloys. *IUCrJ* 6, 218–225. doi: 10.1107/S2052252518017578

Wu, W., Liu, Y., Li, S., Zhong, C., Yu, Z. M., Sheng, X. L., et al. (2018). Nodal surface semimetals: theory and material realization. *Phys. Rev. B* 97:115125. doi: 10.1103/PhysRevB.97.115125

Xu, Q., Yu, R., Fang, Z., Dai, X., and Weng, H. (2017). Topological nodal line semimetals in the CaP_3 family of materials. *Phys. Rev. B* 95:045136. doi: 10.1103/PhysRevB.95.045136

Xu, S. G., Chen, Z. J., Zhao, Y. J., Zhang, X., Xu, H., and Yang, X. B. (2020). Realizing graphene-like Dirac cones in triangular boron sheets by chemical functionalization. *J. Mater. Chem. C* 8, 2798–2805. doi: 10.1039/C9TC06464H

Yan, Z., Bi, R., Shen, H., Lu, L., Zhang, S. C., and Wang, Z. (2017). Nodal-link semimetals. *Phys. Rev. B* 96:041103. doi: 10.1103/PhysRevB.96.041103

Zeugner, A., Nietschke, F., Wolter, A. U., Ga,ß, S., Vidal, R. C., Peixoto, T. R., et al. (2019). Chemical aspects of the candidate antiferromagnetic topological insulator $MnBi_2Te_4$. *Chem. Mater.* 31, 2795–2806. doi: 10.1021/acs.chemmater.8b05017

Zhang, G., Qin, H., Chen, J., He, X., Lu, L., Li, Y., et al. (2011). Growth of topological insulator Bi_2Se_3 thin films on $SrTiO_3$ with large tunability in chemical potential. *Adv. Funct. Mater.* 21, 2351–2355. doi: 10.1002/adfm.201002667

Zhang, M., Yang, Z., and Wang, G. (2018c). Coexistence of Type-I and Type-II Weyl points in the Weyl-semimetal OsC_2. *J. Phys. Chem. C* 122, 3533–3538. doi: 10.1021/acs.jpcc.8b00920

Zhang, X., Fu, B., Jin, L., Dai, X., Liu, G., and Yao, Y. (2019). Topological nodal line electrides: realization of an ideal nodal line state nearly immune from spin–orbit coupling. *J. Phys. Chem. C* 123, 25871–25876. doi: 10.1021/acs.jpcc.9b08446

Zhang, X., Guo, R., Jin, L., Dai, X., and Liu, G. (2018a). Intermetallic Ca_3Pb: a topological zero-dimensional electride material. *J. Mater. Chem. C* 6, 575–581. doi: 10.1039/C7TC04989G

Zhang, X., Liu, Q., Xu, Q., Dai, X., and Zunger, A. (2018b). Topological insulators versus topological Dirac semimetals in honeycomb compounds. *J. Am. Chem. Soc.* 140, 13687–13694. doi: 10.1021/jacs.8b06652

Zhao, B., Guo, C., Garcia, C. A., Narang, P., and Fan, S. (2020). Axion-field-enabled nonreciprocal thermal radiation in Weyl semimetals. *Nano Lett.* 20, 1923–1927. doi: 10.1021/acs.nanolett.9b05179

Zhao, X., and Ma, F. (2020). Hexagonal wurtzite MnO in ferromagnetic state: A magnetic topological spin-gapless Weyl semimetal. *Phys. Lett. A* 384:126494. doi: 10.1016/j.physleta.2020.126494

Zhao, Z., Zhang, Z., and Guo, W. (2020). A family of all sp2-bonded carbon allotropes of topological semimetals with strain-robust nodal-lines. *J. Mater. Chem. C* 8, 1548–1555. doi: 10.1039/C9TC05470G

Zhong, C., Chen, Y., Xie, Y., Sun, Y. Y., and Zhang, S. (2017). Semi-Dirac semimetal in silicene oxide. *Phys. Chem. Chem. Phys.* 19, 3820–3825. doi: 10.1039/C6CP08439G

Zhong, C., Chen, Y., Xie, Y., Yang, S. A., Cohen, M. L., and Zhang, S. B. (2016). Towards three-dimensional Weyl-surface semimetals in graphene networks. *Nanoscale* 8, 7232–7239. doi: 10.1039/C6NR00882H

Zhou, F., Ding, G., Cheng, Z., Surucu, G., Chen, H., and Wang, X. (2020). Pnma metal hydride system LiBH: a superior topological semimetal with the coexistence of twofold and quadruple degenerate topological nodal lines. *J. Phys.* 32:365502. doi: 10.1088/1361-648X/ab8f5d

Zhou, P., Ma, Z. S., and Sun, L. Z. (2018). Coexistence of open and closed type nodal line topological semimetals in two dimensional B2C. *J. Mater. Chem. C* 6, 1206–1214. doi: 10.1039/C7TC05095J

Zhou, Y., Zhao, Y. Q., Zeng, Z. Y., Chen, X. R., and Geng, H. Y. (2019). Anisotropic thermoelectric properties of Weyl semimetal NbX (X = P and As) a potential thermoelectric material. *Phys. Chem. Chem. Phys.* 21, 15167–15176. doi: 10.1039/C9CP02020A

Conflict of Interest: The authors declare that the research was conducted in the absence of any commercial or financial relationships that could be construed as a potential conflict of interest.

frontiers in Chemistry

ORIGINAL RESEARCH
published: 11 December 2020
doi: 10.3389/fchem.2020.546947

Phase Transition and Electronic Structures of All-*d*-Metal Heusler-Type X_2MnTi Compounds (X = Pd, Pt, Ag, Au, Cu, and Ni)

Mengxin Wu[1], *Feng Zhou*[1], *Rabah Khenata*[2], *Minquan Kuang*[1]* *and Xiaotian Wang*[1]*

[1] School of Physical Science and Technology, Southwest University, Chongqing, China, [2] Laboratoire de Physique Quantique de la Matière et de la Modélisation Mathématique (LPQ3M), Université de Mascara, Mascara, Algeria

In this work, we investigated the phase transition and electronic structures of some newly designed all-*d*-metal Heusler compounds, X_2MnTi (X = Pd, Pt, Ag, Au, Cu, and Ni), by means of the first principles. The competition between the XA and $L2_1$ structures of these materials was studied, and we found that X_2MnTi favors to feature the $L2_1$-type structure, which is consistent with the well-known site-preference rule (SPR). Under the $L2_1$ structure, we have studied the most stable magnetic state of these materials, and we found that the ferromagnetic state is the most stable due to its lower energy. Through tetragonal deformation, we found that the $L2_1$ structure is no longer the most stable structure, and a more stable tetragonal $L1_0$ structure appeared. That is, under the tetragonal strain, the material enjoys a tetragonal phase transformation (i.e., from cubic $L2_1$ to tetragonal $L1_0$ structure). This mechanism of $L2_1$-$L1_0$ structure transition is discussed in detail based on the calculated density of states. Moreover, we found that the energy difference between the most stable phases of $L1_0$ and $L2_1$, defined as ΔE_M ($\Delta E_M = E_{Cubic}$-$E_{Tetragonal}$), can be adjusted by the uniform strain. Finally, the phonon spectra of all tetragonal X_2MnTi (X = Pd, Pt, Ag, Au, Cu, and Ni) phases are exhibited, which provides a powerful evidence for the stability of the tetragonal $L1_0$ state. We hope that our research can provide a theoretical guidance for future experimental investigations.

Keywords: spintronic, electronic structure, DFT, electronic properties, Heusler alloys

OPEN ACCESS

Edited by:
Lalith Perera,
National Institute of Environmental Health Sciences (NIEHS), United States

Reviewed by:
Xin Zhou,
Harbin Institute of Technology, China
Qiang Wang,
Nanjing Tech University, China
Shubin Liu,
University of North Carolina at Chapel Hill, United States

***Correspondence:**
Minquan Kuang
mqkuang@swu.edu.cn
Xiaotian Wang
xiaotianwang@swu.edu.cn

Specialty section:
This article was submitted to Theoretical and Computational Chemistry, a section of the journal Frontiers in Chemistry

Received: *30 March 2020*
Accepted: *21 October 2020*
Published: *11 December 2020*

Citation:
Wu M, Zhou F, Khenata R, Kuang M and Wang X (2020) Phase Transition and Electronic Structures of All-d-Metal Heusler-Type X_2MnTi Compounds (X = Pd, Pt, Ag, Au, Cu, and Ni). Front. Chem. 8:546947. doi: 10.3389/fchem.2020.546947

INTRODUCTION

Magnetic shape memory compounds (MSMAs) (O'Handley, 1998) are a new type of intelligent materials which integrates magnetic controlled shape memory and magnetic field-induced strain simultaneously. It can be used as key components of sensors and brakes in the future. MSMAs have both thermoplastic martensitic transformation (Oikawa et al., 2001) and magnetic transformation (Oikawa et al., 2002), and their shape memory effect can be controlled by the magnetic field. That is to say, under the effect of magnetic field, their size or volume will be changed, resulting in a great strain, i.e., the magnetostrictive effect (Populoh et al., 2012). In addition, MSMAs enjoy magnetoresistance (Ullakko et al., 1996) and magnetocaloric (GschneidnerJr et al., 2005) effects, so they have been regarded as a research hot spot in recent years.

Heusler (Graf et al., 2011; Birkel et al., 2013; Ahmadian and Salary, 2014; Kirievsky et al., 2014; Xue et al., 2016; Miranda and Gruhn, 2017; Ghunaim et al., 2018; Li et al., 2019, 2020) compounds

belong to intermetallic compounds. Heusler compounds naturally have many excellent properties, such as high Curie temperature (T_C) (Wurmehl et al., 2005), adjustable electronic structure, suitable semiconductor lattice constants, and various magnetic properties. Therefore, Heusler compounds can be seen as good candidates for spin gapless semiconductors (SGSs) (Gao and Yao, 2013; Skaftouros et al., 2013; Wang et al., 2016; Wang X. et al., 2017), thermoelectric materials (Downie et al., 2013; Huang et al., 2018; Mallick and Vitta, 2018), shape memory compounds (SMAs) (Aksoy et al., 2009; Li et al., 2018), half metals (Shigeta et al., 2018; Singh and Gupta, 2019; Hao et al., 2020), and topological insulators (Hou et al., 2015; Lin et al., 2015). Because Heusler compounds possess excellent properties, they have been regarded as a research hot spot over the past 100 years. To date, researchers have discovered thousands of Heusler compounds. Heusler compounds roughly can be divided into three structures, namely, full Heusler (Wang X. T. et al., 2017), half Heusler (Silpawilawan et al., 2017), and quaternary Heusler (Cui et al., 2019), whose stoichiometric compositions are X_2YZ, XYZ, and XYMZ, respectively. X, Y, and M are usually transition elements, while the Z atom is a main group element. In recent years, a new type of Heusler compounds has been found by researchers, and this type of Heusler compounds is named as all-*d*-metal Heusler compounds (Wei et al., 2015).

In the early 1990s, all-*d*-metal Heusler compounds Zn_2AuAg and Zn_2CuAu (Muldawer, 1966) were synthesized experimentally, which proved that all-*d*-metal Heusler compounds can be successfully prepared. This interesting study opened up a new direction for the research of Heusler compounds. All-*d*-metal Heusler compounds are different from common Heusler compounds in that they are composed of transition metal elements without the participation of main group elements. Compared with common Heusler compounds, all-*d*-metal Heusler compounds have the following advantages: (1) all-*d*-metal Heusler compounds do have not many restrictions on atomic site preference, so they can show more phase space and versatility than traditional materials; (2) they have high strength and toughness; and (3) in addition to magnetic phase transitions, all-*d*-metal Heusler compounds also have many untouched physical properties, such as spintronics properties.

Recently, an effective method, i.e., adjusting composition, was proposed by Tan et al. (2019) to make regular the phase transition of all-*d*-metal Heusler compounds. In their work, the atomic ordering, structural stability, tetragonal deformation, magnetism, and electronic structures of the Mn–Ni–V system, including $Mn_{2-x}Ni_{1.5+x}V_{0.5}$, $Mn_{2-x}Ni_{1+x}V$, and $Mn_{2-x}Ni_{0.5+x}V_{1.5}$ compounds, are studied by employing the first principles. They stated that the tetragonal phase is more stable than the cubic phase for these all-*d*-metal Heusler compounds: $MnNi_2V$, $Mn_{1.25}Ni_{1.75}V$, $MnNi_{2.5}V_{0.5}$, and $Mn_{0.5}Ni_2V_{1.5}$.

Based on the above information, we focus on the electronic structures and phase transition of all-*d*-metal Heusler compounds X_2MnTi (X = Pd, Pt, Ag, Au, Cu, and Ni) with the help of the first principles. To the best of knowledge, the physical properties of the X_2MnTi system have not been studied yet by other researchers up to now. We will reflect that a $L2_1$-$L1_0$ phase transition can be found in all-*d*-metal Heusler compounds X_2MnTi (X = Pd, Pt, Ag, Au, Cu, and Ni) under the tetragonal distortion. The effect of uniform strain on the cubic–tetragonal transition for this X_2MnTi system was also discussed in detail in this work. The mechanism of the $L2_1$-$L1_0$ phase transition is discussed according to the calculated density of states in both cubic and tetragonal phases, and finally, we will further prove the stability of the tetragonal phase by calculating the phonon spectrum of the tetragonal $L1_0$ phase.

COMPUTATIONAL METHODS

Electronic structure calculations were performed using density functional theory (DFT), within the VASP code (Hafner, 2007). The exchange–correlation potential is treated by using the generalized gradient approximation (GGA) (Perdew et al., 1996) with the Perdew–Burke–Ernzerhof (PBE) (Perdew et al., 1998) functional. We also use the projection enhanced wave (PAW) (Kresse and Furthmüller, 1996) method to deal with the interaction between the ion nucleus and valence electron. In the calculations, the cutoff energy was set at 450 eV. A Monkhorst-Pack special 12 × 12 × 12 k-point mesh was used in the Brillouin zone (BZ) integration. The unit cell was optimized until the force and total energy were <0.001 eV/Å and 1×10^{-5} eV, respectively. The crystal models of cubic $L2_1$ phase and tetragonal $L1_0$ phase of Heusler alloys are built *via* VESTA. To calculate the dynamical stabilities of these alloys, phonon dispersion is obtained by means of the force-constants method using Nanodcal code. For the $L2_1$-type X_2MnTi alloys, two magnetic states are considered: one is the ferromagnetic state with spin orderings of X-1, X-2, Mn, and Ti that are ↑↑↑↑; the other one is the antiferromagnetic state with spin orderings of X-1, X-2, Mn, and Ti that are ↓↓↑↓, respectively.

RESULTS AND DISCUSSION

The Crystal and Magnetic Structures of the X_2MnTi (X = Pd, Pt, Ag, Au, Cu, and Ni) Heusler Compounds

Heusler compounds, X_2YZ, enjoy a highly ordered cubic structure (Han et al., 2019a). There are generally four different positions in a primitive cell, namely, A (0, 0, 0), B (0.25, 0.25, 0.25), C (0.5, 0.5, 0.5), and D (0.75, 0.75, 0.75), respectively. The transition metal elements X and Y occupy the A, B, and C positions, and the main group element Z is preferred to occupy the D position. Different occupation positions of X and Y atoms will lead to different structures, namely, $L2_1$ and XA structures (Suzuki and Kyono, 2004) (as shown in **Figures 1A,B**). In the former, two X atoms occupy A and C positions, and Y and Z atoms enter B and D positions, respectively; in the latter, two X atoms occupy A and B positions, and Y and Z atoms are located at C and D positions, respectively.

Next, we studied the competition between the XA structure and the $L2_1$ structure of X_2MnTi. In **Figure 2**, the total energy

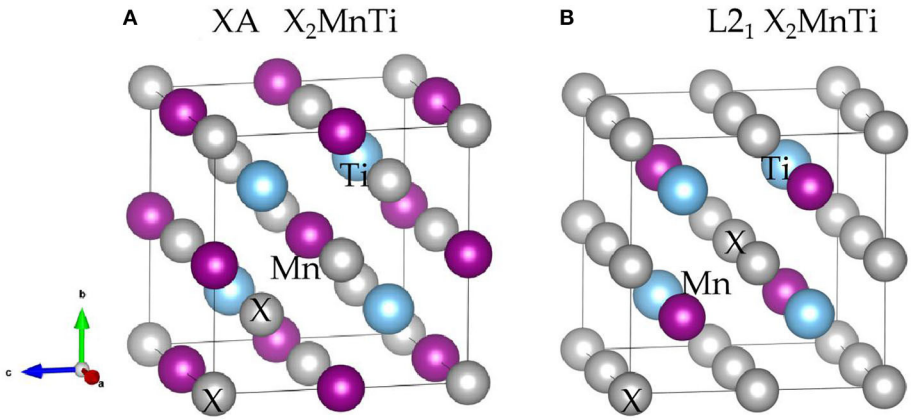

FIGURE 1 | Crystal structure of the **(A)** XA-type X_2MnTi and **(B)** $L2_1$-type X_2MnTi (X = Pd, Pt, Ag, Au, Cu, and Ni); X is highlighted by gray balls, Ti is marked by blue balls, and Mn is marked by purple balls, respectively.

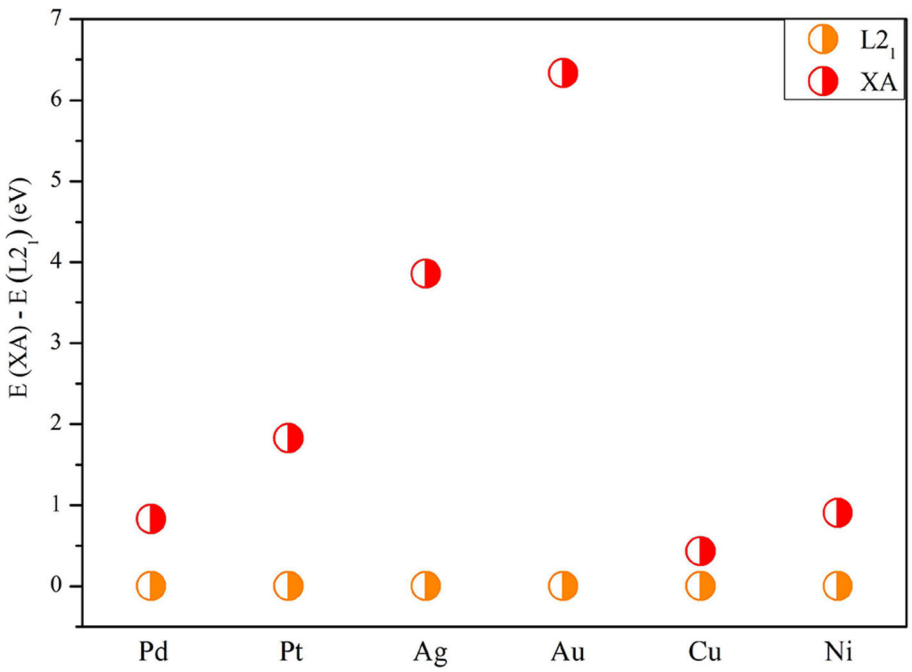

FIGURE 2 | Total energy difference E(XA) – E($L2_1$) of X_2MnTi under the $L2_1$ and XA structure (in FM state) with the energy of $L2_1$ set as 0 eV for reference.

of X_2MnTi at the ground state with different structures ($L2_1$ and XA) is determined, and we set the ground state energy of the $L2_1$ structure as 0 eV as reference. One can clearly see that, for X_2MnTi, the total energy of XA is higher than $L2_1$, reflecting that the most stable ordered structure is $L2_1$ for the X_2MnTi system. In **Figure 3**, we further give a comparison of the total energy of two magnetic states [ferromagnetic (FM) and antiferromagnetic (AFM)] for the $L2_1$-type X_2MnTi. We set the total energy of AFM to 0 eV as reference. As shown in **Figure 3**, the energy of X_2MnTi in the FM structure is lower than 0, which indicates that the X_2MnTi tends to exhibit the FM magnetic state.

The $L2_1$-$L1_0$ Phase Transition of All-*d*-Metal Heusler-Type X_2MnTi

In this section, our research goal is to explore the possible competition between the $L2_1$ (see **Figure 4A**) and $L1_0$ (see **Figure 4B**) of the all-*d*-metal Heusler compounds X_2MnTi. We used Bain paths to investigate the reversible transformation between the ordered $L2_1$ and $L1_0$ phases during tetragonal distortion. Bain paths (Alippi et al., 1997) have tetragonal states along the geometries which connect the bcc and fcc phases of a material. It is assumed that there is no cell volume change after applying deformation on the cubic phase, then the energy

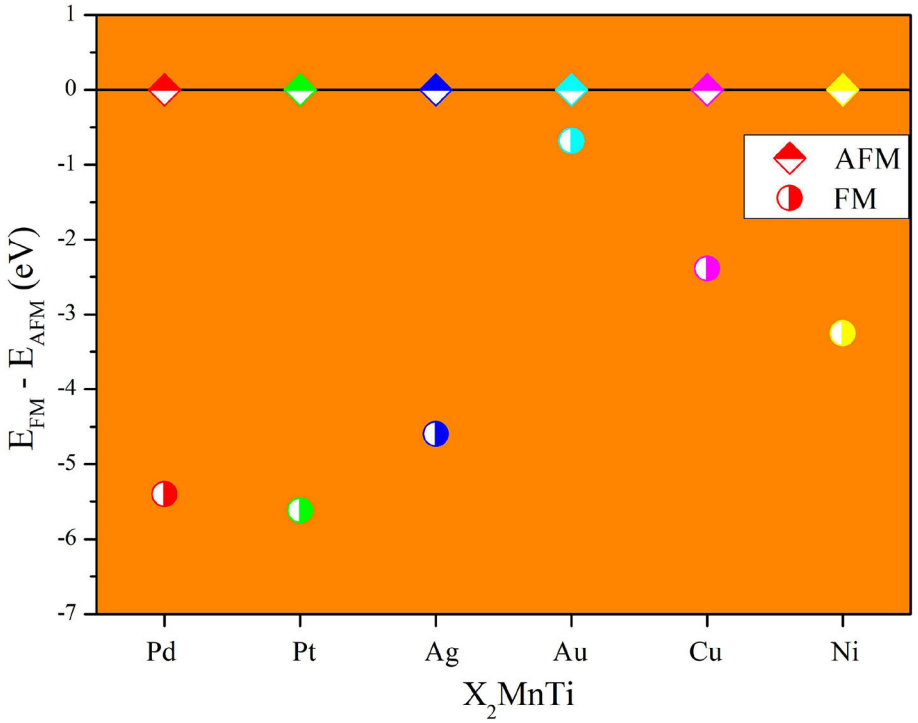

FIGURE 3 | Total energy difference ($E_{FM} - E_{AFM}$) of different magnetic states (AFM and FM) of X_2MnTi ($L2_1$ structure) with the total energy of AFM set as 0 eV.

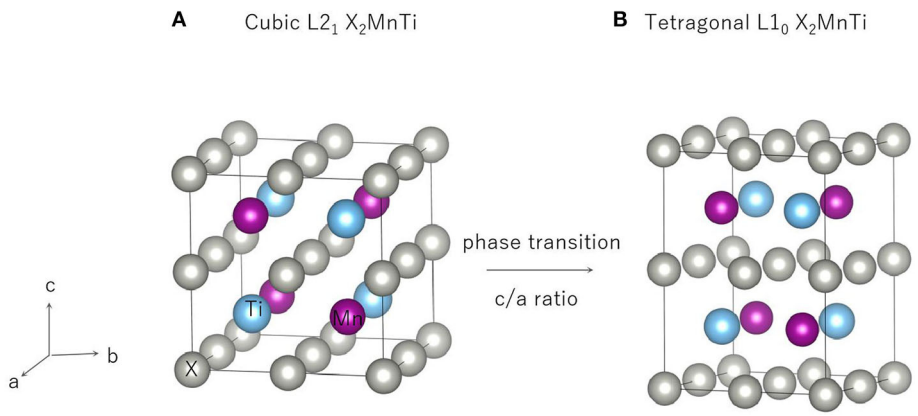

FIGURE 4 | Cubic phase ($L2_1$) **(A)** and tetragonal phase ($L1_0$) **(B)** of X_2MnTi compounds.

difference ΔE in respect to c/a ratios is calculated to estimate whether it is a stable or metastable phase. It is a commonly used method to predict reversible transformation, and a number of literature (Barman et al., 2007; Özdemir Kart et al., 2008; Qawasmeh and Bothina, 2012; Zeleny et al., 2014) have used this method to estimate shape memory effect in Heusler FSMAs, such as Ni_2MnGa and Mn_2NiGa.

In **Figure 5**, we can see that all X_2MnTi (X = Pd, Pt, Ag, Au, Cu, and Ni) compounds present a $L2_1$-$L1_0$ (possible martensitic transformation) under the effect of tetragonal distortion. In detail, we found that X_2MnTi (except for X = Au) compounds have two local minimum energies, one locates at $c/a < 1$ and the other locates at $c/a > 1$. The value of the local minimum energy with $c/a > 1$ is lower than that of the local minimum energy with $c/a < 1$, which means that the local minimum energy with $c/a > 1$ is the most stable state. Moreover, when $c/a < 1$, the local minimum energy of X_2MnTi (except for X = Au) is a metastable phase. For the Au_2MnTi compound, there is only one local minimum energy, which locates at $c/a > 1$. This local minimum energy is the most stable phase and there is no

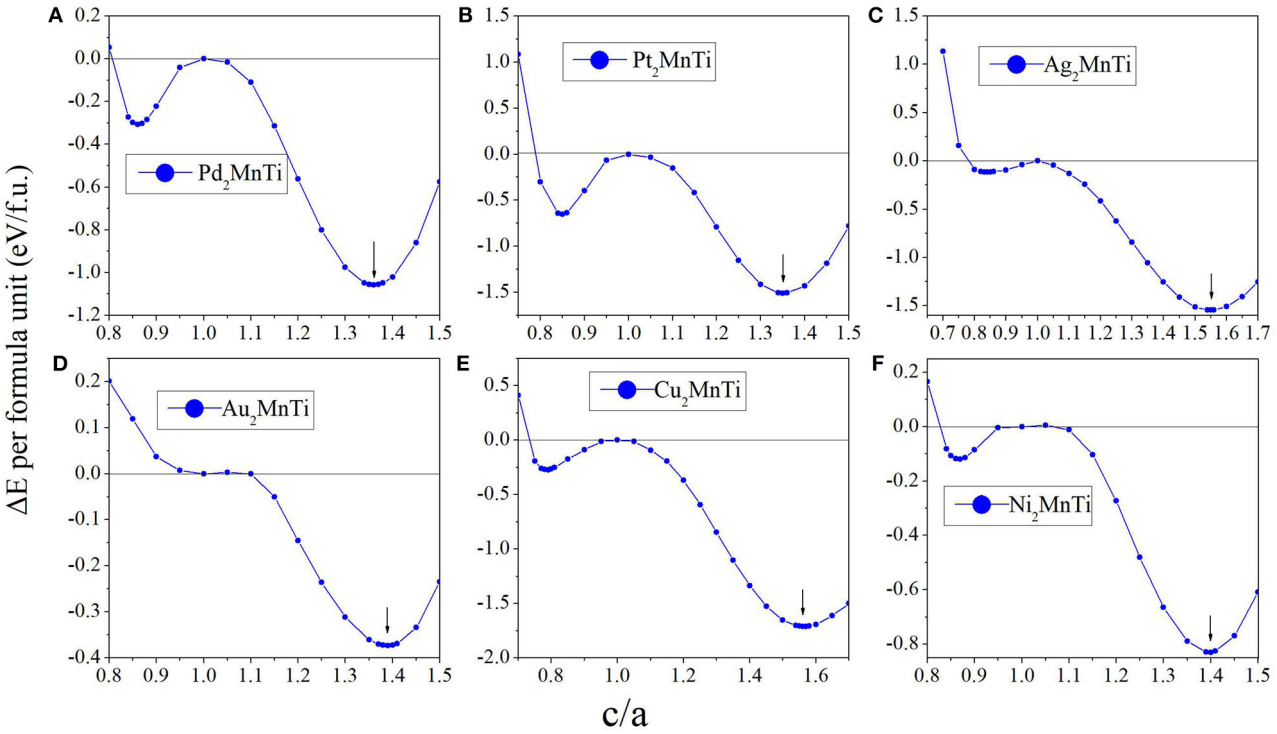

FIGURE 5 | (A–F) Relationship between the *c*/*a* ratio and ΔE ($\Delta E = E_T - E_C$) for X_2MnTi (X = Pd, Pt, Ag, Au, Cu, and Ni) compounds.

metastable structure during the cubic–tetragonal transformation. The *c*/*a* ratio values of the most stable tetragonal $L1_0$ structure of these materials are summarized in **Table 2**.

Next, we studied the influence of uniform strain on the competitiveness of the $L2_1$ and $L1_0$ structures. We give Cu_2MnTi and Ni_2MnTi as examples in **Figure 6** for a detailed discussion.

By adjusting the lattice parameters of X_2MnTi (X = Cu, Ni), their volume was changed between −2 and +2%, and then tetragonal distortion is applied to the cubic crystal structures. As shown in **Figure 6**, under the effect of tetragonal distortion, we can see that all substances with a volume of −2 and +2% still have two local energy minimums, which is the same as the optimized volume (V_{opt}). However, the difference is that during the volume changes from +2 to −2%, the minimum value of local energy gradually becomes lower, that is, the $L1_0$ state becomes more and more stable as the volume decreases.

In addition, it can be seen that the value of the *c*/*a* ratio for the most stable $L1_0$ phase also changes with the volume changes. During the volume changes from −2% to +2%, the *c*/*a* ratio (for the most stable $L1_0$ phase) gradually decreases. A smaller *c*/*a* ratio means a smaller degree of tetragonal distortion.

The Calculated Density of States of All-*d*-Metal Heusler-Type Compounds X_2MnTi

We calculated their total density of states (TDOSs) and partial state density of states (PDOSs) (Han et al., 2019b) in cubic and tetragonal states, respectively, and we plotted them in **Figures 7**, **8**.

We found that the TDOS of tetragonal structure around the Fermi level is softer than the cubic TDOS. For example, we can find some strong peaks (see the red lines) near the Fermi level in the spin-down direction and some small peaks in the spin-up direction (see the black line) for the cubic phase (see **Figure 7A**). Note that one of the contributions to the total energy is the band energy $E_{band} = \int_{E_{min}}^{E_F} dEDOS(E)E$; a reduction of the DOS near E_F in a tetragonal phase, in conjunction with the conservation of the integral for the number of valence electrons $N_V = \int_{E_{min}}^{E_F} dEDOS(E)$, often leads to a lower band energy and, thus, to a lower total energy for the tetragonal phase than for the cubic phase. As shown in **Figure 7**, we can find that, under the effect of the tetragonal strain, the energy states near E_F tend to decrease or move to a high energy level. We give two more detailed explanations as follows: (1) as shown in **Figures 7A,C–F**, we can clearly observe that the local energy states (blue lines) near the Fermi level of the tetragonal $L1_0$ phase are significantly lower than those of the cubic $L2_1$ phase (black lines). Thanks to the TDOSs above, the total energy of the system will be released, resulting in cubic–tetragonal transformation; (2) as shown in **Figures 7A,C**, we find that the peaks (red line) of the cubic structure near the Fermi level disappeared in the tetragonal structure; however, a very small valley at the same energy (see the pink line) occurred. The peak to valley transition of TDOS near the Fermi level also proves that the tetragonal $L1_0$ structure is more stable for X_2MnTi compounds.

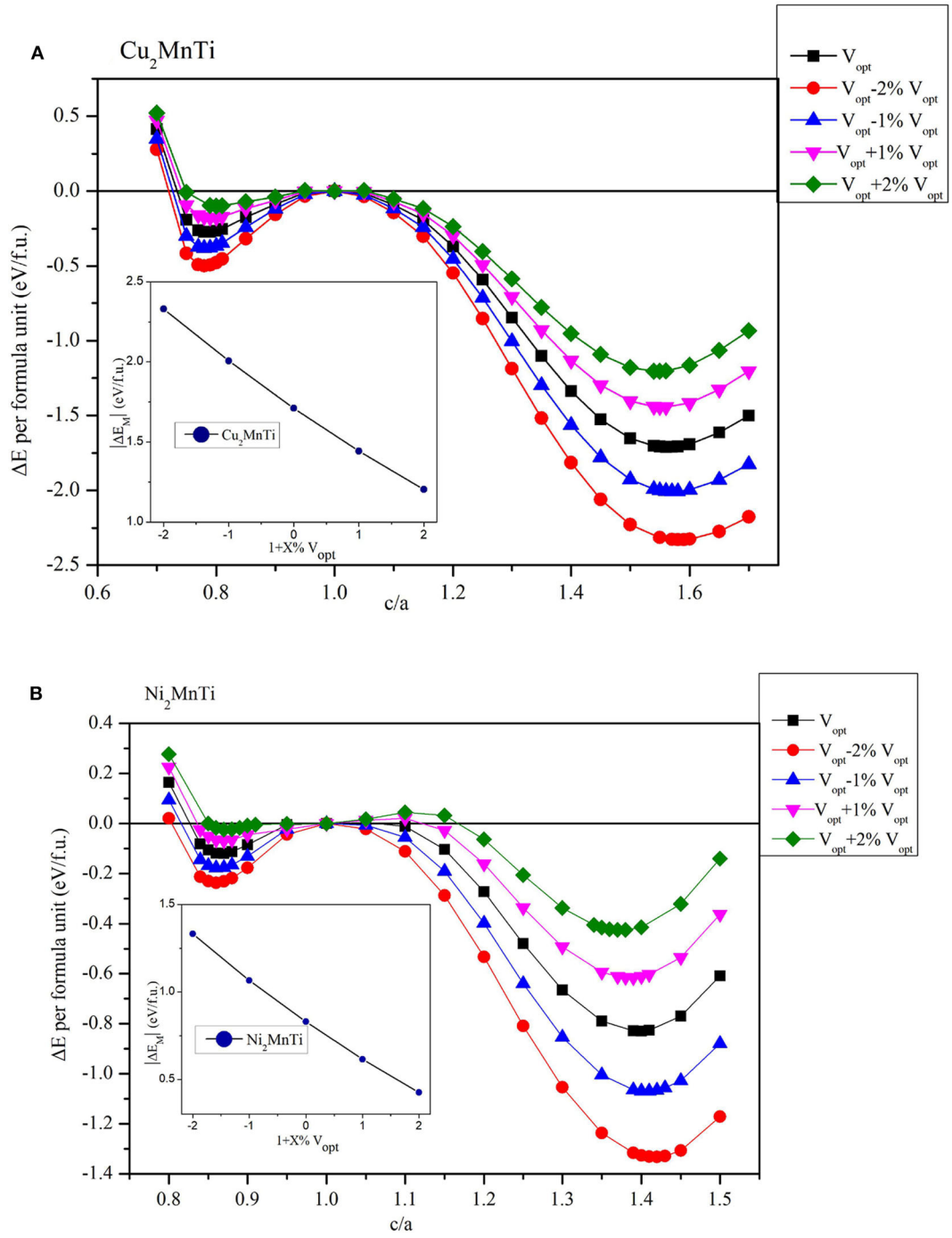

FIGURE 6 | Relationship between *c/a* ratio and ΔE ($\Delta E = E_T - E_C$) with different volumes (insert figures: the relationship between the $|\Delta E_M|$ and $1 + X\%V_{opt}$) for **(A)** the Cu_2MnTi compound and **(B)** the Ni_2MnTi compound.

In **Figure 8**, we also show the PDOSs of each atom in the cubic and tetragonal phases. As shown in **Figure 8A**, the PDOS of the $L2_1$-type Ag orbitals is almost located in the energy areas of −4.5 to −6 eV. In this region, the spin-up and spin-down PDOSs of Ag-d are almost symmetrical, reflecting that the contribution of Ag atoms to the total magnetism is relatively small. In the energy range from −1.5 to −4 eV, two large energy peaks, which come from the Mn-d orbitals, can be found in the spin-up channel; however, the DOS in the spin-down is nearly flat. Above the Fermi level, the TDOS in the spin-up channel is coming from the Ti-d orbital, and the TDOS in the spin-down channel is arising from the hybridization between the Ti-d and Mn-d orbitals. A

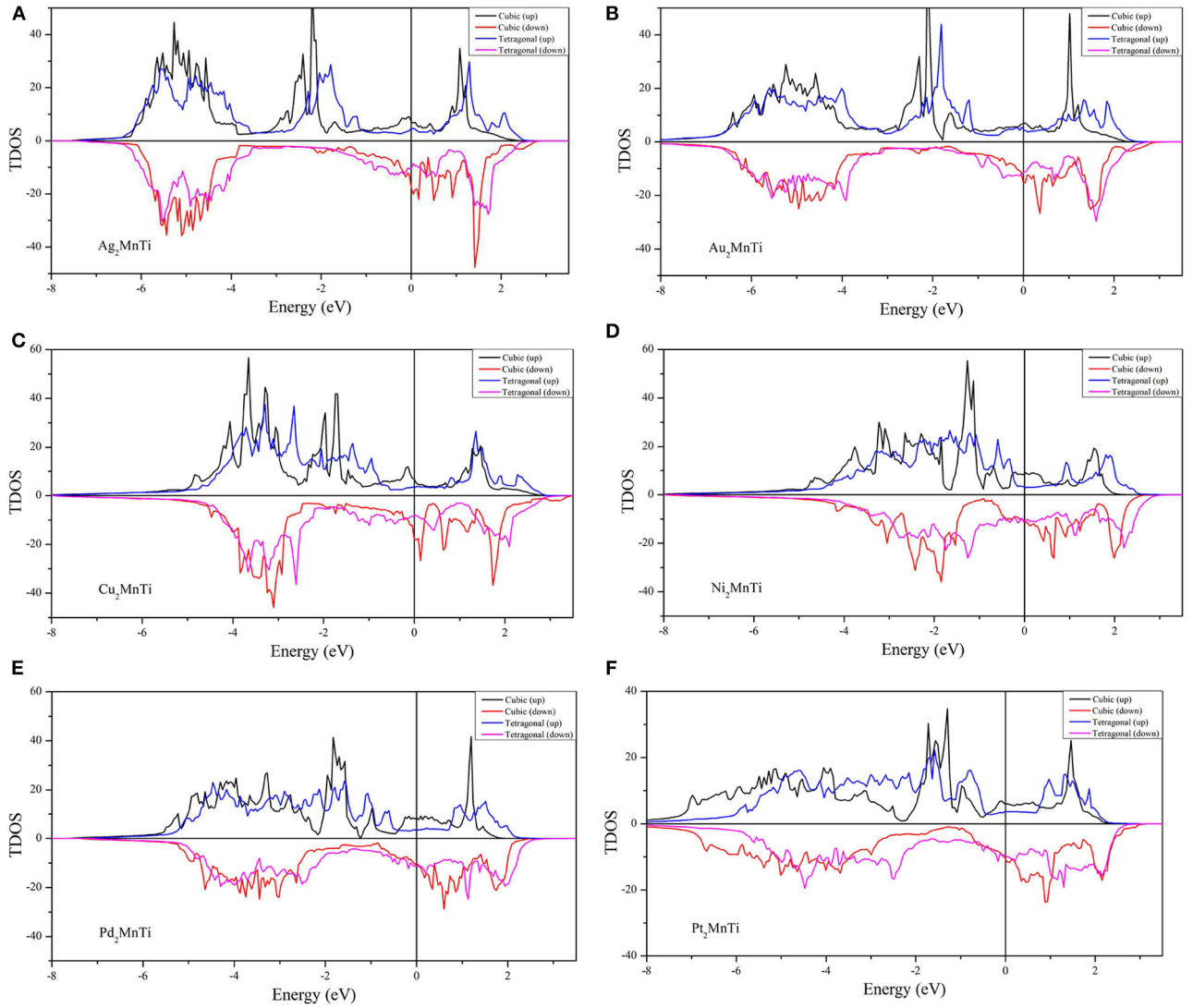

FIGURE 7 | (A–F) Calculated TDOSs of X_2MnTi (X = Pd, Pt, Ag, Au, Cu, and Ni) compounds in cubic and tetragonal phases.

similar phenomenon can also be found in $L2_1$-type Au_2MnTi as shown in **Figure 8B**.

As shown in **Figures 8C–F**, some large peaks can be obviously found below the Fermi level in the spin-up channel for the $L2_1$-type X_2MnTi (X = Ni, Cu, Pd, Pt) alloys. The formation of these peaks owes to the hybridization between X-d and Mn-d orbitals. For Ni_2MnTi, the energy peak of the Ni-d orbital is larger than that of the Mn-d orbital around −1.2 eV; however, for the other three cases, the energy peaks of the X-d orbital are smaller than those of the X-d orbitals. Above the Fermi level, the TDOS is mainly coming from the Mn-d orbital in the spin-up channel and from the Mn-d and X-d orbitals in the spin-down channel.

As shown in **Figure 8**, near the Fermi level, PDOSs of the Mn atom will produce a strong spin splitting in two spin channels, and then result in strong magnetism. Thus, the total magnetism of X_2MnTi is mainly coming from the Mn atoms. We also exhibit the total and atomic magnetic moments in **Tables 1**, **2**.

Finally, we calculated the phonon spectrum of the X_2MnTi (X = Pd, Pt, Ag, Au, Cu, and Ni) tetragonal $L1_0$ phase by means of the force-constants method using Nanodcal code and the results are collected in **Figure 9**. In **Figure 9**, we can clearly see that there are no virtual frequencies in the phonon spectrum of the X_2MnTi, and the absence of virtual frequencies further confirms that their tetragonal $L1_0$ states are theoretically stable. Unfortunately, the possible $L2_1$-$L1_0$ phase transition of X_2MnTi (X = Pd, Pt, Ag, Au, Cu, and Ni) has not been studied experimentally, and therefore, a comparison between the theoretical and experimental results cannot be shown in the current work. However, this investigation can help in understanding the physics in all-*d*-metal alloys. Moreover, we

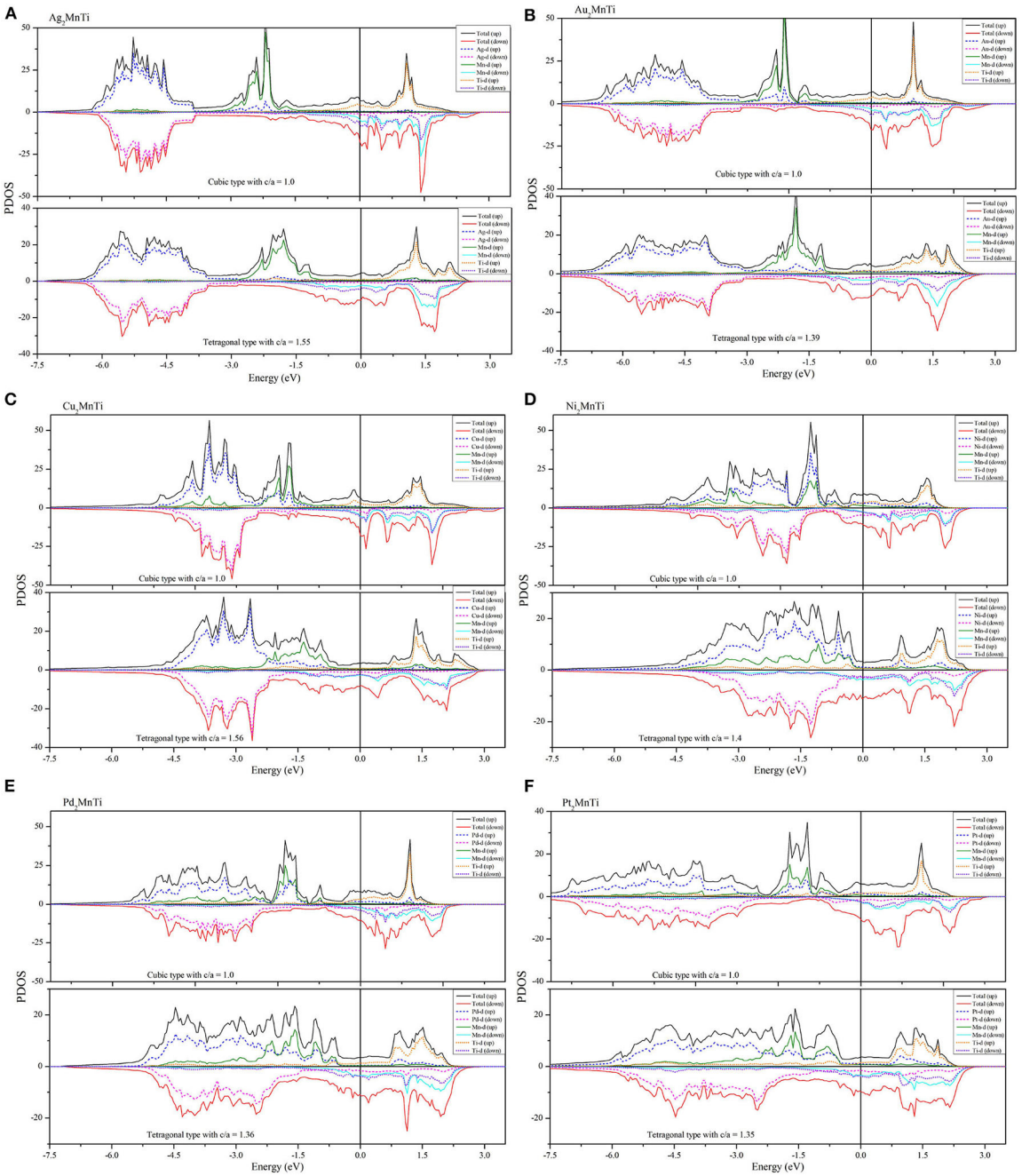

FIGURE 8 | (A–F) PDOS diagrams of X_2MnTi (X = Pd, Pt, Ag, Au, Cu, and Ni) compounds in cubic and tetragonal phases.

TABLE 1 | Total and atomic magnetic moments for cubic $L2_1$ type X_2MnTi (X = Pd, Pt, Cu, Ni, Ag, Au).

Compounds X_2MnTi	Mt (μ_B/f.u.)	M_{Mn} (μ_B)	M_{Ti} (μ_B)	M_{X-1} (μ_B)	M_{X-2} (μ_B)
Pd_2MnTi	3.9295	3.792	−0.108	0.123	0.123
Pt_2MnTi	4.17525	3.774	0.008	0.157	0.157
Cu_2MnTi	3.4385	3.415	−0.117	0.069	0.069
Ni_2MnTi	3.90075	3.372	−0.098	0.313	0.313
Ag_2MnTi	3.45975	3.79	−0.376	0.022	0.022
Au_2MnTi	3.60475	3.76	−0.215	0.03	0.03

TABLE 2 | Total and atomic magnetic moments, and c / a ratio for tetragonal $L1_0$ type X_2MnTi (X = Pd, Pt, Cu, Ni, Ag, Au).

Compounds X_2MnTi	Mt (μ_B/f.u.)	M_{Mn} (μ_B)	M_{Ti} (μ_B)	M_{X-1} (μ_B)	M_{X-2} (μ_B)	c/a
Pd_2MnTi	3.18775	3.446	−0.526	0.134	0.134	1.36
Pt_2MnTi	3.3185	3.429	−0.396	0.143	0.143	1.35
Cu_2MnTi	1.77925	2.487	−0.722	0.007	0.007	1.56
Ni_2MnTi	3.092	2.799	−0.415	0.323	0.323	1.4
Ag_2MnTi	2.01	3.198	−1.147	−0.02	−0.02	1.55
Au_2MnTi	2.42525	3.352	−0.919	−0.004	−0.004	1.39

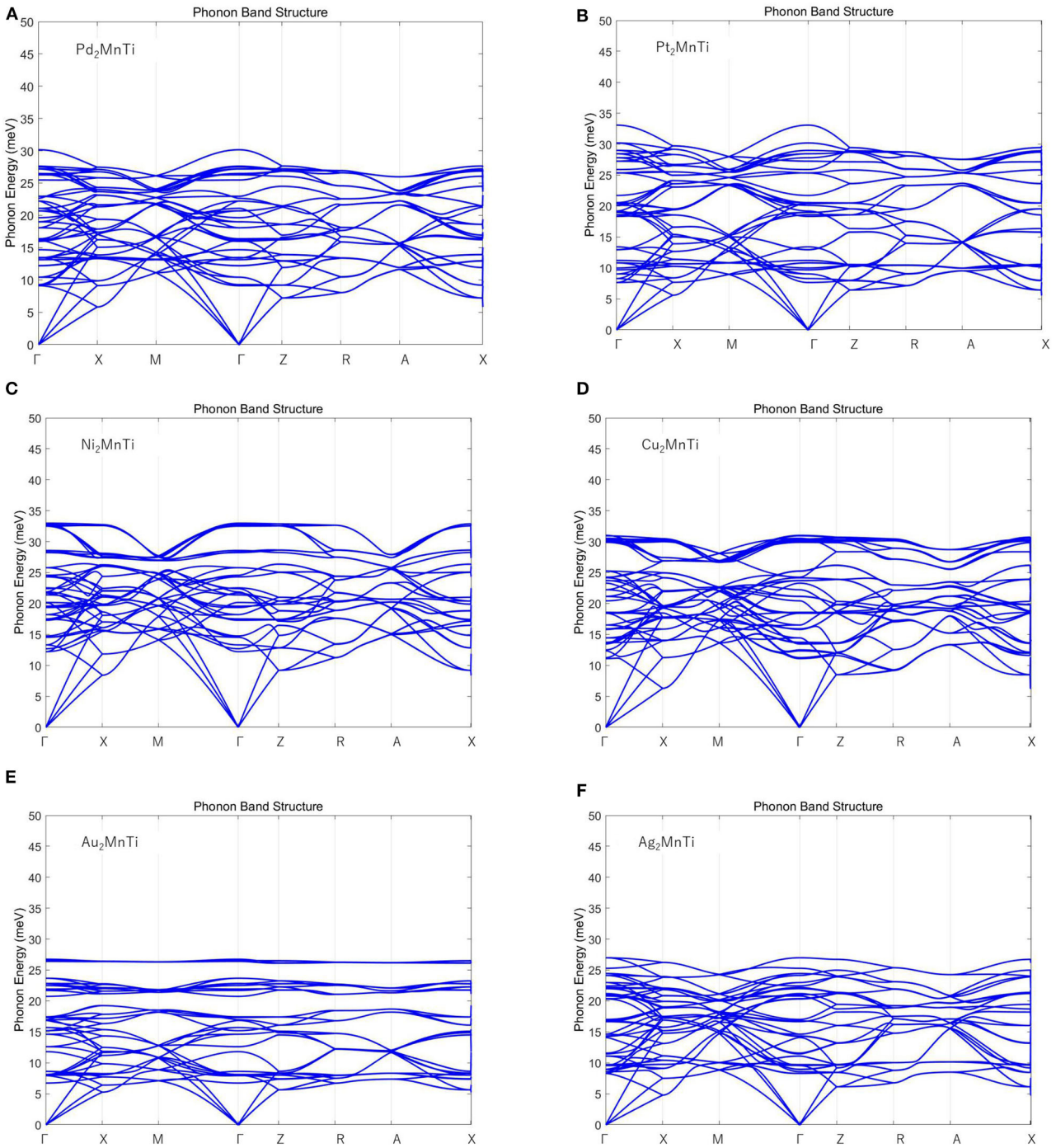

FIGURE 9 | (A–F) Calculated phonon energy of X_2MnTi (X = Pd, Pt, Ag, Au, Cu, and Ni) with tetragonal $L1_0$ phase.

would like to point out that Bain paths are a sophisticated way to investigate the reversible transformation between the $L2_1$ and $L1_0$ phases during the tetragonal distortion. This method has been widely used to design new MSMAs, and some designed MSMAs have been experimentally verified, such as the Mn–Ni–Co–Ti system.

CONCLUSIONS

In this study, we investigated the phase transition and electronic structures of X_2MnTi (X = Pd, Pt, Ag, Au, Cu, and Ni) compounds based on first-principle calculations. First, we examined the $L2_1$ and XA competition of Heusler compounds

X_2MnTi (X = Pd, Pt, Ag, Au, Cu, and Ni). The results show that the $L2_1$ type is the most stable ordered structure for these newly designed materials. Based on the $L2_1$ structure, we also compared the total energies of the $L2_1$ X_2MnTi system with different magnetic states, i.e., FM and AFM. We found that these compounds have lower ground state energy when in the FM state, that is, the most stable state of X_2MnTi is the FM state under the $L2_1$ structure. Subsequently, we studied the possible tetragonal transformation of Heusler compounds X_2MnTi (X = Pd, Pt, Ag, Au, Cu, and Ni) and found that these materials all feature a stable $L1_0$ tetragonal phase. The energy difference ΔE_M (E_T – E_C) in X_2MnTi can be adjusted by a uniform strain. By analyzing the DOS diagram, it can be found that the magnetic moment of X_2MnTi mainly comes from Mn atoms, which is due to their strong spin splitting around E_F. The lower TDOS of the tetragonal $L1_0$ state near the Fermi level can be used to explain the stability of the tetragonal $L1_0$ state of X_2MnTi. Finally, we gave the phonon spectra of the tetragonal $L1_0$ phase of X_2MnTi (X = Pd, Pt, Ag, Au, Cu, and Ni) to further prove their stability.

DATA AVAILABILITY STATEMENT

The raw data supporting the conclusions of this article will be made available by the authors, without undue reservation.

AUTHOR CONTRIBUTIONS

MW: conceptualization, methodology, software, and writing—original draft preparation. FZ and RK: software and writing—original draft preparation. MK and XW: supervision. All authors contributed to the article and approved the submitted version.

FUNDING

This study has been funded by the National Natural Science Foundation of China (Grant No. 11704315) and the Fundamental Research Funds for the Central Universities (Grant No. XDJK2019C112).

REFERENCES

Ahmadian, F., and Salary, A. (2014). Half-metallicity in the Inverse Heusler compounds Sc_2MnZ (Z = C, Si, Ge, and Sn). *Intermetallics*. 46, 243–249. doi: 10.1016/j.intermet.2013.11.021

Aksoy, S., Acet, M., Deen, P. P., Manosa, L., and Planes, A. (2009). Magnetic correlations in martensitic Ni-Mn-based Heusler shape-memory compounds: neutron polarization analysis. *Phys. Rev. B*. 79:212401. doi: 10.1103/PhysRevB.79.212401

Alippi, P., Marcus, P. M., and Scheffler, M. (1997). Strained tetragonal states and Bain paths in metals. *Phys. Rev. Lett*. 78:3892. doi: 10.1103/PhysRevLett.78.3892

Barman, S. R., Banik, S., Shukla, A. K., Kamal, C., and Chakrabarti, A. (2007). Martensitic transition, ferrimagnetism and Fermi surface nesting in Mn_2NiGa. *EPL* 80:57002. doi: 10.1209/0295-5075/80/57002

Birkel, C. S., Douglas, J. E., Lettiere, B. R., Seward, G., Verma, N., Zhang, Y., et al. (2013). Improving the thermoelectric properties of half-Heusler TiNiSn through inclusion of a second full-Heusler phase: microwave preparation and spark plasma sintering of $TiNi_{1+x}Sn$. *Phys. Chem. Chem. Phys*. 15:6990. doi: 10.1039/c3cp50918d

Cui, Z., Wu, B., Xin, R., Zhou, Q., and Feng, Y. (2019). Enhancing the half-metallicity of equiatomic quaternary Heusler compound CoFeCrGe via atomic doping. *Results Phys*. 15:102533. doi: 10.1016/j.rinp.2019.102533

Downie, R. A., Maclaren, D. A., Smith, R. I., and Bos, J. W. G. (2013). Enhanced thermoelectric performance in TiNiSn-based half-Heuslers. *Chem. Commun*. 49:4184 doi: 10.1039/c2cc37121a

Gao, G. Y., and Yao, K. L. (2013). Antiferromagnetic half-metals, gapless half-metals, and spin gapless semiconductors: The DO_3-type Heusler compounds. *Appl. Phys. Lett*. 103:232409. doi: 10.1063/1.4840318

Ghunaim, R., Ecker, V., Scholz, M., Gellesch, S., and Wurmehl, D. (2018). Carbon nanotube-assisted synthesis of ferromagnetic Heusler nanoparticles of Fe3Ga (Nano-Galfenol). *J. Mater. Chem. C* 6:1255. doi: 10.1039/C7TC04618A

Graf, T., Felser, C., and Parkin, S. S. P. (2011). Simple rules for the understanding of Heusler compounds. *Progr. Solid State Chem*. 39, 1–50. doi: 10.1016/j.progsolidstchem.2011.02.001

GschneidnerJr, K. A., Pecharsky, V. K., and Tsokol, A. O. (2005). Recent developments in magnetocaloric materials. *Rep. Progr. Phys*. 68:1479. doi: 10.1088/0034-4885/68/6/R04

Hafner, J. (2007). Materials simulations using VASP—a quantum perspective to materials science. *Comput. Phys. Commun*. 177, 6–13. doi: 10.1016/j.cpc.2007.02.045

Han, Y., Chen, Z., Kuang, M., Liu, Z., Wang, X., and Wang, X. (2019a). 171 Scandium-based full Heusler compounds: A comprehensive study of competition between XA and $L2_1$ atomic ordering. *Results Phys*. 12, 435–446. doi: 10.1016/j.rinp.2018.11.079

Han, Y., Wu, M., Feng, Y., Cheng, Z. X., and Wang, X. T. (2019b). Competition between cubic and tetragonal phases in all-*d*-metal Heusler compounds, $X_{2--x}Mn_{1+x}V$ (X = Pd, Ni, Pt, Ag, Au, Ir, Co; x = 1, 0): a new potential direction of the Heusler family. *IUCrJ*. 6, 465–472 doi: 10.1107/S2052252519004007

Hao, Z. P., Liu, R., Fan, Y. H., and Wang, L. L. (2020). First-principles calculations of a new half-metallic Heusler compound FeCrAs. *J. Comp Comp*. 820:153118. doi: 10.1016/j.jallcom.2019.153118

Hou, Z., Wang, W., Xu, G., Zhang, X., Wei, Z., Shen, S., et al. (2015). High electron mobility and large magnetoresistance in the half-Heusler semimetal LuPtBi. *Phys. Rev. B*. 92:235134. doi: 10.1103/PhysRevB.92.235134

Huang, S., Liu, X., Zheng, W., Guo, J., Xiong, R., Wang, Z., et al. (2018). Dramatically improving thermoelectric performance of topological half-Heusler compound LuPtSb via hydrostatic pressure. *J. Mater. Chem. A*. 6:20069. doi: 10.1039/C8TA07350C

Kirievsky, K., Shlimovich, M., Fuks, D., and Gelbstein, Y. (2014). An ab initio study of the thermoelectric enhancement potential in nano-grained TiNiSn. *Phys. Chemi. Chem. Phys*. 16:20023. doi: 10.1039/C4CP02868F

Kresse, G., and Furthmüller, J. (1996). Efficient iterative schemes for ab initio total-energy calculations using a plane-wave basis set. *Phys RevB*. 54:11169. doi: 10.1103/PhysRevB.54.11169

Li, F., Yang, B., Zhang, J., Han, X., and Yan, Y. (2020). Interface-induced perpendicular magnetic anisotropy in $Co_2FeAl/NiFe_2O_4$ superlattice: first-principles study. *Phys. Chemi. Chem. Phys*. 22:716. doi: 10.1039/C9CP05703J

Li, J., Zhang, G., Peng, C., Wang, W., and Yang, J. (2019). Magneto-Seebeck effect in $Co_2FeAl/MgO/Co_2FeAl$: First-principles calculations. *Phys. Chemi. Chem. Phys*. 21:5803. doi: 10.1039/C8CP07697A

Li, Z., Jiang, Y., Li, Z., Valdés, C. F. S., and Liang, Z. (2018). Phase transition and magnetocaloric properties of $Mn_{50}Ni_{42--x}Co_xSn_8$ ($0 \leq x \leq 10$) melt-spun ribbons. *IUCrJ*. 5, 54–66. doi: 10.1107/S2052525517016220

Lin, S. Y., Chen, M., Yang, X. B., Zhao, Y. J., Wu, S. C., Felser, C., et al. (2015). Theoretical search for half-Heusler topological insulators. *Phys. Rev. B*. 91:094107. doi: 10.1103/PhysRevB.91.094107

Mallick, M. M., and Vitta, S. (2018). Enhancing the thermoelectric performance of a p-type half-Heusler alloy, HfCoSb by incorporation of a band-matched chalcogenide, Cu_2Te. *J. Mater. Chem. A*. 6:14709. doi: 10.1039/C8TA04372H

Miranda, J., and Gruhn, T. (2017). Demixing and ordering in Ni(Ti,Zr)(Sb,Sn) Half-Huesler materials. *Phys. Chemi. Chem. Phys*. 19:30695. doi: 10.1039/C7CP05513G

Muldawer, L. (1966). X-ray Study of Ternary Ordering of the Noble Metals in $AgAuZn_2$ and $CuAuZn_2$. *J. Appl. Phys*. 37, 2062–2066. doi: 10.1063/1.1708670

O'Handley, R. C. (1998). Model for strain and magnetization in magnetic shape-memory compounds. *J. Appl. Phys*. 83, 3263–3270. doi: 10.1063/1.367094

Oikawa, K., Ota, T., Ohmori, T., Tanaka, Y., Morito, H., Fujita, A., et al. (2002). Magnetic and martensitic phase transitions in ferromagnetic Ni–Ga–Fe shape memory compounds. *Appl. Phys. Lett*. 81, 5201–5203. doi: 10.1063/1.1532105

Oikawa, K., Wulff, L., Iijima, T., Gejima, F., Ohmori, T., Fujita, A., et al. (2001). Promising ferromagnetic Ni–Co–Al shape memory compound system. *Appl. Phys. Lett*. 79, 3290–3292. doi: 10.1063/1.1418259

Özdemir Kart, S., Uludogan, M., Karaman, I., and Cagin, T. (2008). DFT studies on structure, mechanics and phase behavior of magnetic shape memory alloys: Ni_2MnGa. *Phys. Status Solidi (a)*. 205, 1026–1035. doi: 10.1002/pssa.200776453

Perdew, J. P., Burke, K., and Ernzerhof, M. (1996). Generalized gradient approximation made simple. *Phys. Rev. Lett*. 77:3865. doi: 10.1103/PhysRevLett.77.3865

Perdew, J. P., Burke, K., and Ernzerhof, M. (1998). Perdew, burke, and ernzerhof reply. *Phys. Rev. Lett*. 80:891. doi: 10.1103/PhysRevLett.80.891

Populoh, S., Aguirre, M. H., Brunko, O. C., Galazka, K., Lu, Y., and Weidenkaff, A. (2012). High figure of merit in (Ti, Zr, Hf)NiSn half-Heusler compounds. *Scr. Mater*. 66, 1073–1076. doi: 10.1016/j.scriptamat.2012.03.002

Qawasmeh, Y., and Bothina, H. (2012). Investigation of the structural, electronic, and magnetic properties of Ni-based Heusler alloys from first principles. *J. Appl. Phys* 111:033905. doi: 10.1063/1.3681286

Shigeta, I., Kubota, T., Sakuraba, Y., Kimura, S., and Awaji, S. (2018). Transport properties of epitaxial films for superconductor NbN and half-metallic Heusler compound Co_2MnSi under high magnetic fields. *Phys B Cond. Matt*. 536, 310–313. doi: 10.1016/j.physb.2017.09.074

Silpawilawan, W., Kurosaki, K., Ohishi, Y., Muta, H., and Yamanaka, S. (2017). FeNbSb p-type half-heusler compound: beneficial thermomechanical properties and high-temperature stability for thermoelectrics. *J. Mater. Chem. C*. 5:6677. doi: 10.1039/C7TC01570D

Singh, S., and Gupta, D. C. (2019). Lanthanum based quaternary Heusler compounds LaCoCrX (X = Al, Ga): Hunt for half-metallicity and high thermoelectric efficiency. *Results Phys*. 13:102300. doi: 10.1016/j.rinp.2019.102300

Skaftouros, S., Ozdogan, K., Sasioglu, E., and Galanakis, I. (2013). Search for spin gapless semiconductors: The case of inverse Heusler compounds. *Appl. Phys. Lett*. 102:022402. doi: 10.1063/1.4775599

Suzuki, R. O., and Kyono, T. (2004). Thermoelectric properties of Fe_2TiAl Heusler compounds. *J. Comp. Comp*. 377, 38–42. doi: 10.1016/j.jallcom.2004.01.035

Tan, J. G., Liu, Z. H., Zhang, Y. J., Li, G. T., Zhang, H. G., Liu, G. D., et al. (2019). Site preference and tetragonal distortion of Heusler compound Mn-Ni-V. *Results Phys*. 12, 1182–1189. doi: 10.1016/j.rinp.2018.12.096

Ullakko, K., Huang, J. K., Kantner, C., Ohandley, R. C., and Kokorin, V. V. (1996). Large magnetic-field-induced strains in Ni_2MnGa single crystals. *Appl. Phys. Lett*. 69, 1966–1968. doi: 10.1063/1.117637

Wang, X., Cheng, Z., Liu, G., Dai, X., and Bouhemadou, A. (2017). Rare earth-based quaternary Heusler compounds MCoVZ (M = Lu, Y; Z= Si, Ge) with tunable band characteristics for potential spintronic applications. *IUCrJ*. 4, 758–768. doi: 10.1107/S2052252517013264

Wang, X., Cheng, Z., Wang, J., Wang, X., and Liu, G. (2016). Recent advances in the Heusler based spin-gapless semiconductors. *J. Mater. Chem. C*. 4, 7176–7192. doi: 10.1039/C6TC01343K

Wang, X. T., Cheng, Z. X., Yuan, H. K., and Khenata, R. (2017). $L2_1$ and XA ordering competition in titanium-based full-heusler alloys. *J. Mater. Chem. C*. 5:11559. doi: 10.1039/C7TC03909C

Wei, Z. Y., Liu, E. K., Chen, J. H., Li, Y., Liu, G. D., Luo, H. Z., et al. (2015). Realization of multifunctional shape-memory ferromagnets in all-*d*-metal Heusler phases. *Appl. Phys. Lett*. 107:022406. doi: 10.1063/1.4927058

Wurmehl, S., Fecher, G. H., Kandpal, H. C., Ksenofontov, V., Felser, C., Lin, H. J., et al. (2005). Geometric, electronic, and magnetic structure of Co_2FeSi: Curie temperature and magnetic moment measurements and calculations. *Phys. Rev. B*. 72:184434. doi: 10.1103/PhysRevB.72.184434

Xue, Q. Y., Liu, H. J., Fan, D. D., Cheng, L., Zhao, B. Y., and Shi, J. (2016). LaPtSb: a half-Heusler compound with high thermoelectric performance. *Phys. Chemi. Chem. Phys*. 18:17912. doi: 10.1039/C6CP03211G

Zeleny, M., Sozinov, A., Straka, L., Björkman, T., and Nieminen, R. M. (2014). First-principles study of Co-and Cu-doped Ni_2MnGa along the tetragonal deformation path. *Phys. Rev. B*. 89:184103. doi: 10.1103/PhysRevB.89.184103

Conflict of Interest: The authors declare that the research was conducted in the absence of any commercial or financial relationships that could be construed as a potential conflict of interest.

frontiers in Materials

ORIGINAL RESEARCH
published: 23 February 2021
doi: 10.3389/fmats.2020.595953

Ferromagnetism With High Curie Temperature of Cu Doped LiMgN New Dilute Magnetic Semiconductors

Junquan Deng, Wuqing Yang, Aiyuan Hu, Peng Yu, Yuting Cui, Shoubing Ding and Zhimin Wu**

Chongqing Key Laboratory of Photoelectric Functional Materials, College of Physics and Electronic Engineering, Chongqing Normal University, Chongqing, China

New diluted magnetic semiconductors represented by Li(Zn,Mn)As with decoupled charge and spin doping have received much attention due to their potential applications for spintronics. However, their low Curie temperature seriously restricts the wide application of these spintronic devices. In this work, the electronic structures, ferromagnetic properties, formation energy, and Curie temperature of Cu doped LiMgN and the corresponding Li deficient system are calculated by using the first principles method based on density functional theory, combined with Heisenberg model in the Mean-Field Approximation. We find that the Cu doped systems have high temperature ferromagnetism, and the highest Curie temperature is up to 573K, much higher than the room temperature. Li($Mg_{0.875}Cu_{0.125}$)N is a half metallic ferromagnet and its net magnetic moments are 2.0 μ_B. When Li is deficient, the half metallic ferromagnetism becomes stronger, the magnetic moments increase to 3.0 μ_B. The bonding and differential charge density indicate that the half metallic ferromagnetism can be mainly attributed to the strong hybridization between N 2p and doped Cu 3d orbitals. The results show that Cu doped LiMgN is a kind of ideal new dilute magnetic semiconductor that will benefit potential spintronics applications.

Keywords: Cu doped LiMgN, electronic structures, ferromagnetism, Curie temperature, first-principles

OPEN ACCESS

Edited by:
Xiaotian Wang,
Southwest University, China

Reviewed by:
Xu Li,
Chengdu University of Information Technology, China
Yongtian Wang,
North China Electric Power University, China
Liu Jun,
Chongqing University of Posts and Telecommunications, China

****Correspondence:***
Shoubing Ding
shoubingding@cqnu.edu.cn
Zhimin Wu
zmwu@cqnu.edu.cn

Specialty section:
This article was submitted to Computational Materials Science, a section of the journal Frontiers in Materials

Received: *18 August 2020*
Accepted: *28 September 2020*
Published: *23 February 2021*

Citation:
Deng J, Yang W, Hu A, Yu P, Cui Y, Ding S and Wu Z (2021) Ferromagnetism With High Curie Temperature of Cu Doped LiMgN New Dilute Magnetic Semiconductors. Front. Mater. 7:595953. doi: 10.3389/fmats.2020.595953

INTRODUCTION

In the modern information technology, the transmission and processing of information mainly use the charge of electrons, while the storage of information mainly uses the spin of electrons. The two degrees of freedom are independent of each other. Diluted magnetic semiconductors (DMS) utilize the electron's charge and spin degrees of freedom simultaneously to achieve novel quantum functionalities, which can combine the properties of semiconductor with ferromagnetism and have potential applications in spintronics (Ohno, 1998). Therefore, the designed spintronic devices have the advantages of lower energy consumption, faster running speed and smaller volume (Zutic et al., 2004; Dietl, 2010; Kacimi et al., 2014). However, there are some insurmountable difficulties for traditional III-V group based dilute magnetic semiconductors prepared by doping transition metals. For example, since the magnetic moments and carriers are provided by the same doped element, the binding effect of the spin and charge precludes the possibility of tuning electric and magnetic properties individually (Kaczkowski and Jezierski, 2009). The heterovalent substitution of Mn^{2+} into Ga^{3+} leads to severely chemical solubility of the magnetic ions (Potashnik et al., 2001). The average solubility for Mn is less than 1%, and only metastable films can be formed, resulting in that it is

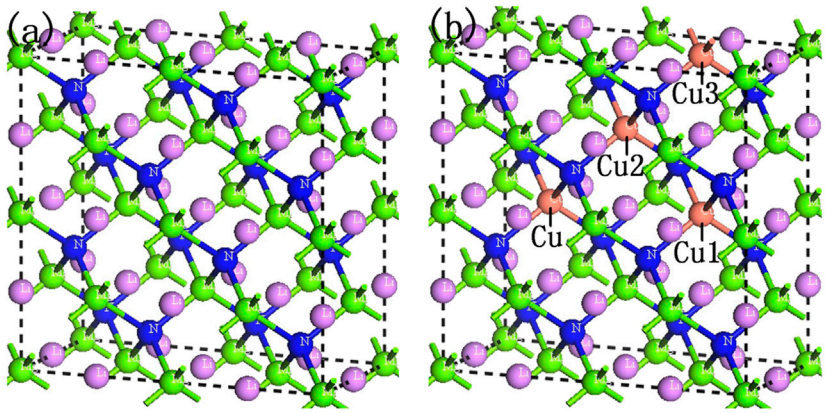

FIGURE 1 | Supercell structures of LiMgN with 48 atoms: **(A)** LiMgN, **(B)** $Li(Mg_{0.875}Cu_{0.125})N$.

difficult to study the origin and mechanism of magnetism in dilute magnetic semiconductors Potashnik et al., 2001). Besides, the impurity ions often have higher ionization energy, restricting the contribution of free carriers in the system (Yan et al., 2007).

To overcome these difficulties, Mašek et al. (2007) theoretically proposed a kind of new diluted magnetic semiconductor Li(Zn,Mn)As based on I-II-V group elements, wherein magnetism due to isovalent substitution can be decoupled from carrier doping with excess/deficient Li concentrations. Deng et al. (2011), Jin et al. (2013) successfully prepared polycrystalline Li(Zn,Mn)As bulk materials with T_C as high as ~50 K. Muon spin rotation measurements have established that the magnetically ordered volume reaches 100% below T_C, and the magnitudes of the ferromagnetic exchange coupling and the ordered moment are comparable to those of (Ga,Mn)As (Deng et al., 2011). Sato et al. (2012) theoretically calculated the electronic structures of Mn doped LiZnAs, LiZnP and LiZnN, and found that introduced Li vacancies could strongly suppress spinodal decomposition, induce ferromagnetic interaction and improve T_c in these systems. Following this, a series of new generation diluted ferromagnetic semiconductors, e.g., "111" type Li(Zn,Mn)P (Deng et al., 2013; Ding et al., 2013) and Li(Cd,Mn)P (Han et al., 2019), "122" type (Ba,K) $(Zn,Mn)_2As_2$ (Zhao et al., 2013; Zhao et al., 2014),"1111" type (La,Ca)(Zn,Mn)SbO (Ding et al., 2014), and "32522" type $(Sr_3La_2O_5)(Zn,Mn)_2As_2$ (Man et al., 2014), were successfully synthesized. A number of progresses of these new DMSs have been made on both fundamental studies and potential applications. Among them, the highest T_c is 230 K of the (Ba,K)$(Zn,Mn)_2As_2$ system (Zhao et al., 2014). However, it remains below room temperature.

Improvement of T_C is always a fundamental issue for diluted ferromagnetic semiconductor materials. To explore new dilute magnetic semiconductor materials with better performance, in this work, the electronic structures, ferromagnetic properties, formation energy, and Curie temperature of Cu doped LiMgN and the corresponding Li deficient system are investigated by using the first principle calculation method based on density functional theory (DFT), combined with Heisenberg model in the Mean-Field Approximation. We find that the Cu doped systems have high temperature ferromagnetism, the highest T_c is up to 573 K, which indicate that Cu doped LiMgN is a kind of ideal new dilute magnetic semiconductor.

COMPUTATIONAL DETAILS

LiMgN is an antifluorite structure (Kuriyama et al., 2002) with the lattice constant $a = b = c = 4.955$ Å, belongs to the space group $F\text{-}43$ m. It can be prepared by the reaction of Li, Mg and N_2 at high temperature (800°C) (Kuriyama et al., 2002). The LiMgN tetrahedral lattice can be viewed as a zinc blende MgN binary compound, analogous to GaN, filled with Li atoms at tetrahedral interstitial sites near N. In the present work, a $2 \times 2 \times 1$ (48 atoms) supercell of ZB-type LiMgN was constructed, containing 16 Li, 16 Mg and 16 N atoms, as shown in **Figure 1A**. Two Mg atoms were substituted by two Cu atoms, thus the doping concentration was 12.5%. When one Cu atom was fixed, another Cu atom was selected three asymmetric positions for comparison (as shown in **Figure 1B**). One Li atom closest to the Cu atom was removed in order to introduce a Li vacancy (V_{Li}) in the $2 \times 2 \times 1$ supercell.

All the first-principles calculations were carried out with the Cambridge Serial Total Energy Package (CASTEP) code (Segall et al., 2002) based on the density functional theory (DFT) method. The periodic boundary conditions were applied in all calculations, and the generalized gradient approximation (GGA) in Perdew Burke Ernzerhof (PBE) (Perdew et al., 1996) was performed to deal with the electronic exchange-correlation potential energy. In order to reduce the number of the plane wave basis vectors groups, the plane-wave ultrasoft pseudo potential (USPP) method (Vanderbilt, 1990) was implemented to describe the interaction between ionic core and valence electrons. The valence electronic states were Li:$2s^1$, Mg:$2p^6 3s^2$, N:$2s^2 2p^3$ and Cu:$3d^{10} 4s^1$, respectively. The cut-off energy for the plane-wave was 400 eV, and the Monkhorst-Pack mesh was $3 \times 3 \times 6$ for the integral calculation of the total energy and charge

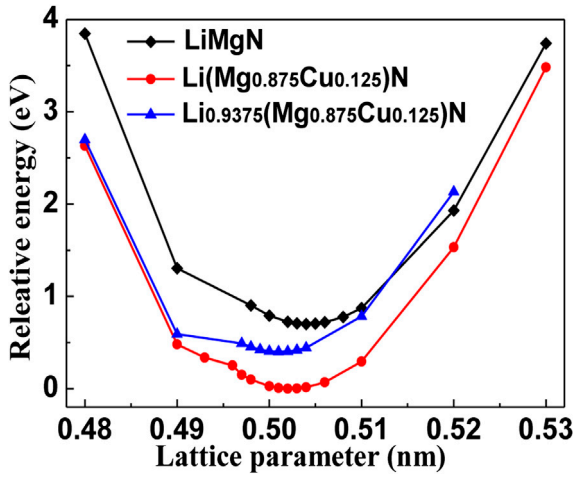

FIGURE 2 | The relative energy as a function of lattice constants for $Li_{1-y}(Mg_{1-x}Cu_x)N$.

density in the Brillouin zone. The self-consistent convergence accuracy was set at 2.0×10^{-6} eV/atom. The structures of each doped configuration were optimized before the calculations of total energies and the electronic structures.

RESULTS AND DISCUSSION

Electronic Structures

In order to achieve the equilibrium lattice constants, the structures of $Li_{1-y}(Mg_{1-x}Cu_x)N$ were optimized firstly. The geometry optimization curves are plotted in **Figure 2**. It can be seen that the optimized lattice constant for LiMgN is 5.04 Å, which is slightly overestimated comparing with the experimental value (4.955 Å) (Kuriyama et al., 2002). The optimized lattice constants of Li ($Mg_{0.875}Cu_{0.125}$) and $Li_{0.9375}$ ($Mg_{0.875}Cu_{0.125}$) N are 5.02 and 5.01 Å respectively, slightly less than that of the pure LiMgN.

Pure LiMgN is a direct band gap semiconductor. The valence band is mainly composed of N-2p, Mg-2p state and Li-2s electronic states, and the conduction band is mainly composed of Mg-2p and Mg-3s electronic states. **Figure 3** shows the spin polarized energy band structures of Cu doped LiMgN and the corresponding Li deficient system, and the inset is enlarged views of the vicinity of Fermi level. It can be seen in **Figures 3A,B** that some impurity levels are introduced near the Fermi level by Cu doping. In the majority-spin bands, the impurity bands merge into the valence band top, and the Fermi level still lies in the band gap, so the majority-spin bands remain semiconducting nature. While in the minority-spin bands, the Fermi level penetrates through the impurity bands, resulting in that two of the impurity levels cross the Fermi level, which demonstrates that the minority-spin bands exhibit metallic properties. So the Cu doped LiMgN system becomes a half-metallic material with 100% spin-polarized ratio of conduction electron. The spin-flip band gap is 0.13 eV (shown in **Table 1**). **Figures 3C,D** are the energy band structures of Cu doped LiMgN with Li vacancies. They are similar to that of Cu doped LiMgN, indicates that $Li_{0.9375}(Mg_{0.875}Cu_{0.125})N$ also exhibits half metallic property. However, the minority-spin bands are somewhat different. The impurity levels across the Fermi level increase to three, and the spin-flip band gap increases to 0.22 eV, which indicates that the more robust half-metallic behavior to lattice deformation and temperature for Li deficient system.

TABLE 1 | The band gaps (E_g), the spin-flip/half-metallic gaps (HM gap), magnetic moments (M), and formation energies (E_f) of $Li_{1-y}(Mg_{0.875}Cu_{0.125})N$.

Li_{1-y} $(Mg_{1-x}Cu_x)N$	E_g (eV)	HM gap (eV)	M (μ_B)	E_f (eV)
$Li(Mg_{0.875}Cu_{0.125})N$	2.23	0.13	2.0	1.98
$Li_{0.9375}(Mg_{0.875}Cu_{0.125})N$	1.98	0.22	3.0	3.56

Figure 4 shows the density of states (DOS) of Cu doped LiMgN and the corresponding Li deficient system. It can be seen in **Figure 4A** that the sub-bands crossing the Fermi level mainly come from Li-2s, N-2p and Cu-3d states of the minority-spin. Besides, one can also note that a resonance peak appears near the Fermi surface, indicating that the electron orbitals of Li-2s, N-2p and Cu-3d states have strong sp-d hybridization near the Fermi

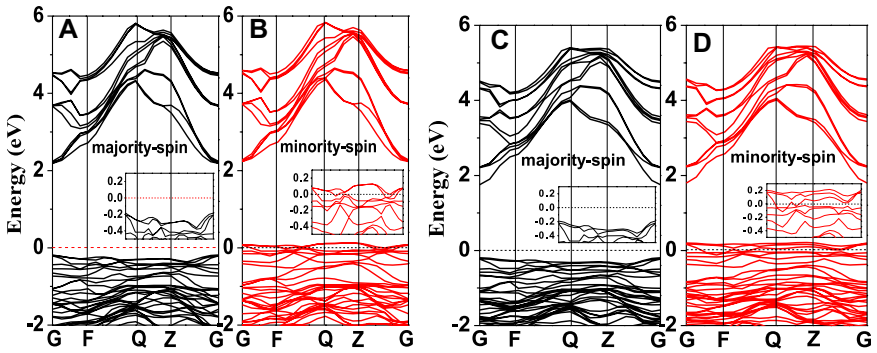

FIGURE 3 | The spin polarized band structures of $Li(Mg_{0.875}Cu_{0.125})N$ **(A,B)**; and $Li_{0.9375}(Mg_{0.875}Cu_{0.125})N$ **(C,D)**. Inset: Enlarged views near Fermi level.

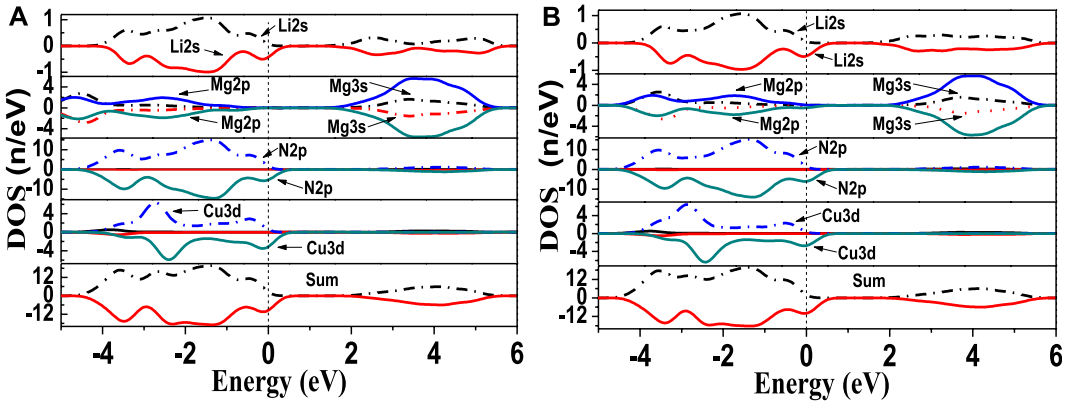

FIGURE 4 | The density of states of Li($Mg_{0.875}Cu_{0.125}$)N **(A)**; $Li_{0.9375}$($Mg_{0.875}Cu_{0.125}$) **(B)**.

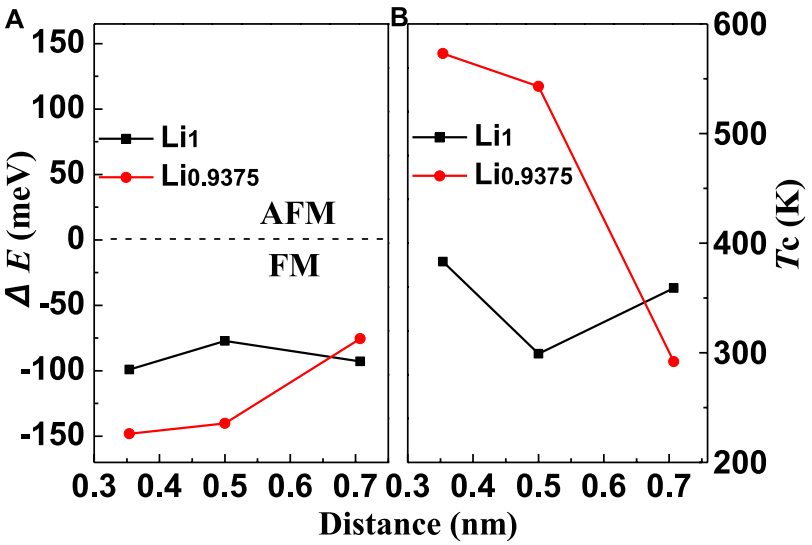

FIGURE 5 | The energy difference of the ferromagnetic and antiferromagnetic state **(A)** and the Curie temperature **(B)** as a function of the two doped Cu atoms distance for Li_{1-y} ($Mg_{0.875}Cu_{0.125}$)N.

level. The t_{2g} energy level split from Cu-3d states of the minority-spin is pushed across the Fermi level, which makes it become a half-filled state. This causes that the states of the majority-spin are slightly more than those of the minority-spin, resulting in the net magnetic moments. The calculated net magnetic moments are 2.0 μ_B for Li($Mg_{0.875}Cu_{0.125}$)N as shown in **Table 1**. **Figure 4B** shows that when Li is deficient, the DOS of Li-2s, N-2p and Cu-3d states near the Fermi level increase obviously. This indicates that the Li vacancies enhance the sp-d orbital hybridization. The t_{2g} energy levels are pushed further above the Fermi level, which makes none of the three levels is occupied by electrons. This increases the spin-flip band gap and net magnetic moments for $Li_{0.9375}$($Mg_{0.875}Cu_{0.125}$)N. The formation energy of the two systems is also calculated and shown in **Table 1**. The stability of the doped system decreases slightly with respect to pure LiMgN.

Ferromagnetism and Bonding

To explore the magnetic properties of the systems, the ferromagnetic and antiferromagnetic coupling energy of Li_{1-y}($Mg_{0.875}Cu_{0.125}$)N with different Cu doped position are calculated and shown in **Table 2**, where E_{FM} is the ferromagnetic coupling energy of the systems, E_{AFM} is the antiferromagnetic coupling energy, and ΔE is the difference between the ferromagnetic and antiferromagnetic coupling energy. It can be seen obviously that $\Delta E < 0$ for each doped position, indicating that the ferromagnetic order is more stable than the antiferromagnetic order. The Cu doped LiMgN systems are half-metallic ferromagnet. To further understand the ferromagnetic properties of Li_{1-y}($Mg_{0.875}Cu_{0.125}$)N, the variation of ΔE with the distance between two Cu atoms is plotted in **Figure 5A**. It can be seen that ΔE decreases with the distance, implying that the half-metallic ferromagnetism

TABLE 2 | The ferromagnetic and anti-ferromagnetic coupling energy of $Li_{1-y}(Mg_{0.875}Cu_{0.125})N$ with different Cu doped position.

$Li_{1-y}(Mg_{1-x}Cu_x)N$	Cu atoms distance (nm)	E_{FM} (eV)	E_{AFM} (eV)	$\Delta E = E_{FM} - E_{AFM}$ (meV)
$Li(Mg_{0.875}Cu_{0.125})N$-1	0.500	−23988.64142	−23988.56416	−77.26
$Li(Mg_{0.875}Cu_{0.125})N$-2	0.354	−23988.84502	−23988.74593	−99.09
$Li(Mg_{0.875}Cu_{0.125})N$-3	0.707	−23988.67494	−23988.58214	−92.80
$Li_{0.9375}(Mg_{0.875}Cu_{0.125})N$-1	0.500	−23796.27993	−23796.13969	−140.24
$Li_{0.9375}(Mg_{0.875}Cu_{0.125})N$-2	0.354	−23796.48006	−23796.33201	−148.05
$Li_{0.9375}(Mg_{0.875}Cu_{0.125})N$-3	0.707	−23796.38217	−23796.30667	−75.50

TABLE 3 | The charge population overlap and bond length of the chemical bonds for $Li_{1-y}(Mg_{1-x}Cu_x)N$.

$Li_{1-y}(Mg_{1-x}Cu_x)N$	Chemical bonds	Charge population overlap	Bond length (Å)
LiMgN	Li-N	−0.02	2.182
	Mg-N	−0.03	2.182
$Li(Mg_{0.875}Cu_{0.125})N$	Li-N	−0.11	2.173
	Mg-N	−0.08	2.173
	Cu-N	0.70	2.173
$Li_{0.9375}(Mg_{0.875}Cu_{0.125})N$	Li-N	−0.12	2.169
	Mg-N	−0.25	2.169
	Cu-N	0.71	2.169

become stronger as the two Cu atoms is closer. Moreover, when Li is deficient, the half-metallic ferromagnetism is further enhanced.

The ideal DMS should have Curie temperature (T_c) higher than the room temperature. The Curie temperature of the Cu doped LiMgN systems is estimated by using the Heisenberg model in the Mean-Field Approximation (Sato et al., 2003):

$$K_B \bullet T_c = 2\Delta E/3x \quad (1)$$

where x is the number of doped particles, ΔE is the difference between the ferromagnetic and antiferromagnetic coupling energy, and K_B is the Boltzmann constant. The variation of T_c with the distance between two Cu atoms is shown in **Figure 5B**. It can be seen that T_c of the doped systems is significantly enhanced when Li is deficient, and the maximum T_c is up to 573 K, much higher than the room temperature. Which shows that Cu doped LiMgN is a kind of ideal new dilute magnetic semiconductor that will benefit potential spintronics applications.

Table 3 shows the bond length and charge population overlap of the doped systems. It is found that the numbers of the charge population overlap for the Li-N and Mg-N bonds in pure LiMgN are negative, which indicates that they are ionic bonds. For Cu doped system, the numbers of the charge population overlap for Li-N and Mg-N bonds decrease. Meanwhile, the number of the charge population overlap for Cu-N bond is positive, demonstrating the covalent nature for the Cu-N bond, which is due to the strong hybridization between N 2p and doped Cu 3d orbitals. In general, the radius of Cu ion is larger than that of Mg ion. However, the bond length decreases for Cu doped system because of the Cu-N covalent bond nature, resulting in that the lattice constant also decreases. When Li is deficient, the numbers of the charge population overlap for Li-N and Mg-N bonds further decreases, whereas that of Cu-N bond further increases. This indicates that more charges transfer from the Li and Mg atoms to the Cu and N atoms, resulting in that the covalent nature for the Cu-N bond become stronger.

Figure 6 shows the charge density for $Li_{1-y}(Mg_{1-x}Cu_x)N$ along (2,2,1) plane. It can be seen that the values of charge density around Li and Mg atoms (**Figure 6B**) also decrease compared with those of pure LiMgN (**Figure 6A**). Besides, we can find that the charges transfer from the Li and Mg atoms to the Cu and N atoms, resulting in that the interaction between Cu and N atoms is stronger than that between Mg and N atoms. When Li is deficient, the charges further transfers and the interaction between Cu and N atoms become stronger. These results indicate that the effect of Cu doping on the ferromagnetic properties and bonding of the doped system is mainly

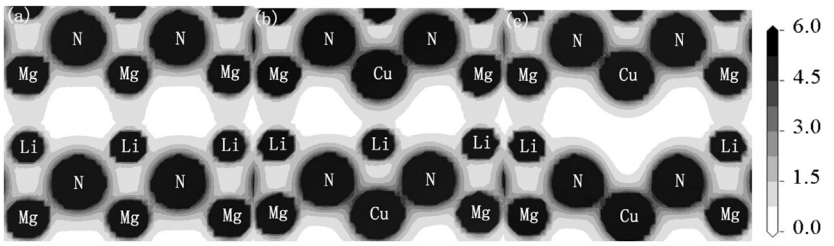

FIGURE 6 | The maps of charge density for $Li_{1-y}(Mg_{1-x}Cu_x)N$ in (2,2,1) surface. **(A)** LiMgN; **(B)** $Li(Mg_{0.875}Cu_{0.125})N$; **(C)** $Li_{0.9375}(Mg_{0.875}Cu_{0.125})N$.

attributed to the strong hybridization between N 2p and doped Cu 3d orbitals.

CONCLUSION

In this work, the electronic structures, ferromagnetism, formation energy, and Curie temperature of Cu doped LiMgN and the corresponding Li deficient system are calculated by using the first principles method based on density functional theory, combined with Heisenberg model in the Mean-Field Approximation. We find that the Cu doped systems exhibit half-metallic ferromagnetism, which is helpful for spin injection. The net magnetic moments for $Li(Mg_{0.875}Cu_{0.125})N$ are 2.0 μ_B. When Li is deficient, the half-metallic ferromagnetism becomes stronger, the magnetic moments increase to 3.0 μ_B. The density of states, bonding and charge density indicate that the half-metallic ferromagnetism can be mainly attributed to the strong hybridization between N 2p and doped Cu 3d orbitals. Besides, we also find that the highest Curie temperature is up to 573 K when Li is deficient, much higher than the room temperature. These results indicate that Cu doped LiMgN is a kind of ideal new dilute magnetic semiconductor and will benefit potential spintronics applications.

DATA AVAILABILITY STATEMENT

All datasets presented in this study are included in the article/ Supplementary Material.

AUTHOR CONTRIBUTIONS

All authors listed have made a substantial, direct, and intellectual contribution to the work and approved it for publication.

FUNDING

The work described in this paper is supported by Chongqing Natural Science Foundation of China (Grant No. cstc2019jcyj-msxmX0251).

REFERENCES

Deng, Z., Jin, C. Q., Liu, Q. Q., Wang, X. C., Zhu, J. L., Feng, S. M., et al. (2011). Li(Zn,Mn)As as a new generation ferromagnet based on a I-II-V semiconductor. *Nat. Commun.* 2, 422. doi:10.1038/ncomms1425

Deng, Z., Zhao, K., Gu, B., Han, W., Zhu, J. L., Wang, X. C., et al. (2013). Diluted ferromagnetic semiconductor Li(Zn,Mn)P with decoupled charge and spin doping. *Phys. Rev. B* 88, 081203. doi:10.1103/PhysRevB.88.081203

Dietl, T. (2010). A ten-year perspective on dilute magnetic semiconductors and oxides. *Nat. Mater.* 9, 965. doi:10.1038/nmat2898

Ding, C., Gong, X., Man, H., Zhi, G., Guo, S., Zhao, Y., et al. (2014). The suppression of curie temperature by Sr doping in diluted ferromagnetic semiconductor $(La_{1-x}Sr_x)$ $(Zn_{1-y}Mn_y)$ AsO. *Eur. Phys. Lett.* 107, 17004. doi:10.1209/0295-5075/107/17004

Ding, C., Qin, C., Man, H. Y., Imai, T., and Ning, F. L. (2013). NMR investigation of the diluted magnetic semiconductor $Li(Zn_{1-x}Mn_x)P$ ($x = 0.1$). *Phys. Rev. B* 88, 041108. doi:10.1103/PhysRevB.88.041102

Han, W., Chen, B. J., Gu, B., Zhao, G. Q., Yu, S., Wang, X. C., et al. (2019). Li(Cd,Mn)P: a new cadmium based diluted ferromagnetic semiconductor with independent spin & charge doping. *Sci. Rep.* 9, 7490. doi:10.1038/s41598-019-43754-x

Jin, C. Q., Wang, X. C., Liu, Q. Q., SiJia, Z., ShaoMin, F., Zheng, D., et al. (2013). New quantum matters: build up versus high pressure tuning. *Sci. China Phys. Mech. Astron.* 56, 2337. doi:10.1007/s11433-013-5356-2

Kacimi, S., Mehnane, H., and Zaoui, A. (2014). I–II–V and I–III–IV half-Heusler compounds for optoelectronic applications: comparative ab initio study. *J. Alloy. Compd.* 587, 451. doi:10.1016/j.jallcom.2013.10.046

Kaczkowski, J., and Jezierski, A. (2009). Ab initio calculations of magnetic properties of wurtzite $Al_{0.9375}TM_{0.0625}N$ (TM = V, Cr, Mn, Fe, Co, Ni). *Acta Phys. Pol. A* 115, 275. doi:10.12693/APhysPolA.115.275

Kuriyama, K., Nagasawa, K., and Kushida, K. (2002). Growth and band gap of the filled tetrahedral semiconductor LiMgN. *J. Crys. Grow.* 237, 2019–2022. doi:10.1016/S0022-0248(01)02249-7

Man, H., Qin, C., Ding, C., Wang, Q., Gong, X., Guo, S., et al. (2014). $(Sr_3La_2O_5)(Zn_{1-x}Mn_x)_2As_2$: a bulk form diluted magnetic semiconductor isostructural to the "32522" Fe-based superconductors. *Eur. Phys. Lett.* 105, 67004. doi:10.1209/0295-5075/105/67004

Mašek, J., Kudrnovský, J., Máca, F., Gallagher, B. L., Campion, R. P., Gregory, D. H., et al. (2007). Dilute moment n-type ferromagnetic semiconductor Li(Zn,Mn)As. *Phys. Rev. Lett.* 98, 067202, doi:10.1103/PhysRevLett.98.067202

Ohno, H. (1998). Making nonmagnetic semiconductors ferromagnetic. *Science* 281, 951. doi:10.1126/science.281.5379.951

Perdew, J. P., Burke, K., and Ernzerhof, M. (1996). Generalized gradient approximation made simple. *Phys. Rev. Lett.* 77, 3865. doi:10.1103/PhysRevLett.77.3865

Potashnik, S. J., Ku, K. C., Chun, S. H., Berry, J. J., Samarth, N., and Schiffer, P., (2001). Effects of annealing time on defect-controlled ferromagnetism in $Ga_{1-x}Mn_xAs$. *Appl. Phys. Lett.* 79, 1495. doi:10.1063/1.1398619

Sato, K., Dederichs, P. H., and Katayama-Yoshida, H. (2003). Curie temperatures of III-V diluted magnetic semiconductors calculated from first principles. *Europhys. Lett.* 61, 403. doi:10.1209/epl/i2003-00191-8

Sato, K., Fujimoto, S., Fujii, H., Fukushima, T., and Katayama-Yoshida, H., (2012). Computational materials design of filled tetrahedral compound magnetic semiconductors. *Physica B* 407, 2950. doi:10.1016/j.physb.2011.09.036

Segall, M. D., Lindan, P. J. D., Probert, M. J., Pickard, C. J., Hasnip, P. J., Clark, S. J., et al. (2002). First-principles simulation: ideas, illustrations and the CASTEP code. *J. Phys. Condens. Matter* 14, 2717. doi:10.1088/0953-8984/14/11/301

Vanderbilt, D. (1990). Soft self-consistent pseudopotentials in a generalized eigenvalue formalism. *Phys. Rev. B Condens Matter* 41, 7892. doi:10.1103/physrevb.41.7892

Yan, Y., Li, J., Wei, S. H., and Al-Jassim, M. M. (2007). Possible approach to overcome the doping asymmetry in wideband gap semiconductors. *Phys. Rev. Lett.* 98, 135506. doi:10.1103/PhysRevLett.98.135506

Zhao, K., Deng, Z., Wang, X. C., Han, W., Zhu, J. L., Li, X., et al. (2013). New diluted ferromagnetic semiconductor with Curie temperature up to 180 K and isostructural to the '122' iron-based superconductors. *Nat. Commun.* 4, 1442. doi:10.1038/ncomms2447

Zhao, K., Chen, B. J., Zhao, G. Q., Yuan, Z., Liu, Q., Deng, D., et al. (2014). Ferromagnetism at 230 K in $(Ba_{0.7}K_{0.3})(Zn_{0.85}Mn_{0.15})_2As_2$ diluted magnetic semiconductor. *Chin. Sci. Bull.* 59, 2524. doi:10.1007/s11434-014-0398-z

Zutic, I., Fabian, J., and Das Sarma, S. (2004). Spintronics: fundamentals and applications. *Rev. Mod. Phys.* 76, 323. doi:10.1103/RevModPhys.76.323

Conflict of Interest: The authors declare that the research was conducted in the absence of any commercial or financial relationships that could be construed as a potential conflict of interest.

Advantages of publishing in Frontiers

OPEN ACCESS
Articles are free to read for greatest visibility and readership

FAST PUBLICATION
Around 90 days from submission to decision

HIGH QUALITY PEER-REVIEW
Rigorous, collaborative, and constructive peer-review

TRANSPARENT PEER-REVIEW
Editors and reviewers acknowledged by name on published articles

Frontiers
Avenue du Tribunal-Fédéral 34
1005 Lausanne | Switzerland

Visit us: www.frontiersin.org
Contact us: frontiersin.org/about/contact

REPRODUCIBILITY OF RESEARCH
Support open data and methods to enhance research reproducibility

DIGITAL PUBLISHING
Articles designed for optimal readership across devices

FOLLOW US
@frontiersin

IMPACT METRICS
Advanced article metrics track visibility across digital media

EXTENSIVE PROMOTION
Marketing and promotion of impactful research

LOOP RESEARCH NETWORK
Our network increases your article's readership